Physics of the Solid State, Vol. 43, No. 3, 2001, pp. 401–407. Translated from Fizika Tverdogo Tela, Vol. 43, No. 3, 2001, pp. 385–390.
Original Russian Text Copyright © 2001 by Wolf, Fedorov.

METALS AND SUPERCONDUCTORS

The Self-Consistent Response of the Electron Density of a Crystal Copper Film to an External Electrostatic Field

G. V. Wolf and D. V. Fedorov

Physicotechnical Institute, Ural Division, Russian Academy of Sciences, ul. Kirova 132, Izhevsk, 426001 Russia
e-mail: wolf@otf.fti.udmurtia.su

Received April 3, 2000; in final form, June 13, 2000

Abstract—The response of the electrons of an fcc copper (001) film to an external electrostatic field is calculated. In order to determine the distribution of the screening charge, the equations of the electron density-functional theory are solved self-consistently by an original method. The position of the “image plane,” which is involved in a correct asymptotic expression for the exchange-correlation potential in the vacuum region, is first determined when performing a quantum-mechanical calculation for an anisotropic crystal film. The nonlinear electron response is characterized by the evolution of the “center of gravity” of the induced charge, which is also investigated. The calculations take into account the crystal structure of the film, and the results differ essentially from the predictions of the “jelly” model. © *2001 MAIK “Nauka/Interperiodica”.*

INTRODUCTION

Correct treatment of the screening of an external electrostatic field by a metal surface is essential for understanding many physical phenomena: atom and electron scattering at a metal surface, tunneling through a surface barrier, lattice dynamics of clean and adsorbent-covered crystals, generation of the second harmonic of an electromagnetic field on its reflection from the surface of a metal, etc. The physics of these phenomena consists in the nonlocal response of conduction electrons to the external electric field. After the classical work of Lang and Kohn [1], many studies were devoted to this problem. However, all of them, with rare exception, are based on the jelly model, which does not take into account the anisotropy of the lattice of a real crystal. Only in [2–5] were quantum-mechanical calculations of the induced electron density performed for the (001) surfaces of Al and Ag in a realistic model of the crystal potential, and the results differ essentially from those obtained in the jelly model.

In this paper, a self-consistent calculation of the electron response to an external electrostatic field is first carried out for an (001) film of fcc copper, a metal for which the jelly model is certain to be inadequate.

1. MODEL AND CALCULATION TECHNIQUE

In order to find the electron states of a (001) film of copper, we self-consistently solve a set of equations of the electron density-functional (EDF) theory written in atomic units ($e = \hbar = m = 1$):

$$\left\{-\frac{1}{2}\Delta + V[\rho;\, \mathbf{r}, q]\right\}\Psi_{n\mathbf{k}}(\mathbf{r}, q) = E_n(\mathbf{k}, q)\Psi_{n\mathbf{k}}(\mathbf{r}, q), \quad (1)$$

$$\rho(\mathbf{r}, q) = \sum_{n,\,\mathbf{k}} |\Psi_{n\mathbf{k}}(\mathbf{r}, q)|^2 \Theta(E_F(q) - E_n(\mathbf{k}, q)) \quad (2)$$

[$\Theta(x)$ is the Heaviside step function], with boundary conditions corresponding to the electron bound states lying below the continuous spectrum. For a crystal film oriented perpendicular to the z axis, this means that

$$\Psi_{n\mathbf{k}}(\mathbf{r}, q) = \exp(-i\mathbf{k}\mathbf{R}_n)\Psi_{n\mathbf{k}}(\mathbf{r} + \mathbf{R}_n, q), \quad (3)$$

$$\int_\Omega |\Psi_{n\mathbf{k}}(\mathbf{r}, q)|^2 d\mathbf{r} = 1, \quad (4)$$

where $\mathbf{R}_n$ is a two-dimensional lattice translation vector and q is the number of uncompensated electrons in a unit cell Ω of the film.

According to Eq. (2), the electron density $\rho(\mathbf{r}, q)$ is the sum over all energy bands n and quasi-momenta $\mathbf{k}$ corresponding to the occupied one-particle states with energies $E_n(\mathbf{k}, q)$ lying below the Fermi level $E_F(q)$.

The Coulomb contribution to the effective potential $V[\rho;\, \mathbf{r}, q]$ is calculated by a method described in [6]; the method explicitly takes into account the electrical neutrality of the volume of the metal film (Fig. 1):

$$\rho(\mathbf{r}, q) = \begin{cases} \rho_\infty(\mathbf{r}), & \mathbf{r} \in \Omega_{\mathrm{I}} \\ \rho_s(\mathbf{r}, q), & \mathbf{r} \in \Omega_{\mathrm{II}} + \Omega_{\mathrm{III}}, \end{cases} \quad (5)$$

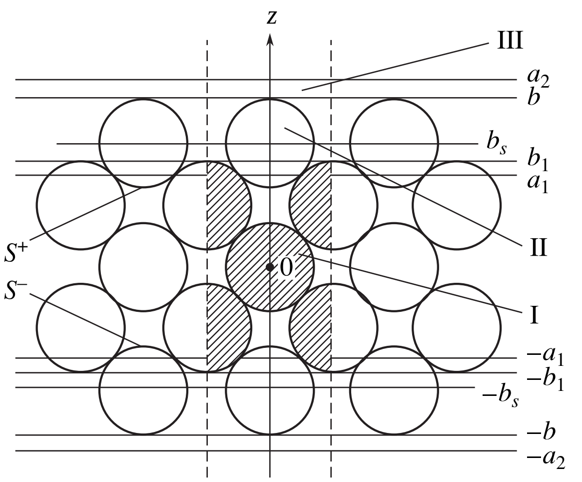

Fig. 1. Different regions of the unit cell of the film. I (Ω_{I}) is the bulk region, II (Ω_{II}) is the surface region, and III (Ω_{III}) is the vacuum region (the portions of MT spheres situated in the bulk region of the unit cell are hatched).

where $\rho_\infty(\mathbf{r})$ is the self-consistent electron density of the electrically neutral infinite crystal. This “frozen electron bulk density” model is based on a strict asymptotic form of the electron wave function deep within the crystal film [7] and agrees with self-consistent calculations of the electronic structure of metal films. The model allows one to improve the stability of self-consistent calculations for a charged film and, on the other hand, to achieve much progress toward analytical solution of the Poisson equation with non-muffin-tin electron density $\rho(\mathbf{r}, q)$. In combination with the calculational technique described below, this model makes it possible to considerably simplify a self-consistent solution of the Kohn–Sham equations (1) and (2) and to take advantage of the available numerous calculations of the electronic structure of infinite crystals.

The exchange-correlation contribution to $V[\rho; \mathbf{r}, q]$ is written in the local density approximation by using the Hedin–Lundqvist interpolation formula with the parameters presented in [8].

For an electrically neutral system ($q = 0$), the boundary conditions in the vacuum region [Eq. (4)] correspond to a potential which asymptotically tends to zero (the wave functions of the discrete spectrum fall off exponentially). In the case of a charged film, the electrostatic potential in the vacuum region varies linearly with the distance from the film surface, as is the case with the potential of a charged surface [6]. For this reason, as in many other papers concerned with calculations of the electronic structure of charged films, we assume that, in vacuum, on either side of the film, there is an infinitely high potential barrier at a distance z_B from the film surface, where the electron density is negligibly small. This barrier is placed far from the film, and its effect on the occupied states can be ignored if the condition $V[\rho; z_B, q] > E_F(q)$ is fulfilled. At the same time, its presence makes it possible to treat the effect of uncompensated charges of both signs in terms of stationary states.

Equations (1)–(4) are solved self-consistently by an original method described in detail in [9, 10]. In this method, the set of coordinate functions chosen for the Ritz variational procedure is such that the surface region and the bulk of the film can be effectively separated and the computational effort is greatly reduced. In some sense, our method is analogous to the “embedding” method (as applied to the case of a film), which was employed in [2, 3] for calculating the electron response of semi-infinite Al and Ag crystals.

In our method, when performing the Ritz variational procedure, the following expansion of the wave function is used:

$$\Psi_{n\mathbf{k}}(\mathbf{r}, q) = \sum_{j=1}^{J_s} c_{jn\mathbf{k}}(q)\phi_{j\mathbf{k}}(\mathbf{r})\tilde{\Theta}(\mathbf{r}) + \sum_{j=J_s+1}^{J_N} d_{jn\mathbf{k}}(q)\xi_{j\mathbf{k}}(\mathbf{r}, q)(1-\tilde{\Theta}(\mathbf{r})), \tag{6}$$

where $\tilde{\Theta}(\mathbf{r}) = 1$ if $\mathbf{r}$ lies in the volume Ω_{I} of the film (Fig. 1); otherwise, we have $\tilde{\Theta}(\mathbf{r}) = 0$.

In Eq. (6), $\phi_{j\mathbf{k}}(\mathbf{r})$ are the eigenfunctions of the Hamiltonian for the infinite crystal

$$\left\{-\frac{1}{2}\Delta + V_\infty[\rho_\infty; \mathbf{r}]\right\}\phi_{j\mathbf{k}}(\mathbf{r}) = \varepsilon_j(\mathbf{k})\phi_{j\mathbf{k}}(\mathbf{r}). \tag{7}$$

These eigenfunctions are subject to the Bloch boundary conditions in Eq. (3) in the film plane and to the homogeneous boundary conditions at the $z = \pm b_s$ planes lying in the surface region (Fig. 1),

$$\frac{\partial}{\partial \mathbf{n}}\phi_{j\mathbf{k}}(\mathbf{r}) = L_s\phi_{j\mathbf{k}}(\mathbf{r}), \tag{8}$$

where $\mathbf{n}$ is an outward normal to the surface of the region bounded by the $z = \pm b_s$ planes and L_s is a constant. In what follows, we assume that the film is symmetrical relative to the $z = 0$ plane; therefore, the functions $\Psi^{(p)}_{n\mathbf{k}}(\mathbf{r}, q)$ possess a definite parity p. Clearly, the Sturm–Liouville problem specified by Eqs. (7) and (8) meets the requirements imposed by symmetry on the functions $\phi^{(p)}_{j\mathbf{k}}(\mathbf{r})$.

It is known that, in fcc copper, the potential in the bulk is closely approximated by the muffin-tin (MT) potential, and Eq. (7) can be solved efficiently by the film version of Green’s function method [9–12].

As in the embedding method, the function $\xi^{(p)}_{j\mathbf{k}}(\mathbf{r}, q)$ is taken in the form of a linearized augmented-plane wave (LAPW) [13] in the film surface regions lying above the S^+ and below the S^- surfaces (Fig. 1). In the space between the sphere in the film surface region, we have

$$\xi^{(p)}_{j\mathbf{k}}(\mathbf{r}, q) = \frac{(z/|z|)^p}{\sqrt{a_2 - a_1}}\cos(k_n(|z| - a_2)) \times \exp(i(\mathbf{k} + \mathbf{K}_\mu)\mathbf{u}), \tag{9}$$

where the parity p coincides with the parity of the state, $\mathbf{K}_\mu$ is a reciprocal lattice vector of the film, $\mathbf{r} = (\mathbf{u}, z)$, $j = \{n, \mu\}$, and $k_n = n\pi/(a_2 - a_1)$, with $n = 0, 1, 2, \ldots$.

The convergence of the variational calculation depends heavily on the position of the $z = a_1$ and $z = a_2$ planes (Fig. 1). For a (001) film of fcc copper, the optimal positions are $a_1 = t - 3.5r_s$ and $a_2 = t + 3.5r_s$, where $z = t$ is the uppermost atomic plane and $r_s = A\sqrt{2}/4$ is the radius of the MT sphere (the lattice parameter A = 6.8309 a.u. is taken to be equal to its bulk value for copper).

Within the ith MT sphere in the surface layer, we have

$$\xi^{(p)}_{j\mathbf{k}}(\mathbf{r}, q) = \sum_{lm}\{G^{p,i}_{lm,j}(\mathbf{k})R^{(i)}_l(r_i; E_l, q) + S^{p,i}_{lm,j}(\mathbf{k})\dot{R}^{(i)}_l(r_i; E_l, q)\}i^l Y_{lm}(\mathbf{r}_i), \tag{10}$$

where $R^{(i)}_l(r_i; E_l, q)$ is a solution (normalized in the MT sphere) to the Schrödinger equation with effective potential $V[\rho; r_i, q]$ averaged over the angles corresponding to the energy E_l; $\dot{R}^{(i)}_l(r_i; E_l, q)$ is its derivative with respect to energy; $\mathbf{r}_i = \mathbf{r} - \mathbf{t}_i$, where $\mathbf{t}_i$ is the position vector of the ith atom of the surface layer; and $Y_{lm}(\mathbf{r}_i)$ are the spherical functions of the polar angles of the vector $\mathbf{r}_i$.

In the vacuum region, $\xi^{(p)}_{j\mathbf{k}}(\mathbf{r}, q)$ is a linear combination of the solution (corresponding to the energy E_v and normalized in volume Ω_{III}, see Fig. 1) to the equation with effective potential $V[\rho; \mathbf{r}, q]$ averaged over the film plane

$$\left(-\frac{1}{2}\frac{d^2}{dz^2} + V[\rho; z, q] - E_v + \frac{1}{2}(\mathbf{k} + \mathbf{K}_\mu)^2\right) \times g_{\mathbf{k},\mu}(z, E_v) = 0 \tag{11}$$

and the derivative to this solution $\dot{g}_{\mathbf{k}\mu}$ with respect to the energy. At $z > 0$, we have

$$\xi^{(p)}_{j\mathbf{k}}(\mathbf{r}, q) = [A^{p,+}_{j\mathbf{k}}g_{\mathbf{k},\mu}(z; E_v, q) + B^{p,+}_{j\mathbf{k}}\dot{g}_{\mathbf{k},\mu}(z; E_v, q)]\exp(i(\mathbf{k} + \mathbf{K}_\mu)\mathbf{u}). \tag{12}$$

The coefficients $G^{p,j}_{lm}(\mathbf{k})$, $S^{p,i}_{lm}(\mathbf{k})$, $A^{p,+}_{j\mathbf{k}}$, and $B^{p,+}_{j\mathbf{k}}$ are determined from the condition for continuous differentiability of the basis functions at the surfaces of the MT spheres and at the film surface $z = b$.

It should be stressed that, as in the LAPW method, the film muffin-tin (FMT) potential is used only for constructing the set of coordinate functions. The effective potential in the surface region is not of the MT form in our method, which is quite important and should be taken into account when describing the electron states of a metal film [10].

The basis functions defined above suffer a discontinuity at the surface-and-bulk region interfaces $S^\pm$. For this reason, the functional to be minimized is written in the form [14]

$$I = \int\limits_{\Omega_{\text{I}} + \Omega_{\text{II}} + \Omega_{\text{III}}} \Psi^*(\hat{H} - E)\Psi d\mathbf{r} + \frac{1}{2}\int\limits_{S^\pm}(\Psi_{\text{II}} - \Psi_{\text{I}})\left(\frac{d}{d\mathbf{n}}\Psi^*_{\text{II}} + \frac{d}{d\mathbf{n}}\Psi^*_{\text{I}}\right)d\mathbf{S} + \frac{1}{2}\int\limits_{S^\pm}(\Psi^*_{\text{II}} + \Psi^*_{\text{I}})\left(\frac{d}{d\mathbf{n}}\Psi_{\text{I}} - \frac{d}{d\mathbf{n}}\Psi_{\text{II}}\right)d\mathbf{S}, \tag{13}$$

where the Hamiltonian $\hat{H} = -\frac{1}{2}\Delta + V[\rho; \mathbf{r}, q]$ is given everywhere over the unit cell Ω of the film; Ψ_{I} and Ψ_{II} are the wave functions in the bulk (Ω_{I}) and surface (Ω_{II}) regions, respectively; and $\mathbf{n}$ is an outward normal to the boundary of Ω_{I}. Minimizing this functional with the functions in Eq. (6) leads to a set of homogeneous linear equations,

$$\begin{pmatrix} S^{(p)}_{11}(E) & S^{(p)}_{12} \\ S^{(p)}_{21} & S_{22}(E) \end{pmatrix}\begin{pmatrix} c^{(p)}_j \\ d^{(p)}_j \end{pmatrix} = 0, \tag{14}$$

whose matrix is Hermitian and has a block form. Only the elements of the diagonal blocks $S^{(p)}_{11}$ and S_{22} are linear functions of the energy, $(S_{ij})_{JJ} = (H_{ij} - EO_{ij})_{JJ}$, whereas the elements of the Hermitian conjugate blocks $S^{(p)}_{12}$ and $S^{(p)}_{21}$ are E independent. Thus, the problem is reduced to a generalized eigenvalue problem and single minimization allows one to determine all eigenvalues $E_n(\mathbf{k})$ in a given energy interval.

It is significant that the surface-layer potential affects only the elements of the block S_{22}, whose dimension is determined by the number of surface layers. This block is the same for even and odd states, which reduces the computational effort. The blocks S_{11}, S_{12}, and S_{21} need not be recalculated when surface perturbations are taken into account or when the self-consistency procedure is carried out, if the self-consistent bulk electron density is used. Details of the derivation of Eq. (14) and an explicit form of the matrix elements

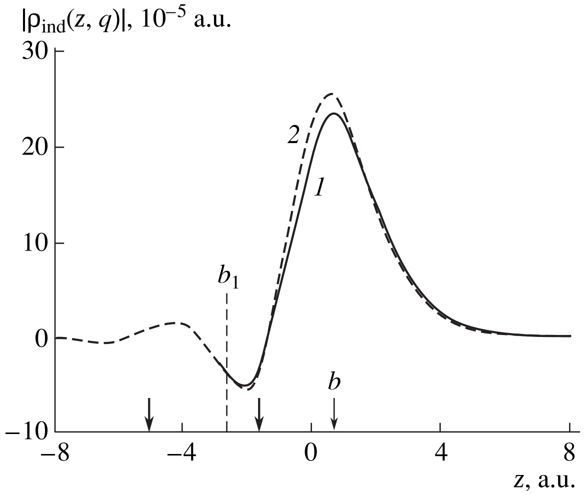

Fig. 2. Distribution of the induced electron density for the uncompensated electron number q equal to (*1*) 0.03 and (*2*) –0.03. The distance is measured from the geometrical surface of the crystal (arrows indicate the positions of the film surface $z = b$ and atomic planes).

are presented in [9]. In [9, 10], it was shown that the accuracy of the electronic-structure calculation method described above is comparable to that of the film LAPW method. The effect of the coordinate function parameters on the rate of convergence of the variation procedure was also analyzed in those papers. The effect of the centers of linearization of LAPW functions is identical to that in the film LAPW method [15]. The Sturm parameters noticeably affect only the rate of convergence of the variation procedure. After the parameters a_1 and a_2 had been optimized, we used 80 LAPW functions and about ten Sturm functions for the states of the same parity. The dimensionality of the basis was verified by comparing the calculation for the electrically neutral film with other available calculations and the experiment.

Table 1. Distribution of the uncompensated electron number q over different surface regions of a (001) film of copper: q_{vac} is in the vacuum region, q_{inter} is in the regions between the spheres of the surface layer, and q_{spher} is in the MT spheres

q	q_{vac}	q_{inter}	q_{spher}
–0.03	–0.0176	–0.0100	–0.0024
–0.02	–0.0123	–0.0069	–0.0008
–0.01	–0.0063	–0.0033	–0.0004
0.01	0.0061	0.0031	0.0008
0.02	0.0117	0.0053	0.0030
0.03	0.0183	0.0083	0.0034

2. SCREENING OF AN ELECTRIC FIELD BY A (001) FILM OF COPPER

An investigation of the electron response of metals to an external electrostatic field in the framework of the EDF theory is of considerable interest for two principal reasons. First, at the present time, this is the only method by which the effect of exchange correlation on the response functions of inhomogeneous systems can be treated. Second, the EDF theory makes it possible to go beyond the linear response regime, since one can easily calculate the electron density induced by an external field of strength $\mathcal{E} = -\frac{4\pi}{S_{\omega s}}\frac{q}{2}$ ($S_{\omega s}$ is the area of the cross section of the unit cell by the plane z = const):

$$\rho_{\text{ind}}(\mathbf{r}, q) = \rho(\mathbf{r}, q) - \rho(\mathbf{r}, 0). \tag{15}$$

In what follows, we consider the case of fields $|\mathcal{E}| \le 4.2 \times 10^9$ V/m ($|q| \le 0.03$), which are practicable [16] and, at the same time, satisfy the condition $V[\rho; z_B, q] \ge E_F(q)$, which rules out the presence of artificial states near the infinite barrier at sufficiently large z_B for negatively charged films. The fulfillment of this condition was checked at each calculation stage.

Figure 2 shows a typical distribution of the induced electron density over a straight line that is normal to the (001) surface of a Cu film and passes through the nucleus of an atom in the second surface layer. From Fig. 2 and Table 1, which lists data on the distribution of the induced charge over different regions of the surface layer, it is seen that most of the screening charge is concentrated in the very thin layer near the film surface ($z = b$). The peak of $\rho_{\text{ind}}(z, q)$ is shifted from the last atomic plane toward the vacuum region by approximately half the spacing between the atomic planes. This distribution of the screening charge in a (001) film of Cu is similar to that obtained by calculating the electron response of the (001) surfaces of Ag [3] and Al [2]. The fraction of q contained in a surface MT sphere is small, but the polarization of the screening charge in this region is significant (Fig. 3). We note that calculations revealed no noticeable polarization of the electronic charge in a surface MT sphere in Al [2], but in a metal with d electrons (Ag), this effect was observed [3].

Friedel oscillations of the electron density in the bulk of the crystal are suppressed in the frozen bulk density model (5) employed in this paper. We estimated the error associated with this approximation in the jelly model, according to which, in the bulk of the crystal, we have [17]

$$\rho_{\text{ind}}(q, z) = A(q)\frac{\cos(2k_F z + \alpha(q))}{z^2} + O\left(\frac{1}{z^3}\right), \tag{16}$$

where $k_F = (3\pi^2\bar{n})^{1/3}$ and $\bar{n} = 0.0125a_0^{-3}$ (a_0 is the Bohr radius) is the bulk value for a copper crystal. The coefficients $A(q)$ and $\alpha(q)$ are determined by matching Eq. (16) with the calculated induced electron density at interfaces S^+ and S^-. The corresponding distribution for $q = 0.03$ is represented by the dashed curve in Fig. 2. The number of uncompensated electrons outside the surface region as calculated by Eq. (16) is -3.9×10^{-5}. This justifies the approximation in which only one atomic layer of the surface region is taken into account in the case of a (001) film of fcc copper. When electrons are present in excess ($q > 0$), the peak of the induced density distribution (Fig. 2) is lower and its shift toward the vacuum region is larger than in the case of a deficit of electrons ($q < 0$). This effect is physically clear and takes place in both the jelly model [16] and models taking the crystal structure into account [2, 3].

However, the magnitude of the shift of the center of gravity of the induced charge,

$$z_q = \int\limits_{\Omega_{\mathrm{II}}+\Omega_{\mathrm{III}}} z\rho_{\mathrm{ind}}(\mathbf{r}, q)d\mathbf{r} \Big/ \int\limits_{\Omega_{\mathrm{II}}+\Omega_{\mathrm{III}}} \rho_{\mathrm{ind}}(\mathbf{r}, q)d\mathbf{r}, \qquad (17)$$

in the (001) film of fcc copper (Fig. 4), which depends on the nonlinear response of the electron density, differs essentially from the jelly model prediction [16]. In the limit as $q \longrightarrow 0$, this quantity gives the position of the image plane z_0 of the metal, which is involved in a correct asymptotic expression for the exchange-correlation potential given by the EDF theory for a finite crystal [1, 17]:

$$\lim_{|z| \to \infty} V[\rho;\, \mathbf{r}, q = 0] = -\frac{1}{4|z - z_0|}; \qquad (18)$$

the image plane is of primary importance in the physics of many surface phenomena. In order to decrease the error when calculating the quantity

$$z_0 = 2\frac{\partial}{\partial q} \int\limits_{\Omega_{\mathrm{II}}+\Omega_{\mathrm{III}}} z\rho_{\mathrm{ind}}(\mathbf{r}, q)d\mathbf{r}\Big|_{q=0}, \qquad (19)$$

we regularize the differentiation, as in [3], by smoothing the calculated z_q dependence by the method of least squares (Fig. 4). For the distance measured from the geometrical surface of the crystal, we obtain

$$z_q = z_0 + z_1 q = 1.03 + 4.03q \text{ (a.u.)}. \qquad (20)$$

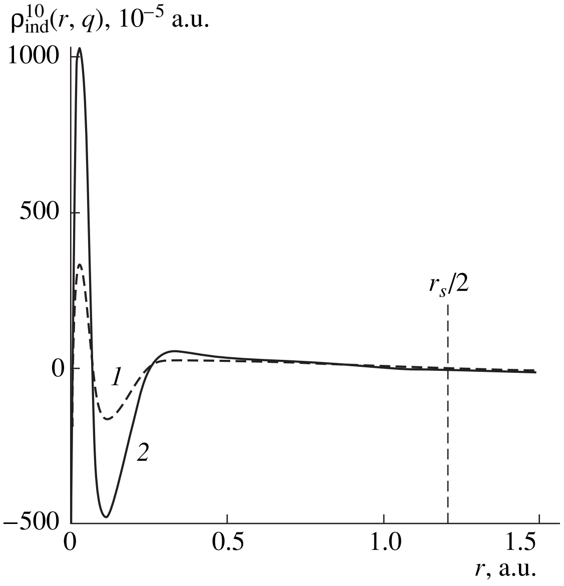

Fig. 3. Variation of the dipolar component of the induced electron density in a surface MT sphere for q equal to (*1*) 0.01 and (*2*) 0.03.

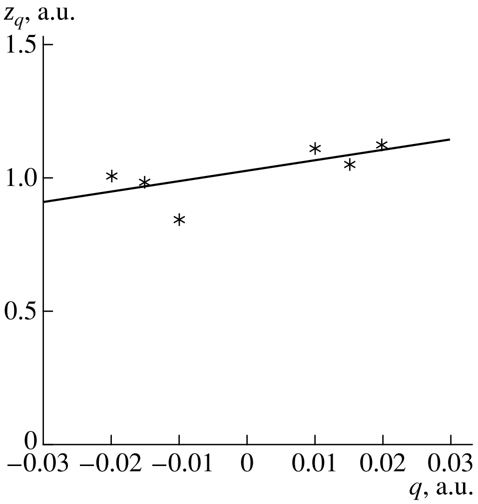

Fig. 4. Center of gravity z_q of the induced electron density for the charge q (the distance is measured relative to the geometrical surface of the crystal).

The error in determining z_q associated with the suppression of Friedel oscillations in the film volume Ω_{I} can be estimated from Eq. (16) and does not exceed 0.01 a.u. A comparison with the results of other papers is performed in Table 2. The data listed in the "Jelly model" column are obtained by linear interpolation of the calculations from the cited papers for the density parameters $r_e/a_0 = 2$ and 3 to a value of $r_e/a_0 = 2.67$ corresponding to a copper crystal. The values of z_0 presented in the "Experiment" column are model calculations with fitting parameters found from the experimental data (the energies of states of the Rydberg type) having a direct relationship to the position of the image plane. From Table 2, it is seen that our results lie in the middle between the jelly model results and the calculations based on the fitting parameters.

Table 2. Position of the image plane for (001) Cu (relative to the geometrical surface of the crystal, in a.u.)

Jelly model				Experiment		Our calculation
[18]	[18]	[19]	[20]	[21]	[22]	
1.42	1.32	1.43	1.35	0.57	0.48	1.03

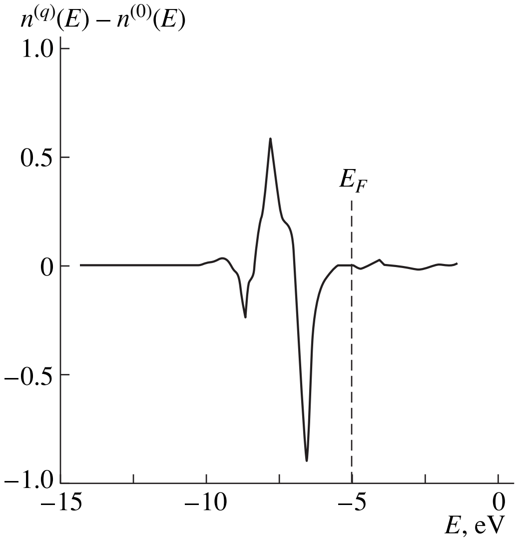

Fig. 5. Difference in the density of states between the charged ($q = 0.01$) and neutral (001) films of Cu.

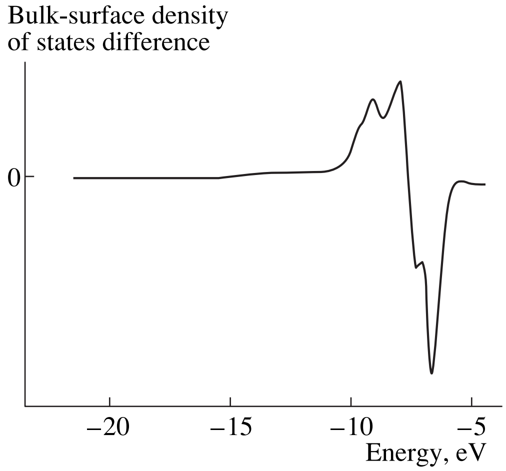

Fig. 6. Difference in the local density of states between the bulk and surface atomic layers of the (001) film of copper (data from [24]).

The coefficient of the term linear in q in Eq. (20) is related to the quadratic response of the electron density $\rho_2(\mathbf{r})$. Indeed, we have

$$\rho_{\mathrm{ind}}(\mathbf{r}, q) = q\rho_1(\mathbf{r}) + q^2\rho_2(\mathbf{r}) + \ldots \tag{21}$$

and, therefore,

$$z_1 = 2\int\limits_{\Omega_{\mathrm{II}} + \Omega_{\mathrm{III}}} z\rho_2(\mathbf{r})d\mathbf{r}. \tag{22}$$

According to [23], in the low-frequency limit ($\omega/\omega_p < 0.1$, where ω_p is the plasma frequency in the bulk of the crystal), we have

$$\rho_{2\omega}(z) = -\frac{1}{2}\mathcal{E}_0^2\rho_2(z) + O(\mathcal{E}_0^4), \tag{23}$$

where $\rho_{2\omega}(z)$ is the second-harmonic amplitude of the electron density in a time-harmonic uniform electric field of amplitude $\mathcal{E}_0$ applied perpendicular to the metal surface. Thus, the coefficient of q in Eq. (20) characterizes the second-harmonic intensity generated on reflection of low-frequency electromagnetic waves at the metal surface. The value of z_1 calculated in [23] in the jelly model for $r_e/a_0 = 3$ is 8.14 a.u. Our calculated value of z_1 for a (001) film of copper equals 4.03 a.u., which is about half as large as the jelly model prediction and differs from the hydrodynamic model result [23] by a factor of about 100. We note that, when the electron screening is calculated for the (001) surface of Ag with allowance made for the crystal structure [3], the value of z_1 is found to be about a third as large as the jelly model result. Thus, it is important to take the crystal structure into account when the nonlinear response is treated theoretically.

Figure 5 shows the dependence of the electron density of states on the external electrostatic field for a (001) film of copper. From Fig. 2 and the results of [3], it follows that the charge induced in a metal by an external electrostatic field is a perturbation strongly localized near the surface. Therefore, according to perturbation theory at small values of q, the difference in the density of states between the electrically neutral and the charged film (Fig. 5) is most significant for surface states. This conclusion correlates well with the data from [24] on the difference in the local density of states between the bulk and surface regions of a (001) film of copper (Fig. 6), which is additional support for the results obtained and, on the other hand, suggests a simple method for determining the energy localization of surface states.

The Stark shift of surface states lying 1.5 eV below the Fermi level (Fig. 5) equals $\frac{\partial E}{\partial \mathcal{E}} = \frac{\partial E}{\partial q}\frac{\partial q}{\partial \mathcal{E}} \approx \frac{\Delta E}{\Delta q}\frac{S_{\omega s}}{2\pi} \approx$ 0.1 a.u., which is of the same order of magnitude as the Stark shift of occupied (001) surface states of Ag in an external electrostatic field.

REFERENCES

1. N. D. Lang and W. Kohn, Phys. Rev. B **7**, 3541 (1973).
2. J. E. Inglesfield, Surf. Sci. **188**, L701 (1987).
3. G. C. Aers and J. E. Inglesfield, Surf. Sci. **217**, 367 (1989).
4. S. Clarke, M. Nekovee, P. K. de Boer, and J. E. Inglesfield, J. Phys.: Condens. Matter **10**, 7777 (1998).
5. V. M. Silkin, L. Yurchishin, E. V. Chulkov, and M. Stenslitskaya, Poverkhnost, No. 7, 36 (1994).
6. G. V. Wolf and D. V. Fedorov, Poverkhnost, No. 5, 105 (1998).
7. Yu. P. Chuburin, Teor. Mat. Fiz. **77** (3), 472 (1988).
8. O. Gunnarson and B. I. Lundqvist, Phys. Rev. B **13**, 4274 (1976).
9. G. V. Wolf and D. V. Fedorov, Available from VINITI, No. 2361-V98 (1998).

10. G. V. Wolf and D. V. Fedorov, Kondens. Sredy Mezhfaz. Granitsy **1** (2), 120 (1999).
11. W. Kohn, Phys. Rev. B **11**, 3756 (1975).
12. N. Kar and P. Soven, Phys. Rev. B **11**, 3761 (1975).
13. G. A. Benesh and J. E. Inglesfield, J. Phys. C **17**, 1595 (1984).
14. H. Schlosser and P. M. Marcus, Phys. Rev. **131**, 1112 (1963).
15. H. Krakauer, M. Posternak, and A. J. Freeman, Phys. Rev. B **19**, 1706 (1979).
16. P. Gies and R. R. Gerhardts, Phys. Rev. B **33**, 982 (1986).
17. N. D. Lang, in *Theory of the Inhomogeneous Electron Gas*, Ed. by S. Lundqvist and N. H. March (Plenum, New York, 1983; Mir, Moscow, 1987).
18. P. A. Serena, J. M. Soler, and N. García, Phys. Rev. B **34**, 6767 (1986).
19. A. Kiejna, Phys. Rev. B **43**, 14695 (1991).
20. S. Ossicini, F. Finocchi, and C. M. Bertoni, Surf. Sci. **189/190**, 776 (1987).
21. E. V. Chulkov, V. M. Silkin, and P. M. Echenique, Surf. Sci. **391**, L1217 (1997).
22. N. V. Smith, C. T. Chen, and M. Weinert, Phys. Rev. B **40**, 7565 (1989).
23. M. Weber and A. Liebsch, Phys. Rev. B **35**, 7411 (1987).
24. J. R. Smith, J. G. Gay, and F. J. Arlinghaus, Phys. Rev. B **21**, 2201 (1980).

Translated by Yu. Epifanov

Physics of the Solid State, Vol. 43, No. 3, 2001, pp. 408–412. Translated from Fizika Tverdogo Tela, Vol. 43, No. 3, 2001, pp. 391–395.
Original Russian Text Copyright © 2001 by T. Popik, Shpenik, Yu. Popik.

METALS AND SUPERCONDUCTORS

Study of the Electronic Spectra of Noble Metals by Low-Energy Electron Backscattering

T. Yu. Popik*, O. B. Shpenik*, and Yu. V. Popik**
**Institute of Electron Physics, National Academy of Sciences of Ukraine, Uzhgorod, 88000 Ukraine*
e-mail: an@zvl.iep.uzhgorod.ua
***Uzhgorod State University, Uzhgorod, 88000 Ukraine*

Received February 28, 2000; in final form, July 7, 2000

Abstract—The density of filled electronic states of noble metals (Au, Ag, Cu) below the Fermi level is studied by low-energy electron backscattering spectroscopy (0–10 eV) by using a specially designed hypocycloidal electron spectrometer capable of high energy (≤50 meV) and angular (~1°–5°) resolution. The features observed in the electron scattering spectra are established to agree well with the extrema of the theoretically calculated density-of-states distributions. The results obtained amplify substantially the information provided by UV and x-ray photoelectron spectroscopy. © *2001 MAIK “Nauka/Interperiodica”.*

The energy structure of the valence bands of noble metals is very complex, and their density of states exhibits a number of features. Analysis of the available literature data shows that high-energy (>100 eV) electrons are hardly suitable to probe the features in the valence-band structure. Therefore, the information on the density of states in the valence bands of metals has thus far been obtained primarily by ultraviolet and x-ray photoelectron spectroscopy (UPS and XPS, respectively) with a high angular resolution [1–6]. The development and use of electron spectrometers capable of a high energy resolution (6–50 meV) offers the possibility of obtaining more detailed information on the density-of-states distribution of both filled and empty bands in metals, as well as on the density of the surface states [7, 8]. Bombardment of a surface by low-energy electrons (particularly near the threshold for inelastic scattering) results in a strong perturbation of the target orbitals, and the electron–target potential suffers a noticeable deformation [9]. This perturbation accounts for the excitation of the transitions in solids which are optically forbidden or IR inactive [3, 9] by low-energy electrons.

The experiments were carried out on a high-vacuum setup with oil-free pumping, which consisted of the following main units: an ultrahigh-vacuum chamber housing a hypocycloidal electron spectrometer, a goniometer with the samples to be studied, an electron-heated sample holder and an effusion atom source, a power supply, and a multichannel system for the primary- and scattered-electron current measurement. The chamber was placed inside Helmholtz coils, which produced the uniform magnetic field necessary for the spectrometer operation.

The hypocycloidal electron spectrometer designed by us [10] and shown schematically in Fig. 1 served to produce a monoenergetic electron beam and to analyze the elastically and inelastically scattered electrons. It consists of two successively placed electron-energy analyzers, one of which operates as a monochromator and the other is used to analyze the elastically or inelastically scattered electrons. The spectrometer makes use of the fact that electrons acted upon by crossed electric and magnetic fields, besides propagating forward, drift in a transverse direction, i.e., perpendicular to both **E** and **H**. Note that the magnitude of the drift does not depend on the electron velocity vector. Therefore, on passing the crossed analyzer fields, the electrons scattered through 180° are displaced a certain distance from the primary beam axis. By placing the collector at this distance, one can detect the elastically backscattered electrons. The detection of the inelastically scattered electrons is made possible by the provision of segment-shaped diaphragms in the analyzer electrodes [10].

The main characteristics of the spectrometer are as follows: primary beam current ~10^{-8} A, scattered-electron current ~10^{-9} to 10^{-10} A, beam diameter ~0.5 mm, full width of the electron energy distribution in the beam ~14–20 meV, and the energy resolution ~20–50 meV. The instrument is unique in that it can operate at very low energies (practically from zero up), with the primary electron-beam intensity being practically energy-independent and the spectrometer transmission being ~95%.

Prior to measurements, the electron spectrometer and the samples were heated at a temperature $T \sim 1000$–1300 K in a vacuum of 10^{-6} Pa for 50–60 h, after which the surface was cleaned by high-energy electrons. The vacuum in the chamber during the measurements was ~10^{-8} Pa. The sample surface cleanness was monitored by checking for the presence of the fine structure in the measured relations.

This equipment permitted performing experiments of the following two types.

(1) Measurement of the energy dependence of electrons scattered elastically through 180°. To do this, one applies optimum constant potentials to the monochromator and analyzer electrodes and measures the current to collector *15* as a function of the electron energy, which is determined by the potential difference between electrodes *1* (cathode) and *14* (sample) (Fig. 1). The incident electron energy is varied from 0 to 10 eV in 0.02-meV steps. Because, as was already mentioned, the primary beam intensity does not depend on energy, the opening of the inelastic scattering channels should become manifest in the form of minima in the energy dependence of the intensity of elastically scattered electrons.

(2) Detection of electrons with a constant residual energy E_r, down to practically zero energy. These measurements are done by maintaining a constant potential difference between analyzer *9* and sample *14* while varying the incident electron energy. In this case, the features in the scattering will be seen as maxima in the energy dependences.

The spectrometer operation and the experimental technique used are described in detail in [10].

This paper reports on testing these techniques for their applicability to the investigation of the electronic energy structure in solids. Because the electrons scattered elastically from metal targets are sensitive only to specific features in the density of filled states, we chose noble metals for our study; their band structure has been studied most thoroughly, both theoretically and experimentally [1]. As was shown in [4], electrons with energies from 30 to 200 eV have the smallest mean free path in solids, whereas for electrons of energy ~1 eV it can reach 10^3 Å. The latter means that electrons with energies of 0–10 eV can be used to probe not only the surface but also the bulk electronic states.

The complexity of the band structure of noble metals is due to their having two groups of *s*, *p*, and *d* electrons differing strongly in the degree of localization. Unlike the *s* and *p* electrons, the *d* electrons are strongly localized, although more weakly than in free atoms. Hybridization of the *s*, *p*, and *d* states gives rise to a superimposition of the localized *d* states on the broad, smoothly varying background of the *s*- and *p*-state distribution, which brings about the formation of resonant *d* states [1].

For this study, we chose bulk polycrystalline samples of gold, silver, and copper with their surface polished to grade 12 perfection.

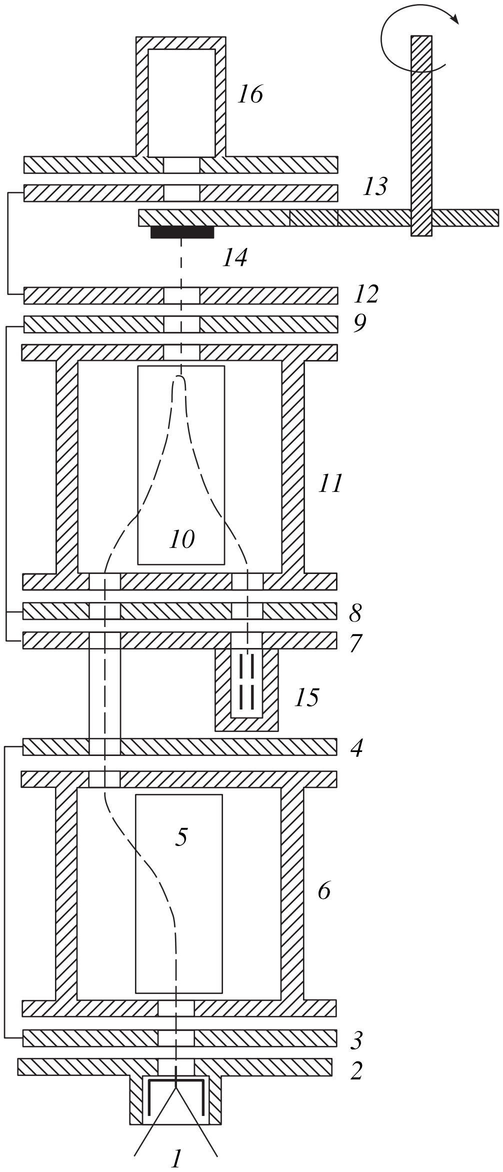

Fig. 1. Schematic of the hypocycloidal electron-backscattering spectrometer. (*1*) Indirectly heated oxide cathode; (*2*) extraction electrode; (*3*, *4*) input and output selector electrodes, respectively; (*5*, *6*) inner and outer electrodes of the cylindrical selector capacitor, respectively; (*7*–*9*) analyzer input and output electrodes; (*10*, *11*) inner and outer electrodes of the analyzer cylindrical capacitor, respectively; (*12*, *13*) spectrometer accelerating electrodes; (*14*) sample; (*15*) collector of backscattered electrons; and (*16*) primary electron-beam monitoring collector.

Figures 2–4 present elastic scattering spectra and spectra of constant residual energy obtained in low-energy electron scattering through 180° from Au, Ag, and Cu. While, in order to reveal features in the energy distribution of scattered electrons, the authors of earlier papers had to find the first (and, quite frequently, the second) derivative of the scattered electron intensity with respect to energy, our technique, as seen from the

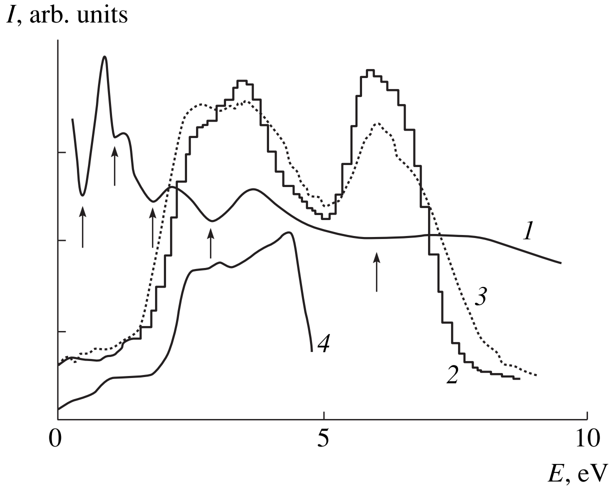

Fig. 2. Valence-electron energy distribution for gold. (*1*) Energy dependence of the elastically backscattered electron intensity, (*2*) calculated density-of-states function [11], (*3*) experimental valence-band photoelectron spectrum [12], and (*4*) valence-band photoelectron spectrum obtained with a synchrotron beam at 10.2-eV exciting photon energy [13].

figures, allows this to be obtained without any additional processing of the measured relations.

Gold is one of the best studied noble metals. Photoemission spectra [12] (curve *3* in Fig. 2) and theoretical calculations of the density of states [11] (curve *2* in Fig. 2) reveal two broad maxima in the density of electronic states in the valence band at ~3–4 eV and ~6–7 eV, with the latter maximum, as shown by calculations [11], being due to the contribution of relativistic interaction effects. Synchrotron radiation was used [13] to study the electron spectra at energies from 10.2 to 90 eV. The photoelectron intensity distribution in energy obtained at a photon energy of 10.2 eV was found to have the shape of curve *4* in Fig. 2, with a clearly pronounced fine structure within the 0- to 2-eV interval and one broad maximum from 2.5 to 4.5 eV. As the exciting photon energy increases, the photoelectron spectrum deforms strongly and, at excitation energies above 50 eV, acquires the shape of curve *3* in Fig. 2. Because we studied the intensity of elastically scattered electrons at energies below 10 eV (curve *1* in Fig. 2), the feature at ~6.0 eV is only weakly pronounced here. However, within the 0- to 3-eV interval, the fine structure of the spectrum is more distinct than that in curve *4*. This confirms the strong dependence of the matrix elements determining the electron excitation probability from filled states below the Fermi level on the energy of exciting particles in the case of gold. The absence of features in the 0- to 2-eV interval in the calculated bulk density-of-states functions and their presence in photoelectron spectra at comparatively low exciting-photon

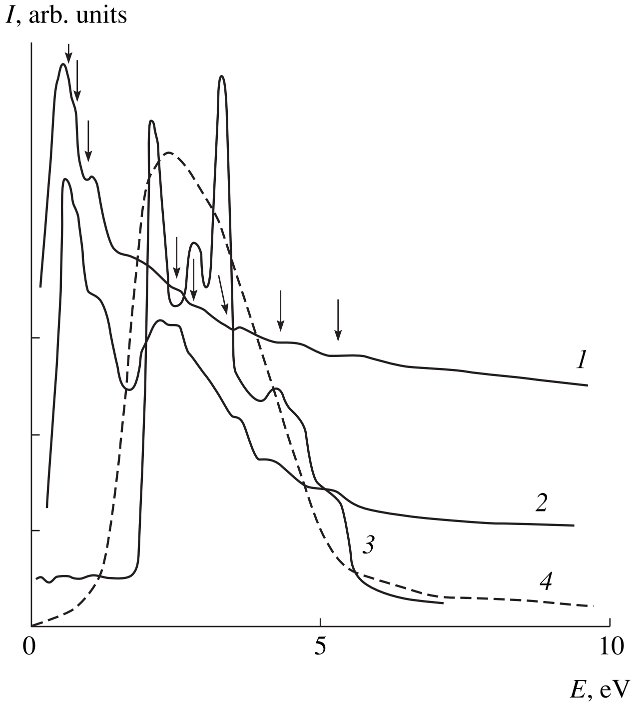

Fig. 3. Valence-electron energy distribution for silver. (*1*) Energy dependence of the elastically backscattered electron intensity, (*2*) electron backscattering spectrum of constant residual energy E_r ~ 0 eV, (*3*) theoretically calculated density-of-states function [14], and (*4*) experimental valence-band photoelectron spectrum [15].

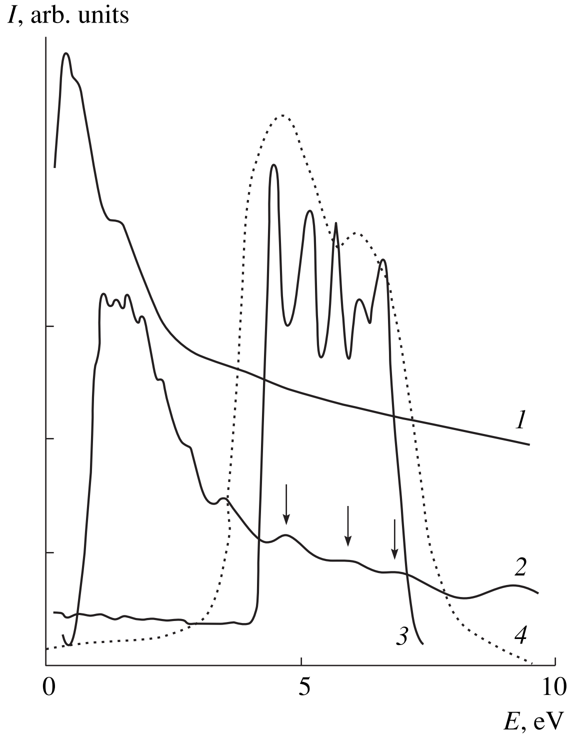

Fig. 4. Valence-electron energy distribution for copper. (*1*) Energy dependence of the elastically backscattered electron intensity, (*2*) electron backscattering spectrum of constant residual energy E_r ~ 0 eV, (*3*) theoretically calculated density-of-states function [1], and (*4*) experimental valence-band photoelectron spectrum [16].

energies and in the spectra of elastically scattered electrons give one grounds to relate the features in curve *1* located at 0.50, 1.00, and 1.70 eV to surface electronic states below the Fermi level, excitation from which has a resonant nature.

The theoretical and experimental photoelectron spectra of silver are summarized in monograph [1]. By calculations [14], the density-of-states function and the photoelectron spectra of valence-band electrons should exhibit five maxima at energies 4–7 eV below the Fermi level, with one of them being substantially weaker in intensity than the other four (curve *3* in Fig. 3). In the experimental XPS and UPS spectra, one sees only two maxima, while at energies from 0 to 4 eV no fine structure was found at all [15] (curve *4* in Fig. 3). Practically no fine structure is seen in the energy dependence of the elastically backscattered intensity at 3–8 eV measured for silver either (curve *1* in Fig. 3). At the same time, the spectra of constant residual energy of scattered electrons (curve *2* in Fig. 3) follow a radically different pattern. These spectra exhibit four clearly pronounced maxima at 3–7 eV, with their energy positions being in satisfactory agreement with calculations. The maxima at energies below 3 eV should be assigned to surface states lying below the Fermi level.

The valence band in copper is formed by the filled 3*d* band overlapping with the half-filled 4*s* and empty 4*p* bands to produce one partially filled band, in which the upper edge of the filled levels lies slightly lower than that of the 3*d* band [17, 18]. This is what accounts for the complex valence-band structure of copper [1]. The calculated and UPS and XPS data for the density of states of valence electrons and photoelectron spectra can be found in [4, 16, 19–21]. Theoretical calculations suggest that the photoelectron spectra should have three distinct and two weak maxima (curve *3* in Fig. 4). The experimental x-ray and photoelectron spectra exhibit only one broad maximum with a very weakly pronounced fine structure (curve *4* in Fig. 4). Only the spectra of photoelectrons emitted perpendicular to the Cu(111) surface have three maxima at photon energies of ~11 eV and only two maxima at 6–9 eV (see Fig. 3.57a in [4]). Note that an increase in photon energy gives rise not only to an increase in the intensity of the second and third maxima, but also to a noticeable increase in the separation between all maxima. For copper, unlike gold and silver, a maximum whose position is independent of the incident photon energy is observed in the region 0–4 eV below the Fermi level. This maximum is assigned to the emission of electrons from surface states. The fine structure of the valence band obtained in our spectra of elastically scattered electrons (curve *1* in Fig. 4) is less distinct than in the spectra of constant electron residual energy (curve *2* in Fig. 4). In contrast to UPS and XPS, our spectra of electrons elastically backscattered through 180° exhibit five features in the 2- to 6-eV interval and their positions agree with the calculated maxima in the valence-band density-of-states function below the Fermi level. According to [4, 22], the features at 0.60–0.80 eV should be identified with surface states located below the Fermi level in the bulk. The features with energies of ~1.00 and ~1.50 eV are also apparently of the surface nature, because they are not seen in the calculated bulk spectra.

The above results permit the following conclusions: (1) The backscattering spectra of low-energy electrons are very sensitive to features in the energy distribution of the density of states in the valence band and can be employed to study the electron energy spectrum in metals. (2) The proposed technique is suitable for probing not only the surface but also the bulk electronic states of solids. (3) Low-energy electron backscattering spectra yield more complete information on details in the density of filled states distribution than the UPS and XPS methods which are currently widely used. This advantage becomes particularly significant when the matrix elements determining the excitation probability depend strongly on the energy of exciting particles.

REFERENCES

1. V. V. Nemoshkalenko and V. G. Aleshin, *Electron Spectroscopy of Crystals* (Naukova Dumka, Kiev, 1983).
2. *Electron and Ion Spectroscopy of Solids*, Ed. by L. Fiermans, J. Vennik, and W. Dekeyser (Plenum, New York, 1978; Mir, Moscow, 1981).
3. *Electron Spectroscopy for Surface Analysis*, Ed. by H. Ibach (Springer-Verlag, New York, 1977; Zinatne, Riga, 1980).
4. D. Woodruff and T. Delchar, *Modern Techniques of Space Science* (Cambridge Univ. Press, Cambridge, 1986; Mir, Moscow, 1989).
5. T. A. Carlson, *Photoelectron and Auger Spectroscopy* (Plenum, New York, 1975; Mashinostroenie, Leningrad, 1981).
6. *Practical Surface Analysis by Auger and X-ray Photoelectron Spectroscopy*, Ed. by D. Briggs and M. Seah (Wiley, New York, 1983; Mir, Moscow, 1987).
7. *Methods of Surface Analysis*, Ed. by A. W. Czanderna (Elsevier, New York, 1975; Mir, Moscow, 1979).
8. S. A. Komolov, *Integral Secondary-Electron Spectroscopy of Surface* (Leningrad. Gos. Univ., Leningrad, 1986).
9. Leon Sanche, J. Chem. Phys. **71** (12), 4860 (1979).
10. O. B. Shpenik, N. M. Erdevdy, N. I. Romanyuk, *et al.*, Prib. Tekh. Éksp. **41** (1), 66 (1998).
11. N. E. Christensen and B. O. Seraphin, Phys. Rev. B **4**, 3321 (1971).
12. D. A. Shirley, Phys. Rev. B **5** (12), 4709 (1972).
13. J. L. Freeouf, M. Erbudak, and D. E. Eastman, Solid State Commun. **13** (7), 771 (1973).
14. S. Hüfner, G. K. Wertheim, N. V. Smith, and M. M. Traum, Solid State Commun. **11** (2), 323 (1972).

15. V. V. Nemoshkalenko, A. I. Senkevich, M. A. Midlina, and V. G. Aleshin, Phys. Status Solidi B **56** (2), 771 (1973).
16. S. Hüfner and G. K. Wertheim, Phys. Lett. A **47** (5), 349 (1974).
17. S. A. Fridrikhov and S. M. Movin, *Physical Foundations of Electronic Engineering* (Vysshaya Shkola, Moscow, 1982).
18. V. N. Strokov, A. V. Shtan'ko, and S. A. Komolov, Vestn. Leningr. Univ. **4** (1), 7 (1990).
19. R. C. Dobbyn, M. L. Williams, J. R. Cuthill, and A. J. McAlister, Phys. Rev. B **2** (16), 1563 (1970).
20. J. A. Knapp, F. J. Himpsel, and D. E. Eastman, Phys. Rev. B **19**, 4952 (1979).
21. N. V. Smith, R. L. Benbow, and Z. Hurych, Phys. Rev. B **21**, 4331 (1980).
22. A. Zangwill, *Physics at Surfaces* (Cambridge Univ. Press, Cambridge, 1988; Mir, Moscow, 1990).

Translated by G. Skrebtsov

Physics of the Solid State, Vol. 43, No. 3, 2001, pp. 413–415. Translated from Fizika Tverdogo Tela, Vol. 43, No. 3, 2001, pp. 396–398.
Original Russian Text Copyright © 2001 by Taĭlanov, Yakhshiev.

METALS AND SUPERCONDUCTORS

Nonlinear Thermomagnetic Waves in the Resistive State of Superconductors

N. A. Taĭlanov and U. T. Yakhshiev
Research Institute of Applied Physics, National University of Uzbekistan,
Universitetskaya ul. 95, Vuzgorodok, Tashkent, 700095 Uzbekistan

Received May 12, 2000

Abstract—The evolution of thermomagnetic perturbations in the resistive state of superconductors is considered. A qualitative pattern of the formation and further development of nonlinear stationary structures that describe the final stage of thermal and electromagnetic perturbations in a superconductor is investigated. The wave propagation velocity and the wave front width in a superconductor are estimated. © *2001 MAIK "Nauka/Interperiodica".*

Energy dissipation during the motion of vortices leads to ohmic heating of a superconductor. As a result, a certain region of the superconductor is heated to a temperature $T > T_c$, where T_c is the critical temperature. An increase in the temperature in a local region of the sample brings about a decrease in the critical current j_c and the emergence of a vortex electric field E at the same region.

The effect of superconductivity quenching due to thermal heating of the vortex lattice has been experimentally studied for a long time. Early experiments [1] revealed that the vortex electric field E is induced under ohmic heating in a superconductor through which a direct current with a density j_c flows. According to the balance between dissipative and nonlinear effects, the transition to the resistive state is accompanied by the emergence of various modes of the "switching wave" type, i.e., the regime of a wave motion that switches a sample from the superconducting to the normal state. Examples of these modes can be provided by thermal waves, namely, a steady-state propagation of a normal zone [2] or nonlinear thermomagnetic waves [3] in superconductors.

In this work, we studied the qualitative pattern of formation and the profile of nonlinear dissipative structures, i.e., stationary traveling waves which describe the final stage of the evolution of thermal and electromagnetic perturbations in the resistive state of superconductors.

The evolution of thermal and electromagnetic perturbations in a superconductor is described by the nonlinear one-dimensional heat conduction equation [3]

$$\nu\frac{dT}{dt} = \kappa\frac{d^2T}{dx^2} + \mathbf{JE}, \tag{1}$$

the Maxwell equation

$$\frac{4\pi}{c^2}\frac{d\mathbf{j}}{dt} = \frac{d^2\mathbf{E}}{dx^2}, \tag{2}$$

and their related equation of the critical state

$$\mathbf{j} = \mathbf{j}_c(T, \mathbf{H}) + \mathbf{j}_r(\mathbf{E}), \tag{3}$$

where ν and κ are the heat capacity and thermal conductivity coefficients, respectively; and $\mathbf{j}_c$ and $\mathbf{j}_r$ are the densities of the critical and resistive currents, respectively.

The model under consideration is essentially nonlinear, because the right-hand side of Eq. (1) contains a term describing the Joule heat generation in the region of the resistive phase. An exact solution to the essentially nonlinear parabolic partial differential equations (1)–(3) does not exist.

Note that the evolution of perturbations of the temperature $T(x, t)$ and the fields $E(x, t)$ and $H(x, t)$ is determined by the equation of critical state (3). Because of considerable analytical difficulties, we will restrict ourselves to considering the Bean model [4] and assume that the critical current density is independent of the external magnetic field; i.e., $dj_c/dH = 0$. The dependence $j_c(T)$ is described by the relationship $j_c(T) = j_0 - a(T - T_0)$, where T_0 is the initial temperature of the superconductor and the quantity $a = |dj_c/dT|_{T = T_0}$ describes the thermally activated weakening of the Abrikosov vortex pinning by lattice defects. The dependence $j(T)$ in the region of the electric field $E > E_f$ (E_f is the boundary of the linear section in the current–voltage characteristic of the superconductor) can be approximated by a piecewise linear function $j(E) \sim \sigma_f E$, where σ_f is the effective conductivity. The dependence $j(E)$ is essentially nonlinear in the flux creep region $E < E_f$ [5]. Here, we will consider a perturbation with a suf-

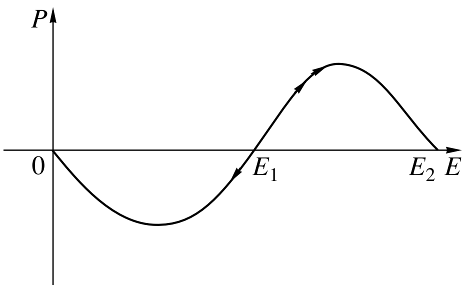

Fig. 1. Phase portrait of Eq. (10).

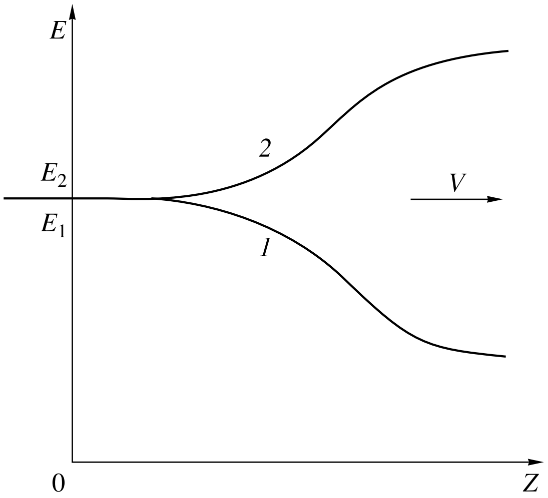

Fig. 2. Nonlinear waves of two types.

ficiently high amplitude ($E > E_f$) and use the linear dependence $j_r(E)$.

We seek a solution to the initial set of equations as a function of the new self-simulated variable $\xi(x, t)$; that is,

$$T = \Theta[\xi(x, t)], \quad E = E[\xi(x, t)], \quad H = H[\xi(x, t)]; \quad \xi = x - Vt, \tag{4}$$

which describes a traveling wave that moves with a constant velocity V along the x axis [3].

After substitution of relationships (4) into the initial set of equations and performing a trivial differentiation, we obtain the following set of equations for the variable $\xi(x, t)$:

$$-\nu V\frac{dT}{d\xi} = \frac{d}{d\xi}\left[\kappa\frac{dT}{d\xi}\right] + jE, \tag{5}$$

$$\frac{dE}{d\xi} = -\frac{4\pi V}{c^2}j, \tag{6}$$

$$E = \frac{V}{c}H. \tag{7}$$

The corresponding thermal and electrodynamic boundary conditions for Eqs. (5)–(7) have the form

$$T(\xi \longrightarrow +\infty) = T_0, \quad \frac{dT}{dx}(\xi \longrightarrow -\infty) = 0, \quad E(\xi \longrightarrow +\infty) = 0, \quad E(\xi \longrightarrow -\infty) = E_e. \tag{8}$$

It should be noted that inclusion of the temperature dependences of the parameters κ and ν substantially complicates analytical calculations of the wave evolution dynamics that is described by the set of Eqs. (5)–(7). In most cases, changes in the local values of these parameters in the sample can be considered small compared to the characteristic scale of temperature variations. Hence, we can take these parameters to be constant. Indeed, the investigation revealed that the thermal conductivity almost does not affect the character of the stationary wave propagation. This stems from the fact that the thermal flux $\kappa(dT/d\xi)$ vanishes at stationary points of the system at $\xi \longrightarrow \pm\infty$. However, the temperature dependence of the heat capacity should be taken into account. Such a dependence is represented as $\nu \approx \nu_0(T/T_0)$ over a wide range of temperatures [5].

By eliminating variables $T(x, t)$ and $H(x, t)$ with the aid of relationships (5) and (7) and employing the boundary conditions (8), we obtain a differential equation for the E wave distribution:

$$\frac{d^2E}{dz^2} - 2\pi\frac{\nu T_0}{E_\kappa}\frac{V^2}{c^2}\left[\left(1 + \frac{\sigma_f E}{aT_0} + \frac{c^2}{4\pi a V T_0}\frac{dE}{dz}\right)^4 - 1\right] + \beta\tau\frac{dE}{dz} = \frac{E^2}{2E_\kappa}. \tag{9}$$

Here, we introduced the following dimensionless parameters:

$$z = \frac{\xi}{L}, \quad L = \frac{cH_e}{4\pi j_0}, \quad E_\kappa = \frac{\kappa}{aL^2},$$

$$\beta = \frac{Vt_\kappa}{L}, \quad \tau = \frac{4\pi\sigma_f\kappa}{c^2\nu}, \quad t_\kappa = \frac{\nu L^2}{\kappa},$$

where L is the depth of the magnetic field penetration into the sample and t_κ is the thermal time of the problem.

According to the qualitative theory [6], the equilibrium states are found from the condition

$$2\pi\nu_0 T_0\frac{V^2}{c^2}\left[\left(1 + \frac{\sigma_f E}{aT_0}\right)^4 - 1\right] = E^2. \tag{10}$$

An evident property of set (10) is the absence of closed curves that are fully composed of the phase trajectories in the phase plane (E, $dE/d\xi$). The proof of this statement can be based on the Bendixson criterion [7]. The number of stationary points (one or three) and their type are determined by the parameter

$$P = 2\pi\nu_0 T_0 \frac{v^2}{c^2}. \tag{11}$$

The three equilibrium points $E = 0$, $E = E_1$, and $E = E_2$ correspond to the condition $P < P_k = 1/2$ (Fig. 1). There is only one singular point $E_0 = 0$ at $P > P_k$. The parabola and the quartic curve in Eq. (10) are tangent at $P = P_k$; i.e., this condition corresponds to the coincidence $E_1 = E_2 = E^* = 6/7(aT_0/\sigma_f)$.

The direct solution of Eq. (10) yields the following waves:

$$(1)\quad E_{1,2} = E^*[1 + 2.2(P_k - P)^{1/2}], \quad \left(\frac{P_k - P}{P_k}\right) \ll 1; \tag{12}$$

$$(2)\quad E_1 = 8\pi\frac{\sigma_f \nu_0}{a}\frac{v^2}{c^2}, \quad E_2 = (2\pi)^{1/2}\frac{\sigma_f^2 \nu_0^2}{a^2}\frac{c}{v} \gg E_1,$$

$$P_k \gg P.$$

Analysis of the phase plane shows that the points $E_0 = 0$ and $E = E_2$ are stable nodes and that $E = E_1$ is a saddle. In addition to the separatrix E_1E_0, set (10) has the separatrix E_1E_2 connecting the points E_1 and E_2 (Fig. 2). This means that two types of waves with amplitudes $\Delta E = E_1$ and $E_2 - E_1$ can exist in the superconductor. Evidently, wave *1* has an amplitude of the order E_k at $P \longrightarrow P_k$; its velocity is determined by equality (10) at $E = E_1$. Equation (10) has two stationary points at $P \ll P_k$: $E_0 = 0$ is a stable node and $E_1 = 2\beta^2\tau E_\kappa$ is a saddle.

The separatrix that connects these two equilibrium states corresponds to a "difference"-type solution with amplitude E_e, which is related to the wave velocity v_E and the wave front width Δz by the following equations:

$$v_E = \frac{L}{t_\kappa}\left[\frac{E_e}{2\tau E_\kappa}\right]^{1/2}, \tag{13}$$

$$\Delta z = 16\frac{1 + \tau}{\tau^{1/2}}\left[\frac{E_\kappa}{E_e}\right]^{1/2}. \tag{14}$$

Wave *2* has a small amplitude at $P \longrightarrow P_k$,

$$\frac{\Delta E}{E_k} = 4.4(P_k - P)^{1/2} \ll 1, \tag{15}$$

and its velocity is inversely proportional to the amplitude at $P \ll P_k$. Such an exotic dependence of v_E on $\Delta E = E_e$ most likely means that the waves of this type are unstable. Note that observation of the second-type waves becomes possible in finite-sized samples with asymmetric boundary conditions.

In conclusion, it should be noted that the above investigations prove the possibility of applying the results obtained to high-temperature superconductors cooled to liquid-nitrogen temperatures ($T = 77$ K), providing that the values of the physical parameters of the sample are known.

REFERENCES

1. V. A. Al'tov, V. B. Zenkevich, M. G. Kremlev, and V. V. Sychev, *Stabilization of Superconducting Magnetic Systems* (Énergoatomizdat, Moscow, 1984).
2. A. V. Gurevich and R. G. Mints, *Heat Autowaves in Normal Metals and Superconductors* (Nauka, Moscow, 1987).
3. I. L. Maksimov, Yu. N. Mastakov, and N. A. Taĭlanov, Fiz. Tverd. Tela (Leningrad) **28** (8), 2323 (1986) [Sov. Phys. Solid State **28**, 1300 (1986)].
4. C. P. Bean, Phys. Rev. Lett. **8** (6), 250 (1962).
5. R. G. Mints and A. L. Rakhmanov, *Instabilities in Superconductors* (Nauka, Moscow, 1984).
6. V. I. Karpman, *Non-Linear Waves in Dispersive Media* (Nauka, Moscow, 1973; Pergamon, Oxford, 1975).
7. A. A. Andronov, A. A. Vitt, and S. É. Khaĭkin, *Theory of Oscillators* (Nauka, Moscow, 1981; Pergamon, Oxford, 1966).

Translated by M. Lebedkin

Physics of the Solid State, Vol. 43, No. 3, 2001, pp. 416–419. Translated from Fizika Tverdogo Tela, Vol. 43, No. 3, 2001, pp. 399–402.
Original Russian Text Copyright © 2001 by Korshunov, Ovchinnikov.

METALS AND SUPERCONDUCTORS

The Effective Hamiltonian of the Singlet–Triplet Model for Copper Oxides

M. M. Korshunov* and S. G. Ovchinnikov**
**Krasnoyarsk State University, Krasnoyarsk, 660062 Russia*
e-mail: kite ent co@xoommail.com
***Kirenskiĭ Institute of Physics, Siberian Division, Russian Academy of Sciences,*
Akademgorodok, Krasnoyarsk, 660036 Russia
e-mail: sgo@post.krascience.rssi.ru

Received June 20, 2000

Abstract—The effective Hamiltonian for a realistic multiband *p–d* model is developed. In the case of electron doping, the Hamiltonian coincides with that for the standard *t–J* model. For hole doping, the singlet–triplet *t–J* model takes place. © *2001 MAIK “Nauka/Interperiodica”.*

In recent years, more and more attention has been paid to investigations of the electronic structure and properties of systems with strong electron correlations (SEC), as an understanding of the processes occurring in these systems is the key in the explanation of the phenomenon of high-temperature superconductivity (HTSC). It is widely believed that the most interesting in this respect is the consideration of a CuO_2 layer, as such high values of the critical temperatures T_c of compounds containing this layer are most likely to be due to the presence of this layer and to the transformation of the electronic structure in it caused by doping. One of the problems appearing here is to construct an adequate model which will make it possible to describe the main HTSC properties completely enough.

The aim of this work is to find the effective Hamiltonian for the multiband *p–d* model [1] in the case of the presence of two-particle singlet and triplet states in the system in addition to the one-particle states. It is shown that this singlet–triplet model is asymmetric with respect to electron and hole doping.

The single-band Hubbard model [2] is one of the simplest models describing, at the same time, the main low-energy properties of the systems with SEC. However, the chemical composition of copper oxides can in no way be taken into account in this model. This drawback was partly eliminated in the three-band *p–d* model, which is a generalization of the Hubbard model for the CuO_2 layer [3]. A lot of spectral methods with high excitation energies, such as x-ray spectroscopy and x-ray electron spectroscopy, have been described in the framework of this model.

There are some essential points that still remain unclear. One point is the difference in behavior between the electron- and hole-doped systems. The issue is that a spin exciton, associated with singlet–triplet excitation of the two-hole term, is created in the hole-doped systems. This excitation is absent in the electron-doped systems [4]. Another fact which is ignored by the three-band model is the nonzero occupancy of d_{z^2} orbitals, which is evident from experiments on the polarization dependence of CuL_3 x-ray absorption spectra [5]. The correlation between the T_c and the occupancy of d_{z^2} orbitals was also detected there. Taking this into account, it can be stated that a more realistic model of the CuO_2 layer must involve $d_{x^2-y^2}$ and d_{z^2} orbitals of copper, as well as p_x and p_y orbitals of each oxygen ion. When considering the systems which involve the apical oxygen, it is necessary to account for the p_z orbital of oxygen. A similar model was proposed in [1], the Hamiltonian of which has the form

$$H_{p-d} = \sum_r H_d(r) + \sum_i H_p(i) + \sum_{\langle r, i\rangle} H_{pd}(r, i) + \sum_{\langle i, j\rangle} H_{pp}(i, j), \tag{1}$$

where

$$H_d(r) = \sum_{\lambda, \sigma}\Bigg[\varepsilon_\lambda^d d_{\lambda r\sigma}^+ d_{\lambda r\sigma} + \frac{U_\lambda^d}{2} n_{\lambda r}^\sigma n_{\lambda r}^{\bar\sigma} - \sum_{\lambda', \sigma'}\Bigg(J_{\lambda\lambda'}^{dd} d_{\lambda r\sigma}^+ d_{\lambda r\sigma'} d_{\lambda' r\sigma'}^+ d_{\lambda' r\sigma} - \sum_{r'} V_{\lambda\lambda'}^{dd} n_{\lambda r}^\sigma n_{\lambda' r'}^{\sigma'}\Bigg)\Bigg],$$

$$H_p(i) = \sum_{\alpha,\sigma}\Bigg[\varepsilon^p_\alpha \overset{+}{p}_{\alpha i\sigma} p_{\alpha i\sigma} + \frac{U^p_\alpha}{2} n^\sigma_{\alpha i} n^{\bar\sigma}_{\alpha i}$$

$$-\sum_{\alpha',\sigma'}\left(J^{pp}_{\alpha\alpha'} \overset{+}{p}_{\alpha i\sigma} p_{\alpha i\sigma'} \overset{+}{p}_{\alpha' i\sigma'} p_{\alpha' i\sigma} - \sum_{i'} V^{pp}_{\alpha\alpha'} n^\sigma_{\alpha i} n^{\sigma'}_{\alpha' i'}\right)\Bigg],$$

$$H_{pd}(r,i) = \sum_{\alpha,\lambda,\sigma,\sigma'}((t^{pd}_{\lambda\alpha} \overset{+}{p}_{\alpha i\sigma} d_{\lambda r\sigma} + \text{H.c.}) + V^{pd}_{\alpha\lambda} n^\sigma_{\alpha i} n^{\sigma'}_{\lambda r}),$$

$$H_{pp}(i,j) = \sum_{\alpha,\beta,\sigma}(t^{pp}_{\alpha\beta} \overset{+}{p}_{\alpha i\sigma} p_{\beta j\sigma} + \text{H.c.}).$$

Here, r and i are sites of copper and oxygen; $\lambda = \{d_{x^2-y^2}, d_{z^2}\}$ and $\alpha = \{p_x, p_y, p_z\}$ are orbital indices for a given site of copper and oxygen, respectively; ε^d and ε^p are the energies of $d_{x^2-y^2}$ and d_z^2 holes on copper and of the p_x, p_y, p_z states of oxygen, measured from the level of the chemical potential μ; U^d and U^p are the on-site Coulomb interactions; t^{pd} is the transfer integral between the nearest neighbors of copper and oxygen; t^{pp} is the oxygen–oxygen transfer integral; V^{dd}, V^{pp}, and V^{pd} are the interatomic Coulomb interactions; and J^{dd} and J^{pp} are the exchange interaction integrals.

As can be seen, the Hamiltonian (1) accounts for all the main types of the relevant interactions in copper oxides. The simplest calculation in this model has been done for CuO_4 [4] and CuO_6 clusters [6] by the precise-diagonalization method. It has been shown that the energy difference between the two-particle singlet ${}^1A_{1g}$ and triplet ${}^3B_{1g}$ is intimately related to the involvement of the d_{z^2} orbitals. With this orbital neglected, it turns out that the triplet with energy ε_{2t} lies above the singlet with energy ε_{2S} by an amount of the order of 2 eV and, therefore, can be ignored in a low-energy description, which leads to the three-band model. However, as the energy of the d_{z^2} orbitals approaches the energy of the $d_{x^2-y^2}$ orbitals, the singlet–triplet splitting decreases, and, at certain values of the parameters, the crossover of the singlet and triplet occurs. A similar result was obtained for the CuO_6 cluster by the self-consistent-field method [7] and also by the perturbation theory [8]. This gives reason for a thorough investigation of the processes associated with the presence of not only the two-particle singlet in the system but also the triplet.

For copper oxides and, particularly, a CuO_2 layer, the CuO_6 cluster is the unit cell they have in common. This cell was considered in [9], where by using the cluster perturbation theory first stated in [10] the following Hamiltonian was obtained on the basis of Eq. (1):

$$H = \sum_f\left(\varepsilon_1\sum_\sigma X_f^{\sigma\sigma} + \varepsilon_{2S}X_f^{SS} + \varepsilon_{2t}\sum_M X_f^{tMtM}\right)$$

$$+\sum_{\langle f,g\rangle,\sigma}[t^{00}_{fg}X_f^{\sigma 0}X_g^{0\sigma} + 2\sigma t^{0b}_{fg}(X_f^{\sigma 0}X_g^{\bar\sigma S} + X_f^{S\bar\sigma}X_g^{0\sigma})$$

$$+ t^{bb}_{fg}X_f^{S\bar\sigma}X_g^{\bar\sigma S}] + \sum_{\langle f,g\rangle,\sigma} t^{aa}_{fg}(\sigma\sqrt{2}X_f^{t0\bar\sigma} - X_f^{t2\sigma\sigma}) \qquad (2)$$

$$\times(\sigma\sqrt{2}X_g^{\bar\sigma t0} - X_g^{\sigma t2\sigma}) + \sum_{\langle f,g\rangle,\sigma} t^{ab}_{fg}$$

$$\times[(\sigma\sqrt{2}X_f^{t0\bar\sigma} - X_f^{t2\sigma\sigma})(-\nu X_g^{0\sigma} + 2\sigma\gamma_b X_g^{\bar\sigma S}) + \text{H.c.}].$$

Here, the energies ε_1, ε_{2S}, and ε_{2t} are related to the level of the chemical potential μ and superscripts 0, a, and b on the transfer integral t_{fg} indicate the appearance of the quasiparticle in the lower (0), the upper singlet (b), and in the upper triplet (a) Hubbard bands.

In this case, the local basis is constituted by the functions which correspond to the no-hole and one-hole terms, namely, $|0\rangle$ for $n_h = 0$ and $|\sigma\rangle \equiv \{|\uparrow\rangle, |\downarrow\rangle\}$ for $n_h = 1$, and also to the two-hole terms with the singlet state (S) $|2\rangle \equiv |\downarrow, \uparrow\rangle$ and the triplet state (t) $|tM\rangle \equiv \{|t0\rangle, |t2\sigma\rangle, |t2\bar\sigma\rangle\}$.

For this basis, the condition of its completeness is written as

$$X_i^{00} + \sum_\sigma X_i^{\sigma\sigma} + X_i^{SS} + \sum_M X_i^{tMtM} = 1. \qquad (3)$$

Using the Hamiltonian (2) as the original one, we can obtain an effective Hamiltonian of the singlet–triplet model by excluding the interband (between the lower and upper Hubbard bands) transitions from it. For this purpose, we use the method proposed in [11].

First, we define projection operators P_1 and P_2

$$P_1 = \left(X_i^{00} + \sum_\sigma X_i^{\sigma\sigma}\right)\left(X_j^{00} + \sum_\sigma X_j^{\sigma\sigma}\right). \qquad (4)$$

The operator P_2 can be determined from the condition for completeness of the basis of the projection operators

$$P_2 = 1 - P_1. \qquad (5)$$

It is clear that P_1 and P_2 follow the rule for multiplication of projection operators

$$P_n P_m = \delta_{mn} P_n. \qquad (6)$$

Left and right multiplications of the Hamiltonian (2) by the operators P_n yield the following four relationships:

$$P_1HP_1 = \varepsilon_1\sum_{i,\sigma}X_i^{\sigma\sigma} + \sum_{\langle i,j\rangle,\sigma} t_{ij}^{00}X_i^{\sigma 0}X_j^{0\sigma}, \tag{7}$$

$$\begin{aligned}P_1HP_2 = \sum_{\langle i,j\rangle,\sigma}[2\sigma t_{ij}^{0b}X_i^{\bar{\sigma}S}X_j^{\sigma 0}\\ -\nu t_{ij}^{ab}(\sigma\sqrt{2}X_i^{\bar{\sigma}t0} - X_i^{\sigma t2\sigma})X_j^{\sigma 0}],\end{aligned} \tag{8}$$

$$P_2HP_1 = (P_1HP_2)^+, \tag{9}$$

$$\begin{aligned}P_2HP_2 = \sum_i\left(\varepsilon_{2S}X_i^{SS} + \varepsilon_{2t}\sum_M X_i^{tMtM}\right) + \sum_{\langle i,j\rangle,\sigma} t_{ij}^{bb}X_i^{S\bar{\sigma}}X_j^{\bar{\sigma}S}\\ + \sum_{\langle i,j\rangle,\sigma} t_{fg}^{aa}(\sigma\sqrt{2}X_i^{t0\bar{\sigma}} - X_i^{t2\sigma\sigma})(\sigma\sqrt{2}X_j^{\bar{\sigma}t0} - X_j^{\sigma t2\sigma})\\ + \sum_{\langle i,j\rangle,\sigma} t_{ij}^{ab}2\sigma\gamma_b[X_i^{S\bar{\sigma}}(\sigma\sqrt{2}X_j^{\bar{\sigma}t0} - X_j^{\sigma t2\sigma}) + \text{H.c.}].\end{aligned} \tag{10}$$

As can be seen from the above relationships, P_1HP_1 and P_2HP_2 describe the processes in the lower and upper Hubbard bands, respectively. The interband transitions are described by the terms P_1HP_2 and P_2HP_1.

The interband transitions may be further excluded by using an operator method of the perturbation theory. We present the Hamiltonian in the form

$$H_\eta = H' + \eta H'', \tag{11}$$

where $H' = P_1HP_1 + P_2HP_2$, $H'' = P_1HP_2 + P_2HP_1$, and η is a formal parameter (we ultimately put it equal to unity). The essence of this method is in the following: applying the canonical transformation

$$\tilde{H} = \exp(-i\eta F)H\exp(i\eta F), \tag{12}$$

we can choose the operator F such that the terms of the Hamiltonian $\tilde{H}$ that are linear in η, namely, the terms responsible for the interband transitions, will be equal to zero.

As can be readily shown, the requirement imposed brings about the following equation for the operator F:

$$H'' + i[H', F] = 0. \tag{13}$$

Then, $\tilde{H}$ is defined as

$$\tilde{H} = \tilde{H}(\eta = 1) = H' + \frac{1}{2}i[H'', F]. \tag{14}$$

Omitting the solutions of Eqs. (13) and (14) presented in [11], we obtain as a result

$$\tilde{H} = P_1HP_1 + P_2HP_2 = \frac{1}{E_{\text{ct}}}[P_1HP_2, P_2HP_1], \tag{15}$$

where $E_{\text{ct}} = \langle P_2HP_2\rangle - \langle P_1HP_1\rangle$ is the charge-transfer energy between the lower and upper Hubbard bands.

When studying the low-energy processes, one can consider the processes in the lower and upper Hubbard bands separately, because there is an appreciable energy gap (2–4 eV) between them.

For the systems with electron doping (n-type systems), the Fermi level ε_F is situated in the lower Hubbard band. In this case, the influence of the upper band can be ignored resulting in the common t–J model (see, e.g., [11, 12]). The corresponding Hamiltonian has the form

$$\begin{aligned}H_{t-J} = \sum_{i,\sigma}\varepsilon_1X_i^{\sigma\sigma} + \sum_{\langle i,j\rangle,\sigma}t_{ij}^{00}X_i^{\sigma 0}X_j^{0\sigma}\\ + \sum_{\langle i,j\rangle,\sigma}J_{ij}\left(\mathbf{S_iS_j} - \frac{1}{4}n_in_j\right),\end{aligned} \tag{16}$$

with J_{ij} being the exchange integral

$$J_{ij} = 4\frac{(t_{ij}^{0b})^2}{E_{ct}}. \tag{17}$$

It has also been accounted for that

$$\mathbf{S_iS_j} - \frac{1}{4}n_in_j = \frac{1}{2}\sum_\sigma(X_i^{\sigma\bar{\sigma}}X_j^{\bar{\sigma}\sigma} - X_i^{\sigma\sigma}X_j^{\bar{\sigma}\bar{\sigma}}).$$

For the systems with hole doping (p-type systems), the ε_F is situated in the upper band. In this case, we have a model which takes into account the transitions involving the two-particle singlet and triplet. We shall further refer to this model as the singlet–triplet model.

By applying the commutation relations for the Hubbard operators and omitting the three-center terms, we find the Hamiltonian of the singlet–triplet model in the form

$$\tilde{H} = H_0 + H_t + H_J, \tag{18}$$

where H_t is the kinetic part of the Hamiltonian and H_J is the term involving all processes associated with the exchange interaction.

In an explicit form, these terms are written as

$$H_0 = \sum_i\left(\varepsilon_1\sum_\sigma X_i^{\sigma\sigma} + \varepsilon_{2S}X_i^{SS} + \varepsilon_{2t}\sum_M X_i^{tMtM}\right),$$

$$\begin{aligned}H_t = \sum_{\langle i,j\rangle,\sigma}t_{ij}^{bb}X_i^{S\bar{\sigma}}X_j^{\bar{\sigma}S}\\ + \sum_{\langle i,j\rangle,\sigma}t_{fg}^{aa}(\sigma\sqrt{2}X_i^{t0\bar{\sigma}} - X_i^{t2\sigma\sigma})(\sigma\sqrt{2}X_j^{\bar{\sigma}t0} - X_j^{\sigma t2\sigma})\\ + \sum_{\langle i,j\rangle,\sigma}t_{ij}^{ab}2\sigma\gamma_b[X_i^{S\bar{\sigma}}(\sigma\sqrt{2}X_j^{\bar{\sigma}t0} - X_j^{\sigma t2\sigma}) + \text{H.c.}],\end{aligned}$$

$$H_J = \frac{1}{2}\sum_{\langle i,j\rangle,\sigma}(J_{ij}+\delta J_{ij})\left(\mathbf{S_i}\mathbf{S_j}-\frac{1}{4}n_i n_j\right) - \frac{1}{2}\sum_{\langle i,j\rangle,\sigma}\delta J_{ij}X_i^{\sigma\sigma}X_j^{\sigma\sigma}.$$

Here, δJ_{ij} is a correction to the exchange integral J_{ij} in Eq. (17) due to the contribution from the triplet

$$\delta J_{ij} = 2\nu^2\frac{(t_{ij}^{ab})^2}{E_{\mathrm{ct}}}. \quad (19)$$

In closing, it should be noted that the obtained effective Hamiltonian of the singlet–triplet model in Eq. (18) is the generalization of the *t–J* model to the case of the presence of the two-particle triplet in the system. However, the allowance for this triplet results in quite appreciable changes in the Hamiltonian, such as the renormalization of the exchange integral in Eq. (17) and also the appearance of the term of the “density–density” type, $X_i^{\sigma\sigma}X_j^{\sigma\sigma}$.

A more important feature of the singlet–triplet model is the asymmetry regarding the systems of the *n* and *p* type. This effect was experimentally observed. In particular, the fact that holes suppress antiferromagnetism more strongly than electrons do was observed in $La_{2-x}Sr_xCuO_4$ in contrast to $Nd_{2-x}Ge_xCuO_4$ [13]. The conditions for the existence of the superconducting phases are also different for the hole and electron superconductors. Restricting ourselves to only the electronic mechanisms of superconductivity, we also see that the spin-fluctuation mechanism, known for the *t–J* model (see review [14]), operates in *n*-type superconductors, while, in addition to the spin-fluctuation mechanism of the creation of the pairs, the pairing due to the singlet–triplet transitions can occur in *p*-type superconductors with the complicated band structure at the top of the valence band described by the Hamiltonian H_t. A similar pairing mechanism was proposed for multiband metals as early as 1969 [15].

ACKNOWLEDGMENTS

This work was supported by the Federal Program “Integratsiya,” project no. A0019, and the RF State Program “Modern Problems in the Condensed Matter Physics,” “High-Temperature Superconductivity” section, grant no. 99019.

REFERENCES

1. Yu. B. Gaididei and V. M. Loktev, Phys. Status Solidi B **147**, 307 (1988).
2. J. C. Hubbard, Proc. R. Soc. London, Ser. A **276**, 238 (1963).
3. V. J. Emery, Phys. Rev. Lett. **58** (26), 2794 (1987).
4. S. G. Ovchinnikov, Pis’ma Zh. Éksp. Teor. Fiz. **64** (1), 23 (1996) [JETP Lett. **64**, 25 (1996)].
5. A. Bianconi, M. de Santis, A. di Cicco, *et al.*, Phys. Rev. B **38** (10), 7196 (1988).
6. V. A. Gavrichkov and S. G. Ovchinnikov, Fiz. Tverd. Tela (St. Petersburg) **40** (2), 184 (1998) [Phys. Solid State **40**, 163 (1998)].
7. H. Kamimura and M. Eto, J. Phys. Soc. Jpn. **59**, 3053 (1990).
8. H. Eskes, L. H. Tjeng, and G. A. Sawatzky, Phys. Rev. B **41** (1), 288 (1990).
9. V. A. Gavrichkov, S. G. Ovchinnikov, A. A. Borisov, and E. G. Goryachev, Zh. Éksp. Teor. Fiz. **118**, 422 (2000) [JETP **91**, 369 (2000)].
10. S. G. Ovchinnicov and I. S. Sandalov, Physica C (Amsterdam) **161**, 607 (1989).
11. K. A. Chao, J. Spalek, and A. M. Oles, J. Phys. C **10**, 271 (1977).
12. L. N. Bulaevskiĭ, É. L. Nagaev, and D. I. Kholmskiĭ, Zh. Éksp. Teor. Fiz. **54** (5), 1562 (1968) [Sov. Phys. JETP **27**, 836 (1968)].
13. B. Keimer, N. Belk, R. J. Birgeneau, *et al.*, Phys. Rev. B **46** (21), 14034 (1992).
14. Yu. A. Izyumov, Usp. Fiz. Nauk **169** (3), 225 (1999).
15. B. T. Geĭlikman and V. Z. Kresin, Usp. Fiz. Nauk **99** (1), 51 (1969) [Sov. Phys. Usp. **12**, 620 (1970)].

Translated by N. Kovaleva

Physics of the Solid State, Vol. 43, No. 3, 2001, pp. 420–429. Translated from Fizika Tverdogo Tela, Vol. 43, No. 3, 2001, pp. 403–413.
Original Russian Text Copyright © 2001 by Kuleev, Arapova.

SEMICONDUCTORS AND DIELECTRICS

Spatial Ordering and Interference Scattering of Electrons by a System of Mixed-Valence Iron Ions in HgSe : Fe Crystals

I. G. Kuleev and I. Yu. Arapova
Institute of Metal Physics, Ural Division, Russian Academy of Sciences, ul. S. Kovalevskoĭ 18, Yekaterinburg, 620219 Russia
e-mail: kuleev@imp.uran.ru

Received May 16, 2000

Abstract—The spatial ordering of charges in mixed-valence systems is considered. The dependence of the correlation sphere radius on the iron impurity content is obtained from the balance equation for the *d* holes and neutral centers in the short-range order cluster of a Fe^{3+} ion. The penetrating hard sphere model is proposed for the rigorous description of the spatial ordering in mixed-valence systems and the calculation of correlation functions. *© 2001 MAIK “Nauka/Interperiodica”.*

1. INTRODUCTION

Experimental investigations of HgSe : Fe crystals (see reviews [1, 2]) showed that the anomalous dependences of kinetic characteristics, such as the conductivity [3, 4], thermopower [5], longitudinal and transverse Nernst–Ettingshausen effects [6–9], and others, on the iron impurity concentration n_{Fe} and the temperature T are determined by the specific features of electron scattering by a spatially correlated system of mixed-valence iron ions. The study of spatial ordering is of considerable importance for the interpretation of the unusual physical properties and other mixed-valence systems [1–12].

Crystals HgSe : Fe are convenient model objects for investigating the role of interimpurity Coulomb correlations in mixed-valence systems. In these crystals, the mixed-valence Fe^{3+}–Fe^{2+} state is formed at concentrations $n_{Fe} > n^* = 4.5 \times 10^{18}$ cm^{-3} when the Fermi level reaches the iron d level ($\varepsilon_d = 0.21$ eV) and is fixed at it. [1]. A further increase in the iron impurity content does not affect the concentration of Fe^{3+} ions ($n_+ = n^*$) and leads only to an increase in the concentration of Fe^{2+} ions which are neutral in the lattice ($n_0 = n_{Fe} - n_+$). In the system of Fe^{2+} and Fe^{3+} ions with the same energy, positive charges on iron ions (*d* holes) can be redistributed over lattice sites occupied by iron ions. Therefore, the Coulomb repulsion between *d* holes in mixed-valence systems results in spatial correlations in their arrangement: the higher the iron impurity concentration n_{Fe}, the larger the number of free sites for the redistribution of *d* holes and the higher the degree of ordering of the correlated system of Fe^{3+} ions. The spatial ordering of Fe^{3+} ions brings about a change in the character of electron scattering by the correlated system of Fe^{3+} ions and in low-temperature anomalies of the thermogalvanomagnetic effects in HgSe : Fe crystals [2–9].

The change in the Coulomb energy with an increase in the degree of ordering of *d* holes was analyzed in [13]. It was proved that the Coulomb repulsion primarily results in an increase in the distance between the closest spaced *d* holes, which provides the maximum gain in the free energy. Hence, a correlation sphere of radius r_c is formed around each Fe^{3+} ion. This sphere is free of other *d* holes. These holes pass into a spherical layer in the region $r_c < r < r_1$, where r_1 is the radius of the first coordination sphere for a perfect face-centered close packing of Fe^{3+} ions (for the Coulomb repulsion, the face-centered close packing possesses the minimum free energy). This redistribution of charges in systems of mixed-valence iron ions furnishes a means for approximating the system of Fe^{3+} ions by a system of hard spheres with the diameter $d = r_c$. In the framework of this model, Fe^{3+} ions cannot be separated by distances less than the hard sphere diameter. The degree of ordering in the hard sphere system is determined by the packing parameter $\eta = (\pi n_+ d^3)/6$, which is equal to the ratio between the volume occupied by hard spheres and the total volume of the system.

In order to describe the spatial ordering of Fe^{3+} ions, Wilamowski *et al.* [14] proposed the short-range correlation model (SRCMI) which is based on the approximation of the pair correlation function by a step function. As was shown in [3], the SRCMI variant of the short-range correlation model is limited by weak interimpurity correlations. Another variant of the short-range correlation model (SRCMII), which is valid for arbitrary magnitudes of Coulomb correlations in the system of Fe^{3+} ions, was proposed in [3]. The latter model made it possible to calculate quantitatively the dependence of the electron mobility $\mu(n_{Fe})$ over a wide range of iron concentrations. The calculated dependence of the mobility was in good agreement with the experimental data. This allowed the authors to determine the empirical dependence of the packing parameter [the correlation sphere radius $r_c(n_{\mathrm{Fe}})$] on the iron impurity content. The SRCMII model was substantiated in [13, 15].

Within the same model, the spatial ordering of Fe^{3+} ions in the mixed-valence system of HgSe : Fe crystals was treated in [16]. However, consideration was given to a nonaveraged short-range order cluster at $n_0 < n_+$ when the value of $r_c(n_{\mathrm{Fe}})$ is limited by the number of free sites n_0 in the spherical layer $r_c < r < r_1$. The dependence of the correlation sphere radius on the iron impurity content, which was obtained in [16], turned out to be considerably weaker than those derived in [2, 3, 17]. Reasoning from this discrepancy, the author of [16] concluded that the results of calculations carried out in [2, 3, 17] are invalid. In fact, the situation is quite the opposite. Only one configuration of the short-range order cluster out of an infinitely large number of possible configurations was taken into account in analysis of the spatial ordering in the system of mixed-valence iron ions in [16]. Below, it will be shown that the statistical weight of this configuration in the formation of the correlation sphere is equal to zero. In Section 2, we consider the balance equation for the *d* holes and neutral centers that participate in the formation of the correlation sphere and obtain the dependence of the correlation sphere radius $r_c(n_{\mathrm{Fe}})$. It is shown the Coulomb repulsion of positive charges on iron ions leads to the correlated arrangement of neutral centers with respect to charged centers. Contrary to the inference made in [16], this is responsible for the interference scattering of electrons. In this case, the reciprocal of the electron relaxation time is not an additive sum of contributions from neutral and charged centers. The method for calculating the partial distribution functions for a system of mixed-valence ions within the penetrating hard sphere model is proposed in Section 3. In Section 4, we discuss the dependence of the electron mobility $\mu(n_{\mathrm{Fe}})$ in the framework of both the model proposed in our earlier works [3, 13, 17] and the concepts advanced in [16].

2. MODEL DESCRIPTION OF SPATIAL ORDERING IN A SYSTEM OF MIXED-VALENCE IRON IONS

Let us consider the spatial ordering in the system of mixed-valence ions in HgSe : Fe crystals. Assume that iron ions with the concentration $n_{\mathrm{Fe}} > n_+$ (n_+ is the concentration of Fe^{3+} ions or *d* holes) are randomly distributed over lattice sites. In the absence of the Coulomb repulsion between *d* holes, the subsystems of charged and neutral centers are spatially distributed in a chaotic way. These subsystems can be treated as statistically independent. It is assumed that the temperature T is equal to 0, and vacant (Fe^{3+}) and filled (Fe^{2+}) *d* states of iron impurities have the same energy. At $t = -\infty$, we adiabatically slowly switch on the Coulomb repulsion $[U(t) = \sum_{i,j}\exp(-\varepsilon t)U(R_{i,j})]$ between *d* holes, which can be redistributed over randomly arranged Fe^{2+} sites. At the instant $t = 0$ (in the presence of the Coulomb repulsion), a correlation sphere of radius r_c is formed around each Fe^{3+} ion. This sphere does not contain other *d* holes, which pass into the spherical layer region that corresponds to the first peak in the pair correlation function $g(r)$ ([13, Fig. 1]). Therefore, the dependence $r_c(n_{\mathrm{Fe}})$ should be found from the balance equation for *d* holes and neutral centers that participate in the transfers between the correlation sphere and the spherical layer.

Another scheme for determining the $r_c(n_{\mathrm{Fe}})$ dependence was proposed in [16]. The probability $W(n_+, r_c, r_1)$ of finding an iron impurity for which the nearest *d* holes are located in the spherical layer $r_c < r < r_1$ was introduced. It was assumed that the concentration n_+ of *d* holes can be represented in terms of this probability

$$n_+ = n_{\mathrm{Fe}}W(n_+, r_c, r_1). \tag{1}$$

It was argued that the probability of a correlated arrangement of particles $W(n_+, r_c, r_1)$ can be determined by considering a random distribution of particles in the system of mixed-valence iron ions (in the absence of Coulomb repulsion between *d* holes). The probability W_N that the subsystem composed of N particles occupying the volume V will be found in the system comprised of N_0 particles filling the volume V_0 can be obtained using the combinatorics [18]

$$W_N = \frac{N_0!}{N!(N_0-N)!}\left(\frac{V}{V_0}\right)^N\left(1-\frac{V}{V_0}\right)^{N_0-N}. \tag{2}$$

According to [16], substitution of $N = 0$, $V = V_c$, $V_0 = V_1$, and $N_0 = n_+V_1$ (where V_1 is the volume of the first coordination sphere) into relationship (2) gives the sought probability $W(n_+, r_c, r_1)$

$$W(n_+, r_c, r_1) = W_0 = \left(1-\frac{V_c}{V_1}\right)^{n_+V_1}, \tag{3}$$

where W_0 is the probability that no *d* holes occur in the volume V_c at a random distribution of particles. The basic equation of the theory developed in [16] is derived from formulas (1) and (3)

$$\eta(N_{\mathrm{Fe}}) = \frac{n_+V_c}{8} = \frac{N_+V_1}{8}\left[1-\left(\frac{n_+}{n_{\mathrm{Fe}}}\right)^{\frac{1}{n_+V_1}}\right]. \tag{4}$$

First and foremost, we note that N and N_0 in relationship (2) are integers [18], whereas N_0 in formula (3) is a fraction: $N_0 = \overline{N}_1 = n_+V_1 = 5.92$, where $\overline{N}_1 = \sum_{N=0}^{N_0} NW_N$ is the mean number of particles in the volume V_1. An interesting situation arises when calculating the mean number of particles $\overline{N}_c$ in the correlation sphere V_c with the use of formula (2) under the assumption that $N_0 = \overline{N}_1 = 5.92$: $\overline{N}_c = \sum_{N=0}^{\overline{N}_1} NW_N(V_c, V_1)$. In this case, the value of $\overline{N}_c = n_+V_c$ can be obtained only at $V_c \longrightarrow 0$

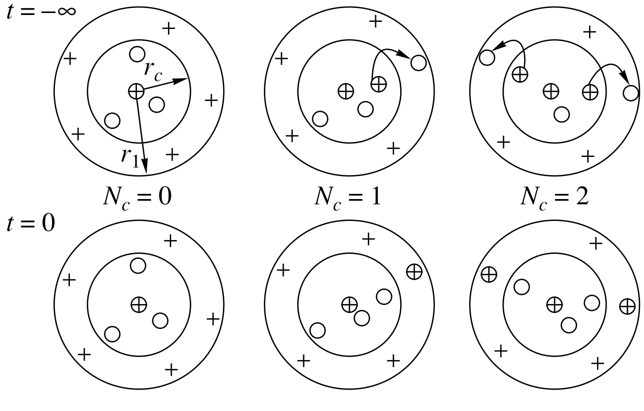

Fig. 1. A scheme for spatial redistribution of *d* holes at different fillings of a short-range order cluster. Circles are neutral centers, and crosses are charged centers.

and $N_0 = [\bar{N}_1]$. These misunderstandings are associated with introducing the notions of the density and the mean number of particles for the microscopic volumes V_c and V_1. The point is that, according to [18], V_0 and N_0 in formula (2) are macroscopic quantities (the total volume and the number of particles in it), for which it is possible to introduce the mean number of particles $\bar{N} = nV$ in the volume V. However, the probability W_N of finding N particles in the volume V at a specified value of $\bar{N}$ should be defined by the Poisson formula (see [18, formula (114.3)])

$$W_N = \frac{\bar{N}^N \exp(-\bar{N})}{N!}. \tag{5}$$

Then, $W_0 = \exp(-n_+V_c)$, and, from formula (3) derived in [16], we have

$$\eta(N_{\mathrm{Fe}}) = \frac{n_+V_c}{8} = \frac{1}{8}\ln\left(1 + \frac{n_0}{n_+}\right). \tag{4a}$$

At $n_0/n_+ \ll 1$, it follows from relationship (4a) [as from relationship (4)] that $\eta(N_{\mathrm{Fe}}) \sim 1/8n_0/n_+$. However, at $n_0 \gg n_+$, the packing parameter increases infinitely, whereas, according to the initial assumptions [16], the subsystem of *d* holes at $n_0/n_+ \longrightarrow \infty$ forms a Wigner crystal with a cubic structure and $\eta(N_{\mathrm{Fe}}) < 0.74$. These contradictions indicate that formula (3) derived in [16] is incorrect and gives no way of determining the $r_c(N_{\mathrm{Fe}})$ dependence. Below, we will show that the sole configuration with zero filling W_0 of the short-range order cluster, which was taken into consideration in [16], remains unchanged upon switching-on of the Coulomb repulsion between *d* holes and does not contribute to the formation of correlation spheres for the subsystem of charged centers.

For this purpose, we now analyze the balance of *d* holes and neutral centers that participate in the transfers between the correlation sphere of radius r_c and the spherical layer $r_c < r < r_1$ upon switching-on of the Coulomb repulsion between *d* holes. Let us draw the correlation sphere of radius r_c around each Fe^{3+} ion and determine the mean number $\bar{N}_c$ of *d* holes in the volume V_c and also the mean number of vacant sites (neutral centers) $\bar{N}_0$ for their redistribution in the spherical layer $V_1 - V_c = (4\pi/3)(r_1^3 - r_c^3)$ at the instant $t = -\infty$. At $n_0 < n_+$, the volume of the correlation sphere is limited from above by the number of vacant sites in the spherical layer $r_c < r < r_1$. In this case, at $t = 0$, *d* holes fill all the vacant sites in the spherical layer (the lattice sites occupied by Fe^{2+} ions). Therefore, the mean value of $V_c(n_{\mathrm{Fe}})$ at the given concentrations n_{Fe}, n_+, and n_0 can be found from the equality $\bar{N}_c = \bar{N}_0$. A scheme for this redistribution at different fillings of the short-range order cluster is displayed in Fig. 1. As can be seen from Fig. 1, the configuration with $N_c = 0$ remains unaltered after the switching-on of the Coulomb repulsion between *d* holes, and hence, its contribution to the balance equation will be equal to zero. According to [16], the probability $W(n_+, r_c, r_1)$ involves such configurations of the short-range order cluster in which a neutral ion Fe^{2+} is located at the center of the correlation sphere. It is clear that these configurations are nonphysical—they are unstable with respect to the switching-on of the Coulomb repulsion between *d* holes and should be excluded from consideration. Their inclusion leads to the fact that the probability $W(n_+, r_c, r_1)$ tends to zero when the concentration of neutral centers tends to infinity ($n_0 \longrightarrow \infty$) and the system of positive charges on iron ions tends to the maximum degree of ordering (in [16], this is a Wigner crystal with a cubic structure).

Unlike [16], we take the total volume of the system as the volume V_0 and $N_0 = n_{\mathrm{Fe}}V_0$, where $n_{\mathrm{Fe}} > 5 \times 10^{18}$ cm^{-3}. Then, the Poisson formula (5) can be used for the probability of different fillings of the correlation sphere V_c. Since $\sum_{N_c=0}^{\infty} N_c W_{N_c} = \bar{N}_c = n_+V_c$, for the mean number of *d* holes that leave the correlation sphere by the time $t = 0$, we obtain the same result as in [13]. In a similar manner, it can be demonstrated that the mean number of vacant sites $\bar{N}_0$ in the spherical layer is defined as

$$\bar{N}_0 = \sum_{N_0=0}^{\infty} N_0 W_{N_0} = n_0(V_1 - V_c). \tag{6}$$

From the equality $\bar{N}_c = \bar{N}_0$, with due regard for $r_c = d$, we find at $n_0 < n_+$

$$\eta(N_{\mathrm{Fe}}) = \frac{n_+V_c}{8} = \frac{1}{8}\Delta N_1\left(\frac{n_0}{n_{\mathrm{Fe}}}\right) \approx 0.74\left(\frac{n_0}{n_{\mathrm{Fe}}}\right), \qquad \Delta N_1 = n_+V_1. \tag{7}$$

These expressions allow for the fact that ΔN_1 for the face-centered close packing is approximately equal to

5.92. Out of 12 atoms that form the first coordination sphere, only 5.92 atoms leave the region with $r < r_1$. In the framework of the proposed scheme, it is possible to treat the problem rigorously at low concentrations of neutral centers $n_0 \ll n_+$. In this case, $\overline{N}_c \ll 1$ and $\overline{N}_0 \ll 1$, and, hence, we can restrict our consideration to the only configuration with $N_c = 1$. Then, from the equality

$$\overline{N}_c \exp(-\overline{N}_c) = \overline{N}_0 \exp(-\overline{N}_0), \qquad (8)$$

by expanding the exponents into a series in terms of a small parameter, we again have relationship (7). Thus, the obtained dependence of the packing parameter on the iron impurity concentration is identical to that derived in the work [13], in which analysis was performed for the averaged short-range order cluster.

In analysis of the spatial ordering of *d* holes in the system of mixed-valence iron ions, the author of [16] used a number of physically incorrect assumptions. First, in the probability $W(n_+, r_c, r_1)$, he included nonphysical configurations of the short-range order cluster, in which a Fe^{2+} ion neutral in the lattice is located at the center of the correlation sphere. Second, he accounted for the sole configuration W_0 of a random distribution of *d* holes (whose statistical weight in the formation of the correlation sphere is equal to zero) and equated it to the probability $W(n_+, r_c, r_1)$. Hence, the basic equation of the theory proposed in [16] is incorrect. The dependence of the packing parameter at $n_0 < n_+$ is approximately described by relationship (7). Our result agrees with the empirical equation obtained for the packing parameter in [3]. It should be noted that further reasoning in [16] about the estimate of the packing parameter, the effect of fluctuations on the correlation sphere radius, and the width of the peak of the first coordination sphere start from false assumptions which are supported neither by experimental data nor by theoretical calculations.

A superficial approach to the complex problem of the spatial ordering in the system of mixed-valence iron ions led the author of [16] to the categorical conclusion that the interference electron scattering by charged and neutral centers in the system of mixed-valence iron ions is absent. Unfortunately, any mathematical calculations that confirm this inference are absent in [16]. We do not intend to dispute the well-known fact that the structure factor is $S_{+0}(q) = 0$ and the interference electron scattering by neutral and charged centers is absent for a random distribution of ions in mixed-valence systems. However, the distribution of neutral centers (Fe^{2+} ions) in the mixed-valence system is not random [17]. Since *d* holes and neutral centers can only exchange places with each other, the sites of *d* holes in the correlation sphere will be occupied by neutral centers. Therefore, the local concentration of *d* holes in the correlation sphere is equal to zero and the concentration of neutral centers is determined by the total concentration of iron impurities (Fig. 2). In the region of the peak that corresponds to the first coordination sphere, at $n_0 < n_+$, the situation is the reverse: the concentration of neutral centers is equal to zero, and the concentration of *d* holes is determined by the total concentration of iron impurities. As a result, the function $g_{++}(r)$ that describes correlations in the system of charged centers (++) and the function $g_{+0}(r)$ that includes correlations in the system (+0) substantially deviate from unity, which corresponds to a chaotic distribution of particles in the short-range order cluster.

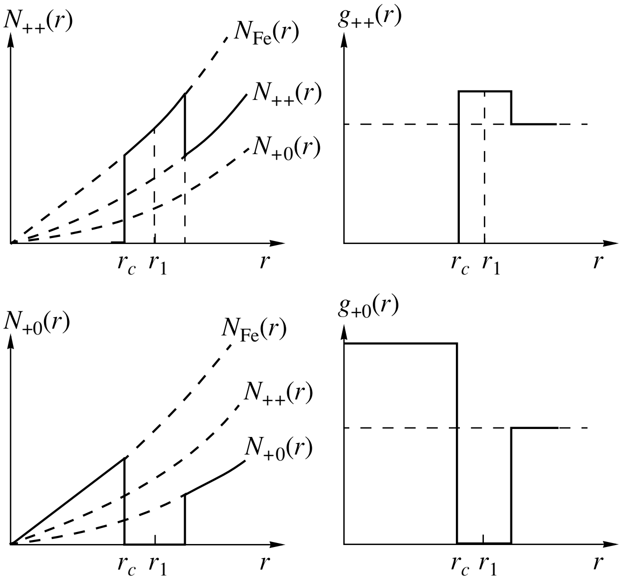

Fig. 2. A scheme for spatial redistribution of *d* holes in a short-range order cluster for one Fe^{3+} ion. $N_{Fe}(r)$, $N_{++}(r)$, and $N_{+0}(r)$ are the radial distribution functions of iron impurities, *d* holes, and neutral centers, respectively, for a random system (dashed lines) and a correlated mixed-valence Fe^{3+}–Fe^{2+} system (solid lines). $g_{++}(r)$ and $g_{+0}(r)$ are the pair correlation functions.

Figure 2 shows a scheme for the redistribution of *d* holes and neutral centers in the averaged short-range order cluster for one Fe^{3+} ion. In this case, it is possible to introduce the partial radial distribution functions $N_{\alpha\beta}(r) = 4\pi r^2 N_\beta g_{\alpha\beta}(r)$ [17]. The quantity $N_{\alpha\beta}(r)dr$ gives the number of particles of the $\beta(0+)$ sort in the spherical layer from r to $r + dr$ when a particle of the $\alpha(0+)$ sort is placed at the origin of the coordinates. For a chaotic distribution of particles, $g_{\alpha\beta}(r) = 1$ and the number of particles in the volume V_c is equal to the product of the concentration by volume. As is seen from Fig. 2, the region V_c in which the local concentration of neutral centers at $n_0 \ll n_+$ can appreciably exceed n_0 is formed near each charged center. Consequently, it can be stated that the Coulomb repulsion between *d* holes brings about an efficient attraction of neutral and charged centers. Thus, the Coulomb repulsion between *d* holes in the system of mixed-valence iron impurities results not only in the spatial ordering of charged centers (Fe^{3+} ions) but also in the correlated arrangement of neutral centers with respect to charged centers. Therefore, the redistribution of charges in the mixed-valence Fe^{3+}–Fe^{2+} system leads to the interference scattering and can considerably affect the kinetic characteristics of HgSe : Fe crystals.

3. PARTIAL DISTRIBUTION FUNCTIONS FOR A MIXED-VALENCE SYSTEM WITHIN THE PENETRATING HARD SPHERE MODEL

In order to describe rigorously the spatial ordering of ions in the mixed-valence Fe^{2+}–Fe^{3+} system, it is necessary to introduce four partial correlation functions $g_{\alpha\beta}(R_{12})$, which characterize the probability of finding an ion of the $\alpha(0, +)$ sort at the point $\mathbf{r}_2$ when an ion of the $\beta(0, +)$ sort is located at the point $\mathbf{r}_1$ (where $\mathbf{R}_{12} = \mathbf{r}_1 - \mathbf{r}_2$). It is unlikely that first-principles calculations of the $g_{\alpha\beta}(R_{12})$ functions with the use of Bogoliubov–Born–Green–Kirkwood–Yvon-like chains of equations can be applied to this system, because an equation for the fourth-order correlation function $g_{\alpha\beta}(\mathbf{r}_1, \mathbf{r}_2, \mathbf{r}_3, \mathbf{r}_4)$ should be uncoupled to obtain physically reasonable results even for single-component systems [19]. Therefore, in the present work, as in [3, 17], the $g_{\alpha\beta}(r)$ functions will be determined using a set of the Ornstein–Zernike equations and the Percus–Yevick approximation. The results obtained within this approximation are in good agreement with Monte Carlo and molecular dynamics calculations. This approach was successfully applied to the calculation of thermodynamic and kinetic properties for liquid metals and alloys [19]. The set of the Ornstein–Zernike equations relates the total correlation functions $h_{\alpha\beta} = g_{\alpha\beta} - 1$ to the direct correlation functions $c_{\alpha\beta}$

$$h_{\alpha\beta}(r_{12}) = c_{\alpha\beta}(r_{12}) + \sum_{\gamma = +,\,0} n_\gamma \int dr_3 c_{\alpha\beta}(r_{13}) h_{\alpha\beta}(r_{32}). \quad (9)$$

The Percus–Yevick approximation enables us to close the set of the Ornstein–Zernike equations by expressing the $c_{\alpha\beta}(r)$ functions (which describe direct correlations between particles) through the pair correlation functions

$$c_{\alpha\beta}(r_{12}) = \{1 - \exp(U_{\alpha\beta}(r_{12})/kT)\} g_{\alpha\beta}(r_{12}), \quad (10)$$

where $U_{\alpha\beta}(r_{12})$ is the interaction potential of the α and β ions located at the points $\mathbf{r}_2$ and $\mathbf{r}_1$, respectively. Substitution of relationship (10) into formula (9) gives the set of nonlinear integral equations whose rigorous solution was obtained only for a model system of a hard sphere mixture [20].

Before proceeding to the solution of the problem, we note a number of aspects which are determined by the specific features of the mixed-valence system.

(i) Iron impurity ions replace Hg^{2+} ions in the lattice sites, and their distribution over the sites as a whole is random. Therefore, there exists the minimum distance $\Delta R_{\min} \sim a_0$ (where $a_0 = 6.2 \times 10^{-8}$ cm is the lattice constant) between iron ions. Taking into account Coulomb correlations of iron ions at the temperature of sample preparation $T \sim 10^3$ K, we obtain $\Delta R_{\min} \sim 10^{-7}$ cm.

(ii) An important circumstance simplifying the problem is the fact that not all the $g_{\alpha\beta}(r)$ functions are independent. If an iron ion occupies the α site, this is a Fe^{2+} ion with the probability $x_0 = n_0/n_{Fe}$ or a Fe^{3+} ion with the probability $x_+ = n_+/n_{Fe}$. Since the total probability of finding either the Fe^{2+} ion or the Fe^{3+} ion at the given distance r from the considered ion of the α sort is equal to the probability of finding the iron impurity, the partial functions $g_{\alpha\beta}(r)$ obey the identities [19]

$$\begin{gathered} x_+ g_{++}(r) + x_0 g_{+0}(r) = G(r), \quad x_+ = \frac{n_+}{n_{Fe}}, \quad x_0 = \frac{n_0}{n_{Fe}}, \\ x_+ g_{0+}(r) + x_0 g_{00}(r) = G(r), \\ x_+ + x_0 = 1, \quad g_{0+}(r) = g_{+0}(r), \end{gathered} \quad (11)$$

where $G(r)$ is the pair correlation function of the distribution of iron impurity ions. By ignoring the occurrence of the minimum distance between iron impurity ions ($|r| > \Delta R_{\min}$), the function $G(r)$ can be taken equal to unity due to a random distribution of iron ions over the lattice sites. When the condition $|r| > \Delta R_{\min}$ is taken into account, the system of iron impurities can be approximated by a system of hard spheres with the diameter $d_f = \Delta R_{\min}$ and the packing parameter $\eta_f = (\pi n_{Fe} d_f^3)/6$. In this case, the $G(r)$ function is determined from the solution of the Ornstein–Zernike equation for a single-component system of hard spheres [21]

$$H_f(r) = c_f(r) + n_{Fe} \int d\mathbf{r}' c_f(r') H_f(|r - r'|). \quad (12)$$

This equation was solved in [21]. The direct correlation function has the form

$$-c(\rho) = \begin{cases} \alpha + \beta\rho + \gamma\rho^3, & \rho = r/d_f \le 1 \\ 0, & \rho > 1, \end{cases}$$
$$\alpha = \frac{(1 + 2\eta)^2}{(1 - \eta)^4}, \quad \beta = \frac{-6\eta(1 + 0.5\eta)^2}{(1 - \eta)^4}, \quad \gamma = \frac{1}{2}\eta\alpha. \quad (13)$$

Since the Coulomb repulsion between d holes at $n_0 > 0$ leads to the formation of correlation spheres in the subsystem of charged centers with $r_c > d_f$, the spatial ordering of charges in the mixed-valence system can be described within the penetrating hard sphere model [22, 23]. For a number of specific cases, a system of the Ornstein–Zernike equations in the Percus–Yevick approximation for the penetrating hard sphere model was approximately solved in [22, 23].

It follows from relationships (11) that, in order to determine the spatial distribution of ions in the mixed-valence system in the framework of the penetrating hard sphere model, it is sufficient to find one partial pair distribution function, for example, $g_{++}(r)$, and the other functions can be expressed in terms of this function. Therefore, the system of the Ornstein–Zernike nonlinear integral equations can be reduced to the sole equation. For further manipulations, it is convenient to take the Fourier transform of system (9), because the system of integral equations for the Fourier components $h_{\alpha\beta}(q)$ and $c_{\alpha\beta}(q)$ transforms into the system of algebraic equations

$$h_{\alpha\beta}(q) = c_{\alpha\beta}(q) + \sum_{\gamma = +,\,0} n_\gamma c_{\alpha\beta}(q) h_{\alpha\beta}(q). \qquad (14)$$

This system can be solved for the Fourier components of the direct correlation functions

$$\begin{aligned} c_{++}(q) &= \frac{1}{D_c}\{h_{++}(q)(1 + n_0 h_{00}(q)) \\ &\quad - n_0 h_{+0}(q) h_{+0}(q)\}, \\ c_{+0}(q) &= c_{0+}(q) = \frac{h_{+0}(q)}{D_c}, \\ c_{00}(q) &= \frac{1}{D_c}\{h_{00}(q)(1 + n_+ h_{++}(q)) \\ &\quad - n_+ h_{0+}(q) h_{0+}(q)\}, \\ D_c &= (1 + n_+ h_{++}(q))(1 + n_0 h_{00}(q)) \\ &\quad - n_+ n_0 h_{+0}(q) h_{0+}(q). \end{aligned} \qquad (15)$$

From expressions (11), it is possible to obtain the relationships for the Fourier components of the total correlation functions

$$\begin{aligned} x_+ h_{++}(q) + x_0 h_{+0}(q) &= H_f(q), \\ H_f(q) &= \frac{c_f(q)}{1 - n_{\mathrm{Fe}} c_f(q)}, \\ x_+ h_{0+}(q) + x_0 h_{00}(q) &= H_f(q), \\ h_{+0}(q) &= h_0(q), \end{aligned} \qquad (16)$$

where $c_f(q)$ is the Fourier transform of the direct correlation function for iron impurities [2]. From formulas (15) and (16), it follows that the direct correlation functions in the penetrating hard sphere model are related by the expressions

$$\begin{aligned} x_+ c_{++}(q) + x_0 c_{+0}(q) &= c_f(q), \\ x_+ c_{0+}(q) + x_0 c_{00}(q) &= c_f(q), \quad c_{+0}(q) = c_{0+}(q). \end{aligned} \qquad (17)$$

Let us introduce the designations $\tilde{h}_{\alpha\beta}(q) = h_{\alpha\beta}(q) - H_f(q)$ and $\tilde{c}_{\alpha\beta}(q) = c_{\alpha\beta}(q) - c_f(q)$. Then, for the $\tilde{h}_{\alpha\beta}(q)$ functions, we obtain

$$\begin{aligned} \tilde{h}_{++}(q) &= \tilde{c}_{++}(q)\left\{1 - n_+\left(1 + \frac{n_+}{n_0}\right)\tilde{c}_{++}(q)\right\}^{-1}, \\ \tilde{h}_{+0}(q) &= \tilde{h}_{0+}(q) = -\frac{n_+}{n_0}\tilde{h}_{++}(q), \\ \tilde{h}_{00}(q) &= \left(\frac{n_+}{n_0}\right)^2 \tilde{h}_{++}(q). \end{aligned} \qquad (18)$$

At $n_0 \longrightarrow 0$, $\tilde{c}_{\alpha\beta}(q) \longrightarrow 0$ and the partial distribution functions $h_{\alpha\beta}(q)$ tend to $H_f(q)$. Since $\tilde{h}_{00} \longrightarrow 0$ at $n_0 \longrightarrow 0$, $(n_+/n_0)^2 \tilde{c}_{++}(q) \longrightarrow 0$, and, hence, $\tilde{c}_{++}(q)$ tends to zero faster as compared to $(n_0)^2$. In the limiting case of high iron impurity concentrations $(n_+/n_0) \ll 1$, we have $h_{00}(q) \longrightarrow H_f(q)$ and the system of neutral centers turns out to be disordered due to a chaotic distribution of iron ions over the lattice sites. In the coordinate space, the Ornstein–Zernike equation within the penetrating hard sphere model takes the form

$$\begin{aligned} \tilde{h}_{++}(r) &= \tilde{c}_{++}(r) + n_+\left(1 + \frac{n_+}{n_0}\right)\int dr\, \tilde{c}_{++}(r')\tilde{h}_{++}(|r - r'|), \\ \tilde{h}_{++}(r) &= h_{++}(r) - H_f(r), \\ c_{++}(r) &= \left[1 - \exp\left(\frac{U_{++}(r)}{k_{\mathrm{B}}T}\right)\right] g_{++}(r), \\ \tilde{c}_{++}(r) &= \begin{cases} c_{++}(r) - c_f(r), & 0 < |r| < d_f \\ c_{++}(r), & d_f < r < r_c = d_+ \\ 0, & r > r_c. \end{cases} \end{aligned} \qquad (19)$$

At $n_0 \longrightarrow 0$, we have $h_{++}(r) \longrightarrow H(r)$ and $c_{++}(r) \longrightarrow c_f(r)$ and, correspondingly, $\tilde{h}_{+}(r) \longrightarrow 0$ and $\tilde{c}_{++}(r) \longrightarrow 0$.

Detailed analysis of Eq. (19) and its solution is a sufficiently tedious problem and will be published in a separate work. Here, the influence of the interference scattering on the dependences of the electron mobility $\mu(N_{\mathrm{Fe}})$ will be examined using an approximate scheme for calculating the partial correlation functions $g_{a3}(r)$ and the corresponding structure factors [17]. The structure factor $S_{++}(q)$ is determined from the solution of the Ornstein–Zernike equation in the Percus–Yevick approximation for the subsystem of d holes within the hard sphere model in much the same manner as was done in [2–4, 13]. The pair correlation functions $g_{+0}(r)$ and $g_{00}(r)$ and the corresponding structure factors $S_{+0}(q)$ and $S_{00}(q)$ are derived from relationships (11).

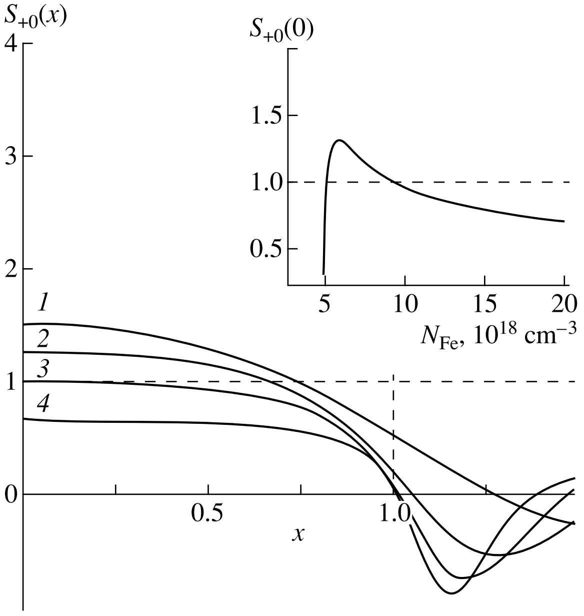

Fig. 3. Dependences of the structure factor S_{+0} on the reduced wave vector $x = q/2k_F$ at different iron impurity concentrations N_{Fe}, 10^{18} cm^{-3}: (*1*) 5, (*2*) 7, (*3*) 9, and (*4*) 15. The vertical line $x = 1$ separates the range of wave vectors $q < 2k_F$ which contribute to the electron momentum relaxation. The inset shows the dependence of $S_{+0}(x = 0)$ on the iron impurity concentration.

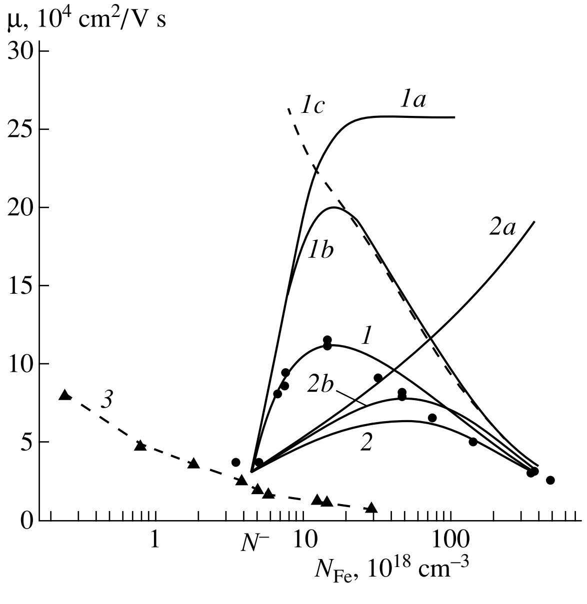

Fig. 4. Dependences of the electron mobility on the iron impurity concentration at the alloy scattering parameter $\Lambda = 0.2$. Curves *1, 1a, 1b,* and *1c* are calculated using the empirical equation for $\eta(N_{Fe})$. Curves *2, 2a,* and *2b* are determined with the use of $r_c(N_{Fe})$ defined by formula (4) derived in [16]. (*1a*, *2a*) Contributions to the mobility due to the scattering by a correlated system of Fe^{3+} ions, (*1b*, *2b*) dependences of the mobility without inclusion of the interference scattering of electrons [$S_{+0}(q) = 0$], (*1c*) contribution to the mobility due to the alloy scattering $\mu_{al}(N_{Fe})$, and (*3*) the electron mobility upon scattering by a random system of donors. Symbols indicate the experimental data on $\mu(N_{Fe})$, taken from [1] (circles) and [25] (triangles).

Setting $G(r) = 1$, we obtain

$$\begin{aligned} S_{++}(q) &= (1 - n_+ c_{++}(q))^{-1}, \\ S_{+0}(q) &= S_{0+}(q) = \sqrt{\frac{n_+}{n_0}}(1 - S_{++}(q)), \\ S_{00}(q) &= 1 + \left(\frac{n_+}{n_0}\right)(S_{++}(q) - 1). \end{aligned} \tag{20}$$

The formula for the Fourier transform of the direct correlation function $C_{++}(q)$ is given in [2, 3, 24]. The structure factors (20) correspond to the solution of the set of the Ornstein–Zernike equations for the partial pair correlation functions when neglecting the effect of the ordering of neutral centers on spatial correlations in the system of Fe^{3+} ions. At $N_0 \longrightarrow 0$, correlations in the system of d holes disappear; in this case, $S_{++}(q) \longrightarrow 1$ and $S_{+0}(q) \longrightarrow 0$. Note that, at high concentrations ($N_0 \gg N_+$), the structure factor $S_{+0}(q)$ tends to 0 and $S_{00}(q) \longrightarrow 1$, as should be expected for a random distribution of particles.

The dependences $S_{+0}(q)$ at different iron impurity concentrations are depicted in Fig. 3. As is seen from this figure, the structure factor $S_{+0}(q)$ only slightly varies in the wave vector range of interest and it is possible to assume with a good approximation that $S_{+0}(q) = S_{+0}(0)$. From the inset in Fig. 3, it can be seen that the value of $S_{+0}(0)$ insignificantly deviates from unity in the range of an increase and a maximum of the electron mobility $\mu(N_{Fe})$. In the phenomenological description of $\mu(N_{Fe})$ in [3], it was assumed that $S_{+0}(q) = 1$. As will be shown below, the effective value of $S_{+0}(q)$ is actually somewhat less than unity. Therefore, the authors of [3] appeared to be substantially closer to the truth as compared to the author of [16], who believed that $S_{+0}(q) = 0$.

4. INTERFERENCE SCATTERING OF ELECTRONS BY A SYSTEM OF MIXED-VALENCE IRON IONS IN HgSe : Fe CRYSTALS

Now, we analyze how the interference scattering of electrons affects the dependence of the electron mobility $\mu(N_{Fe})$ on the iron impurity content. As in [2–4], assume that the value of μ_{BH} is equal to 3×10^4 cm^2/V s upon electron scattering by randomly distributed donors with the concentration $N_d = N^*$. However, as can be seen from Fig. 4, the experimental value of μ^*_{BH} in the concentration range 4×10^{18} cm^{-3} $< N_d < 5 \times 10^{18}$ cm^{-3} is somewhat less [25]. Let us express $\mu(N_{Fe})$ in terms of μ_{BH} for the electron scattering by the system of mixed-valence iron ions [17]

$$\mu(N_{\mathrm{Fe}}) = \mu^*_{BH}\Phi_{BH}(k_F)/\Phi(k_F),$$

$$\mu(N_{\mathrm{Fe}}) = \left(\mu_{++}^{-1}(N_{\mathrm{Fe}}) + \mu_{+0}^{-1}(N_{\mathrm{Fe}}) + \mu_{00}^{-1}(N_{\mathrm{Fe}})\right)^{-1}, \qquad (21)$$

$$\Phi(k_F) = \Phi_{++}(k_F) + \Lambda\left[2\left(\frac{n_0}{n_+}\right)^{1/2}\Phi_{+0}(k_F) + \Lambda\Phi_{00}(k_F)\frac{n_0}{n_+}\right],$$

where $\Phi_{BH} \approx 2.26$ [3], Λ is the alloy scattering parameter, and

$$\Phi_{\alpha\beta}(k_F) = 2\int_0^1 \frac{x^3 S_{\alpha\beta}(2k_F x)}{(x^2 + b_s^{-1})^{\nu}}dx, \quad b_s = 2k_F r_s. \qquad (22)$$

Here, $\nu = 2$ for Φ_{++}, $\nu = 1$ for Φ_{0+}, and $\nu = 0$ for Φ_{00}. Thus, the relaxation of the electron momentum by the correlated system Fe^{2+}–Fe^{3+} in the general case is determined by three contributions: the scattering by charged centers, the scattering by neutral centers, and the interference contribution. Figure 4 shows the dependences $\mu(N_{\mathrm{Fe}})$ and also the contributions $\mu_{++}(N_{\mathrm{Fe}})$ and $\mu_{\mathrm{al}}(N_{\mathrm{Fe}})$ (alloy scattering) to the mobility, which were calculated in the framework of our model [3, 17] and the concepts proposed in [16]. In order to avoid errors associated with the use of the weak spatial correlation model in the determination of $g_{++}(r)$ (formula (8) for $f(r_c, r)$ in [16]), the mobility was calculated using the structure factors $S_{\alpha\beta}(q)$ (20) obtained from the solution of the Ornstein–Zernike equations in the Percus–Yevick approximation. Curves *1*, *1a*, *1b*, and *1c* were computed with the empirical equation for the packing parameter $\eta(N_{\mathrm{Fe}})$ [3]

$$\eta = \eta_L\left[1 - \exp\left(-\frac{\eta}{\eta_L}\frac{N_{\mathrm{Fe}}}{N_+}\right)\right], \qquad (23)$$

where $\eta_L = 0.45$. Curves *2*, *2a*, and *2b* were obtained with expression (4) derived in [16] for the packing parameter.

It is seen from Fig. 4 that the $\mu(N_{\mathrm{Fe}})$ values calculated without regard for the interference scattering of electrons by charged and neutral (in the lattice) iron ions (curve *1b* in Fig. 4) lie considerably higher than the experimental data. It is evident that the interference mechanism plays an important part in the relaxation of electron momentum in HgSe : Fe crystals and should be included in calculation of the electron mobility. A comparison between curves *1* and *2*, which are calculated at the same parameters and differ only in the dependences $r_c(N_{\mathrm{Fe}})$, does not count in favor of the model proposed in [16]. Taking into account two fitting parameters (Λ and η_L) and assumptions made in calculations, a good quantitative agreement between $\mu(N_{\mathrm{Fe}})$ in our model (curve *1*) and the experimental data should not be excessively overrated. However, within the model advanced in [3, 13, 17], it is possible to describe the dependence $\mu(N_{\mathrm{Fe}})$ over a wide range of iron impurity concentrations. The use of the dependence $r_c(N_{\mathrm{Fe}})$ represented by formula (4) derived in [16] leads to a very slow increase in the packing parameter and, correspondingly, $\mu_{++}(N_{\mathrm{Fe}})$ with an increase in the iron impurity concentration (Fig. 4, curve *1a*). As a consequence, the discrepancy between the results obtained within the approach proposed in [16] and the experimental data from [1] in the range of an increase and a maximum of the mobility appears to be sufficiently large: the value of $[(\mu(N_{\mathrm{Fe}}) - \mu_{BH})/\mu_{BH}]$ is less than the experimental value by a factor of two or three. In the framework of this approach, the dependence $\mu(N_{\mathrm{Fe}})$ at any fitting parameters Λ and r_1 cannot be described in the range of an increase and a maximum of the mobility.

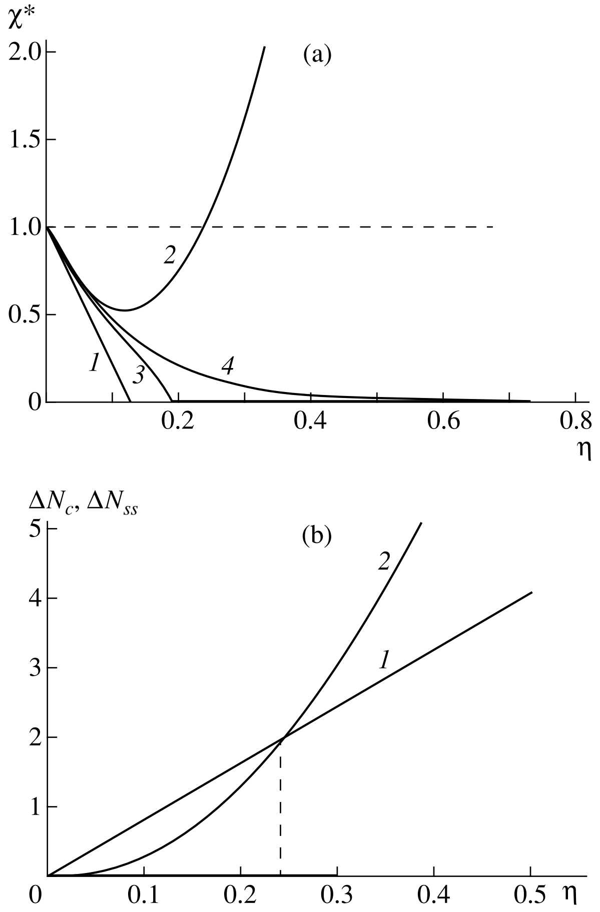

Fig. 5. (a) Dependences of the reduced compressibility $\chi^* = \chi(T, \eta)/\chi(T, 0)$ on the density η (packing parameter) for the system. Curves *1*–*3* are calculated from the expansion of the structure factor in a power series of the density with inclusion of (*1*) first-order terms $\chi^* = 1 - 8\eta$ [14], (*2*) second-order terms $\chi^* = 1 - 8\eta + 34\eta^2$ [16], and (*3*) third-order terms $\chi^* = 1 - 8\eta + 34\eta^2 - 108\eta^3$. Curve *4* is determined from the solution of the Ornstein–Zernike equation within the Percus–Yevick approximation. (b) Dependences of the number of *d* holes (*1*) ΔN_c in the correlation sphere and (*2*) ΔN_{ss} in the spherical layer $r_c < r < 2r_c$ on the density η (packing parameter).

Let us now consider the problem concerning the correctness of using $S_{++}(q)$ and the pair correlation function $f(r_c, r)$ defined in the model of weak Coulomb correlations between Fe^{3+} impurity ions [16]. To accomplish this, let us examine the behavior of such a physical quantity as the isothermal compressibility $\chi(T, \eta)$ with an increase in the density of the system (packing parameter) [19]

$$\chi(T, \eta) \cong n_+ k_\mathrm{B} T S_{++}(0).$$

The value of $S_{++}(0) = (1 - \eta)^4/(1 + 2\eta)^2$ determined from the solution of the Ornstein–Zernike equation within the Percus–Yevick approximation [5] monotonically decreases with an increase in the packing parameter (Fig. 5). In the framework of the weak correlation model [14], upon approximation of $g(r)$ by a step function, $S_{++}(0) = 1 - 8\eta$ and the compressibility of the system becomes negative at $\eta > 1/8$. According to [16], the inclusion of the next expansion term results in $S_{++}(0) = 1 - 8\eta + 34\eta^2$. In this case, as the packing parameter η increases, the compressibility of the system decreases at $\eta < 1/8$, sharply increases at $\eta > 1/8$, and becomes larger than the compressibility of an ideal gas $[S_{++}(0) = 1]$ at $\eta > 0.235$. This behavior of the compressibility indicates that the weak correlation model can be used only at $\eta < 1/8$. Another more serious circumstance that cast some doubt on the results obtained within this model is the violation of the particle conservation law upon ordering of d holes. The mean number of d holes that passed from the correlation sphere $(0 < r < r_c)$ $\Delta N_c = n_+ V_c = 8\eta$ should be equal to the excess number of d holes that appeared in the region $r > r_c$

$$\Delta N_{ss} = 4\pi n_+ \int\limits_{r > r_c} r^2 h_{++}(r) dr.$$

For the pair correlation function $f(r_c, r)$ defined in the model of weak Coulomb correlations between Fe^{3+} impurity ions [16], $\Delta N_{ss} = 34\eta^2$. The particle conservation law is violated over the entire range of packing parameters with the exception of the value $\eta = 0.235$, at which the weak correlation model has already been inapplicable (Fig. 5).

The nonphysical behavior of $\chi(T, \eta)$ at $\eta > 1/8$ and the violation of the particle conservation law suggest that the use of the weak correlation model [16] cannot be treated as justified. The main thing resides in the fact that the application of this model makes no sense. First, for the hard sphere system, there is the rigorous analytical solution of the Ornstein–Zernike equation within the Percus–Yevick approximation [19, 21], which is free of the above disadvantages. This solution can be used in the range of both weak and strong Coulomb correlations of d holes in the system of mixed-valence iron ions. Second, the experimentally observed increase in the mobility cannot be explained within the weak correlation approximation: the experimental ratio $\mu_\mathrm{max}(N_\mathrm{Fe})/\mu_{BH}$ is equal to ~4 at $N_\mathrm{Fe} \sim (1–2) \times 10^{19}$ cm^{-3}, whereas the ratio calculated according to [16] (even without regard for the alloy scattering) is two times less $[\mu_{++}(N_\mathrm{Fe})/\mu_{BH} \le 2]$. Our calculations give $\mu_{++}(N_\mathrm{Fe})/\mu_{BH} \sim 8$ in this concentration range. Therefore, the experimental dependence of the electron mobility on the iron impurity content in HgSe : Fe crystals at low temperatures cannot be described within the approximations made in [16].

5. CONCLUSION

Thus, in the present work, the spatial ordering of charges was considered for the mixed-valence system. The dependence of the correlation sphere radius on the iron impurity content was obtained from the balance equation for d holes and neutral centers in the short-range order cluster of the Fe^{3+} ion. It was demonstrated that the basic equation that determines the dependence $r_c(N_\mathrm{Fe})$ in [16] is incorrect. The penetrating hard sphere model was proposed for the rigorous description of the spatial ordering in the mixed-valence system and the calculation of partial correlation functions. The relationships between the direct correlation functions were derived. This made it possible to reduce sets of four Ornstein–Zernike equations to one nonlinear integral equation for the pair correlation function of d holes in the mixed-valence system. Detailed critical analysis of the results obtained in [16] was carried out. Contrary to the conclusion drawn in [16], we proved that the spatial redistribution of charges in the mixed-valence system leads both to spatial correlations in the subsystem of charged centers and to the correlated arrangement of neutral centers with respect to charged centers. This is responsible for the interference scattering, which plays an important role in the relaxation of electron momentum and should be taken into consideration in calculations of the electron mobility. It was shown that the use of the weak Coulomb correlation model cannot be treated as justified. This model gives no way of fitting the results of calculations to the experimental mobilities in HgSe : Fe crystals.

ACKNOWLEDGMENTS

We are grateful to A.P. Tankeev for his participation in discussions of the results and helpful remarks.

This work was supported by the Russian Foundation for Basic Research, project no. 00-02-16299.

REFERENCES

1. I. M. Tsidil’kovskiĭ, Usp. Fiz. Nauk **162** (2), 63 (1992) [Sov. Phys. Usp. **35**, 85 (1992)].
2. I. M. Tsidilkovskii and I. G. Kuleyev, Semicond. Sci. Technol. **11**, 625 (1996).
3. I. G. Kuleev, I. I. Lyapilin, and I. M. Tsidil’kovskiĭ, Zh. Éksp. Teor. Fiz. **102** (5), 1652 (1992) [Sov. Phys. JETP **75**, 893 (1992)].
4. I. G. Kuleev, I. I. Lyapilin, and I. M. Tsidil’kovskiĭ, Fiz. Tverd. Tela (St. Petersburg) **37** (8), 2360 (1995) [Phys. Solid State **37**, 1291 (1995)].

5. I. G. Kuleev, A. T. Lonchakov, I. Yu. Arapova, and G. I. Kuleev, Zh. Éksp. Teor. Fiz. **114** (1), 199 (1998) [JETP **87**, 106 (1998)].
6. I. G. Kuleev, I. I. Lyapilin, A. T. Lonchakov, and I. M. Tsidil'kovskiĭ, Zh. Éksp. Teor. Fiz. **103** (4), 1447 (1993) [JETP **76**, 707 (1993)].
7. I. G. Kuleev, I. I. Lyapilin, A. T. Lonchakov, and I. M. Tsidil'kovskiĭ, Fiz. Tekh. Poluprovodn. (St. Petersburg) **28** (6), 937 (1994) [Semiconductors **28**, 544 (1994)].
8. I. G. Kuleev, I. I. Lyapilin, A. T. Lonchakov, and I. M. Tsidil'kovskiĭ, Zh. Éksp. Teor. Fiz. **106**, 1205 (1994) [JETP **79**, 653 (1994)].
9. I. G. Kuleev, A. T. Lonchakov, G. L. Shtrapenin, and I. Yu. Arapova, Fiz. Tverd. Tela (St. Petersburg) **39** (10), 1767 (1997) [Phys. Solid State **39**, 1575 (1997)].
10. D. I. Khomskiĭ, Usp. Fiz. Nauk **129** (3), 443 (1979) [Sov. Phys. Usp. **22**, 879 (1979)].
11. C. M. Varma, Rev. Mod. Phys. **48** (2), 219 (1976).
12. P. W. Anderson, Phys. Rev. **124** (1), 41 (1961).
13. I. G. Kuleev, Fiz. Tverd. Tela (St. Petersburg) **39** (2), 250 (1997) [Phys. Solid State **39**, 219 (1997)].
14. Z. Wilamowski, K. Swiatek, T. Dietl, and J. Kossut, Solid State Commun. **74**, 833 (1990); Z. Wilamowski, Acta Phys. Pol. A **77**, 133 (1990).
15. I. G. Kuleev, Fiz. Tverd. Tela (St. Petersburg) **40** (3), 425 (1998) [Phys. Solid State **40**, 389 (1998)].
16. V. M. Mikheev, Fiz. Tverd. Tela (St. Petersburg) **41** (11), 1994 (1999) [Phys. Solid State **41**, 1830 (1999)].
17. I. G. Kuleev and I. Yu. Arapova, Fiz. Met. Metallogr. **88** (3), 43 (1999).
18. L. D. Landau and E. M. Lifshitz, *Statistical Physics* (Nauka, Moscow, 1976; Pergamon, Oxford, 1980), Part 1.
19. J. M. Ziman, *Models of Disorder: The Theoretical Physics of Homogeneously Disordered Systems* (Cambridge Univ. Press, Cambridge, 1979; Mir, Moscow, 1982).
20. J. L. Lebowitz, Phys. Rev. A **133** (3), 895 (1964).
21. M. S. Wertheim, Phys. Rev. Lett. **10** (8), 321 (1963); J. Math. Phys. **5** (5), 643 (1964).
22. J. L. Lebowitz and D. Zomick, J. Chem. Phys. **54** (8), 3335 (1971).
23. M. I. Guerrero, J. S. Rowlinson, and B. L. Sawford, Mol. Phys. **28** (6), 1603 (1974).
24. E. I. Khar'kov, V. I. Lysov, and V. E. Fedorov, *Physics of Liquid Metals* (Vishcha Shkola, Kiev, 1979).
25. T. Dietl and W. Szymanska, J. Phys. Chem. Solids **39** (10), 1041 (1978).

Translated by O. Borovik-Romanova

Physics of the Solid State, Vol. 43, No. 3, 2001, pp. 430–438. Translated from Fizika Tverdogo Tela, Vol. 43, No. 3, 2001, pp. 414–422.
Original Russian Text Copyright © 2001 by Mikheev.

SEMICONDUCTORS AND DIELECTRICS

Mobility of Electrons upon Scattering by a Multicomponent Correlated System of Impurity Centers

V. M. Mikheev

Institute of Metal Physics, Ural Division, Russian Academy of Sciences, ul. S. Kovalevskoĭ 18, Yekaterinburg, 620219 Russia
e-mail: mikheev@imp.uran.ru

Received February 8, 2000; in final form, May 23, 2000

Abstract—A system that contains two sorts of impurity centers spatially distributed in a random way is considered. Not all impurities of the first sort are ionized, and all the impurities of the second sort are ionized. Spatial correlations in the system of impurity ions of the first sort are investigated under conditions when the correlation radius of an impurity ion is limited from above due to a deficit of neutral impurities. The influence of randomly spatially arranged small-sized donors (impurities of the second sort) on correlations in the system of impurity ions is analyzed. The equations for describing the effect of small-sized donors on correlations in the system of impurity ions are obtained. The electron mobility at zero temperature is calculated by the example of HgSe : Fe (the correlated system of impurity centers consists of iron atoms and small-sized donors whose concentration is higher than the Mott concentration). © *2001 MAIK "Nauka/Interperiodica".*

1. INTRODUCTION

Impurity scattering makes the main contribution to the electron mobility in semiconductors at low temperatures. Under normal conditions, when the multiple scattering is negligibly small, the coherent component of scattering is associated with the correlations in the spatial arrangement of impurity centers. In recent years, the interference scattering effects that lead to an increase in the electron mobility have been extensively studied in HgSe : Fe compounds in which correlations in the arrangement of Fe^{3+} iron ions are significant [1, 2]. Earlier [3], I proposed a theory for describing the spatial correlations of impurity ions in solids and considered the specific case when particles of one sort served as correlated scatterers. The theory was applied to analysis of the electron mobility in HgSe : Fe upon scattering by the correlated system of iron ions [3]. However, real impurity systems are multicomponent systems involving impurity centers of different sorts. Particularly, in the case of HgSe : Fe, the mobility is determined by the scattering from Fe^{3+} iron ions, Fe^{2+} iron atoms neutral with respect to a lattice, and the so-called intrinsic donors whose concentration depends on the degree of sample purification and is an uncontrollable quantity. In this respect, the calculation of the mobility upon scattering of electrons by a multicomponent system of correlated impurity ions is a topical problem. In the present work, the theory proposed in [3] was generalized to this case and the electron mobility in HgSe : Fe compounds at low temperatures was considered as an example.

2. RELATIONSHIP BETWEEN CORRELATION FUNCTIONS AND THE MOBILITY UPON ELECTRON SCATTERING BY MULTICOMPONENT IMPURITY SYSTEMS

Our theory is based on the relationship obtained within the Born approximation at $T = 0$ for the relaxation time of electron momentum upon elastic scattering by a system of impurity centers [4, 5], that is,

$$\begin{aligned}\frac{1}{\tau} &= \frac{2}{3}\frac{m}{(2\pi\hbar)^3 n_e}\int_0^{2k_F} q^3 dq \sum_{\alpha,\beta} V_\alpha(q) V_\beta^*(q) \\ &\times \left\langle \sum_{i=1}^{n_\alpha}\sum_{j=1}^{n_\beta} \exp(i\mathbf{q}(\mathbf{r}_i^\alpha - \mathbf{r}_j^\beta))\right\rangle \\ &\times \left\langle \sum_{i=1}^{n_\alpha}\sum_{j=1}^{n_\beta} \exp(i\mathbf{q}(\mathbf{r}_i^\alpha - \mathbf{r}_j^\beta))\right\rangle \\ &= \begin{cases} n_\alpha \delta_{\alpha\beta} & (\mathbf{r}_i^\alpha = \mathbf{r}_j^\beta) \\ n_\alpha n_\beta g_{\alpha\beta}(q) & (\mathbf{r}_i^\alpha \neq \mathbf{r}_j^\beta). \end{cases}\end{aligned} \qquad (1)$$

For a homogeneous and isotropic spatial distribution of impurity centers, we have

$$\begin{aligned} g_{\alpha\beta}(q) &= \int d\mathbf{r} \exp(i\mathbf{q}\mathbf{r})[\tilde{g}_{\alpha\beta}(r) - 1], \\ g_{\alpha\beta}(q) &= g_{\alpha\beta}(q). \end{aligned} \qquad (2)$$

Here, $\tilde{g}_{\alpha\beta}(r)$ is the pair correlation function, which relates the mutual arrangement of impurity centers of the α and β sorts; $V_\alpha(q)$ is the matrix element of the

1063-7834/01/4303-0430$21.00 © 2001 MAIK "Nauka/Interperiodica"

scattering potential; n_α is the partial concentration of impurity centers; n_e is the electron concentration; and ε_F is the Fermi energy. For simplicity, the volume V of the system under consideration is taken equal to unity.

The boundaries of the applicability of our simple theory are determined by two conditions. The condition of validity of the Boltzmann kinetic equation for a degenerate electron gas is represented by the inequality $\hbar/\tau\varepsilon_F \ll 1$. The condition of validity of the Born approximation is defined by the inequality $|V| \ll \frac{\hbar^2}{ma^2}k_F a$. Here, k_F is the wave number of an electron at the Fermi surface and a is the effective range of the potential.

Formulas (1) and (2) allow us to calculate numerically the mobility $\mu = e\tau/m$ only in two specific cases: either when all the scattering centers are spatially distributed in a random way or for the scattering by a correlated distribution of scatterers of one sort. In the case of multicomponent correlated systems of scatterers, the calculation of the mobility μ from formulas (1) and (2) can be brought to completion only under additional model assumptions that reflect specific features of the problem. As such a particular system, let us consider correlated impurity centers in HgSe : Fe and also examine the behavior of the electron mobility at $T = 0$.

In HgSe : Fe, the impurity scattering is contributed by iron atoms, whose concentration n_F is specified in the sample preparation, and intrinsic donors, whose concentration n_D is an uncontrollable quantity and characterizes the sample purity. The sources of electrons in the conduction band are iron atoms, whose energy level lies in the conduction band, and intrinsic donors, whose concentration is higher than the Mott concentration that corresponds to the metal–dielectric transition. At electron concentrations lower than a certain critical value n_c, all the iron atoms are ionized, and the concentration of impurity ions is $n^+ = n_e = n_F^+ + n_D$, where n_F^+ is the concentration of Fe^{3+} ions. When the condition $n_e = n_c$ is met, the Fermi level is fixed at the resonance level of iron [1, 2]. Therefore, at $n_F + n_D > n_c$, the concentration of iron ions becomes constant and a part of iron atoms remain in the Fe^{2+} state, which is neutral with respect to the lattice. In this case, the concentrations of impurity centers are related to each other by the expressions

$$\begin{aligned} n_r &= n_F + n_D, \\ n_F &= n_F^+ + n_F^0, \qquad (3) \\ n^+ &= n_F^+ + n_D. \end{aligned}$$

Here, n_r is the total concentration of all impurity centers and n_F^0 is the concentration of Fe^{2+} atoms neutral with respect to the lattice. It is assumed that all the impurity centers are spatially arranged in a random manner. However, iron ions under the repulsion of the Coulomb forces are spatially redistributed and tend to be spaced as far apart as possible, which leads to correlations in the system of impurity centers [2]. Let us introduce the partial correlation functions $\tilde{g}_{++}^{FF}(r)$, $\tilde{g}_{++}^{DD}(r)$, and $\tilde{g}_{00}^{FF}(r)$, which describe correlations in the mutual spatial arrangement of iron ions, small-sized donor ions, and neutral iron atoms, respectively. Furthermore, the mixed correlation function $\tilde{g}_{0+}^{FF}(r)$ determines correlations in the arrangement of iron ions relative to neutral iron atoms, the function $\tilde{g}_{++}^{FD}(r)$ defines correlations in the location of iron ions with respect to small-sized donor ions, and the function $\tilde{g}_{0+}^{FD}(r)$ describes correlations in the arrangement of neutral iron atoms relative to small-sized donor ions.

Then, in the framework of the model used [2], the relaxation time τ according to formulas (1) and (2) is expressed through the Fourier transforms of six partial correlation functions

$$\begin{aligned} \frac{1}{\tau} = \frac{2}{3}\frac{m}{(2\pi\hbar)^3 n_e}\int_0^{2k_F} q^3 dq\{|V_0(g)|^2(n_F^0 + n_F^{0\,2} g_{00}^{FF}(q)) \\ + |V_+(q)|^2[n^+ + n_F^{+2} g_{++}^{FF}(q) + n_D^2 g_{++}^{FF}(q) \qquad (4) \\ + 2n_F^+ n_D g_{++}^{FD}(q)] + [V_0(q)V_+^*(q) + V_0^*(q)V_+(q)] \\ \times [n_F^0 n_F^+ g_{0+}^{FF}(q) + n_F^0 n_D g_{0+}^{FD}(q)]\}. \end{aligned}$$

Here, $V_0(q)$ is the matrix element of the potential of scattering by a neutral iron atom; $V_+(q)$ is the matrix element of the potential of scattering by the impurity ion (we assume that all the impurity ions irrespective of their nature have the same scattering potential); and $g_{++}^{FF}(q)$, $g_{++}^{DD}(q)$, $g_{00}^{FF}(q)$, $g_{0+}^{FF}(q)$, $g_{++}^{FD}(q)$, and $g_{0+}^{FD}(q)$ are the Fourier transforms of the partial correlation functions.

The specificity of multicomponent systems resides in the fact that the partial correlation functions in these systems are not independent, but are related to each other by universal equations. These universal equations make it possible to reduce the number of partial correlation functions to be calculated by choosing an appropriate model. One universal equation can be obtained by expressing the total correlation function $\tilde{g}_{rr}(r)$ (describing correlations in the system of impurity centers) in terms of the partial correlation functions

$$\begin{aligned} n_r^2\tilde{g}_{rr}(r) = n_F^{+2}\tilde{g}_{++}^{FF}(r) + n_F^{0\,2}\tilde{g}_{00}^{FF}(r) + n_D^2\tilde{g}_{++}^{DD}(r) \qquad (5) \\ + 2n_F^+ n_F^0 \tilde{g}_{0+}^{FF}(r) + 2n_F^+ n_D\tilde{g}_{++}^{FD}(r) + 2n_F^0 n_D\tilde{g}_{0+}^{FD}(r). \end{aligned}$$

The second universal equation is derived when the total correlation function $\tilde{g}_{FF}(r)$ of the subsystem consisting of iron atoms is expressed through the partial correlation functions

$$\overset{}{n}_F^2\tilde{g}_{FF}(r) = \overset{+}{n}{}_F^2\tilde{g}_{++}^{FF}(r) + \overset{0}{n}{}_F^2\tilde{g}_{00}^{FF}(r) + 2\overset{0}{n}_F\overset{+}{n}_F\tilde{g}_{0+}^{FF}(r). \quad (6)$$

Since all the impurity centers are spatially arranged in a random fashion, we have the equality

$$\tilde{g}_{rr}(r) = \tilde{g}_{FF}(r) = \tilde{g}_{++}^{DD}(r) = 1. \quad (7)$$

Recall that correlations in the system of scatterers are determined solely by the ordering of Fe^{3+} ions. The Coulomb repulsion redistributes iron ions in such a way that a sphere of radius r_c, inside which iron ions are absent, can be drawn around each iron ion. This implies that the correlation function $\tilde{g}_{++}^{FF}(r)$ differs from unity. On the other hand, neutral iron atoms occur in the sphere of radius r_c, which surrounds an iron ion, and, hence, the correlation function $\tilde{g}_{0+}^{FF}(r)$ also differs from unity. Similarly, correlations in the arrangement of iron ions with respect to an intrinsic donor ion $[\tilde{g}_{++}^{FD}(r) \neq 1]$ result in the correlation in the location of neutral iron atoms relative to a small-sized donor ion $[\tilde{g}_{0+}^{FD}(r) \neq 1]$. In this case, it is essential that the spatial redistribution of iron ions should not bring about correlations in the mutual arrangement of neutral iron atoms. Actually, since iron atoms themselves are spatially arranged in a random way, the density of iron atoms and, hence, the density of iron ions fluctuate in the space. In spatial regions, where the density of iron ions is anomalously large, the energy of the Coulomb repulsion is also anomalously high. As the concentration of iron atoms increases, iron ions are redistributed in such a way as to reduce the energy of the Coulomb repulsion. In this case, it is clear that the distribution of neutral iron atoms in regions with an anomalously large density of ions most efficiently decreases the energy of the system. Since density fluctuations are spatially distributed in a random manner, the mutual arrangement of neutral iron atoms also turns out to be close to random. In this respect, within our model, we assume that the distribution of neutral iron atoms is close to random and set

$$\tilde{g}_{00}^{FF}(r) = 1. \quad (8)$$

Note that the problem concerning the relation between the partial correlation functions in HgSe : Fe in the idealized case of pure sample ($n_D = 0$) was considered in [6]. Certain heuristic equations that relate the partial correlation functions in the system composed of particles of two sorts (A and B) were taken by the authors of [6] from [7]. These equations (formulas (1) and (2) in [7]) were obtained under the assumption that the correlation functions that describe the mutual arrangement of particles of the A sort relative to each other and particles of the B sort with respect to each other differ little [“when $g_A(r)$ and $g_B(r)$ are the same”]. In the case of HgSe : Fe, the energy of interaction between neutral iron atoms is small as compared to the energy of the Coulomb repulsion between iron ions. Therefore, the correlation functions $\tilde{g}_{++}^{FF}(r)$ and $\tilde{g}_{00}^{FF}(r)$ bear no similarities to each other, and the heuristic equations (obtained in [7]) in our case are inapplicable. In our theory, the relations between the partial correlation functions were derived using the universal Eqs. (5) and (6), which follow from the definition of the total correlation function for a system involving particles of several sorts.

By using the Fourier transform of Eqs. (5) and (6) with due regard for relationships (7) and (8), the partial correlation functions that describe correlations in the arrangement of neutral atoms can be expressed in terms of the partial correlation functions that determine correlations in the system of impurity ions

$$\begin{aligned} g_{0+}^{FD}(q) &= -\frac{\overset{+}{n}_F}{\overset{0}{n}_F}g_{++}^{FD}(q), \\ g_{0+}^{FF}(q) &= -\frac{1}{2}\frac{\overset{+}{n}_F}{\overset{0}{n}_F}g_{++}^{FF}(q). \end{aligned} \quad (9)$$

Substitution of expression (7)–(9) into formula (4) gives the final relationship for the relaxation time τ of the electron momentum

$$\begin{aligned} \frac{1}{\tau} = \frac{2}{3}\frac{m}{(2\pi\hbar)^3 n_e}\int_0^{2k_F} q^3 dq \Big\{ |V_0(q)|^2 \overset{0}{n}_F \\ + |V_+(q)|^2(\overset{+}{n}_F + n_D) + \frac{1}{2}[V_+(q)(V_+^*(q) - V_0^*(q)) \quad (10) \\ + V_+^*(q)(V_+(q) - V_0(q))][\overset{+}{n}{}_F^2 g_{++}^{FF}(q) + 2\overset{+}{n}_F n_D g_{++}^{FD}(q)] \Big\}. \end{aligned}$$

According to formula (10), the interference scattering term expressed through the partial correlation functions is the larger, the larger the difference between the scattering potentials, and tends to zero in the limit $V_+(q) \longrightarrow V_0(q)$. This property of formula (10) is a consequence of our model assumptions, according to which impurity centers are spatially distributed in a random way [relationship (7)], and correlations are determined solely by the spatial arrangement of iron ions. Therefore, the interference terms in the scattering appear only owing to the difference between the potentials of scattering by neutral centers and ions.

Since the potential of electron scattering by neutral iron atoms is small compared to that by iron ions, we take into account the inequality $V_0(q) \ll V_+(q)$ and set $V_0(q) = 0$ in the term involving the correlation functions in formula (10). Within this approximation, correlations in the arrangement of neutral iron atoms make zero contribution to the interference and the formulas for the calculation of the electron mobility μ take the form

$$\mu = \mu_0\mu_+/[\mu_0 + \mu_+],$$

$$\mu_0 = \frac{e}{m}/\{|V_0(q)|^2/|V_+(q)|^2\}n_F^0, \qquad (11)$$

$$\mu_+ = \frac{e}{m}/[\{1\}n^+ + \{g_{++}^{FF}(q)\}\overset{+}{n}{}_F^2 + 2\overset{+}{n}_F n_D\{g_{++}^{FD}(q)\}],$$

where

$$\{f(q)\} = \frac{2}{3}\frac{m}{(2\pi\hbar)^3 n_e}\int_0^{2k_F} q^3 dq|V_+(q)|^2 f(q).$$

Here, μ_0 is the electron mobility associated with the scattering by neutral iron atoms and μ_+ is the mobility stemming from the scattering by impurity ions.

3. CALCULATION OF CORRELATION FUNCTIONS

The correlation function $g_{++}^{FF}(q)$ for HgSe : Fe compounds in the idealized case of pure samples ($n_D = 0$) was calculated within the "hard" sphere model in [2, 3, 8]. The hard sphere diameter r_c (in our case, this quantity plays the role of the correlation sphere radius) was identified with the minimum distance between iron ions. The larger the ratio $C = n_F/\overset{+}{n}_F$, the larger the distance that can separate iron ions, and, hence, the larger the value of r_c. In each of the works [2, 3, 8], the authors used their own basic equation of the theory that relates the hard sphere diameter r_c to the concentrations of iron atoms n_F and iron ions $\overset{+}{n}_F$ and this is the main difference between these works. The influence of intrinsic donors on the correlation effects in HgSe : Fe compounds was taken into consideration in [9, 10]. This was achieved by a simple modification of the basic equation of the theory that was written for $n_D = 0$. Before proceeding to the construction of a more realistic model that includes intrinsic donors, it is necessary to examine the basic equation of the theory for the case of $n_D = 0$.

First and foremost, we consider the limiting case $C \longrightarrow 1$. In this case, $V_c\overset{+}{n}_F \ll 1$ ($V_c = 4\pi r_c^3/3$ is the correlation sphere volume) and the correlation sphere do not overlap. By definition, only neutral iron atoms occur in the correlation sphere. Consequently, the volume occupied by iron ions is equal to $1 - V_c\overset{+}{n}_F$. The concentration of iron ions is equal to the iron atom concentration multiplied by the volume occupied by iron ions. Therefore, in the limiting case $C \longrightarrow 1$ (recall that $C = n_F/\overset{+}{n}_F$), we have

$$\overset{+}{n}_F = n_F(1 - V_c\overset{+}{n}_F). \qquad (12)$$

In the limit $n_F/\overset{+}{n}_F \longrightarrow 1$, the basic equation of the theory should transform into Eq. (12) (in this case, $(d\eta/dC) \longrightarrow 1/8$, where $\eta = V_c\overset{+}{n}_F/8$ is the packing coefficient). Now, we compare the asymptotics of the basic equations underlying the theories proposed in [2, 3, 8] with Eq. (12).

In [2], the basic equation of the theory was postulated in the form

$$V_c\overset{+}{n}_F = 1 - \exp(-V_c n_F).$$

In the limit $C \longrightarrow 1$, this equation takes the form

$$\overset{+}{n}_F = n_F\left(1 - \frac{1}{2}V_c n_F\right)$$

and $(d\eta/dC) \longrightarrow 1/4$. Therefore, the equation derived in [2] has an incorrect asymptotics and overestimates the rate of increase in the packing coefficient by a factor of two.

In [8], the postulated basic equation of the theory was as follows:

$$\frac{\eta}{\eta_L} = 1 - \exp\left(-\frac{\eta}{\eta_L}\frac{n_F}{\overset{+}{n}_F}\right),$$

where the fitting parameter η_L is equal to 0.45. In the limit $C \longrightarrow 1$, this equation has the form

$$\overset{+}{n}_F = n_F\left(1 - \frac{1}{16\eta_L}V_c n_F\right)$$

and $(d\eta/dC) \longrightarrow 2\eta_L$. Consequently, the asymptotics of the equation derived in [8] is also incorrect. Moreover, this equation overestimates the rate of increase in the packing coefficient by one order of magnitude. Thus, the calculations in [2, 8] were based on the equations that exhibit an incorrect asymptotics in the limit $C = n_F/\overset{+}{n}_F \longrightarrow 1$. Therefore, the estimates performed in these works cannot lay claim to the quantitative description.

In my previous work [3], the basic equation of the theory was derived by methods of statistical physics and takes the form

$$n^+ = n\left(1 - \frac{V_c}{V_m}\right)^{n_m}, \qquad (13)$$

where n^+ is the concentration of impurity ions, n is the concentration of impurity centers, V_m is the maximum value of the correlation volume V_c, and $n_m = n^+V_m$ is the number of impurity ions that are redistributed from this volume to the spherical layer $r_c < r < r_m$. Upon redistribution of iron ions, $V_m = V_1 = 2\pi r_1^3/3$ (where r_1 is the radius of the first coordination sphere for a face-centered cubic structure) and $n_m = a = 5.92$ [3]. Equation (13) has the correct asymptotics and transforms into Eq. (12) in the limit $n_F/n_F^+ \longrightarrow 1$. Thus, our theory that includes the influence of small-sized donors on correlations in the arrangement of iron ions is based on Eq. (13).

In order to calculate the mobility μ by formulas (11), it is necessary to compute two correlation functions $g_{++}^{FF}(q)$ and $g_{++}^{FD}(q)$ in the framework of the hard sphere model. In this case, it should be taken into account that the presence of small-sized donors spatially arranged in a random manner weakens correlations in the location of iron ions. At sufficiently large concentrations of small-sized donors, when the energy of interaction between iron ions is considerably less than the energy of interaction between iron ions and small-sized donors, the correlation function $g_{++}^{FF}(q)$ is equal to zero $[g_{++}^{FF}(r) = 1]$ and correlations in the system of impurity ions are described only by the function $g_{++}^{FD}(q)$, which defines correlations in the arrangement of iron ions with respect to small-sized donors. We will restrict our consideration to not very high concentrations of small-sized donors. In this case, it is possible to construct a simple model that furnishes a means of performing numerical calculations. Let the condition $n_F + n_D > n_c$ be met. Then, an increase in the iron concentration leads to the ordering of iron ions, which tend to be spaced as far apart as possible. In doing so, it is clear that each small-sized donor can be surrounded by a correlation sphere of certain radius $\tilde{r}_c$ such that only neutral iron atoms occur in the correlation volume $\tilde{V}_c = 4\pi\tilde{r}^3/3$ around each small-sized donor. For iron ions, it is energetically unfavorable to be inside these correlation volumes due to the Coulomb repulsion between iron ions and small-sized donors. Therefore, iron ions are redistributed only over iron atoms that are located outside the correlation spheres of radius $\tilde{r}_c$. Let us eliminate these iron atoms from consideration by cutting the correlation volumes $\tilde{V}_c$ together with small-sized donors (the centers of these volumes) from the system of impurity centers and calculate the correlation function that describes the mutual arrangement of iron ions in this "perforated" system. Since small-sized donors are spatially arranged in a random way, the location of iron atoms in this perforated system is also random. Hence, it is assumed that the correlation functions in this perforated system should be calculated in the same way as in the system that is comprised of randomly arranged iron atoms in the ideal sample ($n_D = 0$). Note that Eq. (13) in which the iron atom concentration n_F is replaced by the effective concentration $\tilde{n}_F = n_F(1 - \tilde{V}_c n_D)$ should be used as the basic equation of the theory. As a result, the equation for the determination of the V_c parameter takes the form

$$n_F^+ = n_F(1 - \tilde{V}_c n_D)\left(1 - \frac{V_c}{V_1}\right)^a. \tag{14}$$

The basic equation (14) of the theory enables us to calculate the correlation function $g_{++}^{FF}(q)$ provided that the correlation volume $\tilde{V}_c$ is known.

Evidently, upon redistribution of iron ions with respect to the spatially fixed small-sized donor ions, the maximum correlation volume $\tilde{V}_c$ is equal to the volume per impurity ion, i.e., $V_m = 1/n^+$, and the number of ions n_m redistributed from this volume is equal to unity. Substitution of $V_m = 1/n^+$ and $n_m = 1$ into Eq. (13) gives the second equation in our set of equations for determining the correlation volume $\tilde{V}_c$

$$n_F^+ = n_F(1 - \tilde{V}_c n^+). \tag{15}$$

In the limiting case $n_F/n_F^+ \longrightarrow 1$, when the correlation spheres do not overlap, the volume occupied by iron ions is equal to $1 - V_c n_F^+ - \tilde{V}_c n_D$. Consequently, in this limiting case, the correlation volumes and the concentrations of impurity ions are related by the equation

$$n_F^+ = n_F(1 - V_c n_F^+ - \tilde{V}_c n_D). \tag{16}$$

At $n_F/n_F^+ \longrightarrow 1$, Eq. (14) transforms into Eq. (16), and, since $V_c \longrightarrow \tilde{V}_c$, Eq. (15) coincides with Eq. (16). Therefore, Eqs. (14) and (15) have the correct asymptotics. If the expression for the correlation volume $\tilde{V}_c$ from Eq. (15) is substituted into Eq. (14), instead of the set of two coupled equations (14) and (15) we can write the equivalent set consisting of two independent equations

$$\tilde{V}_c n_c = 1 - \frac{n_F^+}{n_F}, \tag{17a}$$

$$\eta = \frac{1}{8}a\left[1 - \left[\frac{n_c}{n_F(1 + n_D/n_F)}\right]^{1/a}\right]. \tag{17b}$$

The condition $n_F + n_D > n_c$ determines the lower boundary of the n_F values at which the set of Eqs. (17) is valid. The upper boundary can be obtained from the following reasoning. The correlation radius r_c cannot be larger than the screening length, because, at larger distances, the Coulomb interaction between ions is negligibly small and ions are not redistributed. The screening length can be calculated by the Thomas–Fermi formula $r_{\mathrm{TF}} = 6\pi n_e e^2/\kappa\varepsilon_F$. The maximum packing coefficient is estimated as $\eta_m = \pi r_{\mathrm{TF}} F^3 n_F^+/6$. The set of Eqs. (17) is valid only in the range of iron atom concentrations n_F

at which $r_c < r_{\mathrm{TF}}$, because the packing coefficient only in this range is limited from above by a deficit of iron atoms. Therefore, at high concentrations of iron atoms, we are forced to restrict ourselves to an estimate and to set $\eta = \eta_m$. The numerical estimates were obtained using the following parameters: $n_c = 4.5 \times 10^{18}$ cm^{-3}, $\varepsilon_F = 210$ meV, $m = 0.07m_0$, and $\kappa = 20$ [1]. At these parameters, the Thomas–Fermi screening length r_{TF} is equal to 6.8×10^{-7} cm and the packing coefficient is limited from above by $\eta_m = 0.475(n_c - n_D)/n_c$.

The set of Eqs. (17) permits us to calculate the correlation functions in the framework of the hard sphere model. The correlation function $\tilde{g}^{FD}_{++}(r)$, which describes the arrangement of small-sized donors relative to an iron atom, is computed by the formula

$$\tilde{g}^{FD}_{++}(r) = \begin{cases} 0 & r < \tilde{r}_c \\ 1 & r \ge \tilde{r}_c. \end{cases} \qquad (18)$$

The correlation function $\tilde{g}^{FF}_{++}(r)$, which defines the mutual arrangement of iron ions, is calculated by the Percus–Yevick method [5].

Here, it is pertinent to recall that the mobility in our theory is calculated from the Boltzmann kinetic equation in the Born approximation with due regard for the screening of the Coulomb potential for impurity ions within the Thomas–Fermi linear theory. The fulfillment of the corresponding conditions requires the smallness of a number of parameters, which for HgTe : Fe in the order of magnitude are as follows: $\hbar/\tau\varepsilon_F \approx 3 \times 10^{-3}$ (condition for applicability of the Boltzmann equation), $(k_F a_{\mathrm{B}})^{-1} \approx 0.1$ (condition for applicability of the Born approximation in the case of the Coulomb scattering potential), and $e^2/\kappa\bar{r}\,\varepsilon_F \approx 5 \times 10^{-2}$ (condition for applicability of the Thomas–Fermi theory). Here, $\bar{r}$ is the mean distance between electrons; a_{B} is the Bohr radius; and τ is the relaxation time of electron momentum, which was estimated from the mobility $\mu = 4 \times 10^4$ cm^2/V s. The above estimates indicate that the high concentration of conduction electrons ($n_e \approx 4.5 \times 10^{18}$ cm^{-3}) in the case of HgSe : Fe ensures the smallness of the basic parameters of our theory developed for calculating the mobility in a degenerate electron gas.

4. ELECTRON MOBILITY AT $T = 0$

We start the discussion of the results of calculations with the mobility μ^+ associated with the scattering by impurity ions, which is calculated by formulas (11), (17), and (18). The results of calculations are conveniently analyzed by separating two relative contributions to the electrical resistivity from formula (11) for μ^+: the contribution $\Delta\rho_{FD}/\rho_0$ from the interference due to the correlation in the arrangement of iron ions with respect to small-sized donors and the contribution $\Delta\rho_{FF}/\rho_0$ from the interference due to the correlation in the mutual arrangement of iron ions, that is,

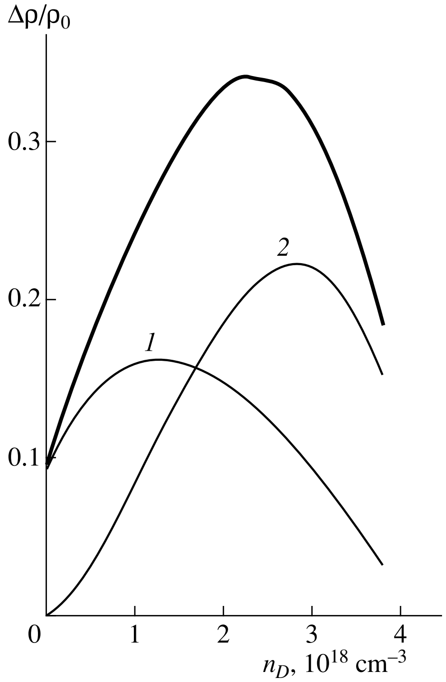

Fig. 1. Dependences of the electrical resistivity on the concentration of small-sized donors n_D. Contributions of the interference to the resistivity: the heavy line corresponds to the contribution of the interference $-\Delta\rho/\rho_0$ upon scattering by impurity ions, curve *1* represents the contribution of the interference $-\Delta\rho_F/\rho_0$ upon scattering by iron ions, and curve *2* shows the contribution of the interference $-\Delta\rho_{FD}/\rho_0$ upon scattering by iron ions and small-sized donors. Concentration of iron atoms $n_F = 5 \times 10^{18}$ cm^{-3}.

$$\begin{aligned} \frac{\Delta\rho_{FD}}{\rho_0} &= \frac{2\overset{+}{n}_F n_D}{n_c}\frac{\{g^{FD}_{++}(q)\}}{\{1\}}, \\ \frac{\Delta\rho_{FF}}{\rho_0} &= \frac{\overset{+}{n}{}_F^{2}}{n_c}\frac{\{g^{FF}_{++}(q)\}}{\{1\}}, \end{aligned} \qquad (19)$$

where

$$\{f(q)\} = \frac{2}{3}\frac{m}{(2\pi\hbar)^3 n_e}\int_0^{2k_F} q^3 dq |V_+(q)|^2 f(q).$$

Here, ρ_0 is the resistivity calculated for a random distribution of impurity ions. The total contribution $\Delta\rho$ from the interference effects to the resistivity is equal to $\Delta\rho_{FD} + \Delta\rho_{FF}$. The electron scattering by the impurity ion will be described as the scattering by a screened Coulomb center with $V_+(q) = (4\pi e^2)/\kappa(q^2 + r_{TF}^{-2})$. Within this approximation, formula (11) for μ_+ in the limit $g^{FF}_{++}(q) \longrightarrow 0$ and $g^{FD}_{++}(q) \longrightarrow 0$ transforms into the well-known Brooks–Herring formula for the mobility.

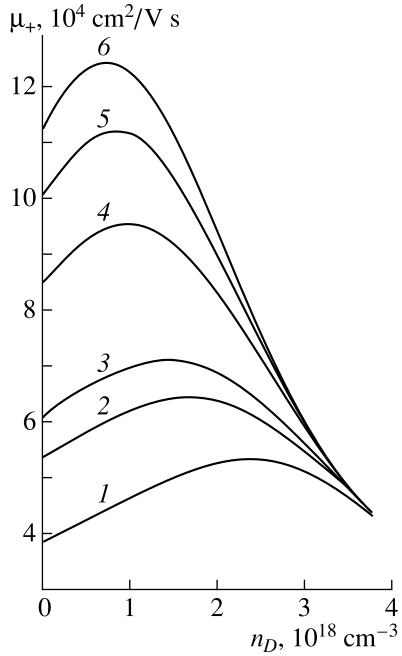

Fig. 2. Dependences of the mobility μ_+ upon scattering by impurity ions on the concentration of small-sized donors n_D at different concentrations of iron atoms n_F, 10^{18} cm^{-3}: (*1*) 5, (*2*) 8, (*3*) 10, (*4*) 20, (*5*) 30, and (*6*) 40.

Figure 1 displays the numerical data on the electrical resistivity as a function of n_D for the specific case $n_F = 5 \times 10^{18}$ cm^{-3}. Curve *1* shows the contribution $-\Delta\rho_{FF}/\rho_0$ (from the interference upon scattering by iron ions) to the resistivity. This contribution to the electrical resistivity (19) is the product of the integral involving the correlation function by the concentration factor n_F^{+2}/n_c, which monotonically decreases with an increase in n_D. According to relationship (17b), the packing coefficient $\eta = \pi r_c^3(n_c - n_D)/6$ can only increase with an increase in the concentration of small-sized donors, and, hence, the hard sphere diameter r_c increases with an increase in n_D. Therefore, at $r_c < r_{\mathrm{TF}}$, the integral $\{g_{++}^{FF}(q)\}$ is a monotonically increasing function of n_D and the quantity $-\Delta\rho_F/\rho_0$, which is the product of a monotonically decreasing function by a monotonically increasing function, reaches a maximum at a certain concentration of small-sized donors. Curve *2* depicts the contribution $-\Delta\rho_{FD}/\rho_0$ (from the interference associated with the correlation in the arrangement of iron ions with respect to small-sized donors) to the resistivity. As follows from Eq. (17a), the hard sphere diameter $\tilde{r}_c$ monotonically increases with an increase in n_D. As a consequence, the integral $\{g_{++}^{FD}(q)\}$ monotonically increases with an increase in n_D, while the concentration factor $\overset{+}{n}_F n_D$ reaches a maximum at $n_D = n_c/2$. Therefore, the resistivity $-\Delta\rho_{FD}/\rho_0$ reaches a maximum at the small-sized donor concentration close to $n_c/2$. The total contribution $-\Delta\rho$ (heavy line in Fig. 1) from the interference to the electrical resistivity contains two terms and also exhibits a maximum. Since the contribution from the interference to the electrical resistivity is negative, the dependence of the electron mobility μ^+ upon scattering by impurity ions on the concentration of small-sized donors has a maximum.

The dependences of the electron mobility μ_+ on the concentration of small-sized donors are depicted in Fig. 2. The value of $\mu_{+0} = 3.5 \times 10^4$ cm^2/V s (where $\mu_{+0} = e/mn^+\{1\}$ is the electron mobility upon scattering by randomly arranged impurity ions) was used in calculations. As can be seen from Fig. 2, the relative mobility at a maximum $\Delta\mu_+/\mu_{+0}$ decreases with an increase in the iron concentration. For example, $\Delta\mu_+/\mu_{+0} = 0.4$ at $n_F = 5 \times 10^{18}$ cm^{-3} (curve *1*) and $\Delta\mu_+/\mu_{+0} = 0.1$ at $n_F = 4 \times 10^{19}$ cm^{-3} (curve *6*). This behavior directly follows from formulas (17), according to which the higher the concentration of iron atoms, the closer the hard sphere diameter to its limiting value, and, hence, the smaller the possible increment in the hard sphere diameter upon an increase in the concentration of small-sized donors. As the concentration of iron atoms n_F increases, the location of the maximum in the $\mu_+(n_D)$ curve shifts toward the range of small concentrations n_D. As follows from our calculations, the maximum mobility is observed at small-sized donor concentrations $n_{Dm} \leq 2 \times 10^{18}$ cm^{-3}.

The influence of small-sized donors on the electron mobility in HgSe : Fe was first studied in [9]. The computational scheme used in this work involved two inconsistencies. First, the calculations were based on the basic equation of the theory for the determination of the hard sphere diameter, which was postulated in [2]. This equation has an incorrect asymptotics in the limit $\overset{+}{n}_F \longrightarrow n_F$ and, hence, cannot be used for the description of correlation in the arrangement of iron ions. Second, the authors of [9] assumed that $g_{++}^{FF}(q) = g_{++}^{FD}(q)$. However, correlations in the mutual arrangement of iron ions and correlations in the arrangement of iron ions with respect to a spatially fixed small-sized donor ion are described by different correlation functions. It is natural that the results obtained in the present work quantitatively differ from the results derived in [9], even though the essence and the main features of this phenomenon were correctly described and interpreted in [9]. In this work, the dependence of the electron mobility on the concentration of small-sized donors was experimentally investigated using HgSe : Fe samples doped with Ga ($n_F = 10^{19}$ cm^{-3}, and $n_{\mathrm{Ga}} = 0.2 \times 10^{18}$ cm^{-3}). Randomly arranged Ga atoms are ionized, because they correspond to the metallic side of the Mott transition, and represent small-sized donors whose concentration can be determined experimentally. The concentration

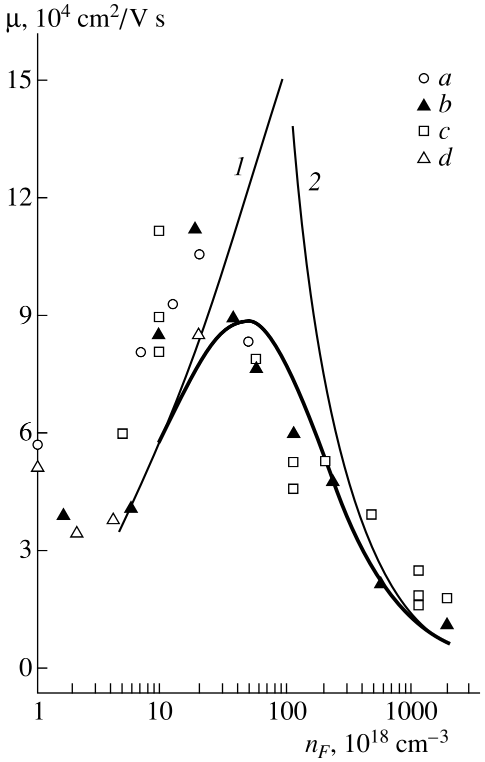

Fig. 3. Dependences of the mobility μ on the concentration of iron atoms n_F: (*1*) the mobility μ_+ determined by the impurity ion scattering and (*2*) the mobility μ_0 due to scattering by neutral iron atoms. The heavy line indicates the total mobility μ associated with the scattering by impurity centers. Points are the experimental data taken from (*a*) [12], (*b*) [11], (*c*) [13], and (*d*) [14].

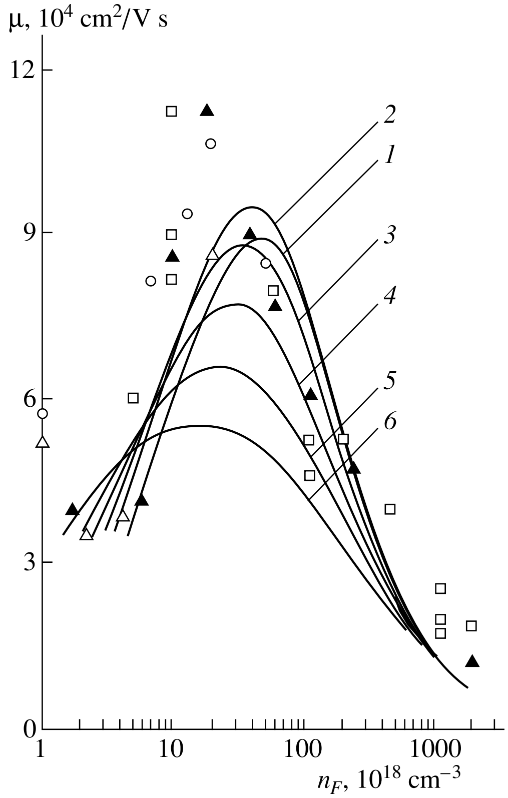

Fig. 4. Dependences of the mobility μ on the concentration of iron atoms n_F at different concentrations of small-sized donors n_D, 10^{18} cm^{-3}: (*1*) 0, (*2*) 1, (*3*) 1.5, (*4*) 2, (*5*) 2.5, and (*6*) 3. Points are the same experimental data as in Fig. 3.

of intrinsic small-sized donors in these samples was assumed to be negligibly small as compared to the concentration of Ga atoms. However, the study of these samples did not allow the authors to reveal a nonmonotonic character of the $\mu_+(n_D)$ dependence. The reason for the negative result can easily be seen from Fig. 2, in which calculated curve *4* corresponds to $n_F = 2 \times 10^{19}$ cm^{-3}. Actually, according to our calculations, the mobility at $n_D = 0$ is larger than that at $n_D = 2 \times 10^{18}$ cm^{-3}. In order to find the nonmonotonic behavior, it is necessary to have a set of sufficiently pure samples with Ga concentrations in the range $0 < n_{\text{Ga}} < 2 \times 10^{18}$ cm^{-3}. Moreover, it is desirable to choose samples with low iron concentrations $n_F \geq 4.5 \times 10^{18}$ cm^{-3}. In the wake of the work [9], the effect of Ga on the electron mobility in HgSe : Fe was considered in [10]. The calculations in this work were based on the equation for the determination of the hard sphere diameter, which was postulated in [8]. In our work, it was demonstrated that this equation in the limit $n_F^+/n_F \longrightarrow 1$ has an incorrect asymptotics and overestimates the rate of increase in the packing coefficient by one order of magnitude with an increase in the concentration of iron atoms. Hence, we will not compare the estimates obtained in [10] with the results of our calculations.

Now, let us dwell on the contribution from the electron scattering by neutral iron atoms to the mobility. As follows from formulas (11), the total electron mobility μ is expressed in terms of the mobility μ_+ associated with the scattering by impurity ions and the mobility μ_0 due to the scattering by neutral impurities through the formula $\mu^{-1} = \mu_+^{-1} + \mu_0^{-1}$. Here, $\mu_0 = A/(n_F - n_F^+)$, where A is the constant independent of the concentration of neutral iron atoms. The constant A was determined from the experimental data taken from [11], according to which $\mu = 2.2 \times 10^4$ cm^2/V s at the concentration of iron atoms $n_F = 5.8 \times 10^{20}$ cm^{-3}. At this concentration n_F and the concentration of small-sized donors $n_D = 1.5 \times 10^{18}$ cm^{-3}, the calculated mobility μ_+ is equal to 1.9×10^5 cm^2/V s and the constant A is 1.46×10^{25} cm^{-1} V^{-1} s^{-1}.

The results of calculations of the mobility for the ideally pure sample ($n_D = 0$) are shown in Fig. 3. As the iron concentration increases, the mobility μ_+ (curve *1*) increases as a result of a partial ordering in the arrangement of iron ions, and the mobility μ_0 (curve *2*) decreases owing to an increase in the concentration of neutral iron atoms that are spatially arranged in a random way. As a consequence, the dependence of the total mobility μ on the concentration n_F exhibits a maximum. The maximum mobility $\mu = 9 \times 10^4$ cm^2/V s is reached at the concentration of iron atoms $n_F = 5 \times 10^{19}$ cm^{-3}. In this case, $\mu_+ = 1.2 \times 10^5$ cm^2/V s and $\mu_0 = 3.2 \times 10^5$ cm^2/V s. The experimental data displayed in Fig. 3 are taken from [11–14]. In experiments, the maximum electron mobility $\mu = 1.1 \times 10^5$ cm^2/V s was observed at the iron concentration $n_F = 2 \times 10^{19}$ cm^{-3}. It should be remembered that the calculated data shown in Fig. 3 were obtained for the ideally pure sample ($n_D = 0$). In real HgSe : Fe samples, the concentration of small-sized donors that are spatially arranged in a random manner can be as high as $n_D = 2 \times 10^{18}$ cm^{-3}. Since the presence of small-sized donors at concentrations in the range $0 < n_D < 2 \times 10^{18}$ cm^{-3} favors an increase in the degree of ordering in the system of impurity ions, we calculated the mobilities $\mu(n_F)$ at different concentrations n_D. Curves *1–6* in Fig. 4 correspond to the concentrations n_D = 0, 1, 1.5, 2, 2.5, and 3×10^{18} cm^{-3}. According to our calculations, the maximum mobility $\mu = 9.5 \times 10^4$ cm^2/V s is observed at $n_D = 10^{18}$ cm^{-3} (curve *2*). At concentrations $n_D > 10^{18}$ cm^{-3}, the electron mobility decreases with an increase in the concentration of intrinsic donors.

5. CONCLUSION

Thus, in the present work, the basic equation of the theory proposed in [3] for the ideally pure sample ($n_D = 0$) was generalized to the real case of systems containing a sufficiently large amount of small-sized impurity donors. The application of the developed theory to the specific case of HgSe : Fe made it possible to calculate the dominant contribution (more than 80%) to an increase in the mobility. In our opinion, a good agreement with the experimental data suggests that the theory advanced can be useful for interpreting experiments related to investigations of interimpurity correlations in semiconductors.

REFERENCES

1. I. M. Tsidilkovski, in *Springer Series in Solid State Sciences*, Vol. 116: *Electron Spectrum of Gapless Semiconductors* (Springer-Verlag, Berlin, 1997).
2. Z. Wilamowski, K. Swatek, T. Dietl, and J. Kossut, Solid State Commun. **74** (8), 833 (1990); Z. Wilamowski, Acta Phys. Pol. A **77** (1), 133 (1990).
3. V. M. Mikheev, Fiz. Tverd. Tela (St. Petersburg) **41** (11), 1994 (1999) [Phys. Solid State **41**, 1830 (1999)].
4. J. M. Ziman, *Models of Disorder: The Theoretical Physics of Homogeneously Disordered Systems* (Cambridge Univ. Press, Cambridge, 1979; Mir, Moscow, 1982).
5. R. Balescu, *Equilibrium and Nonequilibrium Statistical Mechanics* (Wiley, New York, 1975; Mir, Moscow, 1978), Vol. 1.
6. I. G. Kuleev and I. Yu. Arapova, Fiz. Met. Metallogr. **88** (3), 43 (1999).
7. P. Laty, J. C. Joud, J. C. Mathieu, and P. Desre, Philos. Mag. B **38** (1), 1 (1978).
8. I. G. Kuleev, I. I. Lyapilin, and I. M. Tsidil'kovskiĭ, Zh. Éksp. Teor. Fiz. **102** (5), 1652 (1992) [Sov. Phys. JETP **75**, 893 (1992)].
9. C. Skierbiszewski, Z. Wilamowski, T. Suski, and J. Kossut, Semicond. Sci. Technol. **8** (1S), S40 (1993).
10. I. M. Tsidil'kovskiĭ, I. G. Kuleev, N. K. Lerinman, *et al.*, Fiz. Tekh. Poluprovodn. (St. Petersburg) **30** (12), 2113 (1996) [Semiconductors **30**, 1101 (1996)].
11. W. Dobrowolski, K. Dybko, S. Skierbiszewski, *et al.*, in *Proceedings of the 19th International Conference on Physics of Semiconductors, Warsaw, 1988*, Vol. 2, p. 1247.
12. F. Pool, J. Kossut, U. Debska, and R. Reifenberger, Phys. Rev. B **35** (8), 3900 (1987).
13. N. G. Gluzman, L. D. Sabirzyanova, I. M. Tsidil'kovskiĭ, *et al.*, Fiz. Tekh. Poluprovodn. (Leningrad) **20** (1), 94 (1986) [Sov. Phys. Semicond. **20**, 55 (1986)].
14. C. Skierbiszewski, T. Suski, W. Dobrowolski, *et al.*, Semicond. Sci. Technol. **4** (4), 293 (1989).

Translated by O. Borovik-Romanova

Physics of the Solid State, Vol. 43, No. 3, 2001, pp. 439–442. Translated from Fizika Tverdogo Tela, Vol. 43, No. 3, 2001, pp. 423–426.
Original Russian Text Copyright © 2001 by Kaminskiĭ, Solov'ev.

SEMICONDUCTORS AND DIELECTRICS

Emf Induced by a Change in the Samarium Ion Valence as a Result of a Phase Transition in SmS Single Crystals

V. V. Kaminskiĭ and S. M. Solov'ev
Ioffe Physicotechnical Institute, Russian Academy of Sciences, Politekhnicheskaya ul. 26, St. Petersburg, 194021 Russia
e-mail: Vladimir.Kaminski@shuvpop.ioffe.rssi.ru
e-mail: Serge.Soloviev@shuvpop.ioffe.rssi.ru

Received June 29, 2000

Abstract—The mechanism of the emf appearing in a semiconductor under heating in the absence of external temperature gradients, an effect revealed by the present authors, is considered. The experiments were performed on samarium sulfide (SmS) single crystals. It is shown that the emf is generated by an abrupt change in the samarium ion valence, which results from the ion screening by the electrons activated into the conduction band. We succeeded in obtaining emf pulses 1.3 s long with an amplitude of up to 2.5 V at $T \sim 460$ K, as well as CW emf generation within the 375- to 405-K temperature interval with a maximum value of ~50 mV. *© 2001 MAIK "Nauka/Interperiodica".*

Earlier, we reported on the anomalous behavior of the thermopower in samarium monosulfide (SmS) single crystals at $T = 435$–455 K, which consisted in the generation of emf spikes of amplitude larger than 10 mV [1]. This effect was assumed to be connected with the semiconductor–metal phase transition in SmS. This work aimed at studying this effect and revealing the mechanism of the emf generation in the course of the phase transition.

Samarium monosulfide undergoes an abrupt isostructural (NaCl–NaCl) transition from the semiconducting to metallic state after the electrons have reached a critical concentration in the conduction band [2]. This concentration has been experimentally reached in two ways to date, namely, by doping SmS and by acting on a sample mechanically [3]. In the latter case, the phase transition can be induced by a pressure (hydrostatic, uniaxial, indentor) which is the lowest on record for semiconducting materials [3–5]. The mechanism of this phase transition is based on the screening of the samarium-ion electric potential by the conduction electrons. The pressure-induced transition proceeds in two stages: (1) an abrupt increase in the conduction electron concentration through activation from ions which occupy interstitial lattice sites and have an activation energy $E_i \sim 0.045$ eV ($Sm^{2+} \longrightarrow Sm^{3+} + \bar{e}$) and (2) a similar change in the valence state of the samarium ions sitting at lattice sites through activation of electrons from the $4f$ levels with an activation energy $E_f = 0.23$ eV. Both transitions are of the Mott type and terminate in the expulsion of the E_i impurity levels and of the $4f^6$ levels into the conduction band. Stage (1) stimulates stage (2) in that it donates electrons to the conduction band in a sufficient amount [6]. The realization of stage (2) is also made possible by the fact that, at the critical phase-transition pressure (650 MPa), the $4f^6$ levels approach the conduction band bottom by ~0.1 eV, so that their pressure-induced shift is ~0.16 meV/MPa [1].

This work considers the possibility of inducing a phase transition by heating SmS single crystals. Heating within the temperature interval studied can stimulate only stage (1) of the phase transition [1]. Because the concentration of the interstitial samarium ions in SmS is $N_i \sim 10^{20}$ cm^{-3} [6], the conduction band should acquire ~10^{20} cm^{-3} additional electrons. However, impurity ions are distributed nonuniformly over the sample volume; therefore, the Mott transition in the defect system should not occur simultaneously throughout the sample. As a result, a concentration gradient of the conduction electrons will appear. Thus, by measuring the signal from two arbitrarily chosen points of the sample, one will generally observe the generation of an emf. It is this consideration that governed the configuration of our experiments.

Besides the emf measurements, we studied the thermal regimes of the sample regions to which the emf signal wires were connected, as well as the temperature variation dynamics in these regions. The temperature was measured by two copper–constantan thermocouples attached to the opposite end faces of the sample. The emf signal was obtained from the same faces. The sample was placed into an ampoule not much larger in volume than the sample and filled with vacuum oil. The ampoule was mounted in a container, likewise filled with oil and also with SiO_2 powder to preclude convective flows. The container was suspended inside a vessel with oil which was heated. In this way, we succeeded in eliminating practically all the temperature drops forming over a sample under heating and, as a consequence,

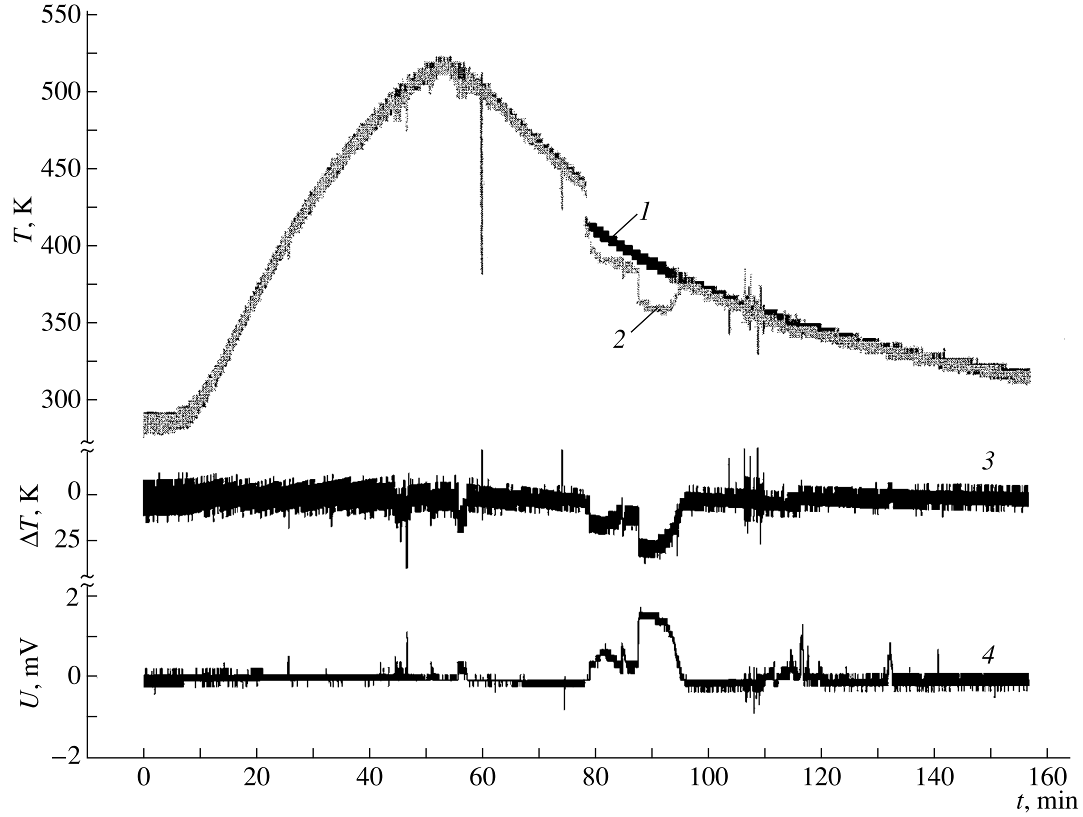

Fig. 1. Dynamics (*1*, *2*) of temperature variation at the sample end faces, (*3*) of their temperature difference, and (*4*) of the emf generated in the course of the heating and cooling of a SmS single crystal.

parasitic emf signals. The signals from the two thermocouples were computer processed and displayed in the course of the experiment.

The samples were SmS single crystals ~2.5 × 2 × 1 mm in size, which were cleaved along the [100], [010], and [001] planes from a larger single crystal and had a conduction electron concentration $n = (3–4) \times 10^{18}$ cm^{-3}. This value was derived from Hall measurements made on a large number of single crystals cleaved from the large crystal investigated and reflects not the measurement error but the expected difference in the values of n in the different regions of the samples studied.

Figure 1 plots the temperatures of both end faces of the sample (curves *1*, *2*), the difference between their temperatures (curve *3*), and the output signal (curve *4*) versus time.

The temperatures of the end faces are seen to vary synchronously under heating, which implies the absence of a temperature gradient across the sample. A similar situation is observed when the sample is cooled down to $T = 440$ K. At this temperature, the sample undergoes a jumplike drop in temperature recorded simultaneously at both its faces. This drop is equal to $\Delta T \approx 28$ K. As the temperature is further decreased, the temperatures of the two end faces vary differently; namely, the temperature of one of them decreases smoothly (curve *1*), whereas that of the other exhibits irregular downward deviations (curve *2*). This behavior is accounted for by the generation of an emf (curve *4*). Note the following features of the effect, which are in agreement with its proposed model: (1) Depending on the actual temperature, SmS can exist in two states (phases). (2) The transition from the high- to the low-temperature region involves an absorption of thermal energy. (3) Generation takes place only if the sample regions to which the signal wires are attached are at different temperatures.

Consider these features in more detail.

(1) Because the temperature $T = 440$ K separating the regions of existence of the two assumed SmS states lies in the region of thermopower (α) anomalies, we may invoke here the data of [1]. While the low-temperature phase of SmS is obviously its semiconducting state, which is characteristic of room and lower temperatures and has a conduction-electron activation energy $E_i = 0.05$ eV, the high-temperature phase has a conduction activation energy of ~0.2 eV. The two phases also differ in the temperature dependence of the thermopower; namely, the low-temperature one exhibits a decrease in α with increasing T, which is typical of semiconductors, whereas in the high-temperature phase, α is small, constant, and even rises slightly with

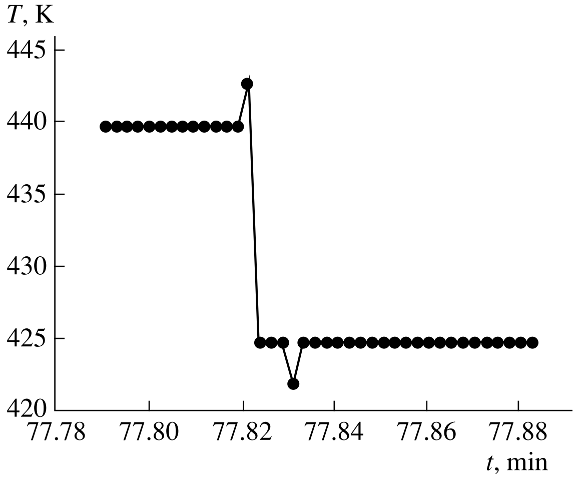

Fig. 2. Determination of the characteristic time of the SmS single-crystal transition from the high- to low-temperature phase (the point-to-point time interval is 0.1428 s).

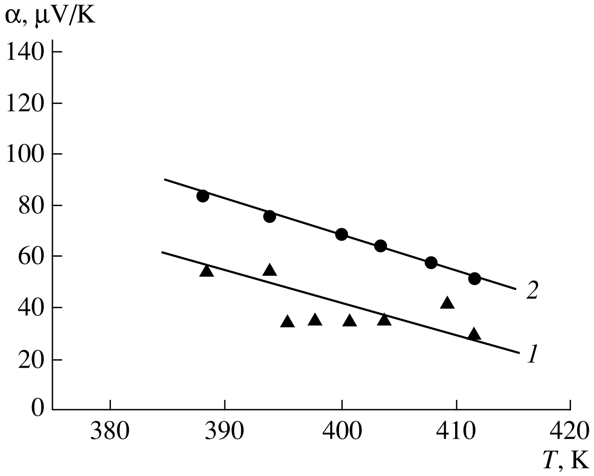

Fig. 3. Temperature dependences of the thermopower of SmS single crystals: (*1*) data of Fig. 1 and (*2*) from [1].

T [1]. Within the proposed model of the effect, the abrupt increase in the activation energy to a value close to that of the samarium ion $4f$ levels, $E_f = 0.23$ eV, can be explained as being due to the disappearance of the E_i states as a result of the Mott-type phase transition (ionization of all Sm^{2+} interstitials with increasing temperature). The behavior of $\alpha(T)$ is in agreement with this explanation [1].

(2) The absorption of energy in the transition from the high- to the low-temperature phase may be associated with the structural changes the SmS undergoes when the interstitial samarium ions transfer from the tri- to divalent state, because the radius of Sm^{3+} is considerably larger than that of Sm^{3+} (1.14 and 0.96 Å, respectively [7]). We attempted to estimate the characteristic transition time τ from the duration of the jump in T. Figure 2 presents the dependence of T on time in the region of the jump, which was obtained in the same conditions as the curves in Fig. 1, but in another heating cycle of the sample. The measured value is $\tau \sim 0.1$ s.[1] It is small enough to permit a rough estimation of the energy expended in the phase transformation of the sample, $Q = cv\Delta T$, where $c = 1.8$ J/(cm^3 K) is the heat capacity of the semiconducting SmS [8] and $v \approx 0.005$ cm^3 is the sample volume. The result is $Q \approx 0.23$ J. This yields 46 J/cm^3 (8.3×10^3 J/kg) for the specific energy of the phase transition under study. This value is less by two orders of magnitude than the metal–semiconductor phase-transition energy in SmS [8, 9], which is in good agreement with the fact that, according to the model under consideration, the number of samarium ions transferring from the tri- to divalent state in the SmS metal–semiconductor transition is larger by two orders of magnitude than in our case (~10^{22} and 10^{20} cm^{-3}, respectively).

(3) The last feature gives one grounds to maintain that the emf generated in this experiment originates from the thermopower. In this case, the temperature gradient across the sample arises due to the transition from the high- to low-temperature phase proceeding incoherently over the sample volume. This can be verified by calculating the temperature dependence of the thermopower from the data in Fig. 1, i.e., by dividing the values of the emf on curve *4* by the values of ΔT taken from curve *3*. The $\alpha(T)$ relation obtained in this way for the 385- to 415-K interval, where $\Delta T \neq 0$, is displayed in Fig. 3. It behaves in agreement with the $\alpha(T)$ relation obtained in [1], which attests to the mechanisms of the effects having a common nature.

One can thus maintain that one of the mechanisms of the emf generation observed under heating of SmS single crystals consists in the onset of temperature gradients in the sample volume as the system of strained samarium ions undergoes local phase transitions, and it is these gradients that generate the emf by the conventional thermoelectric mechanism.

The maximum value of the gradient recorded in our experiment is $\Delta T \approx 125$ K. Considering that α in SmS does not exceed 100 μV/K for $T \geq 400$ K, the magnitude of the emf generated by the above mechanism should not exceed 12 mV. However, emf spikes as high as 80 mV were observed [1], which certainly cannot be fully accounted for within this mechanism of the effect.

The maximum emf spike that we succeeded in detecting in this work was 2.5 V in a pulse 1.3 s long (Fig. 4). The pulse occurred at the temperatures of the sample end faces equal to 445 and 480 K, respectively. This pulse may be due to a large conduction-electron concentration gradient setting in at the phase transition in the strained samarium ion system ($Sm^{2+} \longrightarrow Sm^{3+} + \bar{e}$), which occurs locally near one of the end faces. As follows from an electrostatics calculation, generation of a

---

[1] This value may prove to be an overestimate because of the limited possibilities of this experiment.

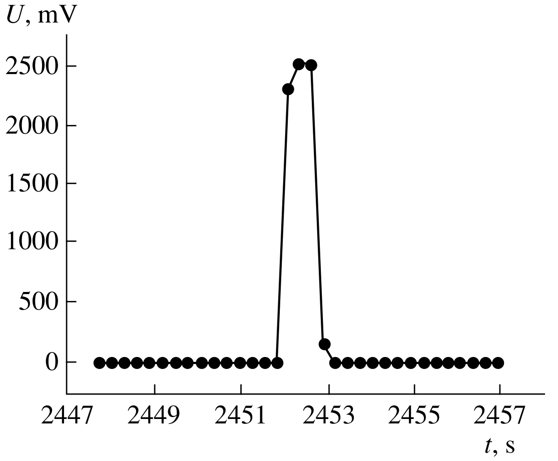

Fig. 4. Maximum emf pulse obtained when heating a SmS single crystal.

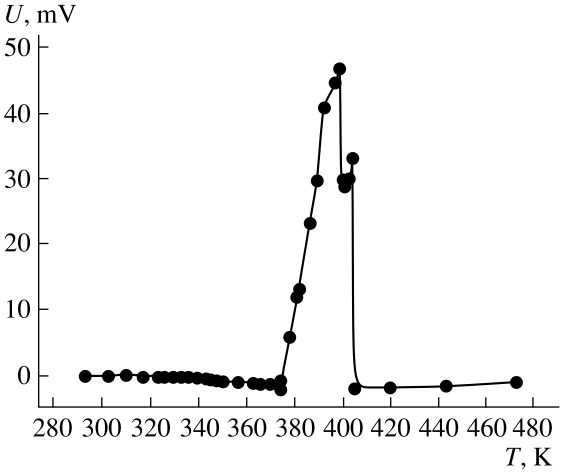

Fig. 5. Temperature dependence of the emf generated in a heated SmS single crystal.

potential-difference pulse with an amplitude of 2.5 V may be expected for the actual sample and contact geometry if a phase transition takes place in a region of radius ~0.2 μm.[2] This second mechanism of emf generation is more sensitive than the first one to selection of the points of wire attachment to the sample, as well as to the actual conditions of heat influx and removal. By properly varying these experimental parameters on a larger single-crystal SmS sample measuring 9.5 × 5 × 5 mm and having $n = 2 \times 10^{19}$ cm^{-3}, we succeeded in obtaining CW generation with a signal of ~50 mV (Fig. 5). This signal may be assumed to be an envelope of a large number of pulsed signals. The region where this effect is observed, 375–405 K, is shifted toward lower temperatures compared to the one recorded in [1], which is in accord with the proposed model, because the magnitude of n in this sample was higher than that in the sample studied in [1].

Thus, heating SmS single crystals gives rise to emf generation. This effect is associated with a change in the samarium ion valence as a result of a Mott-type phase transition occurring in the system of impurity (interstitial) Sm^{2+} ions. There are two grounds for the generation of the emf: (i) the onset of temperature gradients in the sample as a result of absorption and release of the phase-transition energy and (ii) the formation of conduction-electron concentration gradients because of a change in the valence $Sm^{2+} \rightleftarrows Sm^{3+} + \bar{e}$. The results obtained, in particular, those presented in Fig. 4, suggest the possibility of applying this effect to the conversion of thermal to electrical energy.

ACKNOWLEDGMENTS

The authors are grateful to A.V. Golubkov for providing SmS single crystals and to M.V. Romanova for the sample characterization.

This work was supported by the Russian Foundation for Basic Research, grant no. 00-02-16947.

REFERENCES

1. M. M. Kazanin, V. V. Kaminskiĭ, and S. M. Solov'ev, Zh. Tekh. Fiz. **71** (5), 144 (2000) [Tech. Phys. **45**, 659 (2000)].
2. S. I. Grebinskiĭ, V. V. Kaminskiĭ, A. V. Ryabov, and N. N. Stepanov, Fiz. Tverd. Tela (Leningrad) **24** (6), 1874 (1982) [Sov. Phys. Solid State **24**, 1069 (1982)].
3. I. A. Smirnov and V. S. Oskotskiĭ, Usp. Fiz. Nauk **124** (2), 241 (1978) [Sov. Phys. Usp. **21**, 117 (1978)].
4. V. V. Kaminskiĭ, A. A. Vinogradov, N. N. Stepanov, and I. A. Smirnov, Pis'ma Zh. Tekh. Fiz. **9** (10), 624 (1983) [Sov. Tech. Phys. Lett. **9**, 269 (1983)].
5. V. V. Kaminskiĭ and Sh. Lani, Zh. Tekh. Fiz. **68** (3), 53 (1998) [Tech. Phys. **43**, 314 (1998)].
6. V. V. Kaminskiĭ, V. A. Kapustin, and I. A. Smirnov, Fiz. Tverd. Tela (Leningrad) **22**, 3568 (1980) [Sov. Phys. Solid State **22**, 2091 (1980)].
7. A. V. Golubkov, N. F. Kartenko, V. M. Sergeeva, and I. A. Smirnov, Fiz. Tverd. Tela (Leningrad) **20** (1), 228 (1978) [Sov. Phys. Solid State **20**, 126 (1978)].
8. V. V. Kaminskiĭ, Yu. F. Solomonov, V. E. Egorov, *et al.*, Fiz. Tverd. Tela (Leningrad) **18** (10), 3135 (1976) [Sov. Phys. Solid State **18**, 1830 (1976)].
9. V. V. Kaminskiĭ, Fiz. Tverd. Tela (Leningrad) **20** (6), 1742 (1978) [Sov. Phys. Solid State **20**, 1008 (1978)].
10. V. Zelezny, J. Petzelt, V. V. Kaminski, *et al.*, Solid State Commun. **72** (1), 43 (1989).

Translated by G. Skrebtsov

---

[2] We calculated the potential difference between two points (where the wires were attached to the sample) of the electrostatic field of a sphere (the sample region where the phase transition occurs), which was charged uniformly with a volume charge density $\rho = 10^{20}\bar{e}$ cm^{-3} and was placed in a medium with a dielectric permittivity $\varepsilon = 18$ (semiconducting SmS [10]).

Physics of the Solid State, Vol. 43, No. 3, 2001, pp. 443–446. Translated from Fizika Tverdogo Tela, Vol. 43, No. 3, 2001, pp. 427–430.
Original Russian Text Copyright © 2001 by Mustafaeva, Kerimova, Gasanov.

SEMICONDUCTORS AND DIELECTRICS

Exciton Characteristics of $Tl_{1-x}Cu_xInS_2$ Single Crystals

S. N. Mustafaeva, É. M. Kerimova, and N. Z. Gasanov
Institute of Physics, Academy of Sciences of Azerbaijan, pr. Narimanova 33, Baku, 370143 Azerbaijan

Received July 25, 2000

Abstract—The absorption spectra of $Tl_{1-x}Cu_xInS_2$ single crystals (x = 0; 0.005; 0.010; 0.015) are interpreted using experimental data. The allowed interband direct transitions are determined, and the energy gap, binding energy, temperature-shift coefficient, Bohr radius, and reduced effective mass of the exciton are estimated. © *2001 MAIK "Nauka/Interperiodica".*

An investigation of the physical properties of $TlMC_2^{VI}$ compounds (M is In, Ga; C is S, Se, Te) and solid solutions based on these compounds is of practical importance in establishing the relationship between the properties and the composition of these materials and in controlling their optical properties.

According to crystallographic data, layered $TlInS_2$ single crystals are described by the C_{2h}^6–$C2/c$ space group. There are 16 $TlInS_2$ formula units in the unit cell and $Z = 8$ in the primitive cell [1]. It has been shown [2] that the fundamental absorption edge in $TlInS_2$ crystals corresponds to the energy 2.512 eV at 77 K and 2.363 eV at 300 K. Two exciton peaks at 2.58 and 2.87 eV have been revealed in the absorption spectra of $TlInS_2$ single crystals at 10 K [3]. It is also known [4] that $CuInS_2$ crystals have a direct band gap and are characterized by a large absorption coefficient ($\alpha \geq 10^4$ cm^{-1}), which makes them a perspective material for fabricating photocells.

It seems to be of interest to study the $TlInS_2$–$CuInS_2$ system, namely, the effect of the partial replacement of thallium ions by copper ions on the exciton characteristics of layered $TlInS_2$ single crystals. Such an investigation is the subject of the present paper.

To determine the mutual solubility of the $TlInS_2$–$CuInS_2$ compounds, samples of the $Tl_{1-x}Cu_xInS_2$ alloys were fabricated by fusing stoichiometric alloying compositions in quartz ampoules, pumped down to a vacuum of 1.3×10^{-3} Pa, by the two-temperature synthesis method. The differential thermal and x-ray phase analyses were used to control the single-phase state of the alloys over the entire concentration interval. The equilibrium diagram of the $TlInS_2$–$CuInS_2$ system [5] was constructed on the basis of the data of the differential thermal and x-ray phase analyses and resistivity measurements. This diagram is a quasi-binary section of the quaternary Tl–Cu–In–S system and represents an eutectic diagram (the eutectic alloy contains 50 mol % $TlInS_2$ and $CuInS_2$ and melts at 995 K) with the solid-solution regions restricted to 3.0 mol % on the $TlInS_2$ side and to 2.0 mol % on the $CuInS_2$ side. The layered $Tl_{1-x}Cu_xInS_2$ single crystals with x = 0; 0.005; 0.010; 0.015 were grown by the Bridgman–Stockbarger method.

The $Tl_{1-x}Cu_xInS_2$ samples used to measure the optical properties were obtained by cutting massive single crystals along the natural cleavage plane and were approximately 20 μm thick. When making measurements, the cleavage plane of the crystals was oriented perpendicular to the optical axis of the experimental setup. The exciton spectra of the $Tl_{1-x}Cu_xInS_2$ samples were studied on a special setup for integrated investigations of the optical and photoelectric spectra of semiconductor crystals by modulation spectroscopy methods. The setup was based on a KSVU-6M computing complex, which makes it possible to automate recording and mathematical processing of the spectra. The setup resolution was 0.1 meV. The investigations were performed in a wide temperature range by using a

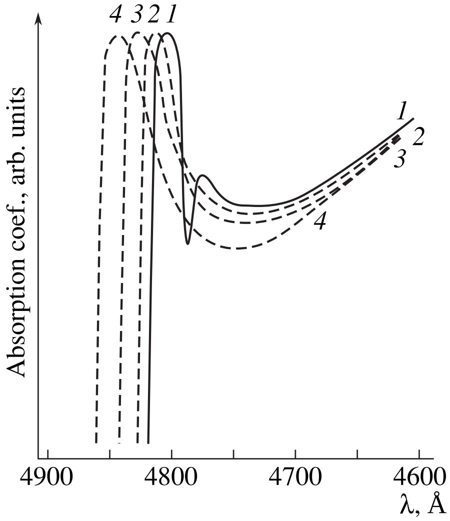

Fig. 1. Absorption spectra of a $TlInS_2$ single crystal at different temperatures: (*1*) 20, (*2*) 40, (*3*) 60, and (*4*) 80 K; the crystal thickness is 23 μm.

1063-7834/01/4303-0443$21.00 © 2001 MAIK "Nauka/Interperiodica"

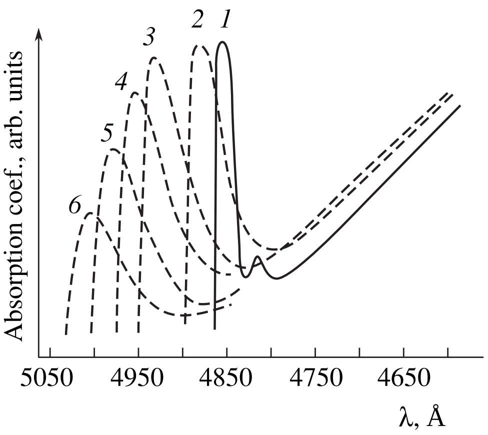

Fig. 2. Absorption spectra of the $Tl_{0.995}Cu_{0.005}InS_2$ single crystal at different temperatures: (*1*) 20, (*2*) 70, (*3*) 120, (*4*) 140, (*5*) 160, and (*6*) 180 K; the crystal thickness is 20 μm.

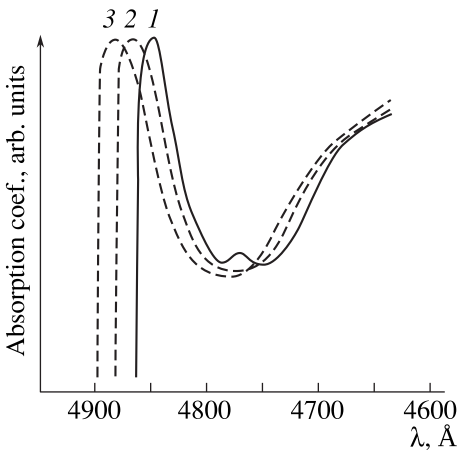

Fig. 3. Absorption spectra of the $Tl_{0.99}Cu_{0.01}InS_2$ single crystal at different temperatures: (*1*) 20, (*2*) 60, and (*3*) 80 K; the crystal thickness is 18 μm.

helium optical cryostat UTREKS with a temperature-stabilizing system (the stabilization precision was 0.02 K). The optical measurements were carried out in the temperature interval 20–200 K.

Figure 1 shows the absorption spectra of a $TlInS_2$ single crystal at different temperatures. The spectra of $Tl_{1-x}Cu_xInS_2$ crystals at $x = 0.005$, 0.010, and 0.015 are shown in Figs. 2, 3, and 4, respectively. The wavelength range investigated was 4600–5050 Å.

The investigation of the absorption spectra of the $Tl_{1-x}Cu_xInS_2$ single crystals showed that the absorption edge shifts to higher energies with decreasing temperature, and a clearly pronounced absorption band associated with direct transitions to the exciton state was observed in the vicinity of the fundamental absorption edge. An exciton peak at 2.58 eV was revealed in $TlInS_2$ at 20 K (Fig. 1). As was mentioned above, the same exciton peak in $TlInS_2$ was also revealed in [3] at 10 K. As the temperature decreased from 200 to 20 K, the exciton absorption maximum shifted to higher energies.

It can be seen from Figs. 1–4 that, for the crystals studied, the intensity of the exciton peaks decreases only slightly with the temperature growth from 20 to 80 K and diminishes considerably with a further

Table 1. Energy positions of the maxima of the exciton peaks in the $Tl_{1-x}Cu_xInS_2$ single crystals (x = 0; 0.005; 0.010; 0.015) at different temperatures

T, K	$E^{ex}(n = 1)$, eV			
	$TlInS_2$	$Tl_{0.995}Cu_{0.005}InS_2$	$Tl_{0.99}Cu_{0.01}InS_2$	$Tl_{0.985}Cu_{0.015}InS_2$
20	2.5800	2.5483	2.5609	2.5493
30		2.5462		
40	2.5758	2.5452	2.5583	2.5457
50		2.5415		
60	2.5680	2.5389	2.5504	2.5415
70		2.5337		
80	2.5588	2.5301	2.5415	2.5327
90		2.5255		
100		2.5198	2.5332	2.5229
110		2.5137		
120		2.5091	2.5249	2.5127
140	2.5250	2.4990	2.5132	2.4995
160		2.4870	2.5005	2.4880
180		2.4741	2.4890	2.4750
200	2.4915		2.4775	2.4608

increase in temperature from 80 to 200 K. In addition, the exciton peaks broaden noticeably with increasing temperature. In comparison with the $TlInS_2$ single crystals, the exciton absorption band in the $Tl_{1-x}Cu_xInS_2$ single crystals was shifted to lower energies. The energies corresponding to the exciton-peak maxima at different temperatures are presented in Table 1.

As can be seen from Figs. 1–4, broadening of the exciton absorption band was observed with an increase in the content of copper in the crystals investigated.

Figure 5 shows the temperature dependence of the spectral position of the maximum of the exciton absorption band in the $Tl_{0.985}Cu_{0.015}InS_2$ single crystal (curve *2*). The $E^{ex}(T)$ dependence for $TlInS_2$ is also presented here for comparison (curve *1*). The experimental $E^{ex}(T)$ dependence is characterized by two slopes. In the interval $20 \leq T \leq 60$ K, the temperature-shift coefficient of the exciton peak in $TlInS_2$ is $\partial E^{ex}/\partial T = -2.8 \times 10^{-4}$ eV/K; in the interval $60 \leq T \leq 200$ K, it is -5.8×10^{-4} eV/K. Partial replacement of thallium ions in $TlInS_2$ by copper ions affects the temperature-shift coefficient of this exciton peak only slightly. For example, for $Tl_{0.985}Cu_{0.015}InS_2$, we have $\partial E^{ex}/\partial T = -2.2 \times 10^{-4}$ eV/K within the interval $20 \leq T \leq 60$ K and -6.1×10^{-4} eV/K within the interval $60 \leq T \leq 200$ K.

Along with the main exciton band, a second band corresponding to $n = 2$ was observed at low temperatures ($T = 20$ K) in the absorption spectra of the $Tl_{1-x}Cu_xInS_2$ crystals at $x = 0$; 0.005; and 0.010 (Figs. 1–3). The second exciton peak was highest in the $TlInS_2$ crystals. The amplitude of this peak decreased with an increasing content of copper, and, finally, at $x = 0.015$, the second exciton peak was not revealed at all (Fig. 4). Using the energy difference between the maxima corresponding to the ground and first excited exciton states, we determined the exciton binding energy E_b^{ex} in the crystals studied (Table 2).

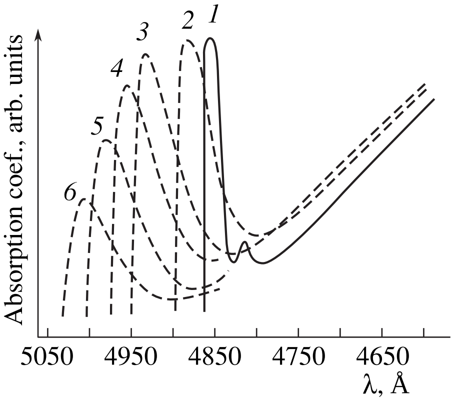

Fig. 4. Absorption spectra of the $Tl_{0.985}Cu_{0.015}InS_2$ single crystal at different temperatures: (*1*) 20, (*2*) 60, (*3*) 100, (*4*) 140, (*5*) 160, and (*6*) 180 K; the crystal thickness is 17 μm.

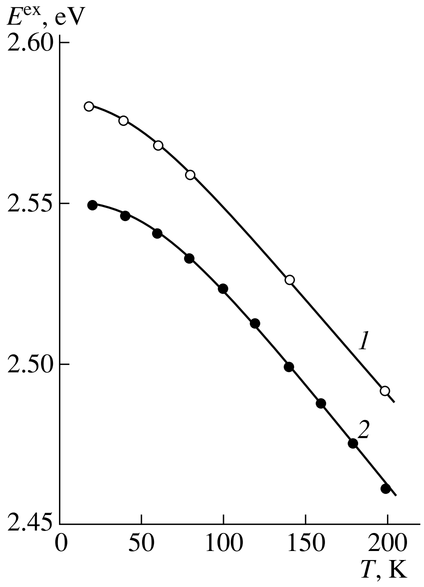

Fig. 5. Temperature dependence of the energy position of the maximum of the exciton absorption band in the (*1*) $TlInS_2$ and (*2*) $Tl_{0.985}Cu_{0.015}InS_2$ single crystals.

It should be pointed out that the exciton binding energy grew as the content of copper in the $TlInS_2$ crystals increased. From the low-temperature ($T \approx 25$ K) data on the absorption spectra of the $TlInS_2$ single crystals [6], the exciton binding energy was calculated to be 25 meV. This result is consistent with our data. The obtained values of the exciton binding energy made it possible to estimate the exciton Bohr radius (a^*) and reduced effective mass (m^*) of the exciton in the $Tl_{1-x}Cu_xInS_2$ crystals whose values are also presented in Table 2. The value of the dielectric constant ($\varepsilon \approx 11$) used in calculating a^* and m^* was taken from [7].

Table 2. Exciton characteristics of the $Tl_{1-x}Cu_xInS_2$ single crystals at $T = 20$ K

Crystal composition	Crystal thickness, μm	E_1^{ex}, eV ($n = 1$)	E_2^{ex}, eV ($n = 2$)	E_b^{ex}, meV	a^*, Å	m^*
$TlInS_2$	23	2.5800	2.5947	20	33	$0.17m_0$
$Tl_{0.995}Cu_{0.005}InS_2$	20	2.5483	2.5710	31	21	$0.27m_0$
$Tl_{0.99}Cu_{0.01}InS_2$	18	2.5609	2.6012	54	12	$0.46m_0$

Using the values of the exciton binding energy, we also determined the energy gap. For example, at T = 20 K, E_g is equal to 2.60 eV for $TlInS_2$ and 2.5793 eV for $Tl_{0.995}Cu_{0.005}InS_2$.

Thus, it can be concluded that partial replacement of thallium by copper in $TlInS_2$ single crystals results in a modification of the absorption spectra and a change in the exciton characteristics, which makes it possible to control the optical parameters of these single crystals.

REFERENCES

1. D. Müller and H. Hahn, Z. Anorg. Allg. Chem. **438**, 258 (1978).
2. G. D. Guseinov, E. Mooser, E. M. Kerimova, *et al.*, Phys. Status Solidi **34**, 33 (1969).
3. J. A. Kalomiros and A. N. Anagnostopolus, Phys. Rev. B **50** (11), 7488 (1994).
4. I. V. Bodnar’, Neorg. Mater. **36** (2), 157 (2000).
5. E. M. Kerimova, G. D. Guseinov, and F. Mamedov, Turk. J. Phys. **21** (2), 225 (1997).
6. M. Ya. Bakirov, G. I. Abutalybov, and N. M. Zeĭnalov, Fiz. Tekh. Poluprovodn. (Leningrad) **17** (7), 1357 (1983) [Sov. Phys. Semicond. **17**, 863 (1983)].
7. S. N. Mustafaeva, M. M. Asadov, and V. A. Ramazanzade, Fiz. Tverd. Tela (St. Petersburg) **38** (1), 14 (1996) [Phys. Solid State **38**, 7 (1996)].

Translated by A. Poushnov

Physics of the Solid State, Vol. 43, No. 3, 2001, pp. 447–457. Translated from Fizika Tverdogo Tela, Vol. 43, No. 3, 2001, pp. 431–441.
Original Russian Text Copyright © 2001 by Firsov, Kudinov.

SEMICONDUCTORS AND DIELECTRICS

The Polaron State of a Crystal

Yu. A. Firsov and E. K. Kudinov
Ioffe Physicotechnical Institute, Russian Academy of Sciences, Politekhnicheskaya ul. 26, St. Petersburg, 194021 Russia
e-mail: kudinov@ekk.ioffe.rssi.ru

Received July 31, 2000

Abstract—The quantum mechanics of an electron–nuclear system with strong electron–phonon coupling is considered. First, a two-site model is treated in the adiabatic approximation. As the coupling constant increases, electron transfer undergoes qualitative changes; more specifically, a potential barrier forms in the adiabatic potential, the electron transfer becomes associated with the tunneling of nuclei through the barrier, and the level splitting in the system falls off exponentially. The properties of a similar crystal model are discussed. It is shown that electron transfer in a crystal in the case of strong coupling is likewise associated with the tunneling of nuclei through barriers in the deformation space. Strong coupling modifies the electron–electron interaction terms. The Hamiltonian (exchange) terms, which are not associated with electron transfer, are only weakly modified. At the same time, the terms involving transfer (the band terms) undergo exponential reduction and vanish in the limit as $M \longrightarrow \infty$ (M is the ion mass) and the carriers become small polarons. This reduction provides a basis for the natural mechanism of enhancement of the isotope effect. *© 2001 MAIK “Nauka/Interperiodica”.*

Recent years have witnessed increasing interest in phenomena associated with strong electron–phonon coupling (the polaron effect). This interest was initiated by the observation of a colossal magnetoresistance in a number of manganates (a discovery promising a considerable application potential), which stimulated intense investigation of their properties (structural, magnetic, optical, transport, etc. [1–5]). One of the most important results of that investigation is certainly the establishment of the essential role of electron–phonon coupling (EPC), in particular, of polaron effects, which should be taken into account when interpreting experimental data. Note the discovery of a giant isotope effect in these compounds [6]. It was found [7] that substitution of O^{18} for the O^{16} isotope transferred some insulating manganates to the conducting state; that is, isotope substitution changed the nature of the ground state. This phenomenon could hardly be possible in the absence of a mechanism of enhancement of the isotope effect, which is readily realized under strong EPC.

Earlier, attention was focused on polarons in connection with the discovery of high-temperature superconductivity, where the bipolaron model [8] was considered as a candidate capable of interpreting the mechanism of the phenomenon. Irrespective of the success (or failure) in this field, the interest in this model as an alternative to the BCS theory is fully justified and its study may reveal a number of characteristics of the superconducting state which the BCS model leaves unclarified.

This paper reports a study of the behavior of an electron interacting with lattice vibrations as a function of the strength of this interaction, which is made within the adiabatic approximation. We consider the simplest one-electron two-site model (a pair of cation–anion complexes), which allows detailed investigation of its properties.[1] This model is used as a basis to discuss how these properties manifest themselves in a crystal. It is pointed out that for a strong enough EPC, a number of characteristics of the crystal undergo qualitative changes. In particular, the Hamiltonian terms describing electron–electron interaction become substantially modified.

1. ADIABATIC POTENTIALS IN THE TWO-SITE MODEL

The Hamiltonian of the two-site model under study has the form

$$\begin{gathered} H = H_0 + V, \quad H_0 = T + U(x_1, x_2), \\ T = \frac{1}{2m}(\hat{p}_1^2 + \hat{p}_2^2), \\ U = \frac{M\omega^2(x_1^2 + x_2^2)}{2} - \sqrt{2}g(\hat{n}_1 x_1 + \hat{n}_2 x_2), \\ V = -J(\hat{a}_1^+\hat{a}_2 + \hat{a}_2^+\hat{a}_1), \quad \hat{n}_i \equiv \hat{a}_i^+\hat{a}_i, \end{gathered} \tag{1}$$

where $\hat{p}_i = i\hbar d/dx_i$ is the momentum operator of nucleus i; $\hat{a}_i^+$ and $\hat{a}_i$ are the operators of creation and annihilation of the electron at site i, respectively; $i = 1, 2$;

---

[1] The usefulness of such a study was pointed out by us in [9]. Note that this model treated in terms of the adiabatic approximation was the subject of investigation in numerous publications. However, we have found it reasonable to give here a fairly complete account of it, while focusing attention on the points of particular significance for crystals.

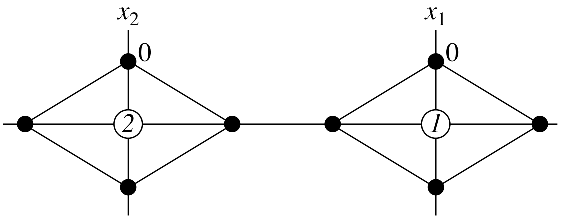

Fig. 1. Two-site model. Filled circles are anions and open circles are cations.

M and ω are the nuclear mass and vibration frequency, respectively; x_i is the nuclear coordinate; g is the EPC constant; and J is an energy constant depending on the wave function overlap of electrons at different sites and determining the electron level splitting at $g = 0$. The Hamiltonian in Eq. (1) is invariant under a simultaneous interchange of indices $(1, 2) \longrightarrow (2, 1)$ of the electronic and nuclear operators (see [9]). We shall limit ourselves here to considering only the one-electron states, which makes valid the relation

$$\hat{n}_1 + \hat{n}_2 = 1. \tag{2}$$

A possible realization of this model is shown in Fig. 1, where two identical cation–anion complexes are depicted. The complex consists of four anions which are located at the vertices of a rhombus centered on a cation. The electron migrates among the cations. It is assumed that deformation changes only the length of the rhombus diagonal. The deformation may be characterized by the position x_i ($i = 1, 2$) of one of the vertices. The reckoning is done from the equilibrium position in the absence of the electron.

In the one-electron problem, the EPC in this model depends only on the difference $x_1 - x_2$. In our earlier study [9], we considered only the two-site model and, therefore, the terms depending on $x_1 + x_2$ were dropped. Having in mind an analysis of a more general model, we intend to retain both variables x_1 and x_2 up to a certain moment. [All the parameters of the Hamiltonian in Eq. (1) coincide with those introduced in [9], but the energy is displaced by $-g^2/2M\omega^2$.]

Now, we shall look for the steady-state wave function of Hamiltonian (1) in the form

$$\Psi = C_1(x_1, x_2)a_1^+|0\rangle + C_2(x_1, x_2)a_2^+|0\rangle. \tag{3}$$

The quantities $C_i(x_1, x_2)$ satisfy the coupled equations

$$\begin{aligned} H_1(x_1, x_2)C_1 + JC_2 &= EC_1, \\ JC_1 + H_2(x_1, x_2)C_2 &= EC_2, \\ H_i(x) \equiv T + \frac{M\omega^2(x_1^2 + x_2^2)}{2} &- \sqrt{2}gx_i. \end{aligned} \tag{4}$$

We determine the adiabatic potentials $E_\pm(x_1, x_2)$ by dropping the kinetic energy terms in Eq. (4),

$$\begin{aligned} \left(\frac{M\omega^2(x_1^2 + x_2^2)}{2} - \sqrt{2}gx_1 - E\right)C_1 + JC_2 &= 0, \\ JC_1 + \left(\frac{M\omega^2(x_1^2 + x_2^2)}{2} - \sqrt{2}gx_2 - E\right)C_1 &= 0, \end{aligned} \tag{5}$$

and by equating the determinant of system (5) to zero,

$$\begin{aligned} \Delta \equiv \bar{E}^2 + \bar{E}\sqrt{2}g(x_1 + x_2) + 2g^2x_1x_2 - J^2 &= 0, \\ \bar{E} = E - \frac{M\omega^2(x_1^2 + x_2^2)}{2}&. \end{aligned} \tag{6}$$

The coefficients in Eq. (6) are symmetric functions of x_1 and x_2; therefore, the adiabatic potentials $E_\pm$ should likewise be symmetric functions of x_1, x_2.

In the specific case of $J = 0$, there are two nonsymmetric terms:

$$\begin{aligned} E_1 &= \frac{M\omega^2(x_1^2 + x_2^2)}{2} - \sqrt{2}gx_1, \\ E_2 &= \frac{M\omega^2(x_1^2 + x_2^2)}{2} - \sqrt{2}gx_2. \end{aligned} \tag{7}$$

For $E_1(x_1) \geq -E_p$, these terms cross at the $x_1 = x_2$ line, where $E_1 = E_2 = M\omega^2x_1^2 - \sqrt{2}gx_1$. The equality sign corresponds to $x_c = \sqrt{2}g/M\omega^2$. An arbitrarily small finite value of J symmetrizes the potential, because the terms diverge by $\pm|J|$ at the x_c point.

Introduce the variables $z_i = x_i/x_0$ and $x_0 = g/M\omega^2$ and the notation:[2]

$$E_p = \frac{g^2}{2M\omega^2} = \frac{M\omega^2x_0^2}{2}, \quad \eta = \frac{1}{2E_p}. \tag{8}$$

Thus, we obtain for the adiabatic terms $E_\pm(x_1, x_2)$,

$$\begin{aligned} E_\pm(x_1, x_2) = E_p\Bigg(&z_1^2 + z_2^2 - \sqrt{2}(z_1 + z_2) \\ &\pm 2\sqrt{\left(\frac{z_1 - z_2}{\sqrt{2}}\right)^2 + \eta^2}\Bigg) \equiv E_p\varepsilon_\pm(z_1, z_2) \end{aligned} \tag{9}$$

(see Fig. 2). (Note that $\varepsilon_\pm(z_1, z_2)$ are analytical functions of $z_{1,2}$, because for real $J \neq 0$, the branching points of the functions in Eq. (9) lie off the real axis. An excep-

---

[2] The dimensionless parameter η does not depend on the ion mass and is the most important characteristic of the adiabatic potential. It coincides with the parameter η_1 introduced by Holstein [10] (for other reasons) and defines the boundary between the large, $\eta_1 > 1$, and small, $\eta_1 < 1$, polarons. (Note that the quantity E_p in Eq. (8) is half the polaron shift introduced in [10].)

tion to the case is $J = 0$, where the derivatives suffer a discontinuity.) For $C_1(z_1, z_2)$ and $C_2(z_1, z_2)$, we obtain

$$\begin{aligned} C_1(z_1, z_2) &= \pm\sqrt{\frac{1}{2}\left(1 \mp \frac{(z_1 - z_2)/\sqrt{2}}{\sqrt{((z_1 - z_2)/\sqrt{2})^2 + \eta^2}}\right)}, \\ C_2(z_1, z_2) &= \frac{J}{|J|}\sqrt{\frac{1}{2}\left(1 \pm \frac{(z_1 - z_2)/\sqrt{2}}{\sqrt{((z_1 - z_2)/\sqrt{2})^2 + \eta^2}}\right)}. \end{aligned} \tag{10}$$

The extrema of the adiabatic terms are defined by the expressions

$$\frac{\partial\varepsilon_\pm(z_1, z_2)}{\partial z_1} = 2z_1 - \sqrt{2} \pm \sqrt{2}\frac{(z_1 - z_2)/\sqrt{2}}{\sqrt{((z_1 - z_2)/\sqrt{2})^2 + \eta^2}} = 0,$$

$$\frac{\partial\varepsilon_\pm(z_1, z_2)}{\partial z_2} = 2z_2 - \sqrt{2} \mp \sqrt{2}\frac{(z_1 - z_2)/\sqrt{2}}{\sqrt{((z_1 - z_2)/\sqrt{2})^2 + \eta^2}} = 0,$$

from which

$$z_1 + z_2 = \sqrt{2}, \tag{11a}$$

$$(z_1 - z_2)\left(1 \pm \frac{1}{\sqrt{((z_1 - z_2)/\sqrt{2})^2 + \eta^2}}\right) = 0. \tag{11b}$$

The term E_+ has its only minimum at $(1/\sqrt{2}, 1/\sqrt{2})$ in the (z_1, z_2) space. The term E_- also has a minimum at point $(1/\sqrt{2}, 1/\sqrt{2})$, if $\eta^2 > 1$. For $\eta^2 < 1$, the $(1/\sqrt{2}, 1/\sqrt{2})$ point becomes a maximum, with two minima appearing at the points

$$\left(\frac{1 + \sqrt{1 - \eta^2}}{\sqrt{2}}, \frac{1 - \sqrt{1 - \eta^2}}{\sqrt{2}}\right)$$

and

$$\left(\frac{1 - \sqrt{1 - \eta^2}}{\sqrt{2}}, \frac{1 + \sqrt{1 - \eta^2}}{\sqrt{2}}\right).$$

Thus, in the absence of EPC ($g = 0$), the level surfaces of the adiabatic potentials $E_\pm(x_1, x_2)$ are paraboloids of rotation displaced vertically by $\pm J$, with minima at the (0, 0) point. Introducing a nonzero EPC lowers the symmetry (to reflection through the $x_1 = x_2$ plane and rotation by π about the vertical axis passing through $x_1 = x_0/\sqrt{2}$, $x_2 = x_0/\sqrt{2}$) and displaces the minima to the $(x_0/\sqrt{2}, x_0/\sqrt{2})$ point. If g exceeds the threshold value g_c (see Appendix 1) corresponding to $\eta = 1$, the lower term E_- undergoes a qualitative change, namely, the extremum at point $(x_0/\sqrt{2}, x_0/\sqrt{2})$ splits into three extrema, more specifically, a maximum at $(x_0/\sqrt{2}, x_0/\sqrt{2})$ and two minima of equal depth. The adiabatic change in deformation from one minimum to the other is accompanied by an electron transfer between the sites and involves overcoming the energy barrier in the (x_1, x_2) space.

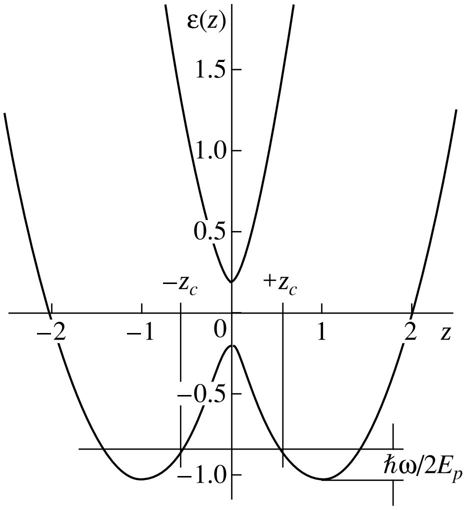

Fig. 2. Adiabatic terms $\varepsilon_\pm(z) \equiv E_\pm(z)/E_p$ of the two-site model. $\pm z_c$ are the turning points for the lowest energy level $\hbar\omega/2$. The region between them is classically inaccessible.

It is appropriate now to cross over to the variables

$$X = \frac{x_1 + x_2}{\sqrt{2}}, \quad x = \frac{x_1 - x_2}{\sqrt{2}}. \tag{12}$$

In these variables, the Hamiltonian in Eq. (1) will take the form

$$\begin{gathered} H = H_0 + V, \quad H_0 = T + U_1(X) + U_2(x), \\ T = \frac{1}{2m}(\hat{P}^2 + \hat{p}^2), \\ U_1(X) = \frac{M\omega^2(X - x_0)^2}{2} - E_p, \\ U_2(X) = \frac{M\omega^2 x^2}{2} - g(\hat{n}_1 - \hat{n}_2)x, \end{gathered} \tag{1a}$$

where $\hat{P}$ and $\hat{p}$ are the corresponding momentum operators.[3] The X-dependent terms in Eq. (1a) do not couple with the electronic variables, and, therefore, in an analysis of the electron system, it is sufficient to retain only the $U_2(x)$ term in the Hamiltonian and to look for the wave function in the form

$$\Psi = (C_1(x)a_1^+ + C_2(x)a_2^+)|0\rangle. \tag{3a}$$

---

[3] The model described by the Hamiltonian in Eq. (1a) was used in the classical papers of Holstein [10, 11], as well as in the treatment of the problem of interband light absorption by a small polaron in [12].

The coupled equations (4) can now be recast as

$$\begin{aligned} H_-(x)C_1 + JC_2 &= EC_1, \\ JC_1 + H_+(x)C_2 &= EC_2. \end{aligned} \tag{4a}$$

In Eq. (4), we have introduced the notation

$$H_\mp(x) \equiv \frac{\hat{p}^2}{2M} + \frac{M\omega^2 x^2}{2} \mp gx.$$

Equation (9) yields a relation for the adiabatic terms ($z \equiv x/x_0$),

$$E_\pm(z) = E_p(z^2 \pm 2\sqrt{z^2 + \eta^2}) \equiv E_p\varepsilon(z), \tag{9a}$$

and, from Eq. (10), the C_1 and C_2 coefficients are found to be

$$\begin{aligned} C_1 &= \pm\sqrt{\frac{1}{2}\left(1 \mp \frac{z}{\sqrt{z^2+\eta^2}}\right)}, \\ C_2 &= \frac{J}{|J|}\sqrt{\frac{1}{2}\left(1 \pm \frac{z}{\sqrt{z^2+\eta^2}}\right)}. \end{aligned} \tag{10a}$$

We now find the first and second derivatives of $E_\pm(z)$ with respect to z to determine the extrema and renormalize the frequency:

$$\frac{1}{E_p}\frac{dE_\pm}{dz} = 2z\left(1 \pm \frac{1}{\sqrt{z^2+\eta^2}}\right), \tag{13}$$

$$\frac{1}{E_p}\frac{d^2E_\pm}{dz^2} = 2\left(1 \pm \frac{\eta^2}{(z^2+\eta^2)^{3/2}}\right). \tag{14}$$

The extrema of the adiabatic terms $E_\pm(z)$ lie at $z = 0$ and

$$z = \pm z_c, \quad z_c = \pm\sqrt{1-\eta^2}, \quad \eta < 1. \tag{15}$$

Note that $E_\pm|_{z=0} = \pm J$. The upper adiabatic term $E_+(z)$ has only one extremum, a minimum at $z = 0$. The lower term, $E_-(z)$, has its only minimum at $z = 0$ for $\eta > 1$ and one maximum at $z = 0$ and two minima at $z = \pm z_c$ for $\eta < 1$, so that for $\eta < 1$, there is a potential barrier (see Fig. 2). For the energies at the minima in Eq. (15), we obtain

$$\left.\frac{E_-(z)}{E_p}\right|_{z=\pm z_c} = -1 - \eta^2. \tag{16}$$

The barrier height is the difference between $E_-(0)$ and $E_-(z_c)$:

$$E_b = E_p(1-\eta)^2. \tag{17}$$

The frequency renormalization is given by the term in parentheses in Eq. (14) for $z = z_c$:

$$\tilde{\omega}^2 = (1 \pm \eta^2)\omega^2 \tag{18}$$

(the vibration mode corresponding to the minus sign softens, and that corresponding to the plus sign hardens). At $z = 0$, $\tilde{\omega}^2 = (1 \pm \eta^{-1})\omega^2$. Note that the ion mass enters Eqs. (5)–(16) only through the combination $M\omega^2$, which has the meaning of the elastic constant and in fact does not depend on M. The dependence on M appears only when solving the Schrödinger equation with potential energy $E_\pm(x)$.

2. NUCLEAR VIBRATIONS

Now, let us take into account the term with the nuclear kinetic energy. As can be seen from Eq. (5), the coefficients $C_1(x_1, x_2)$ and $C_2(x_1, x_2)$ are determined to within the factor $\chi(x_1, x_2)$. Therefore, solutions $\tilde{C}_1(x)$ and $\tilde{C}_2(x)$ to the coupled equations (4a) should be looked for in the form

$$\tilde{C}_1(x) = \chi(x)C_1(x), \quad \tilde{C}_2(x) = \chi(x)C_2(x); \tag{19}$$

in other words, the vibronic electron wave function can be written as

$$\Psi = \chi(x)(C_1(x)a_1^+ + C_2(x)a_2^+)|0\rangle, \tag{20}$$

where $C_1(x)$ and $C_2(x)$ are defined by Eq. (10a). Note that for $z = z_c$,

$$\begin{aligned} C_1(z_c) &= \pm\sqrt{\frac{1 \mp \sqrt{1-\eta^2}}{2}}, \\ C_2(z_c) &= \frac{J}{|J|}\sqrt{\frac{1 \pm \sqrt{1-\eta^2}}{2}} \end{aligned} \tag{21}$$

and for $z = 0$,

$$C_1(0) = \pm\frac{1}{\sqrt{2}}, \quad C_2(0) = \frac{J}{|J|}\frac{1}{\sqrt{2}}. \tag{22}$$

One readily obtains

$$\begin{aligned} T(\chi(x)C_1(x)) + E_\pm(x)\chi(x)C_1(x) &= E\chi(x)C_1(x), \\ T(\chi(x)C_2(x)) + E_\pm(x)\chi(x)C_2(x) &= E\chi(x)C_2(x). \end{aligned} \tag{23}$$

Here, $T(x)$ is the kinetic energy operator of the vibrating system:

$$T(x) = -\frac{\hbar^2}{2M}\frac{d^2}{dx^2} = -E_p\left(\frac{\hbar\omega}{2E_p}\right)^2\frac{d^2}{dz^2}. \tag{24}$$

Taking into account the kinetic energy gives rise to the appearance of a second dimensionless parameter (in addition to η):

$$\nu = J/\hbar\omega. \tag{25}$$

This is customarily called the adiabaticity parameter, because the condition of applicability of the adiabatic approximation is $\nu \gg 1$. Straightforward estimation gives $\nu \sim (M/m^*)^{1/2} = \kappa^{-2}$, where κ is a fundamental parameter of the Born–Oppenheimer approximation [13]. It should be stressed that it does not depend on the EPC constant g.

As follows from Eq. (23), the $\chi(x)$ function should satisfy two different equations, which, generally speaking, is impossible. This implies that the concept of the adiabatic potential is valid only under certain conditions imposed on the parameters of the problem.[4] Indeed, the problem under study here has two length dimension parameters, namely, $x_0 = g/M\omega^2$, which is determined by the actual form of the potential energy and is independent of the nuclear mass, and $l_n = \sqrt{n\hbar/2M\omega} \propto \sqrt{M}$, the oscillator length, which determines the radius of the nth oscillator state. The ratio $(l_n/x_0)^2$ can be written as

$$\frac{l_n^2}{x_0^2} = \frac{n\hbar\omega}{4E_p}. \tag{26}$$

If this ratio is small and the parameter η is not too small, then, for low energy levels in Eq. (23), one may neglect the action of the kinetic energy operator on the $C_i(x)$ functions and recast the first terms in Eq. (23) in the form $C_i(x)T\chi(x)$. Then, Eqs. (23) reduce to one equation:

$$-\frac{\hbar^2}{2M}\frac{d^2\chi}{dx^2} + E_\pm(x)\chi = E\chi. \tag{27}$$

For $\eta < 1$, the potential $E_-(x)$ describes two potential wells separated by a barrier. If we formally make the barrier infinite (by making J and E_p infinite at a fixed $J/E_p = 2\eta$ ratio), then in a steady state, the nuclear wave function will be localized in one of the wells and its amplitude in the other well will be zero. Each energy level will be twofold degenerate and the wave functions can be written as $\chi(x - x_0z_c)$ and $\chi(x + x_0z_c)$ and will not overlap. The total electron–nucleus functions of the doublet will be

$$\begin{aligned}\Psi_{1,2} &= \chi(x \mp x_0z_c)\frac{1}{\sqrt{2}}\Big(-\sqrt{1 \pm \sqrt{1-\eta^2}}\,a_1^+ \\ &\quad + \frac{J}{|J|}\sqrt{1 \mp \sqrt{1-\eta^2}}\,a_2^+\Big)|0\rangle.\end{aligned} \tag{28}$$

Because of χ being sharply decreasing functions, we have replaced $C_i(x)$ in the right-hand part of Eq. (28) by their values at x corresponding to the points of the minima of the adiabatic potential E_-. Obviously enough, the matrix element of any operator coupling the Ψ_1 and Ψ_2 states is zero. Therefore, the probability of electron hopping between the sites is zero. Note that in the states in Eq. (28), there is a certain correlation between the state of the vibrational system and the electron charge distribution between the sites. For instance, in the Ψ_1 state, the fractions of the charge at sites *1* and *2* are $(1 + \sqrt{1-\eta^2})/2$ and $(1 - \sqrt{1-\eta^2})/2$, respectively, with the deformation being localized near site *1* (Fig. 1). Note also that taking into account EPC in the adiabatic approximation makes the electronic charge density spread to the adjacent site *2* with a weight $(1 - \sqrt{1-\eta^2})^2/4$.

If the barrier height is finite, the $\chi(x \mp x_0 z_c)$ functions overlap and the electron can now hop between the sites, thus splitting the doublet in Eq. (28). We shall call this situation at $\eta < 1$ the strong-coupling case (having in mind strong electron–phonon coupling).

For $\eta > 1$, the barrier vanishes and the $E_\pm$ terms have the only extremum, namely, a minimum at $z_c = 0$. Recalling Eq. (22), the wave function can be presented in the form

$$\Psi = \chi(x)\frac{1}{\sqrt{2}}(a_1^+ \pm a_2^+)|0\rangle. \tag{29}$$

Because both electron states have equal weights, the above correlation no longer operates, as in the case of EPC neglect. The part played by the EPC consists in making the adiabatic potentials nonparabolic and in producing corrections to the electron wave function. For $\eta \gg 1$, the wave functions and the energies of the low-energy states are close to the corresponding quantities for the system in the absence of EPC (the weak-coupling case):

$$\begin{aligned}\Psi_{n\pm}^{(0)}(x) &= \psi_n^{(0)}(x)\frac{1}{\sqrt{2}}(a_1^+ \pm a_2^+)|0\rangle, \\ E_{n\pm} &= \pm J + \left(n + \frac{1}{2}\right)\hbar\omega.\end{aligned} \tag{30}$$

[Here, $\psi_n^{(0)}(x)$ are the eigenfunctions of the harmonic oscillator.] The corresponding effects can, in principle, be treated, making a perturbation expansion in weak electron–phonon coupling.

Thus, in our system, we have a realization of one of the two qualitatively different states described by Eqs. (28) and (29), depending on the presence or absence of an energy barrier in the lowest adiabatic term E_-. This barrier is a consequence of the formation of two minima in $E_-(x_1, x_2)$ for $\eta < 1$. The transition between these two states occurs in the vicinity of $\eta = 1$, where a singularity can exist in the parameter space. Analytical study of the region of disappearance of the barrier is fairly difficult to perform even in terms of the two-site problem. (It would be expedient to carry out this study numerically on the basis of the above considerations.)

---

[4] In order for Eq. (23) to be satisfied, one should look for a solution, in place of Eq. (19), in the form $\tilde{C}_i(x) + \Delta C_i(x)$. The limited nature of the concept of the adiabatic potential is discussed in [13, Chapter 4, Appendices VII, VIII].

3. LEVEL SPLITTING IN THE ADIABATIC APPROXIMATION

To find the level splitting, which originates from the existence of an energy barrier in the lowest adiabatic term, we shall use the quasi-classical approximation (QA). Generally speaking, the QA is valid for strongly excited levels. However, the harmonic oscillator levels determined in the QA coincide with their exact values. Because the adiabatic potentials in our problem are oscillator-like in the region of interest to us here, it can be assumed that the QA also remains adequate in the region of small quantum numbers *n*. In the strong coupling case, the adiabatic potential $E_-(x)$ represents two wells separated by a barrier (Fig. 2). A solution to the problem on the splitting ΔE of a deep level with energy *E* of the order of $-E_p$ obtained for such a potential in the QA is given in [14, problem 3, p. 208]:

$$\Delta E = \frac{\hbar\tilde{\omega}}{\pi}\exp\left(-\frac{1}{\hbar}\int_a^b p\,dx\right),\qquad p = \sqrt{2M|E - E_-(x)|}. \tag{31}$$

The nuclear wave functions of the doublet can be written as

$$\chi_\pm(x) = \frac{1}{\sqrt{2}}(\varphi_1(x) \pm \varphi_2(x)), \tag{32}$$

where $\varphi_i(x)$ is the quasi-classical wave function for the *i*th well. The integration is performed between the turning points *a* and *b*; $\tilde{\omega}$ is the frequency of classical motion with energy *E* in the potential well $E_-(x)$. [The argument of the exponential in Eq. (31) decreases with increasing excitation energy if tunneling occurs from an excited state.]

Consider the splitting of the lowest level with a quantum number $n = 0$. The energy of this excitation (the zero-point energy) is $\hbar\tilde{\omega}/2$, where $\tilde{\omega} = \omega\sqrt{1-\eta^2}$ [which coincides with Eq. (18)]. The result depends on the product of the parameters $\eta\nu \equiv \eta_3 = J^2/(\hbar\omega E_p)$. For $\eta_3 < 1$, one obtains

$$\Delta E = \frac{2\sqrt{2}}{\pi}\sqrt{\hbar\omega E_p}\exp\left(-\frac{2E_p}{\hbar\omega}\right). \tag{33}$$

For $\eta_3 > 1$ (to be *more exact*, in the adiabatic limit of $M \longrightarrow \infty$), one can neglect the zero-point energy and integrate from $-x_0$ to x_0. The prefactor in Eq. (31) remains the same, so that the integral in the argument of the exponential in Eq. (31) will be

$$\frac{1}{\hbar}\int_{-x_c}^{+x_c} p\,dx = \frac{2E_p}{\hbar\omega}f(\eta),\qquad f(\eta) = \sqrt{1-\eta^2} - \eta^2\ln\frac{1+\sqrt{1-\eta^2}}{\eta}. \tag{34}$$

Thus, in this case, we have[5]

$$\Delta E = \frac{\hbar\tilde{\omega}}{\pi}\exp\left(-\frac{2E_p}{\hbar\omega}f(\eta)\right). \tag{35}$$

In a number of cases, estimates can be made by means of the approximate expression

$$f(\eta) = 1 - \eta. \tag{36}$$

In this approximation, in view of Eq. (32), the doublet wave functions can be expressed through the wave functions in Eq. (28) in the form

$$\Psi_\pm = \frac{1}{\sqrt{2}}(\Psi_1 \pm \Psi_2). \tag{37}$$

In contrast to Eq. (28), they match the symmetry of the Hamiltonian in Eq. (1) [i.e., they possess a definite parity under the interchange of indices $(1, 2) \longrightarrow (2, 1)$]. Note the structural similarity of these functions to the wave functions in the strong-coupling approximation (or the MO LCAO approximation in molecular theory), where the steady-state wave function is constructed as a superposition of site-localized electron functions with universal coefficients determined by the symmetry of the system. However, in this case, the localized "atomic" functions are actually electron–deformation complexes. This two-site model was studied in [9] in the "antiadiabatic" limit $\nu < 1$ by using a perturbation expansion in *J*, an approximation opposite to ours.[6] In this model, there is an analog of the above barrier and, hence, an analog of the splitting of the lower doublet. This splitting J^* was found to be

$$J^* = J\exp(-2E_p/\hbar\omega). \tag{38}$$

---

[5] In [11, expression (116)] for ΔE obtained by the WKB method is presented without derivation. It coincides with our Eq. (33) to within a factor of the order of unity (~0.87).

[6] The question of the smallness parameter remains open. While the condition $\nu < 1$ ensures decreased expansion terms with increasing order, it is actually not fully realistic, because it assumes the quantity *J* (which is of the order of the electronic energy E_e) to be small compared with $\hbar\omega$, which is of the order of $\sim E_e\sqrt{m/M}$ (*m* is the electronic mass). At the same time, the expansion in powers of *J* also contains the combination $J/2E_p \equiv \eta$, i.e., a parameter which is small in the strong-coupling case. In reality, the expansion in powers of a quantity of the kind of $\eta^\alpha\nu^{1-\alpha}$ may take place [for instance, $(\eta\nu)^{1/2} \equiv \eta_3^{1/2}$] and the condition of validity of the approach in [9] will turn out to be less restrictive than $\nu < 1$.

When Eqs. (33) and (35) are compared with J^* in Eq. (38), calculated to the first order in J, it is seen that the quantity ΔE always contains a phonon exponential,[7] but the prefactor J is replaced by $(2\sqrt{2}/\pi)\sqrt{\hbar\omega E_p}$ or $\hbar\tilde{\omega}/\pi$. Thus, while in the adiabatic region the prefactor J^* is no longer substantially dependent on J,[8] the dependence on this quantity becomes manifest in its argument because of the factor $f(\eta)$.

Note that, in Eq. (35) for ΔE, only the quantities ω and $\tilde{\omega} \propto \sqrt{1/M}$ depend on the ion mass M. Therefore, as $M \longrightarrow \infty$ in the $\eta < 1$ region, the value of ΔE decays exponentially as $\exp(-\sqrt{M})$; in this limit, the electrons are strongly localized at the sites and no charge transfer takes place between the sites. As is shown in [9], this exponential smallness is present in all those terms of the power series expansion in J that are responsible for the splitting of the term; that is, the presence was established outside the bounds of the adiabatic approximation, with the latter serving only as a method for summation of the series. As for the terms responsible for the shift of the doublet centroid (the corrections to the polaron shift), they remain finite in the limit as $M \longrightarrow \infty$.[9]

In the weak-coupling limit, all terms of the perturbative expansion in EPC for ΔE vanish for $M \longrightarrow \infty$ and the electronic states are delocalized and form an unperturbed doublet with a splitting $2J$:

$$\psi_{\pm} = \frac{1}{\sqrt{2}}(\hat{a}_1^+ \pm \hat{a}_2^+)|0\rangle, \quad E_{\pm} = \pm J. \tag{39}$$

Thus, depending on the value of the parameter η, the problem under study allows two branches of solutions, namely, the weak-coupling limit in Eq. (39) for $\eta > 1$ and the strong-coupling limit in Eq. (28) for $\eta < 1$. The most substantial effect of the strong coupling is the appearance of the exponentially small factor $\exp(-E_p/\hbar\omega)$, which is capable of reducing some characteristic parameters by several orders of magnitude. The exponential in Eq. (35) also accounts for the enhancement of the isotope effect [6].[10] Indeed, the replacement of a nucleus of mass M with a nucleus of mass $M + \Delta M$ results in Eq. (35) becoming multiplied by

$$\exp\left(-\frac{E_p}{\hbar\omega}\frac{\Delta M}{M}\right). \tag{40}$$

For a realistic value $\lambda = 10$ of the EPC parameter and $\Delta M/M = 0.1$, isotopic substitution should change the magnitude of J^* by e times, which can radically affect the electronic characteristics (for instance, convert an insulator to a metal). Therefore, the results of [7] can also be treated as a weighty argument for the existence of substances in which the above strong coupling is realized.

Note that the "barrier" exponential, which results in an effective decrease of J^* (the "barrier effect") and accounts for the enhancement mechanism, appears already in the lowest order terms in J, with further growth of J for $\eta < 1$ only modifying it.

4. MODEL OF A POLARON CRYSTAL

Consider the simplest model of a crystal consisting of the above cation–anion complexes, namely, a regular n-gon, where n can be arbitrarily large. The Hamiltonian of this model can be written as

$$\begin{aligned}&\sum_{m=1}^{n}\left(\frac{\hat{p}_m^2}{2M} + \frac{M\omega^2 x_i^2}{2} - \sqrt{2}g\hat{n}_m x_m\right)\\ &\quad - \sum_{m=1}^{n-1} J(\hat{a}_m^+\hat{a}_{m+1} + \hat{a}_{m+1}^+\hat{a}_m).\end{aligned} \tag{41}$$

The canonical transformation [16]

$$\begin{aligned}U &= \prod_{m=1}^{n}\exp\left(\frac{i}{\hbar}\frac{\sqrt{2}g}{M\omega^2}\hat{n}_m\hat{p}_m\right)\\ &\equiv \prod_{m=1}^{n}\exp\left(\frac{i}{\hbar}\sqrt{2}x_0\hat{n}_m\hat{p}_m\right)\end{aligned} \tag{42}$$

eliminates the Hamiltonian terms linear in x_i and transforms the electron operators

$$\begin{aligned}\tilde{a}_m^+ &= \exp\left(\frac{i}{\hbar}\sqrt{2}x_0\hat{p}_m\right)\hat{a}_m^+,\\ \tilde{a}_m &= \exp\left(-\frac{i}{\hbar}\sqrt{2}x_0\hat{p}_m\right)\hat{a}_m.\end{aligned} \tag{43}$$

The canonical transformation preserves the commutation relations, and, therefore, $\tilde{a}_m^+$ and $\tilde{a}_m$ are Fermi operators. We thus come to

$$\begin{aligned}\tilde{H} &= \sum_{m=1}^{n}\left(\frac{\hat{p}_m^2}{2m} + \frac{M\omega^2 x_m^2}{2}\right) - 2E_p\sum_{m=1}^{n} n_m\\ &\quad - \sum_{m=1}^{n-1} J(\tilde{a}_m^+\tilde{a}_{m+1} + \tilde{a}_{m+1}^+\tilde{a}_m).\end{aligned} \tag{44}$$

The transformed operator $\tilde{a}_m^+$ creates an electron at site m and the corresponding optimum deformation. For

---

[7] Perturbation theory does not impose any restrictions on the magnitude of the argument of the exponential in Eq. (38). However, only the case of this argument being large in magnitude is of interest.

[8] Strictly speaking, the prefactor depends on J because of the appearance of the factor $1 \pm \eta^2$ [see Eq. (18)], which brings about its additional decrease for the lowest (corresponding to the minus sign) term.

[9] The prefactor scales with M as $M^{-1/4}$ in Eq. (33) or as $M^{-1/2}$ in Eq. (35).

[10] This mechanism was considered in connection with the model of the bipolaron superconductor [15].

$\eta < 1$, this complex is a small polaron. For $J = 0$, this transformation exactly diagonalizes the Hamiltonian and, in the strong-coupling case, $\eta < 1$, offers the possibility of constructing perturbation theory in J. For $J = 0$, there is n-fold degeneracy with respect to the site index m. In the lowest energy state, all the oscillator quantum numbers are zero and the polaron energy spectrum is described by the band term of the Hamiltonian with a renormalized J^* defined by Eq. (38) (the polaron-induced band narrowing). The wave function of a polaron with quasi-momentum k can be presented in the form

$$\psi_k = \sum_{m=1}^{n} e^{ikm}\exp\left(\frac{i}{\hbar}\sqrt{2}x_0\hat{p}_m\right)\Phi_0(x_1, \ldots, x_n)a_m^{+}|0\rangle, \tag{45}$$

$$\Phi_0(x_1, \ldots, x_n) = \prod_{m=1}^{n}\psi_0^{(0)}(x_m).$$

The region where the perturbation theory is valid is bounded only by the $\nu < 1$ condition.

Consider this problem in the adiabatic approximation. We proceed as before and finally obtain coupled equations which can be used to determine the coefficients $C_i(x_1, \ldots, x_n)$ and the adiabatic potentials $E_i(x_1, \ldots, x_n)$:

$$U_1C_1 - JC_2 - \ldots - JC_n = EC_1,$$

$$-JC_1 + U_2C_2 - JC_3 - \ldots = EC_2,$$

$$-JC_1 - \ldots - JC_{n-1} + U_nC_n = EC_n.$$

$$U_s = \sum_{m=1}^{n}\frac{M\omega^2x_m^2}{2} - \sqrt{2}gx_s \equiv U_0 - \sqrt{2}gx_s. \tag{46}$$

One can readily verify that the determinant of this system $\Delta(E)$ does not change under cyclic permutation of the indices $(1, 2, \ldots, n)$. Therefore, the coefficients of the algebraic equation $\Delta(E) = 0$ and, hence, the adiabatic potentials $E_i(x_1, \ldots, x_n)$, being functions of the deformations $x_1, \ldots, x_n$, are invariant under these permutations. (For $J = 0$, the adiabatic potentials $E_i = U_0 - \sqrt{2}\,gx_i$ are not invariant under these permutations, but they are symmetrized even for an infinitely small J [see Eq. (9) for the two-site model].)

In the absence of EPC ($g = 0$), the adiabatic potentials are $E_i = U_0 + E_i^0$, with $E_i^0 = \text{const}$. The only extremum (minimum) lies at the point $x_1 = x_2 = \ldots = x_n = 0$. For small enough g, one observes only a shift of this minimum to the point $x_1 = x_2 = \ldots = x_n = x_0^{(i)}$; this shift depends on i and does not break the symmetry of the Hamiltonian.

For an infinitely small J and $g \neq 0$, the lowest adiabatic term has n minima at the points ($x_m = x_0$, $x_{m'} = 0$) with $m' \neq m$ and $m = 1, \ldots, n$). When all $x_i \longrightarrow \infty$, this term asymptotically approaches an n-dimensional paraboloid in the n-dimensional deformation space $(x_1, \ldots, x_n)$. (One should not confuse this space with real space, in which the lattice sites exist.) The low-lying electron states are localized on the complexes. Transfer to an adjacent site ($|m - m'| = 1$) involves overcoming one energy barrier. One can easily estimate its height for an infinitely small J. The depth of the minimum at point $(x_0, 0, \ldots, 0)$ is obviously equal to $2E_p$ (i.e., to the polaron shift). The barrier height corresponds to the minimum energy $E_{\min}$ at the line $x_i = x_j$, at which the energies E_i and E_j,

$$E_i(x_i, \ldots, x_n) = \frac{M\omega^2(x_i - \sqrt{2}x_0)^2}{2} - 2E_p + \sum_{m \neq i}\frac{M\omega^2x_m^2}{2},$$

of the two minima, i and j, coincide. One readily sees that this point is $x = x_0\sqrt{2}$ and $E_{\min} = -E_p$; i.e., that the barrier height is $2E_p$. (In a similar way, one can easily describe the structure of all n adiabatic terms in the $J \longrightarrow 0$ limit; however, this structure is not used in this work and we drop the corresponding consideration.)

Note that an electron transfer from site m to site m' involves overcoming $|m - m'|$ barriers in the deformation space.

In principle, the electron energy spectrum should be determined from the Schrödinger equation in the n-dimensional deformation space, which is similar to Eq. (27). This would entail formidable mathematical difficulties.

Note, however, that the electron Hamiltonian H_e can be reasonably simulated in the strong-coupling approximation by the expression

$$H_\mathrm{e} = \sum_{\{\mathbf{m}, \mathbf{m}'\}, \sigma} I_{\mathbf{m}, \mathbf{m}'}a^{+}_{\mathbf{m}, \sigma}a_{\mathbf{m}', \sigma}, \tag{47}$$

where the summation is run over the nearest-neighbor sites $\mathbf{m}$ and $2I_{\mathbf{m}, \mathbf{m}'}$ is the level splitting in the two-site problem with a pair of sites $\mathbf{m}$, $\mathbf{m}'$. There are grounds to expect that our model of the crystal could be satisfactorily approximated in the $\nu > 1$ adiabatic region by replacing I with the quantity ΔE given by Eq. (35), which has the same meaning. Therefore, in order to describe electron transfer in the adiabatic regime, it is sufficient to renormalize the J parameter. (Note that for small η, the modulus of the argument of the barrier exponential is large.)

In view of the results presented in Section 1 and Appendix 1, it can be maintained that the above set of potentials E_i with n minima forms when g is in excess of a certain g_c; therefore, we have a threshold effect. Because the adiabatic-potential structure is described by the only dimensionless parameter $\eta = J/2E_p$, the corresponding criterion takes on the form $\eta < \eta_c$.

5. ELECTRON–ELECTRON INTERACTION

Now, we consider the changes induced by strong EPC in electron–electron interaction. The Hamiltonian of this interaction in the site representation has the form

$$H_{\mathrm{ee}} = \sum_{m_1, m_2, m_3, m_4} \sum_{\sigma, \sigma'} A(m_1, m_2, m_3, m_4) \times \hat{a}^+_{m_1, \sigma} \hat{a}^+_{m_2, \sigma'} \hat{a}_{m_3, \sigma'} \hat{a}_{m_4, \sigma}, \tag{48}$$

where A are numerical functions and σ is the spin index. The canonical transformation given by Eq. (42) gives rise to the appearance of the following operator products under the summation sign in Eq. (48):

$$\exp\left(\frac{i}{\hbar}\sqrt{2}x_0\hat{p}_{m_1}\right)\exp\left(\frac{i}{\hbar}\sqrt{2}x_0\hat{p}_{m_2}\right) \times \exp\left(-\frac{i}{\hbar}\sqrt{2}x_0\hat{p}_{m_3}\right)\exp\left(-\frac{i}{\hbar}\sqrt{2}x_0\hat{p}_{m_4}\right). \tag{49}$$

The terms of the sum in Eq. (48) satisfying the relations

$$m_1 = m_3, \quad m_2 = m_4 \quad \text{and} \quad m_1 = m_4, \quad m_2 = m_3 \tag{50}$$

are not connected with real electron transfer between the sites (these are the main terms of the Coulomb interaction and of the direct exchange). One readily sees that the operator factor in Eq. (49) for these terms becomes unity. Therefore, strong EPC has no noticeable effect on the phenomena associated with these terms (ferro- and antiferromagnetism), there is no barrier effect, and the mechanism of enhancement of the isotope effect does not operate. This relates in equal measure to the mechanisms of indirect exchange via an intermediate state with the formation of a pair at a site, because the electron transfer is here a virtual process (see Appendix 2). The band-narrowing effect raises the problem of modifying the criterion of realization of the insulating or conducting state (similar to the well-known Mott criterion) because of the need of taking magnetic order into account.

The higher order terms in J will hopefully contain only the ν- (i.e., M-) independent parameter η.

Note also that strong EPC gives rise to the appearance of a negative term $-2E_p$ adding to the Hubbard repulsion, which does not depend on the ion mass.

Consider the terms of Eq. (48) describing the real electron transfer process. These are, for instance, the term with $m_1 \neq m_2$, if neither of these indices coincides with m_3 and m_4. The operator product (49) in these terms is not unity. When considered to the lowest order in J, factors $\exp(-2E_p/\hbar\omega)$ appear at the corresponding coefficients A (which brings about their reduction due to the barrier effect). In particular, the operator product (49) for the term in Eq. (48) with

$$m_1 = m_2, \quad m_3 = m_4, \quad m_1 \neq m_3 \tag{51}$$

is

$$\exp\left(\frac{i}{\hbar}2\sqrt{2}x_0\hat{p}_{m_1}\right)\exp\left(-\frac{i}{\hbar}2\sqrt{2}x_0\hat{p}_{m_3}\right). \tag{52}$$

To the lowest order in J, the corresponding coefficients A renormalize with a factor $\exp(-8E_p/\hbar\omega)$,[11] which is substantially larger than the reduction $\exp(-2E_p/\hbar\omega)$ of the one-electron bandwidth. This reduction accounts for the mechanism of the isotope effect enhancement in the phenomena for which the terms under consideration are responsible.

Note that in crystals where the enhancement of the isotope effect takes place, the possibility of fine control of the parameters by properly varying the isotope composition is offered.

In the $M \longrightarrow \infty$ limit, electrons are fully localized and the model under consideration transforms to the Heitler–London model.

The above estimates are based on the lowest order perturbation theory in J, which is valid for $\nu < 1$. In view of the fairly obvious barrier nature of the phenomena under study here in the $\nu < 1$ case, one can assume with a fair degree of confidence that, in the $\nu > 1$ region, the corresponding quantities should likewise be proportional to the appropriately modified barrier exponential, provided the barrier regime with $\eta < 1$ is realized. (Analysis of a perturbation-series expansion made for the two-site model [9] yielded supportive evidence for this assumption.)

Because all the main parameters involved in the adiabatic approach are of a local nature, it appears reasonable to carry out a comprehensive investigation of the mechanisms of concrete phenomena occurring in the adiabatic region $\nu > 1$ on "small" models similar to the above two-site configuration.

6. DISCUSSION OF RESULTS

There can be no reasonable doubt that the effect of the interaction of an electron with nuclei under weak electron–phonon coupling and in the limit of infinitely heavy nuclei reduces to a static field acting on the electron. The band structure characteristics (the bandwidth ΔE, the effective mass m^*, etc.) remain finite in this limit.

On the other hand, the most remarkable consequence of the formation of the above-considered energy barrier in the adiabatic potential for the process of site-to-site "transfer" of nuclear displacement and of the associated reduction of the effective electron-band width is that the electron transfer mechanism no longer operates in the $M \longrightarrow \infty$ limit; that is, the electrons

---

[11] The presence of this renormalization was pointed out in [17]. One of the present authors (EKK) uses this opportunity to point out that this factor was introduced in [17] with an exponent half as much as it should be (this did not, however, in any way affect the conclusions drawn there).

become fully localized. In this case, $\Delta E \longrightarrow 0$ and $m^* \longrightarrow \infty$ exponentially (with the direct consequence that the isotope effect is enhanced with increasing electron–phonon coupling). This means that there is an essential qualitative difference between the cases of strong and weak electron coupling with phonons. One could think that this result is a consequence of the adiabatic approximation and that going beyond it would make electron transfer possible in this limit. However, the fact that, in the two-site model, the exponentially small factor $\exp(-\sqrt{M})$ is present in all terms of the perturbation-series expansion in J for the doublet splitting indicates that, in actuality, this situation is not realized.

The barrier effect results in a substantial modification of both the band term of the Hamiltonian (with the carriers becoming small polarons) and the interaction terms. [The most important features of this modification become particularly revealing after canonical transformation (42) of the Hamiltonian.] When performing first-principles calculations, the possibility of its realization should be taken into account in their very first stages. The constants g, J, and A entering the model Hamiltonians (41) and (48) will then be expressed through the fundamental constants e, $\hbar$, m, and M. [When analyzing experimental data, one should use the known semiphenomenological estimates of these constants (the Fröhlich constant, etc.) with caution, because the conditions for which they were derived may not apply here.]

We have been primarily considering the region of the well-pronounced barrier effect, $\eta < \eta_c$, where the carriers are known to be small polarons. Large polarons (LP) can form outside this region if the EPC is not too weak. All studies of the LP problem of which we are aware made use of various versions of direct variational methods (which, by their nature itself, cannot be euristically solid) within a narrow interval of parameter variation. This raises the importance of studies in this area, with the region of the intermediate strength of EPC ($\eta \geq \eta_c$) in the limit of $M \longrightarrow \infty$ being of particular interest. One could conceive, in principle, the following alternatives:

(1) Throughout the $\eta > \eta_c$ region and with $M \longrightarrow \infty$, we have $m^* \longrightarrow m_0$ (m_0 is the effective electron mass at $g = 0$) and there is no qualitative difference between the weak-EPC and LP cases.

(2) In the $\eta > \eta_c$ region and with $M \longrightarrow \infty$, we have $m^* \longrightarrow \infty$, but this increase is weaker than an exponential one. (A similar result is presented, e.g., in [18].) As the EPC continues to decrease (i.e., η continues to grow), we have $m^* \longrightarrow m_0$ for $\eta > \eta_1$. This could be interpreted as the formation of an LP, i.e., of the electron–deformation bound state in the $\eta_c < \eta < \eta_1$ region. The appearance of a barrier at $\eta < 1$ brings about an exponential growth of m^* and transformation of the large polaron to a small one.

A self-consistent analytical treatment of the region of the intermediate coupling strength would entail formidable mathematical difficulties, even in terms of the simple model employed in this work. The difficulties originate from the LP extending over many lattice sites, so that using "small" models of the two-site kind would no longer have any sense. Numerical methods seem more appropriate here. Such studies of the model described by Eq. (41) are currently being intensely pursued (see, e.g., [18–25]). The analytical relations for m^* obtained by various authors are reviewed in [21]. These relations are found to agree with the numerical results of both [21] and a number of other publications. They agree fairly well with alternative (1).

However, the behavior of the band characteristics for $M \longrightarrow \infty$ has not been investigated thus far. In the light of the above consideration, it appears to be of interest to carry out such a study based on exact diagonalization of the Hamiltonian by numerical techniques.

APPENDIX 1

THE THRESHOLD EFFECT

The adiabatic potential has the form $E(x_1, x_2) = (M\omega^2/2)(x_1^2 + x_2^2) + \xi(x_1, x_2)$, where $\xi(x_1, x_2)$ does not have singularities and tends to zero with $g \longrightarrow 0$. For $g = 0$, there is a single minimum at $x_1 = x_2 = 0$. As g increases, the formation of additional extrema should be preceded by a flattening of the minimum, which occurs at the critical point

$$\Delta^{(2)} \equiv \frac{\partial^2 E}{\partial x_1^2}\frac{\partial^2 E}{\partial x_2^2} - \left(\frac{\partial^2 E}{\partial x_1 \partial x_2}\right) = 0. \qquad \text{(A1.1)}$$

For $g = 0$, we have $\Delta^{(2)} = (M\omega^2)^2$. For small g, condition (A1.1) cannot be satisfied. The additional extrema appear only after g has exceeded a certain threshold value g_c. These considerations also remain valid in the case of a larger number of the quantities x_i.

APPENDIX 2

INDIRECT-INTERACTION CONSTANTS

The second-order correction to the Hamiltonian determining the splitting of the lowest degenerate level with energy E_0 has the form

$$\Delta H_{ij}^{(2)} = \sum_n \frac{\langle i0|V'|n\rangle \langle n|V'|i'0\rangle}{E_0 - E_n}. \qquad \text{(A2.1)}$$

Here, i and i' are the quantum numbers of this level and V' is the off-diagonal part of the perturbation. The summation runs over all excited states (the denominator is always negative). Let the band term of the Hamiltonian have the form $H_b = \sum_{\mathbf{m},\,\mathbf{g},\,\sigma} J(\mathbf{g})\tilde{a}^+_{\mathbf{m}+\mathbf{g},\,\sigma}\tilde{a}_{\mathbf{m},\,\sigma}$. The correction to the exchange constant due to the formation of a virtual pair can be written as

$$\Delta I_{\mathrm{exc}}(\mathbf{g}) = -\sum_{n_1=0}^{\infty}\sum_{n_2=0}^{\infty}\frac{J^2(\mathbf{g})}{E_{\mathrm{H}} + (n_1+n_2)\hbar\omega} \tag{A2.2}$$

$$\times\langle 0|\tilde{a}^{+}_{\mathbf{m}+\mathbf{g},\sigma}\tilde{a}_{\mathbf{m},\sigma}|n_{\mathbf{m}}, n_{\mathbf{m}+\mathbf{g}}\rangle\langle n_{\mathbf{m}}, n_{\mathbf{m}+\mathbf{g}}|\tilde{a}^{+}_{\mathbf{m},\sigma'}\tilde{a}_{\mathbf{m}+\mathbf{g},\sigma'}|0\rangle.$$

Here, $E_{\mathrm{H}} > 0$ is the Hubbard energy, $|0\rangle$ is the ground state of the unperturbed vibrational system, and $|n_{\mathbf{m}}, n_{\mathbf{m}+\mathbf{g}}\rangle$ are the states of this system with excitations at sites $\mathbf{m}$ and $\mathbf{m}+\mathbf{g}$. Equation (A2.2) can be recast in the form

$$\Delta I_{\mathrm{exc}}(\mathbf{g}) = -\sum_{n_1=0}^{\infty}\sum_{n_2=0}^{\infty}\frac{J^2}{E_{\mathrm{H}} + (n_1+n_2)\hbar\omega}$$

$$\times\langle 0|\exp\left(\frac{i}{\hbar}\sqrt{2}g\hat{p}_{\mathbf{m}+\mathbf{g}}\right)\exp\left(\frac{-i}{\hbar}\sqrt{2}g\hat{p}_{\mathbf{m}}\right)|n_1, n_2\rangle \tag{A2.3}$$

$$\times\langle n_1 n_2|\exp\left(\frac{i}{\hbar}\sqrt{2}g\hat{p}_{m}\right)\exp\left(\frac{-i}{\hbar}\sqrt{2}g\hat{p}_{\mathbf{m}+\mathbf{g}}\right)|0\rangle.$$

Using relations (32) from [9], the sum in Eq. (A2.3) can be transformed to

$$\Delta I_{\mathrm{exc}}(\mathbf{g}) = -\frac{J^2}{E_{\mathrm{H}}}$$

$$\times\int_0^{\infty}\exp\left(-z-\frac{4E_p}{\hbar\omega}(1-\exp(-z\hbar\omega/E_{\mathrm{H}}))\right)dz. \tag{A2.4}$$

For $\hbar\omega/E_{\mathrm{H}} \longrightarrow 0$, ΔI_{exc} is finite, $\Delta I_{\mathrm{exc}} = -J^2/E_{\mathrm{H}}$; that is, as in the first-order term, there is no barrier effect.

ACKNOWLEDGMENTS

The authors are grateful to J. Ranninger and A.S. Aleksandrov for a discussion which stimulated this work to a considerable extent.

This work was supported by the Russian Foundation for Basic Research, grant no. 99-02-1833.

REFERENCES

1. J. van den Brink, W. Stekelenburg, D. I. Khomskii, *et al.*, cond-mat/9802146.
2. M. Quijada, J. Cerne, J. R. Simpson, *et al.*, cond-mat/9803201.
3. K. H. Kim, J. H. Jung, and T. W. Noh, cond-mat/9804167.
4. A. S. Alexandrov and A. M. Bratkovsky, cond-mat/9806030.
5. Yu. Unjong and B. I. Min, cond-mat/9906263.
6. Guo-Meng Zhao, K. Conder, H. Keller, and K. A. Müller, Nature **381**, 676 (1996).
7. N. A. Babushkina, L. M. Belova, V. I. Ozhogin, *et al.*, cond-mat/9805315.
8. A. S. Alexandrov and J. Ranninger, Phys. Rev. B **23** (4), 1796 (1981).
9. Yu. A. Firsov and E. K. Kudinov, Fiz. Tverd. Tela (St. Petersburg) **39** (12), 2159 (1997) [Phys. Solid State **39**, 1930 (1997)].
10. T. Holstein, Ann. Phys. **8**, 325 (1959).
11. T. Holstein, Ann. Phys. **8**, 343 (1959).
12. E. K. Kudinov and Yu. A. Firsov, Fiz. Tverd. Tela (Leningrad) **7** (3), 546 (1965) [Sov. Phys. Solid State **7**, 435 (1965)].
13. M. Born and K. Huang, *Dynamical Theory of Crystal Lattices* (Clarendon, Oxford, 1954; Inostrannaya Literatura, Moscow, 1958).
14. L. D. Landau and E. M. Lifshitz, *Quantum Mechanics: Non-Relativistic Theory* (GITTL, Moscow, 1948; Pergamon, Oxford, 1977).
15. A. S. Aleksandrov, Pis'ma Zh. Éksp. Teor. Fiz. **47** (12), 642 (1988) [JETP Lett. **47**, 741 (1988)].
16. I. G. Lang and Yu. A. Firsov, Zh. Éksp. Teor. Fiz. **43**, 1843 (1962) [Sov. Phys. JETP **16**, 1301 (1963)].
17. A. V. Ivanov and E. K. Kudinov, Fiz. Tverd. Tela (Leningrad) **31** (6), 14 (1989) [Sov. Phys. Solid State **31**, 922 (1989)].
18. S. I. Pekar, *Research on Electron Theory of Crystals* (GTTI, Moscow, 1951); Report AEC-tr-5575, US Atomic Energy Commission (1963).
19. A. Bill, V. Z. Kresin, and S. A. Wolf, cond-mat/9801222.
20. A. H. Romero, D. W. Brown, and K. Lindenberg, cond-mat/9710321.
21. A. H. Romero, D. W. Brown, and K. Lindenberg, cond-mat/9905174.
22. H. de Raedt and A. Lagendijk, Phys. Rev. B **27** (10), 6097 (1983).
23. H. de Raedt and A. Lagendijk, Phys. Rev. B **30** (4), 1671 (1984).
24. A. S. Alexandrov, V. V. Kabanov, and D. K. Ray, Phys. Rev. B **49** (14), 9915 (1994).
25. H. Fehske, H. Röder, G. Wellien, and A. Mistriotis, Phys. Rev. B **51**, 16582 (1995).
26. G. Wellien and H. Fehske, Phys. Rev. B **56**, 4513 (1997).

Translated by G. Skrebtso

Physics of the Solid State, Vol. 43, No. 3, 2001, pp. 458–462. Translated from Fizika Tverdogo Tela, Vol. 43, No. 3, 2001, pp. 442–445.
Original Russian Text Copyright © 2001 by Palchaev, Batdalov, Murlieva, Omarov, Palchaeva, Muradkhanov.

Specific Features of Thermal Resistance of Silicon in the Temperature Range 105–130 K

D. K. Palchaev*, A. B. Batdalov, Zh. Kh. Murlieva*,**
A. K. Omarov*, F. D. Palchaeva, and M. É. Muradkhanov***
**Dagestan State University, Makhachkala, 367025 Dagestan, Russia*
***Institute of Physics, Dagestan Scientific Center, Russian Academy of Sciences,*
ul. 26 Bakinskikh Komissarov 94, Makhachkala, 367003 Dagestan, Russia

Received August 3, 2000

Abstract—Careful experimental investigations into the behavior of the thermal resistance of single-crystal silicon are carried out in the immediate vicinity of the temperature of an anharmonicity sign inversion (T_i = 121.1 K), where phonon thermal resistance approaches zero. An anomalous positive deviation of the total thermal resistance (W) from the linear part of the temperature dependence with a maximum at 121.1 K is found in the temperature range 105–130 K. The temperature behavior of W in this range indicates that the mean free path of phonons is limited by a characteristic size of structural defects and that its temperature dependence exhibits specific features in the vicinity of T_i. It is established that the character of the temperature dependence of W above and below T_i is different. A linear functional relation between the total thermal resistance and the isobaric thermal strain is revealed at positive and negative anharmonicities of atomic vibrations. *© 2001 MAIK “Nauka/Interperiodica”.*

1. INTRODUCTION

The results reported in this paper were obtained in the course of experimental investigations into the temperature dependence of the thermal resistance of silicon upon anharmonicity sign inversion [1]. Careful experimental investigations at temperatures close to 121.1 K made it possible to analyze the specific features of the total thermal resistance (W) for both the positive and negative anharmonicities of atomic vibrations. These investigations are of interest, since the phonon thermal resistance (W^{ph}) and the thermal expansion coefficient β, unlike the heat capacity, are determined only by the anharmonicity of atomic vibrations. It is obvious that W^{ph} should be equal to zero at $\beta = 0$. However, the phenomenon of high-temperature phonon superthermal conductivity upon anharmonicity sign inversion, which is suppressed by scattering at boundaries and defects of crystals, has not yet been investigated.

2. THEORETICAL BACKGROUND AND EMPIRICAL FACTS

The theory [2–5] of scattering upon anharmonic phonon–phonon interactions is based on the quasi-harmonic approximation. Therefore, this theory interprets the dependence $W^{\mathrm{ph}} = f(T)$ only qualitatively at low and high temperatures when the density of phonon energy states approaches saturation. According to [2, 6], the assumption that the disturbing anharmonic term is small in the expansion of the potential energy of interatomic interaction and, especially, the harmonic approximation [7], do not provide clear notions of the phonon scattering mechanism. For the same reason, the obvious singularity in the W^{ph} behavior upon anharmonicity sign inversion has not yet been discussed. Apart from silicon, the anharmonicity sign inversion is typical of almost all loose-packed covalent substances. The specific features of the thermal resistance of these substances manifest themselves as inflection points of the curves $W = f(T)$ at relevant temperatures [8]. An anomalous behavior of the phonon thermal conductivity was found earlier for germanium in the temperature range covering T_i [9].

The Grüneisen constant serves as a parameter of the anharmonicity of thermal vibrations:

$$\mathrm{Gr} = \beta\frac{v^2}{c_p}, \tag{1}$$

where β is the thermal expansion coefficient, ν is the sound velocity, and c_p is the heat capacity. Since all expressions for calculating the phonon thermal resistance [2, 3, 10],

$$W \sim \frac{\mathrm{Gr}^2 T}{M_a a T_{\mathrm{D}}^3},$$

involve the square of the Grüneisen parameter, it is believed that inclusion of the negative thermal resistance is not a particular problem. However, W^{ph} should be singular at Gr = 0, all things being equal. Furthermore, the Grüneisen parameter varies within ~10% with temperature and does not reflect a practically observed increase in the thermal resistance by several orders of magnitude. The temperature dependence of W^{ph} in appropriate expressions is specified by the double scattering integral (determined in the harmonic approximation) and the heat capacity.

As a rule, the authors of experimental studies of the objects under consideration (see [8]) give no data on the thermal resistance in the immediate vicinity of the temperature T_i of the anharmonicity sign inversion. In our earlier work [1], it was demonstrated for the first time that the anomalous deviation from the linear part of the temperature dependence of W increases with a decrease in the contribution of phonon scattering at the boundaries. It was also noted [1] that a one-to-one relation between the thermal resistance and isobaric thermal strain in the form

$$W = W_0 + W^{ph}\beta T \qquad (2)$$

was revealed for more than twenty substances (including silicon) over the entire range of positive anharmonicity. Here, W_0 is the residual thermal resistance, which is determined by the phonon scattering at static defects; W^{ph} is the characteristic phonon thermal resistance; and $\beta T = (dV/dT)_p T/V$. When analyzing the theoretical expressions for W^{ph}, these empirical facts necessitated switching our attention from the Grüneisen parameter, which is responsible for anharmonicity, to the double scattering integral.

3. EXPERIMENTAL TECHNIQUE

The thermal resistance of silicon was investigated by absolute stationary and quasi-stationary methods in the range 80–150 K. The operating parts of the samples were prepared in the form of rods ~25 mm long with cross sections of 3.76 × 3.93 mm and 5.82 × 5.73 mm. The rods were cut from one piece of single-crystal silicon (semiconductor grade) doped with phosphorus ($\rho = 10\ \Omega$ m). The single crystal was grown by the Czochralski technique (in Podol'sk). The dislocation density was no more than 10^6 cm^{-3}. On the one end, each sample had a sprig ~2.5 mm in diameter and ~5 mm in length. This sprig was used to mount the sample through a collet chuck on a rod, which in turn was brought into contact with a thermostating liquid. The temperature gradient was produced along the $\langle 111\rangle$ direction of the crystal growth. In addition to the main (gradient) heater, the measuring cell was equipped with a background heater mounted on a temperature-controlled rod in order to increase the average temperature. The temperature gradient, which was provided by the main heater, was estimated in terms of the field superposition. The temperature difference across the operating part of the sample was measured using a differential copper–constantan thermocouple. The average temperature of the sample operating part was estimated using the formula $T_r = T + (T_2 - T_1)/2$, where $T_2 - T_1$ is the thermoelectric power for a differential thermocouple at a temperature T. The temperature T was measured by an absolute copper–constantan thermocouple mounted on the opposite side of the sample at the level of the lower junction of the differential thermocouple. The junctions of the differential and absolute thermocouples were soldered to silver contacts, which were obtained via fusing a silver paste. The diameter and layer thickness of each contact were no more than 0.5 and 0.01 mm, respectively. The gas pressure maintained in the measuring cell was no more than 0.1 Pa. The problem of accounting for heat transfer from the main heater and other parameters which determine the limiting total error of measurements was solved by comparing the results obtained for the sample with a cross section of 14.78 mm^2 and reference data [3] (standard of the absolute magnitude). The data obtained in [11] (the error of their determination was about ±5%) for a sample of approximately the same cross section (~15 mm^2) were taken as a basis for the quantities recommended in [3]. Since we were interested in the behavior of $W = f(T)$ in the vicinity of T_i, the comparison was performed at temperatures of 100 and 150 K, i.e., outside the range of the anomalous deviation of the dependence $W = f(T)$. The sample with a cross section of 33.95 mm^2 was investigated under the same conditions. For better resolution of the specific features of the dependence $W = f(T)$ in the vicinity of T_i, the sample with a cross section of 33.95 mm^2 was studied in the quasi-stationary regime, which provided a change in the temperature of the alcohol–liquid nitrogen thermostating solution at a rate of less than 2.5×10^{-4} K/s at a constant power of the main heater without switching on the background heater. Repeated measurements demonstrated good reproducibility of the data obtained at a thermal drift velocity of 4×10^{-4} K/s. Temperature gradients of the sample and thermostating liquid were measured with a step of ~0.1 K. The sensitivity to thermal resistance variation with an increase in the temperature in the quasi-stationary regime was limited by the temperature gradient variance, which was no more than ±0.2%. This restriction was related to the detection limit of a R3003 comparator. Since the thermogram of a thermostating liquid in the temperature range under investigation was linear, corrections for the temperature gradient across the sample were applied. The scatter in the data obtained in the stationary regime was substantially larger (±0.7%) because of the necessity of estimating the gradient produced by the background heater. The measurements in the stationary regime were performed in order to investigate the dependence $W = f(T)$ in the vicinity of T_i upon heating and cooling.

4. RESULTS AND DISCUSSION

The difference in thermal resistance of the two silicon samples with cross sections of 14.78 and 33.95 mm^2 was no more than ~ 2%. It seems likely that, for samples with a cross section of more than 15 mm^2, the influence of boundaries on the absolute values of thermal resistance, which was observed in [1], considerably decreases with an increase in the sample cross section.

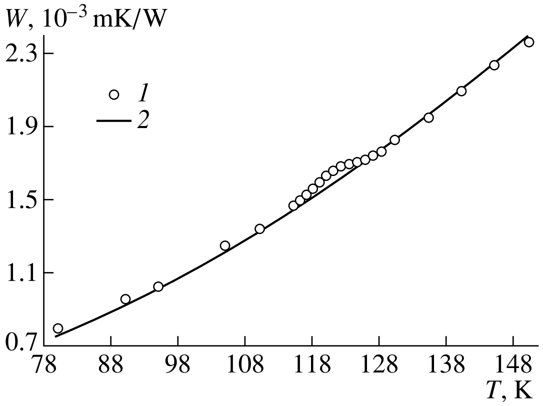

Fig. 1. Temperature dependences of the total thermal resistance of silicon: (*1*) averaged data for the samples with cross sections of 14.78 and 33.95 mm^2 and (*2*) data taken from [8].

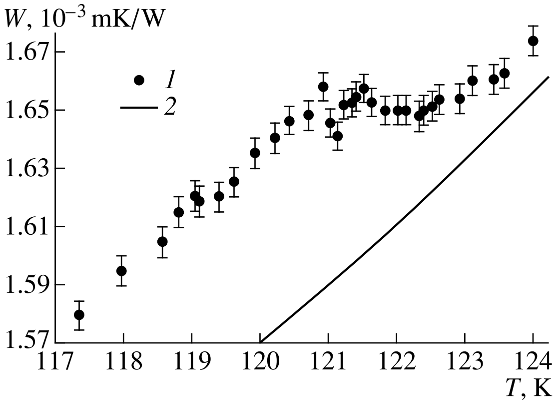

Fig. 2. Temperature dependences of the total thermal resistance of silicon: (*1*) our data for the sample with a cross section of 33.95 mm^2 and (*2*) data taken from [8].

The averaged data on the thermal resistance measured for the two samples upon heating and cooling are displayed in Fig. 1. The variance of the data on W, which restricted the sensitivity of measuring this parameter, was equal to ±0.7%. The maximum thermal resistance for the samples of different sizes was observed at the same temperature, 121.1 K.

The total thermal resistance is determined by the contributions of different scattering mechanisms:

$$W = W_d + W_b + W^{\mathrm{ph}}, \qquad (3)$$

where W_b and W_d are the thermal resistances due to scattering of phonons by the boundaries and defects, respectively. The behavior of the linear part of the temperature dependence of W for both samples is generally determined by the third term in Eq. (3), whereas the discrepancies in the absolute values are determined by the second term, because W_d is identical for both samples. The estimate made for ΔW at T_i according to the formula

$$\Delta W = \frac{K}{c_p \gamma v}\left(\frac{1}{s_1} - \frac{1}{s_2}\right), \qquad (4)$$

where γ is the density and s_1 and s_2 are the thicknesses of the samples, confirms that this difference is small (~3×10^{-5} mK/W) at T_i as compared to the absolute value of W_i (1.65×10^{-3} mK/W). The numerical constant K was determined from the boundary thermal resistance and the size of the silicon sample for which the recommended data were available in the literature.

The theoretical Leibfried–Shleman expression [2, 3] for the phonon thermal resistance has the form

$$W^{\mathrm{ph}} = A\frac{\mathrm{Gr}^2 V_a T}{C_a M_a a^4 T_{\mathrm{D}}^3}\iint \ldots dS dq, \qquad (5)$$

where A is the numerical constant; V_a, M_a, and C_a are the atomic volume, mass, and heat capacity, respectively; a is the lattice parameter; T_{D} is the Debye temperature; and S is the surface containing the wave vectors allowed by the energy conservation law. The Gr^2 values for silicon at temperatures above 200 and below 80 K, which were calculated according to Eq. (1) using the known values for b, β, and c_p [12–14], were equal to approximately 1.5×10^{-2} and decreased to zero at 121.1 K. This trend for Gr^2, according to Eqs. (3) and (5), should provide the minimum value of the total thermal resistance at 121.1 K. The opposite behavior of $W = f(T)$ suggests the decisive role of W_d and its temperature dependence in Eq. (3), which competes with the temperature dependence of W^{ph}. Defects in the form of dislocation loops (swirls) are almost always present in single-crystal silicon [15]. They comprise a spiral vortexlike system with diameter $D > 10^{-6}$ m, which consists of strips extended along the growth direction. The pattern formed by these defects was observed on the end surface of the silicon ingot from which the studied sample was cut. The boundaries of swirls represent lattice distortions with local mass fluctuations. The presence of defects in the form of a dislocation core implies a mass deficit, and as the temperature T_i is approached, the force constants increase. In these cases [2, 3], the mean free path of phonons should exceed the characteristic distance $D \approx 10^{-6}$ m between the defect regions. The mean free path $l \approx 10^{-5}$ m, which was estimated from the maximum value of W, satisfies the condition for Rayleigh scattering, which was observed at wavelengths exceeding the defect size by a factor of 2π. The validity of this interpretation is confirmed by the fact that the lattice distortions in a dislocation core are extended approximately over one or two interatomic distances (a). The preferential length of heat waves at these temperatures is of the order of $(2a)T_{\mathrm{D}}/T$ [10], where T_{D}/T for silicon is approximately equal to 2π.

Phonon scattering by a stress field produced by dislocations usually exceeds scattering by a dislocation core interpreted as a point defect [2, 10]. However, in the case under consideration, the former scattering is small, because the Grüneisen parameter approaches zero at $T \longrightarrow 121.1$ K and the effect revealed is unrelated to scattering by a stress field.

The W^{ph} contribution to the total thermal resistance increases above and below $T_i = 121.1$ K. Figure 2 displays the total thermal resistance W for a sample with a cross section of 33.35 mm^2 in the immediate vicinity of T_i, where the mean free path of phonons approaches infinity and is restricted by the size of defects. The behavior of the dependence $W = f(T)$ in the vicinity of T_i is governed only by the variation in the temperature gradient across the sample at a constant heater power. The reason for this is that the thermogram recorded using an absolute thermocouple is strictly linear in this temperature range. The behavior of $W = f(T)$ above and below T_i (Fig. 2) indicates that the mechanisms of phonon scattering by defects at the positive and negative anharmonicities of atomic vibrations are different. The minimum total thermal resistance W in the range of positive anharmonicity (at 122.2 K) does not contradict the known notions of the scattering theory. Above 121.1 K, the total thermal resistance somewhat decreases when W^{ph} approaches zero at $T \longrightarrow T_i$, because the singularity of the function $W^{\mathrm{ph}} = f(T)$ suppresses the dependence of W_d on T upon scattering of phonons by dislocations. The scattering mechanism at the negative anharmonicity, when the quasi-elastic force in the atomic motion equations changes sign, on average, for all atoms [16], remains unclear. The solution of this problem calls for further theoretical investigations in order to elucidate the specific features of the surfaces containing those wave vectors that are allowed by the energy conservation law at positive and negative anharmonicities.

Analysis demonstrated that the reference data on W for Si [8] (at positive and negative anharmonicities in the ranges from T_i to 1200 K and from 80 K to T_i, respectively[1]) can be approximated by expressions of form (2) with correlation coefficients (r) close to unity:

$$W = 2.03 \times 10^{-3} + 2.11\beta T \; (r = 0.998) \; T > T_i, \quad (6)$$

$$W = 1.63 \times 10^{-3} + 5.04\beta T \; (r = 0.991) \; T < T_i. \quad (7)$$

The linear functional relations between the thermal resistance and isobaric thermal strain above and below T_i also exist for other substances, for example, for InSb [8]:

$$W = 6.03 \times 10^{-3} + 10.55\beta T \; (r = 0.999) \; T > T_i, \quad (8)$$

$$W = 5.84 \times 10^{-3} + 26.13\beta T \; (r = 0.993) \; T < T_i. \quad (9)$$

The angular coefficients in Eqs. (6)–(9) (characteristic thermal resistances) are determined by the characteristic forces of the interatomic interaction, as was shown in [17]. Upon inversion of the anharmonicity sign, these forces undergo a jumplike change according to Eqs. (6)–(9), which indicates the difference in the phonon energy spectra above and below T_i. The first term in these expressions is determined by the contribution $W_0 = W_d + W_b$, and the second term is governed by W^{ph}. Therefore, it is reasonable to suppose that the change in the cross section of phonon scattering by phonons at the positive and negative anharmonicities of atomic vibrations is unambiguously determined by the change in the isobaric thermal strain.

5. CONCLUSION

The above investigations allowed us to make the following conclusions.

(1) Anomalous behavior of the thermal resistance of silicon in the temperature range 105–130 K is determined by the competition between the mechanism of phonon–phonon scattering and the mechanism of phonon scattering by defects, involving the Rayleigh scattering as the specific case.

(2) Phonon scattering by defects is more significant than scattering at boundaries in the vicinity of T_i with an increase in the sample cross section.

(3) The characteristic force of the interatomic interaction changes jumpwise upon a transition from the positive to negative anharmonicity of atomic vibrations in silicon and vice versa. This behavior of W is apparently characteristic of all substances exhibiting inversion of the anharmonicity sign.

REFERENCES

1. D. K. Palchaev, Zh. Kh. Murlieva, A. B. Batdalov, *et al.*, Fiz. Tverd. Tela (St. Petersburg) **38** (3), 684 (1996) [Phys. Solid State **38**, 379 (1996)].
2. J. M. Ziman, *Electrons and Phonons* (Clarendon, Oxford, 1960; Inostrannaya Literatura, Moscow, 1962).
3. B. N. Mogilevskiĭ and A. F. Chudnovskiĭ, *Thermal Conductivity of Semiconductors* (Nauka, Moscow, 1971).
4. V. A. Gurevich, *Kinetics of Phonon Systems* (Nauka, Moscow, 1980).
5. A. P. Zhernov, Fiz. Tverd. Tela (St. Petersburg) **41** (7), 1185 (1999) [Phys. Solid State **41**, 1079 (1999)].
6. R. E. Peierls, *Surprises in Theoretical Physics* (Princeton Univ., Princeton, 1979; Nauka, Moscow, 1988).
7. N. N. Sirota, Dokl. Akad. Nauk SSSR **317** (6), 1380 (1991) [Sov. Phys. Dokl. **36**, 328 (1991)].
8. A. S. Okhotin, R. P. Borovikova, T. V. Nechaeva, and A. S. Pushkarskiĭ, in *Thermal Conductivity of Solids: Handbook*, Ed. by A. S. Okhotin (Énergoatomizdat, Moscow, 1984).
9. V. I. Ozhogin, A. V. Inyushkin, A. N. Taldenkov, *et al.*, Pis'ma Zh. Éksp. Teor. Fiz. **63** (6), 463 (1996) [JETP Lett. **63**, 490 (1996)].

---

[1] At a temperature of ~ 80 K, the negative values of β reach a maximum absolute value.

10. R. Berman, *Thermal Conduction in Solids* (Clarendon, Oxford, 1976; Mir, Moscow, 1979).
11. C. J. Glassenbrenner and G. A. Slack, Phys. Rev. **134** (4A), 1058 (1964).
12. S. I. Novikova, *Thermal Expansion of Solids* (Nauka, Moscow, 1974).
13. I. G. Kozhevnikov and P. A. Novitskiĭ, *Thermophysical Properties of Materials at Low Temperatures* (Mashinostroenie, Moscow, 1982).
14. I. N. Frantsevich, F. F. Voronov, and S. A. Bakuta, *Elastic Constants and Moduli of Metals and Nonmetals* (Naukova Dumka, Kiev, 1982).
15. A. Zeeger, H. Föll, and W. Frank, in *Radiation Effects in Semiconductors*, Ed. by N. B. Urli and J. W. Corbett (Inst. of Physics, Bristol, 1977); *Point Defects in Solids* (Mir, Moscow, 1979).
16. C. H. Xu, C. Z. Wang, C. T. Chan, and K. M. Ho, Phys. Rev. B **43** (6), 5024 (1991).
17. D. K. Palchaev and Zh. H. Murlieva, Phys. Status Solidi B **176**, K5 (1993).

Translated by N. Korovin

Physics of the Solid State, Vol. 43, No. 3, 2001, pp. 463–468. Translated from Fizika Tverdogo Tela, Vol. 43, No. 3, 2001, pp. 446–451.
Original Russian Text Copyright © 2001 by Sharkov, Klokov, Galkina.

Generation of Nonequilibrium Phonons in Semiconductors and Dielectrics by a Pulse-Heated Metallic Film: Model and Experiment

A. I. Sharkov, A. Yu. Klokov, and T. I. Galkina
Lebedev Institute of Physics, Russian Academy of Sciences, Leninskiĭ pr. 53, Moscow, 117924 Russia
e-mail: shark@sci.lebedev.ru

Received July 21, 2000

Abstract—Characteristics of a phonon generator in the form of a pulse-heated metallic film, viz., the time dependences of the film temperature and the kinetics of phonon ejection from the film into a substrate, are considered. The time dependences of the film temperature are calculated for cadmium telluride, diamond, and silicon substrates. It is shown that the duration of film cooling substantially exceeds the heating pulse length and the film continues to generate phonons with lower frequencies at the end of heating pulse. The inference is drawn that the film cooling should be correctly taken into account in analysis of the propagation of nonequilibrium acoustic phonons, specifically for phonon processes occurring in nanostructures.© *2001 MAIK “Nauka/Interperiodica”.*

1. INTRODUCTION

Nanostructure physics, which has rapidly progressed in the last three decades, and the wide practical applications of superlattices and quantum wells in micro- and optoelectronics have required new information in the field of electron–phonon interactions, features of phonon spectra, and specificity of the acoustic phonon propagation in these structures.

For example, the limiting factor in quantum-dot and cascade lasers is the carrier relaxation with emission of optical phonons. After the conversion of optical phonons into acoustic phonons, the acoustic phonon transport is the final stage of the processes occurring in these devices [1, 2].

The quality of surfaces and interfaces can be characterized with phonon pulses, because the wavelengths of phonons used in the heat (phonon) pulse technique are comparable to the scale of inhomogeneities in nanostructures [3].

It should be emphasized that experimental investigations into the kinetics and dynamics of acoustic phonons in nanostructures (heterostructures, double wells, and superlattices) require knowledge of the space–time characteristics of a phonon pulse; otherwise, all the features of scattering by interfaces and, especially, resonance phenomena appear to be “smeared” and the results obtained cannot be interpreted in an adequate way.

The purposes of the present work were as follows. (1) The calculation of the characteristics of a phonon generator—a heated metallic film: the temperature (phonon frequency) and the kinetics of phonon ejection from the film into a substrate. (2) The simulation of the phonon generation process with the use of the generator characteristics in Monte Carlo calculations of heat pulses, which is necessary for analysis of experimental heat pulses.

2. HEAT (PHONON) PULSE TECHNIQUE

The so-called heat pulse technique is virtually the sole method that makes it possible to investigate experimentally the propagation of nonequilibrium acoustic phonons. A general scheme of the experimental heat pulse technique and the principal processes with the participation of nonequilibrium phonons are shown in Fig. 1.

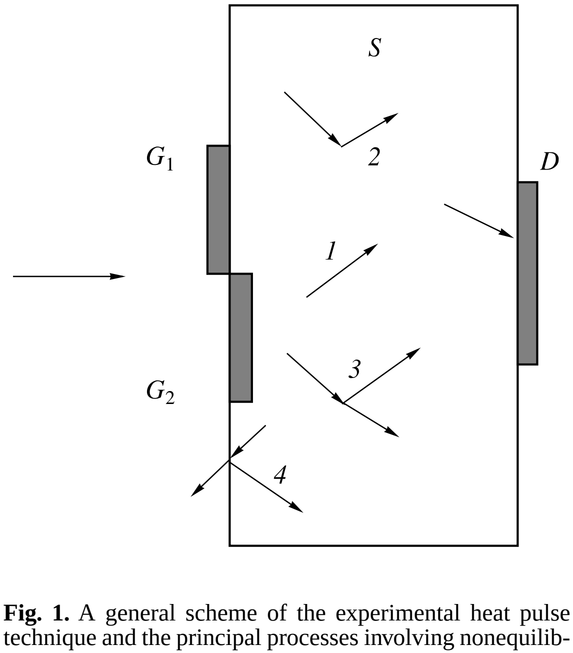

Fig. 1. A general scheme of the experimental heat pulse technique and the principal processes involving nonequilibrium phonons: (*1*) ballistic propagation, (*2*) elastic scattering, (*3*) spontaneous decay, and (*4*) reflection from the boundary or ejection from the sample into a substrate. Designations: G_1 = generation, G_2 = generation, and D = detection.

Nonequilibrium phonons are generated in the sample *S* due to the pulse excitation *P*. The required excitation is usually achieved with light or current heating of a metallic film applied on the sample surface (G_1), when phonons enter the sample through an interface. Moreover, this can be attained by photoexcitation with light characterized by a photon energy larger than the band gap of the studied material (G_2), when the phonons are generated directly in the sample. The generated phonons propagate through the sample (*1*) and undergo processes of elastic scattering (*2*), spontaneous anharmonic decay (*3*), etc. (Fig. 1). Phonons absorbed in detector *D* generate a signal. The features of processes involving nonequilibrium phonons and the conditions of their propagation can be judged from the form of a time-resolved signal.

Analysis of the resulting time-resolved responses of a detector presents considerable difficulties. One way of performing this analysis is to compare the experimental responses with those calculated by the Monte Carlo method [4–6]. This makes it possible to evaluate the features of processes that characterize phonon propagation, for example, the intensity of elastic scattering of nonequilibrium acoustic phonons by point defects in the studied sample [7, 8], the characteristic sizes of grains forming the sample [9], etc.

However, these calculations require the description of all elementary processes with the participation of nonequilibrium phonons. The theoretical treatment of processes such as elastic scattering and decay of phonons has been carried out repeatedly [10–12], and the results of calculations according to the proposed models were confirmed experimentally. At the same time, there are only a few works concerned with the experimental verification of theoretical treatments of certain processes, for example, phonon scattering by interfaces [13].

As regards the phonon generation, the situation is rather complicated because several experimental methods are used for generating nonequilibrium phonons [14, 15]. Let us briefly describe the physical differences in these generation techniques.

Photoexcitation brings about the formation of hot carriers which relax toward conduction band edges for a time of the order of 10^{-12} s with the emission of optical phonons. These phonons decay into longitudinal acoustic phonons with approximately the same energy for a time of the order of 10^{-10} s.

In the case of a pulse-heated metallic film applied on the semiconductor surface, the phonons are generated through a somewhat different mechanism: the energy is absorbed in the metal in which a quasi-equilibrium distribution of phonons is rapidly achieved owing to the electron–phonon interaction and phonons enter the sample through the interface.

The high-frequency phonons generated under photoexcitation are vigorously scattered by point defects, which provides a means of determining the elastic phonon scattering constant [7, 8].

The lower-frequency phonons generated by a metallic film have larger free paths, which enables one to obtain information on the phonon scattering by interfaces [9]. Furthermore, by varying the excitation parameters (energy, pulse length, and excitation spot area), it is possible to change the frequency of phonons generated by the metallic film in the range 0.1–3.0 THz. This is especially important in the study of resonant phonon scattering in superlattices with quantum dots, because the characteristic wavelengths of these phonons (λ = 600–20 Å) coincide with the characteristic sizes of inhomogeneities.

When simulating the phonon generation process, it is necessary to determine the spatial region, the duration of phonon generation, and the distribution of generated phonons over the energy (frequency) and polarization.

Upon photoexcitation with a pulse of length longer than 10^{-10} s, it can be assumed that longitudinal acoustic phonons with energies of an order of half the energy of optical phonons (which is equal, for example, to 20 THz for diamond and 7.5 THz for silicon) are generated during the course of the pulse.

For a heated metallic film, it is believed that the phonon distribution over polarizations is proportional to the density of states [16] and the phonon frequency is determined by the film temperature. Therefore, it is necessary to calculate the temperature and characteristic cooling times of the metallic film.

3. CALCULATION OF THE TIME DEPENDENCE OF THE TEMPERATURE FOR A METALLIC FILM

The problem of determining the temperature of a metallic film on an insulating (semiconductor) substrate upon pulse excitation was posed repeatedly. However, as far as we know, the algorithm that can be used to simulate the phonon generation process by the Monte Carlo method has never been described in the literature. In the case when there is a need to estimate the frequency of phonons emitted by a film into a substrate, it is often assumed that phonons are ejected only during the excitation pulse. Then, their frequency is determined from the equation for the frequency corresponding to a maximum of the Planck distribution

$$h\nu = 2.82k_BT, \tag{1}$$

and the film temperature *T* is derived from the appropriate estimates.

In order to obtain the dependence of the temperature of a metallic film on an insulating substrate, it is necessary to solve the energy balance equation. The problem can be simplified under the following assumptions.

(i) Let the film be “thin”; i.e., its heating time is shorter than the excitation pulse length. This is true even for pulses whose length is only a few fractions of a nanosecond when the duration of film heating is shorter than the excitation pulse length. The heating time of the film does not exceed $\tau^* \sim C\rho d^2/\kappa$ (where C is the heat capacity, ρ is the density, and κ is the thermal conductivity coefficient). For a gold film with thickness $d = 1500$ Å at 20 K, we have $\tau^* = 4.5 \times 10^{-12}$ s. At lower temperatures, this value is even smaller.

(ii) It is assumed that the substrate "is not heated" and, at any instant, its temperature is equal to the ambient temperature T_0. This assumption holds for the majority of single crystals in which the mean free paths of thermal phonons at liquid-helium temperatures are determined by the scattering at sample boundaries and lattice defects and can be as much as several millimeters, so that an equilibrium temperature higher than the ambient temperature is not reached. Otherwise, it is necessary first to estimate the fraction of phonons that return from the substrate to the film and then to solve the self-consistent problem.

(iii) Heat transfer from the film to the surrounding medium (for example, liquid helium) is ignored. This assumption is valid when the sample is placed in vacuum. However, even if the sample resides in helium at high excitation levels when the film temperature becomes higher than the boiling temperature of liquid helium, a gaseous helium "bubble" is formed at the film–helium boundary, thus preventing heat removal.

(iv) Heating of the film in the transverse direction is neglected.

In the general case, under the above assumptions, the equation has the form

$$SW(t) = (dS\rho)C(T)dT/dt + P(T, T_0), \qquad (2)$$

where $W(t)$ is the power density at the excitation pulse; d, S, ρ, and $C(T)$ are the thickness, irradiated area, density, and heat capacity of the film material, respectively; and $P(T, T_0)$ is the heat flux from the film to the surrounding medium.

Within the "short" excitation pulse approximation (adiabatic approximation), when the acquired energy can be considered to be absorbed in the film [$P(T, T_0) = 0$], its maximum temperature T_{AD} can be estimated from the condition

$$E_P = Sd\rho \int_{T_0}^{T_{\mathrm{AD}}} C(T)dT, \qquad (3)$$

where E_P and τ_P are the energy and length of the excitation pulse, respectively, and the integral of the heat capacity $C(T)$ is taken over the ambient temperature from T_0 to T_{AD}. The integral should be calculated taking into account that the heat capacity at low temperatures strongly depends on the temperature.

In the "long" excitation pulse approximation (stationary approximation), the stationary temperature T_{ST} of the film can be evaluated from the condition

$$\frac{E_P}{\tau_P} = P(T_{\mathrm{ST}}, T), \qquad (4)$$

where $P(T_{\mathrm{ST}}, T_0)$ is the heat flux from the film to the surrounding medium. Weis [17] obtained good agreement between the experimentally measured stationary temperatures and those calculated according to the given method when the heat flux was computed within the acoustic matching model [18].

However, it is important to know not only the maximum temperature of the film, but also the time dependence of the film temperature, because the lower-frequency phonons generated by the cooling film can substantially affect the overall pattern of the energy transfer. The energy flux from the film to the substrate was calculated in terms of the acoustic matching theory [18]:

$$P(T, T_0) = \frac{S\pi^2 k_{\mathrm{B}}^4}{60\hbar^3}\left\{\frac{\Gamma_L}{c_L^2} + \frac{2\Gamma_T}{c_T^2}\right\}(T^4 - T_0^4), \qquad (5)$$

where k_{B} is the Boltzmann constant; $\hbar$ is the Planck constant; c_L and c_T are the longitudinal and transverse sound velocities in the film, respectively; T and T_0 are the temperatures in the film and substrate, respectively; and Γ_L and Γ_T are the coefficients of phonon transmission through the interface.

Solution of Eq. (2) with the initial condition $T(t = 0) = T_B$ results in the time dependences of the film temperature and the energy flux from the film to the substrate.

Figure 2 displays the calculated temperature of a gold film on a natural diamond substrate as a function of the pulse energy for typical excitation conditions. As can be seen, the maximum temperature of the film weakly depends on the excitation energy due to a strong

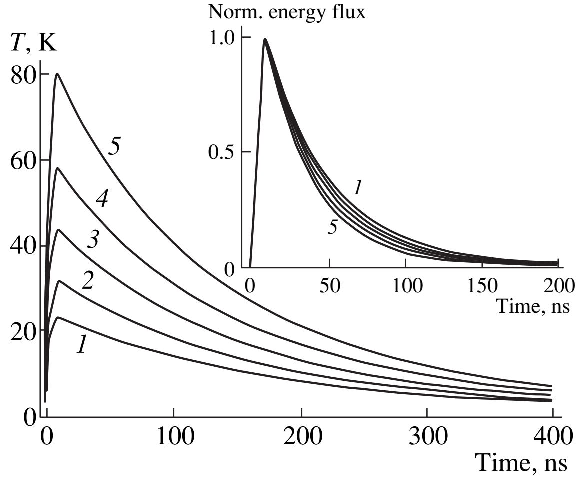

Fig. 2. Time dependences of the temperature of a gold film 1500 Å thick on the diamond substrate at typical excitation energies E_P: (*1*) 0.001, (*2*) 0.003, (*3*) 0.01, (*4*) 0.03, and (*5*) 0.1 μJ. The excitation pulse length τ_P is 10 ns and the excitation spot diameter d_P is 50 μm. The inset shows the normalized time dependences of the energy flux at the same excitation energy densities.

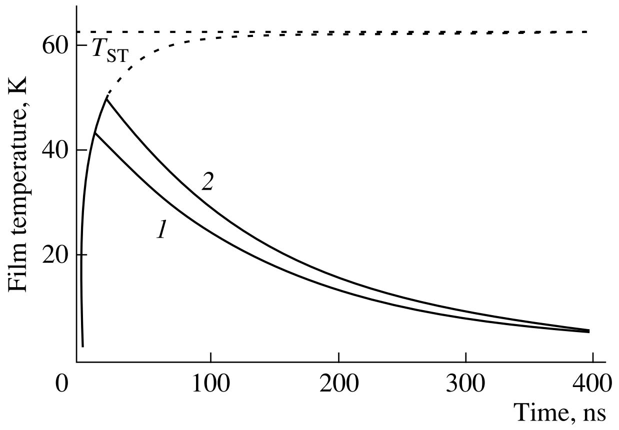

Fig. 3. Time dependences of the temperature of a gold film 1500 Å thick on the diamond substrate at excitation pulse lengths τ_P = (*1*) 10 and (*2*) 20 ns and their comparison with the stationary temperature T_{ST} at the same power density $E_P/(\tau_P \pi^2 d_P^2/4) = 2.0$ kW/mm^2 (see curve *3* in Fig. 2). Dotted lines show further behavior of the temperature in the case of a longer excitation pulse at the same power density.

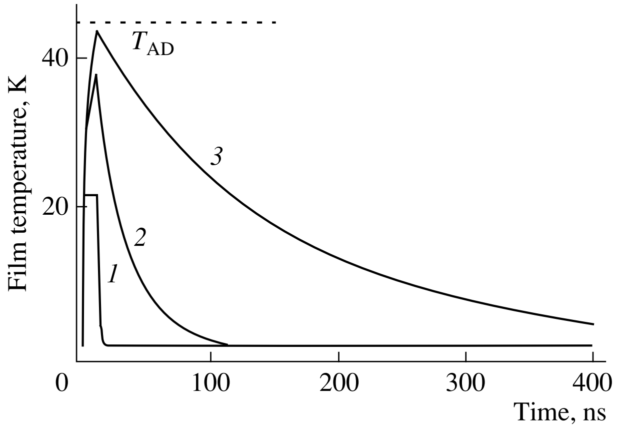

Fig. 4. Time dependences of the temperature of a gold film 1500 Å thick on different substrates: (*1*) CdTe, (*2*) silicon, and (*3*) diamond. Conditions: $\tau_P = 10$ ns, $E_P = 0.01$ μJ, and $d_P = 50$ μm.

temperature dependence of the heat capacity and the fourth power of temperature in the formula for the energy flux from the film to the substrate. For example, for curves *1* and *5*, the excitation energies differ by a factor of 100, whereas the maximum temperatures differ only three times.

The inset in Fig. 2 shows the dependences of the energy flux from the film to the substrate. It should be noted that the times of film cooling are considerable and equal to tens of nanoseconds; all this time, the film generates nonequilibrium phonons.

A comparison of the temperature of the film with the stationary temperature T_{ST} estimated by formula (2) is given in Fig. 3. It can be seen that, in this case, the temperature close to T_{ST} is reached at times longer than 50 ns. It is worth noting that, over the course of tens of nanoseconds when the phonon ejection is still noticeable, the film temperature has already been substantially lower than the estimated temperature. Consequently, the film generates a greater portion of low-frequency nonequilibrium phonons which have appreciably larger free paths compared to elastic scattering by point defects and, thus, can considerably affect the recorded heat pulses. This is the reason why the correct inclusion of the film cooling in simulation of the nonequilibrium phonon propagation is so important for analysis of experimental responses.

Figure 4 depicts the time dependences of the temperature for a gold film on different substrates which are most frequently used in experiments. It is seen that these dependences of the film temperature differ considerably. However, it should be noted that the proposed model disregards the return of phonons from the substrate to the film, which, in actual fact, can occur as a result of vigorous scattering of phonons by lattice defects in the substrate or the formation of a local thermal equilibrium region—a “hot phonon spot” [19]. The effect of this scattering is relatively small for materials such as silicon and diamond in which the mean free paths of phonons with actual frequencies (<3 THz, which correspond to temperatures below 50 K) are equal to hundreds of microns. At the same time, for binary compounds (for example, CdTe), where the mean free paths of phonons are several orders of magnitude smaller, this effect changes the kinetics of film cooling, which, in turn, can lead to an increase in the temperature of the film and the time of its cooling [20].

It should be particularly emphasized that we cannot answer beforehand the question as to which approximation—stationary or adiabatic—gives the most correct estimate of the maximum temperature for a given film/substrate pair of materials or specific excitation conditions.

4. EXPERIMENT

In order to test the proposed model, we performed the following experiment. A gold bolometer in the form of a meander 0.35 × 0.50 mm in size and 1500 Å thick was evaporated onto a sample prepared from the type IIa natural diamond. For the bolometer, the dependence $R(T)$ was linear in the temperature range 4–330 K and the value of dR/dT was equal to 28.2 mΩ/K. The bolometer was irradiated with UV pulses of an LGI-21 nitrogen laser at the liquid-helium temperature $T = 4.2$ K. Upon phonon generation, it is usual practice to decrease the size of a phonon source and, hence, to use a sharp focusing of an excitation beam. However, since the value of dR/dT was small and, moreover, it was necessary to obtain a uniform illumination of the bolometer, the experimental parameters were chosen as follows: the size of the excitation spot was increased to 0.5 mm and the excitation energy was equal to 3.6 μJ. The pulse length was 7.5 ns.

A comparison of the calculated and experimentally measured dependences of the film temperature is given in Fig. 5. It can be seen that the time dependence and the magnitude of the film temperature are in good agreement, which, in our opinion, conclusively proves the correctness of the above treatment.

5. SIMULATION OF NONEQUILIBRIUM PHONON GENERATION BY THE MONTE CARLO METHOD

The Monte Carlo simulation of the generation of nonequilibrium phonons for further calculations of their propagation in the sample consists in computing random coordinates x_i, y_i, and z_i of the point at which the *i*th phonon is generated; the time t_i of its generation; frequency ν_i; polarization p_i; and the direction of its propagation. In the case when the pulse-heated metallic film serves as a phonon generator, the *x* and *y* coordinates are assumed to be uniformly distributed in a specified excitation region, the *z* coordinate corresponds to the irradiated boundary of the sample, and the distributions of initial phonons over frequencies and times of their generation should be chosen in such a way as to reproduce the calculated dependences of the film temperature and the energy flux from the film to the substrate on the time.

The time dependences of the film temperature $T(t)$ and the energy flux $Q(t)$ from the film to the substrate are the initial data for the construction of the algorithm for simulating the generation of nonequilibrium phonons. Since the characteristic frequencies of generated phonons are proportional to the film temperature, the quantity $N(t) = Q(t)/T(t)$ is proportional to the number of phonons generated at a given instant of time. The function

$$p(t) = \int_0^t N(\tau)d\tau \Big/ \int_0^\infty N(\tau)d\tau$$

has the meaning of the probability that a phonon will be generated at an instant of time *t*; i.e., it is the time distribution function of phonon generation. Then, the random quantity $t_i = p^{-1}(r_i)$ (where r_i is the random number uniformly distributed within the interval 0–1) is the time t_i of generation of the *i*th phonon and the dependence $T(t)$ makes it possible to obtain the film temperature T_i at this instant of time. The temperature T_i determines the frequency distribution of phonons generated by the film.

The function $n(u) = u^2/(\exp(u) - 1)$ (where $u = h\nu/k_BT_i$) is proportional to the density of the frequency distribution of the phonon number. Then, the frequency of the *i*th generated phonon is determined by the relationship $\nu_i = u_ik_BT_i/h$, where $u_1 = q^{-1}(r_i)$, r_i is the random number uniformly distributed in the interval 0–1, and $q(u) = \int_0^u n(s)ds / \int_0^\infty n(s)ds$.

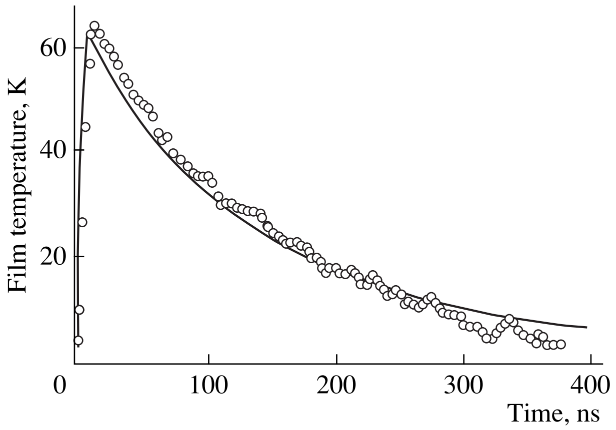

Fig. 5. Comparison of the calculated and experimental dependences of the temperature for a gold film 1500 Å thick on the diamond substrate. Computational and experimental parameters: τ_P = 7.5 ns, E_P = 3.6 μJ, d_P = 0.50 mm, and T_0 = 4 K.

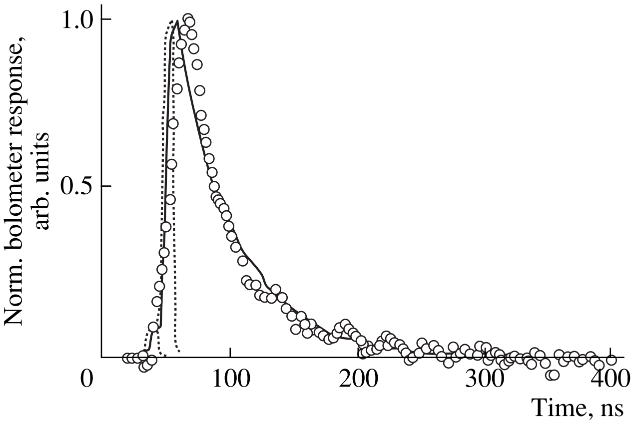

Fig. 6. Comparison of heat pulses calculated using different algorithms for phonon generation and the experimental data. Circles correspond to the experimental response of a detector (gold film 1500 Å thick on diamond substrate, τ_P = 7.5 ns, E_P = 0.005 μJ, d_P = 0.25 mm, and T_0 = 2 K). Dotted lines represent the calculated response upon generation of phonons with a frequency of 0.93 THz (which corresponds to the temperature T_{AD} = 15.8 K) for a time τ_P. The solid line indicates the response calculated within the proposed model of phonon generation.

Since the dependences $T(t)$, $Q(t)$, and others had a complex shape, the integration was performed numerically, the results of calculations were tabulated, and the values of inverse functions were determined by the interpolation and then were also tabulated.

The phonon polarization p_i was chosen in a random way with the probability proportional to the density of states. The Θ_i and ϕ_i angles, which determine the direction of the phonon wavevector, were also randomly chosen in a hemisphere from uniform distributions in the intervals $[0, \pi/2]$ and $[0, 2\pi]$, respectively. Moreover, it is possible to introduce an additional check in order to exclude errors such as the appearance of phonons with frequencies higher than those realized physically.

Thus, the execution of the given algorithm results in a set consisting of the time t_i of generation of the *i*th phonon; its frequency ν_i; the polarization p_i; the coordinates x_i, y_i, and z_i of the point at which the *i*th phonon is generated; and the direction of the wavevector, which is specified by the angles Θ_i and ϕ_i.

Figure 6 illustrates the importance of the correct inclusion of the features of phonon generation.

(i) Circles show the experimental heat pulse, which was measured in a single crystal of the type II*a* natural diamond with the use of the pulse-heated gold film as a phonon generator under the following excitation conditions: $E_P = 0.005$ μJ, $\tau_P = 7.5$ ns, and $d_P = 0.25$ mm. In this case, the estimates of the film temperature give the values $T_{\mathrm{AD}} = 15.8$ K and $T_{\mathrm{ST}} = 25.1$ K.

(ii) The dotted curve represents the heat pulse, which was calculated by the Monte Carlo method under the assumption that phonons are generated only during the excitation pulse, have a frequency of 0.93 THz (which corresponds to a temperature of 15.8 K), and are scattered only by isotopes. In this case, the mean free paths of phonons are equal to tens of centimeters and it seems that the heat pulse should be very sharp. However, taking allowance for the fact that the film cools down for a considerable time and generates phonons all this time results in quite a different situation.

(iii) The solid line in Fig. 6 depicts the results obtained by simulating the propagation of nonequilibrium phonons with inclusion of the above algorithm of phonon generation. It is seen that the results of simulation agree well with the experimental data.

It should be noted that attempts to explain the observed heat pulse length in any one way, for example, by scattering from point defects, lead to very large elastic scattering constants, which are undeniably invalid.

ACKNOWLEDGMENTS

We are grateful to A.A. Gippius and R.A. Khmel'nitskiĭ for supplying the natural diamond samples.

This work was supported by the Russian Foundation for Basic Research, project nos. 99-02-17183 and 98-02-16892.

REFERENCES

1. P. Hawker and A. J. Nemin, Physica B (Amsterdam) **263–264**, 514 (1996).
2. W. S. Capinski and H. J. Maris, Physica B (Amsterdam) **219–220**, 699 (1996).
3. A. G. Kozorezov, J. K. Wigmore, T. Miyasato, and K. Strickland, Physica B (Amsterdam) **219–220**, 748 (1996).
4. M. M. Bonch-Osmolovskiĭ, T. I. Galkina, A. Yu. Klokov, *et al.*, Fiz. Tverd. Tela (St. Petersburg) **38** (4), 1051 (1996) [Phys. Solid State **38**, 582 (1996)].
5. Sh. Tamura, Phys. Rev. B **48** (18), 13502 (1993).
6. B. A. Danil'chenko, D. V. Kazakovtsev, and I. A. Obukhov, Zh. Éksp. Teor. Fiz. **106**, 1439 (1994) [JETP **79**, 777 (1994)].
7. T. I. Galkina, A. Yu. Klokov, R. A. Khmelnitskii, *et al.*, Proc. SPIE **3484**, 222 (1998).
8. S. Tamura, J. A. Shields, M. T. Ramsbey, and J. P. Wolfe, in *Proceedings of VII International Conference on Phonon Scattering in Condensed Matter, 1992*, p. 79.
9. A. I. Sharkov, T. I. Galkina, A. Yu. Klokov, *et al.*, Diamond Relat. Mater. **9** (3–6), 1100 (2000).
10. V. M. Mogilevskiĭ and A. F. Chudnovskiĭ, *Thermal Conductivity of Semiconductors* (Nauka, Moscow, 1972).
11. A. Berke, A. P. Mayer, and R. K. Wehner, Solid State Commun. **54** (5), 395 (1985); H. Schwartz, K. F. Renk, A. Berke, *et al.*, in *Proceedings of the 5th International Conference on Phonon Scattering in Condensed Matter* (Springer-Verlag, Berlin, 1986), p. 362.
12. Sh. Tamura, Phys. Rev. B **31** (4), 2574 (1985).
13. W. S. Kapinski, M. Cardona, D. S. Hatzer, *et al.*, Physica B (Amsterdam) **263–264**, 530 (1999).
14. T. I. Galkina, A. F. Klokov, and A. I. Sharkov, Pis'ma Zh. Tekh. Fiz. **21** (17), 5 (1995) [Tech. Phys. Lett. **21**, 679 (1995)].
15. T. I. Galkina, A. I. Sharkov, A. Yu. Klokov, *et al.*, Pis'ma Zh. Éksp. Teor. Fiz. **64** (4), 270 (1996) [JETP Lett. **64**, 298 (1996)].
16. O. Weis, Z. Angew. Phys. **26** (5), 325 (1969).
17. O. Weis, J. Phys. (Paris) **33** (C4), 48 (1972).
18. W. A. Little, Can. J. Phys. **37**, 334 (1959).
19. D. V. Kazakovtsev and I. B. Levinson, Zh. Éksp. Teor. Fiz. **88** (6), 2228 (1985) [Sov. Phys. JETP **61**, 1318 (1985)].
20. D. V. Kazakovtsev and Y. B. Levinson, Phys. Status Solidi B **136**, 425 (1986).

Translated by O. Borovik-Romanova

Physics of the Solid State, Vol. 43, No. 3, 2001, pp. 469–472. Translated from Fizika Tverdogo Tela, Vol. 43, No. 3, 2001, pp. 452–455.
Original Russian Text Copyright © 2001 by Medvedeva, Ivanovskiĭ.

DEFECTS, DISLOCATIONS, AND PHYSICS OF STRENGTH

Effect of Metal and Carbon Vacancies on the Band Structure of Hexagonal Tungsten Carbide

N. I. Medvedeva and A. L. Ivanovskiĭ

Institute of Solid-State Chemistry, Ural Division, Russian Academy of Sciences,
Pervomaĭskaya ul. 91, Yekaterinburg, 620219 Russia
e-mail: ivanovskii@ihim.uran.ru

Received July 10, 2000

Abstract—The band structure of hexagonal tungsten carbide (β-WC) containing vacancies in metal and carbon sublattices is investigated within the first-principles full-potential linear muffin-tin orbital (LMTO) approach for a model of 16-atom supercells. Specific features of the formation of “vacancy” states are discussed, and the formation energies of defects and their charge states are estimated. The results obtained are compared with previous calculations and available experimental data. *© 2001 MAIK “Nauka/Interperiodica”.*

1. INTRODUCTION

Lattice vacancies belong to the most commonly encountered type of point (zero-dimensional) defects of a crystal lattice. They substantially affect the properties of nonstoichiometric compounds within their homogeneity region.

It is known that no ideal (perfect) crystals occur at $T > 0$. At present, the nonstoichiometry of compounds is associated with its main feature, namely, the experimentally observed discrepancy between the chemical composition and the number of sites in crystal sublattices [1]. In other words, classification of all crystal phases as stoichiometric and nonstoichiometric compounds depends on the potentials of currently available methods for experimental observation of the effects brought about by lattice vacancies.

Cubic (*B*1 type) carbides of Group IV and V transition metals represent one of the most well-known classes of nonstoichiometric compounds with very wide homogeneity regions. For example, titanium carbide with a cubic structure exists in the concentration region from $TiC_{1.00}$ to $TiC_{0.49}$ [2]. The characteristic feature of these phases is the variable concentration of structural vacancies in one (carbon) of the sublattices, whereas the metal sublattice is usually considered as occupied completely [2, 3]. The band structure of carbon-incomplete cubic carbides has been investigated elsewhere [4–7]. Unlike the cubic (*B*1) carbides, the higher group transition metal carbides which belong to other crystallographic types usually have considerably narrower regions of homogeneity [2, 3].

One of the latter carbides of most interest is the tungsten monocarbide (β-WC), which has a hexagonal structure (the D^1_{3h} symmetry). Tungsten monocarbide is one of the most mechanically resistant and refractory carbide materials ($T_{\mathrm{mel}} = 3058$ K); its catalytic activity is comparable to that of platinum [2].

Tungsten monocarbide has a narrow homogeneity region in which the carbon content varies in the range 37–48 at. %. Until recently, the metal lattice of tungsten carbide was assumed to be completed.

Rempel *et al.* [8] were the first to reveal the presence of both C and W vacancies in tungsten carbide. These data were obtained by the electron–positron annihilation technique whose sensitivity to the vacancy content was estimated at $\sim10^{-4}$ vacancies per atom [9].

The purpose of the present work was to investigate the band structure of the hexagonal tungsten carbide containing lattice defects of both types, namely, C and W vacancies. Using the self-consistent nonempirical full-potential linear muffin-tin orbital (FPLMTO) method, we analyzed the nature of vacancy states and general variations observed in the band spectrum of nonstoichiometric WC_x and W_yC due to structural defects. The formation energies of the C and W vacancies were calculated numerically. Based on the analysis of their charge states, we interpreted the experiments on the positron annihilation [8].

Note that, so far, the band-theory calculations have been performed for the electronic structure of “ideal” tungsten carbides with hexagonal (β-WC [4, 10–16]) and metastable cubic (of the *B*1 type [7, 13, 15, 17, 18]) structures.

2. MODEL AND CALCULATION PROCEDURE

Tungsten monocarbide β-WC has a hexagonal structure (space group D^1_{3h}–$P6m2$) formed by packing hexagonal monolayers of W and C atoms in the *ABAB*… stacks. In the β-WC structure, the W and C atoms reside in a trigonal–prismatic environment. In

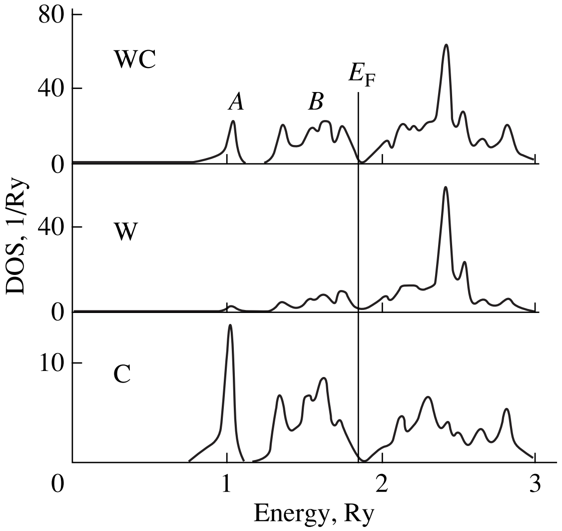

Fig. 1. Total (upper curve) and local densities of states for β-WC.

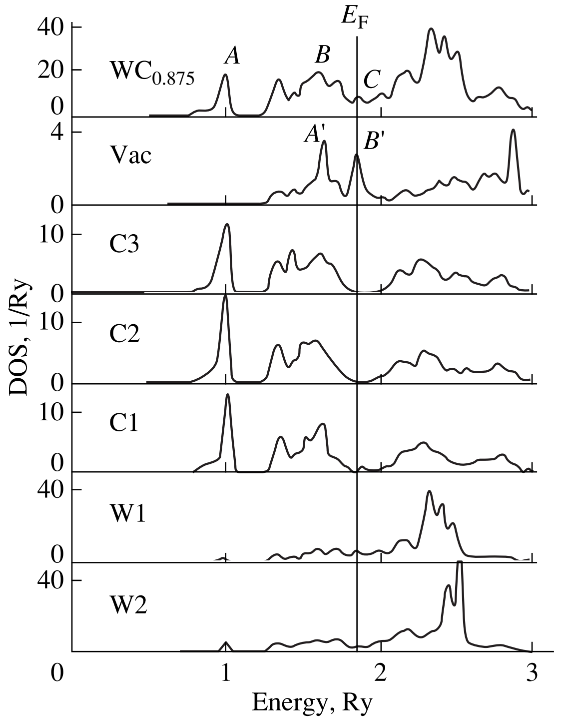

Fig. 2. Total (upper curve) and local densities of states for $WC_{0.875}$. The densities of states for nonequivalent atoms W and C in the $W_8C_7V_C$ supercell are given.

this case, the W and C atoms have $[WC_6W_8]$ and $[CW_6]$ coordination polyhedra, respectively. The unit cell contains one formula unit ($Z = 1$), and the W and C atoms occupy the positions (a) 000 and (d) 1/32/31/3, respectively. The unit cell parameters are $a = 2.9065$ Å and $c = 8.366$ Å [2, 3].

For modeling WC, we used a 16-atom supercell with the initial composition W_8C_8. The $W_8C_7V_C$ and $W_7V_WC_8$ supercells (V_C and V_W denote the vacancies in the C and W sublattices, respectively) corresponded to the defect carbides of the formal stoichiometries $WC_{0.875}$ and $W_{0.875}C$, respectively.

The band structures of WC, $WC_{0.875}$, and $W_{0.875}C$ were calculated by the self-consistent FPLMTO method [19, 20] in the local-electron-density approximation [21]. The actual crystal potential and charge density used in the FPLMTO method make it possible to calculate with a high accuracy the total energy of the system and the physical properties of crystals (lattice dynamics, structural stability, etc. [19–26]), which are determined by the total energy. The muffin-tin orbitals were calculated in the standard 3k basis set with the kinetic energies $-k^2 = 0.01$, 1.0, and 2.3 Ry. The computations were performed in the scalar–relativistic interpretation of valence electrons (6s, 6p, and 5d for W and 2s and 2p for C).

3. RESULTS AND DISCUSSION

The total and local densities of states (TDOS and LDOS, respectively) for β-WC are shown in Fig. 1. According to the previous computations [4, 10–16], the carbide valence band consists of two main subbands (A and B) separated by the energy gap. The lower subband A is formed by the contributions of the C 2s states, whereas the subband B has a substantially hybrid character and is formed by overlapping the W 5d and C 2p states. The Fermi level (E_F) is located close to the local DOS minimum which separates the bands of bonding and antibonding W–C states. These features of the band structure determine the extreme cohesion characteristics of β-WC [4], unlike the metastable cubic carbide phase in which W-5d-like bands of the antibonding type are occupied to a large extent [4, 7].

The total and local densities of states for nonstoichiometric $WC_{0.875}$ and $W_{0.875}C$ are shown in Figs. 2 and 3. Introduction of the C vacancy results in the appearance of the near-Fermi peak of C and the substructure of the DOS distribution for the hybrid B band (Fig. 2). These variations can be explained by the nature of the formation of vacancy states [4, 6]. As is seen from Fig. 2, the vacancy states form two symmetric peaks A' and B', which are separated by the DOS minimum. Their origin is caused by a local distortion of the crystal field in the vicinity of V_C and a partial decrease in the splitting of the d states, which coordinate the defects of W atoms as bonding and antibonding ones. As a result, certain W d states regain their antibonding states. This scheme is clearly illustrated with the local density of states of the C vacancy and the local densities of states of the W atoms which surround the vacancy (Fig. 2). It is seen that the A' and B' LDOS peaks of the V_C defect reflect a decrease in the energy of the bonding W d states (A' peak) and an increase in the energy of the antibonding W d states (B' peak) in the defect region as compared to those in the complete crystal (Fig 1). Judging from the LDOS shape for atoms in the $W_8C_7V_C$ cell, the atoms of at least two coordination spheres undergo a perturbation of the electron density in the presence of a vacancy. This effect is demonstrated by the electron density map for $WC_{0.875}$ (Fig. 4).

The general mechanism of the perturbing effect of the W vacancy is similar to that described previously and is associated with the variation in the electronic states of the carbon atoms nearest to V_W. The transition of a certain portion of C 2*p* states to the region of antibonding states clearly manifests itself in the LDOS profile of the C1 carbon atoms nearest to the vacancy (peak *A*' in Fig. 3). As a result, the C and W vacancies bring about the "depletion" of certain bonding states, E_F shifts downward in the energy scale, and the density of states at the Fermi level substantially increases. Note that the density of states at the Fermi level $N(E_F)$ for metal vacancies increases more rapidly (see table).

Calculations of the cohesion (E_{coh}) and vacancy formation (E_v) energies, which were carried out according to the procedure described in [24, 25], yielded the following results (see table): (i) the presence of vacancies of both types deteriorates the cohesion properties of WC and (ii) $E_v(W) > E_v(C)$ in accordance with the preferential formation of C vacancies in WC. The latter result can be qualitatively explained in terms of interatomic interactions in WC. As follows from computations (see also [4, 10–16]), the chemical bond in WC has a mixed covalent–metallic–ionic character [4]. For this reason, the preferential formation of C vacancies is determined by the lower energy expenditure in breaking six carbon–metal covalent bonds (in a trigonal prism—the [CW_6] coordination polyhedron). By contrast, the formation of a metal vacancy requires the additional breakage of eight metallic bonds between the receded metal atom and the metal atoms forming its second coordination sphere (the [WC_6W_8] coordination polyhedron).

At present, experimental investigations of the electronic structure of nonstoichiometric WC_x and W_yC are practically absent. Rempel *et al.* [8] obtained the evaluated data on the charge density distribution in β-WC by using the electron–positron annihilation technique. These authors measured the positron lifetime τ in the samples exposed to radiation (the electron energies were 1.0 and 2.5 MeV), revealed the bounded (localized) positron states for two types of structural defects, and found that the lifetime of a positron captured by the C vacancy ($\tau_C \sim 136$ ps) was considerably shorter than that in the case of the W vacancy ($\tau_W \sim 175$ ps) [8]. The increased value of τ_W was explained in [8] by the lower electron density in the region of metal vacancies surrounding the carbon atom, whereas the C vacancies are surrounded by tungsten atoms with a higher electron density; hence, it follows that $\tau_C < \tau_W$.

The calculations performed allow direct estimations of the electron density distribution in the coordination spheres of the W and C vacancies (see table). It is seen that $Q(V_W) < Q(V_C)$, which qualitatively correlates with the relationship $\tau_C < \tau_W$ [8]. Taking into account that positrons in β-WC annihilate primarily with the electrons removed from positively charged nuclei [9], we also compared the so-called intersphere electron densities (Q_{is}). The obtained values were $Q_{is}(WC_{0.875})$ =

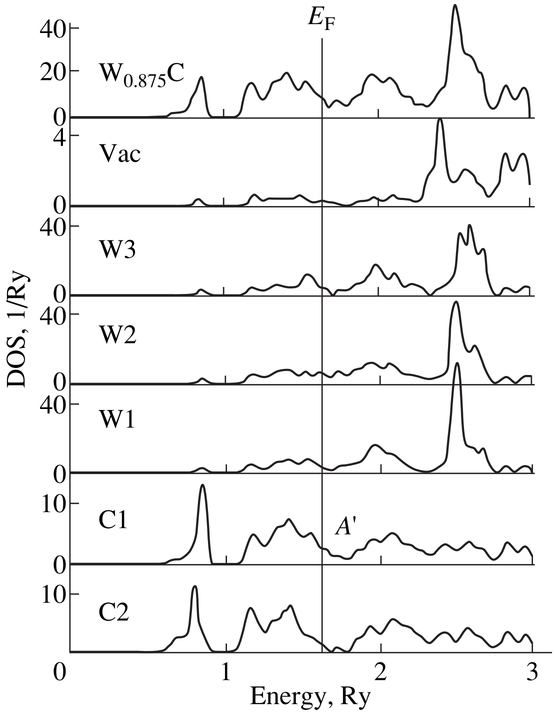

Fig. 3. Total (upper curve) and local densities of states for $W_{0.875}C$. The densities of states for nonequivalent atoms W and C in the $W_7V_WC_8$ supercell are given.

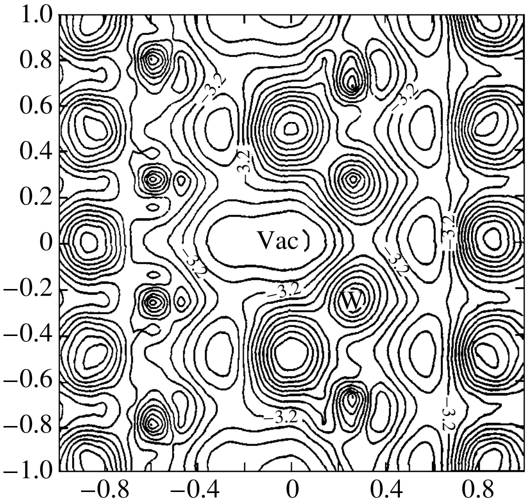

Fig. 4. Distribution of the electron valence–state density for $WC_{0.875}$ in the $W_8C_7V_C$ supercell (V_C stands for vacancies in the carbon sublattice).

Cohesion (E_{coh}), vacancy formation (E_V), and Fermi (E_F) energies (Ry), density of states at the Fermi level ($N(E_F)$, 1/Ry), and charges in the muffin-tin spheres of vacancies (Q, e)

Carbide	E_{coh}	E_V	E_F	$N(E_F)$	Q_{vac}
WC	–1.76	–	1.86	3.16	–
$WC_{0.875}$	–1.63	0.13	1.84	8.26	0.67
$W_{0.875}C$	–1.56	0.20	1.62	9.37	0.51

Note: The radii of vacancy spheres are taken equal to the radii of receded atoms.

$2.98e > Q_{is}(W_{0.875}C) = 2.77e$, which is in agreement with the difference in τ revealed for V_W and V_C in β-WC [8]. Undoubtedly, in order to obtain the quantitative estimate of τ, it is necessary to solve a special problem with the introduction of the positron wavefunctions into the basis set.

ACKNOWLEDGMENTS

We thank A.A. Rempel for preliminary first-hand acquaintance with the results of paper [8] and fruitful discussions.

REFERENCES

1. A. I. Gusev, Usp. Fiz. Nauk **170** (1), 3 (2000).
2. L. E. Toth, *Transition Metal Carbides and Nitrides* (Academic, New York, 1971).
3. G. V. Samsonov and I. M. Vinitskiĭ, *Handbook of Refractory Compounds* (Metallurgiya, Moscow, 1976; Plenum, New York, 1980).
4. A. L. Ivanovskiĭ, V. P. Zhukov, and V. A. Gubanov, *Electronic Structure of Refractory Carbides and Nitrides of Transition Metals* (Nauka, Moscow, 1990).
5. A. L. Ivanovskiĭ, A. I. Gusev, and G. P. Shveĭkin, *Quantum Chemistry in Material Science: Triple Carbides and Nitrides of Transition Metals and Group III–IV Elements* (Ural. Otd. Ross. Akad. Nauk, Yekaterinburg, 1996).
6. A. L. Ivanovskii, V. I. Anisimov, D. L. Novikov, *et al.*, J. Phys. Chem. Solids **49** (5), 465 (1988).
7. M. J. Puska, M. Sob, G. Bauer, and T. Korhonen, J. Phys. IV **5** (2), 135 (1995).
8. A. A. Rempel, R. Wurschum, and H.-E. Schaefer, Phys. Rev. B **61** (9), 5945 (2000).
9. A. A. Rempel, Usp. Fiz. Nauk **166** (1), 33 (1996) [Phys. Usp. **39**, 31 (1996)].
10. L. F. Mattheiss and D. R. Hamann, Phys. Rev. B **30** (4), 1731 (1984).
11. A. L. Ivanovskii, D. L. Novikov, and V. A. Gubanov, Phys. Status Solidi **141** (2), 9 (1987).
12. D. L. Novikov, A. L. Ivanovskiĭ, and V. A. Gubanov, Zh. Neorg. Khim. **33** (10), 2673 (1988).
13. V. P. Zhukov and V. A. Gubanov, Solid State Commun. **56** (1), 51 (1985).
14. J. Liu, R. Wentzcovitch, and M. Cohen, Phys. Rev. B **38** (14), 9483 (1988).
15. D. L. Price and B. R. Cooper, Phys. Rev. B **39** (8), 4945 (1989).
16. S. L. Kas'yanov, V. M. Tapilin, and V. R. Belosludov, J. Struct. Chem. **38** (4), 511 (1997).
17. J. Liu and M. Cohen, Solid State Commun. **67** (10), 907 (1988).
18. M. Rajagopalan, P. Saigeetha, G. Kalpana, and B. Palanivel, Jpn. J. Appl. Phys., Part 1 **33** (4A), 1847 (1994).
19. M. Methfessel, C. Rodríguez, and O. K. Andersen, Phys. Rev. B **40** (3), 2009 (1989).
20. M. Methfessel and M. Scheffler, Physica B (Amsterdam) **172**, 175 (1991).
21. M. Methfessel, Phys. Rev. B **38** (8), 1537 (1988).
22. A. T. Paxton, M. Methfessel, and H. M. Polatoglou, Phys. Rev. B **41** (12), 8127 (1990).
23. V. Schonberger, O. K. Andersen, and M. Methfessel, Acta Metall. Mater. **40**, 81 (1992).
24. N. I. Medvedeva, O. N. Mryasov, Yu. N. Gornostyrev, and A. Freeman, Phys. Rev. B **54** (19), 13506 (1996).
25. N. I. Medvedeva, D. L. Novikov, A. L. Ivanovskii, *et al.*, Phys. Rev. B **58**, 16 042 (1998).
26. A. L. Ivanovskiĭ, N. I. Medvedeva, Yu. E. Medvedeva, and G. P. Shveĭkin, Dokl. Akad. Nauk **361** (5), 642 (1998).

Translated by N. Korovin

Physics of the Solid State, Vol. 43, No. 3, 2001, pp. 473–479. Translated from Fizika Tverdogo Tela, Vol. 43, No. 3, 2001, pp. 456–461.
Original Russian Text Copyright © 2001 by Gorlov, Guseva, Potapov, Rokeakh.

DEFECTS, DISLOCATIONS, AND PHYSICS OF STRENGTH

Superhyperfine Interaction in the Trigonal Center $BaF_2 : Gd^{3+}$ and the Lattice Distortion Analysis in the Vicinity of the Impurity Ion

A. D. Gorlov, V. B. Guseva, A. P. Potapov, and A. I. Rokeakh
Research Institute of Physics and Applied Mathematics, Ural State University, pr. Lenina 51, Yekaterinburg, 620083 Russia
e-mail: Anatoliy.Gorlov@usu.ru

Received April 17, 2000; in final form, August 1, 2000

Abstract—The constants of the superhyperfine interaction of Gd^{3+} with the ^{19}F nuclear spins in the first four coordination shells were determined from the ENDOR spectra of a trigonal $BaF_2 : Gd^{3+}$ center. These data were used for analysis of the crystalline lattice distortions in the vicinity of the impurity ion. It was found that the largest displacements of fluorine nuclei occurred in the vicinity of the ion compensator and the impurity ion. To calculate the anion positions within the first coordinate shell, whose electron–nuclear interaction with Gd^{3+} depends considerably on chemical bonds in the $Gd^{3+}F_8^-$ complex, an empirical model is used for the isotropic constants of the superhyperfine interaction of Gd^{3+} with fluorine nuclei in cubic centers, with allowance made for the impurity ion polarization. © *2001 MAIK “Nauka/Interperiodica”.*

INTRODUCTION

Trigonal impurity centers Gd^{3+} and BaF_2 are formed in the process of crystal growth due to the compensation for the excess positive impurity charge by the F^- ion at the nearest interstitial site along the C_3 axis. Local distortions of the neighboring anion surrounding (the first coordinate shell) of Gd^{3+} produced by the F^k compensator were analyzed by us in [1] on the basis of the superposition model for the spin Hamiltonian (SH) constants of the second and fourth ranks [2]. These constants describe the Stark splitting of the ground state of the $^{157}Gd^{3+}$ trigonal centers in SrF_2 and BaF_2. Some results of our previous investigations of the superhyperfine interaction (SHFI) of Gd^{3+} with BaF_2 ligands are also taken into account. In this work, we consider the local structure of the trigonal Gd^{3+} in the BaF_2 center in detail on the basis of the results of the ENDOR investigation of SHFI of Gd^{3+} with the ^{19}F nuclei (the nuclear spin $I = 1/2$) of the first four coordination shells and with the compensating ion. The SHFI studied by the ENDOR method is determined for the individual Gd^{3+}–^{19}F couple. This allows one to calculate the ligand coordinates relative to the impurity ion, when the Gd^{3+} and ^{19}F ions interact as two point magnetic dipoles. To determine the coordinates of the nearest ligands, for which the short-range interaction contributions (covalence, overlapping of the electron shells of the impurity and of the surrounding ions) to the SHFI are large, a model describing the radial dependences of the electron–nuclear interaction constants is needed. The empirical model taking into account the covalence and the Gd^{3+} and F^- (polarized by the electric field of the surrounding ions) electron shell overlap was proposed in [3] and used by us in [4] for determining the radial dependences of the SHFI constants for the cubic Eu^{2+} and Gd^{3+} centers in crystals with a fluorite-type structure. In this work, such a model, also taking into account the impurity ion polarization, is utilized for description of the isotropic constants of the trigonal Gd^{3+} center in BaF_2.

1. RESULTS OF ENDOR STUDIES AND DISCUSSION

The trigonal and cubic EPR spectra of Gd^{3+} (electron spin $S = 7/2$) with the intensity ratio 20 : 1 were observed in the BaF_2 crystals with the GdF_3 impurity (0.01 wt % in the charge), grown by means of the Stockbarger method. The EPR of the trigonal center at $T = 4.2$ K is well described by the standard SH with parameters given in [5] in the coordinate system (called the laboratory coordinate system in what follows) where the principal symmetry axis of the C_3 center is parallel to Z and to [111], the X axis is parallel to $[\bar{1}\bar{1}2]$, and Y is parallel to $[\bar{1}10]$.

The ENDOR measurements were carried out mainly for the external magnetic field orientation along the crystal symmetry axes (C_3, C_2, C_4). The fragments of angular dependences in the vicinity of these axes were studied in specific cases. Due to the presence of the compensating ion, the local symmetry of some anions was lowered from C_{3v} to C_s and the distances between anions and Gd^{3+} were changed. The latter led to a considerable increase in the number of the ENDOR signals with respect to the case of the cubic Gd^{3+} center in BaF_2. This made the interpretation and description of the spectra more complicated.

1063-7834/01/4303-0473$21.00 © 2001 MAIK “Nauka/Interperiodica”

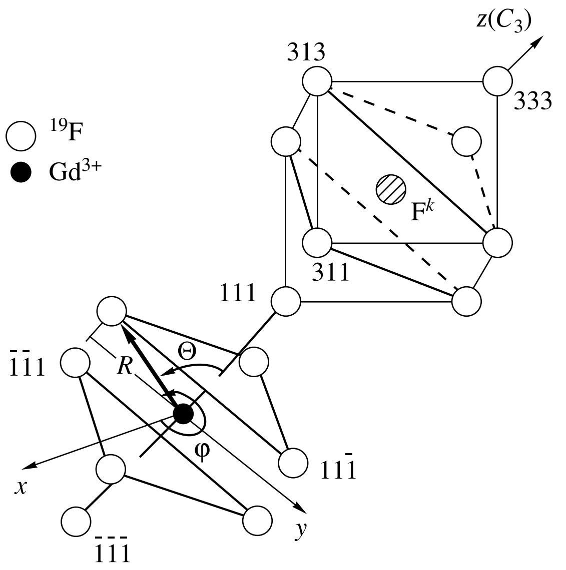

Fig. 1. A part of the local surrounding of the trigonal impurity center in BaF_2. The ligands nearest to Gd^{3+} and the fluorine nuclei of the second to fourth coordination shells that are displaced relative to the cubic center are shown.

For virtually all orientations, the ENDOR signals that were determined by the fluorine nuclei being the nearest neighbors of the impurity ion and situated at equivalent sites (in Fig. 1, they form regular triangles) had a fine structure associated with indirect nuclear interaction through an impurity ion [6, 7].

Our calculations of such a structure showed that its center coincides with the ENDOR signals position in the absence of the indirect interaction. For this reason, the frequencies correspondent to the positions of the structure centers are used for the determination of the SHFI constants.

By symmetry, the eight fluorine nuclei nearest to Gd^{3+} are separated into two groups. Figure 1 shows two non-equivalent nuclei lying on the C_3 axis with the local symmetry C_{3v} (nuclei of the 111 and $\bar{1}\bar{1}\bar{1}$ type) and two nonequivalent equilateral triangles whose planes are perpendicular to the C_3 axis. These triangles consist of the fluorine nuclei of the second type: $11\bar{1}$, $1\bar{1}1$, and $\bar{1}11$, $\bar{1}\bar{1}1$, $\bar{1}1\bar{1}$, $1\bar{1}\bar{1}$ (local symmetry of the nuclei is C_s). Here and henceforth, the figures that specify the type of nuclei correspond to the F^- coordinates in the undistorted lattice.

The SH part that is necessary for description of the SHFI ligands of the C_s symmetry has the following form in the local coordinate system attached to any selected nucleus (the z axis is parallel to the Gd^{3+}–^{19}F bond axis, the x axis lies in the plane containing the bond axis and C_3):

$$\begin{aligned} H_n = {} & (A_s + 2A_p)O_1^0(S)O_1^0(I) + (A_s - A_p - A_E) \\ & \times O_1^1(S)O_1^1(I) + (A_s - A_p + A_E)\Omega_1^1(S)\Omega_1^1(I) \\ & + (A_1 + 4A_2)O_3^0(S)O_1^0(I) + (A_1 - 3A_2) \\ & \times (O_3^1(S)O_1^1(I) + \Omega_3^1(S)\Omega_1^1(I)) - g_n\beta_n(HI). \end{aligned} \tag{1}$$

The notation in Eq. (1) is commonly used [6, 7]. We note that only the S^3I-type terms whose contributions to the ENDOR frequencies are greater than the experimental error (≥5 kHz) are taken into account in the Hamiltonian. The corresponding SH for the C_{3v} symmetry ligands is given by Eq. (1) in which $A_E = (A_{yy} - A_{xx})/2 = 0$.

With a set of experimental and calculated ENDOR frequencies for each nucleus, the SHFI constants were determined by the numerical minimization of the mean square deviation for all orientations of a magnetic field simultaneously. A computer diagonalization of the energy matrix, obtained from the Hamiltonian containing both the part describing the splitting of the ground state [5] and H_n reduced to the laboratory coordinate system, was carried out. The angles Θ and φ transforming the local coordinate system for each fluorine nucleus into the laboratory system (which are the ligand angular coordinates) were included in a standard way [6] into relations for the ENDOR frequencies and were also determined in the course of the minimization process.

Calculations show that the SHFI of Gd^{3+} with the fluorine nuclei of the second and more distant coordination shells, including even F^k (independently of the local ligand symmetry), is described by axially symmetric SHFI tensors (in the local coordinate system) and $A_s = 0$, $A_E = 0$, $A_1 = A_2 = 0$, and $A_{zz} = -2A_{xx} = -2A_{yy} = 2A_p$. Such a situation takes place when the SHFI is determined by the dipole–dipole interaction between the impurity ion and ^{19}F. Thus, the quantity $A'_p = A_p - A_d$ associated with the short-range interaction in the Gd^{3+}–^{19}F couple (usually, $A_s > A'_p$ for fluorides [3, 4, 6–9]) equals zero. In this case, the anisotropic constant $A_p = A_d = gg_n\mu\mu_n/R^3$ [3, 4, 6], where A_d is the dipole–dipole interaction constant and R is the distance between Gd^{3+} and ^{19}F.

The constants of the SHFI compensator and of the anions of the second, third, and fourth coordination shells of the impurity ion are presented in Table 1. Both the calculated coordinates of these ligands in the laboratory coordinate system and their deviations from the corresponding values for the cubic Gd^{3+} center in BaF_2 are also shown. The azimuthal angles φ are not presented, since, in the limits of calculation error, they do not differ from the corresponding values for the cubic center. It is evident from the data of Table 1 that the

Table 1. The SHFI constants and the fluorine nuclei coordinates for the second to fourth coordination shells, including the compensator, in the trigonal Gd^{3+} center in BaF_2, and their deviations $\Delta R = R - R_{cub}$ and $\Delta\Theta = \Theta - \Theta_{cub}$ from the coordinates of the corresponding nuclei in the cubic Gd^{3+} in BaF_2 center [1]

Shell	The nucleus type (the number of nuclei)	A_p, kHz	R, Å	Θ, deg	ΔR, Å	ΔΘ, deg
2	311(3)	534(3)	5.18(1)	31.0(2)	0.10(1)	1.9(3)
	$1\bar{1}3$ (3), $31\bar{1}$ (3)	573(4)	5.06(1)	58.8(2)	–0.02(2)	0.4(3)
	$\bar{1}\bar{1}3$ (3)	567(3)	5.08(1)	80.5(2)	0.00(2)	0.3(3)
	$1\bar{3}1$ (3)	565(3)	5.08(1)	100.0(2)	0.01(1)	0.3(3)
	$1\bar{3}\bar{1}$ (3), $\bar{1}1\bar{3}$ (3)	566(4)	5.08(1)	121.7(2)	0.01(1)	0.3(3)
	$\bar{1}\bar{3}\bar{1}$ (3)	576(3)	5.08(2)	150.6(2)	–0.01(2)	–0.1(3)
3	313(3)	232(2)	6.83(2)	22.7(2)	0.14(3)	0.7(3)
	$3\bar{1}3$ (3)	246(2)	6.70(2)	48.6(4)	0.00(3)	0.0(6)
	$1\bar{3}3$ (3), $3\bar{3}1$ (3)	247(2)	6.70(2)	82.5(3)	0.00(3)	0.1(4)
	$\bar{1}\bar{3}3$ (3), $3\bar{3}\bar{1}$ (3)	247(2)	6.70(1)	97.5(5)	0.00(3)	–0.1(6)
	$\bar{3}\bar{3}1$ (3)	246(4)	6.70(1)	131.5(4)	0.00(3)	0.0(6)
	$\bar{3}\bar{3}\bar{1}$ (3)	249(2)	6.68(3)	157.9(5)	–0.02(5)	–0.2(6)
4	333(1)	137(1)	8.15(2)	0	0.16(5)	0
	511(3)	145(2)	8.00(3)	38.0(3)	0.01(7)	0.1(5)
	$5\bar{1}1$ (3), $\bar{1}51$ (3)	144(2)	8.01(3)	56.4(4)	0.02(7)	0.1(6)
	$\bar{1}\bar{1}5$ (3), $3\bar{3}3$ (3)	145(4)	8.00(7)	70.5(9)	0.0(1)	0(1)
	$11\bar{5}$ (3), $3\bar{3}\bar{3}$ (3)	145(4)	8.00(7)	109.5(9)	0.0(1)	0(1)
	$\bar{1}\bar{5}1$ (3), $\bar{5}1\bar{1}$ (3)	144(2)	8.01(3)	123.6(4)	0.02(7)	–0.1(6)
	$\bar{1}\bar{5}\bar{1}$ (3)	144(2)	8.00(3)	141.0(3)	0.01(7)	–0.1(5)
	$\bar{3}\bar{3}\bar{3}$ (1)	145(2)	7.99(4)	180	0.00(7)	0
	F^k	533(3)	5.18(1)	0	–	–

ligands of the 311, 313, and 333 types, which are located near the compensator (Fig. 1), are displaced the most. This displacement leads to an increase in the spacing in the Gd^{3+}–^{19}F couple and in the polar angles $\Theta \neq 0°, 180°$. The other fluorine ions are localized in the same positions as in the cubic impurity center (within the calculation errors, connected with the dispersion of the ENDOR experimental frequencies) [4]. Thus, one can consider that Gd^{3+} replacing Ba^{2+} is not displaced towards the compensator, while F^k is displaced from the center of the interstice of the perfect BaF_2 lattice towards the impurity ion. Analogous results were obtained in [9], where the trigonal centers Yb^{3+} in SrF_2 and BaF_2 were studied.

The SHFI constants and the Θ angles for the fluorine nuclei nearest to the Gd^{3+} (in their local coordinate system), obtained from the ENDOR spectra, are given in Table 2. The constants A_s are directly connected with the fluorine nuclei in triangles by the Θ angles, since, due to the Coulomb repulsion, one should have $\Theta > \Theta_{cub}$, which is realized for the $11\bar{1}$-type nuclei in the upper triangle (Fig. 1). For nuclei of the $\bar{1}\bar{1}1$ type in the lower triangle, we have $\Theta \cong \Theta_{cub}$. Noticeable angular and radial displacements of nuclei of the first coordination shell are usually accompanied by displacements in the second coordination shell [3, 8, 9]. However, all ^{19}F atoms that are placed near the $\bar{1}\bar{1}1$- and $\bar{1}\bar{1}\bar{1}$-type anions have (within the error limits) the same coordinates as in cubic centers. Taking into account this circumstance and the fact that the impurity ion itself is not displaced, one can assume that the coordinates of the fluorine nuclei nearest to Gd^{3+} and placed far from the compensator, below the XY plane (Fig. 1), are the same as in the

Table 2. The SHFI constants and the angular coordinates of the nearest neighbor ligands in the trigonal Gd^{3+} in BaF_2 center together with the values of distances, induced dipole moments, and isotropic constants calculated in the framework of the proposed model

Type of a nucleus	111	$11\bar{1}$	$\bar{1}\bar{1}1$	$\bar{1}\bar{1}\bar{1}$
The local ligand symmetry	C_{3v}	C_s	C_s	C_{3v}
A_s, MHz	–2.447(5)	–1.755(4)	–1.755(5)	–1.560(4)
A_p, MHz	5.118(3)	4.625(3)	4.598(3)	4.638(2)
A_E, kHz	–	–1(4)	2(4)	–
A_1, kHz	–0.9(3)	–1.1(4)	–0.9(5)	–0.8(3)
A_2, kHz	–0.27(9)	–0.17(7)	–0.12(7)	–0.26(9)
Θ, deg	0	71.0(1)	109.6(1)	180
R, Å (calculation)	2.388	2.408	2.431	2.431
d_z, eÅ (calculation)	0.143	0.097	0.070	0.055
d_x, eÅ (calculation)	0	0.04	0.017	0
A_s, MHz (calculation)	–2.467	–1.751	–1.744	–1.574

cubic impurity center. Thus, the local anion surrounding of Gd^{3+} can be divided into two regions separated by the XY plane. This plane is parallel to {111} and passes through the impurity ion (Fig. 1). In the first region, which contains the compensating ion, the displacements of the ^{19}F atoms (in comparison with the case of the cubic Gd^{3+} center in BaF_2) are noticeable in the shells no more distant than the fourth coordination shell, while in the second region, the displacements are not observed. Therefore, $R(\bar{1}\bar{1}1) = R(\bar{1}\bar{1}\bar{1}\} = 2.431$ Å (the distances of Gd^{3+} to the $\bar{1}\bar{1}1$- $1\bar{1}\bar{1}$-type nuclei) [3]. It is considerably more difficult to evaluate R for the remaining two types of the nearest neighbor anions, since their neighboring fluorine nuclei are displaced with respect to their positions in the case of the cubic impurity center. At the same time, the constants A_s (Table 2), which are determined by the short-range interaction, are large and different. Thus, the analogous contributions to the anisotropic SHFI are, most probably, not equal to zero [3, 4, 8, 9].

It follows from the obtained results that the nearest ligands having the local symmetry C_s are described by the SH of a higher symmetry (since $A_E \approx 0$). We believe that this is connected not only with the restrictions of the experimental precision, but also with the low value of the trigonal distortion. This is supported, by the way, by similar values of the parameter b_4^0 for trigonal and cubic centers [1]. Thus, the SHFI in the Gd^{3+}–^{19}F couple can be analyzed in the same manner as in the cubic center, namely, by taking into account only small changes in the chemical bonds with small changes in the electron structure of these ions caused by the transition from the cubic center to the trigonal one.

2. DETERMINATION OF THE DISTANCES TO THE NEAREST NEIGHBOR LIGANDS

Before we come to the determination of the distance to the ligands nearest to Gd^{3+} in the trigonal center, let us try to get rid of the weaknesses of the empirical SHFI model. This model was proposed by Baker [3] and used by us [4] for description of the A_s and A_p constants in five Gd^{3+} cubic centers in crystals with a fluorite-type structure.

Baker's notion of the reasons for the electric dipole moments D induced at ligands was incorrect and rejected in [4]. However, it was assumed in [4] that the contributions to A_s and A_p associated with the ligand polarization did not depend explicitly upon the distance R in the Gd^{3+}–^{19}F couple and were determined only by the value of $D = d_z = \alpha E_z$ [3] (here, α is the fluorine ion polarizability for a given crystal; E_z is the electric field on ^{19}F directed along the axis of the couple bond; this field is determined by the excess positive charge of the impurity and by the displacements of the surrounding ligands). This approximation can also be rejected, if one represents A_s (and A_p) in the following form (on the basis of theoretical expressions for the SHFI constants derived in the approximation linear in E_z [3]):

$$A_s = A_s(R)(1 + K_s D). \tag{2}$$

Here, $A_s(R) = A_s(R_0)(R_0/R)^n$ is the contribution to the isotropic constant dependent on the distance from the ligand and determined by the covalence parameters and the overlap integrals of the 4f and the polarized 5s and 5p states of Gd^{3+} with the 1s and 2s states of F^- [3, 8, 10–12]; $A_s(R_0)$ is the model parameter, which is equal to the above contribution for $R = R_0 = 2.37$ Å (R_0 is taken to be the same as in [1]). The quantity $A_s(R)K_sD$ is the second contribution, where K_s is the model parameter connected with the mixing of the 2p and 3s states of the fluorine ion. Since this p–s mixing is determined by the matrix element $\langle 2p_z | d_z | 3s \rangle / | E_{3s} - E_{2p} |$, this contribution is proportional to D.

To determine the radial dependence of A_s, which should be same for all Gd^{3+} cubic centers in isostructural crystals, it is necessary to eliminate D. Varying the K_s and n parameters in such a way that the function $A_s(R) = A_s/(1 + K_sD)$ describes all five relations, we obtain $K_s = -4.4(1)1/e$ Å and $n = 3.0(2)$ for $A_s(R_0) = -3.62(6)$ MHz (e is the magnitude of the electron charge).

The $A_s(R)$ function for the cubic impurity centers is plotted in Fig. 2. This is a weak power-law dependence with $n = 3$, which is, probably, due to the fact that the constant A_s depends on two terms which are roughly equal in value, but opposite in sign. These terms are related to the different electron shells of the interacting ions. Indeed, according to evaluations in [3, 8], the $4f$ electrons give a positive contribution to A_s, whereas the contribution from the $5s$ and $5p$ electrons is negative, if one takes into account their overlapping with the $2s$ electrons of F^-. Taking into consideration the $1s$ shell leads to positive contributions to the isotropic constant [3, 6, 8, 10]. Although all these terms have different radial dependences [8], their sum can have a negligible dependence on R over a small range of distances.

The results of the analogous analysis of the isotropic SHFI constant for the Eu^{2+} cubic impurity centers in the same crystals can serve as proof of the adequacy of the chosen description of A_s. In this case, the value of the induced dipole moment D of the fluorine ions is determined only by the ligand displacements [4]. It is found that $K_s = -4.2(2)1/e$ Å, $n = 5.7(3)$, and $A_s(R_0) = -3.94(6)$ MHz. It can be seen that the values of K_s, related to the changes in the electron structure of F^- (i.e., to the partial occupation of the $3s$ states), are approximately the same for the isoelectron impurity ions. This confirms, in our opinion, the validity of the chosen model.

To analyze the case of the trigonal Gd^{3+} in BaF_2, let us first suppose that the distance to all nearest neighbor fluorine atoms $R = 2.431$ Å (as in the cubic center). Calculations show that the dipole moment induced at the $11\bar{1}$-type nucleus is greater than at the nearest neighbor nuclei in the cubic center, i.e., $\Delta D = D_{\text{trig}} - D_{\text{cub}} > 0$ (for $\bar{1}\bar{1}1$, $\Delta D < 0$), and this inequality remains true over the $2.44 > R > 2.38$ Å range. This is due to the fact the d_x component of the induced dipole moment appears for the fluorine nuclei in the trigonal center with the C_s local symmetry. This leads to an additional displacement of the $2p_x$ $3s$ states of F^-. In a linear (with respect to D) approximation, for the trigonal impurity centers, one should use the value $D = d_z + d_x$ in Eq. (2), in contrast with the cubic centers.

Let us compare the values of the isotropic constants for the $11\bar{1}$- and $\bar{1}\bar{1}1$-type nuclei (see Table 2) with the value $A_s = -1.808(6)$ MHz for the cubic impurity center in BaF_2 [4]. According to Eq. (2), one should have for $11\bar{1}$ $\Delta A_s = A_s(\text{trig}) - A_s(\text{cub}) > 0$ ($\Delta A_s < 0$ for $\bar{1}\bar{1}1$). On the contrary, in our case, we have $\Delta A_s > 0$ and virtually the same values of A_s (see Table 2) for both types of fluorine nuclei. We also note that the calculated values of $A_s(R)$ can be divided into two groups for all four types of nuclei (even for the same values of R): two values above and two below the $A_s(R)$ dependence obtained for the cubic impurity centers (Fig. 2). It is impossible to explain such a spread of the $A_s(R)$ values by small changes in only the ligand electron structure due to their polarization. Thus, there is another contribution to A_s as a minimum, which is determined by changes in the Gd^{3+} electron structure as one goes from the cubic to the trigonal centers. An analogous conclusion can made from a comparison of the SHFI constants for the fluorine nuclei situated at the C_3 axis (the C_{3v} local symmetry), where the character of the chemical bonds is the same as in the Gd^{3+} in BaF_2 cubic center.

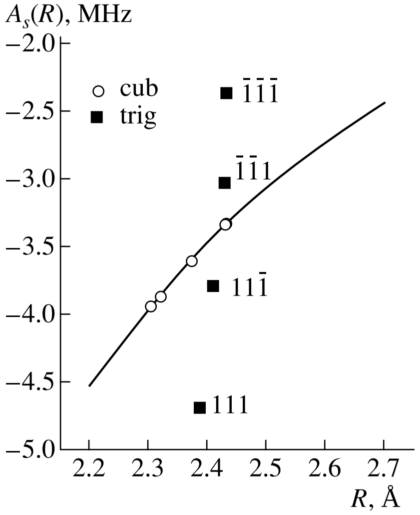

Fig. 2. $A_s(R)$ values for fluorine nuclei nearest to the Gd^{3+} ions in the cubic impurity centers of the following crystals: CaF_2, CdF_2, SrF_2, PbF_2, BaF_2, and in the trigonal center of BaF_2. The curve corresponds to the determined functional dependence for the cubic centers.

On the other hand, it is clear that Gd^{3+} is also polarized and has an induced dipole moment $\mathbf{D}_1 \parallel \mathbf{C}_3$, which is due to electric fields of the compensator and to asymmetric displacement of ligands. This leads to mixing of the Gd^{3+} electron states [6, 7, 10–12] and, as a result, to a change in the unpaired spin density at the ligands.

It is clear from Fig. 2 that, for the $11\bar{1}$- and $\bar{1}\bar{1}1$-type nuclei, the values of $A_s(R)$ are situated below and above the curve, respectively. The values of $\Delta A_s = A_s(R)(\text{trig}) - A_s(R)(\text{cub})$, caused by polarization of Gd^{3+}, are almost equal in value but opposite in sign. The same is true for the D_1 projections along the bond axes. The remaining two fluorine nuclei are also unambiguously connected with the direction of the D_1 projection. They can be directly related to the values of the isotropic constants, in accordance with the sign of ΔA_s (see Table 2). Since we consider the contributions to A_s, we can conclude that the unpaired-spin density of the Gd^{3+} electrons at $^{19}\mathrm{F}$ varies proportionally to $D_1\cos\Theta$ along the bond axis. Hence, for a description of the isotropic constants of the nearest neighbor ligands in the trigonal impurity center, one should add to Eq. (2) the term taking into account the change in the electron structure of Gd^{3+} induced by its polarization

$$A_s = A_s(R)(1 + K_s D) + K_s'(R)D_1\cos\Theta. \qquad (3)$$

In order to obtain the distance R to the nearest neighbor fluorine nuclei, it is necessary to make a comparison between the values of A_s calculated from Eq. (3) and the experimental data. To do this, one should know the model parameters $K_s'(R)$, D, and D_1. These parameters were first estimated assuming that $R = 2.431$ Å. It was found that there is no such value of $K_s'(R)$ which gives values of A_s close to the experimental ones simultaneously for all four types of nuclei. However, a comparison of calculated and experimental values shows that one should have $R(111) < R(\bar{1}\bar{1}\bar{1})$. Such an inequality corresponds to the character of the possible shift of the nearest neighbor ligands, since F^k will, without any doubt, also shift $^{19}\mathrm{F}(111)$ in the same direction, when approaching the impurity ion. Varying the values of $R(111)$ and $R(11\bar{1})$, we obtained that the best agreement with the experiment is realized when $R(111) = 2.388$ Å, $R(11\bar{1}) = 2.408$ Å, and $K_s'(R) = -38.3(2)(R_0/R)^9$ MHz/eÅ.

The induced dipole moments D and D_1 were calculated in the model of point charges and point dipoles. The charge and dipole sources were the impurity ion and all anions inside a shell with the radius larger than ≥10 Å (the center of the shell coincided with the ion at which the dipole moment was determined), as well as the nearest neighbor cations. The positions of anions of the second to fourth coordination shells were known from experiment. The positions of the nearest neighbor cations and of the distant F^- were considered to be the same as their positions in the cubic impurity center [4]. In this case, the dipole moment of Gd^{3+} is $D_1 = 0.0318$ eÅ if $\alpha = 1$ and 0.87 Å^3 for F^- in BaF_2.

Note that the distances to the nearest ligands determined here are close to those obtained from the superposition model for the constants of the initial splitting and of the quadrupole interaction in the trigonal $^{157}\mathrm{Gd}^{3+} : \mathrm{BaF}_2$ center [1].

The additional term in Eq. (3) is, most probably, connected with the partial filling of the empty 5d shell due to the mixing of even and odd states of the polarized Gd^{3+}. This term is proportional to the matrix elements having the form $\langle 4f|D_1|5d\rangle/|E_{4f} - E_{5d}|$ [6, 10–12], since the energy E_{5d}, as it is known, is the lowest one for the exited states. It is clear that this mechanism will lead to a change in the unpaired spin density of the Gd^{3+} electrons at ligands in the trigonal center, in comparison with the cubic center. Thus, it will change the SHFI. For the cubic centers, such a process was first considered in theoretical work [10]. It was assumed there that the main reason for this process was the transfer of an electron from the ligand to the empty 5d and 6s shells. This transfer made a contribution $\Delta A_s = -8$ MHz to the isotropic constant for $\mathrm{CaF}_2 : \mathrm{Gd}^{3+}$. Since the odd components of the crystalline field are absent in the cubic centers, an odd electric field of a virtual hole was introduced in [11, 12], in order to mix the impurity states. This field appears at a ligand due to the electron transfer. A calculation of the contribution to the isotropic constant (using our parameter $K_s'(R)$) from the field of the virtual hole at $^{19}\mathrm{F}$ gives $\Delta A_s \geq 8$ MHz. Adding ΔA_s from [10] to this value, we obtain a change in A_s, which is close to zero. Therefore, the conclusion can be made that the above-discussed mechanism virtually does not change the isotropic constants in the Gd^{3+} cubic impurity centers in fluorites. Note that changes in the electron structure of ligands were not taken into account in [10–12].

Some other physical mechanisms which influence the electron structure of the impurity centers with the cubic local symmetry were also considered in [10–12]. For example, according to [10–12], changes in the population of the 5s and 6s states of impurity centers are possible. In the trigonal center discussed in our work, there is also a direct influence of the odd crystalline field upon the populations of these states. However, the intrinsic electron–nuclei interaction in the $^{157}\mathrm{Gd}$ trigonal center should be changed considerably in comparison with this interaction in the BaF_2 cubic center. Nevertheless, this is not observed [1, 4]. Hence, one may conclude that the spin density at the 5s and 6s states is not changed considerably when one goes from the cubic to the trigonal impurity center in BaF_2.

To analyze the anisotropic constants A_p of the nearest neighbor nuclei, one can use the relations analogous to Eq. (3), where all indices s should be replaced by p, since the change mechanisms for these constants are analogous to those discussed above. It is found that $A_p'(R_0) = -1.94(5)$ MHz, $n = 16(1)$, $K_p = -8(1)$ 1/eÅ (for the cubic centers), and $K_p' = -7(6)$ MHz/eÅ. Due to the presence of a large error in K_p', the anisotropic constants for four types of the nearest neighbor fluorine nuclei in the trigonal center have a worse description than in the cubic centers. Most likely, this is connected with the model imperfection. Indeed, one should take into account the contributions from both σ and π bonds to A_p' [3, 6, 8, 10–12], while we have considered only the changes in σ bonds, since it is not clear at the moment how π bonds should change. Moreover, one should possibly take into account the contributions to A_p from the multipole corrections. These corrections are connected with the deviation from sphericity for polarized Gd^{3+} in the Gd^{3+}–$^{19}\mathrm{F}$ couple [12].

CONCLUSIONS

Thus, the following results are obtained in this work.

(1) Analysis of the distances calculated from the experimentally determined SHFI constants for the trigonal $BaF_2 : Gd^{3+}$ center shows that anion surrounding of Gd^{3+} (the first four coordination shells of the fluorine atoms) can be divided into two regions separated by the plane passing through the impurity ion and located perpendicular to the main symmetry axis of the impurity center. In the first region, there are considerable displacements of the ^{19}F near the compensator and Gd^{3+}. In the second one, which is placed far from the compensator, the fluorine ion coordinates are the same as in the cubic center.

(2) A comparison of the experimental and calculated values of A_s for the fluorine nuclei nearest to the impurity center shows that a model describing the SHFI interaction constants for the Gd^{3+} cubic centers in fluorites can also be successfully used for the trigonal center. To do this, one should take into account the contribution to A_s associated with the change in the electron structure of the impurity due to its polarization by an odd electric field produced by the surroundings.

(3) The distances to the fluorine nuclei of the first coordinate shell are determined. These distances are found to be close to their values as estimated in the framework of the superposition model for the initial splitting and quadruple interaction parameters in the $^{157}Gd^{3+}$ in BaF_2 trigonal center.

(4) The equality (within the experimental error) of the constants of the intrinsic electron–nuclear interaction for the ^{157}Gd isotope in the cubic and trigonal centers of BaF_2 indicates that the Gd^{3+} polarization in the trigonal center does not lead to a noticeable change in the spin densities of any impurity ion s states when compared with the cubic center.

REFERENCES

1. A. D. Gorlov and A. P. Potapov, Fiz. Tverd. Tela (St. Petersburg) **42** (1), 49 (2000) [Phys. Solid State **42**, 51 (2000)].
2. D. J. Newman and W. Urban, Adv. Phys. **24** (6), 793 (1975).
3. J. M. Baker, J. Phys. C **12** (19), 4093 (1979).
4. A. D. Gorlov, V. B. Guseva, A. Yu. Zakharov, *et al.*, Fiz. Tverd. Tela (St. Petersburg) **40** (12), 2172 (1998) [Phys. Solid State **40**, 1969 (1998)].
5. L. A. Boatner, R. V. Reynolds, and M. M. Abraham, J. Chem. Phys. **57** (5), 1248 (1970).
6. A. Abragam and B. Bleaney, *Electron Paramagnetic Resonance of Transition Ions* (Clarendon, Oxford, 1970; Mir, Moscow, 1973).
7. S. A. Al’tshuler and B. M. Kozyrev, *Electron Paramagnetic Resonance* (Nauka, Moscow, 1972; Academic, New York, 1964).
8. J. Casas-Gonzáles, P. Stydzinski, J. Andriessen, *et al.*, J. Phys. C **19** (34), 6767 (1986).
9. O. V. Nazarova and T. I. Sanadze, Soobshch. Akad. Nauk Gruz. SSR **87** (2), 329 (1977).
10. O. A. Anikienok and M. V. Eremin, Fiz. Tverd. Tela (Leningrad) **23** (6), 1792 (1981) [Sov. Phys. Solid State **23**, 1046 (1981)].
11. O. A. Anikienok, M. V. Eremin, M. L. Falin, *et al.*, J. Phys. C **17** (15), 2813 (1984).
12. O. A. Anikienok, M. V. Eremin, and O. G. Khutsishvili, Fiz. Tverd. Tela (Leningrad) **28** (6), 1690 (1986) [Sov. Phys. Solid State **28**, 935 (1986)].

Translated by A. Sonin

Physics of the Solid State, Vol. 43, No. 3, 2001, pp. 480–483. Translated from Fizika Tverdogo Tela, Vol. 43, No. 3, 2001, pp. 462–465.
Original Russian Text Copyright © 2001 by Makara, Steblenko, Gorid'ko, Kravchenko, Kolomiets.

On the Influence of a Constant Magnetic Field on the Electroplastic Effect in Silicon Crystals

V. A. Makara, L. P. Steblenko, N. Ya. Gorid'ko, V. M. Kravchenko, and A. N. Kolomiets

Shevchenko National University, Vladimirskaya ul. 64, Kiev, 01033 Ukraine

e-mail: makara@hq.ups.kiev.ua

Received July 27, 2000

Abstract—The influence of a constant magnetic field on the electroplastic effect induced by an electric current in silicon crystals is investigated. It is found that the preliminary magnetic field treatment of silicon crystals leads to a weakening of the electroplastic effect. A possible mechanism of the phenomena observed is discussed. *© 2001 MAIK "Nauka/Interperiodica".*

1. INTRODUCTION

Earlier [1–7], it was noted that the dislocation behavior in alkali halide crystals, metals, and compound semiconductors in a magnetic field exhibits a number of specific features.

Experiments revealed that application of a magnetic field can substantially affect the plastic properties of crystals. This phenomenon was termed the magnetoplastic effect. The magnetoplastic effects can be positive and negative; that is, the magnetic field can bring about both hardening and softening of crystals, respectively. Application of the magnetic field can result in a drastic increase in the internal friction of dislocations trapped by paramagnetic impurities [1].

The effect of an electric current on the microplasticity stimulated by the magnetic field in aluminum single crystals was also investigated elsewhere [6]. Unfortunately, despite a considerable body of experimental data and a diversity of models interpreting the magnetoplastic effect, there is no consistent theory for describing available experimental data within a unified context.

As regards the class of simple semiconductor crystals (specifically, silicon crystals), the data on the influence of magnetic field on the dislocation mobility in these crystals are virtually not available in the literature.

At the same time, investigation of this phenomenon is undoubtedly an urgent problem of modern semiconductor physics, because its solution can provide a better insight into the physical mechanisms responsible for the plastic and strength properties of semiconductor crystals.

On the other hand, it is well known that the magnetic susceptibility of diamagnetic and paramagnetic crystals is rather sensitive to the presence and the amount of dislocations in these crystals. Novikov *et al.* [8] proved that the presence of nongrowth dislocations in single-crystal silicon samples brings about a decrease in the diamagnetism (the generation of paramagnetic centers) and a change in the static susceptibility of silicon. These authors also revealed a certain correlation between the magnetic susceptibility and the density of nongrowth dislocations. Vavilov *et al.* [9] adduced the relevant experimental and theoretical arguments in support of the possible magnetic ordering of electron spins on dislocation structures in silicon and, in particular, pointed to the possibility of realizing a ferromagnetic ordering in the dislocation core. Thus, there is an inverse effect, namely, the influence of structural defects on the magnetic properties of crystals.

In this respect, it was expedient to elucidate how the constant magnetic field affects the dynamic behavior of dislocations in silicon crystals. The velocity of dislocation motion was chosen as an indicator and a measure of this effect.

In our recent work [10], we carried out a preliminary investigation into the influence of magnetic field on the dynamic behavior of dislocations in initial silicon crystals. It was experimentally found that the applied magnetic field alone does not provide a dislocation motion. Considerable variations in the dynamic behavior of dislocations were observed only in the case when the samples were subjected to mechanical deformation after the magnetic field treatment. The treatment of silicon samples in a magnetic field with magnetic induction B = 0.17 T for a certain time ($t_{\mathrm{MF}} \geq 7$ days) and a further mechanical loading brought about an increase in the starting stresses and the delay time of the onset of dislocation motion and also a decrease in the dislocation velocity approximately by a factor of three. Therefore, silicon crystals underwent a hardening after the preliminary magnetic field treatment. The characteristics of the dislocation mobility turned out to be sensitive only to a magnetic field whose induction reached a specific threshold value (B = 0.17 T). The properties acquired by silicon samples in the course of magnetic treatment did not disappear immediately after the magnetic field was withdrawn, but they were retained for a short time (about 1 h). In other words, the magnetic memory inherent in dislocation-containing silicon samples after their treatment in a magnetic field has a short-term character.

In our opinion, a possible reason for the observed effects can be the changes induced by the magnetic field in a defect system of silicon (decomposition of large-sized complexes, diffusion of individual point defects both from the bulk of the matrix and along the dislocation line toward a dislocation, and increase in the cluster power around dislocations). The magnetic-field-induced change in the system of point defects interacting with elastic fields of dislocations leads to a change in the dynamic behavior of dislocations due to the magnetic field treatment of the samples.

The results obtained demonstrate that the transformations revealed in the structure after the magnetic treatment are somewhat similar to changes observed in the processes of strain ageing in steels after their treatment with a pulsed field [11].

From our point of view, the investigation into the influence of a constant magnetic field on the dislocation mobility is topical by itself and also with relation to the interpretation of the well-known electroplastic effect, which was observed in metals [12] and revealed in silicon crystals in our earlier works [13, 14]. It was of interest to clarify the role played by the magnetic field in the electroplastic effect induced in silicon crystals upon passage of an electric current.

The purpose of the present work was to investigate how the magnetic field affects the electroplastic effect in silicon crystals excited by an electric current.

2. EXPERIMENTAL TECHNIQUE

In experiments, we used *n*-type and *p*-type silicon samples (20 × 4 × 0.4 mm in size), which were grown by the Czochralski technique and doped during the growth with phosphorus and boron, respectively. Stress concentrators—scratches cut in the $[1\bar{1}0]$ direction on the (111) surface—served as a source of dislocation half-loops. The dislocation motion was caused by bending around the $[11\bar{2}]$ axis (the four-support bending method). The length of segments in dislocation half-loops introduced into the samples varied from 10 to 100 μm; i.e., the dislocations under investigation were the short surface dislocations. The starting and terminal positions of dislocation half-loop ends were fixed by chemical etching and then were examined with a metallographic microscope. The silicon samples under investigation were subjected to mechanical tensile stresses. The influence of magnetic field on the electroplastic effect was studied by the four-support bending method. This method differed from the traditional technique in that the cylindrical tungsten electrodes served as two lower supports. The voltage was applied across these electrodes, which made it possible to pass an electric current through the samples immediately in the course of their mechanical deformation.

After the introduction of isolated dislocations, the silicon samples were subjected to the magnetic treatment: the samples with preliminarily introduced dislocations were placed in a constant magnetic field with the induction $B = 0.17$ T. The duration of the magnetic field treatment was 7 days.

The samples treated in the magnetic field were subjected to a static loading with simultaneous passage of a direct electric current. The fundamental quantity studied in this work was the dislocation path length L. The influence of the magnetic treatment on the dislocation path length was investigated in the temperature range $T = 823$–923 K at the mechanical stress $\sigma = 63.5$ MPa and the current density $j = (0.2 - 1.0) \times 10^6$ A/m^2. Thus, the magnetic treatment was carried out at room temperature and the thermally activated dislocation motion was initiated at temperatures of 823–923 K. After the high-temperature mechanical deformation, the samples were subjected to chemical etching. The dislocation path length was determined from the positions of the dislocation half-loop ends prior to and after the mechanical deformation of the samples.

The experimental data obtained in the present work allowed us to reveal a number of features in the motion of dislocation segments in the silicon crystals which were subjected to the preliminary magnetic treatment.

3. EXPERIMENTAL RESULTS AND DISCUSSION

Let us consider how the magnetic treatment of silicon samples affects the electroplastic effect.

As was noted above, the treatment of the initial silicon crystals in a magnetic field leads to the pinning of dislocations in the starting positions and a decrease in the velocity of dislocation motion. The electroplastic effect manifests itself in the silicon crystals excited by a direct current and implies an increase in the velocity of dislocation motion and a decrease in the starting stresses. Therefore, it can be assumed that the electroplastic effect is unlikely to be caused only by the influence of the dc magnetic field. Most probably, the electroplastic effect is associated with a diversity of other factors.

In our opinion, it is of interest not only to determine the contribution of the dc magnetic field to the electroplastic effect, but also to analyze the influence of the preliminary magnetic field treatment on the magnitude of this effect.

As can be seen from the dependences depicted in Fig. 1, the velocity of dislocation motion upon excitation by the direct electric current in the silicon samples subjected to the magnetic treatment (curve *2*) is less than that in the samples which were not treated in the magnetic field and were excited only by the current (curve *3*). In this case, as follows from the experimental

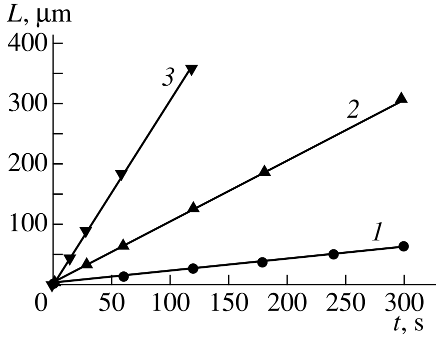

Fig. 1. Dependences of the mean dislocation path length L on the time t of applying the mechanical stress σ = 63.5 MPa at a temperature of 923 K for (*1*) the initial silicon crystal samples (subjected to tensile deformation), (*2*) silicon crystal samples treated in a magnetic field (B = 0.17 T) with subsequent extension under electric current passage ($j = 1 \times 10^6$ A/m^2), and (*3*) silicon samples subjected to tensile deformation with simultaneous passage of an electric current ($j = 1 \times 10^6$ A/m^2).

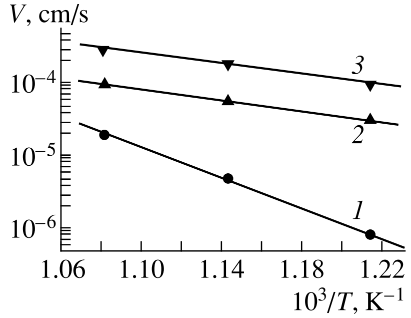

Fig. 2. Temperature dependences of the velocity of dislocation motion in silicon crystals strained under a mechanical stress of 63.5 MPa. The designations are the same as in Fig. 1.

data, the dislocation velocity after the magnetic treatment of samples decreases approximately by a factor of three, irrespective of the density of the current exciting these samples. At the same time, the velocity of dislocation motion in the silicon crystals untreated in the magnetic field depends on the current density [14].

If the magnitude of the electroplastic effect is taken to mean the ratio between the dislocation velocities in the current-excited and initial crystals, it turns out that the magnitude of the electroplastic effect after the magnetic treatment decreases approximately by a factor of three. For example, at a temperature of 923 K, the magnitude of the electroplastic effect is equal to 15 for the samples excited by the direct current and 5 for the crystals treated in the magnetic field. The preliminary investigations revealed that, upon electric insulation of silicon crystal samples subjected to the magnetic treatment, the dislocation velocity in these crystals decreases to zero. Consequently, the electroplastic effect induced by the electric field in the silicon crystals treated in the magnetic field not only decreases (as in the case of electric current), but also changes sign. However, these data require further checking and refinement.

Now, we consider the temperature dependence of the velocity of dislocation motion. Figure 2 displays a series of the experimental dependences $V = f(1/T)$ for the initial samples and the samples treated in the magnetic field. These dependences were used to calculate the activation energies of dislocation motion for the samples which were preliminarily subjected to the magnetic treatment and then were excited by the direct current and the samples which were excited only by the direct current without preliminary treatment in the magnetic field. The activation energies were found to be almost the same for both samples: $E_{\mathrm{MF+I}} \approx E_{\mathrm{I}} \approx 0.75$ eV. For the initial silicon samples, the calculated activation energy E_{init} was equal to ≈2.03 eV.

The observed effect of the magnetic field on the dislocation mobility in diamagnetic silicon can be governed by a diversity of factors. In particular, the change in the dynamic behavior of dislocations in the initial silicon crystals due to their magnetic field treatment can be explained by the rearrangement of a system of point defects and defect complexes which interact with elastic fields of dislocations [15].

Let us analyze the influence of magnetic field on the electroplastic effect. As was noted in our earlier works [13, 14], a possible reason for the electroplastic effect can be the change in the charge state of dislocations and their environment, which results in a decrease in the Coulomb component of the interaction between dislocations and trapping centers and also in the height of barriers that fix dislocations in the starting positions. Moreover, from our point of view, the electroplastic effect can also be associated with the influence of an excess energy that is locally released in the dislocation region upon recombination of carriers during the passage of an electric current in crystals. This energy facilitates the formation and motion of charged double dislocation kinks.

The experimental results obtained in the present work can be qualitatively interpreted by invoking the model proposed by Kveder *et al.* [16]. This model treats the spin-dependent recombination of free carriers through dislocation dangling bonds in magnetic fields. The electron (or hole) trapping from shallow levels into dislocation dangling bonds is a spin-dependent process. In this case, the trapping probability depends on the polarization of a spin chain of dislocation dangling bonds and the direction of the electron spin.

It seems likely that the magnetic field in our experiments brings about a change in the polarization of a paramagnetic spin center and a decrease in the trapping probability. As a result, the probability of carrier recombination decreases.

As follows from the experimental results obtained in this work, in the silicon crystals treated in the magnetic field and excited by the direct current, the velocity of dislocations changes and the activation energy of their motion remains virtually constant. The latter result indicates that the effects observed are associated with the change in the preexponential factor in the empirical formula obtained by Maeda *et al.* [17] for the dislocation velocity in silicon crystals excited by an electron beam. The preexponential factor in this formula involves the recombination frequency ν multiplied by the quantum yield η [17]. According to [17], we can assume that the magnetic field affects the recombination frequency which is determined by the rate of the formation of carriers, their lifetime, and trapping cross section of the kink.

Therefore, as in [16], it can be assumed that silicon crystals contain both purely fluctuation trapping centers and purely spin trapping centers which behave differently in fast capture events in the presence of field effects, in particular, "magnetic" effects. The change in the state of spin trapping centers after the treatment of silicon samples in the magnetic field leads to the change in the magnitude of the electroplastic effect. In the case when the silicon crystals subjected to the preliminary magnetic treatment are excited by the electric current, the electroplastic effect decreases approximately by a factor of three. According to the experimental data, a decrease in the electroplastic effect is characteristic of the entire studied range of current densities. It should be noted that a threefold decrease in the electroplastic effect is observed independently of the density of the current exciting the silicon samples.

The last result suggests that, under the given experimental conditions, the spin-dependent recombination is virtually independent of the current density and, according to [16], depends only on the polarization of a dislocation dangling bond chain with respect to the direction of the electron spin.

All the above experimental findings require a detailed theoretical interpretation. However, it has already been possible to draw the inference about the practical importance of the results obtained in this work.

Since the dangling bonds of silicon are responsible for the spin-dependent recombination channel, it is clear that the magnetic field treatment of silicon samples leads to the "neutralization" of spin trapping centers and a decrease in the recombination probability.

REFERENCES

1. V. I. Al'shits, E. V. Darinskaya, T. M. Perekalina, and A. A. Urusovskaya, Fiz. Tverd. Tela (Leningrad) **29** (2), 467 (1987) [Sov. Phys. Solid State **29**, 265 (1987)].
2. Yu. I. Golovin, O. L. Kazakova, and R. B. Morgunov, Fiz. Tverd. Tela (St. Petersburg) **35** (5), 1384 (1993) [Phys. Solid State **35**, 700 (1993)].
3. V. I. Al'shits, E. V. Darinskaya, and E. A. Petrzhik, Izv. Vyssh. Uchebn. Zaved., Chern. Metall. **10**, 85 (1990).
4. V. I. Al'shits, E. V. Darinskaya, O. L. Kazakova, *et al.*, Pis'ma Zh. Éksp. Teor. Fiz. **63**, 628 (1996) [JETP Lett. **63**, 668 (1996)].
5. Yu. I. Golovin, R. B. Morgunov, V. E. Ivanov, *et al.*, Pis'ma Zh. Éksp. Teor. Fiz. **68**, 400 (1998) [JETP Lett. **68**, 426 (1998)].
6. V. I. Al'shits, E. V. Darinskaya, E. Yu. Mikhina, and E. A. Petrzhik, Pis'ma Zh. Éksp. Teor. Fiz. **67**, 788 (1998) [JETP Lett. **67**, 832 (1998)].
7. E. V. Darinskaya, E. A. Petrzhik, S. A. Erofeeva, and V. P. Kisel, Solid State Phenom. **69–70**, 503 (1999).
8. N. N. Novikov, V. M. Tsmots', Z. F. Ivasiv, *et al.*, Ukr. Fiz. Zh. (Ukr. Ed.) **41** (11–12), 1127 (1996).
9. V. S. Vavilov, V. F. Kiselev, and B. N. Mukashev, *Defects in Silicon and on Its Surface* (Nauka, Moscow, 1990).
10. V. A. Makara, L. P. Steblenko, N. Ya. Gorid'ko, *et al.*, Visn. Kiiv. Univ., Ser. Fiz.–Mat. Nauki **4**, 316 (1999).
11. O. I. Datsko, V. I. Alekseenko, and A. D. Shakhova, Fiz. Tverd. Tela (St. Petersburg) **38** (6), 1799 (1996) [Phys. Solid State **38**, 992 (1996)].
12. V. I. Spitsyn and O. A. Troitskiĭ, *Electroplastic Deformation of Metals* (Nauka, Moscow, 1985).
13. V. A. Makara, L. P. Steblenko, and E. G. Robur, Solid State Phenom. **32–33**, 619 (1993).
14. V. A. Makara, L. P. Steblenko, V. V. Obukhovskiĭ, and E. G. Robur, Fiz. Tverd. Tela (St. Petersburg) **36** (9), 2618 (1994) [Phys. Solid State **36**, 1427 (1994)].
15. V. N. Buzynin, O. I. Datsko, and S. N. Postnikov, Élektron. Obrab. Mater., No. 2 (170), 16 (1993).
16. V. V. Kveder, Yu. A. Osip'yan, and A. I. Shalykin, Zh. Éksp. Teor. Fiz. **83**, 699 (1982) [Sov. Phys. JETP **56**, 389 (1982)].
17. N. Maeda, K. Kimura, and S. Takeuchi, Izv. Akad. Nauk SSSR, Ser. Fiz. **51** (4), 729 (1987).

Translated by O. Borovik-Romanova

Physics of the Solid State, Vol. 43, No. 3, 2001, pp. 484–488. Translated from Fizika Tverdogo Tela, Vol. 43, No. 3, 2001, pp. 466–470.
Original Russian Text Copyright © 2001 by Pukh, Baĭkova, Zvonareva, Ivanov-Omskiĭ, Knyazevskiĭ, Kireenko, Kazannikova, Tikhonova.

DEFECTS, DISLOCATIONS, AND PHYSICS OF STRENGTH

Influence of Amorphous Hydrogenated Carbon Coating on the Strength and Cracking Resistance of a Glass in the High-Strength State

V. P. Pukh, L. G. Baĭkova, T. K. Zvonareva, V. I. Ivanov-Omskiĭ, V. N. Knyazevskiĭ, M. F. Kireenko, T. P. Kazannikova, and L. V. Tikhonova

Ioffe Physicotechnical Institute, Russian Academy of Sciences, Politekhnicheskaya ul. 26, St. Petersburg, 194021 Russia
e-mail: pukh@sglass.ioffe.rssi.ru

Received August 3, 2000

Abstract—The strength of sheet glass treated by etching in a hydrofluoric acid with subsequent deposition of an amorphous hydrogenated carbon coating 50 nm thick is investigated. The carbon coating is applied by ion magnetron sputtering of a chemically pure graphite target. It is shown that the strength of the sheet glass after coating is retained at a level of 2.4 GPa. The leaching of the surface glass layer upon treatment in water at a temperature of 96°C prior to the deposition of a coating leads to an increase in the strength by 12%. The cracking resistance of the glass is examined by the microindentation technique. It is revealed that the load P_c which corresponds to the formation of 50% of all the cracks increases by a factor of three upon deposition of the coating and by a factor of 15 after the preliminary leaching of the glass surface. The assumption is made that the preliminary leaching of the glass surface considerably enhances the adhesion of the hydrogenated carbon film to the glass surface and, thus, improves its protective properties. *© 2001 MAIK “Nauka/Interperiodica”.*

1. INTRODUCTION

In recent years, amorphous hydrogenated carbon or diamond-like coatings have attracted the particular attention of researchers owing to their unique properties, such as high hardness, wear resistance, chemical durability, transparency, etc. [1]. These properties allow the use of diamond-like films as protective coatings by way of their deposition onto various materials.

The structure of diamond-like films, which represents amorphous hydrogenated carbon a-C : H, has been investigated thoroughly [1–3]. It was shown that this structure depends on the preparation conditions and can vary over a wide range from structures close to diamond to a graphite-like structure. As a rule, the structure of a-C : H films is considered a mixture of nanometer-sized structures with carbon in the sp^3- and sp^2-hybridization states. Such properties as the density, microhardness, band gap, and others depend on the fraction of a particular structure and the hydrogen content [4–6].

Note that the protective properties of a film substantially depend on its adhesion to a substrate material. High stresses at the film–substrate interface can result in the peeling of the film and its fracture [7]. These phenomena are observed, for example, upon film deposition onto silicide-forming metals. By contrast, the film deposition onto carbide-forming metals provides a good adhesion of carbon films to the substrate. For this reason, in some cases, improvement in the adhesiveness is achieved with intermediate layers, for example, from silicon [7].

It was of interest to investigate the possibility of applying amorphous hydrogenated coatings on a glass treated by chemical polishing in hydrofluoric acid. It is well known that, after the removal of a surface defect layer by etching in hydrofluoric acid, commercial sheet glasses possess a high strength which is close in the order of magnitude to the theoretical value [8, 9]. On the other hand, it is also known that glasses in a high-strength state are extremely sensitive to mechanical contacts with solids. This is explained by the fact that inorganic glasses upon indentation can undergo a plastic deformation without fracture only within a very limited volume [10]. Therefore, any contact with a solid, especially when sharp and hard dust particles occur in the contact area, usually leads to the formation of microcracks and a decrease in the strength.

The main problem of retaining the high strength of a glass is to prevent the formation of new defects which can serve as stress concentrators on the glass surface.

This problem can be solved in part either by plasticizing the surface layer of a glass [11, 12] or by creating compressive stresses in this layer [13–15]. Another method that can be used in a combination with the above techniques consists in preparing protective coatings on the glass surface.

The aim of the present work was to investigate the influence of thin amorphous hydrogenated carbon (a-C : H) coatings on the strength and cracking resistance (resistance to the formation of cracks) of a glass treated by chemical polishing.

1063-7834/01/4303-0484$21.00 © 2001 MAIK “Nauka/Interperiodica”

2. EXPERIMENTAL TECHNIQUE

An *a*-C : H coating was applied by ion magnetron sputtering of a chemically pure graphite target in a vacuum chamber. In these sputtering systems, electrons emitted by a target are captured by a magnetic field, which prevents their bombardment of substrates and a heating to high temperatures [16]. After the preliminary evacuation to a pressure of 10^{-5}–10^{-6} torr, the chamber was filled with a working gas (80% argon and 20% hydrogen). The working gas pressure was brought up to ~5×10^{-3} torr. In this case, the discharge voltage was 370–400 V and the current strength was maintained equal to 0.5 A. A sample in the form of a glass plate was fastened on a metal disk, which was located at a distance of 130 mm above the cathode target. During the sputtering of the target, the disk was rotated about its axis and along the chamber perimeter, which provided a uniform deposition of the coating. A negative potential of 24 V was applied to the disk.

The thickness of a deposited film was determined by the ellipsometric method with the use of an LÉF-3m instrument operating in a reflection geometry at the wavelength of a He–Ne laser. Under the above sputtering conditions and a sputtering time of 30 min, the coating thickness was equal to ~50 nm.

The optical absorption spectra of the films prepared under the specified sputtering conditions were measured on a Hitachi U-3410 spectrophotometer. It was found that the optical band gap in these films is equal to ~2 eV, which is characteristic of films containing amorphous hydrogenated carbon formed from the nanostructures with the sp^3- and sp^2-hybridizations of carbon electron shells [3].

The amorphous hydrogenated carbon films were deposited onto glass plates 1.4 × 120 × 120 mm in size, which were cut from the commercial sheet soda–lime–silica glass prepared by vertical drawing. The high strength of glass samples of the given size was achieved by chemical polishing (etching to a depth of 0.05 mm) in an aqueous solution of hydrofluoric acid under the conditions which excluded the damage of their operating surfaces [8]. Selected samples after the etching were further treated in water at a temperature of 96°C for 1 h. After the deposition of the coating, each plate was cut into four parts, and the obtained samples 1.3 × 60 × 60 mm in size were tested for strength.

The strength was determined by the central symmetric bending method. The diameter of a ring support was equal to 40 mm and the diameter of a loading ring was 8.5 mm. The formulas for calculating the stresses for a rigid plate [9] could not be used in this case, because the deflection of samples with a strength higher than 0.5 GPa exceeded one-half the sample thickness. Therefore, the calculations of the strength were performed using the calibration curve obtained with the reference tables for flexible plates [17]. The accuracy in determination of the strength was ~5%. At least 25–40 samples were tested in each case.

Experimental data on the strength of a glass treated by etching in hydrofluoric acid prior to and after deposition of the *a*-C : H coating

Conditions of glass surface treatment	Mean strength σ, GPa	Number of samples	Variation coefficient γ, %
Etching in hydrofluoric acid	2.4	42	10
The same with subsequent deposition of the *a*-C : H coating under standard conditions[1]	2.4 1.1[2]	29 11	15 50
The same but at a discharge voltage of 430 V	0.7	18	60
Etching in hydrofluoric acid with subsequent treatment in water at 96°C	2.7	24	14
The same with subsequent deposition of *a*-C : H coating under standard conditions[1]	2.7 1.4[2]	26 18	10 50

[1] Standard conditions of coating deposition: working gas pressure, 5×10^{-3} torr; voltage, 370–400 V; ionic current, 0.5 A; negative bias at the substrate, –24 V; time, 30 min; and coating thickness, 50 nm.

[2] Possible instability in the form of ionic current surges upon bombardment of a target.

The resistance of strengthened glasses to crack formation (cracking resistance) upon contact with solids was studied by the microindentation technique—the indentation of a standard Vickers diamond pyramid with an apex angle of 136° into the glass. Twenty indentations for each load were made with a PMT-3 microhardness gauge. The number of radial cracks emanating from corners of an indentation was measured after the unloading of an indenter. The case when four cracks emanated from four corners in each indentation was taken as 100%. Indentations were produced with loads from 0.5 to 10.2 N. The cracks can be formed immediately after the unloading of the indenter or after a while. Therefore, in order to decrease the scatter in the data, the measurements were performed within 30 min after the unloading of the indenter.

The curves of the probability of forming radial cracks (the number of cracks in percentage) as a function of the indenter load characterize the cracking resistance of a glass prior to and after the deposition of the coating.

3. RESULTS AND DISCUSSION

The results of measuring the strength prior to and after the deposition of the coating are given in the table. The mean strength of the glass treated by etching in hydrofluoric acid is equal to 2.4 GPa with a variation coefficient of 10%, which is close to the data on the strength measured earlier by central symmetric bending of a rigid plate [9].

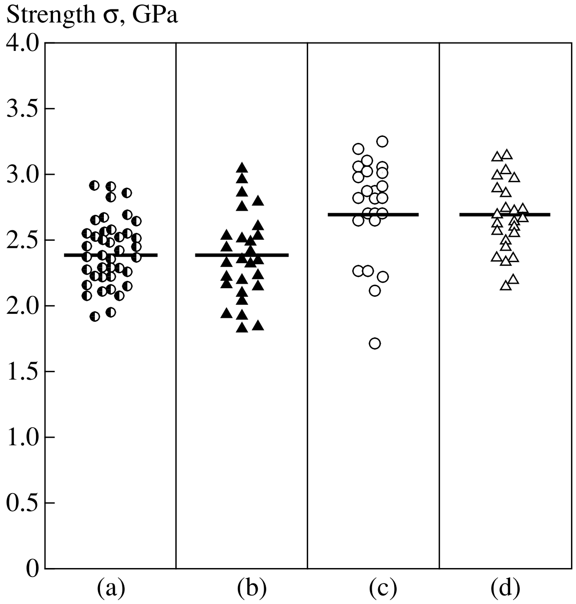

Fig. 1. Strength of the sheet glass subjected to (a) etching in hydrofluoric acid and (b) subsequent deposition of the *a*-C : H coating 50 nm thick and the sheet glass subjected to (c) treatment with water at 96°C for 1h after the etching in hydrofluoric acid and (d) subsequent deposition of the *a*-C : H coating 50 nm thick. Horizontal lines correspond to the mean strengths.

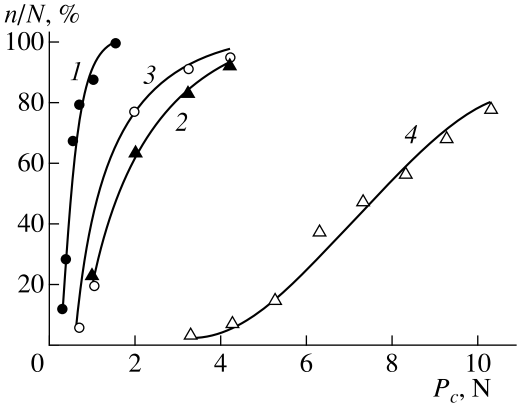

Fig. 2. Dependences of the relative number of cracks (n/N) formed upon indentation of a Vickers diamond pyramid into a glass on the indenter load for the glasses subjected to different surface treatments: (*1*) etching in hydrofluoric acid and (*2*) subsequent deposition of the *a*-C : H coating 50 nm thick and (*3*) treatment with water at 96°C for 1h after the etching in hydrofluoric acid and (*4*) subsequent deposition of the *a*-C : H coating 50 nm thick.

The deposition of coatings can result both in an increase in the strength of a glass due to a decrease in the attack of environment and in a decrease in the strength when, for one reason or other, the deposition of the coating brings about the formation of new defects on the surface.

The tabulated data on the glass strength measured after the deposition of the *a*-C : H coating can be separated into two groups (see table). In the first group, the mean strength is equal to 2.4 GPa (the variation coefficient is 15%), which is virtually identical to the strength of the glass without coating. In the other group of experiments, which were performed under the same conditions of coating deposition, the strength considerably decreases (down to 1 GPa) and the variation coefficient increases to 50%; i.e., in this group of experiments, high values of the strength (greater than 2 GPa) are observed together with very small strengths of ~0.5 GPa.

The amorphous hydrogenated carbon film is formed upon deposition of carbon onto the glass surface under the conditions of an argon–hydrogen plasma. As was shown in our earlier work [18], the bombardment of the glass surface by argon ions at voltages higher than 400 V and a gas pressure of 10^{-1} torr brings about a decrease in the glass strength. At a lower pressure of 10^{-2} torr, the strength virtually does not decrease. Furthermore, it was revealed that the presence of hydrogen in the plasma does not lead to a considerable decrease in the strength [18].

Since the *a*-C : H coating was deposited under a pressure of 10^{-3}–10^{-2} torr and at a voltage of 360–400 V, the presence of argon and hydrogen ions should produce an insignificant negative effect on the strength.

As a rule, a decrease in the strength was observed in the case when the gas discharge became unstable, which manifested itself in short-term ionic current surges. The number of experiments in which the sputtering of coating exhibited instability was as much as ~30% of all the experiments.

An increase in the discharge voltage above 400 V and, correspondingly, in the rate of target sputtering also leads to a decrease in the strength of a glass after the deposition of the coating.

The data on the strength of glass samples subjected to etching with subsequent treatment in water at a temperature of 96°C are also listed in the table. This treatment results in an increase in the strength to 2.7 GPa, i.e., by 12%. The same strength was found after the deposition of the *a*-C : H coating. It should be noted that, in this case, too, the instability of target sputtering and a decrease in the strength were observed in a number of experiments (~30%).

Thus, the results obtained indicate that the amorphous hydrogenated carbon coating does not lead by itself to a decrease in the glass strength (Fig. 1). However, the technique used in the present work for the deposition of coatings by sputtering a solid target is likely characterized by a certain instability which is associated with the structure of the target material and jumps in the intensity of the beam of particles bombarding the target. It is quite possible that, under certain conditions, not only individual ions or atoms but their aggregates can be knocked out of the target. The deposition of these aggregates onto the glass surface (substrate) can bring about a local heating of the surface and, as a consequence, the formation of microdefects.

The next part of this work is concerned with the investigation into the protective properties of the coating. The purpose of this part of the present work is to answer the question of how much the thin amorphous hydrogenated carbon film (~50 nm thick) can increase the cracking resistance of the glass, i.e., the resistance of the glass to formation of cracks upon contact with solids.

Figure 2 shows the dependences of the number of cracks formed upon indentation of a diamond pyramid into the glass on the indenter load. The cracking resistance of materials is usually characterized by the load P_c which corresponds to the formation of 50% of all the cracks.

As can be seen from Fig. 2, this load for the glass treated by etching in a hydrofluoric acid is equal to ~0.5 N (curve *1*). After the deposition of the *a*-C : H coating, the cracking resistance curve is shifted toward the right (curve *2*) and the value of P_c increases to 1.7 N.

The cracking resistance increases still further when the etched glass is treated in water at 96°C for 1 h prior to the deposition of the coating. In this case, the value of P_c increases to 7.5 N, i.e., by a factor of 15 compared to P_c for the glass without coating.

Therefore, the treatment of glass in water at an elevated temperature, which, as is known, leads to the leaching of the surface layer of the glass [19], strongly affects the protective properties of the film. Upon leaching of the glass in water, alkali metal ions leave the surface glass layer, whereas hydrogen ions penetrate into the glass; i.e., the ion-exchange process occurs. For example, upon treatment in boiling water for 1 h, the concentration of hydrogen ions in the surface layer increases two or three times, and the concentration of sodium ions likewise decreases by a factor of two or three [20]. As a result of this process, the structure of the surface glass layer is modified: a sufficiently strong Coulomb cation–oxygen interaction gives way to a considerably weaker interaction between the ≡Si–OH silanol groups due to hydrogen bonding. This leads to an increase in the molecular mobility of the structure of the surface layer and enhances its relaxation ability [11, 12].

Indeed, as can be seen from Fig. 1, the curve characterizing the cracking resistance of the glass without coating is shifted toward the right after the treatment in water; i.e., the resistance to the crack formation increases by almost a factor of 2.5 (P_c = 1.2 N). However, as was shown above, the largest increase in the cracking resistance is observed in the case when a thin layer of the *a*-C : H coating (~50 nm) is deposited onto the leached glass.

It is known that radial cracks are formed under residual tensile stresses which arise on the glass surface after the unloading of the indenter. Kurkjian *et al.* [21] proved that the emergence of radial cracks substantially depends on the attack of the environment: the crack formation increases in a corrosive medium and decreases or ceases in a neutral medium.

In this respect, we believe that the protective properties of a very thin amorphous hydrogenated carbon layer are associated with a decrease in the attack of the environment, namely, water vapors, on the glass surface during the penetration of the indenter and after its unloading. The higher the adhesion of the coating to the glass surface, the stronger its protective properties can be. In the case when the adhesion is insufficient, the film peels at the indenter boundaries or in adjacent regions and water molecules penetrate to stressed bonds, which results in the formation of microcracks.

It seems likely that the treatment of glass in water prior to the deposition of the coating brings about an increase in the adhesion of the hydrogenated carbon film to the glass due to the removal of sodium ions from the glass surface. Electric fields of alkali metal cations can hamper good adhesion of carbon atoms deposited onto the glass surface. By contrast, an increase in the hydrogen content in the surface layer of the glass can encourage the formation of hydrogenated carbon complexes.

4. CONCLUSION

Summarizing the results of the present work, we can draw the following inferences. The deposition of amorphous hydrogenated carbon coatings onto the glass in the high-strength state does not reduce its strength. However, the technique used in this work for the sputtering of a graphite target does not necessarily ensure the stability of the coating deposition process, which, in some cases, leads to a decrease in the glass strength.

The protective properties of the amorphous hydrogenated carbon coating depend on the adhesion of the film to the glass surface. The preliminary leaching of the glass surface upon treatment of the glass in water at a temperature close to the boiling point considerably improves the protective properties of the *a*-C : H film, which brings about an increase in the resistance of glass to the crack formation upon mechanical contacts.

REFERENCES

1. A. Grill and B. S. Meyerson, in *Synthetic Diamond: Emerging CVD Science and Technology*, Ed. by Karl, E. Spear, and J. P. Dismukes (Wiley, New York, 1994), p. 91.
2. X. L. Peng and T. W. Clyne, Thin Solid Films **312**, 207 (1998).
3. V. I. Ivanov-Omskii, V. I. Siklitsky, A. A. Sitnikova, *et al.*, Philos. Mag. B **76** (6), 973 (1997).
4. A. Bubenzer, B. Dischler, G. Brandt, and P. Koidl, J. Appl. Phys. **54** (8), 4590 (1983).
5. S. Kaplan, F. Jansen, and M. Machonkin, Appl. Phys. Lett. **47** (7), 750 (1985).

6. J. W. Zou, K. Reichelt, K. Schmidt, and B. Dischler, J. Appl. Phys. **65** (10), 3914 (1989).
7. A. Grill, B. Meyerson, and V. Patel, J. Mater. Res. **3**, 214 (1988).
8. L. G. Baĭkova, F. F. Vitman, G. S. Pugachev, and V. P. Pukh, Dokl. Akad. Nauk SSSR **163** (3), 617 (1965) [Sov. Phys. Dokl. **10**, 666 (1966)].
9. V. P. Pukh, *Strength and Failure of Glass* (Nauka, Leningrad, 1973).
10. L. G. Baĭkova, F. F. Vitman, T. G. Dmitrieva, and V. P. Pukh, Fiz. Tverd. Tela (Leningrad) **9** (2), 480 (1967) [Sov. Phys. Solid State **9**, 365 (1967)].
11. L. G. Baĭkova, V. A. Bershteĭn, F. F. Vitman, *et al.*, Fiz. Tverd. Tela (Leningrad) **10** (5), 1315 (1968) [Sov. Phys. Solid State **10**, 1046 (1968)].
12. V. A. Bershteĭn, I. V. Dreval’, V. A. Stepanov, and V. G. Chistoserdov, Dokl. Akad. Nauk SSSR **213** (1), 77 (1973) [Sov. Phys. Dokl. **18**, 730 (1973)].
13. F. F. Vitman, I. A. Boguslavskiĭ, and V. P. Pukh, Fiz. Tverd. Tela (Leningrad) **4** (8), 2160 (1962) [Sov. Phys. Solid State **4**, 1582 (1963)].
14. B. R. Lawn, D. B. Marshall, and S. M. Wiederhorn, J. Am. Ceram. Soc. **62** (1–2), 71 (1979).
15. R. Dal Maschio, C. D. Soraru, G. Scarinci, *et al.*, Phys. Chem. Glasses **30** (2), 59 (1989).
16. B. S. Danilin and V. K. Syrchin, *Magnetron Sputtering Systems* (Radio i Svyaz’, Moscow, 1982).
17. M. S. Kornishin and F. S. Isanbaeva, *Flexible Plates and Slabs* (Nauka, Moscow, 1968).
18. V. P. Pukh, L. G. Baĭkova, V. I. Ivanov-Omskiĭ, and T. K. Zvonareva, Fiz. Khim. Stekla **24** (5), 648 (1998) [Glass Phys. Chem. **24** (5), 460 (1998)].
19. A. A. Belyustin, Fiz. Khim. Stekla **7** (3), 257 (1981).
20. G. Soraru, R. Dal Maschio, and G. Della Mea, Glass Technol. **27** (2), 69 (1986).
21. Ch. R. Kurkjian, G. W. Kammlott, and M. M. Chaudhri, J. Am. Ceram. Soc. **78** (3), 737 (1995).

Translated by O. Borovik-Romanova

Physics of the Solid State, Vol. 43, No. 3, 2001, pp. 489–492. From Fizika Tverdogo Tela, Vol. 43, No. 3, 2001, pp. 471–473.

MAGNETISM AND FERROELECTRICITY

Conductivity of $La_{1-x}Ca_xMnO_3$ under Magnetic Resonance of Mn Ions[1]

R. Laĭho*, E. Lähderanta*, L. S. Vlasenko, M. P. Vlasenko**, and V. S. Zakhvalinskiĭ*****
**Wihuri Physical Laboratory, Department of Physics, University of Turku, 20014 Turku, Finland*
e-mail: erlah@utu.fi
***Ioffe Physicotechnical Institute, Russian Academy of Sciences, Politekhnicheskaya ul. 26, St. Petersburg, 194021 Russia*
****Institute of Applied Physics, Academy of Sciences of Moldova, Chisinau MD 2028, Moldova*
Received July 17, 2000

Abstract—A change in the electrical conductivity, σ, is observed in the manganese perovskite $La_{1-x}Ca_xMnO_3$, with $x = 0$ and 0.3 under saturation of the magnetic resonance transitions of Mn ions. This effect has a maximum in the temperature range of the magnetic phase transition of the compounds. Two contributions to the change in σ are found. The first, dominating in $LaMnO_3$, is an increase in σ caused by heating of the sample under magnetic resonance. The second is a σ decrease due to reorientation of the Mn spins, observed in $La_{0.7}Ca_{0.3}MnO_3$. *© 2001 MAIK "Nauka/Interperiodica".*

Recently, much interest has been directed to the properties of the mixed valence compound $La_{1-x}Ca_xMn^{3+}_{1-\delta}Mn^{4+}_{\delta}O_3$ (LCMO) due to the appearance of "colossal" magnetoresistance at the paramagnetic–ferromagnetic (PM–FM) transition. The ferromagnetic coupling is strongest at $x \approx 0.3$–0.4, which gives the maximum Curie temperature $T_C \approx 250$ K [1]. The correlation between the conductivity and magnetic ordering of Mn ions has been attributed to the double-exchange (DE) mechanism [2–4] with a connection to the Jahn–Teller interaction to take into account the electron–lattice interaction [5] and the formation of lattice polarons [6, 7]. Recently, it was shown [8, 9] that the sharp decrease in the resistance of $La_{1-x}Ca_xMnO_3$ ($0.15 < x < 0.4$) near T_C can be explained by the collapse of the carrier density due to the tendency of polarons to form immobile bound pairs in the PM phase and the dissociation of the pairs in the FM phase.

As follows from all the models presented, the resistivity $\rho(T)$ of the manganese perovskites depends strongly on the average spin projection $\langle S_z \rangle$ of the Mn ions. EPR investigations of LCMO in the PM phase [10–13] have shown that all Mn^{3+} and Mn^{4+} ions contribute to a broad unresolved EPR line, characterized near room temperature by a g-factor of about 2 and a linewidth $\Delta B_{pp} = 10$–20 mT. The shape and width of this line depend on the Ca doping x, the temperature, and the sample preparation. Accurate measurements of the EPR line intensity have shown that the magnetic susceptibility is proportional to $\langle S_z \rangle$ and coincides with the susceptibility of the Mn system determined by dc magnetometry [12]. As the temperature is lowered towards the PM–FM transition, the amplitude and the width of the EPR line increase gradually. Upon passing T_C, the EPR line remarkably broadens attaining a width of $\Delta B_{pp} = 100$–200 mT. An additional broad line with $g > 2$ attributed to the FM phase [13] is usually observed below the PM–FM transition.

In the PM phase ($T > T_C$), where the EPR line of the Mn ions is easily detectable, the value of $\langle S_z \rangle$ can be changed by a resonant microwave field strong enough to saturate the EPR transitions. A consequent change can be observed in $\rho(T)$ by using electrical contacts on a sample. This technique of the electrical detection of magnetic resonance (EDMR) gives direct information about the relation between the transport properties and the average spin projection of Mn ions and allows one to detect the contribution of the magnetic field to the conductivity of LCMO in relatively weak magnetic fields $B < 1$ T. So far, the EDMR method has been used only for investigating paramagnetic centers in semiconductors. In this paper, we report the first observation of a change in $\rho(T)$ induced by a microwave resonance field in manganese oxide perovskites.

Ceramic samples of $La_{1-x}Ca_xMnO_3$ with $x = 0$ and 0.3 were synthesized by mixing stoichiometric amounts of high-purity oxides La_2O_3, $CuCO_3$, and MnO_2 and heating them at 1320°C for 35 h with intermediate grindings. Then the powder was pressed into a pellet, sintered at 1375°C in air for 22 h, and finally annealed at 1520°C for 13 h. For the EDMR investigations, samples of the size $0.5 \times 0.5 \times 0.5$ mm were cut from the pellet and provided with electrical contacts soldered with In on two opposite ends. The magnetic properties of the samples were investigated by an *rf*-SQUID magnetometer.

---

[1] This article was submitted by the authors in English.

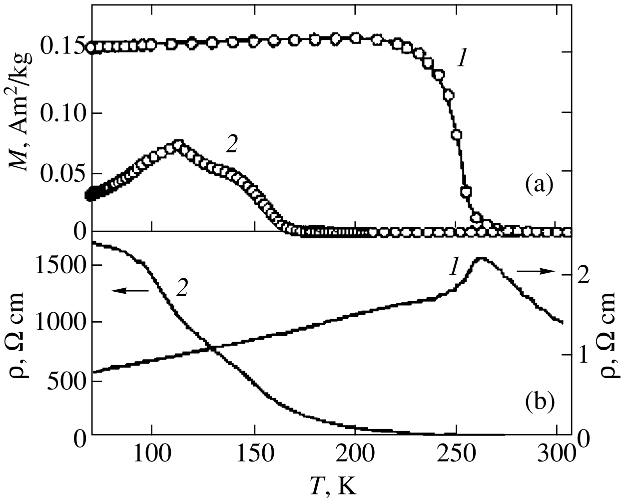

Fig. 1. Temperature dependences of (a) the magnetic moment *M* and (b) the resistivity ρ for (*1*) $La_{0.7}Ca_{0.3}MnO_3$ and (*2*) $LaMnO_3$.

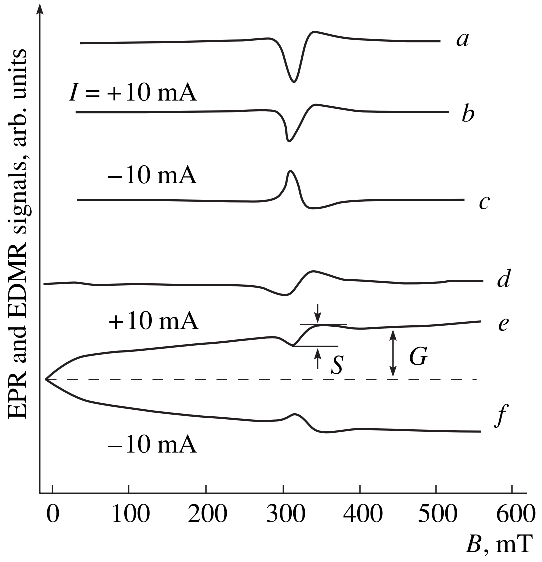

Fig. 2. (*a*, *d*) EPR and (*b*, *c*, *e*, *f*) EDMR signals observed in $La_{0.7}Ca_{0.3}MnO_3$ at (*a*, *b*, *c*) $T = 275$ and (*d*, *e*, *f*) 250 K for the currents *I* obtained by application of a positive and a negative voltage *V* across the sample. All measurements are made for $P = 400$ mW, sufficient to saturate the Mn EPR transitions.

The EDMR experiments were performed with an EPR spectrometer at the microwave frequency of 9.024 GHz and powers up to $P \cong 400$ mW, employing 100-kHz field modulation with an amplitude of $B_m \approx$ 1 mT. The spectrometer allows simultaneous observation of the usual EPR spectra and of the changes in σ under scanning the magnetic field *B*. To establish a stable measurement current of $I = 0.1$–20 mA, in the geometry of **I** || **B**, a dc voltage *V* was applied to the contacts through a load resistor $R_L > 10R_S$, where R_S is the resistance of the sample. The amplitude of the oscillating voltage across the ends of the sample at the 100 kHz field modulation frequency was detected by a lock-in amplifier, allowing us to observe only the field-dependent part of R_S. The temperature of the sample was varied over a range of 70–300 K in a helium gas-flow cryostat.

Figure 1a shows the temperature dependence of the magnetic moment $M(T)$ for the $La_{0.7}Ca_{0.3}MnO_3$ and $LaMnO_3$ samples measured in the field $B = 0.2$ mT after zero field cooling. With these data, the PM–FM transition at $T_C \approx 250$ K can be clearly revealed in LCMO with $x = 0.3$. The magnetic anomaly observed in $LaMnO_3$ below $T \cong 170$ K and the decrease in $M(T)$ for $T < 120$ K can be attributed to antiferromagnetic ordering. The temperature dependences of ρ measured directly in the cavity of the EPR spectrometer at $B \cong 0$ are plotted in Fig. 1b. These measurements were made by a two-point-contact method, such that the resistivity of the contacts can give the contribution to the measured values. The resistivity of $La_{0.7}Ca_{0.3}MnO_3$ has a drop below $T \cong 250$ K corresponding to the PM–FM transition. The resistivity of $LaMnO_3$ shows a semiconductor-like behavior for $T < 300$ K.

The change in ρ under magnetic resonance was found in $La_{0.7}Ca_{0.3}MnO_3$ for microwave powers $100 < P < 400$ mW. The EDMR signals observed at $T = 275$ and 250 K for opposite directions of the current *I* are shown in Fig. 2 (curves *b*, *c*, *e*, and *f*). The shape of these signals is similar to that of the EPR line of Mn ions with $g \approx 2$ (curves *a* and *d*). The change in the sign of the EDMR signal *S* taking place when *I* is reversed can be explained simply by a 180° phase shift of the alternating (100 kHz) voltage appearing across the sample. This confirms that the EDMR signal really originates from a change in ρ under saturation of the EPR transitions. The sign of this change was established independently with the same installation by comparing the sign of the EDMR signal with the sign of the resonance change in the photoconductivity caused by spin-dependent recombination in irradiated silicon [14]. This experiment revealed that the resistivity of $La_{0.7}Ca_{0.3}MnO_3$ increases under magnetic resonance.

The amplitudes of the EPR and EDMR signals increase when the temperature decreases from 300 to 250 K. Below T_C, the EPR and EDMR lines are considerably broadened and disappear below $T \cong 220$–230 K. The amplitude of the EDMR line *S* increases roughly linearly with the square root of the microwave power up to $P \cong 400$ mW, whereas the EPR line exhibits the usual saturation behavior [15] already above $P \cong 20$ mW. Under saturation of the EPR transitions, the ratio between the numbers of Mn ions with spin-up and spin-down orientations decreases. This leads to a decrease in $\langle S_z \rangle$ and,

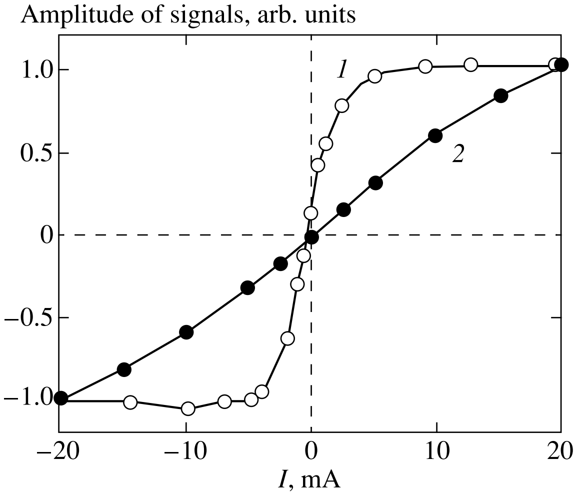

Fig. 3. Dependences of the amplitudes of (*1*) the *S* and (*2*) *G* signals (Fig. 2) on the value of the dc current *I* through the $La_{0.7}Ca_{0.3}MnO_3$ sample at $T = 250$ K.

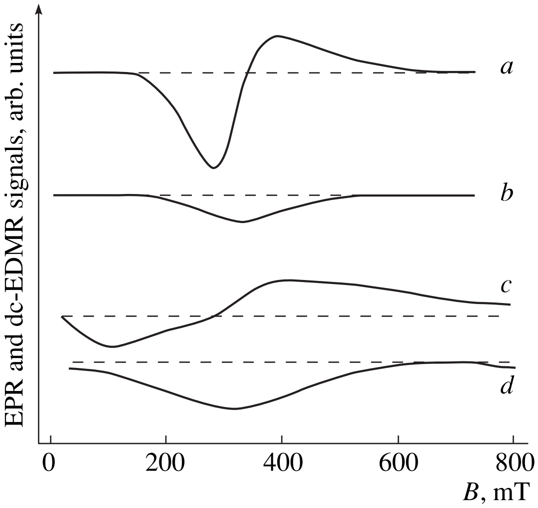

Fig. 4. (*a*, *c*) EPR and (*b*, *d*) dc EDMR signals detected in $LaMnO_3$ at $T = 190$ and 140 K.

consequently, to a decrease in σ, in accordance with the proposed models [2–9]. The relative change in the resistance of the sample under magnetic resonance $\Delta R_S/R_S$ is ~10^{-3}, which is surprisingly low when account is taken of the much larger change of $\Delta\langle S_z\rangle/\langle S_z\rangle \sim 0.1$–0.3 estimated from the saturation of the EPR line.

As can be seen from Fig. 2 (traces *e*, *f*), an additional change *G* in the background signal, depending on the magnetic field, is observed at $T = 250$ K. This is the contribution of the magnetoresistance to the total resistivity of the sample. The electrically detected signals *S* and *G* show different dependences on the value of *I* (Fig. 3). While *S* exhibits a saturation at $I \cong 5$ mA, *G* has no saturation up to $I = 50$ mA. This suggests that different physical mechanisms are responsible for the EDMR line *S* and for the magnetoresistance signal *G*. The saturation of *S* with increasing *I*, as well as the low value of $\Delta R_S/R_S$, can be attributed to scattering of carriers by localized magnetic moments of Mn ions. This interaction can strongly reduce the Mn spin relaxation time, and, therefore, higher microwave power is needed to saturate the EPR transitions. It is equivalent to the reduction of $\Delta\langle S_z\rangle/\langle S_z\rangle$ at a fixed microwave power. This can explain the saturation of *S* when *I* is increased. The *G* signal does not depend on the microwave resonance condition and is, therefore, independent of the Mn relaxation time.

The *S* and *D* signals observed at the 100 kHz modulation frequency of *B* were not found in $LaMnO_3$. Instead, a strong change in σ was detected in the range of $100 < T < 200$ K when measuring the dc component of *I* under magnetic resonance. The recorded traces of the EPR signal and the dc resistivity of $LaMnO_3$ are shown in Fig. 4. The resistivity decreases under EPR, whereas the EDMR signal in $La_{0.7}Ca_{0.3}MnO_3$ corresponds to an increase in ρ. Taking into account the high sensitivity of ρ to temperature (Fig. 1b), the EDMR signals in $LaMnO_3$ can be explained by heating of the sample by the microwave field under the magnetic resonance of Mn ions.

In conclusion, we are the first to apply the EDMR method for investigating the manganese oxide perovskites $La_{0.7}Ca_{0.3}MnO_3$ and $LaMnO_3$. Two contributions leading to EDMR signals of opposite signs are found. The decrease in ρ observed in $LaMnO_3$ is related to heating of the sample by the microwave field under magnetic resonance. Instead, in $La_{0.7}Ca_{0.3}MnO_3$, the increase in ρ is caused by the magnetic resonance reorientation of the Mn spins, in agreement with the DE mechanism [2–4]. Saturation of the EDMR signal with increasing the dc current through the sample and an additional nonresonant change in ρ, related to magnetoresistance, are observed in $La_{0.7}Ca_{0.3}MnO_3$. All these signals have a maximum amplitude near the magnetic phase transitions of the samples.

ACKNOWLEDGMENTS

This work was supported by the Wihuri Foundation, Finland.

REFERENCES

1. P. Schiffer, A. P. Ramírez, W. Bao, and S.-W. Cheong, Phys. Rev. Lett. **75**, 3336 (1995).
2. C. Zener, Phys. Rev. **82**, 403 (1951).
3. P. W. Anderson and H. Hasegawa, Phys. Rev. **100**, 675 (1955).
4. P. G. de Gennes, Phys. Rev. **118**, 141 (1960).
5. A. J. Millis, P. B. Littlewood, and B. I. Shraiman, Phys. Rev. Lett. **74**, 5144 (1995).

6. H. Röder, J. Zang, and R. Bishop, Phys. Rev. Lett. **76**, 1356 (1996).
7. A. J. Millis, B. I. Shraiman, and R. Mueller, Phys. Rev. Lett. **77**, 175 (1996).
8. A. S. Alexandrov and A. M. Bratkovsky, Phys. Rev. Lett. **82**, 141 (1999).
9. A. S. Alexandrov and A. M. Bratkovsky, J. Appl. Phys. **85**, 4349 (1999).
10. S. B. Oseroff, M. Torikachvili, J. Singley, *et al.*, Phys. Rev. B **53**, 6521 (1996).
11. C. Rettori, D. Rao, J. Singley, *et al.*, Phys. Rev. B **55**, 3083 (1997).
12. M. T. Causa, M. Tovar, A. Caneiro, *et al.*, Phys. Rev. B **58**, 3233 (1998).
13. G. Papavassiliou, M. Fardis, F. Milia, *et al.*, Phys. Rev. B **55**, 15000 (1997).
14. L. S. Vlasenko, Y. V. Martynov, T. Gregorkiewicz, and C. A. J. Ammerlaan, Phys. Rev. B **52**, 1144 (1995).
15. J. W. Orton, *Electron Paramagnetic Resonance* (ILIFFE Books, London, 1968), p. 168.

Physics of the Solid State, Vol. 43, No. 3, 2001, pp. 493–495. Translated from Fizika Tverdogo Tela, Vol. 43, No. 3, 2001, pp. 474–476.
Original Russian Text Copyright © 2001 by Petrakovskiĭ, Ryabinkina, Abramova, Velikanov, Bovina.

MAGNETISM AND FERROELECTRICITY

Antiferromagnet–Ferromagnet Transition in α-Mn_xS Manganese Sulfides

G. A. Petrakovskiĭ*, L. I. Ryabinkina*, G. M. Abramova, D. A. Velikanov*, and A. F. Bovina***

**Kirenskiĭ Institute of Physics, Siberian Division, Russian Academy of Sciences,*
Akademgorodok, Krasnoyarsk, 660036 Russia
***Krasnoyarsk State University, Krasnoyarsk, 660041 Russia*
e-mail: ovm@online.ru

Received July 19, 2000

Abstract—Off-stoichiometric manganese monosulfides α-Mn_xS ($1 \le x \le 1.25$) are synthesized, and their crystal structure and magnetic properties are studied in the 4.2- to 300-K range. The compounds have a NaCl fcc lattice. Increasing the manganese ion concentration x in the antiferromagnetic semiconductors α-Mn_xS is found to result in concentration- ($x_c \sim 1.05$) and temperature-driven ($T_c \sim 50$ K) magnetic transitions from the antiferromagnetic to ferromagnetic state, with the cubic structure remaining unchanged. *© 2001 MAIK “Nauka/Interperiodica”.*

It is customarily assumed [1, 2] that manganese monosulfide, similar to MnO and NiO, is a classical second-type antiferromagnet, with the magnetic unit cell being a doubled crystallographic cell. The magnetic moments associated with the Mn^{2+} ions lie in the (111)-type planes and exhibit ferromagnetic in-plane and antiferromagnetic intraplane ordering. This magnetic structure is typical of rare-earth metal oxides with a $LaMnO_3$-type perovskite structure [3]. Interest in manganese monosulfide increased after the discovery in its solid solutions $Fe_xMn_{1-x}S$ of a colossal negative magnetoresistance [4], whose mechanism, as well as ferromagnetic nature, remains unclear. It thus appeared of interest to perform an integrated investigation of the physical properties of manganese monosulfide.

This paper presents the results of an investigation into the temperature behavior of the structure (100–300 K) and magnetic properties (4.2–300 K) of the α-Mn_xS sulfides ($1.00 \le x \le 1.25$). The investigation was carried out on single-crystal ($x = 1.00$) and polycrystalline ($x = 1.00$, 1.05, 1.15, and 1.25) samples. The technology used to prepare the polycrystals was described in [5]. The α-Mn_xS single crystal was obtained by sulfidization of molten metallic manganese. The x-ray characterization of the samples was performed on a DRON-2.0 diffractometer with CuK_α radiation within a grazing angle region of 0° to 70°. The magnetization of the samples was measured with a SQUID magnetometer in the temperature range from 4.2 to 300 K in a magnetic field of 100 Oe.

The x-ray diffraction measurements showed that at 300 K the samples have the fcc NaCl lattice typical of manganese monosulfide. The lattice parameter for the single crystal with $x = 1.00$ is $a = 5.216$ Å, and for the polycrystal, $a = 5.222$ Å, which is close to the data quoted in [2] ($a = 5.22$ Å). At $T \sim 166$ K, the lattice parameter exhibits an anomaly similar to the one observed at 150 K in [2], which indicates a rhombohedral distortion of the cubic lattice. The lattice parameter decreases with decreasing temperature (Fig. 1a); this decrease becomes sharper for $T < 166$ K, but within the $100 < T < 122$ K region, it is practically temperature-independent. The results of the structural study of the single crystal are corroborated by optical measurements made on the same crystal [6]. Optical measure-

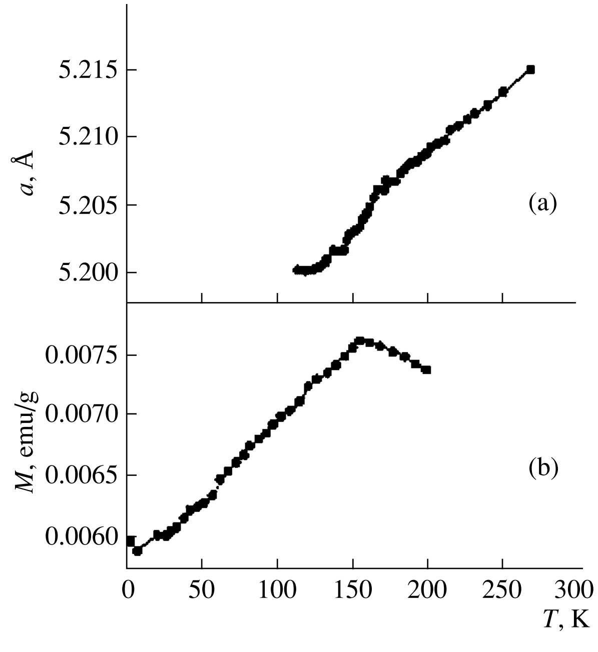

Fig. 1. Temperature dependences of (a) the lattice parameter and (b) magnetization of α-MnS.

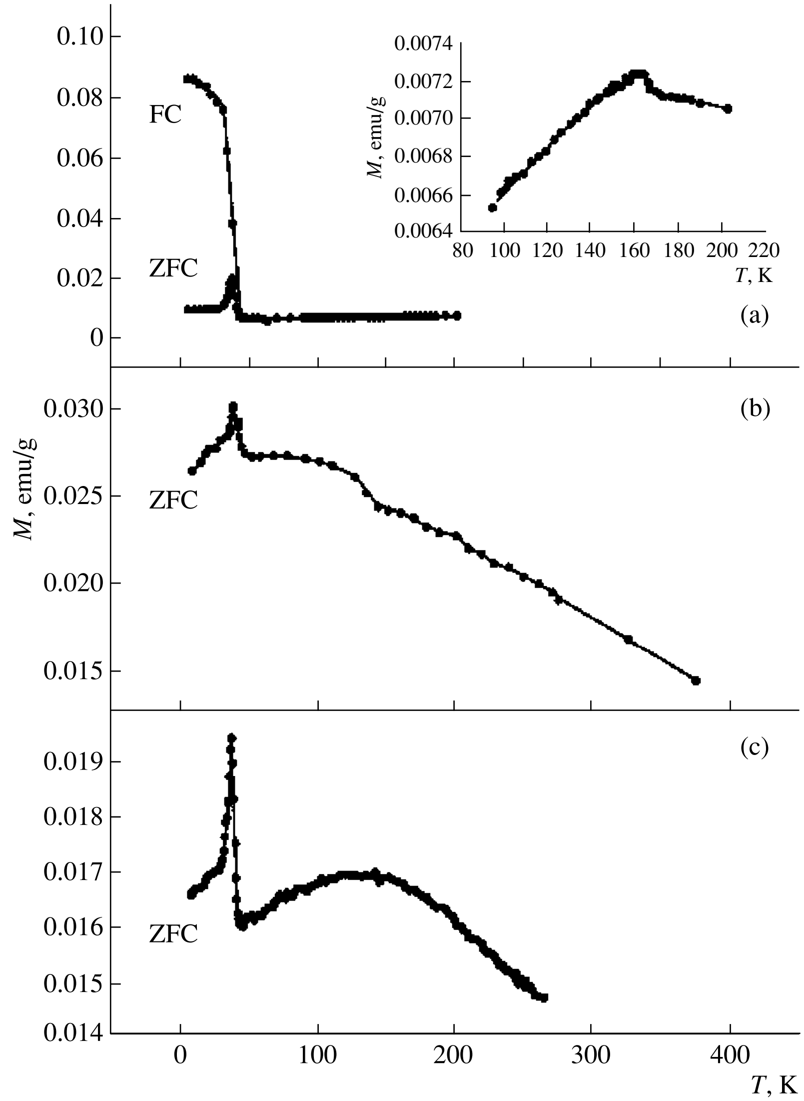

Fig. 2. Temperature dependences of the magnetization of α-Mn_xS with compositions (x): (a) 1.05, (b) 1.15, and (c) 1.25. The inset to Fig. 2a shows the temperature dependence of magnetization obtained for $x = 1.05$ in the 100- to 200-K region.

ments and a calculation of the temperature coefficient of expansion yield $T_s = 162 \pm 2$ K for the temperature of the structural transition in single-crystal manganese monosulfide. As the manganese concentration in Mn_xS ($1.00 \le x \le 1.25$) increases at 300 K, the cubic cell parameter of the polycrystalline sample varies from 5.222 Å ($x = 1.00$) to 5.218 Å ($x = 1.25$).

Figure 1b shows the temperature dependence of the magnetization of single-crystal α-MnS measured in a magnetic field perpendicular to the (100) plane. This dependence is similar to the one reported in [2] and passes through a maximum at $T_N = 157$ K, which is evidence of a transition from the paramagnetic to antiferromagnetic state. Similarly to the α-MnS single crystal studied in [2], in our crystal, the antiferromagnetic transition is observed to occur in the region of existence of the distorted NaCl structure. The magnetic susceptibility of α-MnS at T_N is 76.2×10^{-6} cm^3/g (66.28×10^{-4} cm^3/mol), which is in accord with available data (63.5×10^{-4} cm^3/mol [2]). In the 200–400-K region, the magnetic susceptibility obeys the Curie–Weiss law with a paramagnetic Curie temperature of ~–600 K.

Figure 2a presents the temperature dependence of magnetization for the α-Mn_xS sulfide with $x = 1.05$ measured in a field of 100 Oe. The magnetization of this sample measured within the 45–270-K region behaves similarly to α-MnS manganese monosulfide. At $T_N = 155$ K, one observes a maximum indicating the transition from the paramagnetic to antiferromagnetic state. At the Neél temperature, the magnetic susceptibility for $x = 1.05$ is close to that found for $x = 1.00$. At $T_c \sim 40$ K, a second magnetic transition similar to that observed in the $\text{Cr}_{0.5}\text{Mn}_{0.5}\text{S}$ solid solution [7] was discovered. The temperature dependence of magnetization measured on a ZFC sample exhibits a sharp peak at T_c (the Hopkinson effect) (Fig. 2a). The FC magnetization measured at $H = 100$ Oe is characteristic of ferromagnets and is evidence of a transition from the antiferromagnetic to ferromagnetic state. The ZFC magnetization measured on this sample ($x = 1.05$) at 4.2 K is 95.3×10^{-4} emu/g.

Figure 2b displays the temperature dependence of ZFC magnetization for the $x = 1.15$ sulfide. The magnetization of this sample within the 4.2–50-K interval behaves as it does in the sample with $x = 1.05$ (Fig. 2a). The transition point to the low-temperature ferromagnetic phase in this sulfide is $T_c = 45$ K. For $T > T_c$, the magnetization of the sulfide with $x = 1.15$ differs in behavior from that observed in the previously mentioned samples. As the temperature increases, the magnetization drops to 370 K, with an anomaly seen at $T = 133$ K. In the 133- to 370-K interval, the sample with $x = 1.15$ does not obey the Curie–Weiss law characteristic of the manganese monosulfide ($x = 1.00$) in the paramagnetic region. The magnetization measured at 4.2 K in a field of 100 Oe is 266.7×10^{-4} emu/g, which is an order of magnitude higher than that of samples with lower manganese contents. The temperature dependence of the magnetization of the sulfide with $x = 1.25$ is shown in Fig. 2c; it is similar to that observed in the $x = 1.05$ sample.

On comparing our results with the available data on the conductivity of off-stoichiometric manganese sulfides [5], we note that the increase in magnetization observed to occur in the Mn_xS system at 300 K is accompanied by metallization of the samples, with the electrical resistivity ρ at 300 K decreasing by two orders of magnitude as x varies from 1.00 to 1.05. The temperature dependence of the electrical resistivity of off-stoichiometric manganese sulfides at 77–300 K behaves similarly to $\rho(T)$ for the monosulfide with $x = 1.00$ and exhibits a sharp break at the points of structural and antiferromagnetic transitions.

Thus, we have found that manganese monosulfide undergoes concentration- and temperature-driven magnetic transitions. At room temperature, lattice compression occurring with increasing manganese concentration is accompanied by an increase in the magnetization by an order of magnitude and a decrease in the electrical resistivity by two orders of magnitude. A similar situation is observed to occur in the cation-substituted sulfides $Me_xMn_{1-x}S$ (Me = Cr, Fe) [7]. The similarity between the concentration dependences of the lattice parameter, magnetization, and electrical resistivity suggests that ferromagnetism in the Mn_xS and $Me_xMn_{1-x}S$ sulfides may set in by similar mechanisms.

ACKNOWLEDGMENTS

This work was supported by the Russian Foundation for Basic Research, grant no. 00-02-81059 Bel 2000a.

REFERENCES

1. É. L. Nagaev, *Physics of Magnetic Semiconductors* (Nauka, Moscow, 1979).
2. H. H. Heikens, G. A. Wiegers, and C. F. van Bruggen, Solid State Commun. **24** (3), 205 (1977).
3. É. L. Nagaev, Usp. Fiz. Nauk **166** (8), 833 (1996) [Phys. Usp. **39**, 781 (1996)].
4. G. A. Petrakovskiĭ, L. I. Ryabinkina, G. M. Abramova, *et al.*, Pis'ma Zh. Éksp. Teor. Fiz. **69** (12), 895 (1999) [JETP Lett. **69**, 949 (1999)].
5. G. V. Loseva, L. I. Ryabinkina, L. S. Emel'yanova, and A. V. Baranov, Fiz. Tverd. Tela (Leningrad) **22** (12), 3698 (1980) [Sov. Phys. Solid State **22**, 2165 (1980)].
6. A. V. Malakhovskiĭ, T. P. Morozova, V. N. Zabluda, and L. I. Ryabinkina, Fiz. Tverd. Tela (Leningrad) **32** (4), 1012 (1990) [Sov. Phys. Solid State **32**, 596 (1990)].
7. G. A. Petrakovskiĭ, L. I. Ryabinkina, D. A. Velikanov, *et al.*, Fiz. Tverd. Tela (St. Petersburg) **41** (9), 1660 (1999) [Phys. Solid State **41**, 1520 (1999)].

Translated by G. Skrebtsov

Physics of the Solid State, Vol. 43, No. 3, 2001, pp. 496–500. Translated from Fizika Tverdogo Tela, Vol. 43, No. 3, 2001, pp. 477–481.
Original Russian Text Copyright © 2001 by Guanghua, Levitin, Snegirev, Filippov.

MAGNETISM AND FERROELECTRICITY

Magnetostriction of $SmMn_2Ge_2$ and $GdMn_2Ge_2$ Intermetallic Compounds

Guo Guanghua, R. Z. Levitin, V. V. Snegirev, and D. V. Filippov

Moscow State University, Vorob'evy gory, Moscow, 119899 Russia

Received August 14, 2000

Abstract—Longitudinal and transverse magnetostrictions of polycrystalline samples of intermetallic compounds RMn_2Ge_2 (R = Sm or Gd) are measured in pulsed magnetic fields up to 250 kOe. It is found that linear magnetostrictive strains of about 10^{-3} arise in a temperature range in which the magnetic field causes a change in the magnetic state of a manganese magnetic subsystem. The results obtained are described within the model of a two-sublattice ferrimagnet with a negative exchange interaction in the manganese subsystem in terms of a strong dependence of this interaction on interatomic distances. *© 2001 MAIK "Nauka/Interperiodica".*

Magnetism of intermetallic compounds RMn_2Ge_2 (R is a rare-earth element or yttrium) is determined by two magnetic subsystems which are formed by the magnetic moments of manganese and a rare-earth element, respectively. These compounds have a layered tetragonal crystal structure of the $ThGe_2Si_2$ type (space group $I4/mmm$). The following hierarchy of exchange interactions is realized in these compounds: the Mn–Mn positive exchange in a layer is the strongest exchange interaction; the exchange interactions between the neighboring layers of manganese, as well as the interactions between the rare-earth element and manganese, are one order of magnitude weaker; and the R–R exchange interaction is two orders of magnitude weaker (see review [1] and references therein). An important feature is that the parameter of the Mn–Mn interlayer exchange interaction strongly depends on interatomic distances (primarily, within the layer) and changes sign from positive to negative as the unit cell parameter a increases to a critical value $a_{cr} \approx$ 4.045 Å [1, 2]:

$$\lambda = \rho(a - a_{cr}). \tag{1}$$

Since the unit cell parameter a at room temperature exceeds the critical value a_{cr} for intermetallic compounds with light rare-earth elements (La, Nd, Pr, or Sm), the magnetic ordering of the manganese subsystem in these compounds has a ferromagnetic character. For $SmMn_2Ge_2$, the sign of the Mn–Mn interlayer exchange interaction changes with a decrease in the temperature to 150 K. The reason for this is that the thermal expansion at this temperature results in a decrease in the unit cell parameter a to the a_{cr} value and the manganese subsystem transforms to the antiferromagnetic state [1, 3–5]. In intermetallic compounds with heavy rare-earth elements (Gd, Tb, Dy, Ho, Er, or Tm), the magnetic ordering of the manganese subsystem has an antiferromagnetic character, because $a < a_{cr}$. As the temperature decreases, the transition of a manganese subsystem to the ferromagnetic state is observed in intermetallic compounds with a negative Mn–Mn interlayer exchange interaction (Sm, Gd, Tb, or Dy). This transition is induced by magnetic ordering of the rare-earth subsystem [1]. For Sm- and Gd-containing intermetallic compounds, this transition occurs at a temperature of about 100 K [4–6]. Note that the magnetic transitions associated with the change in the magnetic state of a manganese subsystem are accompanied by considerable magnetoelastic strains. The thermal expansion measurements revealed that the relative variation of the unit cell parameter a is of the order of 10^{-3} [4, 5, 7]. This strain can be explained by the above dependence of the Mn–Mn interlayer exchange interaction on interatomic distances. According to [8], the exchange magnetostriction depends on the θ angle between the directions of magnetic moments $\mathbf{M}$ of manganese in neighboring planes:

$$\Delta a/a = -2\rho M^2 a \cos\theta/N, \tag{2}$$

where M is the magnetic moment of manganese and N is the corresponding elastic modulus.

If the Mn–Mn interplanar exchange interaction is negative, the external magnetic field can also vary the state of the manganese subsystem. Field-induced magnetic phase transitions were observed for $SmMn_2Ge_2$ [2, 4] and $GdMn_2Ge_2$ [9, 10].

The purpose of this work was to investigate the magnetoelastic strains arising upon field-induced magnetic phase transitions in Sm- and Gd-containing intermetallic compounds.

Polycrystalline samples of the $SmMn_2Ge_2$ and $GdMn_2Ge_2$ intermetallic compounds were obtained by melting initial components in an induction furnace under quasi-levitation conditions in an argon atmosphere. The samples were homogenized by annealing at 750°C in a dynamic vacuum for a week. The phase homogeneity of the samples was checked by an x-ray diffraction technique.

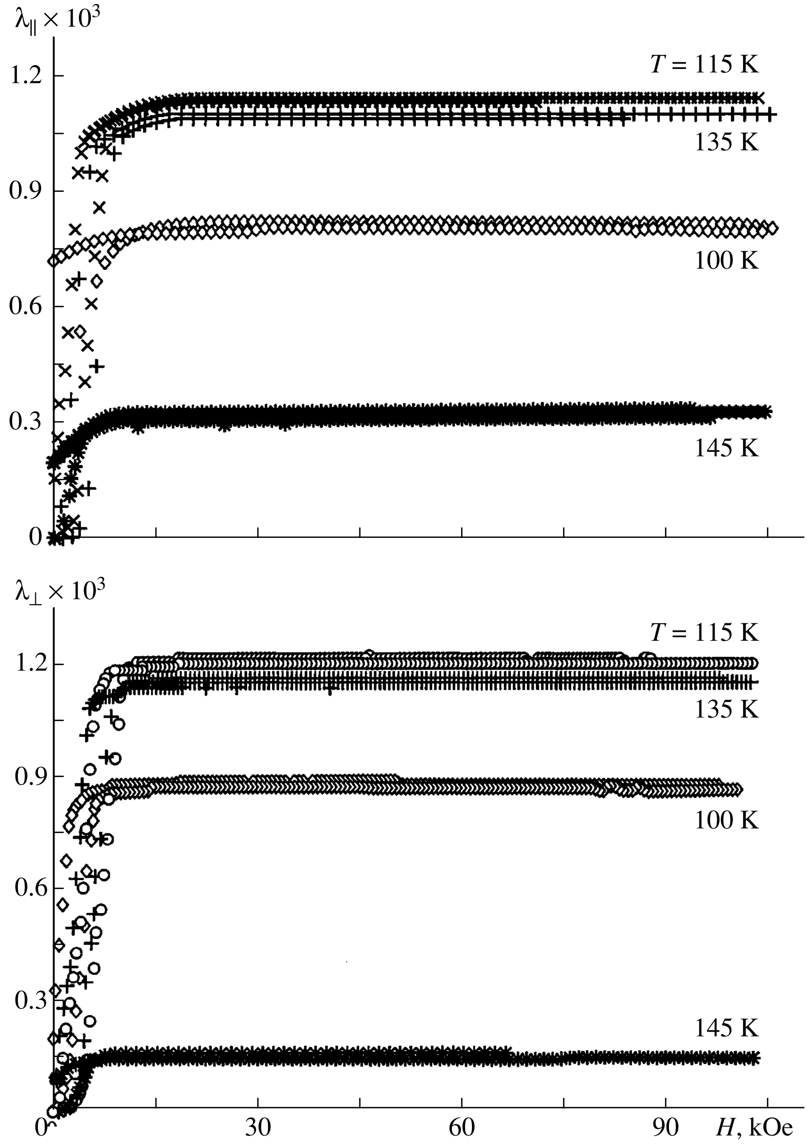

Fig. 1. Field dependences of the longitudinal and transverse magnetostrictions of $SmMn_2Ge_2$ at different temperatures.

The transverse and longitudinal magnetostrictions of the samples were measured in the temperature range 10–300 K in pulsed magnetic fields up to 250 kOe by the method of quartz piezoelectric sensors being glued onto the sample [11]. In order to determine the temperatures of spontaneous magnetic phase transitions, the magnetic susceptibility was measured in alternating magnetic fields of an order of several oersteds.

$SmMn_2Ge_2$. In the $SmMn_2Ge_2$ intermetallic compound, the manganese subsystem is ferromagnetically ordered at room temperature, whereas the samarium subsystem is in the paramagnetic state. Upon cooling, the first-order phase transition of the manganese subsystem to the antiferromagnetic state is caused by the change in the sign of the Mn–Mn interlayer exchange interaction due to thermal expansion, whereas the samarium subsystem remains paramagnetic. As follows from the measurements of magnetic susceptibility and thermal expansion [7], the temperature of this transition in the sample under study is equal to $T_1 = 150$ K. This value agrees well with the available data [4, 5]. Further cooling is accompanied by a reverse first-order transition of the manganese subsystem to the ferromagnetic state. This transition is determined by the ferromagnetic ordering of the samarium subsystem. The temperature of the reverse transition which we determined was $T_2 = 100$ K. This value is also in agreement with the data obtained in [4, 5, 7]. Since the rare-earth–manganese exchange interaction in intermetallic compounds containing light rare-earth elements is positive, the magnetic moments of the samarium and manganese subsystems are parallel to each other.

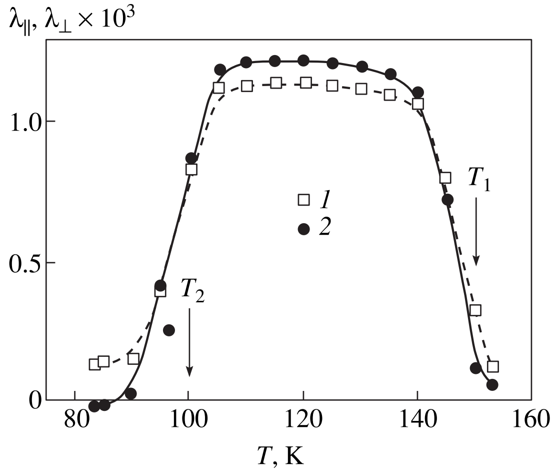

Fig. 2. Temperature dependences of (*1*) the longitudinal and (*2*) transverse saturation magnetostrictions of $SmMn_2Ge_2$. Phase transition temperatures T_1 and T_2 are marked by arrows.

The field dependences of the longitudinal and transverse magnetostrictions of $SmMn_2Ge_2$ at different temperatures are shown in Fig. 1. It is seen that in the temperature range $T_2 < T < T_1$, in which the manganese system is ordered antiferromagnetically, the magnetostriction is substantially larger than that at temperatures outside this range. This is explained by the fact that the field in this temperature range, as was demonstrated in [3, 5], induces the transition of the manganese subsystem to the ferromagnetic state, and the magnetostriction is caused by the magnetoelastic strains arising upon this transition. As is seen from Fig. 1, the magnetostriction associated with the antiferromagnet–ferromagnet transition in the manganese subsystem is positive and almost isotropic ($\lambda_{\parallel} \approx \lambda_{\perp}$). The temperature dependences of the longitudinal and transverse saturation magnetostrictions are shown in Fig. 2. As follows from [4, 5, 7], the spontaneous transition of the manganese subsystem from the ferromagnetic to the antiferromagnetic state at temperature T_1 and the reverse transition to the ferromagnetic state at temperature T_2 are accompanied by a decrease and increase, respectively, in unit cell parameter a. It is reasonable to suppose that the magnetostrictive strains, which arise upon field-induced transition of the manganese subsystem from the antiferromagnetic to the ferromagnetic state, are also caused by the magnetoelastic strains affecting the a parameter. Since the anisotropy at these temperatures is relatively small, the transition from the antiferromagnetic to ferromagnetic state in the field range investigated occurs at any orientation of the magnetic field with respect to the crystal axes [3]. In this case, the longitudinal magnetostriction of a polycrystalline sample should be equal to the transverse magnetostriction:

$$\lambda_{\parallel} = \lambda_{\perp} \approx 2\Delta a/3a, \quad (3)$$

where Δa is the change in unit cell parameter a upon spontaneous transition from the antiferromagnetic to ferromagnetic state. A comparison of the $\lambda_{\parallel}$ and $\lambda_{\perp}$ magnetostrictions with the $\Delta a/a$ ratio taken from [7] justifies this relationship. A small difference between longitudinal and transverse magnetostrictions can be explained by the fact that the polycrystalline sample is not absolutely isotropic and has a certain texture. The influence of the crystal texture on the magnetic properties of the RMn_2Ge_2 intermetallic compounds was also observed in [12].

$GdMn_2Ge_2$. The measurements of the thermal expansion [7] and magnetic susceptibility for the samples under investigation demonstrated that the transition of the manganese subsystem from the antiferromagnetic to ferromagnetic state with a simultaneous ferromagnetic ordering of the gadolinium subsystem occurs upon cooling below $T_2 = 97$ K. Since the gadolinium–manganese exchange interaction is negative, the intermetallic compound is a ferrimagnet at $T < T_2$. For the ferrimagnetic range (below 97 K), as follows from the data obtained in [9, 10], the magnetic field normal to the tetragonal axis of the crystal induces the first-order magnetic phase transition from the ferrimagnetic to the triangular phase in the magnetic field range covered. In this case, the magnetic moments of the gadolinium and manganese subsystems of the ferrimagnetic phase are aligned parallel to the tetragonal axis. In the triangular phase, the magnetic moment of the gadolinium subsystem is parallel to the magnetic field, whereas the magnetic moments of the two neighboring manganese planes deviate variously from this direction and form a certain angle θ. Above 97 K, if the manganese subsystem is antiferromagnetic and the gadolinium subsystem is paramagnetic, the magnetic field oriented along the tetragonal axis induces the first-order phase transition of the manganese subsystem to the ferromagnetic state [9].

The field dependences of the longitudinal and transverse magnetostrictions for one of the $GdMn_2Ge_2$ samples investigated are shown in Fig. 3. It is seen that the magnetostriction has a metamagnetic character both above and below the T_2 temperature; namely, the absolute value of magnetostriction increases after a certain critical field is reached. In this case, the longitudinal and transverse magnetostrictions are negative below the T_2 temperature and positive above this temperature. This character of magnetostriction can be explained under the assumption that the magnetoelastic strains observed are caused by the aforementioned field-induced metamagnetic transitions due to the field-induced change in the magnetic state of the manganese subsystem. Different magnetostriction signs above and below $T_2 = 97$ K can be explained by the fact that, at low temperatures, the field disturbs the ferromagnetic ordering in the manganese subsystem. Above this temperature, the manganese subsystem in the magnetic

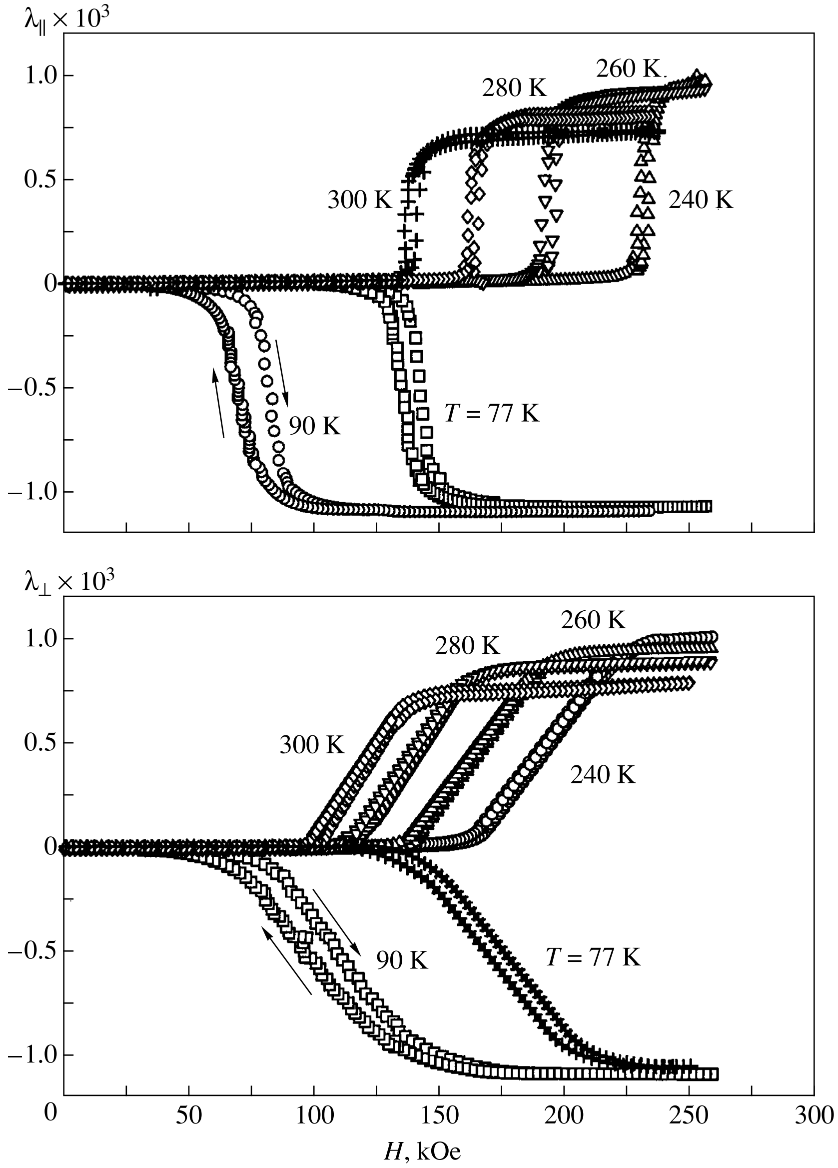

Fig. 3. Field dependences of the longitudinal and transverse magnetostrictions of $GdMn_2Ge_2$ at different temperatures.

field transforms to the ferromagnetic state.[1] Identical signs and approximately equal magnitudes of the longitudinal and transverse magnetostriction of $GdMn_2Ge_2$ indicate that the magnetostriction is essentially a bulk quantity. The temperature dependences of the longitudinal and transverse saturation magnetostrictions of $GdMn_2Ge_2$ are depicted in Fig. 4. These magnetostrictions agree in order of magnitude with the data obtained from the thermal expansion measurements for $GdMn_2Ge_2$ [7].

However, it should be noted that the field dependences of the magnetostriction measured for different

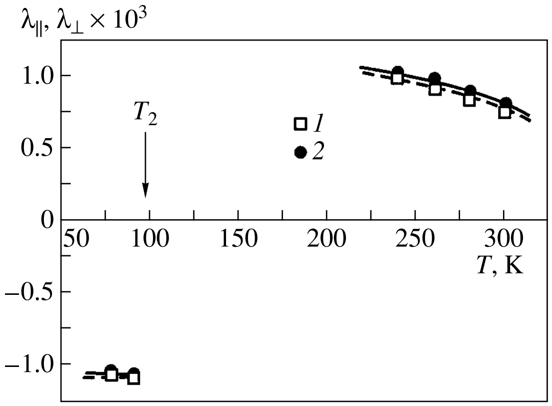

Fig. 4. Temperature dependences of (*1*) the longitudinal and (*2*) transverse saturation magnetostrictions of $GdMn_2Ge_2$. Phase transition temperature T_2 is marked by the arrow.

---

[1] We failed to measure the saturation magnetostriction in the range $T_2 = 97 < T < 240$ K, because the field of the metamagnetic transition at these temperatures exceeds the field of 250 kOe, which was achieved in our experiments.

samples are similar in character but significantly differ in details, specifically in the degree of smearing of the metamagnetic transition. This is clearly seen from comparison of the field dependences for $\lambda_{\parallel}$ and $\lambda_{\perp}$, which are shown in Fig. 4. In these experiments, the $\lambda_{\parallel}$ and $\lambda_{\perp}$ quantities were measured along the same direction, whereas the field was oriented parallel and normal to the direction of the magnetostriction measurements for the longitudinal and transverse magnetostrictions, respectively. The saturation magnetostrictions are also somewhat different. This is apparently caused, as was already noted, by the existence of the crystal texture in the samples. A comparison of the magnetostriction magnitudes for six different $GdMn_2Ge_2$ samples showed that the mean scatter of the absolute magnetostriction values reaches 30%. For this reason, the values of magnetostrictions displayed in Figs. 3 and 4 should be considered only as estimates.

Thus, the measurements demonstrated that a giant magnetostriction is observed for the $SmMn_2Ge_2$ and $GdMn_2Ge_2$ intermetallic compounds due to a change in the magnetic ordering of the manganese subsystem in the magnetic field. The large magnetoelastic effects for the intermetallic compounds investigated confirm the conclusion that the Mn–Mn exchange interactions strongly depend on interatomic distances.

ACKNOWLEDGMENTS

This work was supported by the Russian Foundation for Basic Research (project nos. 99-02-17358 and 00-15-96695) and the Ministry of Science of the Russian Federation (project no. 97-0-7.3-157).

REFERENCES

1. A. Szytula and J. Leciejewicz, in *Handbook of Physics and Chemistry of Rare Earths*, Ed. by K. A. Gschneidner, Jr. and L. Eyring (North-Holland, Amsterdam, 1989), Vol. 12, p. 133.
2. H. Fujii, T. Okamoto, N. Shigeoka, and N. Ivata, Solid State Commun. **53**, 715 (1985).
3. G. Venturini, B. Malaman, and E. Ressouche, J. Alloys Compd. **241**, 135 (1996).
4. E. M. Gyorgy, B. Batlogg, J. P. Remeika, *et al.*, J. Appl. Phys. **61**, 4237 (1987).
5. M. Duraj, R. Duraj, A. Szitula, and Z. Tomkowich, J. Magn. Magn. Mater. **73**, 240 (1988).
6. T. Shigeoka, H. Fujii, H. Fujiwara, *et al.*, J. Magn. Magn. Mater. **31–34**, 209 (1983).
7. I. Yu. Gaĭdukova, Guo Guanghua, S. A. Granovskiĭ, *et al.*, Fiz. Tverd. Tela (St. Petersburg) **41**, 2053 (1999) [Phys. Solid State **41**, 1885 (1999)].
8. C. Kittel, Phys. Rev. **120**, 335 (1960).
9. H. Kobayashi, H. Onodera, and H. Yamomoto, J. Magn. Magn. Mater. **79**, 76 (1989).
10. A. Yu. Sokolov, Guo Guanghua, S. A. Granovskiĭ, *et al.*, Zh. Éksp. Teor. Fiz. **116**, 1346 (1999) [JETP **89**, 723 (1999)].
11. R. Z. Levitin, V. N. Milov, Yu. F. Popov, and V. V. Snegirev, Physica B (Amsterdam) **59**, 177 (1992).
12. T. Ono, H. Onodera, M. Ohashi, *et al.*, J. Magn. Magn. Mater. **123**, 133 (1993).

Translated by N. Korovin

Physics of the Solid State, Vol. 43, No. 3, 2001, pp. 501–507. Translated from Fizika Tverdogo Tela, Vol. 43, No. 3, 2001, pp. 482–488.

MAGNETISM AND FERROELECTRICITY

Transport Effects in $La_{0.67-x}R_xSr_{0.33}MnO_3$ (R = Eu, Gd)

**N. G. Bebenin*, R. I. Zaĭnullina*, V. V. Mashkautsan*, V. V. Ustinov*,
V. G. Vasil'ev**, and B. V. Slobodin****

**Institute of Metal Physics, Ural Division, Russian Academy of Sciences, ul. S. Kovalevskoĭ 18, Yekaterinburg, 620219 Russia
e-mail: bebenin@imp.uran.ru*

***Institute of Solid-State Chemistry, Ural Division, Russian Academy of Sciences,
ul. Pervomaĭskaya 91, Yekaterinburg, 620219 Russia*

Received August 14, 2000

Abstract—An experimental study is reported on the temperature dependences of the magnetic susceptibility, electrical resistivity, magnetoresistance, thermo- and magnetothermopower, and on the Hall effect of the polycrystalline lanthanum manganites $La_{0.67-x}R_xSr_{0.33}MnO_3$ (x = 0 and 0.07, R = Eu, Gd) within the 77- to 430-K temperature range. Replacement of a small amount of lanthanum by europium or gadolinium was found to result in a considerable decrease in the resistivity and in a change in the pattern of its temperature dependence. The temperature dependence of both the ordinary and anomalous Hall coefficients near the Curie temperature is shown to be determined by the change in the number of carriers in delocalized states. A method is proposed for separation of the hole and electronic contributions to thermopower in the ferromagnetic region. The conduction mechanisms are discussed in terms of the concept of mobility edge motion. *© 2001 MAIK "Nauka/Interperiodica".*

INTRODUCTION

The large ("giant") magnetoresistance observed near the Curie temperature T_C in $La_{1-x}D_xMnO_3$ lanthanum manganites (D stands for a divalent metal) accounts for the interest in these materials. It was assumed for a long time that the magnetic and transport effects in these manganites are determined by Mn^{4+} ion content. Recent studies showed, however, that this is an oversimplification and that there is a number of other factors which considerably affect the properties of these complex oxides [1, 2]. For instance, replacement of a part of the lanthanum by yttrium [3, 4] or aluminum [5] noticeably reduces the Curie temperature, although these elements have the same valence. A noticeable change in the Curie temperature and magnetization was observed when a small part of the lanthanum in $La_{0.67-x}Sr_{0.33}MnO_3$ and $La_{0.67}Ba_{0.33}MnO_3$ was replaced by other rare-earth elements [6, 7], and these changes cannot be assigned to deformation of the unit cell induced by substituting an ion of a smaller radius for lanthanum.

This paper reports on an integrated study of the magnetic and transport properties of polycrystalline

$La_{0.67-x}Sr_{0.33}MnO_3$ (LaSr subsequently),

$La_{0.60}Gd_{0.07}Sr_{0.33}MnO_3$ (LaGdSr),

and

$La_{0.60}Eu_{0.07}Sr_{0.33}MnO_3$ (LaEuSr).

A comparison of the temperature dependences of the magnetic properties, resistivity, Hall effect, and thermopower of these compounds permits one to draw certain conclusions on the charge state of the rare-earth element, as well as to reveal the changes in the properties of individual crystallites induced by variation of their size. Comparative analysis of the experimental data obtained and of literature information on the resistivity and thermopower of single crystals of various lanthanum manganites offers the possibility of separating the contributions due to electrons and holes to conduction and thermopower in the ferromagnetic temperature region. The discussion is based on the semiphenomenological theory developed in the next section, which permits description of the main properties of the temperature dependences of the conductivity and thermopower.

1. THEORY

There is no universally accepted interpretation of the anomalies in the transport effects in lanthanum manganites. The microscopic models discussed in reviews [1, 2] contain constants which are difficult to determine; in addition, calculations are usually presented for resistivity only, which precludes their application to integrated studies. A semiphenomenological approach with a small set of parameters, which have a clear physical meaning and allow experimental measurement, currently appears more acceptable. The relations presented below were obtained by generalizing the results published in [8, 9].

We use for the calculation of σ the expression proposed by Mott:

$$\sigma = \int_{E_1}^{E_2}\left(-\frac{\partial F}{\partial E}\right)\sigma_E dE, \qquad (1)$$

where $F(E)$ is the Fermi function and integration is performed between the energies E_1 and E_2, which are the lower and upper mobility edges, respectively. The thermopower S can be conveniently calculated by the Mott–Fritzsche relation [10]:

$$S = -\frac{k_B}{e}\frac{1}{\sigma}\int_{E_1}^{E_2}\frac{E - E_F + D(E)}{T}\left(-\frac{\partial F}{\partial E}\right)\sigma_E dE, \qquad (2)$$

where k_B is the Boltzmann constant, e is the modulus of the electronic charge, and the $D(E)$ function takes into account the contributions of the spin and lattice degrees of freedom to the heat flux. One usually considers the situation in which the Fermi energy E_F lies close to one of these energies while being distant enough from the other, so that either the upper or the lower limit in Eqs. (1) and (2) may be set to infinity. As will be seen later, there are grounds to believe that in lanthanum manganites, both mobility edges are close to the Fermi level. Relations applicable to this situation seem to be lacking in the literature, and, therefore, we present their brief derivation.

The position of the mobility edges is determined by the degree of disorder in the system. At low temperatures, nonmagnetic disorder prevails. The growth of magnetic fluctuations near the Curie temperature shifts the mobility edges toward the band center, so that the region of delocalized states narrows. We shall assume, in accordance with [8, 9], that the variation of E_1 and E_2 induced by the variation of the magnetic field H and temperature can be described as

$$\begin{aligned} E_1(H, T) &= \Delta_{10} + \Delta_{11}m^2, \\ E_2(H, T) &= \Delta_{20} - \Delta_{21}m^2, \end{aligned} \qquad (3)$$

where $m = M/M_s(0)$, $M(H, T)$ is the magnetization, H is the magnetic field, $M_s(T)$ is the spontaneous magnetization, and Δ_{ij} are parameters extracted from the experiment. We shall be primarily interested in the case of the metallic state setting in the ferromagnetic region and of the insulating state in the paramagnetic region.

The crystal resides in the metallic state if the Fermi level lies between E_1 and E_2 and $|E_F - E_1|, |E_F - E_2| \gg T$. In this case, $\sigma = \sigma_{E = E_F}$ and the conductivity changes because of the changing carrier mobility. Relation (2) yields the well-known Mott expression for the thermopower:

$$S = -\frac{k_B}{e}\frac{\pi^2}{3}\frac{\sigma'(E_F)}{\sigma}T, \qquad (4)$$

where $\sigma'(E_F) = (\partial\sigma_E/\partial E)_{E = E_F}$. We here took into account that in the region of metallic conduction, the carrier concentration in delocalized states is high and one should assume that $D = 0$ [9].

Near the Curie temperature, a metal–insulator transition occurs, and the Fermi level turns out to be in the region of localized states. Because Hall measurements suggest that holes are the majority carriers in the materials of interest to us here, we shall assume the transition to be due to the crossing of E_F and E_2, in which case, in the insulating phase, we have $E_F > E_2 > E_1$. Assuming that $\sigma_E = \sigma_m$ (σ_m is the minimum metallic conductivity) for $E_1 < E < E_2$, we obtain from Eq. (1)

$$\sigma = \sigma_m(f(y_2) - f(y_1)), \qquad (5)$$

where $y_{1,2} = (E_F - E_{1,2})/T$ and $f(y) = (e^y + 1)^{-1}$. To derive an expression for the thermopower, we estimate the integral containing the $D(E)$ function by means of the first theorem of the mean, and, as a result, a term proportional to $\bar{D}/T$ will appear in the expression for the thermopower. Assuming, as before, that $\sigma_E = \sigma_m$, we come to

$$S = \frac{k_B}{e} \qquad (6)$$
$$\times\left(\frac{y_2 f(y_2) + \ln(1 + e^{-y_2}) - y_1 f(y_1) - \ln(1 + e^{-y_1})}{f(y_2) - f(y_1)} - \frac{\bar{D}}{T}\right).$$

As is evident from Eqs. (5) and (6), the closeness of the lower mobility edge brings about a decrease in the conductivity and thermopower. These changes are not significant if $y_1 \gg |y_2|$ and $y_1 \gg 1$. In this case, the terms containing y_1 may be disregarded, which yields the following simple expressions in the immediate vicinity of the metal–insulator transition [9]:

$$\rho = \rho_m\left(\exp\left(\frac{E^\rho}{T}\right) + 1\right), \qquad (7)$$

$$S = \frac{k_B}{e}\left(\frac{E^S}{T} + 1\right). \qquad (8)$$

Here, $\rho_m = \sigma_m^{-1}$; the resistivity activation energy is $E^\rho = E_0^\rho - E_1^\rho m^2$, where $E_0^\rho = E_F - \Delta_{20}$ and $E_1^\rho = \Delta_{21}$; and the thermopower activation energy is $E^S = E^\rho - \bar{D}$. The thermopower is typically about 100 μV/K. Using Eqs. (7) and (8), we have succeeded in satisfactorily describing the resistivity peak and the thermopower near T_C in the $La_{0.8}Ba_{0.2}MnO_3$ single crystal in which no metal–insulator transition takes place, but in the ferromagnetic region, the Fermi level does not lie far from the mobility edge [9].

In addition, relation (7) turned out to be valid for the $\rho(T, H)$ relation in the $La_{0.5}Sr_{1.5}MnO_4$ antiferromagnet [11], although, in the latter case, E_1^ρ may have a different meaning. The quantity E_0^ρ decreases with increasing doping, and E_1^ρ is of the order of 10^3 K in all cases, which apparently reflects a similarity in structure of the wave functions in all manganites.

Lanthanum manganites with Mn^{4+} concentrations in excess of 0.5 are insulators at any temperature. Obviously enough, at a slightly lower Mn^{4+} concentration, the $E_2 - E_1$ difference should become small compared to T, at least in the paramagnetic state. In this case, the temperature dependences of the resistivity and thermopower will differ qualitatively in behavior from Eqs. (7) and (8). To verify this, we write the expressions following from Eqs. (5) and (6) for the case $E_2 - E_1 \ll T$, $|E_F - E_{1,2}| \ll T$:

$$\rho = \rho_m \frac{4T}{E_2 - E_1}, \tag{9}$$

$$S = -\frac{k_B}{e}\frac{\bar{E} - E_F}{T}, \tag{10}$$

where $\bar{E} = (E_1 + E_2)/2$. We readily see that the linear growth of resistivity with temperature in the paramagnetic state, where $E_{1,2} = \text{const}$, is not sufficient proof of a “true” metallic state and is fully consistent with the temperature dependence of an activation-type thermopower. The temperature dependences of the resistivity and thermopower of an $La_{0.6}Sr_{0.4}MnO_3$ single crystal [12] suggest that it is this situation that occurs in this single crystal.

The concept of the σ_E function undergoing a jump at the mobility edge is a fairly rough approximation. The σ_E function is actually a continuous function, such that in the vicinity of the mobility edge (for definiteness, the upper one), one can set [13] $\sigma_E = C(E_2 - E)$, $C > 0$ for $E < E_2$. The temperature dependences of the conductivity and thermopower for $y_1 \gg 1$ turn out to follow the same pattern as suggested by Eqs. (4), (7), and (8); however, because $\sigma'_F = -C$ for the region of metallic conduction with $E_2 > E_F > E_1$, one obtains from Eq. (4)

$$S = \frac{k_B}{e}\frac{\pi^2}{3}\frac{T}{E_2 - E_F}. \tag{11}$$

Note that lanthanum manganites with Mn^{4+} contents of the order of 25–30% have carriers of different types. No separation of the corresponding contributions to the transport coefficients has thus far apparently been carried out, although in some favorable cases this is possible. We shall present below an example of such analysis.

2. EXPERIMENTAL RESULTS AND DISCUSSION

The powders of nominal composition $La_{0.67}Sr_{0.33}MnO_3$ and $La_{0.60}R_{0.07}Sr_{0.33}MnO_3$ (R = Eu, Gd) were prepared by coprecipitation from a solution. The precursors thus prepared were pressed at room temperature and annealed afterwards in an oxygen flow at 1200°C for 12 h. The techniques used to measure the magnetic properties, resistivity, thermopower, and the Hall effect were described in our previous publications [9, 14, 15].

Curie temperature and coefficients a_0, a_1, and a_2 in Eq. (14) for $La_{0.67-x}R_xSr_{0.33}MnO_3$ and $La_{0.75}Sr_{0.25}MnO_3$

Sample	T_C, K	a_0, μV/K	a_1, 10^{-2} μV/K^2	a_2, 10^{-4} μV/K^3
LaSr	369	–7.2	6.7	–1.9
LaSrEu	328	–3.9	7.4	–2.5
LaSrGd	349	–4.0	6.7	–2.1
Single crystal $La_{0.75}Sr_{0.25}MnO_3$ (from [12])	342	–3.0	9.1	–2.6

The magnetization curves follow a behavior typical of ferromagnets. The values of the Curie temperature T_C determined by the method of thermodynamic coefficients are listed in the table. Doping with Eu or Gd results in a decrease in T_C. For $T < T_C$ and in magnetic fields $H \geq 6$ kOe, the magnetization M is described by the relation $M = M_s + \chi H$.

Figure 1 presents plots of the temperature dependence of susceptibility $\chi(T)$. LaGdSr exhibits a growth of χ with decreasing T in the ferromagnetic region; for LaEuSr, this growth is less pronounced; and for LaSr, it does not occur at all. The increase in χ with decreasing temperature can be assigned to the presence of paramagnetic ions. In LaGdSr, such ions are obviously the

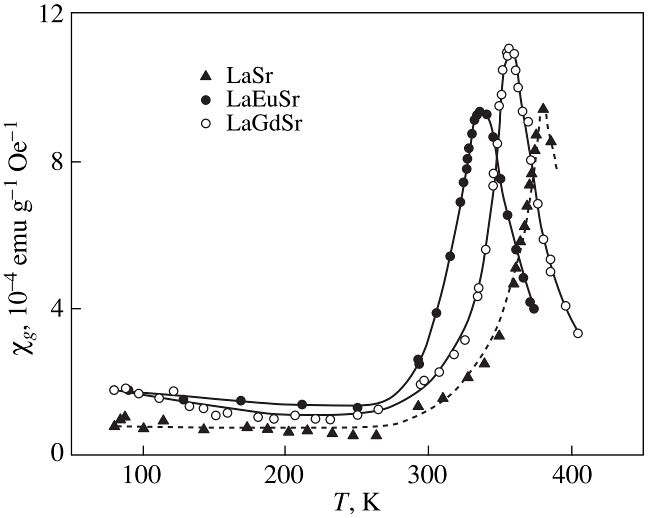

Fig. 1. Temperature dependence of the susceptibility of the paraprocess in $La_{0.67}Sr_{0.33}MnO_3$ (LaSr), $La_{0.60}Eu_{0.07}Sr_{0.33}MnO_3$ (LaEuSr), and $La_{0.60}Gd_{0.07}Sr_{0.33}MnO_3$ (LaGdSr).

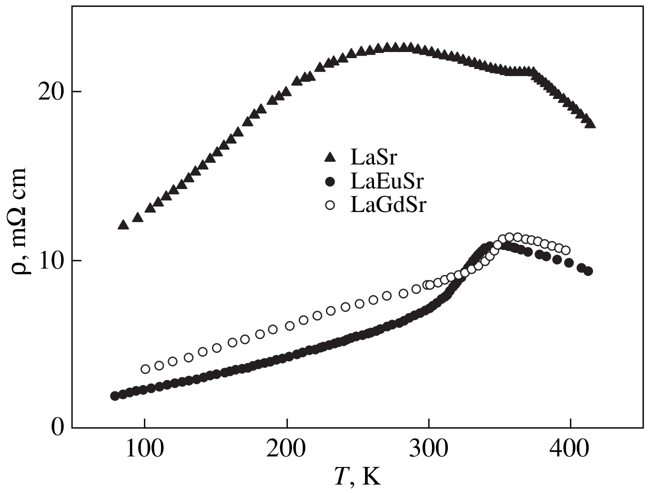

Fig. 2. Temperature dependence of the electrical resistivity of LaSr, LaEuSr, and LaGdSr.

Gd^{3+} ions in the *s* state (spin $S = 7/2$). Because the magnetic moment of the Eu^{3+} ion in the ground state is zero, the presence of paramagnetic ions in LaEuSr implies that these are Eu^{2+}. This provides support for the conjecture [6, 7, 15] that europium resides in LaEuSr in a mixed valence state.

The Curie temperature of polycrystalline LaEuSr is lower than that of LaGdSr, which may be associated with the additional disorder induced by the presence of Eu^{2+} ions with a comparatively large ionic radius. The difference between the T_C values in our samples turned out to be considerably larger than that quoted in [6, 7]. This suggests a high sensitivity of the Curie temperature to defects whose presence is likely to be the reason for the existence of Eu^{2+} ions.

The temperature dependence of resistivity ρ is shown graphically in Fig. 2. The $\rho(T)$ curve for LaSr exhibits two weakly pronounced maxima, one of them lying near the Curie point, and the other, in the ferromagnetic region at $T \approx 280$ K. Doping with europium or gadolinium brings about a considerable decrease in the resistivity, particularly in the ferromagnetic region, with the $\rho(T)$ curves having only one maximum located slightly above T_C. It is known [1] that such differences in temperature behavior and in the value of resistivity of the manganites are due to the contribution of grain boundaries to the sample resistivity increasing with decreasing crystallite size; therefore, one may assume that the crystallites in LaEuSr and LaGdSr samples are considerably larger than those in LaSr.

It would be difficult to make a judgment on the conduction mechanisms from the shape of the $\rho(T)$ curve, because even the presence of a region with $d\rho/dT > 0$ is not proof of transition to the metallic state [9]. Valuable information can be obtained from analysis of the temperature dependence of the ordinary Hall coefficient R_0, which is shown graphically in Fig. 3. In contrast to the $\rho(T)$ curves, the temperature dependences $R_0(T)$ follow the same pattern in all samples. In the ferromagnetic region for $T < 200$ K, the values of R_0 are positive and lie within the interval $(4–6) \times 10^{-12}$ Ω cm/G. Hence, the majority carriers are holes in the metallic state. A straightforward calculation of their concentration using the expression $R_0 = (ecn_h)^{-1}$ yields n_h of the order of 0.8 hole/Mn. The noticeable difference in the calculated value of n_h from the one which can be expected from the doping level is evidence of the existence of an electronic contribution to R_0; analysis of the thermopower data leads one to the same conclusion (see below). The $R_0(T)$ curve for LaSr does not exhibit any features at $T = 280$ K, and, therefore, the maximum in

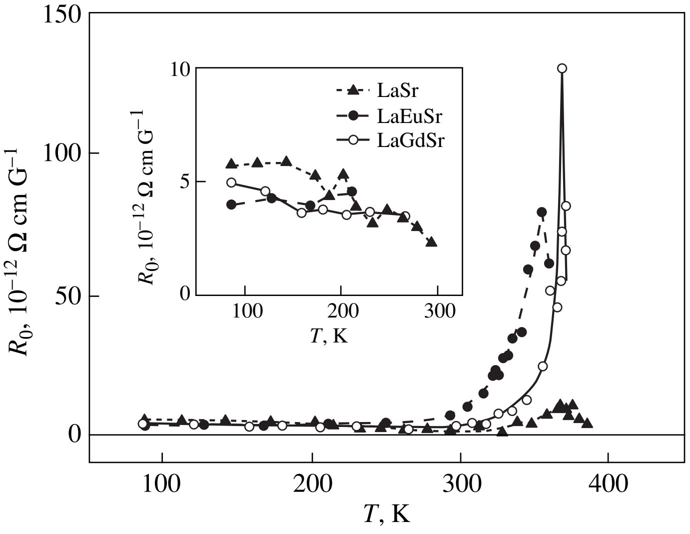

Fig. 3. Temperature dependence of the ordinary Hall coefficient of LaSr, LaEuSr, and LaGdSr.

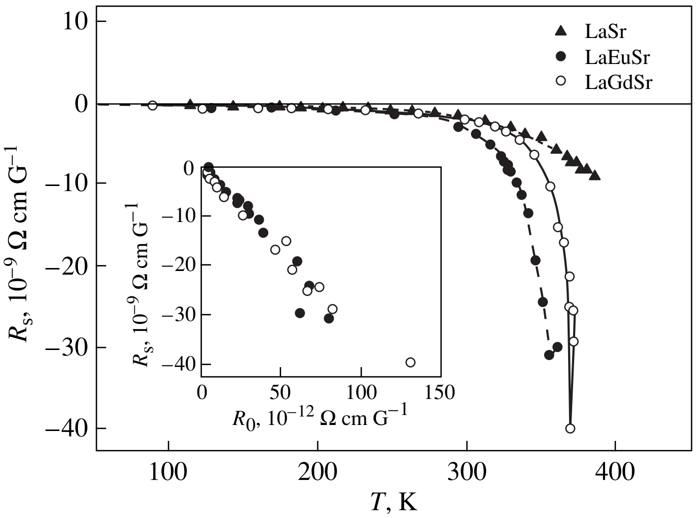

Fig. 4. Temperature dependence of the anomalous Hall coefficient of LaSr, LaEuSr, and LaGdSr.

ρ(T) observed at this temperature cannot originate from intragrain processes. At temperatures of the order of 100 K and lower, the value of R_0 for the LaEuSr sample is slightly smaller than that for LaSr and LaGdSr, which is not in conflict with the conjecture on the presence of Eu^{2+} ions playing the part of additional acceptors.

As one approaches the Curie point, R_0 and the resistivity of the LaEuSr and LaGdSr samples exhibit a rapid growth. It was shown [15] that in LaEuSr, this growth is connected with the motion of the mobility edge and is due to the transition to the insulating state at T_{MI} = 300 K, with the temperature dependence ρ(T) in the region of the peak being described by relation (7) with $E_0^\rho \approx 530$ K and $E_1^\rho \approx 2000$ K. We did not succeed in determining E_0^ρ and E_1^ρ for the LaGdSr and LaSr samples because of the higher values of T_C for these samples. However, because the $R_0(T)$ curves in all three samples are similar, one may assume that T_{MI} in LaGdSr and LaSr also lies below the Curie temperature by approximately 30 K.

The temperature dependences of the anomalous (spontaneous) Hall coefficient R_s follow the same pattern (Fig. 4). For $T < 300$ K, the dependence of R_s on magnetization can be fitted well for all three samples by a second-order polynomial $R_s = (-6.9 + 16.8x - 10.2x^2) \times 10^{-9}$ Ω cm/G, where $x = [M_s(T)/M_s(0)]^2$. In the vicinity of T_C, the anomalous Hall coefficient in LaEuSr and LaGdSr is proportional to the ordinary Hall coefficient (see inset to Fig. 4), whence it follows that the temperature behavior of R_s in this region is governed by the variation of the carrier concentration in delocalized states, i.e., by the motion of the mobility edge.

The temperature dependences of thermopower presented in Fig. 5 have the form typical of lanthanum manganites with a high Mn^{4+} concentration. The $S(T)$ curves for LaEuSr and LaGdSr are similar in behavior while differing noticeably from that for LaSr, which is shifted toward negative values of S. The peak near T_C, which is characteristic of manganites with a comparatively low content of divalent ions, is absent here; the modulus of the derivative $|dS/dT|$ reaches a maximum near the Curie temperature.

The measurements of thermopower and of the Hall effect show the lanthanum manganites to have carriers of both the hole and electron types. The hole contribution S_h to the thermopower in the ferromagnetic region far from T_C is small and proportional to temperature, because the holes are in a metallic state. Analysis of the data obtained on single-crystal samples of $La_{1-x}Sr_xMnO_3$ [12] with x = 0.18, 0.25, and 0.4 suggests that the electrons in these materials have a small activation energy, substantially less than 100 K. Limiting ourselves to the region of $T \geq 100$ K, we may neglect the dependence of the electronic conductivity σ_e and electronic thermopower S_e on temperature. Because the electrons are nonmetallic here, the inequality $|S_e| \gg S_h$ should hold. The resistivity of such single crystals for $T \leq 200$ K is well approximated by the relation [16]

$$\rho(T) = \rho(0) + AT^2. \tag{12}$$

Hence, there are grounds to assume that for $100 < T < 200$ K, the thermopower of the manganites of such compositions can be described by the expression

$$S = S_h - |S_e|\sigma_e\rho. \tag{13}$$

In other words, the $S(T)$ curve should be approximated by a second-order polynomial:

$$S = a_0 + a_1T + a_2T^2, \tag{14}$$

where $a_0 = -|S_e|\sigma_e\rho(0)$, the relation for a_1 follows from Eq. (4), and $a_2 = -|S_e|\sigma_eA$. Obviously enough, a_2/a_0 =

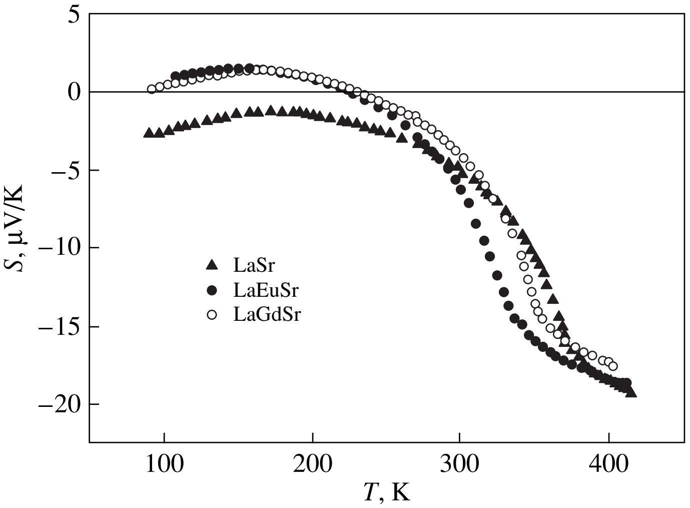

Fig. 5. Temperature dependence of the thermopower of LaSr, LaEuSr, and LaGdSr.

$A/\rho(0)$. As shown by our analysis [12] of the temperature dependence of the thermopower of $La_{0.75}Sr_{0.25}MnO_3$, the $S(T)$ curve for this single crystal is fitted well by the relation of the type $C_1T - C_2\rho$, with C_1 and C_2 being fitting parameters, which is evidence of the validity of the proposed interpretation of the a_i coefficients. Because the strontium content in the above single crystal is close to that in our samples, we treated the $S(T)$ curves obtained on our polycrystals and on the $La_{0.75}Sr_{0.25}MnO_3$ single crystal using Eq. (14). The values of a_i thus obtained are listed in the table. In all our polycrystalline samples, $a_1 \approx 0.07$ μV/K^2, which attests to their hole concentrations being equal. The value of a_1 for $La_{0.75}Sr_{0.25}MnO_3$ is slightly higher, which is in accord with the lower strontium content. Substituting $E_2 - E_F = E_1^\rho - E_0^\rho =$ 1500 K into Eq. (11) yields $a_1 = 0.19$. Because the calculated value is nearly threefold the experimental figure, the mobility edge apparently lies beyond the region where σ_E can be considered a linear function of energy.

The values of $\rho(0)$ and A for $La_{1-x}Sr_xMnO_3$ with $x > 0.2$ are typically 0.1 mΩ cm and 10^{-5} mΩ cm/K^2 [16], which approximately yields 10^{-4} K^{-2} for the $A/\rho(0)$ ratio. In our polycrystals, the ratio a_2/a_0 is of the same order of magnitude: 0.6×10^{-4} for LaEuSr, 0.5×10^{-4} for LaGdSr, and 0.3×10^{-4} K^{-2} for LaSr, which supports the proposed explanation of the temperature dependence of the thermopower. At the same time, it should be pointed out that the magnitude of the coefficient a_0 for the LaSr sample is nearly twofold that for the other samples, while the coefficients a_1 and a_2 differ substantially less. It can be conjectured that the intragrain resistivity in the LaSr sample is about twice that for the other two polycrystals because of increasing imperfection of the material with decreasing crystallite size.

Recalling that the thermopower due to nonmetallic electrons should be of the order of 100 μV/K and setting $|a_0| = 4$ μV/K, we obtain $\sigma_e\rho(0) = 0.04$. As the temperature increases, the contribution of electrons to conductivity also increases; however, in the region of metallic conduction, the σ_e/σ ratio remains less than 10%. This conclusion is in agreement with the Hall data and band-structure calculations [17]. Thus, the significant part played by electrons in the thermopower in the ferromagnetic region is associated not with their large concentration but rather with the small thermopower of the holes in the metallic state.

Near T_C, the ordinary Hall coefficient and the thermopower have opposite signs. As shown above, the main contribution to the conductivity is due to the holes activated to the mobility edge. The negative sign of the thermopower indicates, however, that their contribution to S is substantially smaller than 100 μV/K; hence, it does not follow relation (8). The theoretical considerations presented in the preceding section suggest that the decrease in S_h may be caused by the lower mobility edge approaching the Fermi level at the transition to the paramagnetic phase. In these conditions, the hole conductivity does not decrease as strongly as the thermopower and, therefore, the holes continue to be majority carriers.

Thus, we have shown that codoping $La_{0.67}Sr_{0.33}MnO_3$ with a small amount of Eu or Gd can increase the size of the crystallites and reduce their imperfection without increasing the anneal temperature. Europium resides in $La_{0.60}Eu_{0.07}Sr_{0.33}MnO_3$ in a mixed valence state.

In the vicinity of T_C, the temperature behavior of the ordinary and anomalous Hall coefficients is governed by the variation of the carrier concentration in delocalized states.

In the ferromagnetic region, the concentration of electrons is less by an order of magnitude than that of holes, but the ratio of the hole to electron contributions to the transport coefficients changes as one approaches the Curie temperature. Near T_C, the hole thermopower decreases considerably, which may be associated with the region of existence of delocalized hole states being narrow.

ACKNOWLEDGMENT

This work is supported by the Russian Foundation for Basic Research, grants no. 00-02-17544 and 00-15-96745.

REFERENCES

1. J. M. D. Coey, M. Viret, and S. von Molnar, Adv. Phys. **48** (2), 167 (1999).
2. Y. Tokura and Y. Tomioka, J. Magn. Magn. Mater. **200** (1–3), 1 (1999).
3. S. Jin, H. M. O'Bryan, T. H. Tiefel, *et al.*, Appl. Phys. Lett. **66** (3), 382 (1995).
4. A. Nossov, J. Pierre, V. Vassiliev, and V. Ustinov, J. Phys.: Condens. Matter **8** (44), 8513 (1996).
5. J. Blasco, J. García, J. M. de Teresa, *et al.*, Phys. Rev. B **55** (14), 8905 (1997).
6. A. Nossov, J. Pierre, J. Beille, *et al.*, Eur. Phys. J. B **6**, 467 (1998).
7. J. Pierre, A. Nossov, V. Vassiliev, and V. Ustinov, Phys. Lett. A **250**, 435 (1998).
8. N. G. Bebenin and V. V. Ustinov, J. Phys.: Condens. Matter **10** (28), 6301 (1998).
9. N. G. Bebenin, R. I. Zaĭnullina, V. V. Mashkautsan, *et al.*, Zh. Éksp. Teor. Fiz. **117** (6), 1181 (2000) [JETP **90**, 1027 (2000)].
10. H. Fritzsche, Solid State Commun. **9** (21), 1813 (1971).
11. M. Tokunaga, N. Miura, Y. Moritomo, and Y. Tokura, Phys. Rev. B **59** (17), 11151 (1999).
12. A. Asamitsu, Y. Moritomo, and Y. Tokura, Phys. Rev. B **53** (6), R2952 (1996).
13. P. A. Lee and T. V. Ramakrishnan, Rev. Mod. Phys. **57** (2), 287 (1985).
14. R. I. Zaĭnullina, N. G. Bebenin, V. V. Mashkautsan, *et al.*, Fiz. Tverd. Tela (St. Petersburg) **40** (11), 2085 (1998) [Phys. Solid State **40**, 1889 (1998)].
15. R. I. Zaĭnullina, N. G. Bebenin, V. V. Mashkautsan, *et al.*, Fiz. Tverd. Tela (St. Petersburg) **42** (2), 284 (2000) [Phys. Solid State **42**, 292 (2000)].
16. A. Urushibara, Y. Moritomo, T. Arima, *et al.*, Phys. Rev. B **51** (20), 14103 (1995).
17. W. E. Pickett and D. J. Singh, J. Magn. Magn. Mater. **172**, 237 (1997).

Translated by G. Skrebtsov

Physics of the Solid State, Vol. 43, No. 3, 2001, pp. 508–512. Translated from Fizika Tverdogo Tela, Vol. 43, No. 3, 2001, pp. 489–494.
Original Russian Text Copyright © 2001 by Abdulvakhidov, Mardasova, Myasnikova, Kogan, Spinko, Kupriyanov.

MAGNETISM AND FERROELECTRICITY

Phase Transitions in Lead Scandoniobate $PbSc_{0.5}Nb_{0.5}O_3$

K. G. Abdulvakhidov, I. V. Mardasova, T. P. Myasnikova,
V. A. Kogan, R. I. Spinko, and M. F. Kupriyanov
Rostov State University, pr. Stachki 194, Rostov-on-Don, 344090 Russia
e-mail: kupri@phys.rnd.runnet.ru

Received May 23, 2000; in final form, August 3, 2000

Abstract—Crystals of $PbSc_{0.5}Nb_{0.5}O_3$ are investigated by x-ray diffraction and optical spectroscopy. It is found that the phase transformations in $PbSc_{0.5}Nb_{0.5}O_3$ are governed by two mechanisms: displacive ferroelectric phase transitions and consistent rotations of oxygen octahedra. *© 2001 MAIK “Nauka/Interperiodica”.*

1. INTRODUCTION

The considerable interest expressed by researchers in the structural and physical properties of lead scandoniobate $PbSc_{0.5}Nb_{0.5}O_3$ (PSN) [1–7] is associated with the general problem concerning the microscopic interpretation of the specific features of the ferroelectric state in oxygen-containing perovskites with the composition $Pb(B'_{1-x}B''_x)O_3$ (x = 1/2 and 1/3). Until presently, the particular type of structural ordering in relaxor ferroelectrics has not been established conclusively [8–10]. It has remained unclear whether there is an ordering (disordering) of different-type atoms (B' and B") in the same sublattice of the structure that is controlled by the high-temperature annealing. By now, the experiments have provided a large body of information on this group of perovskites, including ferroelectric $PbSc_{0.5}Nb_{0.5}O_3$. Considerable difficulties in solving structures of ferroelectric phases of these compounds are associated with the problems regarding the correct determination of the structure parameters of the real crystals under investigation [5, 10].

Earlier, it was revealed that $PbSc_{0.5}Nb_{0.5}O_3$ crystals either can undergo a normal phase transition (without indications of relaxation) from the ferroelectric to paraelectric phase [3] or can exhibit pronounced properties of relaxor ferroelectrics [2, 6]. The phase transition temperature of $PbSc_{0.5}Nb_{0.5}O_3$ and its physical properties depend on the thermal prehistory of the crystal. It was reliably established that the heating of the $PbSc_{0.5}Nb_{0.5}O_3$ compound from room temperature to the phase transition point leads to a decrease in the unit cell volume [3, 6, 11]. Moreover, it was shown that $PbSc_{0.5}Nb_{0.5}O_3$ undergoes an usual thermal expansion in the temperature range from 10 to 300 K [11]. The atomic structure of $PbSc_{0.5}Nb_{0.5}O_3$ was determined at different temperatures [11, 12]. Although Malibert *et al.* [11] analyzed the $PbSc_{0.5}Nb_{0.5}O_3$ structure by different methods (neutron diffraction and x-ray diffraction analyses, including techniques with the use of synchrotron radiation), they reported only the neutron diffraction data at 10 and 523 K. For the ferroelectric phase of $PbSc_{0.5}Nb_{0.5}O_3$ at 10 K, it was found that the Sc/Nb atoms are displaced from the center of a perovskite cell along the [111] direction by 0.235 Å, whereas the oxygen atoms at the same values $\delta x = \delta y = 0.051$ are displaced by $\delta z = 0.039$. For the paraelectric phase of $PbSc_{0.5}Nb_{0.5}O_3$ at 523 K, the Debye–Waller factors are as follows: B(Pb) = 4.33 Å^2, B(Sc/Nb) = 0.84 Å^2, B_{11}(O) = B_{22}(O) = 0.043 Å^2, and B_{33}(O) = 0.014 Å^2. According to [12], the Debye–Waller factors for the paraelectric phase of $PbSc_{0.5}Nb_{0.5}O_3$ at 400 K are B(Pb) = 4.15 Å^2, B(Sc/Nb) = 0.95 Å^2, B_{11}(O) = 0.90 Å, and B_{22}(O) = B_{33}(O) = 2.66 Å^2; and the Sc/Nb atoms in the ferroelectric phase at 200 K, as in [11], are displaced along the [111] direction by 0.242 Å. In this case, the oxygen atoms are displaced along the [010] and [001] directions by 0.189 Å and along the [100] direction by 0.123 Å.

It should be noted that a series of extremely weak superstructure reflections was revealed by Caranoni *et al.* [1]. According to [1], these reflections are associated with the possible short-range order in the arrangement of Sc and Nb atoms only in the *xy* planes.

In the present work, we investigated the structure of $PbSc_{0.5}Nb_{0.5}O_3$ crystals, their optical absorption spectra in the visible and IR ranges, and the electrical conductivity in order to elucidate the specific features of the phase states and to reveal the correlation between the possible structural models of these states and their physical properties.

2. EXPERIMENTAL TECHNIQUE

2.1. Crystal growth. Crystals of $PbSc_{0.5}Nb_{0.5}O_3$ were grown from a solution which was preliminarily synthesized by the solid-phase reaction of the $PbSc_{0.5}Nb_{0.5}O_3$ compound with a PbO melt. Two branches of the crystallization indicated its eutectic character. The eutectics corresponded to the 0.9PbO–0.1PSN composition at 860°C. The high volatility of

PbO and a low quality of the $PbSc_{0.5}Nb_{0.5}O_3$ crystals obtained under these conditions necessitate the use of a $PbO–B_2O_3$ mixture as a solvent. The best crystals of $PbSc_{0.5}Nb_{0.5}O_3$ were obtained using the $0.78PbO–0.17B_2O_3–0.05PSN$ composition. Homogenizing of the resultant solution at a temperature of 1100°C for 4 h and its cooling to 950°C at a rate of 5 K/h brought about the formation of high-quality $PbSc_{0.5}Nb_{0.5}O_3$ crystals in the form of plates 0.3 × 0.3 cm in size and cubes with edges as large as 0.4 cm.

2.2. Optical and electrical investigations. Crystals of $PbSc_{0.5}Nb_{0.5}O_3$ were examined with a polarizing microscope for the purpose of revealing the morphology of their block or domain structures. The optical absorption spectra in IR (3500–14 500 cm^{-1}) and visible (400–750 nm) ranges and their temperature evolution were investigated on IKS-14A and SF-14 spectrophotometers. The electrical conductivity of $PbSc_{0.5}Nb_{0.5}O_3$ crystals was studied using a V-483 nanovoltmeter.

2.3. X-ray structure investigations. The crystal structure of the $PbSc_{0.5}Nb_{0.5}O_3$ compound was investigated by the Laue and rotating crystal methods with an HZG-4B diffractometer (CuK_α radiation) and an Enraf–Nonius diffractometer CAD-4 (MoK_α radiation), respectively. The structure amplitudes of 246 reflections were obtained on the Enraf–Nonius diffractometer CAD-4 for a $PbSc_{0.5}Nb_{0.5}O_3$ crystal of spherical form (the data were corrected for the Lorentz and polarization factors and absorption).

No extinction corrections were applied. The temperature investigations of a $PbSc_{0.5}Nb_{0.5}O_3$ powder were performed on a DRON-3.0 diffractometer in a special chamber which ensured the temperature stability in the range from 20 to 200°C with an accuracy of no worse than ±1 K.

3. RESULTS

3.1. The domain structure of $PbSc_{0.5}Nb_{0.5}O_3$ crystals at room temperature in the ferroelectric rhombohedral phase is rather complex and depends on the growth conditions and crystal sizes. Thin lamellar crystals 0.01 × 0.01 cm in size have sufficiently clear domain boundaries which can easily be observed with a polarizing microscope. It is revealed that, upon etching of large-sized crystals of $PbSc_{0.5}Nb_{0.5}O_3$ (the thickness h is of the order of 1 mm), the domain structure has a different configuration (Fig. 1). This can be explained by the presence of growth defects and residual mechanical strains arising upon cooling the crystals and during the ferroelectric phase transition [13].

Figure 2 shows the temperature evolution of the absorption spectra of $PbSc_{0.5}Nb_{0.5}O_3$ lamellar crystals for which the [100] direction is perpendicular to the crystal surface. In the visible range, the spectra contain two absorption bands I and II with maxima at 405 and

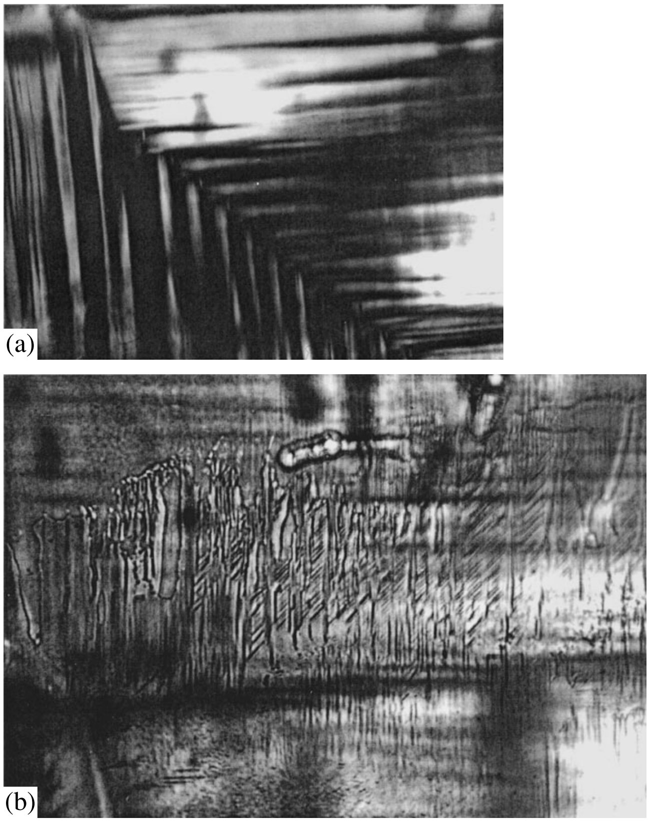

Fig. 1. Fragments of the domain structure at different thicknesses of a $PbSc_{0.5}Nb_{0.5}O_3$ single crystal.

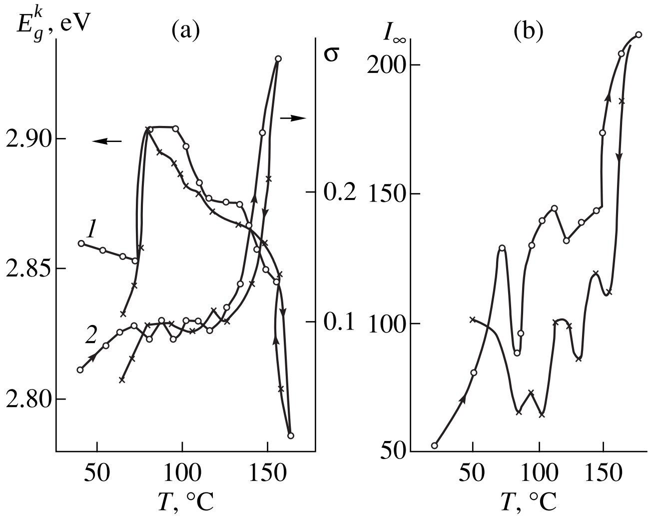

Fig. 2. (a) Temperature dependences of (*1*) the energy location of absorption edge E_g^k at ln$k$ = 5.1 and (*2*) the parameter σ for a $PbSc_{0.5}Nb_{0.5}O_3$ single crystal 0.051 cm thick. Circles and crosses correspond to heating and cooling, respectively. (b) Temperature dependences of the integrated intensity of the absorption band at λ_{max} = 685 nm for a $PbSc_{0.5}Nb_{0.5}O_3$ single crystal.

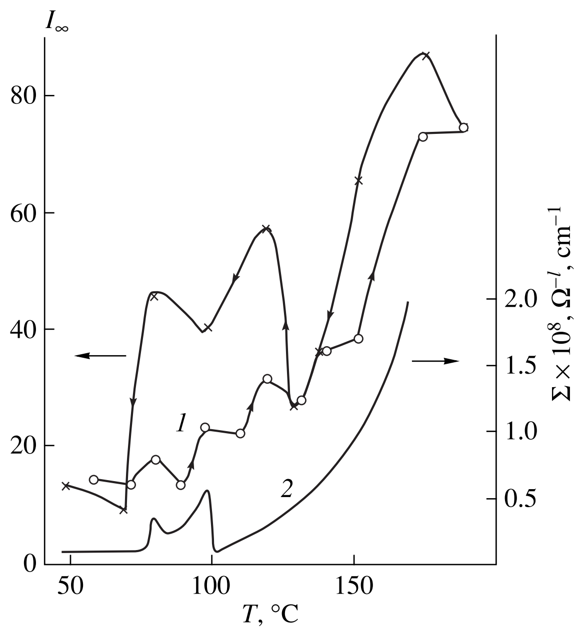

Fig. 3. Temperature dependences of (*1*) the integrated intensity I_∞ of the absorption band at $\omega_{\max}$ = 8600 cm^{-1} and (*2*) the electrical conductivity Σ for a $PbSc_{0.5}Nb_{0.5}O_3$ single crystal.

685 nm, respectively. Upon heating of the crystal, the absorption edge (band *I*) near 70°C shifts toward the short-wavelength range, and above 100°C, it is displaced toward the long-wavelength range and follows the Urbach rule. The parameter $\sigma = (\Delta \ln k/\Delta \hbar\omega)kT$, which characterizes the slope of the linear dependence of the logarithm of the absorption coefficient k on the incident photon energy, has resonance minima at temperatures of 70, 90, and 120°C upon heating of the $PbSc_{0.5}Nb_{0.5}O_3$ crystal and minima at 130 and 100°C upon its cooling (Fig. 2a). The temperature dependence of the energy location of the absorption edge E_g^k (at a constant absorption coefficient) exhibits the following features: upon heating of the crystal, E_g^k jumpwise increases by 0.047 eV near 70°C (at $\ln k = 5.1$), decreases by 0.029 eV near 90°C, and decreases by 0.046 eV near 140°C. The electron–phonon coupling constant g is equal to 3.56 at temperatures below 70°C, 4.36 in the range 70–120°C, and 2.59 above 120°C [14, 15]. The effective phonon energy $\hbar\omega_{\text{eff}}$ is equal to 542 cm^{-1} below 70°C, 526 cm^{-1} above 70°C, and 607 cm^{-1} above 120°C [14, 15]. The absorption band *II* ($\lambda_{\max}$ = 685 nm) is bell-shaped and has a half-width of 0.31 eV at 140°C. This band can be associated with *F*-centers in the $PbSc_{0.5}Nb_{0.5}O_3$ crystal [16, 17]. Upon heating of the $PbSc_{0.5}Nb_{0.5}O_3$ crystal, the absorption band *II* exhibits weak maxima at temperatures of 70 and 100°C and a drastic increase in the integrated intensity I_∞ above 140°C (Fig. 2b). Upon cooling of the crystal, the temperature dependence of the integrated intensity I_∞ has small maxima at 140, 120, and 90°C. Below 80°C, the intensity of band *II* increases with a decrease in the temperature.

In the IR range, the spectrum of the $PbSc_{0.5}Nb_{0.5}O_3$ crystal exhibits a bell-shaped absorption band with the center at 8600 cm^{-1} and a half-width of 1.05 eV at 120°C. Upon heating of the crystal, the integrated intensity I_∞ increases with small anomalies at temperatures of 70 and 110°C and a noticeable maximum at 150°C. Upon cooling, I_∞ has a more pronounced maximum at the same temperatures (Fig. 3). The temperature dependence of the electrical conductivity of the $PbSc_{0.5}Nb_{0.5}O_3$ crystal (curve *2*), its features observed at 70 and 100°C, and a sharp increase in the electrical conductivity at temperatures above 150°C allow us to assign the IR absorption band ($\omega_{\max}$ = 8600 cm^{-1}) to a polaron of small radius with the activation energy E_a = 0.27 eV [16].

3.2. At the first stage of x-ray structure analysis of $PbSc_{0.5}Nb_{0.5}O_3$ crystals with the use of the Laue x-ray patterns and rotating-crystal x-ray photographs, we chose the crystal without indications of twining. In a series of rotating-crystal x-ray photographs obtained at large exposures, we observed weak diffuse superstructure reflections that corresponded to twice the perovskite cell periods. The x-ray diffraction patterns were recorded upon rocking of the crystal about the [111] direction in a perovskite setting. In addition to the above reflections, the x-ray diffraction photographs contained superstructure reflections that corresponded to a more than twofold multiplication of the perovskite cell periods. The diffuse character of the superstructure reflections and their extremely low intensity suggest a limited size of the ordering regions of either the Sc and Nb atoms or antiparallel atomic displacements. These data correlate with the results obtained in [1]. The x-ray diffraction patterns obtained with a Guinier camera also show weak superstructure reflections that correspond to an eightfold multiplication of the perovskite cell parameters for $PbSc_{0.5}Nb_{0.5}O_3$ crystals. A detailed analysis of the superstructure of $PbSc_{0.5}Nb_{0.5}O_3$ crystals will be described in a separate paper.

The structure of the $PbSc_{0.5}Nb_{0.5}O_3$ crystal was refined in the hexagonal setting of a perovskite-type structure with A_H = 5.768(2) Å and C_H = 7.062(3) Å, which corresponds to the rhombohedral perovskite cell with the parameters a_R = 4.079(2) Å and α_R = 89.88(3)°. In the approximation of the complete disordering of Sc and Nb atoms in the lattice, the atomic parameters were determined by the local search method with minimization of the appropriate functional. The refinement led to the structural model for $PbSc_{0.5}Nb_{0.5}O_3$ with the discrepancy factor R = 0.045. The least R value was obtained using the Debye–Waller factors. The refinement of the atomic displacements for oxygen δx_0 by using the *hki*0-type reflections reduced the discrepancy factor to R = 0.012 at δx_H = 0.033. The final refinement

Table 1. Coordinates of oxygen atoms in a hexagonal setting of the unit cell of $PbSc_{0.5}Nb_{0.5}O_3$

Atom	x_H	y_H	z_H
O_I	$1/6 + \delta x_0$	$5/6 - \delta x_0$	$2/3 + \delta z_0$
O_{II}	$1/6 + \delta x_0$	$1/3 + 2\delta x_0$	$2/3 + \delta z_0$
O_{III}	$2/3 - 2\delta x_0$	$5/6 - \delta x_0$	$2/3 + \delta z_0$
O_{IV}	$1/2 + \delta x_0$	$1/2 - \delta x_0$	$0 + \delta z_0$
O_V	$1/2 + \delta x_0$	$0 + 2\delta x_0$	$0 + \delta z_0$
O_{VI}	$-2\delta x_0$	$1/2 - \delta x_0$	δz_0
O_{VII}	$5/6 + \delta x_0$	$1/6 - \delta x_0$	$1/3 + \delta z_0$
O_{VIII}	$5/6 + \delta x_0$	$2/3 + 2\delta x_0$	$1/3 + \delta z_0$
O_{IX}	$4/3 - 2\delta x_0$	$1/6 - \delta x_0$	$1/3 + \delta z_0$

of the atomic structure in the $PbSc_{0.5}Nb_{0.5}O_3$ crystal revealed that, at room temperature, the Sc/Nb atoms are displaced from the center of the perovskite cell along the [111] direction by the distance $\delta z_H(Sc/Nb) = 0.017(2)$ (0.12 Å) at $B_{iso}(Sc/Nb) = 2.3(2)$ Å^2. The oxygen atoms are displaced by the distance $\delta z_H(O) = 0.035(2)$ along the [111] direction and $|\delta y_H(O)| = 0.017(2)$ in perpendicular directions of the [110] type; in this case, $B_{iso}(Sc/Nb) = 2.6(1)$ Å^2. Note that the displacements obtained for the Sc (Nb) and O atoms in [11, 12] exceed those determined at room temperature in the present work by a factor of 2 and 1.5, respectively. In the ferroelectric phase at room temperature, the “mean” Sc/Nb atoms in the found structural model are uniquely displaced along the [111] direction in a perovskite cell (along the [001] direction in a hexagonal setting) and specify the direction of spontaneous polarization. In addition to the displacements along the [111] direction $\delta z_H(O)$, the oxygen atoms undergo additional displacements along the x_H and y_H axes (in a hexagonal setting) according to the space group $R3$m (Table 1).

Table 2 presents the results of structural investigations of the $PbSc_{0.5}Nb_{0.5}O_3$ single crystal and the structure parameters determined by x-ray powder diffraction [18] at different temperatures.

4. DISCUSSION

Since the $PbSc_{0.5}Nb_{0.5}O_3$ structure was refined without regard for the structure amplitudes because of their smallness, we did not considere the effects of superstructural ordering of either the Sc and Nb atoms or antiparallel atomic displacements. However, it should be noted that the oxygen atoms undergo small displacements along the x_H and y_H axes. On the one hand, these displacements can be interpreted as the result of distortions of oxygen octahedra (with respect to their sizes in an ideal cubic phase) with the formation of oxygen triangles in the closest cubic packing planes. These triangles are perpendicular to the threefold polar axis of the ferroelectric rhombohedral phase and can be separated into two types, namely, oxygen triangles with shortened oxygen–oxygen distances and oxygen triangles with lengthened oxygen–oxygen distances. On the other hand, the observed displacements of oxygen atoms can correspond to rotations of oxygen octahedra that are associated with the R_{25} or M_3 modes [19]. An important point is that the consistent rotations of oxygen octahedra are accompanied by the following effects: first, a decrease in the lattice parameter and, second, the formation of the superstructure due to anti-

Table 2. Structure of $PbSc_{0.5}Nb_{0.5}O_3$

Parameter	$R3m$ rhombohedral phase				$Pm3m$ cubic phase	
T, K	293*	303	343	358	393	473
A_H, Å	5.768(2)	5.7680(2)	5.7691(2)	5.7695(2)	5.7727(2)	5.7738(2)
C_H, Å	7.082(3)	7.0844(4)	7.0802(4)	7.0772(5)	7.0701(3)	7.0714(3)
a_R, Å	4.082(2)	4.0824(1)	4.0821(1)	4.0817(1)	4.0819(1)	4.0827(1)
α_R, deg	89.88(3)	89.89(3)	89.92(3)	89.94(3)	90.00	90.00
$\delta z_H(Sc/Nb)$	0.017(2)	0.017(2)	0.013(2)	0.002(1)	0	0
$\delta z_H(O)$	0.035(3)	0.032(3)	0.034(2)	0.037(2)	0	0
$\delta x_H(O)$	0.017(2)	0.016(2)	0.017(2)	0.019(2)	0	0
B(Pb), Å^2	1.8(1)	0.79(10)	0.80(10)	2.01(13)	2.82(14)	3.07(16)
B(Sc/Nb), Å^2	2.3(1)	0.79(10)	0.80(10)	2.01(13)	2.82(14)	3.07(16)
B(O), Å^2	2.6(2)	0.79(10)	0.80(10)	2.01(13)	2.82(14)	3.07(16)
Number of reflections N	170	19	19	19	9	9
Number of refined parameters n	6	4	4	4	1	1
R	0.045	0.059	0.058	0.055	0.057	0.064

* Data for the $PbSc_{0.5}Nb_{0.5}O_3$ single crystal.

parallel displacements of oxygen atoms. From this viewpoint, the decrease in the perovskite cell parameter with an increase in the temperature, the constancy of the δx_H values for oxygen atoms below the phase transition point, and the superstructure observed in x-ray diffraction and electron diffraction experiments allow us to assume that, in $PbSc_{0.5}Nb_{0.5}O_3$ crystals, an increase in temperature up to the phase transition point is accompanied by a gradual stabilization in the phase of the R3*c* symmetry with the superstructure unit cell. Such a structural model of the phase states of certain ferroelectric perovskites (characterized by the smeared phase transition, strong effect of the measuring field frequency on the temperature of the permittivity maximum, violation of the classical Curie–Weiss law in paraelectric phases, etc.) is in reasonable agreement with the features of the second-order phase transition described above.

In conclusion, it should be noted that the observed atomic displacements along the z_H (Sc/Nb and O) axis correspond to the spontaneous polarization P_s. The displacements of oxygen atoms δx_H and δy_H are unrelated to the polarization. They are aligned antiparallel, mutually compensated in the unit cell, and hence, cannot be transformed as components of the polarization vector. It is believed that, in real $PbSc_{0.5}Nb_{0.5}O_3$ crystals, the physical properties are associated with the order parameters of different nature. Two mechanisms of phase transformations in $PbSc_{0.5}Nb_{0.5}O_3$ crystals—displacive ferroelectric phase transitions with the emergence of spontaneous polarization with a decrease in temperature of the paraelectric phase and rotational vibrations of oxygen atoms (rotations of oxygen octahedra about the [100] directions as undistorted structural units)—are responsible for the observed features in the physical properties of real $PbSc_{0.5}Nb_{0.5}O_3$ crystals. This provides the explanation for the fact that the properties of $PbSc_{0.5}Nb_{0.5}O_3$ crystals are highly sensitive to the types and the concentration of different defects, which are determined by the prehistory of the crystals, including the conditions of high-temperature annealing.

REFERENCES

1. C. Caranoni, P. Lampin, I. Siny, *et al.*, Phys. Status Solidi A **130**, 25 (1992).
2. K. Bormans, M. Dambekalne, and E. Gerdes, Ferroelectrics **131**, 201 (1992).
3. M. F. Kupriyanov, A. V. Turik, S. M. Zaitsev, and E. G. Fesenko, Phase Transit. **4**, 65 (1983).
4. M. Kupriyanov and V. Kogan, Ferroelectrics **124**, 213 (1991).
5. K. G. Abdulvakhidov and M. F. Kupriyanov, Kristallografiya **41** (6), 1066 (1996) [Crystallogr. Rep. **41**, 1013 (1996)].
6. F. Chu, J. M. Reaney, and N. Setter, J. Appl. Phys. **77** (4), 1671 (1995).
7. N. Takesue, Y. Fuji, M. Jchihara, and H. Chen, Phys. Rev. Lett. **82** (18), 3709 (1999).
8. H. D. Rosenfeld and T. Egami, Ferroelectrics **158**, 351 (1994).
9. B. E. Vugmeister and H. Rabitz, Ferroelectrics **206–208**, 265 (1998).
10. F. Chu, J. M. Reaney, and N. Setter, J. Am. Ceram. Soc. **78** (7), 1947 (1995).
11. C. Malibert, B. Dkhil, J. M. Kiat, *et al.*, J. Phys.: Condens. Matter **9**, 7485 (1997).
12. K. S. Knight and K. Z. Baba-Kishi, Ferroelectrics **173**, 341 (1995).
13. F. Jona and G. Shirane, *Ferroelectric Crystals* (Pergamon, Oxford, 1962; Mir, Moscow, 1965).
14. T. P. Myasnikova, S. G. Gakh, and V. N. Shalaev, Kristallografiya **43** (3), 502 (1998) [Crystallogr. Rep. **43**, 463 (1998)].
15. E. N. Myasnikov, R. I. Spinko, E. A. Shalaeva, and T. P. Myasnikova, Ferroelectrics **214**, 177 (1998).
16. É. V. Bursian, *Nonlinear Crystal: Barium Titanate* (Nauka, Moscow, 1977).
17. S. I. Pekar, *Investigations on the Electron Theory of Crystals* (GITTL, Moscow, 1969).
18. V. Kogan and M. Kupriyanov, J. Appl. Crystallogr. **25**, 16 (1992).
19. V. I. Zinenko, Fiz. Tverd. Tela (Leningrad) **17**, 1064 (1975) [Sov. Phys. Solid State **17**, 678 (1975)].

Translated by O. Borovik-Romanova

Physics of the Solid State, Vol. 43, No. 3, 2001, pp. 513–516. Translated from Fizika Tverdogo Tela, Vol. 43, No. 3, 2001, pp. 495–498.
Original Russian Text Copyright © 2001 by Milov, Strukov.

MAGNETISM AND FERROELECTRICITY

Pyroelectric Effect and Spontaneous Polarization in High-Temperature Ferroelectric $LaBGeO_5$ (LBGO)

E. V. Milov and B. A. Strukov
Moscow State University, Vorob'evy gory, Moscow, 119899 Russia

Received August 7, 2000

Abstract—The temperature dependence of the pyroelectric coefficient of the new high-temperature ferroelectric LBGO in a single-domain state is determined. These data are used to reconstruct and describe the temperature dependence of the spontaneous polarization within the 50- to 540°C range. The possible existence of a second phase transition in this crystal is discussed. © *2001 MAIK "Nauka/Interperiodica".*

The ferroelectric properties of LBGO crystals were discovered in 1992 [1]. These crystals have the stillwellite structure and transfer to the ferroelectric state at $T_c = 532°C$, and the temperature dependence of the low-frequency dielectric permittivity in the paraelectric phase obeys the Curie–Weiss law with a constant C = 3200–3600 K [1, 2]. This value, as well as the magnitude of the excess entropy of the phase transition $\Delta S = 0.1R$ [2], indicated that the phase transition in LBGO is intermediate between the displacive- and order–disorder-type. Raman scattering data [3] and a high-precision neutron diffraction analysis [4] confirmed the complex character of the structure rearrangement the crystal undergoes when transferring to the polar phase. In some cases, LBGO exhibits a "splitting" of the phase transition, so that the permittivity, the loss tangent, and the heat capacity have two anomalies separated by a temperature interval of 1–5 K, which may correspond to an intermediate phase [1, 2].

Remarkably, the comparatively high phase transition temperature makes spontaneous polarization measurements difficult because of a fairly high temperature-dependent electrical conductivity and a strong increase in the coercive field below 300°C [5]. The available experimental data on the temperature dependence of the spontaneous polarization, which are derived from measurements of the second-harmonic generation (SHG) intensity performed on a finely disperse powder [1] and calorimetric studies [2], provide strongly differing results (P_s = 12 in [1] and 3 $\mu C/cm^2$ in [2] at room temperature). Symmetric hysteresis loops distorted by conduction were observed above 400°C, while below 250°C, no switching of spontaneous polarization at 60 Hz was observed to occur in fields of up to 6 kV/cm [5]. The high electrical conduction also hindered measurements of the pyroelectric coefficient; the available data obtained at temperatures up to ~400°C [1] are at odds with the figures expected from the temperature dependence of the SHG intensity.

This uncertainty in the temperature dependence and in the spontaneous polarization, an important parameter of the ferroelectric phase transition in LBGO crystals, stimulated our interest in a more comprehensive investigation of the pyroelectric properties of this crystal over a broad temperature region and around the phase transition. Application of an improved technique for measuring small (down to 1 pA) currents at a comparatively small (~10 kΩ) input resistance of the measuring system permitted us to carry out an extensive study of the pyroelectric properties of the LBGO crystals and to determine and describe the temperature dependence of their spontaneous polarization.

1. EXPERIMENTAL TECHNIQUES

The samples of the LBGO crystal were plates, ~1 cm^2 in area and 2 mm thick, cut perpendicular to the polar c axis of the crystal, which has trigonal symmetry $P3_1$ in the polar phase. The polished samples were transparent and did not reveal visible inhomogeneities. Gold electrodes ~1 μm thick were deposited by RF cathode sputtering on the plate faces. To exclude generation of parasitic thermopower, the wire leads into the high-temperature chamber were made of gold. The insulating components of the high-temperature lead-in and of the sample holder were made of quartz glass. All measurements were carried out under heating at a rate of ~0.15 K/s, which was maintained by means of a heating controller within the temperature range of 30 to 600°C. The temperature was measured with a chromel–alumel thermocouple with an absolute error of ±1.5 K and a sensitivity of 0.1 K.

Our technique of closed-circuit measurement of the pyroelectric current, with the sample temperature varied at a constant rate, permitted the distortions due to the intrinsic conductivity of the crystal to be reduced to a minimum. To increase the charge sensitivity and the accuracy of charge integration, as well as to reduce the input resistance of the setup, we used the modulation

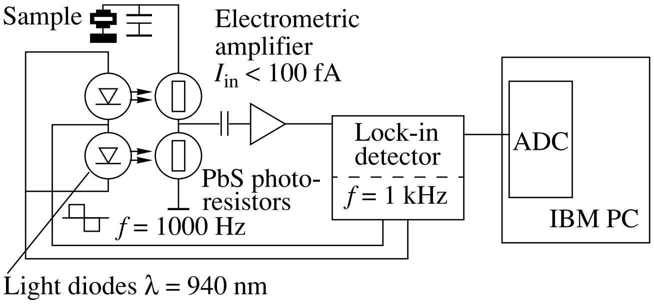

Fig. 1. Block diagram of the setup for pyroelectric current measurements.

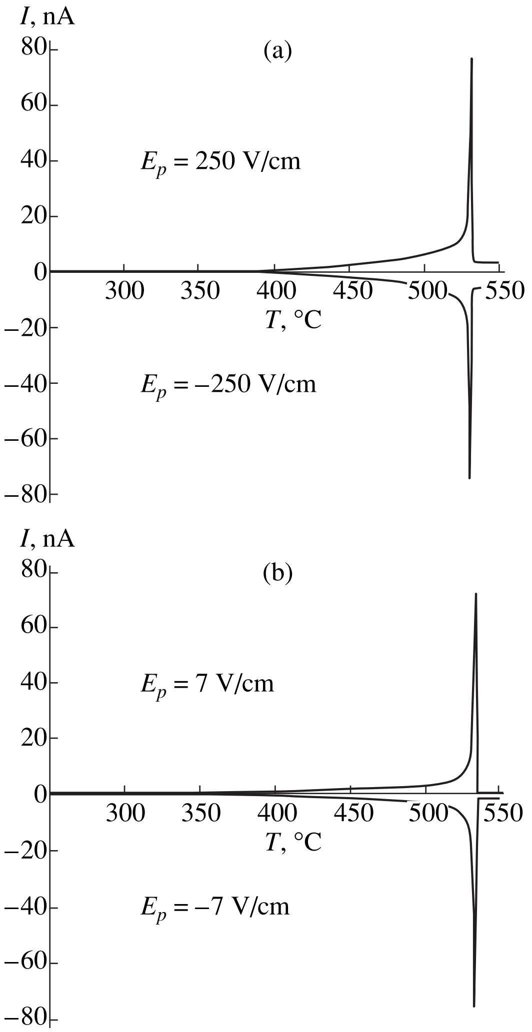

Fig. 2. Temperature dependence of the pyroelectric current in LBGO crystals obtained for two values of the field applied to make the sample single-domain: (a) ±250 and (b) ±7 V/cm.

method, whose essence is explained in Fig. 1. The current generated in the heated sample is fed into a photoresistor modulator consisting of two fast, alternately illuminated PbS photoresistors. The modulator converts the slowly varying current in the sample circuit to an ac voltage of 1 kHz, which will be subsequently amplified by an electrometric amplifier. The signal thus obtained passes lock-in detection and is sent through a 16-bit ADC to a computer, which performs on-line digital integration to yield the pyroelectric current and the total charge passed. It is essential that using the modulation method permitted us to increase the input resistance of the setup to 75 kΩ at the lowest sample resistance of ~5 MΩ in the temperature range covered. Thus, the error introduced by the intrinsic sample conductivity into the sample pyroelectric current measurements did not exceed 1.5%.

Prior to measurements, the sample was first heated in a closed circuit at 630°C for 30 min to reduce the current presumably associated with the electret effect and then cooled in a dc electric field E_p to the temperature at which the measurements were started. We are going to present the data for two values of E_p, 250 and 7 V/cm below. As we shall see, a field of 7 V/cm is high enough to make the samples single-domain.

2. EXPERIMENTAL RESULTS

Figure 2 presents temperature dependences of the current passing through the sample circuit when heated at a constant rate of 0.15 K/s. The sample was subjected preliminarily to dc fields of opposite polarities of the magnitude specified above; by convention, the top parts of Figs. 2a and 2b relate to the positive direction of the electric field, and the lower parts, to the negative one. The sign of the pyroelectric current in the circuit is seen to depend on the direction of the field E_p, that is, on the direction of the spontaneous polarization in the crystal. The sample that had not been subjected to prepolarization exhibited pyroelectric currents lower, on average, by an order of magnitude than those shown in Fig. 2, which indicated the polydomain state of the crystal. As is evident from a comparison of Figs. 2a and 2b, cooling a sample already in a 7-V/cm field results in its becoming completely single-domain; indeed, the results of pyroelectric current integration on cooling in the fields of 7 and 250 V/cm are practically identical, provided one neglects the parasitic current flowing through the sample above the phase-transition point after the sample is made single-domain in a field of 250 V/cm. This current, clearly seen in Fig. 2a, is apparently associated with the spread of the space charge, which appears in a sample cooled through the Curie point in a high enough electric field. This effect is more clearly pronounced for negatively directed E_p (the lower part of Fig. 2a). For us, it was essential that after polarization in the 7-V/cm field, there was no parasitic current in the positive field, and this provided grounds for believing that the behavior of the current flowing through the crystal is governed in this case only by the variation of the spontaneous polarization.

Two features in the behavior of the pyroelectric coefficient p (connected with the pyroelectric current through the relation $i_p = pSdT/dt$) are of interest to us here, namely, its absolute magnitude within the “working” temperature interval and in the immediate vicinity of the Curie point. The corresponding data are displayed in Fig. 3. One readily sees that the magnitude of p lies, over a broad temperature interval, within 2–3 nC K^{-1} cm^{-2}; the inset to Fig. 3 shows a gradual growth of the pyroelectric coefficient with $T \longrightarrow T_c$ and its sharp drop at the transition point to the paraelectric phase. Note also the shoulder in the temperature course of the pyroelectric coefficient at the temperature $T_c - 1$ K seen for both directions of E_p.

The temperature dependence of the spontaneous polarization obtained by integrating the pyroelectric current within a broad temperature interval is shown in Fig. 4. The curve is seen to have the “classical” pattern characteristic of second-order phase transitions. The magnitude of the spontaneous polarization was found to be nearly three times lower than that quoted in [1], but again one-half larger than that given in [2].

3. DISCUSSION OF RESULTS

The temperature dependence of the LBGO spontaneous polarization obtained was treated in terms of Landau’s theory of second-order phase transitions. We used the expansion of the thermodynamic potential in even powers of polarization through the sixth order, which is standard for a uniaxial ferroelectric, and the attendant relation for the temperature dependence of spontaneous polarization [6]:

$$P_s = \pm\alpha/2\gamma[\{(\beta/\alpha)^2 - 4(T - T_c)\gamma/\alpha\}^{1/2} - \beta/\alpha]^{1/2}.$$

Here, α, β, and γ are constant coefficients of the terms $P^2/2$, $P^4/4$, and $P^6/6$, respectively, in the thermodynamic potential. The ratios β/α and γ/α were determined by the least-squares technique within the temperature interval (T_c – 16 K)–T_c:

$$\beta/\alpha = (9.5 \pm 0.3) \times 10^{-8} \text{ CGSE},$$

$$\gamma/\alpha = (1.13 \pm 0.01) \times 10^{-14} \text{ CGSE},$$

with the temperature corresponding to the pyroelectric current maximum, $T_c = 533.6$°C, accepted as the phase-transition point. The coefficient α was preliminarily derived from permittivity measurements made for $T > T_c$, $\alpha = 4\pi/C$. In accordance with [2], $C = 3600$ K and $\alpha = 3.49 \times 10^{-3}$ K^{-1}. We obtain finally $\beta = 3.32 \times 10^{-10}$ CGSE and $\gamma = 3.94 \times 10^{-17}$ CGSE. As can be seen from Fig. 5, the ratio used provides a good fit to the experimental curve over a broad enough temperature interval of about 75 K.

Note that this set of coefficients differs somewhat from the one obtained from calorimetric measurements in [2], where $\beta = 2.40 \times 10^{-10}$ CGSE and $\gamma = 6.05 \times 10^{-18}$ CGSE. The reason for such a substantial disagreement in the magnitude of the γ coefficient remains unclear; one could suggest that calculations based on calorimetric data are valid only near the Curie point.

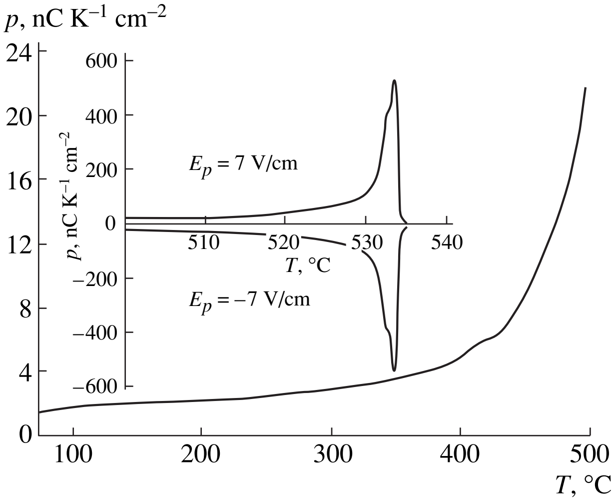

Fig. 3. Temperature dependence of the pyroelectric coefficient of an LBGO crystal. Inset: the same near the phase-transition temperature for $E_p = \pm 7$ V/cm.

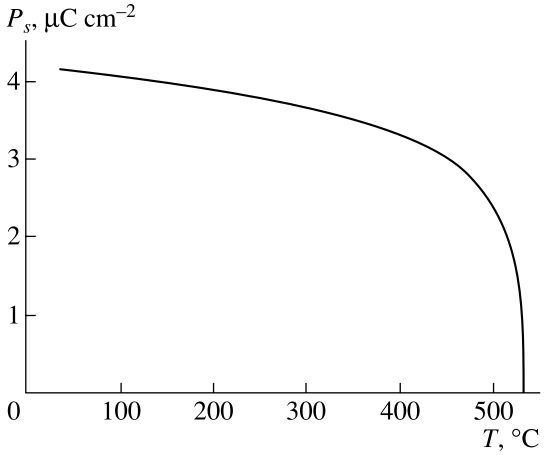

Fig. 4. Temperature dependence of the spontaneous polarization of an LBGO crystal within a broad temperature interval.

As can be seen from Fig. 5, within the temperature interval $T_c \pm 2.5$ K, the experimental points deviate from the temperature course predicted by the Landau theory. This is associated, to a certain extent, with the additional shoulder-type anomaly of the pyroelectric coefficient near T_c; this anomaly becomes manifest in the temperature behavior of the spontaneous polarization as a break, which could be related to a second phase transition in this crystal, which was discussed earlier in the literature. One can also not rule out the effect of lattice defects, which make a phase transition diffuse [7, 8]. As can be seen from Fig. 3, in our case, the broadening is observed to occur within a temperature interval ~1 K,

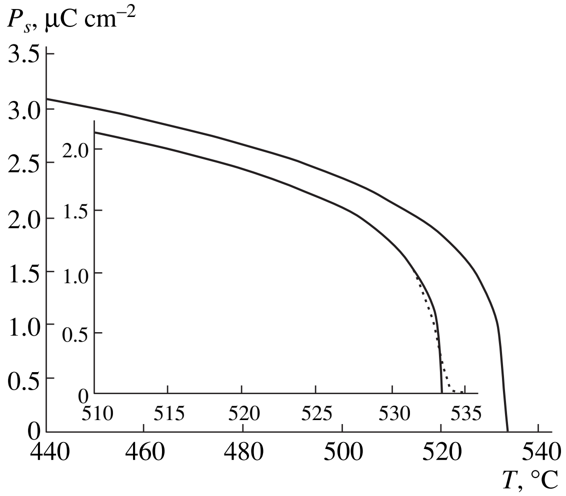

Fig. 5. Comparison of the experimental temperature dependence $P_s(T)$ with Eq. (1) plotted by a solid line. Inset: the same near the phase-transition temperature.

which is comparable to the temperature difference between T_c and the temperature of the possible second phase transition.

Thus, the problem of the existence of a second phase transition can be resolved only by measurements on high-quality samples; this work is being carried out presently.

We note in conclusion that we have established the possibility of creating a stable single-domain state in crystals of high-temperature ferroelectric LBGO, obtained the temperature dependence of the pyroelectric coefficient over a broad temperature interval and in the phase-transition region by a specially developed technique of low-current measurement, measured the temperature dependence of the spontaneous polarization of LBGO crystals, and proposed its quantitative description in terms of the phenomenological theory.

ACKNOWLEDGMENTS

The authors are indebted to B.V. Mill' for providing LBGO samples for our studies.

This work was supported by the "Universities of Russia" program and the Russian Foundation for Basic Research, grant no. 99-02-16319.

REFERENCES

1. S. Yu. Stefanovich, B. V. Mill', and A. V. Butashin, Kristallografiya **37**, 965 (1992) [Sov. Phys. Crystallogr. **37**, 513 (1992)].
2. A. Onodera, B. A. Strukov, A. A. Belov, *et al.*, J. Phys. Soc. Jpn. **62**, 4311 (1993).
3. R. V. Pisarev and M. Serhane, Fiz. Tverd. Tela (St. Petersburg) **37**, 3669 (1995) [Phys. Solid State **37**, 2022 (1995)].
4. E. L. Belokoneva, W. I. F. David, J. B. Forsyth, and K. S. Knigth, J. Phys.: Condens. Matter **9**, 3503 (1997).
5. Y. Uesu, N. Horiuchi, E. Osakabe, *et al.*, J. Phys. Soc. Jpn. **62**, 2522 (1993).
6. B. A. Strukov and A. P. Levanyuk, *Ferroelectric Phenomena in Crystals* (Springer-Verlag, Heidelberg, 1998).
7. A. P. Levanyuk and A. S. Sigov, *Defects and Structural Phase Transitions* (Gordon and Breach, New York, 1988).
8. B. A. Strukov, Y. Uesu, A. Onodera, *et al.*, Ferroelectrics **218**, 249 (1998).

Translated by G. Skrebtsov

Physics of the Solid State, Vol. 43, No. 3, 2001, pp. 517–521. Translated from Fizika Tverdogo Tela, Vol. 43, No. 3, 2001, pp. 499–503.
Original Russian Text Copyright © 2001 by Meshcheryakov.

LOW-DIMENSIONAL SYSTEMS AND SURFACE PHYSICS

Quantum Generation of Angular Momenta of Crystallites in a Nanocrystalline Material

V. V. Meshcheryakov
Moscow Institute of Steel and Alloys, Leninskiĭ pr. 4, Moscow, 117936 Russia
e-mail: valery@meshcheryakov.misa.ac.ru

Received June 22, 2000

Abstract—It is shown that, under the effect of a point force, ordered deformation states of the Fermi type can arise in a nanocrystal. These states are characterized by an angular momentum whose magnitude (estimated in the units of Planck’s constant) depends on the number of atoms in the deformed nanocrystals and can accept macroscopic values. A qualitative explanation is given to the evolution of the strength, diffusive, and damping properties of compact nanocrystalline materials based on the assumption that the quantum generation of angular momenta of crystallites can result in states of rotational motion. *© 2001 MAIK “Nauka/Interperiodica”.*

The main feature of compact nanocrystalline materials that differentiates them from the conventional materials is related to the higher values of their strength characteristics in combination with better damping properties and a higher diffusive mobility of atoms in them [1]. Numerous attempts that were undertaken to explain this feature are based on the estimation of differences in structural and (or) thermodynamic properties of individual crystallites and intercrystalline boundaries. In spite of a certain successfulness of these attempts (especially, in the phenomenological description of some experimental dependences), we can suppose that the existence of these clearly pronounced “anomalous” dependences follows from a sufficiently simple mechanism that explains the formation of “nanocrystalline properties.” Without resorting to a detailed consideration of this mechanism, it turns out to be possible to find, in the solution of the problem of the microscopic deformation of a crystal, such aspects in the behavior of an ensemble of nanocrystallites that directly indicate the differences of the properties of nanocrystalline materials from the macrocrystalline ones.

In [2], we made an attempt to solve the problem of the deformation of a finite crystal by point force sources by quantizing stationary displacements of atoms from lattice sites. The main result of the solution consisted in the fact that, in crystals with dimensions of an order of a few nanometers, there can arise deformation states which, in their spatial and energy characteristics, qualitatively differ from the known states. The field of charge displacements in these states is represented in the form of a limited set of Fourier harmonics of zero-point vibrations of the crystal whose quantization leads to an energy spectrum of the Fermi type. An assumption on the possibility of thermal excitation of negative-energy states suggests the existence, in an elastically polarized or deformed crystal, of quasiparticle excitations whose characteristics depend on the properties of the crystal and of the external force source.

In this work, we show that the specific features of the energy spectrum of deformation excitations permit the existence of quantum ordered states corresponding to a macroscopic value of the angular momentum of a crystal whose dimensions fall into the nanoscopic range. From the viewpoint of the properties of nanocrystalline materials, this result agrees well with the long-known mechanical model in which force interactions (induced by an external factor) between individual nanocrystallites may generate rotational moments and, consequently, create new, and suppress some of the existing, degrees of freedom of crystallites during arbitrary changes of the shape of these materials.

Quantized deformation states of a crystal have the following spectrum:

$$\tilde{\varepsilon}_a(p) = \frac{v}{2}[p - 2n_a\tilde{p}_{0a}^3/p^2], \tag{1}$$

which includes momentum components of the zero-point energy of the crystal and of the energy of its monopole deformation by an extraneous force source [2]. Formula (1) includes the following quantities: $v = ne(\chi/\rho)^{1/2}$ is the velocity of propagation of phonon states, where n is the number of charges e per atomic volume Ω and χ is the phenomenological constant of interatomic bonding; $\rho = m/\Omega$ is the crystal density; n_a is the number of phonon states that determines the component of the wave vector $k_a = 2\pi n_a/L_a$, where L_a is the length of the crystal along a preferred direction;

$$\tilde{p}_{0a} = p_{\mathrm{D}}(m_a/n_aN)^{1/3} \tag{2}$$

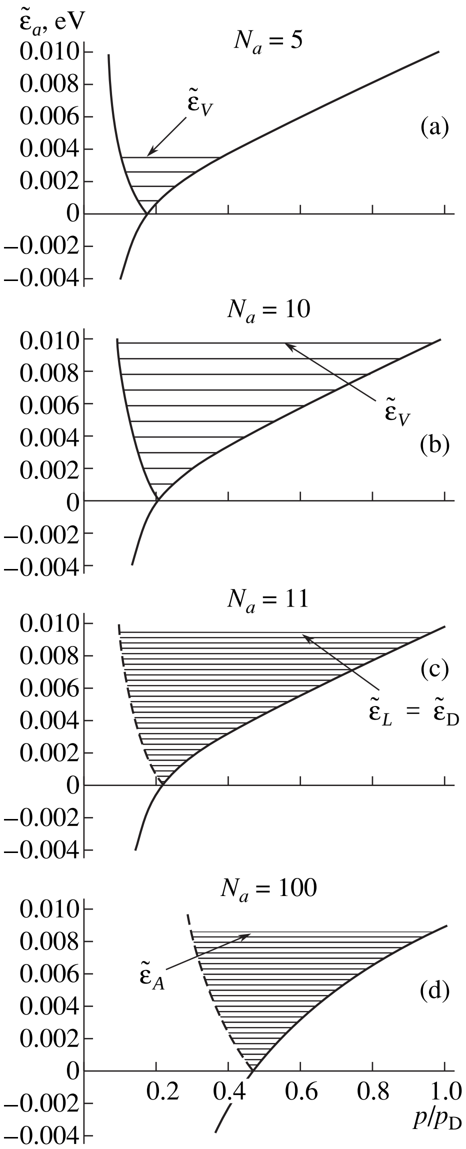

Fig. 1. Spectra of deformation vibration states of a nanocrystal with a total number of ions $N = 10^3$. As the number N_a of displaced ions in the region of the force nonuniformity increases, the character of the spectrum evolution is determined by an increase in the magnitude of the Fermi momentum $\tilde{p}_{0a}$ from p_L to p_D. The transition from (a) $N_a = 5$ to (b) $N_a = 10$ causes, in accordance with (10), an increase in the number of levels $N_a - 1$ and in the number of states of the deformation mode $2N_a$. Transition from (c) $N_a = N_{ac} = 11$ to (d) $N_a = 100$ causes, in accordance with Eq. (11), a decrease in the number of levels $N - N_a$ and, as before, an increase in the number of states $2N_a$.

is the boundary momentum, where $p_D = \pi\hbar/\Omega^{1/3}$ is the Debye momentum; $N = V/\Omega$ is the total number of atoms in the crystal with a volume V; and $m_a = E_{1a}^2/\pi^3\hbar v\chi$ is the number of quantized deformation states of the crystal deformed by an external electrostatic field with a component E_{1a}.

The calculations of the energies $\tilde{\varepsilon}_a$ of excited states for the cases of $p \le \tilde{p}_{0a}$ and $p \ge \tilde{p}_{0a}$ yield

$$\tilde{\varepsilon}_A = \varepsilon_D(1 - N_a/N), \tag{3}$$

$$\tilde{\varepsilon}_V = \varepsilon_D(N_a - 1)/N^{1/3}, \tag{4}$$

respectively, where N_a is the number of monopole-displaced ions in the region of the force nonuniformity of the crystal. For the values $m_a = 2N_a = 2$ at $\tilde{\varepsilon}_V = 0$ and $m_a = 2N_a = 2N$ at $\tilde{\varepsilon}_A = 0$ (which corresponds to either the absence of the field of ion displacements or the complete overlap of the crystal by the deformation field), the values of the number N_a vary from 1 to N.

Excited states with energies (3) are determined by that branch of spectrum (1) that corresponds to the greatest possible momentum p_D, i.e., to the smallest wavelength of the excited state that can propagate through the crystal lattice with an interatomic spacing $\Omega^{1/3}$. These states can correspond to collective vibrations of ions that are permanently displaced from lattice sites. The excited states with energies (4) are determined by another branch of spectrum (1), which corresponds to the smallest possible momentum $p_L = p_D/N^{1/3}$ (i.e., to the greatest wavelength of the excited state which can propagate through the crystal with length $L = (\Omega N)^{1/3}$). The physical meaning of these states is not completely clear. But since this branch is formed by excited states of "holes" that appear in the negative-energy range, we can assume that, in the coordinate space, the energies $\tilde{\varepsilon}_V$ are associated with collective motions of a discrete set of voids that are formed by displaced states of ions. These voids can be referred to by the commonly accepted name "vacancies," but with a "string" that, in contrast to Frenkel's vacancies, they are formed in this model by small displacements of atoms from the equilibrium positions. In what follows, the branch of spectrum (1) that determines the energies $\tilde{\varepsilon}_V$ will be named the vacancy branch, and that which determines the energy $\tilde{\varepsilon}_A$, the atomic branch.

In [2], we considered the case of spectrum (1) determined by the total number N of atoms in the crystal at a specified value of the number N_a of monopole-displaced atoms in the region of force nonuniformity and established the main features of this spectrum. Now, we dwell on the features of this spectrum that can conveniently be revealed by analyzing the variation of $\tilde{\varepsilon}_a$ at N_a, N = const.

Figure 1 shows spectra of deformation-induced vibrational states for the case where the number N_a of monopole-displaced ions changes in the region of the force nonuniformity at a constant total number N of ions in the crystal and $n_a = 1$. The transition from the spectrum $\tilde{\varepsilon}_a(N_a - 1)$ to the spectrum $\tilde{\varepsilon}_a(N_a)$ corresponds to a jumpwise change in the field E_{1a} by a magnitude corresponding to the passage of an ion in the crystal lattice into the next displaced state. The change in N_a from 5 (Fig. 1a) to 10 (Fig. 1b) demonstrates the appearance of a spectrum that is formed by excitations of vacancy character, and the passage from $N_a = 11$ in Fig. 1c to $N_a = 100$ in Fig. 1d shows the disappearance of the spectrum that is formed by excitations of atomic nature. The passage, during the formation of a spectrum, from one branch to the other occurs when the number of displaced atoms becomes equal to

$$N_{ac} = (N + N^{2/3})/(1 + N^{2/3}) \approx N^{1/3} + 1. \qquad (5)$$

The velocity of propagation of deformation excitations of atomic character is

$$v_A = (d\varepsilon/dp)_{p = p_D} \longrightarrow v. \qquad (6)$$

Deformation excitations of vacancy type have a velocity

$$v_V = (d\varepsilon/dp)_{p = p_L} = v m_a \qquad (7)$$

that is m_a times that of the velocity of propagation of acoustic vibrations. The results (6) and (7) suggest that the difference in the velocities of propagation of atomic and vacancy excitations is analogous to the difference in the velocity of the relative displacement of two laths crossed at a small angle on the velocity of the point of their intersection.

A distinctive feature of the spectrum of deformation excitations (1) is the asymmetry of the atomic and vacancy branches relative to the Fermi momentum (2). Apart from the difference in the velocities of excited states, this asymmetry manifests itself in the different character of the change in the energies of excited states (3) and (4) when the number of monopole-displaced ions passes through the value N_{ac} determined by formula (5). In Fig. 2 this difference is illustrated using $\tilde{\varepsilon}_V(N)$ and $\tilde{\varepsilon}_A(N)$ dependences.

Let us estimate the effect of structural features on the variation of the spectrum. For the values $N_a < N_{ac}$, the energy interval between nearest-neighbor levels is written as follows:

$$\Delta\tilde{\varepsilon}_V = \tilde{\varepsilon}_V(N_a + 1) - \tilde{\varepsilon}_V(N_a) = \varepsilon_D/N^{1/3}; \qquad (8)$$

and for $N_a \geq N_{ac}$, as follows:

$$\Delta\tilde{\varepsilon}_A = \tilde{\varepsilon}_A(N_a) - \tilde{\varepsilon}_A(N_a + 1) = \varepsilon_D/N. \qquad (9)$$

The energy intervals (8) and (9) do not depend on the number m_a of quantized states of the spectrum (or the number of monopole-displaced ions) but are determined only by the properties of the deformed crystal. The difference in these intervals leads to differences in the number of levels of the spectrum. At $N_a < N_{ac}$, the number of energy levels that can be occupied by Fermi pairs is equal to

$$N_V = \tilde{\varepsilon}_V/\Delta\tilde{\varepsilon}_V = N_a - 1, \qquad (10)$$

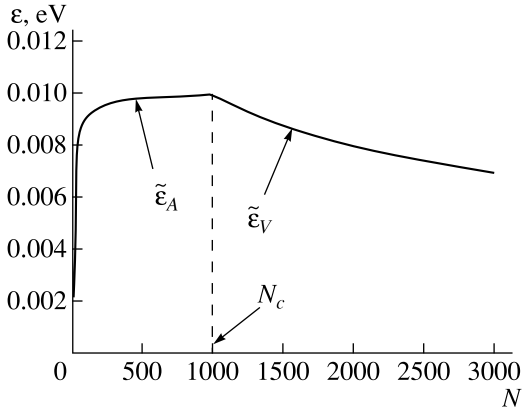

Fig. 2. The energy of the highest excited state as a function of the number N of ions in the crystal. At $N = N_c = 10^3$, the quantity $\tilde{\varepsilon}$ changes from values determined by the atomic branch of the spectrum to values determined by the vacancy branch.

and at $N_a \geq N_{ac}$, to

$$N_A = \tilde{\varepsilon}_A/\Delta\tilde{\varepsilon}_A = N - N_a. \qquad (11)$$

Dependences (10) and (11) are shown in Fig. 3; it is seen that at $N_c = (N_{ac} - 1)^3$, there occurs a sharp change in the number of energy levels of the spectrum.

The main consequence of the change in the number of energy levels upon the passage through the point N_c consists in that the phonon pumping of the spectrum by deformation pairs in the case of the different structure of the levels can lead to differences in the character of their occupation. For example, assuming that all the m_a states became transformed by phonons into excited states, at $N_a < N_{ac}$, we obtain an energy band with a complete occupation of the levels by pairs of oppositely directed deformation spins. At $N_a \geq N_{ac}$, the number of energy levels can exceed the number of pairs, since $N \geq N_a$. At the point $N_a = N_{ac}$, the number of levels $N_c \geqslant m_{ac} = N_{ac}/2$ and, consequently, there is a partially filled energy band, which permits generation of spin excesses from m_a admissible states of Fermi deformation pairs in n_a phonon states of thermal normal vibrations of the crystal.

The assumption that the additional external force action or exchange interaction can cause ordering of deformation spins permits one to determine the possible angular momentum of a nanocrystal:

$$L = \hbar N_a n_a \approx \hbar N^{1/3} n_a.$$

Since all possible phonon states from $n_a = 1$ to $n_a \approx N$ can take part in the formation of collective deformation modes, the angular momentum can take on magnitudes from a lower value

$$L_l \approx \hbar N^{1/3} \qquad (12)$$

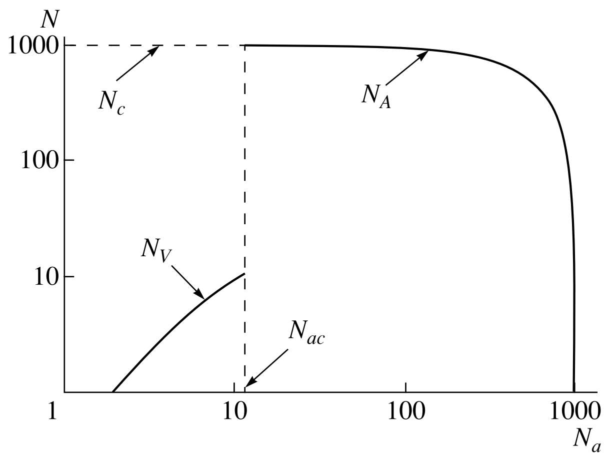

Fig. 3. Variation of the number of energy levels of the spectrum of deformation excitations of a crystal as a function of the number of monopole-displaced ions in the region of the force nonuniformity. At $N_a = N_{ac} = 11$, we have $N - N_{ac} \gg m_{ac}$ for the number of levels of the spectrum (the total number of deformation spins).

to an upper value

$$L_h \approx \hbar N^{4/3}. \quad (13)$$

Formulas (12) and (13) show that for typical values of the number of atoms in nanocrystals, L can take on macroscopic (although in the case under consideration, it would be more correctly to say “nanoscopic”) values and, consequently, cause the appearance of a rotational momentum of a nanocrystal.

Thus, in nanocrystals subjected to deformation by an external force source, ordered states of Fermi deformation modes generated by thermal excitations can arise. These states, in turn, can bring the nanocrystal into a state of rotational motion and determine its instability, e.g., as in the case of instability of small particles on a substrate [3–5].

In compact materials subjected to an external load, the angular momentum L should favor sliding or twisting of nanocrystallites along their boundaries, thereby ensuring the improvement of plastic properties, as is the case in nanoceramic materials, e.g., in nanoceramics based on hydroxyapatite [1] or in ceramics based on polycrystalline zirconium oxide ZrO_2 [6]. It can easily be understood that even in the absence of an external force action, only at the expense of temperature gradients, the force interaction between nanocrystallites is retained and, consequently, the thermal generation of the momenta L is also retained. Therefore, the effect of sliding or twisting of nanocrystals also should occur. In both cases, the rotational motions of nanocrystallites should lead to the acceleration of the diffusion transfer of atoms through the intercrystalline space.

Let us estimate the possible velocities v of motion of surface atoms of a rotating nanocrystallite. Assuming that the mechanical momentum of a nanocrystal is $L = Mvr$, where M is its mass and r is the average radius, and taking, as the basis for calculations, a typical case of $r = 10$ nm for typical solid-state values of the volumes $\Omega \approx 10^{-23}$ cm^3 and densities $\rho \approx 10$ g/cm^3, we find the lower order of magnitude for the velocity

$$v_l = \frac{\hbar N^{1/3}}{Mr} \approx \frac{10^{-27} \times 10^{5/3}}{10^{-17} \times 10^{-6}} \approx 10^{-3} \text{ cm/s}$$

from Eq. (12) and the upper order

$$v_h = \frac{\hbar N^{4/3}}{Mr} \approx \frac{10^{-27} \times 10^{20/3}}{10^{-17} \times 10^{-6}} \approx 10^{2} \text{ cm/s}$$

from Eq. (13).

If we proceed from the case $N = 10^3$ considered in this paper, which, for typical values of parameters, corresponds to a nanocrystal with an average radius $r \approx 1$ nm, we obtain

$$v_l \approx \frac{10^{-27} \times 10}{10^{-19} \times 10^{-7}} \approx 1 \text{ cm/s},$$

$$v_h \approx \frac{10^{-27} \times 10^{4}}{10^{-19} \times 10^{-7}} \approx 10^{3} \text{ cm/s}.$$

The tendency observed is evident: the velocity of rotation of a crystallite increases as its size decreases. The other aspect, namely, the high values of the velocities, which can qualitatively substantiate the exclusively high diffusive mobility of atoms in nanomaterials, is nontrivial [1]. Experimental data indicate that the mobility of atoms in nanomaterials is 5–6 orders of magnitude higher than in conventional polycrystals and, consequently, indirectly corroborates the above estimates.

We can also note that the greatest estimate for the velocities is not very far from the typical value of the velocity of propagation of long-wavelength elastic vibrations $c \approx 10^5$ cm/s. The question that arises is whether or not the phenomenon that is called superplasticity is linked with the fact that the velocity of rotation of the surfaces of nanocrystals coincides with the sound velocity. To answer this question, experiments *in situ* are necessary, such experiments that would permit one to follow the behavior of individual nanocrystallites during deformation.

Now, we consider the higher strength properties of compact nanocrystalline materials as compared to the conventional polycrystals. For example, at normal temperatures, the microhardness of nanomaterials is 2–7 times that of coarse-grained polycrystals [1]. This property seems to be the best studied, perhaps, for the reason that the phenomenon of increasing strength of polycrystals with decreasing grain size has long been known. Neglecting known deviations from this regularity, we nevertheless can believe that the approach to the estimates of microhardness from the viewpoint of the existence of self angular momenta for nanocrystallites can reflect some new aspects of the physics of interaction of two solids.

Investigations of microhardness by the Vickers technique is performed using a diamond pyramid that is impressed into the surface of a material and causes an inhomogeneous stress. The inhomogeneous distribution of the field of stresses imposed onto a disordered structure of the vector field of self angular momenta of nanocrystallites can lead to an ordering of rotations of crystallites.[1] The formation of an ordered structure of the vector field of momenta should make the collective response of nanocrystallites more rigid, at least at the expense of the suppression in such a system of translational degrees of freedom of individual crystallites.

Finally, let us turn to the question of damping properties. In [7], we arrived at a conclusion that an improvement in the damping properties of nanocrystalline materials can be a consequence of cutting out of long-wavelength phonons of the nanocrystal by extended force nonuniformities. In addition, it follows from the results of our previous paper [2] and this paper that the formation of a collective vibrational system of deformation spins is possible only at the extent of cutting out of the long-wavelength portion of the phonon spectrum of the crystal. Based on the geometrical aspect (which is traditional for the investigation of damping properties), we can conclude that the specific features of the collective behavior of rotating nanocrystals in the ordered and disordered states should manifest itself in experimental data on internal friction.

ACKNOWLEDGMENTS

I am grateful to A.G. Lyapin, O.A. Kazakov, and F.I. Manyakhin for fruitful discussions of the paper.

REFERENCES

1. A. I. Gusev, Usp. Fiz. Nauk **168** (1), 55 (1998) [Phys. Usp. **41**, 49 (1998)].
2. V. V. Meshcheryakov, Fiz. Tverd. Tela (St. Petersburg) **42** (9), 1700 (2000) [Phys. Solid State **42**, 1749 (2000)].
3. É. L. Nagaev, Usp. Fiz. Nauk **162** (9), 49 (1992) [Sov. Phys. Usp. **35**, 747 (1992)].
4. S. Iijima and T. Ichihashi, Phys. Rev. Lett. **56** (6), 616 (1986).
5. J.-O. Bovin, R. Wallenberg, and D. J. Smith, Nature **317**, 47 (1985).
6. F. Wakai, S. Sakagushi, and Y. Matsuno, Adv. Ceram. Mater. **1** (3), 259 (1986).
7. V. V. Meshcheryakov, Zh. Éksp. Teor. Fiz. **111** (5), 1845 (1997) [JETP **84**, 1010 (1997)].

Translated by S. Gorin

---

[1] It should perhaps be noted that here we should speak of classical ordering rather than of quantum ordering of deformation spins that form the moment *L*.

Physics of the Solid State, Vol. 43, No. 3, 2001, pp. 522–526. Translated from Fizika Tverdogo Tela, Vol. 43, No. 3, 2001, pp. 504–507.
Original Russian Text Copyright © 2001 by Krevchik, Zaĭtsev .

LOW-DIMENSIONAL SYSTEMS AND SURFACE PHYSICS

Impurity Absorption of Light in Structures with Quantum Dots

V. D. Krevchik* and R. V. Zaĭtsev

Penza State University, Penza, 440017 Russia
**e-mail: physics@diamond.stup.ac.ru*

Received April 7, 2000; in final form, July 27, 2000

Abstract—The impurity absorption of light in a quantum dot with a parabolic potential profile is considered within the framework of the model of a zero radius potential in the effective mass approximation. The sensitivity of the effect of position disorder to the size factor at the transition from a quantum well to a quantum dot is revealed. The spectral dependence of the coefficient of impurity absorption of light is investigated with account of the spread in size of quantum dots. It is shown that the account of spread in size results in smearing of discrete absorption lines. The impurity absorption edge depends on the parameters of quantum dots and the depth of the impurity level. *© 2001 MAIK "Nauka/Interperiodica".*

1. Research into the optical properties of semiconductor quantum dots (QD) synthesized in a glass host is rather urgent for development of new devices of quantum electronics [1]. An important aspect of the research is the reliable identification of optical transitions, which is based on calculation of corresponding oscillator strengths. For example, in the case of interband absorption of light by a spherically symmetric QD, such identification [2] allows one to interpret the results of the experiment [3]. The development of δ-doping technology (a review is given in [4]) stimulates research of impurity absorption of light in structures with QDs. In the present work, the local electron states induced by defects inside semiconductor QDs, which are synthesized in a transparent boron silicate host, are investigated. The QD is described within the framework of the model of a spherical oscillator well. The model of zero radius potential is used for the potential of the defect [5–7]. This model, as known [7], well enough describes D^- states and the states of a negative hydrogen ion. In the effective mass approximation, the coefficient of impurity absorption of light is calculated with account of the size spread of QDs. It is supposed that the spread appears during phase disintegration of an oversaturated solid solution [8, 9] and is satisfactorily described by the Lifshitz–Slezov formula [10]

$$P(u = R_0/\bar{R}_0) = \begin{cases} \dfrac{3eu^2\exp[-1/(1-2u/3)]}{2^{5/3}(3+u)^{7/3}(3/2-u)^{11/3}}, & u < 3/2 \\ 0, \quad u > 3/2, \end{cases} \tag{1}$$

where e is the natural logarithm base and R_0 and $\bar{R}_0$ are the radius of a QD and its average value, respectively.

2. The Lippmann–Schwinger equation for a bound state is written as[1]

$$\Psi_\lambda(\mathbf{r}, \mathbf{R}_a) = \int d\mathbf{r}_1 G(\mathbf{r}, \mathbf{r}_1; E_\lambda) V_\delta(\mathbf{r}, \mathbf{R}_a)\Psi_\lambda(\mathbf{r}_1, \mathbf{R}_a), \tag{2}$$

where $G(\mathbf{r}, \mathbf{r}_1; E_\lambda)$ is the one-electron Green's function which corresponds to a source at the point $\mathbf{R}_a = (x_a, y_a, z_a)$ and to an energy E_λ; $\Psi_\lambda(\mathbf{r}_1, \mathbf{R}_a)$ is the wave function of an electron which is localized by the short-range potential; $E_\lambda = -\hbar^2\lambda^2/(2m^*)$ is the binding energy of the impurity center; and m^* is the effective mass of the electron. Here, $V_\delta(\mathbf{r}, \mathbf{R}_a)$ is a zero radius potential of power $\gamma = 2\pi/\alpha$:

$$V_\delta(\mathbf{r}, \mathbf{R}_a) = \gamma\delta(\mathbf{r} - \mathbf{R}_a)[1 + (\mathbf{r} - \mathbf{R}_a)\nabla_\mathbf{r}]. \tag{3}$$

The parameter α is defined by the binding energy E_i of the electron localized on the same defect in the bulky semiconductor. After substitution of Eq. (3) into Eq. (2), we have

$$\Psi_\lambda(\mathbf{r}, \mathbf{R}_a) = \gamma G(\mathbf{r}, \mathbf{R}_a; E_\lambda)(\hat{T}\Psi_\lambda)(\mathbf{R}_a, \mathbf{R}_a), \tag{4}$$

where

$$(\hat{T}\Psi_\lambda)(\mathbf{R}_a, \mathbf{R}_a) \equiv \lim_{\mathbf{r} \to \mathbf{R}_a}[1 + (\mathbf{r} - \mathbf{R}_a)\nabla_\mathbf{r}]\Psi_\lambda(\mathbf{r}, \mathbf{R}_a). \tag{5}$$

Operating with the operator $\hat{T}$ on both parts of Eq. (4) and summing over quantum numbers with the use of the Möller formula for the generating function [11]

$$\sum_{n=0}^{\infty}\left(\frac{u}{2}\right)^n \frac{H_n(x_1)H_n(x_2)}{n!} = \frac{1}{\sqrt{1-u^2}} \times \exp\left\{\frac{2x_1x_2u - (x_1^2 + x_2^2)u^2}{1-u^2}\right\} \tag{6}$$

---

[1] The impurity center is located at the point $\mathbf{R}_a = (x_a, y_a, z_a)$, and the energy is reckoned from the bottom of a spherical oscillator well that approximates a QD.

1063-7834/01/4303-0522$21.00 © 2001 MAIK "Nauka/Interperiodica"

gives the following equation, which defines the dependence of the bound state energy E_λ of the impurity center on the parameters of the QD and on the position of the defect R_a:

$$\sqrt{\eta^2+\frac{3}{2}\beta^{-1}} = \eta_i - \sqrt{\frac{2}{\beta\pi}}\int_0^\infty dt\exp[-(\beta\eta^2+3/2)t]$$
$$\times\left[\frac{1}{2t\sqrt{2t}}-\frac{1}{(1-\exp(-2t))^{3/2}}\right] \tag{7}$$
$$\times\exp\left(-\frac{R_a^{*2}\beta^{-1}}{2}\frac{1-\exp(-t)}{1+\exp(-t)}\right)\Bigg],$$

where $\eta^2 = |E_\lambda|/E_d$ and $\eta_i^2 = |E_i|/E_d$ are parameters specifying the energies of the bound state of the impurity center in the QD and the bulky semiconductor, respectively; $E_d = m^*e^4/2\hbar^2\varepsilon^2$ is the effective Bohr energy with account of the effective mass m^* and the dielectric permittivity ε; $\beta = R_0^*/4\sqrt{U_0^*}$; $R_0^* = 2R_0/a_d$; $a_d = \varepsilon\hbar^2/m^*e^2$ is the effective Bohr radius; $U_0^* = U_0/E_d$ is the amplitude of the QD potential; and $R_a^* = R_a/a_d$.

The results of numerical analysis of Eq. (7) are presented in Fig. 1, from which it is seen that the effect of position disorder takes place in a QD with impurity centers: $\eta^2(R_a^*)$ is a decreasing function of R_a (curve *1*). Such behavior of $\eta^2(R_a^*)$ is characteristic of quantum-sized films [5, 6] and quantum wells [7]. This behavior is caused by a radical change in the local electron states near the boundary of the system. The growth of the amplitude of the QD potential U_0^* leads to more restrictive conditions for the existence of the bound state (cf. curves *1* and *2*). For comparison, Fig. 1 presents the numerically calculated dependence (curve *3*) of the localization energy on the position of the same defect in a quantum well with a parabolic potential profile, which was obtained in [12]. In our notation, the corresponding equation has the form

$$\sqrt{\eta^2+\frac{1}{2}\beta^{-1}} = \eta_i - \sqrt{\frac{1}{2\beta\pi}}\int_0^\infty \frac{dt}{t}\exp[-(\beta\eta^2+1/2)t]$$
$$\times\left[\frac{1}{\sqrt{2t}}-\frac{1}{(1-\exp(-2t))^{1/2}}\right] \tag{8}$$
$$\times\exp\left(-\frac{a^{*2}\beta^{-1}}{2}\frac{1-\exp(-t)}{1+\exp(-t)}\right)\Bigg],$$

where $a^* = z_a/a_d$, $\beta = L^*/4\sqrt{U_0^*}$, $L^* = L/a_d$, and L is the width of the quantum well.

A comparison of curves *1* and *3* shows that the $2D \longrightarrow 0D$ transition is accompanied by strengthening of the effect of position disorder.

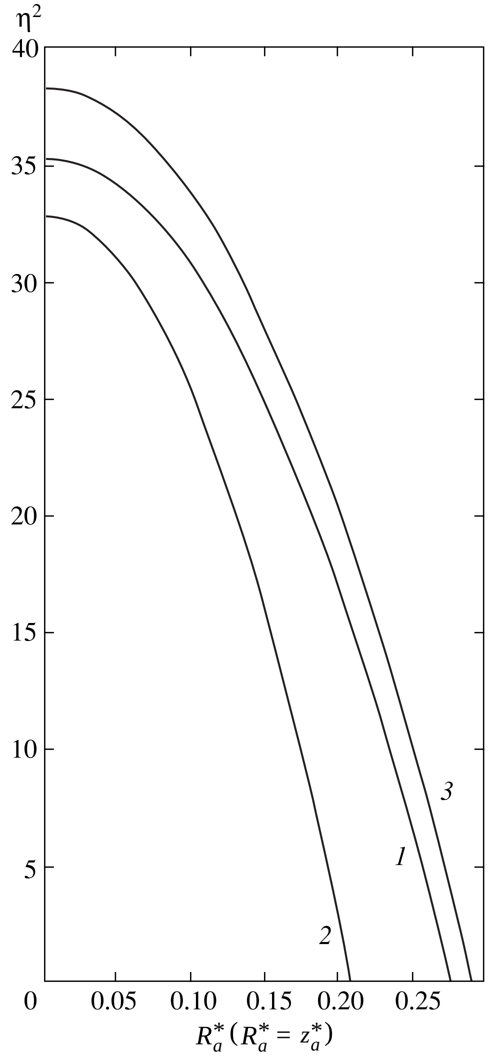

Fig. 1. Position of the localized level $\eta^2 = |E_\lambda|/E_d$ as a function of the coordinate of the impurity center $R_a^* = R_a/a_d$ for various values of the parameters of a quantum dot: (*1*) $U_0^* = 120$, $\eta_i^2 = 40$, $R_0^* = 1$; and (*2*) $U_0^* = 200$, $\eta_i^2 = 40$, $R_0^* = 1$. Curve *3* presents a similar function for a quantum well: $U_0^* = 120$, $\eta_i^2 = 40$, $L^* = 1$.

3. We consider impurity absorption of light in a QD with a parabolic potential profile. The wave function of the electron which is localized by a short-range potential, as one can easily see from Eq. (4), differs only by a constant factor from the one-electron Green's function:

$$\Psi_\lambda(\mathbf{r},\mathbf{R}_a) = C\exp\left(-\frac{r^2+R_a^2}{2a^2}\right)\int_0^\infty dt e^{-\beta t}(1-e^{-2t})^{-3/2}$$
$$\times\exp\left\{-\frac{e^{-2t}(r^2+R_a^2)-2e^{-t}(\mathbf{r},\mathbf{R}_a)}{a^2(1-e^{-2t})}\right\}, \tag{9}$$

where $C = (-\partial/\partial\varepsilon_a G(R_a, R_a; \varepsilon_a)a^3)^{1/2}$ is a normalizing factor, $\varepsilon_a = |E_\lambda|/\hbar\omega_0$, $E_0 = (3/2)\hbar\omega_0$ is the energy of the QD ground state, and $a^2 = \hbar/(m^*\omega_0)$.

We consider the case when an impurity atom is located at the center of the QD ($R_a = 0$). Then, using an integral representation for the Whittaker function [11], relation (9) can be rewritten as

$$\Psi_\lambda(r) = C\left(\frac{r^2}{a^2}\right)^{-3/4}\Gamma\left(\frac{\varepsilon_a + 3/2}{2}\right)W_{-\varepsilon_a/2,\,1/4}\left(\frac{r^2}{a^2}\right), \quad (10)$$

where $\Gamma(x)$ is the gamma function, $W_{\kappa,\,\mu}(x)$ is the Whittaker function, and

$$C = \{2\sqrt{\pi}\Gamma(\varepsilon_a/2 + 7/4)a^3[(\varepsilon_a/2 + 3/4)$$
$$\times(\Psi(\varepsilon_a/2 + 7/4) - \Psi(\varepsilon_a/2 + 1/4)) - 1]/[(\varepsilon_a + 3/2)^2$$
$$\times\Gamma(\varepsilon_a/2 + 1/4)]\}^{-1/2},$$

with $\Psi(x)$ being the logarithmic derivative of the gamma function.

The wave function of the final state is taken as

$$\Psi_{fn,\,l,\,m}(r) = C_{nl}\left(\frac{r}{a}\right)^l\exp\left(-\frac{r^2}{2a^2}\right)\frac{\Gamma(l + 3/2)}{\Gamma(l + 3/2 + n)}$$
$$\times L_n^{l+1/2}\left(\frac{r^2}{a^2}\right)\sqrt{\frac{2l+1}{4\pi}\frac{(l-m)!}{(l+m)!}}P_l^m(\cos\theta)\exp(im\varphi), \quad (11)$$

where $C_{nl} = \sqrt{2n!\Gamma(l + n + 3/2)/a^3}/\Gamma(l + 3/2)$ is the normalizing factor; $L_n^{l+1/2}(r^2/a^2)$ are the generalized Laguerre polynomials; $P_l^m(\cos\theta)$ are the associated Legendre functions of the first kind; n, l, and m are the radial, orbital, and magnetic quantum numbers, respectively; and r, φ, and θ are the spherical coordinates. Such a choice of the wave function of the final state is justified if the inequality $\lambda a \gg 1$ is satisfied (the case of strong localization of the impurity electron).

By virtue of the spherical symmetry of the problem, optical transitions fulfill the usual selection rules in the dipole approximation: only the transitions from the ground s state of the impurity center to the excited p states of the QD are allowed. The square of the modulus of the matrix element that determines the oscillator strength of a dipole optical transition has the form

$$|M_{f\lambda}|^2 = \frac{\pi^{5/2}\alpha^* I_0\lambda_0^2}{6^3\omega}a^2E_0^2(\varepsilon_a + 2n + 5/2)^2$$
$$\times\frac{n!(\varepsilon_a + 3/2)^2\Gamma(\varepsilon_a/2 + 1/4)\Gamma^2(\varepsilon_a/2 + 3/4)}{\Gamma(n + 5/2)\Gamma(\varepsilon_a/2 + 7/4)\{(\varepsilon_a/2 + 3/4)[\Psi(\varepsilon_a/2 + 7/4) - \Psi(\varepsilon_a/2 + 1/4)] - 1\}} \quad (12)$$
$$\times\left\{\sum_{m=0}^{n}(-1)^m\frac{\Gamma(n + 5/2)}{(n-m)!\Gamma(m + 5/2)m!}\frac{(2m+3)!!}{2^m}\frac{\Gamma(m+2)}{\Gamma(m + 2 + \varepsilon_a/2 + 3/4)}\right\}^2,$$

where a^* is the fine structure constant including the permittivity, ω is the frequency of light, I_0 is the intensity of light, and λ_0 is the local-field coefficient.

With account of the size spread of QDs, the impurity absorption coefficient of light K can be written as

$$K = K_0\frac{X}{(X - \eta^2)^3\beta^*}\sum_{n=0}^{N}P(\delta_n)(2n + 5/2)^2$$
$$\times\frac{n!(2\Delta_n + 3/2)^2\Gamma(\Delta_n + 1/4)\Gamma^2(\Delta_n + 3/4)}{\Gamma(n + 5/2)\Gamma(\Delta_n + 7/4)\{(\Delta_n + 3/4)[\Psi(\Delta_n + 7/4) - \Psi(\Delta_n + 1/4)] - 1\}} \quad (13)$$
$$\times\left\{\sum_{m=0}^{n}(-1)^m\frac{\Gamma(n + 5/2)}{(n-m)!\Gamma(m + 5/2)m!}\frac{(2m+3)!!}{2^m}\frac{\Gamma(m+2)}{\Gamma(m + 2 + \Delta_n + 3/4)}\right\}^2,$$

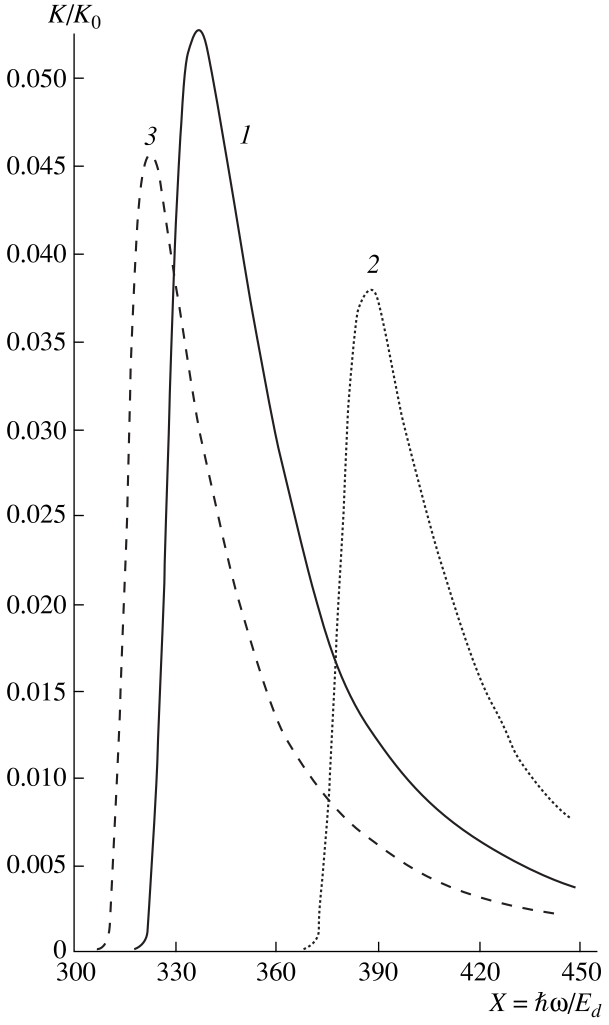

Fig. 2. Spectral distribution of the normalized absorption coefficient K/K_0 for optical transition with a maximal oscillator strength ($n = 0$) for various values of the parameters of a QD: (*1*) $U_0^* = 100$, $\eta_i^2 = 250$, $\bar{R}_0^* = 1.0$; (*2*) $U_0^* = 100$, $\eta_i^2 = 300$, $\bar{R}_0^* = 1.0$; and (*3*) $U_0^* = 100$, $\eta_i^2 = 250$, $\bar{R}_0^* = 1.2$.

where $K_0 = \pi^{7/2}\alpha^*\lambda_0^2 a_d^2 N_0/24$, $\beta^* = \bar{R}_0^*/4\sqrt{U_0^*}$, $\bar{R}_0^* = 2\bar{R}_0/a_d$, $\delta_n = (2n + 5/2)/[(X - \eta^2)\beta^*]$, $X = \hbar\omega E_d$, $N = [C]$ is the integer part of the number $C = [3(X - \eta^2)\beta^*/2 - 5/2]/2$, $\Delta_n = \eta^2(2n + 5/2)/[2(X - \eta^2)]$, the function $P(\delta_n)$ is defined by formula (1), and N_0 is the concentration of QDs in the dielectric host.

In Fig. 2, the spectral distribution of the normalized impurity absorption coefficient K/K_0 is presented, for the optical transition, with a maximal oscillator strength ($n = 0$). One can see that the account of the size spread results in smearing of discrete lines of the impurity absorption of light. The evolution of the spectrum of impurity absorption with a change in the QD size $\bar{R}_0^*$ is shown by curves *2* and *3* in Fig. 2. A decrease in $\bar{R}_0^*$ shifts the edge of impurity absorption to the short-wavelength spectrum range, which reflects the shift of the lower size-quantization level. The sensitivity of the impurity absorption edge to the parameter $\eta^2 = |E_\lambda|/E_d$ is shown by curves *1* and *2*. A decrease in η^2 (i.e., an increase in the radius of the localized state) leads to an appreciable increase in the oscillator strength of the dipole optical transition (cf. curves *1* and *2*), and the edge of impurity absorption is shifted to the long-wavelength spectrum range. This shift satisfies the law ($N = 0$) $X_t = \eta^2 + 5/(3\beta^*)$. This shift can be used for experimental determination of the average radius of nanocrystals (QDs) if the parameters η^2 and U_0^* are known.

4. Thus, the localized state in a short-range potential in a QD with a parabolic potential profile was considered. In this model of the QD, the amplitude of the QD potential U_0^* is an empirical parameter.

In this approximation, the influence of dimensionality on the location of the impurity level is shown to take place in the $2D \longrightarrow 0D$ transition. The account of the size spread of QDs essentially changes the character of the spectral distribution of the impurity absorption coefficient of light. The quantum dot which is filled only by electrons localized by short-range potentials can have higher thresholds for thermal ionization. The reason for this is that the electrons localized by short-range potentials inside the QD are confined to the region between the barriers of height about U_0^* and $U_0^* + \eta^2$. In this connection, the use of an assemblage of QDs with impurity states as an active medium for a laser structure attracts certain interest.

ACKNOWLEDGMENTS

The authors are grateful to A.É. Yunovich and A.A. Gutkin for their interest in this work.

REFERENCES

1. J. Yumoto, S. Fukushima, and K. Kubodera, Opt. Lett. **12**, 832 (1987).
2. Al. L. Éfros and A. L. Éfros, Fiz. Tekh. Poluprovodn. (Leningrad) **16**, 1209 (1982) [Sov. Phys. Semicond. **16**, 772 (1982)].
3. A. I. Ekimov and A. A. Onushchenko, Fiz. Tekh. Poluprovodn. (Leningrad) **16**, 1215 (1982) [Sov. Phys. Semicond. **16**, 775 (1982)].
4. A. Ya. Shik, Fiz. Tekh. Poluprovodn. (St. Petersburg) **26**, 1161 (1992) [Sov. Phys. Semicond. **26**, 649 (1992)].
5. V. D. Krevchik and E. Z. Imamov, Phys. Status Solidi B **114** (1982).

6. V. D. Krevchik and É. Z. Imamov, Fiz. Tekh. Poluprovodn. (Leningrad) **17**, 1235 (1983) [Sov. Phys. Semicond. **17**, 780 (1983)].
7. A. A. Pakhomov, K. V. Khalipov, and I. N. Yassievich, Fiz. Tekh. Poluprovodn. (St. Petersburg) **30**, 1387 (1996) [Semiconductors **30**, 730 (1996)].
8. N. F. Borelli, D. W. Hall, H. J. Holland, and D. W. Smith, J. Appl. Phys. **61** (12), 5399 (1987).
9. N. R. Kulish, V. P. Kunets, and M. P. Lisitsa, Fiz. Tverd. Tela (St. Petersburg) **39**, 1865 (1997) [Phys. Solid State **39**, 1667 (1997)].
10. I. M. Lifshitz and V. V. Slezov, Zh. Éksp. Teor. Fiz. **35** (1), 479 (1958) [Sov. Phys. JETP **8**, 331 (1959)].
11. *Higher Transcendental Functions (Bateman Manuscript Project)*, Ed. by A. Erdelyi (McGraw-Hill, New York, 1953; Nauka, Moscow, 1974), Vol. 2.
12. V. D. Krevchik and R. V. Zaĭtsev, in *Proceedings of the II International Scientific and Technical Conference "Problems and Applied Questions of Physics," Saransk, 1999.*

Translated by O. Ivanov

Physics of the Solid State, Vol. 43, No. 3, 2001, pp. 527–529. Translated from Fizika Tverdogo Tela, Vol. 43, No. 3, 2001, pp. 508–510.
Original Russian Text Copyright © 2001 by Ayukhanov, Shkerdin.

LOW-DIMENSIONAL SYSTEMS AND SURFACE PHYSICS

Effect of Photoelasticity Enhancement Stimulated by Carrier Localization in a Quantum Well near Interband Resonances in Superlattices

R. A. Ayukhanov and G. N. Shkerdin
Institute of Radio Engineering and Electronics (Fryazino Branch), Russian Academy of Sciences,
pl. Vvedenskogo 1, Fryazino, Moscow oblast, 141120 Russia
e-mail: gns277@ire216.msk.su

Received April 18, 2000; in final form, July 31, 2000

Abstract—An analytical expression is obtained for the resonant permittivity and linear photoelasticity coefficients in multiple quantum well structures near interband resonances. It is shown that the resonant photoelasticity in these structures is considerably higher than that in the bulk case and can exceed the photoelasticity near the resonance of a bulk exciton. It is noted that this result is associated with localization of noninteracting electrons and holes in the layer with a quantum well. Similar to the exciton in a bulk crystal, this system determines the elastooptic properties of the superlattice in the vicinity of the interband resonance. © *2001 MAIK "Nauka/Interperiodica".*

As was shown earlier [1], the localization of electrons and holes in a quantum well leads to a significant increase in the linear photoelasticity coefficients in multiple quantum well structures (MQWS) in the vicinity of exciton resonances. This localization imparts the properties of an oscillator to the electron–hole system and can be assumed to increase the photoelasticity coefficients near resonances between discrete levels of free (noninteracting) electrons and holes in the intrinsic quantum wells, with respect to the interband resonance in a bulk crystal. Let us estimate this quantity.

By using the density matrix method [2], which was developed for the case of noninteracting electrons and holes in a quantum well, and the approximation of an infinitely deep well, we obtain an expression for the resonant component of the permittivity in the region of transitions between discrete levels of free electrons and holes in the quantum well:

$$\varepsilon_{ik}(\mathbf{r}, t) = \frac{4\pi e^2}{m^2\omega^2 V_p}$$

$$\times \sum_{n, n', \mathbf{k}_\parallel} \frac{(f^c_{n', \mathbf{k}_\parallel + \kappa_\parallel} - f^v_{n, \mathbf{k}_\parallel}) \dfrac{1}{4L^2}\left[\displaystyle\int_{-L/2}^{L/2} c_{n'}(z) c_n(z) dz\right]^2 L^{nn'}_{ik}}{\hbar\omega + E_{n, \mathbf{k}_\parallel, v} - E_{n', \mathbf{k}_\parallel + \kappa_\parallel, c} + is},$$

$$c_n(z) = (1 - (-1)^n)\cos\frac{\pi n z}{L} + (1 + (-1)^n)\sin\frac{\pi n z}{L},$$

$$L^{nn'}_{ik} = \langle v, n, \mathbf{k}_{0,\parallel}| e^{i\kappa\mathbf{r}} \hat{p}_i | c, n', \mathbf{k}_{0,\parallel} + \kappa_\parallel\rangle$$
$$\times \langle c, n', \mathbf{k}_{0,\parallel} + \kappa_\parallel | e^{i\kappa\mathbf{r}} \hat{p}_k | v, n, \mathbf{k}_{0,\parallel}\rangle, \qquad (1)$$

$$|c, v, n, \mathbf{k}_{0,\parallel}\rangle = \frac{1}{\sqrt{\Omega}} u_{c, v, n, \mathbf{k}_{0,\parallel}}(\mathbf{r}),$$

$$E_{c, n', \mathbf{k}_\parallel + \kappa_\parallel} = E_g + \frac{\hbar^2\pi^2}{2m^*_{e,\perp}L^2}n'^2 + \frac{\hbar^2[(\mathbf{k}_\parallel - \mathbf{k}_{0,\parallel}) + \kappa_\parallel]^2}{2m^*_{e,\parallel}},$$

$$E_{v, n, \mathbf{k}_\parallel} = -\frac{\hbar^2\pi^2}{2m^*_{h,\perp}L^2}n^2 - \frac{\hbar^2(\mathbf{k}_\parallel - \mathbf{k}_{0,\parallel})^2}{2m^*_{h,\parallel}}.$$

Here, $V_p = SL_p$ and $L_p = L + L_B$ denote the volume and the thickness of an MQWS period, respectively; L is the quantum well width; L_B is the barrier width; S is the area of the MQWS surface parallel to the layers; ω and κ stand for the frequency and the wave vector of the electromagnetic wave exciting the electron; E_g is the band gap in the layer constituting the quantum well in the bulk case; $m^*_{e,\perp;\parallel}$ and $m^*_{h,\perp;\parallel}$ are the effective masses of the electron and the hole, respectively, in the directions perpendicular and parallel to the MQWS layers; Ω is the unit cell volume in a three-dimensional crystal used to form the quantum well; $u_{c, v, n, \mathbf{k}_{0,\parallel}}(\mathbf{r})$ is the amplitude of the Bloch function for the conduction (c) or valence (v) band in the state n with the wave vector $\mathbf{k}_{0,\parallel}$ in the layer with a quantum well (it is assumed that the minimum of the conduction band and the maximum of the valence band coincide in the n state and are situated at the point $\mathbf{k}_{0,\parallel}$); $\mathbf{k}_\parallel$ and $\kappa_\parallel$ symbolize the components of the wave vectors $\mathbf{k}$ and κ, respectively, in the plane parallel to the MQWS layers; $n = 1, 2, 3, \ldots$ are the numbers of the discrete spatial-quantization levels of the electron and hole states in the quantum well (this representation of the Bloch function amplitude reflects

1063-7834/01/4303-0527$21.00 © 2001 MAIK "Nauka/Interperiodica"

the situation when the confinement of the well thickness in the direction perpendicular to the MQWS layers transforms the quasi-continuous spectrum of electronic states in the bulk crystal [3] and the quantum numbers k_x, k_y, and k_z, which characterize the Bloch function, are replaced by k_x, k_y, and n); $E_{c,\,v,\,n,\,\mathbf{k}_\parallel}$ and $f^{c,\,v}_{n,\,\mathbf{k}_\parallel}$ represent the energies of electronic states and the electron energy distribution functions, respectively, in the conduction and valence bands which are transformed in the quantum well; $\hat{p}$ is the momentum operator; e and m designate the charge and the mass of the electron, respectively; and s is the linewidth of the resonant transition with the energy difference $E_{c,\,n',\,\mathbf{k}_\parallel+\kappa_\parallel} - E_{v,\,n,\,\mathbf{k}_\parallel}$.

A strain applied to the MQWS, which changes the electronic levels according to the law $E_{c,\,n',\,\mathbf{k}_\parallel+\kappa_\parallel} = E^0_{c,\,n',\,\mathbf{k}_\parallel+\kappa_\parallel} + \Lambda^{c,\,n'}_{ik} u_{ik}$ and $E_{v,\,n,\,\mathbf{k}_\parallel} = E^0_{v,\,n,\,\mathbf{k}_\parallel} + \Lambda^{v,\,n}_{ik} u_{ik}$, in the general case, also changes the resonant permittivity ($E^0_{c,\,v,\,n,\,\mathbf{k}_\parallel}$ denote the energy levels in the absence of strain; $\Lambda^{c,\,v,\,n}_{ik}$ symbolize the tensors of deformation potentials for intraband transitions in the nth subband in the conduction band and the valence band, respectively; and u_{ik} is the strain tensor). In what follows, we will use the linear term in the dependence of the permittivity on u_{ik}. This becomes possible at a small strain, i.e., when $(\Lambda^{c,\,n'}_{ik} - \Lambda^{v,\,n}_{ik})u_{ik} \ll |\hbar\omega + E^0_{v,\,n,\,\mathbf{k}_\parallel} - E^0_{c,\,n',\,\mathbf{k}_\parallel+\kappa_\parallel} + is|$. We assume that $f^{v}_{\mathbf{k}_\parallel} \cong 1$ and $f^{c}_{\mathbf{k}_\parallel+\kappa_\parallel} \cong 0$. Since summation over all quantum numbers n and n' in formula (1) leads to additional difficulties, we neglect the contribution of the levels with $n > 1$ to the resonant permittivity. Analysis showed that the latter assumption is acceptable when $s < \hbar^2\pi^2/(2m^*_{h\perp}L^2)$, because, in this case, the numerator of the first term in the series (i.e., the term with $n = n' = 1$) in formula (1) is maximum and its denominator near the resonance $\hbar\omega \longrightarrow E_{c,\,1,\,\mathbf{k}_\parallel+\kappa_\parallel} - E_{v,\,1,\,\mathbf{k}_\parallel}$ is considerably smaller than the denominators of other nonzero terms in the series. The above criterion can easily be satisfied for standard values of the parameters. Then, we change from summation over $\mathbf{k}_\parallel$ to integration, expand the obtained expression into a power series of $\Delta a = -(\Lambda^{c,\,1}_{ik} - \Lambda^{v,\,1}_{ik})u_{ik}$, and find the linear term of the ε_{ik} expansion in terms of Δa in the simplest case $k_{0,\,\parallel} = 0$; that is,

$$\Delta\varepsilon_{ik} = -A^{11}_{ik}\left(\frac{\hbar^2\pi^2}{2\mu_\parallel L_p^2}\right)^{\frac{1}{2}}\frac{\Delta a}{a+is}. \tag{2}$$

Here, $A^{11}_{ik} = 2e^2L^{11}_{ik}/\pi m^2\omega^2(2\mu/\hbar^2)^{3/2}$, $a = \hbar\omega - E^0_g - \hbar^2\pi^2/(2\mu_\perp L^2)$ is the deviation from the resonance, $\mu_{\perp;\,\parallel} = m^*_{e,\,\perp;\,\parallel}m^*_{h,\,\perp;\,\parallel}/(m^*_{e,\,\perp;\,\parallel} + m^*_{h,\,\perp;\,\parallel})$ is the reduced mass of the electron and the hole in the directions perpendicular and parallel to the quantum well layers, and E^0_g is the band gap in the absence of strain.

Substituting expression (2) into the formula for the linear photoelasticity coefficient in a cubic crystal [1], that is, $P_{111} = -\Delta\varepsilon_{11}/[(\varepsilon^0_{11})^2u_{11}]$, where ε^0_{11} is the component of the stationary permittivity of the layer constituting the quantum well (it is assumed that $\varepsilon^0_{11} = \varepsilon^0_{22} = \varepsilon^0_{33} = \varepsilon_0$, where ε_0 is the stationary permittivity of a bulk crystal), we can estimate the photoelasticity coefficient of the MQWS in the vicinity of the resonance between the ground states of the electron and the hole in the layer with a quantum well

$$P^{\mathrm{MQWS}}_{1111} = -A^{11}_{11}\left(\frac{\hbar^2\pi^2}{2\mu_\parallel L_p^2}\right)^{1/2}\frac{\Lambda_c - \Lambda_v}{(\varepsilon^0_{11})^2(a+is)}. \tag{3}$$

Analysis of the derived expression indicates the importance of the factor $(\hbar^2\pi^2)(2\mu_\parallel L_p^2)^{1/2}$, which is related to the MQWS period or, equivalently, to the quantum well density N_{QW} in the MQWS ($N_{\mathrm{QW}} = N/L_{\mathrm{MQWS}} = 1/L_p$, where N is the number of quantum wells in the MQWS and $L_{\mathrm{MQWS}} = NL$ is the MQWS length in the direction perpendicular to the layers). This is explained by the fact that, upon localization of an electron and a hole in the layer with a quantum well, this system can be considered an oscillator and the density of these oscillators under resonant excitation affects both the linear permittivity (2) and the linear photoelasticity.

A comparison of relationship (3) and the photoelasticity coefficient P^{V}_{1111} near interband resonances in a bulk crystal results in the following relationship (for the same deviations a from the resonance and the same values of s) [4]:

$$\frac{P^{\mathrm{MQWS}}_{1111}}{P^{V}_{1111}} \sim \left[\left(\frac{\hbar^2\pi^2}{2\mu_\parallel L_p^2}\right)/(a+is)\right]^{1/2}. \tag{4}$$

Hence, we have $P^{\mathrm{MQWS}}_{1111} > P^{V}_{1111}$ for $\hbar^2\pi^2/(2\mu_\parallel L_p^2) > |a + is|$. Relationship (4) is qualitatively similar to the relationship between the photoelasticity coefficients $P^{V,\,EX}_{1111}$ and P^{V}_{1111} for the bulk exciton [5]:

$$\frac{P^{V,\,EX}_{1111}}{P^{V}_{1111}} \sim [R/(a+is)]^{3/2}.$$

Here, $R = \mu e^4/(2\varepsilon_0^2\hbar^2)$ is the energy of the ground exciton state and μ is the reduced mass of the electron and the hole in the bulk crystal. Thus, the system of noninteracting electrons and holes in the quantum well behaves as an exciton in which the spatial confinement of the motion of the electron and the hole inside the quantum well plays the role of the Coulomb interaction localizing the electron and the hole together. As follows from a comparison of P_{1111}^{MQWS} and $P_{1111}^{V,\,EX}$,

$$\frac{P_{1111}^{\mathrm{MQWS}}}{P_{1111}^{V,\,EX}} \sim \left\{\left[(a+is)\left(\frac{\hbar^2\pi^2}{2\mu_{\|}L_P^2}\right)^{1/2}\right]^{2/3}/R\right\}^{3/2},$$

the magnitude of P_{1111}^{MQWS} can significantly exceed $P_{1111}^{V,\,EX}$. According to calculations for the standard parameters, this is achieved with deviations from the resonance when $P_{1111}^{V,\,EX}$ has sufficiently large values. For instance, $P_{1111}^{\mathrm{MQWS}} \sim -0.51$ for the GaAs/Al$_x$Ga$_{1-x}$As system at $a \sim 8$ meV, $s \sim 4$ meV, $L_P = 309$ Å ($L = 102$ Å), and $P_{1111}^{V,\,EX} \sim -0.31$.

Thus, the system of noninteracting electrons and holes in a layer constituting the quantum well in the MQWS can be considered an exciton-like oscillator in which the localization of an electron and a hole in the quantum well fulfills the function of a Coulomb interaction in the exciton. The enhancement of the frequency dependence of the permittivity in the immediate vicinity of the resonance in systems of these oscillators in the MQWS leads to an increase in the photoelasticity coefficients as compared to the bulk case. This increase is quite essential and, under certain conditions, can even exceed the resonant photoelasticity near the resonance of a bulk exciton.

The multiple quantum well structures have recently been applied to designing acoustooptic and electrooptic devices for electromagnetic radiation modulation (see, for example, [6]). The efficiency of acoustooptic modulators is primarily determined by photoelasticity coefficients. In this respect, the resonant behavior of photoelasticity coefficients, which is characterized by a substantial increase in their values, is of particular interest. The experimental investigation of the resonant photoelasticity coefficients near interband resonances in the MQWS can be performed according to the standard scheme for determining the resonant photoelasticity in bulk anisotropic crystals with the use of Brillouin scattering, as was done in [7, 8].

ACKNOWLEDGMENTS

We are grateful to Yu.V. Gulyaev for fruitful discussions and A.Yu. Léderman for his continuing interest in the work.

REFERENCES

1. R. A. Ayukhanov and G. N. Shkerdin, Fiz. Tverd. Tela (St. Petersburg) **35** (7), 1916 (1993) [Phys. Solid State **35**, 957 (1993)].
2. S. L. Adler, Phys. Rev. **126** (2), 413 (1962).
3. D. S. Chemla, Helv. Phys. Acta **56**, 607 (1983).
4. Yu. V. Gulyaev and G. N. Shkerdin, Fiz. Tekh. Poluprovodn. (Leningrad) **14** (12), 2397 (1980) [Sov. Phys. Semicond. **14**, 1422 (1980)].
5. R. A. Ayukhanov, Yu. V. Gulyaev, and G. N. Shkerdin, Fiz. Tekh. Poluprovodn. (Leningrad) **16** (12), 2174 (1982) [Sov. Phys. Semicond. **16**, 1402 (1982)].
6. F. C. Jain, K. Bhattachajee, and T. Grudkowski, in *Proceedings of IEEE 1991 Ultrasonic Symposium, Lake Buena Vista, 1991*, Vol. 1, p. 529.
7. R. Berkowicz and T. Skettrup, Phys. Rev. B **11** (6), 2316 (1975).
8. S. Adachi and C. Hamaguchi, Phys. Rev. B **19** (2), 938 (1979).

Translated by M. Lebedkin

Physics of the Solid State, Vol. 43, No. 3, 2001, pp. 530–538. Translated from Fizika Tverdogo Tela, Vol. 43, No. 3, 2001, pp. 511–519.
Original Russian Text Copyright © 2001 by Galkin, Margulis, Shorokhov.

Intraband Absorption of Electromagnetic Radiation by Quantum Nanostructures with Parabolic Confinement Potential

N. G. Galkin, V. A. Margulis, and A. V. Shorokhov
Mordovian State University, Bol'shevistskaya ul. 68, Saransk, 430000 Russia
e-mail: theorphysics@mrsu.ru
e-mail: margulis@mrsu.ru

Received August 11, 2000

Abstract—The intraband absorption of electromagnetic radiation by two types of nanostructures of cylindrical symmetry—by a quantum cylinder (ring) and a quantum wire—is investigated. Analytical expressions for the coefficients of absorption of high-frequency electromagnetic radiation by the electron gas of nanostructures are obtained. It is shown that the absorption curve exhibits resonance peaks and that, in the case of a degenerate gas, these peaks have breaks. © *2001 MAIK "Nauka/Interperiodica".*

1. INTRODUCTION

One of the basic methods for investigating the spectral properties of an electron gas and the lateral-confinement parameters of different low-dimensional structures is examination of intraband electron transitions caused by electromagnetic radiation. This type of examination is of utmost importance for those quantum nanostructures whose confinement may be modeled by a parabolic potential, since, in this case, according to the generalized Kohn theorem, electron–electron interaction usually has no influence on the optical properties of the system. It should be noted that, by means of a parabolic potential, many low-dimensional structures can be described. For example, in [1], it was shown that the parabolic potential is equivalent to the potential produced by a positive charge uniformly distributed over an infinite layer. In this case, the optical properties of the system are independent of both the electron–electron interaction and the number of electrons in the layer. At the present time, progress in nanotechnologies permits one to construct strained GaAs/GaAlAs layers of various curvatures [2] and, in particular, to create cylindrical surfaces exhibiting very interesting physical properties [3, 4].

Another type of structure that can be described by the model of parabolic potential is quantum wires. Recently, the technology for production of high-perfect semiconductor quantum wires with an arbitrary potential profile, in particular, with a parabolic confinement potential, was elaborated [5].

Optical electron transitions in various quantum nanostructures are now widely studied. In particular, intraband transitions in quantum wells [6–8], quantum wires [9], quantum layers [10], and arrays of antiwires [11] have been considered. The hybrid phonon resonance in a quasi-two-dimensional structure was examined in [12]. Multiphonon resonance was studied in [13, 14]. The optical properties of a quantum point junction were investigated in [15]. In [16], the influence of electron correlations on the optical absorption of a quantum point was considered. The theory of magnetooptical absorption by a parabolic quantum channel in a two-dimensional electron gas was expounded in [17].

The aim of this work is to examine the absorption of electromagnetic radiation by quantum structures of two types in a longitudinal magnetic field, namely, by the quantum layer of a finite thickness rolled as a cylinder and by the quantum wire. Moreover, the absorption of electromagnetic radiation by a quantum ring of finite thickness, as the limiting case of the quantum cylinder, was considered. Note that the applied magnetic field can couple the motion along the field with that in the transverse direction and cause hybridization of the spectrum. This fact, in turn, can result in interesting physical effects. In particular, as is shown below, resonance absorption occurs at hybrid frequencies rather than at the cyclotron frequency.

Since only the systems described by parabolic confinement potential are considered in this work, the electron–electron interaction is not taken into account here. However, we note that the Kohn theorem is not true for two basic cases: for multicomponent systems (such as double quantum wells [18]) and for a nonparabolic well [19]. In such systems, electron–electron interaction can have a strong effect on the optical properties of electrons.

In our work, we examine the dependence of the absorption coefficient Γ on the radiation frequency ω for the structures mentioned above. In calculating $\Gamma(\omega)$, we used the approach which was elaborated in [20, 21].

Both the cases of degenerated and nondegenerated gas are considered.

As is shown below, the frequency dependence of electromagnetic radiation absorption is of the resonance type. Note that the resonance absorption takes place only if the broadening of electron energy levels caused by temperature and scattering is sufficiently small.

2. A QUANTUM RING OF FINITE WIDTH AND A QUANTUM CYLINDER OF FINITE THICKNESS

We will model a thin quantum ring and a quantum cylinder with thin walls by using the following approach. Let us consider 2D-electron gas in a quantum channel with parabolic confinement potential. If, in one of the directions, the periodic boundary conditions are imposed on the electron wave function,

$$\Psi(x, y) = \Psi(x + L, y), \tag{1}$$

where L is the channel length, we will obtain the model of a quantum ring of finite width. In this case, the effective ring width coincides with the channel width, $l_{\text{eff}} = \sqrt{\hbar/m^*\omega_0}$.

By adding a term describing free motion along the z axis to the Hamiltonian, we can obtain a model of a quantum cylinder of finite thickness.

It is clear that the resonance character of the absorption will take place only for the transitions in which discrete spectral quantum numbers are changed (the photon polarization vector is perpendicular to the z axis). This conclusion follows from the fact that the motion of electrons along the z axis has no influence on the resonance optical transitions. When the cylinder height tends to zero, we have a ring whose absorption coefficient is the same as that of a cylinder, as will be shown below.

For the cylinder, the Hamiltonian H_0 of one-electron spinless states is of the form

$$H_0 = \frac{1}{2m^*}\left(\mathbf{p} - \frac{e}{c}\mathbf{A}\right)^2 + \frac{m^*\omega_0^2 y^2}{2}, \tag{2}$$

where ω_0 is the frequency of the confinement potential, m^* is the effective mass, and $\mathbf{p}$ is the electron momentum.

The gauge of the vector potential is chosen such that $\mathbf{A} = (-By, 0, 0)$. Then, after imposing periodic boundary conditions along the x axis, we obtain the energy spectrum of the quantum cylinder:

$$\varepsilon_{nmp} = \hbar\Omega\left(n + \frac{1}{2}\right) + \lambda m^2 + \frac{p^2}{2m^*}, \tag{3}$$

where $\Omega = \sqrt{\omega_c^2 + \omega_0^2}$, $\omega_c = |e|B/m^*c$ is the cyclotron frequency, $\lambda = 2\pi\hbar^2\omega_0^2/m^*L^2\Omega^2$ is the energy of the dimensional confinement, p is the electron momentum along the field direction, $m = 0, \pm1, \pm2, \ldots$, and $n = 0, 1, 2, \ldots$.

The wave functions corresponding to the energies in Eq. (3) can be written in the form

$$\Psi_{nmp} = \frac{1}{\sqrt{2\pi\hbar}}\exp\left(\frac{ipz}{\hbar}\right)\frac{1}{2\pi R} \times \exp\left(\frac{imx}{R}\right)\Phi_n\left[\frac{1}{l}\left(y + \frac{\omega_c l^2}{\Omega R}m\right)\right]. \tag{4}$$

Here, $l = \sqrt{\hbar/m^*\Omega}$, $L = 2\pi R$ is the channel length and $\Phi_n(x)$ are the oscillator functions.

In the case of a nondegenerated gas, in the first-order perturbation theory with respect to the constant of electron–photon interaction, the absorption coefficient is described by the following expression, which follows from [20]:

$$\Gamma^{\text{cyl}} = \frac{2\pi\sqrt{\varepsilon(\omega)}}{c\hbar N_{\mathbf{f}}}\left[1 - \exp\left(-\frac{\hbar\omega}{T}\right)\right] \times \sum_{m,n,p}\sum_{m',n',p'} f_0(\varepsilon_{mnp})|\langle m, n, p|H_R|m', n', p'\rangle|^2 \times \delta(\varepsilon_{mnp} - \varepsilon_{m'n'p'} + \hbar\omega), \tag{5}$$

where $\varepsilon(\omega)$ is the real part of the permittivity, $\mathbf{f}$ is the wave vector of the photon, $f_0(\varepsilon_{mnp})$ is the electron distribution function, $N_{\mathbf{f}}$ is the number (per unit volume) of photons of frequency ω, and the factor $(1 - \exp(-\hbar\omega/T))$ allows for stimulated photon emission.

The normalization constant of the distribution function in Eq. (5) is found from the condition

$$\frac{L_z}{2\pi\hbar}\sum_{m=-\infty}^{\infty}\sum_{n=0}^{\infty}\int_{-\infty}^{\infty} f_0^{\text{cyl}}(\varepsilon_{mnp})dp = N. \tag{6}$$

Here, N is the number of electrons per unit volume and L_z is the cylinder length along the z axis.

Hence, the distribution function $f_0^{\text{cyl}}(\varepsilon_{mnp})$ takes the form

$$f_0^{\text{cyl}} = \frac{4\pi N\sinh(\hbar\Omega/2T)}{\sqrt{2\pi m^*T}L_z\Theta_3[\exp(-\lambda/T)]} \times \exp\left\{-\frac{1}{T}\left[\hbar\Omega\left(n + \frac{1}{2}\right) + \lambda m^2 + \frac{p^2}{2m^*}\right]\right\}, \tag{7}$$

where $\Theta_3(x)$ is the Jacobian theta function.

Let the direction of the photon polarization be coincident with the direction of the y axis. Then, the operator of the electron–photon interaction is written in the form

$$H_R = -\frac{ie\hbar}{m^*}\sqrt{\frac{2\pi\hbar N_{\mathbf{f}}}{\varepsilon(\omega)\omega}}\frac{\partial}{\partial y}. \tag{8}$$

In the dipole approximation, the square of the modulus of the matrix element of H_R is easily found to be

$$\begin{aligned}|\langle m, n, p|H_R|m', n', p'\rangle|^2 &= \frac{e^2\hbar^2}{m^{*2}l^2}\left(\frac{2\pi\hbar N_{\mathbf{f}}}{\varepsilon(\omega)\omega}\right)\delta_{m,m'}\delta_{p,p'} \\ &\times\left(\frac{n+1}{2}\delta_{n,n'-1} - \frac{n}{2}\delta_{n,n'+1}\right).\end{aligned} \tag{9}$$

As is evident from Eq. (9), only transitions between the neighboring levels $n' = n \pm 1$ are possible in the dipole approximation.

Substituting Eq. (9) into Eq. (5), we obtain the absorption coefficient:

$$\begin{aligned}\Gamma^{\mathrm{cyl}}(\omega) &= 2\hbar\left(\frac{\pi e}{m^* l}\right)^2\frac{1-\exp(-\hbar\omega/T)}{c\omega\sqrt{\varepsilon(\omega)}} \\ &\times\sum_{m=-\infty}^{\infty}\sum_{n=0}^{\infty} f_0^{\mathrm{cyl}}(\varepsilon_{mn0})[(n+1)\delta(\omega-\Omega) - n\delta(\omega+\Omega)].\end{aligned} \tag{10}$$

From Eq. (10), it is clear that the transitions occur at the resonance frequency $\omega = \Omega$.

To take into account the resonance broadening due to electron scattering, we replace the delta-function peaks by the Lorentzian

$$\delta_\tau = \frac{(\pi\tau)^{-1}}{\tau^{-2} + x^2}. \tag{11}$$

Here, τ is the phenomenological relaxation time. After substitution Eq. (11) into Eq. (10), we obtain

$$\begin{aligned}\Gamma^{\mathrm{cyl}}(\omega) &= \frac{\hbar N}{c\omega}\left(\frac{\pi e}{m^* l}\right)^2\frac{1-\exp(-\hbar\omega/T)}{2\sqrt{\varepsilon(\omega)}\sinh(\hbar\Omega/2T)} \\ &\times\left[\frac{(\pi\tau)^{-1}}{\tau^{-2}+(\omega-\Omega)^2}\exp(\hbar\Omega/2T)\right. \\ &\left.-\frac{(\pi\tau)^{-1}}{\tau^{-2}+(\omega+\Omega)^2}\exp(-\hbar\Omega/2T)\right].\end{aligned} \tag{12}$$

Taking into account that the probability of the spontaneous emission of photons is exponentially small and the hybrid frequency is sufficiently large ($\hbar\Omega \gg T$), we drop the exponentially small terms of the order of $\exp(-\hbar\omega/T)$ and $\exp(-\hbar\Omega/T)$ in Eq. (12). In this case, we obtain the estimation

$$\frac{\Gamma^{\mathrm{cyl}}(\omega)}{\Gamma_0} = \frac{\Omega}{\omega}\frac{1}{1+\tau^2(\omega-\Omega)^2}, \tag{13}$$

where

$$\Gamma_0 = \frac{e^2 N\tau}{\sqrt{\varepsilon(\omega)}cm^*}. \tag{14}$$

As is clear from Eq. (13), there is a unique resonance at the point $\omega = \Omega$ which corresponds to the transition between the neighboring hybrid levels.

For a degenerated gas, the expression for $\Gamma(\omega)$ can be obtained from the initial expression (10) by formal replacement of $f_0(\varepsilon_{mnp})$ by $f_0(\varepsilon_{mnp})[1 - f_0(\varepsilon_{mnp} + \hbar\omega)]$. Here, $f_0(\varepsilon_{mnp})$ is the Fermi distribution function.

Therefore, for the absorption coefficient of the degenerated gas, we obtain the estimation

$$\Gamma^{\mathrm{cyl}}(\omega) = \frac{\Omega}{\omega}\frac{1}{1+\tau^2(\omega-\Omega)^2}\gamma_0(\omega), \tag{15}$$

where

$$\begin{aligned}\gamma_0(\omega) &= \frac{2\pi e^2\tau}{m^* c\sqrt{\varepsilon(\omega)}} \\ &\times\sum_{nmp} f_0(\varepsilon_{mnp})[1 - f_0(\varepsilon_{mnp}+\hbar\omega)](n+1)\end{aligned} \tag{16}$$

and the normalizing volume is taken to be equal to unity.

As is evident from Eq. (15), the response of the electron gas to the perturbation produced by the electromagnetic radiation includes two factors. The first of them refers to the resonance peak in the curve $\Gamma(\omega)$ at the point $\omega = \Omega$. The second one $\gamma_0(\omega)$, as will be shown below, is responsible for the breaks on the resonance curve.

The dependence $\Gamma^{\mathrm{cyl}}(\omega)$ for the nondegenerate gas is shown in Fig. 1. As follows from the resonance conditions and Fig. 1, the peak location in the curve $\Gamma(\omega)$ depends on the magnitude of the magnetic field.

In the case when the cylinder height is small enough, the wave function and the spectrum of the one-electron states have the form

$$\Phi_{nm} = \frac{1}{2\pi R}\exp\left(\frac{imx}{R}\right)\Phi_n\left[\frac{1}{l}\left(y + \frac{\omega_c l^2}{\Omega R}m\right)\right]\varphi(z), \tag{17}$$

$$E_{nm} = \hbar\Omega\left(n+\frac{1}{2}\right) + \lambda m^2, \tag{18}$$

where $\varphi(z)$ is the part of the wave function that describes the motion along the z axis.

This case corresponds to a thin quantum ring of effective width $\sqrt{\hbar/m^*\omega_0}$. For the case of a nondegenerate gas, the expression for Γ^{ring} is the same as the expression for Γ^{cyl}, as was indicated above.

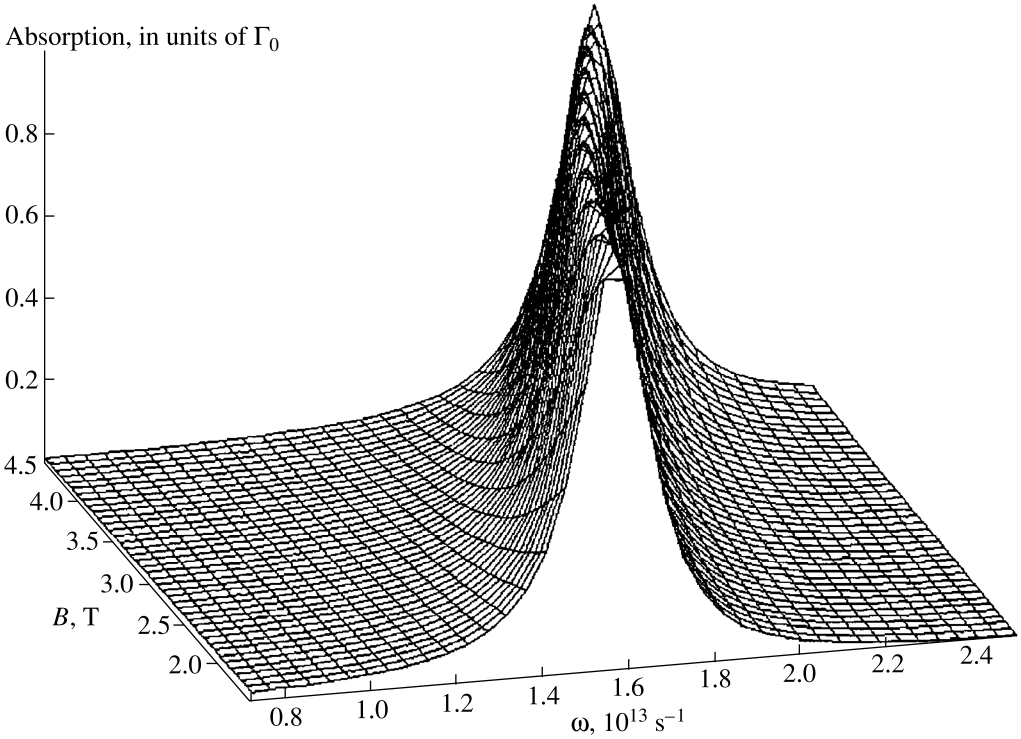

Fig. 1. Absorption coefficient of the quantum cylinder as a function of the frequency of the electromagnetic radiation and the magnetic field in the case of a nondegenerate gas; $\omega_0 = 1.5 \times 10^{13}$ s^{-1} and $\tau = 10^{-12}$ s.

3. ABSORPTION COEFFICIENT FOR THE QUANTUM WIRE

Now, we consider the quantum wire of a circular cross section in a longitudinal magnetic field characterized by vector potential $\mathbf{A} = (-yB/2, xB/2, 0)$. The confinement potential is assumed to be the sum of two parabolic potentials of the same characteristic frequencies. The spectrum of the parabolic quantum wire has the well-known form

$$E_{mnp} = \frac{\hbar\omega_c}{2}m + \frac{\hbar\Omega}{2}(2n + |m| + 1) + \frac{p^2}{2m^*}, \qquad (19)$$

where $m = 0, \pm1, \pm2, \ldots$; $n = 0, 1, 2, \ldots$; p is the momentum along the field direction; and $\Omega = \sqrt{\omega_c^2 + 4\omega_0^2}$, ω_0 is the frequency of the parabolic potential.

In the cylindrical coordinates, the wave functions corresponding to the energies in Eq. (19) are of the form

$$|m, n, p\rangle = \frac{1}{\sqrt{2\pi}}\exp\left(\frac{ipz}{\hbar}\right)\exp(im\varphi)R_{m,n}(\rho), \qquad (20)$$

where $R_{m,n}(\rho) = C_{mn}\rho^{|m|}\exp(-\rho^2/4l_0^2)L_n^{|m|}(-\rho^2/2l_0^2)$, $L_n^{|m|}$ is the Laguerre polynomial, $l_0 = \sqrt{\hbar/m^*\Omega}$, and $C_{mn} = (1/l_0^{|m|+1})\sqrt{n!/2^{|m|}(n+|m|)!}$.

The absorption coefficient of the wire can be found with formula (5) by replacing ε_{mnp} with E_{mnp}.

Let the direction of the electromagnetic wave polarization be coincident with the y axis. Then, the operator of the electron–photon interaction can be written in the form

$$H_R = -\frac{ie\hbar}{m^*}\sqrt{\frac{2\pi\hbar N_{\mathbf{f}}}{\varepsilon(\omega)\omega}}\left(\frac{\partial}{\partial y} - \frac{i}{2l_B^2}x\right), \qquad (21)$$

where $l_B^2 = c\hbar/|e|B$. By passing to the cylindrical coordinates, we obtain from Eq. (21)

$$H_R = -\frac{ie\hbar}{m^*}\sqrt{\frac{2\pi\hbar N_{\mathbf{f}}}{\varepsilon(\omega)\omega}} \times\left(\sin\varphi\frac{\partial}{\partial\rho} + \frac{\cos\varphi}{\rho}\frac{\partial}{\partial\varphi} - \frac{i}{2l_B^2}\rho\cos\varphi\right). \qquad (22)$$

The matrix elements of H_R are of the form

$$\langle m, n, p|H_R|m', n', p'\rangle = \frac{e\hbar}{2m^*}\sqrt{\frac{2\pi\hbar N_{\mathbf{f}}}{\varepsilon(\omega)\omega}} \times\left[\delta_{m,m'+1}\left\langle R_{m,n}\left|-\frac{\partial}{\partial\rho} + \frac{m'}{\rho} - \frac{\rho}{2l_B^2}\right|R_{m',n'}\right\rangle + \delta_{m,m'-1}\left\langle R_{m,n}\left|\frac{\partial}{\partial\rho} + \frac{m'}{\rho} - \frac{\rho}{2l_B^2}\right|R_{m',n'}\right\rangle\right]\delta_{pp'}. \qquad (23)$$

The quantities that are multiplied by $\delta_{m, m'+1}$ and $\delta_{m, m'-1}$ in Eq. (23) are conveniently calculated separately. Since the modulus of m is contained in the expression for $R_{m, n}$, it is necessary to consider three cases: $m \geq 1$, $m \leq -1$, and $m = 0$. After long mathematical manipulation, we obtain expressions for the squares of the matrix elements of H_R (see Appendix).

First, let us consider the case of a nondegenerate electron gas. After calculating the normalizing constant by using a condition similar to Eq. (6), we obtain

$$f_0^{\text{wire}} = \frac{4\pi\hbar N}{\sqrt{2\pi m^* T}L_z}\left(\cosh\frac{\hbar\Omega}{2T} - \cosh\frac{\hbar\omega_c}{2T}\right) \times \exp(-E_{mnp}/T). \tag{24}$$

It is convenient to represent the expression for the absorption coefficient as a sum of three terms, $\Gamma^{\text{wire}}(\omega) = \Gamma^{(+)} + \Gamma^{(-)} + \Gamma^{(0)}$, where $\Gamma^{(+)}$ corresponds to the case of $m \geq 1$:

$$\begin{aligned}\Gamma^{(+)} = A\sum_{m,n,p} f_0(E_{mnp})\Bigg[&(n+m)\left(\frac{1}{l_0^2} - \frac{1}{l_B^2}\right)^2 \\ &\times\delta\left(\omega + \frac{1}{2}(\omega_c + \Omega)\right) + (n+1)\left(\frac{1}{l_0^2} + \frac{1}{l_B^2}\right)^2 \\ &\times\delta\left(\omega + \frac{1}{2}(\omega_c - \Omega)\right) + 4(m+1)^2 \\ &\times\sum_{n'}\frac{n'!(n+m)!}{n!(n'+m+1)!}\left[\frac{\theta(n'-n)}{l_0^2} - \frac{(-1)^{n'}}{l_B^2}\right]^2 \\ &\times\delta\left(\omega - \Omega(n'-n) - \frac{1}{2}(\omega_c + \Omega)\right)\Bigg];\end{aligned} \tag{25}$$

and $\Gamma^{(-)}$ corresponds to the case of $m \leq -1$:

$$\begin{aligned}\Gamma^{(-)} = A\sum_{s,n,p} f_0(E_{snp})\Bigg[&(s+n)\left(\frac{1}{l_0^2} + \frac{1}{l_B^2}\right)^2 \\ &\times\delta\left(\omega + \frac{1}{2}(\omega_c - \Omega)\right) + (n+1)\left(\frac{1}{l_0^2} - \frac{1}{l_B^2}\right)^2 \\ &\times\delta\left(\omega - \frac{1}{2}(\omega_c + \Omega)\right) + 4(s+1)^2 \\ &\times\sum_{n'}\frac{n'!(n+s)!}{n!(n'+s+1)!}\left[\frac{\theta(n'-n)}{l_0^2} + \frac{(-1)^{n'}}{l_B^2}\right]^2 \\ &\times\delta\left(\omega - \Omega(n'-n) + \frac{1}{2}(\omega_c - \Omega)\right)\Bigg].\end{aligned} \tag{26}$$

Here, $s = |m|$, $E_{snp} = \hbar\Omega(n + 1/2) + \hbar(\Omega - \omega_c)s/2 + p^2/2m^*$. Finally, $\Gamma^{(0)}$ corresponds to the case of $m = 0$:

$$\begin{aligned}\Gamma^{(0)} = 4A\sum_{n,n',p} f_0(E_{0np})\frac{1}{n'+1}\Bigg[&\left(\frac{1}{l_0^2} + \frac{(-1)^{n'}}{l_B^2}\right)^2 \\ &\times\delta\left(\omega - \frac{1}{2}(\omega_c + \Omega) - \Omega(n'-n)\right) + \left(\frac{1}{l_0^2} - \frac{(-1)^{n'}}{l_B^2}\right)^2 \\ &\times\delta\left(\omega + \frac{1}{2}(\omega_c - \Omega) - \Omega(n'-n)\right)\Bigg].\end{aligned} \tag{27}$$

In Eqs. (25)–(27), we introduced the notation

$$A(\omega) = \frac{\pi^2 e^2 \hbar l_0^2(1 - e^{-\hbar\omega/T})}{2m^{*2}c\sqrt{\varepsilon(\omega)}\omega}, \quad \theta(x) = \begin{cases}1, & x > 0 \\ 0, & x \leq 0.\end{cases}$$

As follows from Eqs. (25)–(27), there are four kinds of resonance points:

$$\omega_{1,2} = \frac{\Omega \mp \omega_c}{2}, \quad \omega_{3,4} = \frac{\Omega \mp \omega_c}{2} + \Omega(n'-n), \quad n' > n. \tag{28}$$

Let us rearrange the terms in $\Gamma^{\text{wire}}(\omega)$ according to their behavior at the resonance points. As a result, we obtain $\Gamma^{\text{wire}} = \Gamma^{(1)} + \Gamma^{(2)} + \Gamma^{(3)} + \Gamma^{(4)}$, where the term containing the singularities of the first type has the form

$$\begin{aligned}\Gamma^{(1)} = A\Bigg[&\sum_{m,n,p} f_0(E_{mnp})(n+1)\left(\frac{1}{l_0^2} + \frac{1}{l_B^2}\right)^2 \\ &+ 4\sum_{s,n,p} f_0(E_{snp})(s+1)^2\left(\frac{1}{l_0^2} + \frac{(-1)^n}{l_B^2}\right)^2\frac{1}{n+s+1} \\ &+ 4\sum_{n,p} f_0(E_{0np})\frac{1}{n+1}\left(\frac{1}{l_0^2} - \frac{(-1)^n}{l_B^2}\right)^2\Bigg]\delta\left(\omega + \frac{\omega_c - \Omega}{2}\right),\end{aligned} \tag{29}$$

while the term containing the singularities of the second type has the form

$$\begin{aligned}\Gamma^{(2)} = A\Bigg[&\sum_{s,n,p} f_0(E_{snp})(n+1)\left(\frac{1}{l_0^2} - \frac{1}{l_B^2}\right)^2 \\ &+ 4\sum_{m,n,p} f_0(E_{mnp})(m+1)^2\left(\frac{1}{l_0^2} - \frac{(-1)^n}{l_B^2}\right)^2\frac{1}{n+m+1} \\ &+ 4\sum_{n,p} f_0(E_{0np})\frac{1}{n+1}\left(\frac{1}{l_0^2} + \frac{(-1)^n}{l_B^2}\right)^2\Bigg]\delta\left(\omega - \frac{\omega_c + \Omega}{2}\right).\end{aligned} \tag{30}$$

The term having singularities of the third type is of the form

$$\begin{aligned}\Gamma^{(3)} = 4A\Bigg[&\sum_{snp} f_0(E_{snp})(s+1)^2 \sum_{n'>n}\left(\frac{1}{l_0^2}+\frac{(-1)^{n'}}{l_B^2}\right)^2\\ &+\frac{n'!(n+s)!}{n!(n'+s+1)!}+\sum_{n,\,n'>n,\,p} f_0(E_{0np})\frac{1}{n'+1}\\ &\times\left(\frac{1}{l_0^2}-\frac{(-1)^{n'}}{l_B^2}\right)^2\Bigg]\delta\left(\omega+\frac{\omega_c-\Omega}{2}-\Omega(n'-n)\right),\end{aligned} \tag{31}$$

and, finally, the term having singularities of the fourth type is of the form

$$\begin{aligned}\Gamma^{(4)} = 4A\Bigg[&\sum_{mnp} f_0(E_{mnp})(m+1)^2 \sum_{n'>n}\left(\frac{1}{l_0^2}-\frac{(-1)^{n'}}{l_B^2}\right)^2\\ &+\frac{n'!(n+m)!}{n!(n'+m+1)!}+\sum_{n,\,n'>n,\,p} f_0(E_{0np})\frac{1}{n'+1}\\ &\times\left(\frac{1}{l_0^2}+\frac{(-1)^{n'}}{l_B^2}\right)^2\Bigg]\delta\left(\omega-\frac{\omega_c+\Omega}{2}-\Omega(n'-n)\right).\end{aligned} \tag{32}$$

Note that, in $\Gamma^{(3)}$ and $\Gamma^{(4)}$, the inequality $n' > n$ is fulfilled, since $\omega_c < \Omega$.

In the vicinity of a resonance point, where ω is such that $(2\omega \mp \omega_c - \Omega)/2\Omega$ is an integer, the dominant contribution to $\Gamma^{(3)}$ and $\Gamma^{(4)}$ comes from only one term in the sum over n'. We introduce the notation

$$N^{\pm} = \left[\frac{2\omega\pm\omega_c-\Omega}{2\Omega}\right], \tag{33}$$

where plus corresponds to $\Gamma^{(3)}$, minus corresponds to $\Gamma^{(4)}$, and the integer part of the variable x is denoted by $[x]$. Then, n' can be written as $n' = N^{\pm} + n$.

In order to take level broadening into account, we replace the delta-function peaks by the Lorentzian $\delta_\tau(\Delta\omega_i)$, where $\Delta\omega_i = \omega - \omega_i$ is the resonance detuning ($i = 1, 2, 3, 4$).

After substituting the distribution function (24) into Eqs. (29)–(32) and dropping the exponentially small terms of the same order as in Eq. (12), we obtain a final expression for Γ^{wire}. For the term containing the resonance points of the first type, we obtain

$$\begin{aligned}\frac{\Gamma^{(1)}}{\Gamma_0} = 4\frac{\Omega}{\omega}\Bigg[&\sum_{s,\,n} g_{sn}(s+1)^2\left(1+\frac{(-1)^n\omega_c}{\Omega}\right)^2\frac{1}{n+s+1}\\ &+\sum_n g_{0n}\left(1-\frac{(-1)^n\omega_c}{\Omega}\right)^2\frac{1}{n+1}\Bigg]\frac{1}{1+\tau^2(\omega-\omega_1)^2}.\end{aligned} \tag{34}$$

For the term containing the resonance points of the second type, we find

$$\begin{aligned}\frac{\Gamma^{(2)}}{\Gamma_0} = 4\frac{\Omega}{\omega}\Bigg[&\sum_{m,\,n} g_{mn}(m+1)^2\left(1-\frac{(-1)^n\omega_c}{\Omega}\right)^2\frac{1}{n+m+1}\\ &+\sum_n g_{0n}\left(1+\frac{(-1)^n\omega_c}{\Omega}\right)^2\frac{1}{n+1}\Bigg]\frac{1}{1+\tau^2(\omega-\omega_2)^2}.\end{aligned} \tag{35}$$

The term containing the resonance points of the third type is of the form

$$\begin{aligned}\frac{\Gamma^{(3)}}{\Gamma_0} = 4\frac{\Omega}{\omega}\Bigg[&\sum_{s,\,n} g_{sn}(s+1)^2\left(1+\frac{(-1)^{n+N^+}\omega_c}{\Omega}\right)^2\\ &\times\frac{(n+N^+)!(n+s)!}{n!(n+N^++s+1)!}+\sum_n g_{0n}\frac{1}{n+N^++1}\\ &\times\left(1-\frac{(-1)^{n+N^+}\omega_c}{\Omega}\right)^2\Bigg]\frac{1}{1+\tau^2(\omega-\omega_3)^2}.\end{aligned} \tag{36}$$

Finally, for $\Gamma^{(4)}$, we obtain

$$\begin{aligned}\frac{\Gamma^{(4)}}{\Gamma_0} = 4\frac{\Omega}{\omega}\Bigg[&\sum_{m,\,n} g_{mn}(m+1)^2\left(1-\frac{(-1)^{n+N^-}\omega_c}{\Omega}\right)^2\\ &\times\frac{(m+1)^2(n+N^-)!(n+m)!}{n!(n+m+N^-+1)!}+\sum_n g_{0n}\frac{1}{n+N^-+1}\\ &\times\left(1+\frac{(-1)^{n+N^-}\omega_c}{\Omega}\right)^2\Bigg]\frac{1}{1+\tau^2(\omega-\omega_4)^2}.\end{aligned} \tag{37}$$

Here, $g_{mn} = \exp[-(\hbar(\omega_c + \Omega)m + 2\hbar\Omega n)/2T]$, $g_{sn} = \exp[-(\hbar(\Omega - \omega_c)s + 2\hbar\Omega n)/2T]$, $\omega_1 = (\Omega - \omega_c)/2$, $\omega_2 = (\Omega + \omega_c)/2$, $\omega_3 = \Omega N^+ - (\omega_c - \Omega)/2$, and $\omega_4 = (\Omega + \omega_c)/2 + \Omega N^-$.

Thus, in the case of a quantum wire, the resonance points are given by the common formula $\omega = \Omega(k + 1/2) \pm \omega_c/2$, where $k = 0, 1, 2, \ldots$.

The $\Gamma^{\text{wire}}(\omega)$ dependence for the case of a nondegenerate gas is shown in Fig. 2.

In the case of a degenerate gas, it is convenient to write the absorption coefficient in a form similar to that in the nondegenerate case. To do this, we transform the integral over the momentum in $\Gamma(\omega)$ into a series by summing the residues at the simple poles:

$$\begin{aligned}&\frac{L_z}{2\pi\hbar}\int f_0(E_{mnp})[1-f_0(E_{mnp}+\hbar\omega)]dp\\ &\quad= \frac{L_z}{8\hbar}\sqrt{\frac{m^*T}{2}}\frac{\exp(-\hbar\omega/2T)}{\sinh(\hbar\omega/2T)}I_{mn},\end{aligned} \tag{38}$$

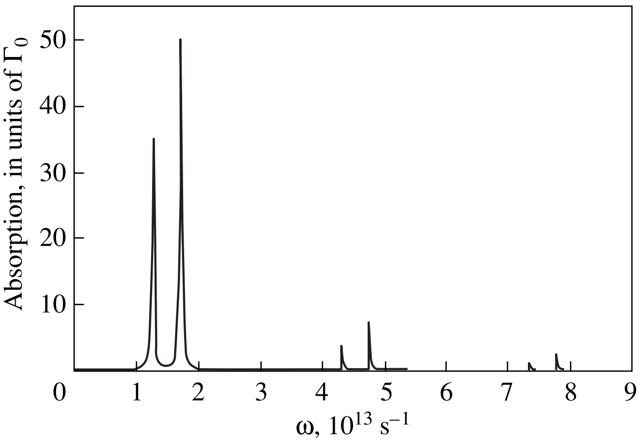

Fig. 2. Absorption coefficient of the quantum wire versus the frequency of the electromagnetic radiation in the case of a nondegenerate gas; $\omega_0 = 1.5 \times 10^{13}$ s^{-1}, $\tau = 5 \times 10^{-12}$ s, $B = 1.5$ T, and $T = 100$ K.

where

$$I_{mn} = \sum_{k=0}^{\infty}\left[\frac{(\mu-\varepsilon_{mn})/T}{\{(\mu-\varepsilon_{mn})^2/T^2+\pi^2(2k+1)^2\}^{3/4}} - \frac{(\mu-\varepsilon_{mn}-\hbar\omega)/T}{\{(\mu-\varepsilon_{mn}-\hbar\omega)^2/T^2+\pi^2(2k+1)^2\}^{3/4}}\right]. \quad (39)$$

Note that Eq. (38) is true only at $T > 0$ because of the method by which it was obtained. In this case, the absorption coefficient $\Gamma^{\text{wire}} = \Gamma^{(1)} + \Gamma^{(2)} + \Gamma^{(3)} + \Gamma^{(4)}$ is of the same form as in the nondegenerate case, if Γ_0 in Eqs. (34)–(37) is formally replaced by Γ_0' and g_{mn} is replaced by I_{mn}, where $\gamma_0' = \pi\tau L_z e^2\sqrt{m^*T}/16\sqrt{2}\,m^*c\sqrt{\varepsilon}\,\hbar$.

4. DISCUSSION

In this work, we obtained relations for the absorption coefficients of high-frequency electromagnetic radiation for a number of quantum nanostructures with a parabolic confinement potential, namely, for a quantum ring of finite width, a quantum wire, and a quantum cylinder of finite thickness. For each of these structures, the absorption curve has resonance peaks due to transitions between certain electron energy levels. In the cases of a quantum ring and quantum cylinder, there is only one resonance point $\omega = \Omega$ in the $\Gamma(\omega)$ curve associated with electron transitions between neighboring levels $n \longrightarrow n + 1$. The transitions accompanied by a change in quantum number m are forbidden. Note that, in the case of a nondegenerated gas, the absorption coefficients for the ring and the cylinder are the same, which is because the motion of electrons along the z axis has no effect on the relevant electron transitions.

In the case of a quantum wire, the situation is much more complex: in the dipole approximation, only the transitions accompanied by a change in both quantum numbers, m and n, take place. In this case, as follows from the relations for $g_{mn}(\omega)$ and $g_{sn}(\omega)$, the peaks of the largest amplitude are located at the resonance frequencies $(\Omega + \omega_c)/2$ and $(\Omega - \omega_c)/2$. The amplitude of the peaks at the frequencies $\omega = \Omega(k + 1/2) \pm \omega_c/2$ (k = 1, 2, …) decreases abruptly with frequency growth (Fig. 2).

From the above discussion, it follows that a series of peaks arises in the $\Gamma(\omega)$ curve, which, in the general case, have a doublet structure, with the spacing between doublet components being equal to ω_c (Fig. 2). The doublets are located periodically with the period Ω, and the peak height decreases dramatically with ω increase. Note that, at the frequency $\Omega = 2\omega_c$, the distances between the peaks are the same, and, therefore, there is no doublet structure. As is clear from Fig. 2, the

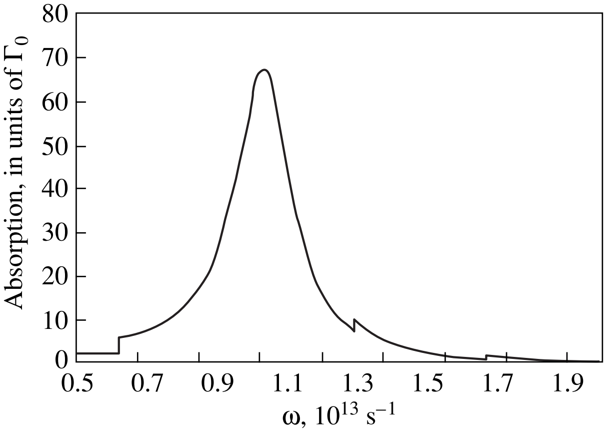

Fig. 3. Absorption coefficient of the quantum cylinder versus the frequency of the electromagnetic radiation in the case of a degenerate gas; $\omega_0 = 10^{13}$ s^{-1}, $\tau = 10^{-12}$ s, $B = 1$ T, $T = 0$ K, and $\mu = 10^{-13}$ erg.

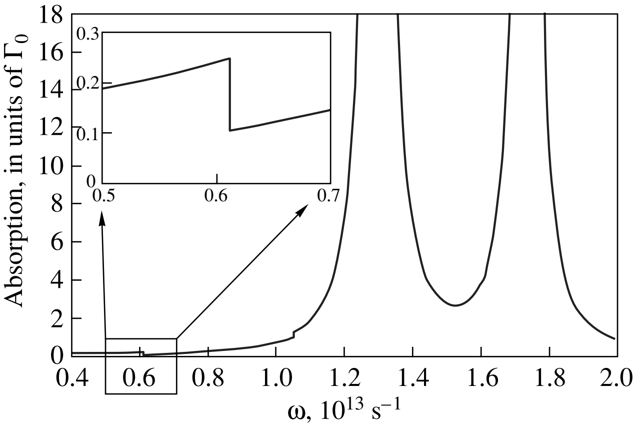

Fig. 4. Absorption coefficient of the quantum wire versus the frequency of the electromagnetic radiation in the case of a degenerate gas; $\omega_0 = 1.5 \times 10^{13}$ s^{-1}, $\tau = 5 \times 10^{-12}$ s, B = 1.5 T, $T = 0$ K, and $\mu = 10^{-13}$ erg.

doublet components are asymmetric. The existence of resonance is independent of the type of electron statistics, and, therefore, the expression for the absorption coefficient in the degenerate case has the same resonance points as in the nondegenerate case. However, in the case of a nondegenerate gas, there can be singularities resultant from gas degeneracy; in this case, there are breaks in the $\Gamma(\omega)$ curve. This is because, at a sufficiently low temperature, only electrons of an energy E higher than the threshold energy ($E > E_{\rm th} = \mu - \hbar\omega$) take part in the absorption. For this reason, when the photon energy $\hbar\omega$ becomes such that the line $\mu - \hbar\omega$ crosses an energy level of the discrete spectrum, there occurs a sharp jump in the density of states, and, as a result, a break appears. Note that the breaks are best-marked only in the resonance region. These breaks can be seen on the $\Gamma(\omega)$ curves presented in Figs. 3 and 4 for the cylinder and the wire, respectively.

For the cylinder, it is easy to estimate the peak height. At the resonance point, we have $\omega = \Omega$, and, therefore, $(\Gamma^{\rm cyl})_{\rm max} = \Gamma_0$. Note that the peak height does not depend on the magnetic field and temperature in this case. We also note that, for the wire, the spacing between the doublet components increases with field growth.

The characteristic feature of the resonance of this type, in contrast with the usual cyclotron resonance, is that the resonance peaks can occur at zero magnetic field. The reason for this lies in the hybridization of the magnetic and dimensional quantization. As a result, the formula for the electron energy levels contains the hybrid frequency Ω in place of ω_c. Therefore, the distance between the levels can be sufficient for the resonance to exist even in the limit of zero magnetic field under the condition, of course, that the dimensional quantization is sufficiently strong.

APPENDIX

Here, we present the squares of the perturbation matrix elements calculated for different values of m.

(1) $m \geq 1$

$$|\langle m, n, p|H_R|m', n', p'\rangle|^2 = D^2\delta_{p,p'}\left\{\frac{l_0^2}{2}\delta_{m,m'+1}\right. \times\left[(n+m)\left(\frac{1}{l_0^2}-\frac{1}{l_B^2}\right)^2\delta_{n,n'} + (n+1)\left(\frac{1}{l_0^2}+\frac{1}{l_B^2}\right)^2\delta_{n,n'-1}\right] + 2l_0^2\delta_{m,m'-1}\frac{n'!(n+m)!}{n!(n'+m+1)!}(m+1)^2 \left.\times\left[\frac{\theta(n'-n)}{l_0^2}-\frac{(-1)^{n'}}{l_B^2}\right]^2\right\}; \qquad \text{(A.1)}$$

(2) $m \leq -1$ ($s = |m|$)

$$|\langle m, n, p|H_R|m', n', p'\rangle|^2 = D^2\delta_{p,p'}\left\{\frac{l_0^2}{2}\delta_{m,m'-1}\right. \times\left[(n+s)\left(\frac{1}{l_0^2}+\frac{1}{l_B^2}\right)^2\delta_{n,n'} + (n+1)\left(\frac{1}{l_0^2}-\frac{1}{l_B^2}\right)^2\delta_{n,n'-1}\right] + 2l_0^2\delta_{m,m'+1}\frac{n'!(n+s)!}{n!(n'+s+1)!}(s+1)^2 \left.\times\left[\frac{\theta(n'-n)}{l_0^2}+\frac{(-1)^{n'}}{l_B^2}\right]^2\right\}; \qquad \text{(A.2)}$$

(3) $m = 0$ ($s = 0$)

$$|\langle m, n, p|H_R|m', n', p'\rangle|^2 = D^2\frac{2l_0^2}{n'+1}\delta_{p,p'}\left\{\left[\frac{\theta(n'-n)}{l_0^2}+\frac{(-1)^{n'}}{l_B^2}\right]^2\delta_{0,m'-1} + \left[\frac{\theta(n'-n)}{l_0^2}-\frac{(-1)^{n'}}{l_B^2}\right]^2\delta_{0,m'+1}\right\}. \qquad \text{(A.3)}$$

Here,

$$D = \frac{e\hbar}{2m^*}\sqrt{\frac{2\pi\hbar N_{\mathbf{f}}}{\varepsilon(\omega)\omega}}.$$

ACKNOWLEDGMENTS

The work was supported by the Ministry of Education of Russia, project no. 97-7.1-210, and the Program "Universities of Russia—Fundamental Researches," project no. 53/33-98.

REFERENCES

1. L. Brey, N. Johnson, and B. J. Halperin, Phys. Rev. B **40**, 10647 (1989).
2. V. Ya. Prinz, V. A. Seleznev, V. A. Samoylov, and A. K. Gutakovsky, Microelectron. Eng. **30**, 439 (1996); V. Ya. Prinz, V. A. Seleznev, and A. K. Gutakovsky, in *Abstracts of 24th Conference on Semiconductor Physics, Jerusalem, 1998.*
3. V. A. Geĭler, V. A. Margulis, and A. V. Shorokhov, Zh. Éksp. Teor. Fiz. **115**, 1450 (1999) [JETP **88**, 800 (1999)].
4. L. I. Magaril and A. V. Chaplik, Zh. Éksp. Teor. Fiz. **115**, 1478 (1999) [JETP **88**, 815 (1999)].
5. W. Geiselbrecht, U. Sahr, A. Masten, *et al.*, Physica E (Amsterdam) **2**, 106 (1998).
6. É. P. Sinyavskiĭ and S. M. Sokovnich, Fiz. Tverd. Tela (St. Petersburg) **42** (9), 1685 (2000) [Phys. Solid State **42**, 1734 (2000)].
7. Rui Q. Yang and J. M. Xu, Phys. Rev. B **50**, 7474 (1994).
8. L. V. Butov, A. A. Shashkin, V. T. Dolgopolov, *et al.*, Phys. Rev. B **60**, 8753 (1999).
9. S. Blom, L.Y. Gorelik, M. Jonson, *et al.*, Phys. Rev. B **58**, 16305 (1998).

10. Yu. A. Uspenskii and B. N. Harmon, Phys. Rev. B **61**, 10571 (2000).
11. D. Huang, G. Gumbs, and N. Horing, Phys. Rev. B **49**, 11463 (1994).
12. V. A. Margulis, Zh. Éksp. Teor. Fiz. **111**, 1092 (1997) [JETP **84**, 603 (1997)].
13. Jai Yon Ryu, Y. Hu, and R. F. O'Connell, Phys. Rev. B **49**, 10437 (1994).
14. É. P. Sinyavskiĭ and S. M. Sokovnich, Fiz. Tverd. Tela (St. Petersburg) **42** (9), 1695 (2000) [Phys. Solid State **42**, 1744 (2000)].
15. A. Grincwajg, M. Jonson, and R. I. Shekhter, Phys. Rev. B **49**, 7557 (1994).
16. V. Halonen, P. Pietilainen, and T. Chakraborty, Europhys. Lett. **33**, 377 (1996).
17. L. Wendler and V. G. Grigoryan, Physica B (Amsterdam) **245**, 127 (1998).
18. Yu. B. Vasilyev, K. V. Klitzing, and K. Eberl, Physica E (Amsterdam) **2**, 116 (1998).
19. A. H. MacDonald and C. Kallin, Phys. Rev. B **40**, 5795 (1989).
20. F. G. Bass and I. B. Levinson, Zh. Éksp. Teor. Fiz. **49**, 914 (1965) [Sov. Phys. JETP **22**, 635 (1966)].
21. R. K. Bakanas, Fiz. Tverd. Tela (Leningrad) **12** (11), 3409 (1970) [Sov. Phys. Solid State **12**, 2769 (1970)].

Translated by N. Ostrovskaya

Physics of the Solid State, Vol. 43, No. 3, 2001, pp. 539–548. Translated from Fizika Tverdogo Tela, Vol. 43, No. 3, 2001, pp. 520–528.
Original Russian Text Copyright © 2001 by Romanov, Romanova.

Dynamical Electron Localization and Self-Induced Transparency in Semiconductor Superlattices

Yu. A. Romanov and Yu. Yu. Romanova

Institute of Physics of Microstructures, Russian Academy of Sciences, Nizhni Novgorod, 603600 Russia
e-mail: jul@ipm.sci-nnov.ru
e-mail: romanov@ipm.sci-nnov.ru

Received April 12, 2000; in final form, August 15, 2000

Abstract—The mechanisms of the occurrence of self-induced and selective transparencies of semiconductor superlattices in a strong time-dependent electric field are investigated. The association of these mechanisms with Bloch oscillations, dynamical localization, and collapse of electron quasi-energy minibands is analyzed, and a comparison with the properties of Josephson junctions is made. It is shown that the self-induced transparency is due to the fact that the current-contributing component of the electron distribution function is destroyed by collisions at discrete values of the amplitude of the time-harmonic field, while the selective transparency is associated with the nonmonotonic dependence of the spectrum of nonlinear electron oscillations in the electric field on the amplitude of the field. The dynamical localization and collapse of quasi-energy minibands lead to the field energy dissipation and are favorable to destruction of the transparency states of the superlattice. *© 2001 MAIK “Nauka/Interperiodica”.*

INTRODUCTION

An important property of semiconductor superlattices (SSLs) is the occurrence of electromagnetic transparency of three types, namely, self-induced (SIT) [1, 2], induced [1, 3], and selective transparencies [1]. The SIT in an SSL was apparently first observed in [4], but more conclusive experimental evidence for its occurrence was provided in [5]. Observations of the induced and selective transparencies in SSLs have not yet been reported in the literature. After [1–3], a number of theoretical papers were published [6–9] in which attempts were made to physically interpret the transparency effects in SSLs. Based on those papers, it is erroneously believed that the transparency of SSLs is identical to the dynamical localization (DL) of electrons [6, 9]; i.e., it is a macroscopic manifestation of this localization or, in quantum-mechanical terms, it is a consequence of the collapse of quasi-energy minibands [8, 10]. Unfortunately, this misinterpretation is sometimes drawn on when discussing experimental data on the nonlinear effects in SSLs [5, 11] and considering nonlinear transmission of terahertz radiation through these media [12–14]. It is not surprising that the authors of the papers mentioned above arrived at conflicting conclusions, as was indicated with good reason in [15]. The authors of [8] also showed that the collapse of minibands cannot cause the SIT to occur in an SSL, but they made the erroneous inference from this that the SIT does not occur at all.

In this paper, we develop a consistent theory (in the τ approximation) of the transparency effects in SSLs, elucidate the mechanisms for the occurrence of the transparency, and make a comparison with Josephson junctions.

1. GENERAL PROPERTIES OF BLOCH OSCILLATIONS

We start from the dispersion relation for an electron in the SSL derived in the tight-binding approximation:

$$\varepsilon(\mathbf{k}) = \frac{\Delta}{2}(1-\cos(k_3 d)) + \frac{\hbar^2 k_\perp^2}{2m}, \tag{1}$$

where Δ is the miniband width; d is the SSL period; $\hbar k_3$ and $\hbar k_\perp$ are the longitudinal and transverse (relative to the SSL axis) components of the electron momentum $\hbar\mathbf{k}$, respectively; m is the transverse electron mass; and $\hbar$ is the Planck constant. Let us consider the dynamics of such an electron moving in a time-harmonic electric field directed along the SSL axis:

$$E(t) = E_0\cos(\omega t). \tag{2}$$

Nonlinear oscillations of the superlattice electron in this field are characterized by the velocity

$$\begin{aligned} V(k_0, t_0, t) &= V_m\sin[k_0 d + g(\sin(\omega t) - \sin(\omega t_0))] \\ &= V_m[c_S(k_0, t_0)\psi_S(t) + c_a(k_0, t_0)\psi_a(t)], \end{aligned} \tag{3}$$

where

$$\begin{aligned}\psi_S(t) &= \cos(g\sin(\omega t))\\ &= J_0(g) + 2\sum_{n=1}^{\infty} J_{2n}(g)\cos(2n\omega t),\\ \psi_a(t) &= \sin(g\sin(\omega t))\\ &= 2\sum_{n=1}^{\infty} J_{2n-1}(g)\sin((2n-1)\omega t),\\ c_S(k_0, t_0) &= \sin[k_0 d - g\sin(\omega t_0)],\\ c_a(k_0, t_0) &= \cos[k_0 d - g\sin(\omega t_0)],\end{aligned} \tag{4}$$

$V_m = \Delta d/2\hbar$ is the maximum longitudinal velocity of the electron, $\mathbf{k}_0$ is the longitudinal electron momentum at time t_0, $g = \Omega/\omega$, $\Omega = eEd/\hbar$, $J_n(g)$ is the Bessel function, and e is the electron charge. It is known that, in a static field of any strength E_C, an electron is localized in space and performs periodic Bloch oscillations (BO) no matter what its dispersion relation and initial momentum $\mathbf{k}_0$. These oscillations have a Stark frequency $\Omega_C = eE_Cd/\hbar$ [see Eq. (3) for $\omega \longrightarrow 0$] and amplitudes $\delta V = V_m = \text{const}$ and $\delta x = d\Delta/\hbar\Omega_C$. The initial momentum $\mathbf{k}_0$ determines the initial phase of the BO. Collisions do not affect the BO energy (time-averaged kinetic electron energy), but change the position of the center of the oscillations (and, hence, the average potential energy of the electron). The time-harmonic field has a phase of its own and two characteristic times, namely, the period $2\pi/\omega$ and the electron transit time over the Brillouin minizone (the latter time is determined by the amplitude of the harmonic field). For this reason, Bloch oscillations in a harmonic field (BOHF), described by Eq. (3), possess the following properties, which are different from those of BO in a static field:

(1) The motion of the electron in the momentum space is independent of its dispersion relation and is periodic, with its period being equal to that of the electric field $2\pi/\omega$. Bragg reflections from the minizone boundaries do not lead to an additional period (in contrast to the case of a static field); they merely modulate the electron oscillations within a field period. Therefore, the BOHF spectrum contains only harmonics with frequencies which are multiples of the field frequency and the amplitudes of the harmonics depend nonmonotonically upon the field amplitude.

(2) The electron localization in real space occurs only at discrete values of the field amplitude (see below).

(3) The initial momentum $\mathbf{k}_0$ determines the time-averaged energy and velocity of the electron, i.e., the two BOHF amplitudes, c_S and c_a, of the packets of the even (ψ_S) and odd (ψ_a) velocity harmonics, respectively (as is the case with a two-level system). The amplitudes and "eigenfunctions" of the packets ψ_S and ψ_a are related by the normalization conditions $c_S^2 + c_a^2 = 1$ and $\psi_S^2(t) + \psi_a^2(t) = 1$. The phases of the BOHF harmonics are determined, to within a multiple of π, by the phase of the field. Collisions affect the amplitudes c_S and c_a, the kinetic energy, and the position of the BOHF center and destroy its low-frequency harmonics. When $\omega\tau \gg 1$, the BOHF can be thought of as a long-lived quasiparticle (spin) with two vibrational degrees of freedom.

(4) From the last property, it follows that, in a time-harmonic field with $\omega\tau \gg 1$, all the even and/or odd harmonics (rather than some of them) in the macroscopic current can simultaneously change and even disappear because of collisions.

If the SSL is placed in a combination of a time-harmonic and a static bias field

$$E(t) = E_C + E\cos(\omega t), \tag{5}$$

then, instead of Eq. (3), we will have

$$\begin{aligned}V(k_0, t) &= V_m\sin\{k_0 d + \Omega_C(t - t_0)\\ &+ g[\sin(\omega t) - \sin(\omega t_0)]\} = V_m\sum_{n=-\infty}^{\infty} J_n(g)\\ &\times \sin\{k_0 d + \Omega_C(t - t_0) + n\omega t - g\sin(\omega t_0)\}.\end{aligned} \tag{6}$$

From Eq. (6), it is seen that the static field shifts the BOHF spectrum as a whole by the Stark frequency Ω_C, but the harmonic amplitudes remain unchanged [in Eq. (6), the positive and negative frequencies are not considered identical for the sake of convenience]. This shift can be conveniently thought of as the amplitude modulation of BOHF in the time-harmonic field (2) by Bloch oscillations [see Eqs. (3) and (4), with k_0d being replaced by $k_0d + \Omega_C(t - t_0)$]. For an arbitrary E_C, the BOHF are not periodic, because their spectrum contains only harmonics with incommensurate frequencies $\Omega_C \pm n\omega$. However, since E_C has no phase of its own, the Stark frequency shift is destroyed when its phase is randomly changed by collisions (i.e., by amplitude modulation with a random phase). For this reason, only harmonics with frequencies $n\omega$ will be in the steady-state macroscopic current (see below). In this case, as before, the spectra of oscillations (BOHF) of individual electrons will contain only combination frequencies and no field harmonics. In the Stark resonance $\Omega_C = n\omega$, the BOHF become periodic again. Periodicity of the trajectories in $\mathbf{k}$ space and of the velocity oscillations also takes place in a more general case where Ω_C and ω are commensurate, $n_1\Omega_C = n_2\omega$, where $n_{1,2} = 1, 2, \ldots$. In this case, the oscillation period is $T = 2n_1\pi/\omega$ (n_2/n_1 is noninteger); that is, it becomes n_1 times longer. However, this new periodicity is destroyed by collisions.

Thus, due to collisions, the static field, even in combination with a time-harmonic field, cannot induce steady-state current oscillations in the SSL, in contrast to the case of Josephson junctions. There is also no analogy with the behavior of a magnetized electron plasma [16], since the magnetic field (in contrast to the electric field) does no work.

2. THE SPECTRUM OF BLOCH OSCILLATIONS AND DYNAMICAL ELECTRON LOCALIZATION

Let us investigate the BOHF spectrum as a function of the dimensionless amplitude of the harmonic field g. We consider the zeroth harmonic first. It is easily shown that, for any dispersion law, the relative time for which the electron occupies the states with a wave vector $\mathbf{k}_3$ being within a unit interval is

$$P(k_0, k_3) = \frac{d}{2\pi}\left[1 + \sum_{\nu=1}^{\infty} J_0(\nu g)\cos[\nu(k_3 - k_0)d]\right]. \quad (7)$$

From Eqs. (3) and (7), we find the following quantities averaged over a period of oscillations (for $t_0 = 0$): velocity (zeroth BOHF harmonic), energy, squared velocity, oscillating velocity, and oscillating displacement:

$$\bar{V}(k_0) = V_m \sin(k_0 d) J_0(g), \quad (8)$$

$$\bar{\varepsilon}(k_0) = \frac{\Delta}{2}[1 - \cos(k_0 d) J_0(g)], \quad (9)$$

$$\bar{V}^2(k_0) = \frac{1}{2}V_m^2[1 - \cos(2k_0 d) J_0(2g)], \quad (10)$$

$$\overline{V_\sim^2} = \frac{1}{2}V_m^2 \times \{1 - J_0^2(g) + \cos(2k_0 d)[J_0^2(g) - J_0(2g)]\}, \quad (11)$$

$$\bar{x}_\sim^2 = 2\left(\frac{V_m}{\omega}\right)^2\left[\sin^2(k_0 d)\sum_{n=1}^{\infty}(2n)^{-2}J_{2n}^2(g) + \cos^2(k_0 d)\sum_{n=0}^{\infty}(2n+1)^{-2}J_{2n+1}^2(g)\right], \quad (12)$$

respectively. In the case of $t_0 \neq 0$, the quantity $k_0 d$ should be replaced by $k_0 d - g\sin(\omega t_0)$. If the field amplitude is such that $J_0(g) = 0$, we will have

$$\bar{V}(k_0) = 0, \quad \bar{\varepsilon}(k_0) = \frac{\Delta}{2}; \quad (13)$$

that is, the motion of the electron in such a field is finite, no matter what the initial electron momentum [6]. In the case of finite motion, the electron has a discrete energy spectrum, which is manifested by the collapse of the one-dimensional quasi-energy miniband of the electron:

$$\tilde{\varepsilon}(k_3) = \frac{\Delta}{2}[1 - J_0(g)\cos(k_3 d)] + n\hbar\omega, \quad n = 0, \pm 1, \pm 2, \ldots \quad (14)$$

at $J_0(g) = 0$ [8]. In terms of classical and quantum theories, this is called dynamical localization (DL). This effect is purely classical in the one-miniband approximation. Its quantum-mechanical treatment both in the Wannier representation [6, 9] and in quasi-energy terms [8] revealed no new features.

At $J_0(g) = 0$, the $\nu = 1$ harmonic disappears in the spectrum of the average momentum distribution in Eq. (7). This is the only harmonic that contributes to the average electron velocity in the case of the dispersion law given by Eq. (1). Several (even two) harmonics with different ν cannot disappear simultaneously. Therefore, the DL in a time-harmonic field can occur only in the case of a harmonic dispersion law. It can be shown that, in this case, the DL can also occur in a multifrequency (in particular, biharmonic) field. For an arbitrary dispersion law, the DL can take place only in a multifrequency field.

Now, we consider the other BOHF harmonics. From the expressions for the eigenfunctions $\psi_S(t)$ and $\psi_a(t)$, it follows that, as the field amplitude increases, the nth harmonics (among them the zeroth one) corresponding to the zeros of $J_n(g)$ disappear in turn in the electron oscillation spectrum irrespective of $\mathbf{k}_0$. In the absence of collisions, this will lead to the disappearance of the nth harmonic in the macroscopic current for any initial electron distribution function, that is, to selective transparency. In contrast to the SIT, the selective transparency is determined by the electron dynamics alone and is independent of the momentum distribution of electrons. The DL, which implies the disappearance of the zeroth harmonic in the electron oscillation spectrum, is a special case of selective transparency.

As indicated above, in a field containing a static and a time-harmonic component [Eq. (5)], the BOHF spectrum is shifted by the Stark frequency [see Eq. (6)]. Therefore, the DL occurs at any g if $\Omega_C \neq \nu\omega$. However, the periodicity of motion in $\mathbf{k}$ space is absent and $\bar{V}(\mathbf{k}_0)$ vanishes only after its averaging over an infinitely long time interval. In the Stark resonance ($\Omega_C = \nu\omega$), the BOHF periodicity is restored and the quasi-energy spectrum and the average quantum-mechanical velocity of the electron are given by

$$\tilde{\varepsilon}(k_3) = \frac{\Delta}{2}[1 - (-1)^\nu J_\nu(g)\cos(k_3 d)] + n\hbar\omega, \quad (15)$$

$$\tilde{V}(k_3) = \frac{1}{\hbar}\frac{\partial\varepsilon}{\partial k_3} = (-1)^\nu \sin(k_3 d) J_\nu(g). \quad (16)$$

In this case, the DL and the collapse of quasi-energy minibands occur only if the BOHF spectrum does not contain the νth harmonic at $E_C = 0$, i.e., if $J_n(g) = 0$. Otherwise [at $J_\nu(g) \neq 0$], the electron is delocalized and $j_C \neq 0$. This provides further support for the view that the DL and the collapse of the quasi-energy miniband are an important, but no more than specific, case of the selective transparency associated with the nonmonotonic dependence of the BOHF spectra on the field amplitude.

The quantities given by Eqs. (8)–(12) depend on the initial electron momentum, which is not convenient for their analysis. For this reason, we average Eqs. (10)–(12) over $\mathbf{k}_0$ and obtain, for an "average" electron, the expressions

$$\bar{x}_{\sim}^2 = \left(\frac{V_m}{\omega}\right)^2 B(g), \quad \bar{V}^2 = \frac{1}{2}V_m^2 J_0^2(g),$$
$$\overline{V_{\sim}^2} = \frac{1}{2}V_m^2[1 - J_0^2(g)], \tag{17}$$

where

$$B(g) = \sum_{n=1}^{\infty} n^{-2} J_n^2(g). \tag{18}$$

It is seen from Eqs. (8), (10), and (17) that the mean square velocity of the "average" electron, which contains the oscillating and constant components, is independent of the field amplitude ($g > 0$); the value of this velocity is merely redistributed between its components as g is varied. When $J_0(g)$ vanishes, the translational motion of the electron entirely transforms into an oscillatory motion. In this case, the oscillating velocity is maximal, the amplitude of the coordinate oscillations is large, and the average energy equals $\Delta/2$ for any values of $\mathbf{k}_0$ rather than for an "average" electron only (this is a consequence of the collapse of the quasi-energy miniband). The last feature is important, because it implies that all electrons are on equal terms in collisions and in energy exchange with the field.

Thus, when the DL and the collapse of quasi-energy minibands take place, the energy exchange between individual electrons and the field is the most efficient and the electron oscillation amplitude is the largest. From this, it was erroneously concluded in [8] that there is no SIT in the superlattice in this case (this conclusion is true for Josephson junctions). Indeed, the large oscillating velocities of some electrons do not signify that the macroscopic current is large, since the electrons move incoherently because of collisions. One might expect just an increase in the absorption of the electromagnetic field, because this effect is incoherent in the given-field approximation.

2. SELF-INDUCED AND SELECTIVE TRANSPARENCIES

We start from the Boltzmann equation with the collision integral taken in the τ approximation:

$$\frac{\partial f(\mathbf{k}, t)}{\partial t} + \frac{eE(t)}{\hbar}\frac{\partial f(\mathbf{k}, t)}{\partial \mathbf{k}} = -\frac{f(\mathbf{k}, t) - f_0(\mathbf{k})}{\tau},$$
$$f(\mathbf{k}, t) = f_0(\mathbf{k}), \tag{19}$$

where $f(\mathbf{k}, t)$ and $f_0(\mathbf{k})$ are the nonequilibrium (perturbed by the field) and equilibrium electron distribution functions, respectively, and τ is the relaxation time. Since the distribution function is periodic in $\mathbf{k}$ space, it can be expanded in a Fourier series:

$$f(\mathbf{k}, t) = \sum_{\nu=-\infty}^{\infty} F_\nu(k_\perp)\exp(i\nu k_3 d)\Phi_\nu(t),$$
$$\Phi_\nu = \Phi_{-\nu}^*, \tag{20}$$

where

$$F_\nu(k_\perp) = \frac{d}{2\pi}\int_{-\pi/d}^{\pi/d} f_0(k)\exp(-i\nu k_3 d)dk_3,$$
$$F_\nu = F_{-\nu}^*. \tag{21}$$

From Eqs. (19)–(21), it follows that the multicomponent function $\Phi_\nu(t)$ satisfies the equation

$$\tau\frac{d\Phi_\nu(t)}{dt} + [1 + i\nu\tau\Omega(t)]\Phi_\nu(t) = 1,$$
$$\Omega(t) = \frac{edE(t)}{\hbar} \tag{22}$$

with the initial conditions

$$\Phi_\nu(0) = 1. \tag{23}$$

Given $\Phi_\nu(t)$, one can find all average quantities (energy, velocities, current, etc.):

$$\varepsilon(t) = \sum_{\nu=-\infty}^{\infty} \bar{\varepsilon}(-\nu)\Phi_\nu(t), \tag{24}$$

$$j(t) = \frac{i}{2}\sum_{\nu=1}^{\infty} j_{0\nu}\Phi_\nu(t) + c.c., \tag{25}$$

where

$$j_{0\nu} = -2ine\bar{V}_3(-\nu) = -2ned\hbar^{-1}\nu\bar{\varepsilon}(-\nu)$$
$$= -\frac{4ed}{\hbar}\nu\int F_\nu(k_\perp)\varepsilon(\mathbf{k})\exp(i\nu k_3 d)\frac{d^3k}{(2\pi)^3} \tag{26}$$

and n is the electron concentration. For the dispersion law given by Eq. (1), we have from Eqs. (24) and (25)

$$j(t) = -j_0\mathrm{Im}(\Phi_1(t)), \quad j_0 = \frac{end}{\hbar}\left(\frac{\Delta}{2} - \langle\varepsilon_3\rangle_0\right), \tag{27}$$

$$\varepsilon(t) - \frac{\Delta}{2} = \left(\langle\varepsilon_3\rangle_0 - \frac{\Delta}{2}\right)\mathrm{Re}(\Phi_1(t)), \tag{28}$$

where $\langle\varepsilon_3\rangle_0$ is the average equilibrium longitudinal electron energy and $f_0(\mathbf{k})$ is assumed to be a symmetric function. We will refer to the momentum harmonics in the distribution function that make a nonzero contribution to the current as current-contributing harmonics.

In the case of an arbitrary time dependence of the field $E(t)$ and an arbitrary electron dispersion law, we conveniently separate the BOHF by representing $\Phi_\nu(t)$ in the form

$$\Phi_\nu(t) = a_\nu(t)\psi_\nu(t), \tag{29}$$

where

$$\psi_\nu(t) = [\psi_1(t)]^\nu = \exp\left(-i\nu\int_0^t \Omega(t_1)dt_1\right) \tag{30}$$

is the BOHF eigenfunction that is a solution to the kinetic equation (22) without the collision integral and describes the dynamical (i.e., collisionless) modulation of the electron distribution function caused by the field. For a time-harmonic field, we have

$$\psi_1(t) = \psi_S(t) - i\psi_a(t), \tag{31}$$

where $\psi_S(t)$ and $\psi_a(t)$ are defined in Eq. (4). The dissipative function $a_\nu(t)$ describing the changes in the amplitude and in the spectrum of the νth momentum harmonic of the distribution function caused by collisions (i.e., the departures from the BOHF expressions) satisfies the equation

$$\dot{a}_\nu(t) + \tau^{-1}a_\nu(t) = \tau^{-1}\psi_\nu^*(t). \tag{32}$$

A solution to this equation has the form

$$a_\nu(t) = \Phi_\nu(0)\exp\left(-\frac{t}{\tau}\right) + \int_0^t \exp\left(-\frac{t-t_1}{\tau}\right)\psi_\nu^*(t_1)dt_1. \tag{33}$$

In the absence of collisions, we have $a_\nu(t) \equiv 1$. Passing over from $\Phi_\nu(t)$ to $a_\nu(t)$ implies that we go over to a generalized quasi-momentum representation, i.e., to a new frame of reference K_0 that oscillates synchronously with a collisionless electron in the momentum space. For each electron (or, more precisely, for each mode of BOHF), there is a fixed point $\mathbf{k}_0$ in frame K_0. The distribution of these points is changed only by collisions. If collisions are of infrequent occurrence, the changes over a field period are small, but the changes caused by several collisions can accumulate. At the same time, the equilibrium distribution function in frame K_0 is modulated by the field (dynamical modulation) and becomes a periodic function of time:

$$\begin{aligned} f_0(k_3) &= f_0\left(k_0 - \frac{1}{d}\int_0^t \Omega(t_1)dt_1\right) \\ &= \sum_{\nu=-\infty}^{\infty} F_\nu(k_\perp)\exp(-i\nu k_3 d)\psi_\nu^*(t). \end{aligned} \tag{34}$$

This is reflected in Eq. (32), where the second (loss) term corresponds to usual relaxation, while the gain term is a dynamically modulated equilibrium distribution function. This description enables one to go beyond the τ approximation by introducing matrices $(\tau^{-1})_{\mu\nu}$ that allow for transitions between different momentum harmonics ν (see below).

If the BOHF are high-frequency, that is, the spectrum of these oscillations contains only frequencies $\omega = 0$ and $\omega \gg \tau^{-1}$, they are weakly affected by collisions [see property (3) in the preceding section]. Averaging Eq. (32) over the time interval $\omega^{-1} \ll \Delta t \ll \tau$ yields

$$\begin{aligned} a_\nu(t) &= \Phi_\nu(0)\exp\left(-\frac{t}{\tau}\right) \\ &+ \left[1 - \exp\left(-\frac{t}{\tau}\right)\right]\overline{\psi_\nu^*}(t) + O\left(\frac{1}{\omega\tau}\right). \end{aligned} \tag{35}$$

From Eqs. (32) and (35), it follows that, when $\overline{\psi_\nu^*}(t) = 0$, the electrons do not return to the νth state in the average (in the $\tau = \text{const}$ approximation), because collisions destroy this momentum harmonic of the distribution function for the time of the order of τ. This signifies that the BOHF cease to be coherent in such a field. Since the equalities $\overline{\psi_\nu^*}(t) = 0$ cannot be fulfilled for all values of ν simultaneously, the coherence of the BOHF is not completely destroyed in the general case (i.e., the distribution function is not a constant in the momentum space). The destruction of coherence can be complete in a multifrequency field with incommensurate frequencies:

$$E(t) = \sum_{\nu=1}^{\infty} E_\nu\cos(\omega_\nu t + \delta_\nu). \tag{36}$$

In this field, the functions

$$\overline{\psi_\nu}(t) = \prod_{\alpha=1}^{\infty} J_0(\nu g_\alpha) \tag{37}$$

vanish simultaneously when $J_0(\nu g_\nu) = 0$. It can easily be shown that under these conditions, the dynamical electron localization also occurs for any dispersion law, which can be employed to investigate this law.

Let us consider the behavior of the SSL in a harmonic field in more detail. In this field, we have

$$\overline{\psi_\nu}(t) = J_0(\nu g). \tag{38}$$

By substituting Eqs. (31), (35), and (38) into Eq. (29) and putting $\Phi_\nu(0) = 1$, we obtain, for $\omega\tau \gg 1$,

$$\Phi_\nu(t) = \exp[-i\nu g\sin(\omega t)] \times\left\{\exp\left(-\frac{t}{\tau}\right) + \left[1-\exp\left(-\frac{t}{\tau}\right)\right]J_0(\nu g)\right\} + O\left(\frac{1}{\omega\tau}\right). \qquad (39)$$

For arbitrary values of $\omega\tau$ and $E_C \neq 0$, we have, instead of Eq. (39),

$$\begin{aligned}\Phi_\nu(t) = {} & \sum_{\mu=-\infty}^{\infty} J_\mu(\nu g)\left[1-\sum_{n=-\infty}^{\infty}\frac{J_n(\nu g)}{1+i(\nu\Omega_C+n\omega)\tau}\right] \\ & \times\exp\{-[\tau^{-1}+i(\nu\Omega_C+\mu\omega)]t\} \qquad (40) \\ & + \sum_{\mu,\,n=-\infty}^{\infty}\frac{J_n(\nu g)J_{n+\mu}(\nu g)}{1+i(\nu\Omega_C+n\omega)\tau}\exp(-i\mu\omega t).\end{aligned}$$

By substituting Eq. (39) into Eq. (20) and using Eq. (25), the distribution function and the current are found to be

$$\begin{aligned}f(\mathbf{k}, t) = {} & F_0(k_\perp) + 2\sum_{\nu=1}^{\infty}F_\nu(k_\perp)\cos[\nu(k_3d - g\sin(\omega t))] \qquad (41) \\ & \times\left[\exp\left(-\frac{t}{\tau}\right) + \left(1-\exp\left(-\frac{t}{\tau}\right)\right)J_0(\nu g)\right] + O\left(\frac{1}{\omega\tau}\right),\end{aligned}$$

$$\begin{aligned}j(t) = {} & 2\sum_{\nu=1}^{\infty}\left[\exp\left(-\frac{t}{\tau}\right) + \left(1-\exp\left(-\frac{t}{\tau}\right)\right)J_0(\nu g)\right] \\ & \times\left\{\operatorname{Re}j_{0\nu}\sum_{\mu=1}^{\infty}J_{2\mu-1}(\nu g)\sin[(2\mu-1)\omega t]\right. \\ & \left.-\operatorname{Im}j_{0\nu}\left[\frac{1}{2}J_0(\nu g) + \sum_{\mu=1}^{\infty}J_{2\mu}(\nu g)\cos(2\mu\omega t)\right]\right\} \\ & + \frac{2}{\omega\tau}\sum_{\mu,\,\nu=1}^{\infty}\{\operatorname{Re}j_{0\nu}A_{2\mu-1}(\nu g)\cos[(2\mu-1)\omega t] \\ & + \operatorname{Im}j_{0\nu}A_{2\mu}(\nu g)\sin(2\mu\omega t)\} \qquad (42) \\ & - \frac{1}{\omega\tau}\sum_{\nu=1}^{\infty}C(\nu g)\{\operatorname{Re}j_{0\nu}\cos[\nu g\sin(\omega t)] \\ & - \operatorname{Im}j_{0\nu}\sin[\nu g\sin(\omega t)]\}\exp\left(-\frac{t}{\tau}\right),\end{aligned}$$

where

$$\begin{aligned}A_\nu(x) = {} & \sum_{n=-\infty}^{\infty}{}' \, n^{-1}J_n(x)J_{n+\nu}(x) \\ = {} & \frac{2}{x}[\delta_{\nu 1} - J_0(x)J_{\nu-1}(x)] + \frac{2\nu-1}{x}A_{\nu-1}(x) - A_{\nu-2}(x), \\ & A_0 = 0, \quad A_1(x) = x^{-1}[1-J_0^2(x)], \qquad (43) \\ & C(x) = \sum_{n=-\infty}^{\infty}{}' \, n^{-1}J_n(x),\end{aligned}$$

and $\delta_{\nu 1}$ is the Kronecker symbol. In contrast to Eq. (39), Eq. (43) contains terms of the order of $(\omega\tau)^{-1}$, which have been calculated using Eq. (40). For the sinusoidal dispersion law given in Eq. (1), we have

$$j_{0\nu} = \delta_{\nu 1}j_0, \quad j_0 = \frac{end}{\hbar}\left(\frac{\Delta}{2} - \langle\varepsilon_3\rangle_0\right) - ien\langle V\rangle_0, \qquad (44)$$

where $\langle V\rangle_0$ is the electron velocity averaged by using the distribution function $f_0(\mathbf{k})$. For the Maxwell statistics, the distribution function averaged over the transverse momentum is found to be

$$F_0 = \frac{nd}{2}, \quad F_\nu = F_0 I_\nu\left(\frac{\Delta}{2T}\right)I_0^{-1}\left(\frac{\Delta}{2T}\right), \qquad (45)$$

where T is the lattice temperature and $I_\nu(x)$ are the modified Bessel functions. For the Fermi statistics at $T = 0$ and the Fermi level $\mu > \Delta$, we have

$$F_0 = \frac{nd}{2}, \quad F_1 = \frac{m\Delta}{(2\pi\hbar)^2}, \quad F_\nu = 0, \quad \nu \geq 2. \qquad (46)$$

It is seen from Eq. (41) that the νth momentum harmonics in the electron distribution function disappear in turn as g increases and the condition $J_0(\nu g) = 0$ is fulfilled. Formally, this effect can be thought of as selective transparency in a momentum space or in the νth harmonics space (except for dynamical localization, because the zeroth harmonic of the distribution function remains unchanged). However, the mechanism of this transparency is related not only to the dynamics of an individual electron. The corresponding modulation of the distribution function in the momentum space is a combined effect of the field and collisions. If the dynamical modulation of the equilibrium distribution function is such that its νth momentum harmonic being averaged over one temporal period vanishes (the νth momentum harmonic of the BOHF contains no zeroth time harmonic and, therefore, when averaged over a temporal period, the gain term in the collision integral becomes zero), then collisions completely destroy this harmonic within a time of the order of τ. In the case of a sinusoidal distribution law, only the harmonic with $\nu = 1$ contributes to the current. Therefore, if the field amplitude is such that $J_0(g) = 0$, then, within a time of the order of τ after the field is turned on, the SSL becomes transparent [see Eq. (42)]; that is, the SSL behaves as a dielectric with permittivity equal to that of the basic semiconductor lattice and with relatively weak nonlinear resonance absorption. This is the SIT effect. In the case corresponding to Eq. (46) and $J_0(g) = 0$, the electrons are distributed uniformly over the miniband. It is obvious that the current equals zero for this distribution, as is the case with any entirely filled band. The occurrence of the SIT is the most descriptive in this case.

In accordance with the general consideration, it also follows from Eq. (42) that the spectrum of the macroscopic current coincides [to within terms of the order $(\omega\tau)^{-1}$] with the spectrum of the first momentum harmonic of BOHF [see Eq. (3)]. Therefore, in SSLs, in addition to the SIT, there occurs the selective-transparency effect, i.e., the alternate disappearance of the time harmonics in the current, the constant component included. One can say that the selective transparency in the current is a macroscopic manifestation of the BOHF spectrum. In contrast to the SIT, this effect occurs immediately after the field is turned on. Collisions do nothing but uniformly change the amplitudes of all time harmonics of the current.

A completely different type of situation occurs when $E_C \neq 0$ [see Eq. (40)]. In this case, averaging over a long time interval yields $\overline{\psi_v}(t) = 0$. Therefore, in the current, all harmonics with combination frequencies $\Omega_C \pm n\omega$ (of which the oscillation spectrum of each electron alone consists) decay within the time τ after the field is turned on and only harmonics $n\omega$ (including the constant component), which are absent in the BOHF, remain in the current. As indicated above, this is due to the chaotic change in the phase of the BOHF amplitude modulation caused by the static field. The exception to this is provided by resonance fields with frequency $\Omega_C = n_0\omega$. In these fields, we have $\overline{\psi_v}(t) = J_{n_0}(g)$; therefore, under the static field, the SIT in the SSL is shifted to the region where $J_{n_0}(g) = 0$. The conditions for selective transparency are also changed. Thus, due to collisions, the oscillation spectra of the macroscopic quantities in the SSL become different from those of individual electrons. In this respect, the SSL differs essentially from Josephson junctions, where collisions do not destroy the coherence of Cooper pairs and, therefore, the macroscopic current contains harmonics with combination frequencies.

It is significant that, in Eq. (42), the function $J_0(g)$ enters both into the common modulation factor responsible for the SIT and into the separate term responsible for the DL. The coincidence of the mathematical conditions for the DL and the SIT was, perhaps, the reason why these physically different effects were erroneously considered to be the same [5, 9–14]. It is to be noted that there is no common modulation factor both in the current flowing through a Josephson junction and in the BOHF.

Let us consider the field energy dissipation. According to Eqs. (42) and (43), in the case of the dispersion law given by Eq. (1), the field energy absorption loss is

$$Q = \frac{\omega}{2\pi}\int\limits_{t}^{t+2\pi/\omega} j(t)E(t)dt$$

$$= Q_0\left[1 - J_0^2(g) + (1 - J_0^2(g))^2\exp\left(-\frac{t}{\tau}\right)\right], \qquad (47)$$

$$Q_0 = \frac{\hbar j_0}{ed\tau} = \frac{n}{\tau}\left(\frac{\Delta}{2} - \langle\varepsilon_3\rangle_0\right).$$

At the initial stage ($t \le \tau$), the absorption loss is higher than its steady-state value, because an extra amount of energy is required to heat the electron gas. The absorption loss in Eq. (47) is maximal in the case of DL [$J_0(g) = 0$] and is equal to that in a static field when $\Omega_C\tau \gg 1$. It should be noted here that the average electron energy and the absorption loss reach their maximum values at the same field amplitudes. This is in accordance with the above discussion of the resonance incoherent interaction of individual electrons with the field when the DL occurs.

We found the quantitative conditions for the occurrence of the SSL transparency in the single-relaxation-time approximation, where the momentum harmonics of the distribution function are not mixed by collisions. In actuality, this mixing takes place [e.g., in the case of $\tau = \tau(k)$], which can affect the conditions for the occurrence of the SIT effect and even lead to its suppression. Such is not the case for the selective transparency, which is determined by the electron dynamics alone. In order to analyze the mixing effect, we return to Eq. (3) and the properties of BOHF. From Eq. (3), it follows that, for an SSL with a sinusoidal dispersion law and arbitrary scattering mechanisms (the only condition is that the scattering itself be momentary), the current can be written in the form

$$j(t) = ne\left\{\left[\frac{d}{\hbar}\left\langle\left(\frac{\Delta}{2} - \varepsilon_S(t_0)\right)\psi_S(t_0)\right\rangle\right.\right.$$

$$\left. + \langle V_S(t_0)\psi_a(t_0)\rangle\right]\psi_a(t) + \left[\langle V_S(t_0)\psi_S(t_0)\rangle\right. \qquad (48)$$

$$\left.\left. - \frac{d}{\hbar}\left\langle\left(\frac{\Delta}{2} - \varepsilon_S(t_0)\right)\psi_a(t_0)\right\rangle\right]\psi_S(t)\right\},$$

where $\varepsilon_S(t_0)$ and $V_S(t_0)$ are the average energy and velocity of electrons scattered at time t_0, respectively, and the angular brackets signify averaging over the last collision acts preceding the time of observation t. In the general case, the average is dependent on t. It can easily be shown that $V_S(t)$ contains only odd field harmonics, while $\varepsilon_S(t)$ contains only even ones. At $\omega\tau \gg 1$, the probability that an electron having experienced a collision during the time interval dt_0 will move ballistically can be closely approximated by

$$P(t-t_0) = \exp\left(-\frac{t-t_0}{\tau}\right)W(t_0)\frac{dt_0}{\tau}, \qquad (49)$$

where $W(t_0)$ is a periodic function equal to the relative number of collisions of the electron during a field period, $\frac{\omega}{\pi}\int_0^{\pi/\omega} W(t)dt = 1$. In this approximation, from Eq. (48) we obtain the condition for the occurrence of the SIT:

$$\left[\frac{\Delta}{2} - \alpha_0(g)\right]J_0(g) - 2\sum_{n=1}^{\infty}\alpha_{2n}(g)J_{2n}(g) + 2\sum_{n=1}^{\infty}\beta_{2n-1}(g)J_{2n-1}(g) = 0, \qquad (50)$$

where

$$\alpha_n(g) = \frac{\omega}{\pi}\int_0^{\pi/\omega}\varepsilon_S(t)W(t)\cos(n\omega t)dt,$$
$$\beta_n(g) = \frac{\omega}{\pi}\int_0^{\pi/\omega}V_S(t)\sin(n\omega t)dt, \qquad (51)$$

and $\alpha_0 \approx \langle\varepsilon_3\rangle_0 < \Delta/2$. If electron collisions are absolutely random [$W(t) = 1$] and the distributions of scattered electrons are independent of t_0 [i.e., $\varepsilon_S(t_0) = \text{const}$, $V_S(t_0) = 0$], then, using the time reversal invariance of the equations of motion, one can write

$$j \sim \sum_{\mathbf{k}_0}\int_{t-2\pi/\omega}^{t}V(\mathbf{k}_0, t_0, t)dt_0 = \left[\sum_{\mathbf{k}_0}\bar{V}(\mathbf{k}_0, t_0)\right]_{t_0 = t}, \qquad (52)$$

where, now, the bar signifies averaging over the time of observation t. Therefore, strictly speaking, only in this case does the alternating current vanish under the condition that $\bar{V}(\mathbf{k}_0, t_0) = 0$ for any $\mathbf{k}_0$; that is, in the strict sense, only in this case does the DL (in combination with collisions) lead to the occurrence of the SIT. When $\varepsilon_S(t)$, $V_S(t)$, and $W(t)$ depend on t only slightly, Eq. (50) approximately coincides with the equation $J_0(g) = 0$. But if the collision probability depends heavily on time (momentum), Eq. (50) can possess no solution and the SIT does not occur. This situation can take place when the main mechanism of electron scattering is the emission of optical phonons.

If mixing of the different momentum harmonics of the distribution function is taken into account by adding the corresponding terms to Eq. (32), the following generalized condition for the occurrence of the SIT can be obtained:

$$\sum_{\nu=1}^{\infty}a_\nu J_0(\nu g) = 0, \quad a_\nu = \text{const}. \qquad (53)$$

In [7], the condition for the transparency was found to be

$$J_0(g) + J_2(g) = 0, \qquad (54)$$

which also does not coincide with the condition for the occurrence of the DL. (Unfortunately, they used a nonphysical collision integral.)

It is appropriate to analyze the condition for the SIT effect in the frequently used one-dimensional two-relaxation-time model [2, 16] (which, however, inadequately allows for the electron gas heating [17]). In this model, the collision integral being integrated over $k_\perp$ has the form [16]

$$\frac{f(k_3, t) - f_0(k_3)}{\tau} + \frac{f(k_3, t) - f(-k_3, t)}{\tau_1}, \qquad (55)$$

where the second (additional) term allows for those elastic collisions that reverse the three-dimensional momentum (the probability of these collisions is infinitely small, but we, following [2, 16] and other incorrect papers, assume that $\tau_1 \ll \tau$). This collision integral does not mix the different νth momentum harmonics, and, therefore, the SIT occurs under the same condition, $J_0(g) = 0$, as the DL does [16]. For the purposes of illustration, we will show how this result is obtained for a degenerate electron gas with $\mu > \Delta$ [see Eq. (46)]. Assume for the moment that the second term in Eq. (55) is absent. In this case, as was shown above, at $J_0(g) = 0$ (and $\omega_1\tau \gg 1$), the electron distribution function $f(k_3, t)$ is a constant and, hence, the SIT occurs. Now, we take into account "elastic" collisions represented by the second term in Eq. (55). For $f(k_3, t) = \text{const}$, this term is identically equal to zero and, therefore, the solution to the kinetic equation remains unaffected. Thus, the introduction of two relaxation times in the one-dimensional model of an SSL [2] does not lead to separation of the regions where the SIT and DL effects occur. It can easily be shown that this statement is true for any equilibrium distribution function.

4. COMPARISON WITH JOSEPHSON JUNCTIONS

As was repeatedly indicated (see, e.g., [11]), the collisionless dynamics of a superlattice electron is mathematically identical to the behavior of the superconduction current in a Josephson junction. This suggests the possible development of the so-called Bloch (continuous-wave) oscillator at the Stark frequency (in accordance with the non-steady-state Josephson effect). The special properties of the Josephson junctions are associated with the fact that the current in them consists of two components: superconducting and normal (dissipative). These components correspond to two different groups of electrons passing through the junction: condensed Cooper pairs (superconducting electrons) and one-electron excitations, respectively. All superconducting electrons are described by a common wave function. Due to the coherence of the Cooper pairs, the phase of this wave function is a macroscopic quantity and is not affected by collisions. The dissipative current can be thought of as a shunt current, being one of the components of the total current flowing through the junction. In an SSL, the electrons cannot be separated into coherent and normal ones, because they have no common phase and all undergo collisions. Therefore, the resistance and reactance of the SSL are in series, rather than in parallel as in a Josephson junction. In addition, the BO and BOHF in the SSL essentially manifest themselves in a different manner in dissipative processes (e.g., in current–voltage characteristics), because dissipation in Josephson junctions is associated with electrons whose dispersion law is different from that of superlattice electrons. For this reason, even infrequent collisions lead to a dissimilarity of macroscopic properties between SSLs and Josephson junctions. Therefore, the Bloch oscillator is impossible (the SSL conductivity at the Stark frequency is always positive). However, amplification of signals at shifted resonance frequencies can occur. The macroscopic properties of SSLs and Josephson junctions associated with Bloch oscillations remain similar only in processes of duration $\Delta t \leq \tau$. These can be transients caused by the static field turning on, or by its sharp change, or by sharp optical excitation of electrons in the presence of a static field [14, 18]; these can also be short solitons [16]. Only selective transparency effects, including the DL, are similar in nature in the Josephson junctions and SSLs.

Thus, the nonlinear conductivity of an SSL is a nonmonotonic function of the field amplitude, which manifests itself most clearly in the selective transparency and SIT effects. Selective transparency is determined solely by the dynamics of collisionless electrons and is a direct consequence of the absence of the corresponding harmonics in the BOHF. The SIT is a combined effect of the time-harmonic field and collisions which produce the special electron distribution modulated in the momentum space; this distribution does not contain the harmonic that contributes to the current. In contrast to selective transparency, the SIT does not occur in the absence of collisions. The dynamical localization (the absence of the zeroth harmonic in the BOHF) and the collapse of quasi-energy minibands, corresponding to a special case of selective transparency, are accompanied by complete transformation of the energy of translational motion of electrons into the energy of their oscillations. As a consequence, the energy exchange between the field and individual electrons is enhanced, which causes the dissipative current to increase sharply and can give rise to dissipative instabilities. In particular, the DL is favorable for the absolute conductivity becoming negative. In the relaxation time approximation (τ = const), the DL and SIT occur at the same values of the field amplitude which are determined from the equation $J_0(g) = 0$. In all the models proposed, the DL, as well as the selective transparency effect, occurs immediately after the field is turned on, while the SIT occurs after a time of the order of τ. Beyond the τ = const approximation, the DL and the SIT occur at different values of the field amplitude and the question of whether these two effects are identical does not arise. In contrast to the DL, the conditions for the occurrence of the SIT are sensitive to the relaxation mechanisms and, hence, depend on the temperature and the electron concentration. When investigating the transparency effect in SSLs experimentally, especially in SSLs with nonharmonic dispersion low, it is advisable to use multifrequency fields.

Since the properties of SSLs are similar to those of two-level systems [1], the effects considered in this paper also occur in structures with separate quantum wells.

ACKNOWLEDGMENTS

This work was supported by the INTAS FEBR, grant no. 95-0615, and the Russian Interdisciplinary Research and Development Program FTNS, grant no. 99-1129.

REFERENCES

1. Yu. A. Romanov, in *Multilayer Semiconductor Structures and Superlattices*, Ed. by A. M. Belyantsev and Yu. A. Romanov (Gorki, 1984).
2. A. A. Ignatov and Yu. A. Romanov, Fiz. Tverd. Tela (Leningrad) **17** (11), 3388 (1975) [Sov. Phys. Solid State **17**, 2216 (1975)]; Phys. Status Solidi B **73**, 327 (1976).
3. Yu. A. Romanov and L. K. Orlov, Fiz. Tverd. Tela (Leningrad) **18** (3), 728 (1977) [Sov. Phys. Solid State **19**, 421 (1978)]; Yu. A. Romanov, L. K. Orlov, and V. P. Bovin, Fiz. Tekh. Poluprovodn. (Leningrad) **12**, 1665 (1978) [Sov. Phys. Semicond. **12**, 987 (1977)].
4. A. A. Kostenko, O. A. Kuznetsov, V. A. Tolomasov, *et al.*, Dokl. Akad. Nauk SSSR **271**, 1360 (1983) [Sov. Phys. Dokl. **28**, 670 (1983)].
5. M. C. Wanke, A. G. Markelz, K. Unterrainer, *et al.*, in *Physics of Semiconductors*, Ed. by N. Scheffter and R. Zimmerman (World Scientific, Singapore, 1996), p. 1791.
6. O. N. Dunlap and V. M. Kenkre, Phys. Rev. B **34**, 3625 (1986); Phys. Lett. A **127**, 438 (1988).
7. J. F. Lam, B. D. Guenther, and D. D. Skatrud, Appl. Phys. Lett. **56**, 773 (1990).
8. M. Holthaus, Z. Phys. B **89**, 251 (1992); Phys. Rev. Lett. **69**, 351 (1992); M. Holthaus and D. Hone, Phys. Rev. B **47**, 6499 (1993); M. Holthaus and D. Hone, Phys. Rev. B **49**, 16605 (1994).
9. O. M. Yevtuhenko and A. P. Panchekha, Phys. Lett. A **200**, 453 (1995).

10. J. Rotvig, A.-P. Jauho, and H. Smith, Phys. Rev. Lett. **74** (10), 1831 (1995).
11. B. J. Keay, S. Zeuner, S. J. Allen, *et al.*, Phys. Rev. Lett. **75**, 4102 (1995).
12. A. W. Ghosh, A. V. Kuznetsov, and J. W. Wilkins, Phys. Rev. Lett. **79**, 3494 (1997).
13. A. W. Ghosh, M. C. Wanke, S. J. Allen, and J. W. Wilkins, Appl. Phys. Lett. **74**, 2164 (1999).
14. M. W. Feise and D. S. Citrin, Appl. Phys. Lett. **75**, 3536 (1999).
15. G. Bastard and R. Ferreira, C. R. Acad. Sci. **312**, 971 (1991); R. Ferreira and G. Bastard, Surf. Sci. **229**, 424 (1990).
16. F. G. Bass, A. A. Bulgakov, and A. P. Tetervov, *High-Frequency Properties of Semiconductors with Superlattices* (Nauka, Moscow, 1989).
17. E. V. Demidov, Yu. A. Romanov, and Yu. Yu. Romanova, in *Abstracts of 10th International Symposium on Ultrafast Phenomena in Semiconductors, 1998*, p. 138; Yu. A. Romanov and E. V. Demidov, Fiz. Tverd. Tela (St. Petersburg) **41** (9), 1698 (1999) [Phys. Solid State **41**, 1555 (1999)].
18. C. Waschke, H. G. Roskos, R. Schwedler, *et al.*, Phys. Rev. Lett. **70**, 3319 (1993); M. Sudzius, V. G. Lyssenko, G. Valusis, *et al.*, Physica E (Amsterdam) **2**, 437 (1998).

Translated by Yu. Epifanov

Physics of the Solid State, Vol. 43, No. 3, 2001, pp. 549–555. Translated from Fizika Tverdogo Tela, Vol. 43, No. 3, 2001, pp. 529–535.
Original Russian Text Copyright © 2001 by Grinyaev, Razzhuvalov.

LOW-DIMENSIONAL SYSTEMS AND SURFACE PHYSICS

Resonant Electron Tunneling in GaN/$Ga_{1-x}Al_xN$(0001) Strained Structures with Spontaneous Polarization and Piezoeffect

S. N. Grinyaev and A. N. Razzhuvalov

Kuznetsov Siberian Physicotechnical Institute, pl. Revolyutsii 1, Tomsk, 634050 Russia
e-mail: gsn@phys.tsu.ru

Received May 18, 2000; in final form, August 15, 2000

Abstract—Electron tunneling through the GaN/$Ga_{1-x}Al_xN$(0001) wurtzite strained structures is investigated by the pseudopotential and scattering matrix methods. It is shown that the results of multiband calculations at low aluminum concentrations ($x < 0.3$) are adequately described within the single-valley model in the envelope wave function method accounting for the dependences of the effective mass on the energy and strain. Upon electron tunneling through two-barrier structures, sharp resonance peaks are observed at a barrier thickness of several monolayers and the characteristic collision time in the resonance region is equal to ~1 ps. The internal electric fields associated with spontaneous and piezoelectric polarizations lead to a "red" or "blue" shift in the resonance energy according to the thickness and location of barriers with respect to the polar axis. In the $(GaN)_n(Ga_{1-x}Al_xN)_m$ superlattices, the internal fields can form the Stark ladder of electronic states at a small number of ultrathin layers even in the absence of external fields. © *2001 MAIK "Nauka/Interperiodica".*

1. INTRODUCTION

The wide-gap wurtzite structures GaN/$Ga_{1-x}Al_xN$(0001) are of considerable interest for ultraviolet opto- and high-frequency nanoelectronics. These structures have already been used in fabricating "blue" light-emitting [1] and multiple-well laser [2] diodes and fast field-effect transistors [3]. Moreover, they are promising materials for the development of high-sensitive sensors [4]. The specific feature of these materials is a record-high value of the spontaneous polarization and piezoelectric tensor components [5, 6], which are responsible for the generation of strong internal electric fields (~10^7 V/cm). These fields substantially affect the electron transport [7, 8], defect formation [8], and optical properties [9–11].

A number of parameters determined for nitride compounds in recent studies [5, 6, 12, 13] make modeling the physical properties of heterostructures with inclusion of polarization fields and strains possible. Despite extensive investigations, the effect of these fields on fundamental electronic processes has not been adequately explored. Theoretical investigations are usually performed within the effective mass method in the flat band approximation or with allowance made only for piezoelectric fields [4, 8, 9], whereas the spontaneous polarization in nitride compounds can induce fields even with a higher strength [13]. Recently, it was shown that the spontaneous polarization makes the main contribution to the "red" Stark shift in the energies of optical transitions in GaN quantum wells [14]. The strength and orientation of internal fields depend on the thickness of layers, their chemical composition, doping, the type of substrate, etc., which considerably extends the possibilities of controlling instrumental characteristics [15]. The known effects which are associated with external electric fields (Bloch oscillations, Stark localization of states, and band-to-band tunneling) are substantially modified in the presence of internal polarization and can manifest themselves even at a small number of ultrathin layers in heterostructures. For example, in the $(GaAs)_n(Ga_{1-x}Al_xAs)_m$ superlattices with a layer thickness of ~30 Å, the Stark localization of charges in GaAs wells is observed in considerably weaker external fields (~10^5 V/cm) [16]. However, piezoelectric fields in these crystals are not very high and the spontaneous polarization is forbidden by the cubic symmetry.

For the most part, the investigations of nitride structures are concerned with the optical properties which determine their use in optoelectronics. At the same time, the considerable conduction band discontinuity at GaN/AlN heterointerfaces (~1 eV, as in GaAs/AlAs structures) [12, 13], fast (at a distance of the order of one lattice spacing) attenuation of electron waves in barrier regions, and simple single-valley structure of the low-lying conduction band, which excludes undesirable intervalley mixing effects (leading to an increase in the tunneling time in GaAs/AlAs structures [17]), render these compounds interesting for the design of fast resonant-tunnel subatomic structures.

These structures, as their binary components, are stable to extreme external effects (high temperatures, external stresses, irradiation, etc.) [18]. It is evident that strong polarization fields should substantially change all the characteristics of tunneling processes. Note that the forms of their manifestation can be diverse due to the dependence of the field strength on heterostructure parameters.

Faithful description and design of simplified models for electronic states in heterostructures with inclusion of built-in fields are based on fundamental methods for calculating electronic energy spectra (methods of pseudopotential, augmented plane waves, etc.). The parameters of spontaneous and piezoelectric polarizations and the band discontinuities at the heterointerfaces of GaN/AlN strained structures were determined with *ab initio* pseudopotentials [12, 13]. A more correct description of the band structure can be achieved within the quasiparticle approach [19]. However, the nonlocal character of *ab initio* pseudopotentials complicates the determination of states with complex values of the wave vectors which appear in solving the problem of electron scattering. In this respect, in the present work, the electron tunneling through the $GaN/Ga_{1-x}Al_xN(0001)$ strained heterostructures was investigated by the local pseudopotential method [20], which made it possible to use an efficient technique for determining the general solutions of the Schrödinger equation [21]. The calculated complex band structure enabled us to devise a simplified model within which we studied the effects brought about by built-in polarization fields upon electron tunneling through nitride heterostructures.

2. COMPUTATIONAL TECHNIQUE

Self-consistent calculations of the electronic spectrum of $(GaN)_n(AlN)_n(0001)$ superlattices demonstrate that the internal electric fields at distances of the order of one monolayer from boundaries are well described within the macroscopic approach [13]. Therefore, the nitride structures with layer thickness of several periods can be studied in the framework of the model with a crystal potential discontinuity at the heterointerfaces. In this case, the interface dipoles are approximately taken into account through the change in band discontinuities and the monopole shielding with allowance made for the lattice relaxation is included with the use of the static permittivity [13].

In order to illustrate the effects associated with the internal fields, we considered the $GaN/Ga_{0.7}Al_{0.3}N$ structure with the (0001) natural growth boundary. Barrier layers were taken to be thin (several lattice spacings); hence, their lattice constant in the boundary plane matched the lattice constant of GaN contact regions. The experimental structure parameters used for free crystals were as follows [18]: $a(\mathrm{GaN}) = 3.189$ Å, $c(\mathrm{GaN}) = 5.185$ Å, $a(\mathrm{AlN}) = 3.111$ Å, and $c(\mathrm{AlN}) = 4.98$ Å. The misfit of the lattice constants for GaN and AlN (~4%) leads to considerable strains of layers in the heterostructure. The compression of barrier layers along the axis is defined by the relationship $\Delta c = -2(c_{13}/c_{33})(\Delta a/a)c$ [22]. The strains induce the piezoelectric polarization whose projection onto the hexagonal axis is given by the expression $P_{\mathrm{piezo}} = 2e_{31}\Delta a/a + e_{33}\Delta c/c$ [22]. The elastic moduli in the $Ga_{1-x}Al_xN$ solution were determined by interpolating the experimental data taken from [23]: $c_{13} = (10.5 + 1.1x)$ dyn/cm^2 and $c_{33} = 39$ dyn/cm^2. The piezoelectric tensor components e_{31} and e_{33} and the spontaneous polarization P_{spont} were derived from the results of calculations [13]: $e_{31} = (-0.49 - 0.11x)$ C/m^2, $e_{33} = (0.73 + 0.73x)$ C/m^2, and $P_{\mathrm{spont}} = (-0.029 - 0.052x)$ C/m^2. The piezoelectric polarization in barriers was $P_{\mathrm{piezo}}(Ga_{0.7}Al_{0.3}N) = -0.012$ C/m^2. The total polarization (spontaneous and piezoelectric) along the hexagonal axis $P_{w,b}$ (where the subscripts w and b designate the well and the barrier, respectively) in the barrier region ($P_b = -0.057$ C/m^2) is 80% contributed by the spontaneous polarization and is almost twice as large as the polarization in the well ($P_w = -0.029$ C/m^2). The discontinuity of the macroscopic polarization at the heterointerfaces gives rise to surface charges. From the continuity condition for the normal component of the dielectric induction at the layer boundary follows the relationship between the electric field strengths $F_{w,b}$ [24]: $\varepsilon_w F_w - \varepsilon_b F_b = -(P_w - P_b)/\varepsilon_0$, where e_w and e_b are the static permittivities (the value of $\varepsilon = 9.5$ [25] was used for all compositions) and ε_0 is the permittivity of free space.

The strengths and orientations of fields in layers depend on the boundary conditions. The internal field in the heterostructure is inhomogeneous due to the difference in the polarization of layers. Bernardini and Fiorentini [13] used the periodic boundary conditions, which corresponds to the complete compensation for the homogeneous component of the internal electric field over the superlattice period. In real structures, the compensation for the homogeneous component of the internal field F_0 in the active region can be achieved by different methods, for example, through the screening of doped contact regions by free charges [15]. In the case when the external field strength is considerably less than F_0, the external field can be ignored in the boundary condition. Then, the compensation condition is determined by the relationship $\sum_i l_i F_i = 0$, where l_i is the thickness of the ith layer and the summation is performed over the active region layers. For the active region composed of a finite superlattice $(GaN)_n(Ga_{1-x}Al_xN)_{n+1}$ (where n is the number of periods along the hexagonal axis) with a spacer layer (of thickness l_s) from the same solid solution, which are arranged between the GaN contact regions, the compensation condition leads to the relationship for the potential shift $\Delta V = l_w(l_b + l_s)(P_b - P_w)/D$ {where $D = [n(l_w\varepsilon_b + l_b\varepsilon_w) + (l_b + l_s)\varepsilon_w]\varepsilon_0$} over the superlattice period $d = l_w + l_b$ and the expressions for the internal field strengths in the layers $F_w = -[(n+1)l_b + l_s](P_b - P_w)/D$ and $F_b = F_s = nl_w(P_w - P_b)/D$. In the limit $n \longrightarrow \infty$, these relationships are transformed into the formulas for an infinite superlattice [13]. As a rule, the thickness of the contact regions is much more than the thickness of the active region $d_a = (n+1)l_b + nl_w + l_s$, and, hence, the fields in them are close to zero [15]. Let us consider the possibility of compensating for F_0 by free charges. The value of F_0 is determined by the ratio between the potential jump at an "excess" barrier containing the spacer layer and the active region thickness d_a. Therefore, at comparable layer thicknesses $l_s \sim l_w \sim l_s$, the field F_0 is approximately $(n+1)$ times weaker than the field in the barrier whose magnitude for the structures under consideration is less than 2×10^6 V/cm. Consequently, even for the two-barrier structure ($n = 1$), we have $F_0 < 10^6$ V/cm. As follows from [15, 26], similar fields are efficiently screened at a practically achievable donor concentration of $\sim 10^{19}$ cm^{-3}. The self-consistent solution of the Poisson and Schrödinger equations proved that the redistribution of free charges over the bulk of the structure with the GaN/$Ga_{0.8}Al_{0.2}N$ quantum well brings about noticeable bendings of bands in depleted contact regions and small bendings in the active region [15]. In our case, the field F_0 is substantially weaker than the unscreened field in the well [15], and, hence, the compensation for F_0 was taken into account by neglecting the bendings of bands near interfaces.

The probabilities of electron tunneling through heterostructures were calculated in the framework of the model with a potential discontinuity at the heterointerfaces by using the scattering matrix method [27] that was modified for crystals with a hexagonal symmetry. In the present work, we considered the normal incidence of electrons on the heterointerface. The wave functions of the adjacent layers were matched on planes that contained nitrogen atoms. The general solutions of the Schrödinger equation in layers were sought by calculating the complex band structure [19] with the crystal potential matrix renormalized according to the Löwdin method in the basis set consisting of 73 exactly included plane waves that were constructed around the Γ reference point. Nineteen incident and nineteen reflected Bloch waves were formed in this basis set [27]. In calculations, we used the model pseudopotentials taken from [20]. In order to improve the accuracy of describing the spectrum, these pseudopotentials included additional corrections for nonlocality and energy dependence by way of renormalizing the free electron mass m in the kinetic energy operator $T = -\hbar^2\Delta(1 + \beta/\Omega)/2m$, where Ω is the unit cell volume. The pseudopotential parameters were determined by fitting the calculated energies of band-to-band transitions and side valleys of the low-lying conduction band in *w*-GaN and *w*-AlN, and also the effective masses and deformation potentials, to experimental data and results of *ab initio* calculations. The found parameters of ion pseudopotentials are as follows (in au, $\hbar = m = e = 1$): $v_0(\mathrm{N}) = -4.3$, $R_m(\mathrm{N}) = 2.49$, and $\beta(\mathrm{N}) = 0$; $v_0(\mathrm{Al}) = -0.7$, $R_m(\mathrm{Al}) = 3.34$, and $\beta(\mathrm{Al}) = -60$; and $v_0(\mathrm{Ga}) = -0.8$, $R_m(\mathrm{Ga}) = 4.1$, and $\beta(\mathrm{Ga}) = 0$. The band structure parameters for GaN and AlN, which were calculated with these pseudopotentials in the vicinity of the band gap, are given in the table in comparison with the results of other works. Here, the deformation potentials D_1, D_3 and D_2, D_4 characterize the level shifts with a change in the lattice constants c and a according to [6].

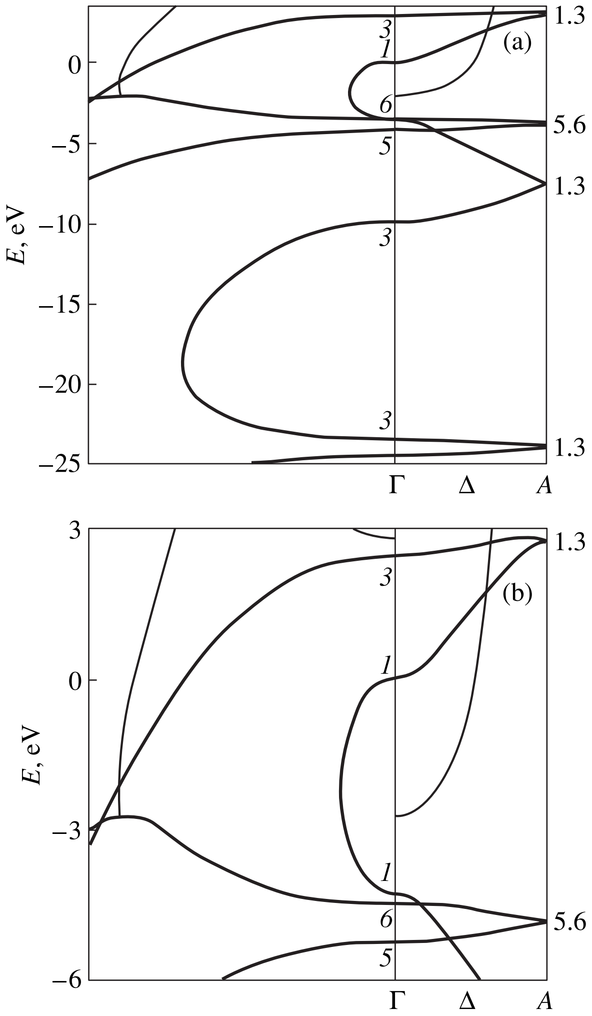

Fig. 1. Fragments of complex band structures for (a) *w*-GaN free crystal and (b) *w*-$Ga_{0.7}Al_{0.3}N$ strained solid solution. The solutions with purely real values of the wave vector along the hexagonal axis (heavy lines) and the real parts of complex solutions (thin lines) are shown to the right of the Γ point. The purely imaginary solutions (heavy lines) and the imaginary parts of complex solutions (thin lines) are displayed to the left of the Γ point.

The electronic states in the $Ga_{1-x}Al_xN$ solutions were calculated within the virtual-crystal approximation. The cation pseudopotential was represented as the mean of the Al and Ga potentials taken with weights proportional to their concentrations. The calculated energy gap appeared to be almost a linear function of the solution composition. Figure 1 depicts the frag-

Band structure parameters for GaN and AlN

Level	GaN		AlN	
	1	2	1	2
Γ_{5v}	–0.7	–1.2 [19]	–0.8	–1.1 [19]
Γ_{6v}	0	0	–0.22	–0.2 [19] –0.176 [6]
Γ_{1v}	–0.08 (–0.022 [28])	–0.02 [19] –0.0504 [6]	0	0
Γ_{1c}	3.52 (3.44 [29])	3.5 [19]	6.28 (6.28 [32])	5.8 [19]
Γ_{3c}	6.5	5.9 [19]	7.7	8.3 [19]
M_{4v}	–0.7	–1.1 [19]	–0.6	–0.9 [19]
M_{1c}	6.5	6.5 [19]	7.6	7.4 [19]
$m^*/m(\Gamma_{1c})$	0.14 (0.22 [30])	0.19 [31]	0.30	0.35 [31]
$D_1(\Gamma_{1v})$	–24.3	–20.0 [6]	–14.3	–17.1 [6]
$D_2(\Gamma_{1v})$	–13.6	–14.2 [6]	–6.6	–7.9 [6]
$D_1(\Gamma_{1c})$	–15.0		–8.6	
$D_2(\Gamma_{1c})$	–13.5		–8.8	
$D_3(\Gamma_{6v})$	10.6 (8.82 [28])	5.8 [6]	8.9	8.84 [6]
$D_4(\Gamma_{6v})$	–3.4 (–4.41 [28])	–3.25 [6]	–1.5	–3.92 [6]

Note: The results of this work are presented in columns 1 (the experimental data are given in parentheses) and the results of other works are listed in columns 2. The energies of levels and the deformation potentials are expressed in electron-volts.

ments of calculated complex band structures along the Δ direction of the hexagonal Brillouin zone at zero wave vector component parallel to the boundary. The energies are measured from the bottom of the conduction band of each compound. The standard designations are used for irreducible representations of the C_{6v}^4 group. As far as we know, the complex band structures of these materials are presented in this work for the first time. Their analysis makes it possible to reveal the states with the least damping decrement, which play a decisive role in tunneling processes. Since the side point A at the Brillouin zone edge is not the point of zero slope of the band spectrum for wurtzite crystals [33], the branches of complex band structure with these damping decrements originate only from the central Γ valley of the low-lying conduction band of the $Ga_{1-x}Al_xN$ solid solutions. The biaxial tension in the boundary plane and the compression along the hexagonal axis of the $Ga_{0.7}Al_{0.3}N$ solution layer lead to the change in the symmetry of the higher-lying state in the valence band and the crystalline splitting from $\Delta_{cr}(\Gamma_{1v} - \Gamma_{6v}) = 0.009$ eV to $\Delta_{cr}(\Gamma_{6v} - \Gamma_{1v}) = 0.202$ eV and also to a decrease in the band gap from $E(\Gamma_{1c} - \Gamma_{6v}) = 4.37$ eV to $E(\Gamma_{1c} - \Gamma_{1v}) = 4.26$ eV and the effective electron mass from 0.191 to 0.177 (in terms of m). The gap discontinuity at the heteroboundary also depends on layer stresses [12, 13, 34]. This discontinuity in structures with strained solid solution layers was taken into consideration by using a linear interpolation (with respect to the composition) of the valence band discontinuity $\Delta E_v = 0.2$ eV [13], which was found for a GaN/AlN heteropair with strained barriers. From the obtained value $\Delta E_v(GaN/Ga_{0.7}Al_{0.3}N) = 0.06$ eV and the calculated energy gaps, the conduction band discontinuity was determined as $\Delta E_c(GaN/Ga_{0.7}Al_{0.3}N) = 0.81$ eV.

3. RESULTS AND DISCUSSION

The calculated coefficient $P(E)$ for transmission of electrons through the symmetric two-barrier structure $GaN/Ga_{0.7}Al_{0.3}N(3c)/GaN(4c)/Ga_{0.7}Al_{0.3}N(3c)/GaN$ is displayed in Fig. 2. The results of multiband calculations were obtained without regard for the internal fields. The resonance states in the well correspond to two peaks in $P(E)$. Under the same conditions, we performed the approximate calculations in which the exact matching matrix accounted for “interactions” between the states only of the low-lying conduction band. At electron energies up to ~2 eV from the well bottom, the results of two calculations turned out to be virtually identical. This can be explained by the fact that the states of higher-energy bands with larger damping decrements weakly affect the asymptotics of wave functions of the heterostructure. Therefore, in this energy range, it is possible to apply the effective mass method which takes into account the states of one real branch that connects the states with the Γ_1 symmetry at the band gap edges. In order to simplify our calculations, the envelope wave function was chosen in the form of a plane wave (the Bloch function at the Γ extremum of the conduction band) for which the standard conditions of matching at the boundaries were used with due regard for the dependence of the effective mass on the energy and strain. The transmission coefficient calculated in the framework of this model is in reasonable agreement with the results of multiband calculations (Fig. 2). A small difference in the energies of the low-lying resonance (~0.02 eV) is caused by the influence of states of the valence band. As the aluminum concentration in the barrier layers increases, the energy of resonance approaches the branch point of the complex band structure of solid solution and the discrepancy with exact calculations increases. At small Al concentrations, it is possible to use the single-valley model which was applied for analyzing the effect of internal electric fields on the electron tunneling in the $GaN/Ga_{0.7}Al_{0.3}N$ structures. In this case, the fields in the contact regions were taken equal to zero and the potential of electric field in the layers of the active region was represented in the form of thin square barriers. Figure 2 also shows the transmission coefficient, the phase transmission time $\tau = \hbar\partial\varphi(E)/\partial E$ [where $\varphi(E)$ is the phase shift in the amplitude of the transmitted wave], the profile of effective electron potential, and the charge density (obtained under the condition that the amplitude of the incident wave is equal to unity), which were calculated for the same two-barrier structure with due regard for the internal fields. At the chosen boundary conditions, the internal field is directed from the cation to the nearest anion along the hexagonal axis in the barrier regions (F_b = 1.31×10^6 V/cm) and in the opposite direction in the well region ($F_w = -1.92 \times 10^6$ V/cm). Spontaneous polarization makes the main contribution to these fields.

The internal fields lead to a change in the electron potential in the layers by magnitudes comparable to the gap discontinuities and render the potential asymmetric. As a consequence, the localization of charge density in the well depends on the direction of electron incidence and the probability of tunneling, the energy of the low-lying resonance, and the phase time decrease. These effects enhance with an increase in the Al concentration in the barriers. The occurrence of a polar direction in wurtzite crystals results in the dependence of the transmission coefficient on the mutual arrangement of barriers in the asymmetric two-barrier structures

$$GaN/Ga_{0.7}Al_{0.3}N(4c)/GaN(4c)/Ga_{0.7}Al_{0.3}N(3c)/GaN$$
(Fig. 3a)

and

$$GaN/Ga_{0.7}Al_{0.3}N(3c)/GaN(4c)/Ga_{0.7}Al_{0.3}N(4c)/GaN$$
(Fig. 3b).

The internal field strengths in similar layers of these structures are identical ($F_w = -2.04 \times 10^6$ V/cm, and $F_b = 1.20 \times 10^6$ V/cm), but the potential profiles are different. In the case when the left barrier is thicker, the internal fields bring about a "blue" shift in the first and second resonance peaks (Fig. 3a) due to the effective rise of the well bottom. In the opposite case (Fig. 3b), the "red" shift of the first resonance increases and the energy of the second resonance decreases. Furthermore, since the "powers" of two barriers level off (the left and right barriers become higher and lower, respectively), the probability of tunneling at a resonance, as for a symmetric structure, is close to unity. In all the structures, the times of electron transmission through the region of the low-lying resonance are less than 1 ps, i.e., are of the same order of magnitude as in the GaAs/AlAs structures [17].

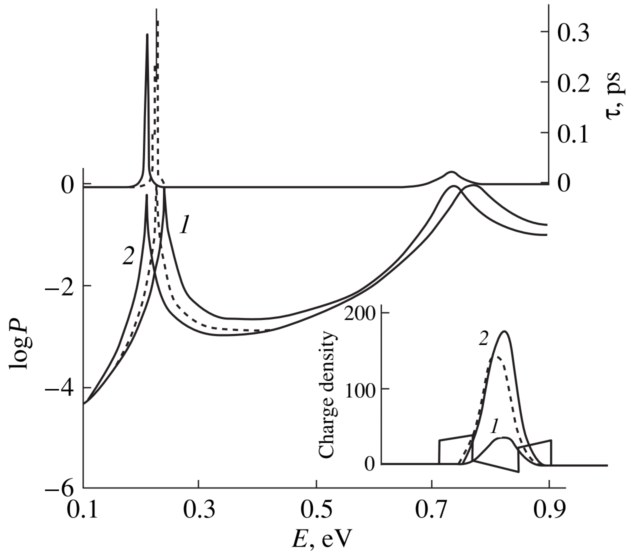

Fig. 2. Coefficients $P(E)$ and phase times $\tau(E)$ for transmission of electrons through the two-barrier structure $GaN/Ga_{0.7}Al_{0.3}N(3c)/GaN(4c)/Ga_{0.7}Al_{0.3}N(3c)/GaN$. Solid line *1* and the dashed line indicate the results of multiband calculations and calculations within the single-valley model without inclusion of electric fields, respectively. Solid line *2* represents the results of calculations in the framework of the single-valley model with inclusion of internal electric fields. The inset shows the effective potential profile and the charge densities of resonance states. The dashed line corresponds to the calculation without fields. Solid lines *1* and *2* display the results of calculations with internal fields upon incidence of electrons from the left and the right, respectively.

Now, we consider the electron tunneling through the finite $(GaN)_4(Ga_{0.7}Al_{0.3}N)_5$ superlattice with a spacer layer of the same solid solution which is located to the left and has a thickness of one lattice constant c (Fig. 4). In the absence of fields, the interaction between the states of separate wells leads to the formation of two minibands which are associated with two levels in the well and whose energies do not overlap. The states of these minibands correspond to the resonance peaks in the transmission coefficient calculated without regard for the fields (Fig. 4). The locations of peaks allow us to determine the difference between the energies of extreme resonance states in the low-lying miniband $\Delta E = 0.037$ eV and the band gap between the adjacent states in the

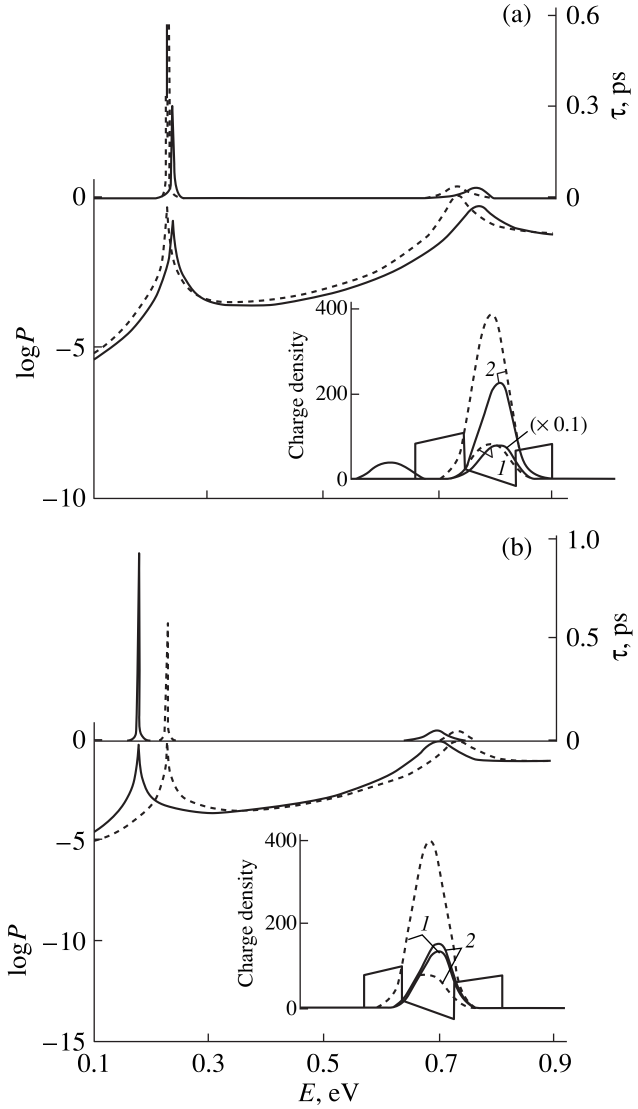

Fig. 3. Coefficients $P(E)$ and phase times $\tau(E)$ for transmission of electrons through the asymmetric two-barrier structures (a) $GaN/Ga_{0.7}Al_{0.3}N(4c)/GaN(4c)/Ga_{0.7}Al_{0.3}N(3c)/GaN$ and (b) $GaN/Ga_{0.7}Al_{0.3}N(3c)/GaN(4c)/Ga_{0.7}Al_{0.3}N(4c)/GaN$ without (dashed lines) and with (solid lines) inclusion of internal electric fields. Insets show the effective potential profiles and the charge densities of resonance states: lines *1* and *2* correspond to the incidence of electrons from the left and the right, respectively.

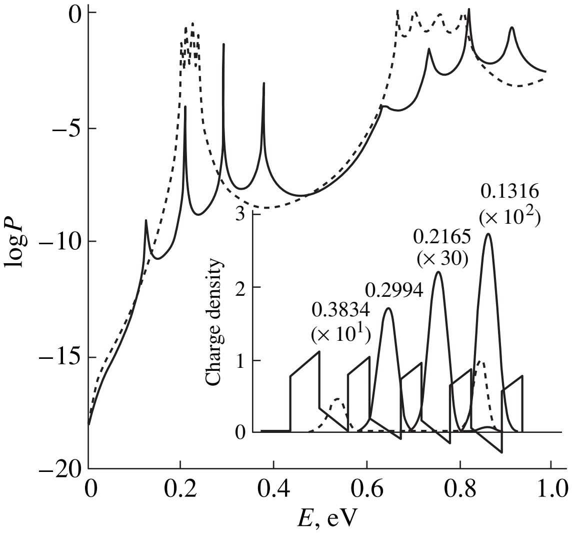

Fig. 4. Coefficients for transmission of electrons through the strained finite superlattice $(GaN)_4(Ga_{0.7}Al_{0.3}N)_5$ with the solid-solution spacer layer. Dashed and solid lines correspond to the calculations without and with inclusion of internal electric fields, respectively. The inset shows the effective potential profile and the charge density of resonances upon incidence of electrons on the structure from the right. The energies of resonances are given in eV.

miniband $\Delta E/n = 0.009$ eV ($n = 4$). With allowance made for the internal fields, the field strengths in the layers are as follows: $F_w = -1.60 \times 10^6$ V/cm and $F_b = 1.64 \times 10^6$ V/cm. As can be seen from the potential profile in Fig. 4, the superlattice potential to the right of the spacer layer appears such as if the superlattice were in a homogeneous external field with the strength $F_{\text{eff}} = -2.3 \times 10^5$ V/cm. The value of F_{eff} is determined from the ratio between the potential shift $\Delta V = 0.084$ eV and the superlattice period d. Since the value of ΔE is close to the limiting value that corresponds to the miniband width for an infinite superlattice [35], it can be used for verifying the fulfillment of the criterion for the formation of the Stark ladder [36]: $\Delta V \gg \Delta E/n$. A comparison of the obtained values demonstrates that the states of the low-lying miniband of the finite superlattice satisfy the above criterion. The presence of the main indications of the Stark ladder (the localization of charge density in separate wells and the equidistant step between resonance levels, which coincides with the potential jump ΔV) is illustrated in Fig. 4. The Stark ladder is formed owing to the disturbance of the superlattice hybridization of states of separate wells by the electric field F_{eff}. For the Stark states with the highest and lowest energies, certain deviations from an “ideal behavior” in the form of density satellites are observed as a result of edge effects upon incidence of electrons on the structure from the right and the left, respectively. At energies $E > 0.6$ eV, the resonance states of the second miniband correspond to more smeared peaks in $P(E)$. These states insufficiently rigorously meet the criterion from [36] ($n\Delta V/\Delta E \sim 2$), and the localization of charge density in wells is absent. Therefore, the formation of the Stark ladder due to the internal fields in finite nitride superlattices depends on the field strength F_{eff} and the dispersion of the miniband. The fulfillment of conditions for its observation can be provided by the proper choice of sizes and compositions of superlattice layers. The typical field strength F_{eff} required in this case, as for external fields, is equal to $\sim 10^5$ V/cm.

ACKNOWLEDGMENTS

We are grateful to G.F. Karavaev and V.G. Tyuterev for their participation in helpful discussions.

REFERENCES

1. S. Nakamura, M. Senoh, S. Nagahama, *et al.*, Jpn. J. Appl. Phys., Part 2 **35** (1B), L74 (1996).
2. D. Korakakis, K. F. Ludwig, and T. D. Moustakas, Appl. Phys. Lett. **72** (9), 1004 (1998).
3. Y.-F. Wu, B. P. Keller, D. Kapolnek, *et al.*, Appl. Phys. Lett. **69**, 1438 (1996).
4. R. Gaska, A. D. Bykhovski, M. S. Shur, *et al.*, J. Appl. Phys. **85** (9), 6932 (1999).
5. F. Bernardini, V. Fiorentini, and D. Vanderbilt, Phys. Rev. B **56** (16), R10024 (1997).
6. K. Shimada, T. Sota, and K. Suzuki, J. Appl. Phys. **84** (9), 4951 (1998).
7. R. Oberhuber, G. Zandler, and P. Vogl, Appl. Phys. Lett. **73** (6), 818 (1998).
8. L. Hsu and W. Walukiewicz, Appl. Phys. Lett. **73** (3), 339 (1998).
9. S.-H. Park and S.-L. Chuang, Appl. Phys. Lett. **72** (24), 3103 (1998).
10. N. Grandjean, B. Damilano, S. Dalmasso, *et al.*, J. Appl. Phys. **86** (7), 3714 (1999).
11. J. S. Im, H. Kollmer, J. Off, *et al.*, Phys. Rev. B **57** (16), R9435 (1998).
12. M. B. Nardelli, K. Rapcewicz, and J. Bernholc, Phys. Rev. B **55** (12), R7323 (1997).
13. F. Bernardini and V. Fiorentini, Phys. Rev. B **57** (16), R9427 (1998).
14. M. Leroux, N. Grandjean, M. Laugt, *et al.*, Phys. Rev. B **58** (20), R13371 (1998); J. Simon, R. Lauger, A. Barski, and N. T. Pelekanos, Phys. Rev. B **61** (11), 7211 (2000).
15. V. Fiorentini, F. Bernardini, F. D. Sala, *et al.*, Phys. Rev. B **60** (12), 8849 (1999).
16. E. E. Méndez, F. Agullo-Rueda, and J. M. Hong, Phys. Rev. Lett. **60** (23), 2426 (1988).
17. G. F. Karavaev and A. A. Voronkov, Fiz. Tekh. Poluprovodn. (St. Petersburg) **32** (11), 1363 (1998) [Semiconductors **32**, 1214 (1998)].
18. *Properties of Group III Nitrides*, Ed. by J. H. Edgar (Kansas State Univ., 1994), emis DATAREVIEWS SERIES No. 11.
19. A. Rubio, J. L. Corkill, and M. L. Cohen, Phys. Rev. B **49** (3), 1952 (1994).
20. S. N. Grinyaev, V. Ya. Malakhov, and V. A. Chaldyshev, Izv. Vyssh. Uchebn. Zaved., Fiz., No. 4, 69 (1986).
21. Y.-C. Chang and J. N. Schulman, Phys. Rev. B **25** (6), 3975 (1982).
22. Yu. I. Sirotin and M. P. Shaskolskaya, *Fundamentals of Crystal Physics* (Nauka, Moscow, 1979; Mir, Moscow, 1982).
23. A. A. Wright, J. Appl. Phys. **82**, 2833 (1997).
24. A. Bykhovski, B. Gelmont, and M. S. Shur, J. Appl. Phys. **74**, 6734 (1993).
25. J. W. Orton and C. T. Foxon, Rep. Prog. Phys. **61**, 1 (1998).
26. T. Deguchi, A. Shikanai, K. Torii, *et al.*, Appl. Phys. Lett. **72**, 3329 (1998).
27. S. N. Grinyaev and V. N. Chernyshov, Fiz. Tekh. Poluprovodn. (St. Petersburg) **26** (12), 2057 (1992) [Sov. Phys. Semicond. **26**, 1157 (1992)].
28. A. Shikanai, T. Azuhata, T. Sota, *et al.*, J. Appl. Phys. **81**, 417 (1997).
29. P. Perlin, I. Gorczyca, S. Porowski, *et al.*, Jpn. J. Appl. Phys. **32**, 334 (1993).
30. W. J. Moore, J. A. Freitas, and R. L. Molnar, Phys. Rev. B **56** (19), 12073 (1997).
31. H. Wang, G. A. Farias, and V. N. Freire, Phys. Rev. B **60** (8), 5705 (1999).
32. P. B. Perry and R. F. Rutz, Appl. Phys. Lett. **33**, 319 (1978).
33. É. I. Rashba, Fiz. Tverd. Tela (Leningrad) **1** (3), 407 (1959) [Sov. Phys. Semicond. **1**, 368 (1959)].
34. S. W. King, C. Ronning, R. F. Davis, *et al.*, J. Appl. Phys. **84** (4), 2086 (1998).
35. D. Y. Ko, G. Edwards, and J. C. Inkson, Semicond. Sci. Technol. **5**, 200 (1990).
36. J. Zak, Phys. Rev. Lett. **20**, 1477 (1968).

Translated by O. Borovik-Romanova

Physics of the Solid State, Vol. 43, No. 3, 2001, pp. 556–562. Translated from Fizika Tverdogo Tela, Vol. 43, No. 3, 2001, pp. 536–542.
Original Russian Text Copyright © 2001 by Dedkov, Kyasov.

LOW-DIMENSIONAL SYSTEMS AND SURFACE PHYSICS

Fluctuational Dissipative Electromagnetic Interaction between a Nanoprobe and a Surface

G. V. Dedkov and A. A. Kyasov
Kabardino-Balkar State University, Nalchik, 360004 Russia
e-mail: gv_dedkov@rekt.kbsu.ru

Received May 30, 2000

Abstract—In the framework of fluctuational electromagnetic theory, analytical expressions are obtained for the dynamic dissipative damping forces acting on the probe of an atomic-force microscope (AFM), as well as between two plane surfaces at their contact. The contacts between materials typical of AFM, quartz-microbalance, and surface-force apparatus experiments are considered. The conditions for nondissipative slide are discussed. A comparison between the calculated oscillator quality factor associated with fluctuational dissipative forces and its values obtained in AFM experiments with a silicon probe and a mica sample shows that they are of the same order of magnitude; therefore, an experimental investigation of such forces is feasible. © *2001 MAIK "Nauka/Interperiodica".*

INTRODUCTION

Nanostructural mechanisms of energy dissipation play a decisive role in the problem of friction as a whole, and the fluctuational dissipative electromagnetic interaction is one of the most important factors in the process of contactless slide of surfaces [1]. This process is typical of the dynamical mode of operation of an atomic-force microscope (AFM), and, therefore, experimental AFM studies of dissipative forces have considerable promise [2, 3].

In our recent papers [4, 5], the problem of damping of atomic and molecular particles moving laterally over the surface of a solid at a nonrelativistic velocity V was treated in detail in the framework of the general theory of fluctuational electromagnetic interactions. The objective of this paper is further development and application of this theory for calculating dissipative forces acting on an AFM probe in the cases of different combinations of the materials of the probe and sample. We also discuss the role of fluctuational electromagnetic forces in measurements with a quartz microbalance [6, 7] and treat the problem on the friction of two plane surfaces, which is the subject of some controversy in the literature [8–10].

1. DAMPING FORCE ON ATOMIC AND MOLECULAR PARTICLES: THE PRINCIPAL THEORETICAL RESULTS

The physical processes resulting in fluctuational dissipative interactions are similar to those that lead to conservative van der Waals attractive forces between solids. The latter forces are due to quantum-mechanical and thermal fluctuations of microscopic electric fields associated with motion of charged particles. These fluctuating fields induce analogous fields in other interacting solids, and, when the solids move relative to each other, the interaction between them is accompanied by Joule loss, which is considered the result of dynamical damping.

In order to strictly calculate the fluctuational dissipative interaction force between an arbitrarily shaped nanoprobe and a plane (or curved) surface in the framework of the theory developed in [4, 5], one should determine the equilibrium fluctuation spectrum of the electromagnetic field in the gap between the solids, which is a complicated mathematical problem in itself. In this case, some geometrical restrictions arise which reflect the fundamental properties of forces of this kind, in particular, of conservative van der Waals forces. In the latter case, fortunately, the assumption of additive interactions between individual particles is a close approximation, which allows one to correctly calculate the dependence of the resultant forces upon the spacing between the solids; only the interaction constant is affected by this approximation [11]. For a convex probe and a plane surface, this constant, as calculated in the additive-interaction approximation, is more than 5–20% in error and can be corrected by its effective renormalization [12].

As a working hypothesis, we assume that the fluctuational dissipative forces are also additive and that this additivity approximation gives the correct distance dependence of the forces. A comparison with calculations that do not involve this approximation is further shown (Section 5) to provide support for this assumption.

Following [4, 5], we consider the case where an atom (molecule) moves at a nonrelativistic velocity V parallel to the surface of a medium with a dielectric function $\varepsilon(\omega)$ and is at a distance h from the surface. A neutral spherical particle is characterized by polarizability $\alpha(\omega)$, while a dipole molecule is assumed to have an arbitrarily oriented constant dipole moment **d**.

In the limit of small velocities (which is of prime interest for the dynamical mode of the AFM operation, in which the typical nanoprobe velocities do not exceed or are much smaller than 1 m/s) and in the range of distances $r_0 \ll h \ll c/\omega_0$ (where r_0 is the characteristic size of atoms and ω_0 is the frequency of orbital motion of electrons), the damping force per atom was found to be [4, 5]

$$F = -\frac{3\hbar V}{8\pi h^5}\int_0^\infty d\omega \left\{ 2\left[\alpha''(\omega)\frac{d\Delta''(\omega)}{d\omega} - \Delta''(\omega)\frac{d\alpha''(\omega)}{d\omega}\right] + \omega\left[\alpha''(\omega)\frac{d^2\Delta''(\omega)}{d\omega^2} - \Delta''(\omega)\frac{d^2\alpha''(\omega)}{d\omega^2}\right]\right\}\coth\left(\frac{\omega\hbar}{2k_{\mathrm{B}}T}\right), \tag{1}$$

where $\Delta(\omega) = (\varepsilon(\omega) - 1)/(\varepsilon(\omega) + 1)$ and the doubly primed quantities are the imaginary parts of the corresponding functions. At $T = 0$, after some mathematical manipulation, Eq. (1) is reduced to a simpler formula:

$$F = -\frac{3\hbar V}{4\pi h^5}\int_0^\infty d\omega\alpha''(\omega)\frac{d\Delta''(\omega)}{d\omega}. \tag{2}$$

We note that the condition $r_0 \ll h \ll c/\omega_0$ allows one to treat the particle as a point dipole and ignore the retardation effects. In this case, the distance to the surface is limited from above by a value of 10–20 nm, which is the exact value at which probing is efficiently performed in the dynamical mode of the AFM operation. At $h \approx r_0$, spatial dispersion effects become significant and the dependence of the dielectric function upon the wave vector should be taken into account. Nonetheless, in this case, too, Eqs. (1) and (2) account for a certain (perhaps, dominant) part of the interaction. Here, the situation is analogous to that which takes place when one calculates the interaction energy between two neutral atoms in the vicinity of the van der Waals minimum: the dipole–dipole interaction makes a significant contribution to the interatomic interaction energy, although, strictly speaking, the atoms cannot be considered as point dipoles when the separation between them is so small.

Damping of motion of a dipole molecule with dipole moment $\mathbf{d} = (d_x, d_y, d_z)$ is characterized by the dissipative force [5]

$$F = -\frac{3(3d_x^2 + d_y^2 + 4d_z^2)V}{32\sigma h^5}, \tag{3}$$

and in the case of a charged particle with charge Z_1e, this force is

$$F = -\frac{(Z_1e)^2}{16\pi\sigma h^3}V, \tag{4}$$

where σ is the static conductivity. In the case where the particle moves perpendicular to the surface, an extra factor of 2 occurs in Eqs. (3) and (4). More general formulas describing damping of a dipole molecule and a charged particle were also derived in [4, 5]. No general formula has yet been derived for the damping force acting on a neutral atom moving perpendicular to the surface.

2. DAMPING FORCE ON THE MOVING NANOPROBE

We assume that the probe has the form of a paraboloid of revolution which is described by the canonical equation $z = d + (x^2 + y^2)/2R$, where z is measured from the surface of the sample, d is the minimum distance from the surface to the apex of the probe, and R is the probe's radius of curvature.

By using the Clausius–Mossotti equation, the atomic polarizability can be expressed in terms of the dielectric function $\varepsilon(\omega)$ of the material of the probe. Thus, we have

$$\alpha''(\omega) = \frac{3}{4\pi N}\mathrm{Im}\frac{\varepsilon(\omega) - 1}{\varepsilon(\omega) + 2}, \tag{5}$$

where N is the volume concentration of atoms. In what follows, the dielectric functions of the probe and the surface under investigation are labeled by indices 1 and 2, respectively. By substituting Eq. (5) into Eq. (1) and integrating over the probe's volume, the resultant lateral damping force can be found to be

$$F = -\frac{3}{64\pi}\frac{\hbar RV}{d^3}J(\varepsilon_1(\omega), \varepsilon_2(\omega)), \tag{6}$$

where $J(\varepsilon_1(w), \varepsilon_2(\omega))$ is the overlap integral of the spectra. The structure of this integral is identical to that of the integrand in Eq. (1), in which the imaginary part of the polarizability is replaced by the imaginary part of the quotient in Eq. (5) [4]. When deriving Eq. (6), it was also taken into account that, in the typical case, the AFM nanoprobe has a large aspect ratio (of height to radius of curvature) and, therefore, the upper limit of integration over the height of the probe can be extended to infinity. At $T = 0$, the numerical factor in Eq. (6) should be replaced by $3/32\pi$ and the integral $J(\varepsilon_1(\omega), \varepsilon_2(\omega))$ becomes identical to the integral in Eq. (2) with the substitution for the function $\alpha''(\omega)$ indicated above.

The dominating contribution to $J(\varepsilon_1(w), \varepsilon_2(\omega))$ comes from the frequency ranges where the absorption bands of the interacting solids strongly overlap. Therefore, the contributions from the different mechanisms operating in different spectral ranges should, in gen-

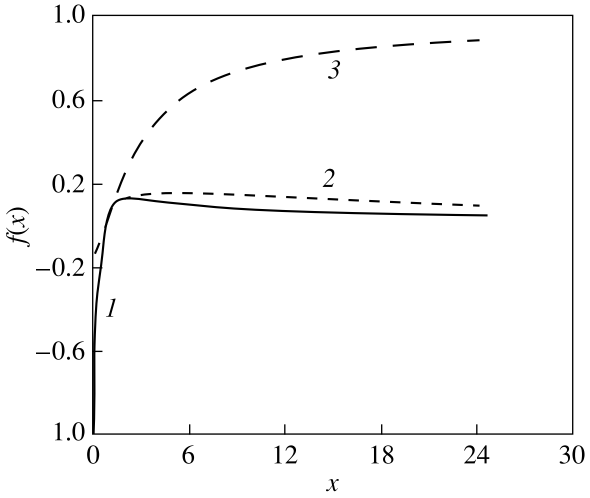

Fig. 1. Characteristic functions $f_1(x)$, $f_2(x)$, and $xf_1(x)$ (curves *1, 2, 3,* respectively). The ranges where these functions are negative correspond to nondissipative lateral forces.

eral, be taken into account. For uniform contacts, the functional $J(\varepsilon_1(\omega), \varepsilon_2(\omega))$ for some model dielectric functions was calculated numerically in our recent papers [4, 13]. However, analytical expressions for the friction forces are of prime interest. It turns out that closed expressions for these forces can be derived in the case where absorption in the low-frequency range of the electromagnetic spectra plays a dominant role.

First, we consider two conducting materials being in contact and represent the dielectric functions in the standard form:

$$\varepsilon_{1,2}(\omega) = 1 + i\frac{4\pi\sigma_{1,2}}{\omega}, \tag{7}$$

where $\sigma_{1,2}$ are the static conductivities. In order to take high-frequency spectral ranges into account, one should draw on formulas for the dynamical conductivities.

In the case of $\omega\hbar/2k_BT \ll 1$, where the temperature effects are significant, it is appropriate to use Eq. (1). By substituting Eqs. (5) and (7) into Eq. (1), the functional $J(\varepsilon_1(\omega), \varepsilon_2(\omega))$ can be represented in the form

$$\begin{aligned} J_1(a, b) = \int_0^\infty \frac{dx}{x}\Bigg\{ & 2\left[f_1(x)\frac{df_2(x)}{dx} - f_2(x)\frac{df_1(x)}{dx}\right] \\ & + x\left[f_1(x)\frac{d^2f_2(x)}{dx^2} - f_2(x)\frac{d^2f_1(x)}{dx^2}\right]\Bigg\}, \end{aligned} \tag{8}$$

where $f_1(x) = x/(x^2 + a^2)$ and $f_2(x) = x/(x^2 + b^2)$. All integrals in Eq. (8) are reduced to tabulated integrals, and, after complicated algebra, the function $J_1(a, b)$ is found to be

$$J_1(a, b) = \frac{\pi(b-a)}{ab(a+b)^2}. \tag{9}$$

At lower temperatures, where $\omega\hbar/2k_BT \gg 1$, Eq. (2) is more convenient to use, because the hyperbolic cotangent in Eq. (1) can be replaced by unity in this case. By substituting Eqs. (5) and (7) into Eq. (2) and performing integration, we obtain

$$\begin{aligned} J_2(a, b) &= \int_0^\infty dx \frac{x}{x^2 + a^2}\frac{d}{dx}\frac{x}{x^2 + b^2} \\ &= \frac{(a^2 + b^2)\ln(b/a) + (a^2 - b^2)}{(a^2 - b^2)^2}. \end{aligned} \tag{10}$$

With these results, the damping force is written as

$$F = -\frac{9}{128\pi}\frac{k_BTRV}{d^3\sigma_1}f_1(x), \quad T \gg T_0, \tag{11a}$$

$$F = -\frac{3}{32\pi}\frac{\hbar RV}{d^3}f_2(x), \quad T \ll T_0, \tag{11b}$$

$$T_0 = \frac{\pi\hbar}{k_B}\max(2\sigma_1/3, \sigma_2), \quad x = 3\sigma_2/2\sigma_1, \tag{11c}$$

$$f_1(x) = \frac{x-1}{(1+x)^2}, \tag{12}$$

$$f_2(x) = \frac{(1 - x^2 + (1 + x^2)\ln x)x}{(1 + x^2)^2}. \tag{13}$$

Estimations show that T_0 = 300 K for $\max\sigma_{1,2}$ = 1400 Ω^{-1} m^{-1}; therefore, for materials (such as germanium and silicon) showing weak conductivity, smaller than the value indicated above, the temperature effects are significant and the damping force is proportional to the temperature and given by Eq. (11a). For metals, the parameter T_0 is very large and Eq. (11b) is valid in actual practice. Its singularity at $2\sigma_2 = 3\sigma_1$ is a seeming one; analysis shows that in this limit, we have $F = 0$, which is also the case for Eq. (11a) at $T = 0$. Thus, damping vanishes when the critical condition $2\sigma_2 = 3\sigma_1$ is fulfilled. At $2\sigma_2 < 3\sigma_1$, the lateral force on the nanoprobe becomes accelerative, because the probe gains energy from surface plasmons. The functions $f_1(x)$, $f_2(x)$, and $xf_1(x)$ [see Eq. (17a)], in terms of which the damping forces are calculated, are plotted in Fig. 1 (curves *1, 2, 3*).

An important feature of Eqs. (11) is their symmetry relative to interchanging the probe and the surface at $\sigma_1 = \sigma_2$. In this case, at $T = 0$, the damping force is quite independent of the conductivities and equals $F = -0.002\hbar RV/d^3$, which has a value of 0.0003 pN for typical AFM parameters $R = 30$ nm, $d = 0.3$ nm, and $V = 1$ m/s. At room temperature, for silicon–silicon-like tribometric contacts, more frequently used in AFM experiments, the damping force is much larger. For example, for $d = 0.3$ nm, $V = 1$ m/s, $R = 30$ nm, $T = 300$ K, and $\sigma = 0.001\ \Omega^{-1}\ \mathrm{m}^{-1}$, Eq. (11b) gives $F = 1$ nN, which is comparable to the adhesive friction force in the close-contact regime. We note that velocities of 0.06–6 m/s are typical of the dynamical mode of the AFM operation at an oscillation frequency of 1 MHz with amplitudes 10–1000 nm. It is possible that such (and even higher) velocities should also take place for the close-contact mode of the AFM operation in the initial short-run stage of the probe sliding over the surface.

Investigations of the interaction between two insulating materials and between a metal and an insulator are also of practical importance. A surface force apparatus [14] is commonly used to investigate insulator–insulator (e.g., mica–mica) interactions. We will approximate the dielectric functions of insulators in the low-frequency range by the Debye model expression:

$$\varepsilon(\omega) = 1 + \frac{\varepsilon - 1}{1 - i\omega\tau}, \tag{14}$$

where ε is the static permittivity and τ is the relaxation time (for mica, $\tau = 10^{-10}$–10^{-9} s). The approximations in Eq. (14) and Eq. (7) lead to the same functional of the dielectric functions. With Eqs. (9), (10), and (14), the damping forces for different combinations of materials can be written in the following unified form:

(1) For the insulating probe and the insulator surface,

$$F = -\frac{9k_B TRV}{32d^3}\frac{\tau_1(\varepsilon_1 - 1)(\varepsilon_2 - 1)}{(\varepsilon_1 + 2)^2(\varepsilon_2 + 1)} f_1(x), \quad T \gg T_0, \tag{15a}$$

$$F = -\frac{3}{32\pi}\frac{\hbar RV}{d^3}\frac{(\varepsilon_1 - 1)(\varepsilon_2 - 1)}{(\varepsilon_1 + 2)(\varepsilon_2 + 1)} f_2(x), \quad T \ll T_0, \tag{15b}$$

$$\begin{gathered} T_0 = \frac{2\hbar}{k_B}\max((\varepsilon_1 + 2)/3\tau_1;\ (\varepsilon_2 + 1)/2\tau_2), \\ x = 3\tau_1(\varepsilon_2 + 1)/2\tau_2(\varepsilon_1 + 2); \end{gathered} \tag{15c}$$

(2) For the conducting probe and the insulator surface,

$$F = -\frac{9}{128\pi}\frac{k_B TRV}{d^3}\frac{(\varepsilon - 1)}{\sigma(\varepsilon + 1)} f_1(x), \quad T \gg T_0, \tag{16a}$$

$$F = -\frac{3}{32\pi}\frac{\hbar RV}{d^3}\frac{(\varepsilon - 1)}{(\varepsilon + 1)} f_2(x), \quad T \ll T_0, \tag{16b}$$

$$\begin{gathered} T_0 = \frac{2\hbar}{k_B}\max(4\pi\sigma/3,\ (\varepsilon + 1)/2\tau), \\ x = \frac{3(\varepsilon + 1)}{8\pi\sigma\tau}; \end{gathered} \tag{16c}$$

(3) For the insulating probe and the conductor surface,

$$F = -\frac{9}{64\pi}\frac{k_B TRV}{d^3}\frac{(\varepsilon - 1)}{(\varepsilon + 2)\sigma} f_1(x)x, \quad T \gg T_0, \tag{17a}$$

$$F = -\frac{3}{32\pi}\frac{\hbar RV}{d^3}\frac{(\varepsilon - 1)}{(\varepsilon + 2)} f_2(x), \quad T \ll T_0, \tag{17b}$$

$$T_0 = \frac{\hbar}{2k_B}\max\left(\frac{\varepsilon + 2}{3\tau}, 2\pi\sigma\right), \quad x = \frac{6\pi\sigma\tau}{\varepsilon + 2}. \tag{17c}$$

For silicon–mica contacts, we have $T_0 < 0.1$ K and, therefore, Eqs. (15a), (16a), and (17a) are valid under any typical experimental conditions. As seen from Fig. 1, the sign of the lateral force can be different, depending on the ratio between the conductivities, the ratio between the relaxation times, or the product $\sigma\tau$.

It should be stressed once again that the formulas derived in this paper determine only that part of the fluctuational electromagnetic force which is due to absorption in the low-frequency spectral range. Additional contributions can arise if the absorption bands overlap in other spectral ranges.

3. A COMPARISON WITH AFM DATA

It is of considerable interest to compare the theoretically calculated fluctuational dissipative forces with the available experimental AFM data. In [2], the dissipative forces were measured experimentally in the case where the AFM silicon probe moved along a normal to the surface of mica in a vacuum. The cantilever had stiffness $k = 40$ N/m and natural frequency $f = 300$ MHz, and the radius of curvature of the probe was $R = 20$ nm. For an amplitude of $A = 20$ nm, the energy loss per cycle was measured to be $\Delta W = 1$–10 eV, depending on the ratio d/A, where d is the initial spacing between the probe apex and the surface in the absence of oscillations. In this case, the quality factor of the oscillating probe $Q = \pi kA^2/\Delta W$ equals $(0.3$–$3.0) \times 10^5$. It is obvious that, for lateral oscillations of the probe at the same frequency and the same (fixed) spacing between the probe apex and the surface, equal to $h = d - A$, the energy loss rate is somewhat higher and the quality factor is lower.

By representing Eq. (16a) in the form $F = -\gamma RTV/h^3$, the theoretical quality factor associated with fluctuational forces is found to be $Q_t = kh^3/4\pi f\gamma RT$. For $\varepsilon = 6$, $\tau = 10^{-9}$ s, and $\sigma = 0.001\ \Omega^{-1}\ \mathrm{m}^{-1}$, we obtain from Eqs. (16a)–(16c) that $\gamma \approx 0.019k_B\tau$. For the same values of the probe parameters and $h = 0.3$ nm, the quality factor is equal to $Q_t = 5.3 \times 10^7/T$. Therefore, at temperatures 100–300 K, Q_t is of the same order of magnitude as the experimental values [2].

It should be noted that, in the case considered above, Q_t virtually does not depend on the conductivity of the probe, but decreases in inverse proportion to increasing relaxation time of the dielectric. On the whole, we have

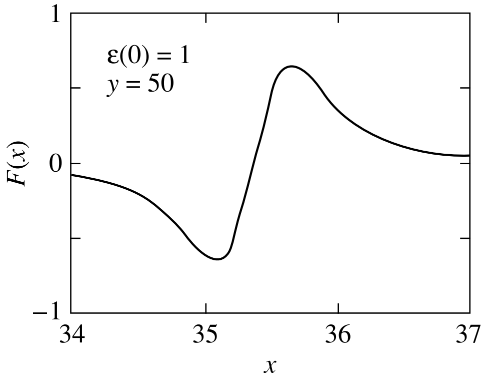

Fig. 2. Function $F(x)$ given by Eq. (21) ($x_i \equiv x$).

$Q_t \propto kh^3/f\tau RT$ in this case; this permits verification of the predictions of the theory, which enables one to measure fluctuational electromagnetic forces. As has already been noted above, a surprising prediction of the theory is that the lateral damping force acting on the probe can vanish and even become positive (Fig. 1). In the case of the silicon–mica contact, the damping force vanishes at $\sigma = 3(\varepsilon + 1)/8\pi\tau$; therefore, for a fixed value of τ, this condition can easily be satisfied by choosing the appropriate doped material for the probe.

In the experiment under discussion, the energy loss can be associated not only with fluctuational dissipative forces, but also with the breaking of adhesion bonds, although the latter mechanism is more typical of the close-contact mode of the AFM operation [1]. However, the damping force due to the breaking of adhesion bonds is independent of the velocity and electrophysical properties and is likely to depend on the temperature only slightly [13]. These specific features can help in the separation of the corresponding contributions to the damping force.

4. FLUCTUATIONAL DISSIPATIVE FORCES AND QUARTZ-MICROBALANCE MEASUREMENTS

Fluctuational dissipative forces can also be determined from crystalline-quartz microbalance experiments [6, 7], in which one measures the oscillation damping of quartz oscillators (metal-coated quartz plates). The presence of a film of adsorbed inert gases on the surface of the plate causes a change in the Q factor of the oscillator and allows one to estimate the characteristic decay time of the translational motion of adsorbed atoms. In the case of krypton on the surface of gold, this time is about 1 ns.

Let us estimate the decay time due to fluctuational electromagnetic forces from Eq. (2). The imaginary part of the atomic polarizability can be written in the most general case as (e and m are the charge and mass of an electron, respectively)

$$\alpha''(\omega) = \frac{e^2}{m}\sum_i \frac{f_i\gamma_i\omega}{(\omega_i^2 - \omega^2)^2 + \gamma_i^2\omega^2}, \tag{18}$$

where the sum is over all electron transitions from the ground state (0) of the atom to the excited states (i) of the discrete spectrum and ω_i, γ_i, and f_i are the transition frequency, linewidth, and oscillator strength, respectively. The high-frequency dielectric function of the metal or semiconductor coating of the plate can be written in the standard Drude approximation as ($\varepsilon = 1$ for the metal coating)

$$\varepsilon(\omega) = \varepsilon - \frac{(\omega_p\tau)^2}{1 + (\omega\tau)^2} + \frac{i(\omega_p\tau)^2}{\omega\tau(1 + (\omega\tau)^2)}, \tag{19}$$

where ω_p is the plasma frequency and τ is the relaxation time for electrons.

By substituting Eqs. (18) and (19) into Eq. (2) and going to the limit $\gamma_i \longrightarrow 0$, we obtain

$$F = \frac{3\hbar e^2\tau^2 V}{4mz^5}\Phi(a, y), \tag{20}$$

$$\begin{aligned}\Phi(a, y) &= \sum_i \frac{f_i y^2(3a^2x_i^4 - 2ax_i^2y^2 + a^2x_i^2 - y^4)}{x_i(a^2x_i^4 - 2ax_i^2y^2 + a^2x_i^2 + y^4)^2} \\ &= \sum_i F_i(a, y, x_i) f_i y^2,\end{aligned} \tag{21}$$

where $a = \varepsilon + 1$, $x_i = \omega_i\tau$, and $y = \omega_p\tau$.

Analysis shows that the terms in the sum in Eq. (21) can have any sign. For metals, we have $y \gg 1$ and the $F_i(a, y, x_i)$ vanish at $\sqrt{2}\,w_i \approx w_p$ for fixed values of x_i. The contributions from the transition frequencies $w_i \geq w_p/\sqrt{2}$ correspond to an accelerative force; the other frequencies contribute to the damping force. In order to compute the function $\Phi(a, y)$, the specific distribution of oscillator strengths should be given.

Figure 2 shows the dependence of $F_i(a, y, x_i)$ on x_i for the parameter values typical of gold: $\omega_p = 8.8$ eV, $\tau = 3.7 \times 10^{-15}$ s, $a = 2$, $y = 50.2$, and $f_i \equiv 1$. It is seen from Fig. 2 that $F_i(a, y, x_i)$ has no singularities, because $x_i > 0$; however, this function exhibits a characteristic nonmonotonic change in the narrow spectral range around $x_i \approx y/\sqrt{2}$, and, therefore, the dominant contribution to $\tilde{\Phi}(a, y)$ comes from these transition frequencies. By putting $f_i \approx 0.1$ and $df/dx \propto x^{-3.5}$ (which adequately describes the optical and UV ranges of the spectrum) and converting the sum in Eq. (21) to an integral, we arrive at the function $\tilde{\Phi}(a, y)$ plotted in Fig. 3. It is seen that, where the lateral force is negative,

$\tilde{\Phi}(a, y) < 0$, which corresponds to the case of usual damping.

For the surface of gold, we have $\tilde{\Phi}(2, 50.2) = -0.093$. Using this result and Eq. (20), for the case of a Kr atom adsorbed at a distance of 0.4 nm from the surface, we obtain the decay time $\Delta t = MV/F \approx 0.6$ ns (M is the mass of a Kr atom), which is close to the experimental value. It should be noted, however, that the value of Δt is very sensitive to variations in τ, ω_p, and z, as is seen from Eqs. (20) and (21) and Fig. 3.

If adsorbed atoms form a film, an additional contribution to the damping force can arise because of absorption in the low-frequency spectral range. Another factor leading to an increase in the damping force can be the appearance of localized dipole moments and electric charges on adsorbed atoms. The corresponding damping forces are given by Eqs. (3) and (4), and these are fairly small in the case of good conductors, such as gold. For example, for $Z_1 = 1$, the dipole moment $d = 1$D and $z = 0.4$ nm, the damping forces are 4–5 orders of magnitude smaller than those given by Eq. (20) and can be ignored. A completely different type of situation can occur for the surface of graphite and silicon.

5. THE INTERACTION BETWEEN PLANE SURFACES

The fluctuational dissipative forces per unit area of the interacting surfaces were recently calculated [8–10] using the Maxwell stress tensor for the case where two parallel thick plates divided by a gap of width d move relative to each other. An extended discussion of those calculations is beyond the scope of this paper. However, it should be noted that there is a fundamental discrepancy concerning the finite damping force proportional to the velocity at $T = 0$; in contrast to our paper, this force is missing from the results of the papers mentioned.

It is our opinion that the electric field in the gap was calculated incorrectly in [8–10]. For example, Pendry [8] used a heuristic expression for the field amplitude, which allows for the inherent fluctuating field of one of the plates and the field of the wave reflected from the other plate, with the Fresnel reflection coefficient including the Doppler shift due to the relative motion of the surfaces. Volokitin and Persson [9, 10] used a more general method, but their dynamical generalization of formulas of the Lifshitz fluctuation theory for the electromagnetic field amplitude is not evident and, furthermore, a number of additional approximations were made when passing over from the original relativistic theory to the nonrelativistic case. The expressions derived in [9, 10] for the damping force at $T = 0$ are identical to those obtained by Pendry; however, at $T \neq 0$, the contribution to the damping force proportional to the velocity is quadratic in T.

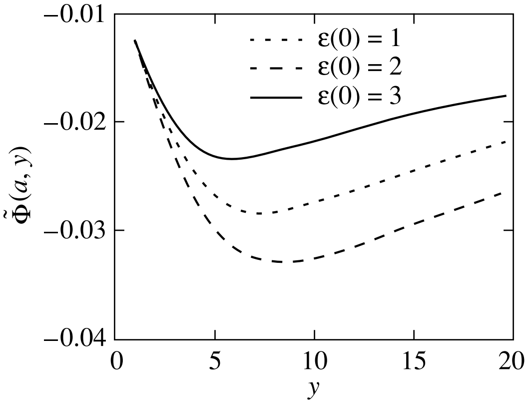

Fig. 3. Function $\tilde{\Phi}(a, y)$.

In order to go to the case of two interacting plates in our formulas for the damping force exerted on the convex probe by the plane surface, it is sufficient, rather than to integrate over the probe volume, to integrate Eq. (1) or Eq. (2) over h (from zero to infinity) and divide the result by the area S of the surface of the plate. Then, e.g., instead of Eq. (6), one obtains

$$\frac{F}{S} = -\frac{9\hbar V}{128\pi^2 d^4} J(\varepsilon_1(\omega), \varepsilon_2(\omega)). \qquad (22)$$

The friction stress F/S for different combinations of materials is obtained by multiplying the right-hand sides of Eqs. (11) and (15)–(17) by a factor of $3/2\pi Rd$. Thus, in the case under discussion, the dependence on the gap width follows a power law with an exponent (in the denominator) larger by unity than that in the case of an interaction between the parabolic probe and the plane surface.

We note that a formula little different from Eq. (22) is derived from an intermediate result obtained by Pendry (Eq. (18) in [8] in the low-velocity limit). In comparison with Eq. (22), this formula has an extra factor 4/9 and, in the spectrum-overlap integral analogous to the integral in Eq. (2), $\alpha''(\omega)$ is replaced by $\mathrm{Im}[(\varepsilon_1(\omega) - 1)/(\varepsilon_1(\omega) + 1)]$. It is clear that the factor 4/9 appears because the contribution from the other plate is not taken into account. However, the original expression is not symmetric under the permutation of indices $1 \longleftrightarrow 2$ and its formal symmetrization, performed in [8], resulted in a final symmetric expression in which the contributions to the damping force linear in velocity canceled each other out. Furthermore, even without symmetrization, the damping force also becomes zero for plates of the same type, in contrast to Eq. (22). This shows once again that the approximation made in [8] suffers from shortcomings. For the purposes of this paper, however, the most important point is that although the results obtained in [8–10] are based on the continuum model and do not involve the assumption that the interactions are additive, these results lead to the same dependence of the damping force on the distance d as that in Eq. (22).

In actual practice, the calculations of the fluctuational forces acting between plane surfaces are of importance in surface-force apparatus experiments [14], in which one measures the friction forces between mica plates covered with surfactants.

6. CONCLUSIONS

Thus, the theoretical model proposed in [4, 5] for calculating nonrelativistic dynamical fluctuational dissipative forces is developed further. We derived closed analytical formulas for the damping forces acting between a parabolic nanoprobe and a plane surface, between a neutral spherical atom and a conducting surface, and between parallel thick plates divided by a gap. The metal–metal, insulator–insulator, metal–insulator, and insulator–metal contacts are considered. The formulas derived allow for absorption of electromagnetic waves in the low-frequency spectral range and predict characteristic dependences of the damping forces upon velocity, temperature, distance, nanoprobe radius, and electrical characteristics of interacting solids. In particular, it is predicted that, in all cases considered in this paper, the damping force proportional to the velocity does not vanish at zero temperature. The conditions for nondissipative slide of surfaces are discussed.

The Q factor of oscillators is estimated for the modulation mode of the AFM operation, and a comparison with the experimental data is made for the case of a silicon nanoprobe interacting with mica. The calculated and experimental fluctuational electromagnetic forces are shown to be of the same order of magnitude (0.001–1 nN), so that their AFM measurement is feasible.

It is also shown that the damping time for moving adatoms measured in quartz microbalance experiments can be associated with fluctuational electromagnetic forces.

REFERENCES

1. G. V. Dedkov, Usp. Fiz. Nauk **170** (6), 585 (2000); Phys. Status Solidi A **179** (1), 2 (2000).
2. B. Gotsmann, C. Seidel, B. Anczykowski, and H. Fuchs, Phys. Rev. B **60** (15), 11051 (1999).
3. I. Dorofeyev, H. Fuchs, G. Wenning, and B. Gotsmann, Phys. Rev. Lett. **83** (12), 2402 (1999).
4. G. V. Dedkov and A. A. Kyasov, Phys. Lett. A **259**, 38 (1999); Pis’ma Zh. Tekh. Fiz. **25** (12), 10 (1999) [Tech. Phys. Lett. **25**, 466 (1999)].
5. G. V. Dedkov and A. A. Kyasov, Fiz. Tverd. Tela (St. Petersburg) **43** (1), 169 (2001) [Phys. Solid State **43**, 176 (2001)]; Surf. Sci. (2000).
6. E. T. Watts, J. Krim, and A. Widom, Phys. Rev. B **41** (6), 3466 (1990).
7. J. Krim, D. H. Solina, and R. Chiarello, Phys. Rev. Lett. **66** (2), 181 (1991).
8. J. B. Pendry, J. Phys. C **9** (8), 10301 (1997).
9. A. I. Volokitin and B. N. J. Persson, Phys. Low-Dimens. Semicond. Struct. **7** (8), 1 (1998).
10. A. I. Volokitin and B. N. J. Persson, J. Phys.: Condens. Matter **11** (2), 345 (1999).
11. P. Johansson and P. Apell, Phys. Rev. B **56** (7), 4159 (1997).
12. Yu. N. Moiseev, V. M. Mostepanenko, and V. I. Panov, Phys. Lett. A **132** (6–7), 354 (1988).
13. G. V. Dedkov, Mater. Lett. **38** (5), 360 (1999); Wear **232** (2), 145 (1999).
14. J. N. Israelachvili, *Intermolecular and Surface Forces* (Academic, New York, 1992).

Translated by Yu. Epifanov

Physics of the Solid State, Vol. 43, No. 3, 2001, pp. 563–568. Translated from Fizika Tverdogo Tela, Vol. 43, No. 3, 2001, pp. 543–548.
Original Russian Text Copyright © 2001 by Avignon, Men'shov, Tugushev.

LOW-DIMENSIONAL SYSTEMS AND SURFACE PHYSICS

Triangular Lattices of Charge- and Spin-Density Waves in Chemisorbed Metal Monolayers on the Surface of Diamond Structure Semiconductors

M. Avignon[1], V. N. Men'shov[2], and V. V. Tugushev[1, 2]
[1]*LEPES CNRS, 25. Av. Martyrs BP166, Grenoble, France*
[2]*Russian Research Centre Kurchatov Institute, pl. Kurchatova 1, Moscow, 107207 Russia*
e-mail: sasha@mail.mics.msu.su

Received June 26, 2000

Abstract—The electronic spectrum of a planar triangular lattice is analyzed, and the possible occurrence of charge (CDWs) and spin density waves (SDWs) in the lattice is discussed. Commensurate CDW and SDW structures of two types are considered in the weak and strong electron–electron interaction approximations. The CDW and SDW models are applied to the specific case of chemisorbed metal monolayers on the (111) surface of diamond structure semiconductors with a coverage close to 1/3. *© 2001 MAIK "Nauka/Interperiodica".*

INTRODUCTION

The ordered structures and phase transitions in monolayers of metals chemisorbed on the surface of diamond structure semiconductors (primarily Si and Ge) have been studied intensively for several decades (see, e.g., [1]). In this paper, however, we do not pursue the goal of giving even a brief overview of all aspects of this field of surface physics.

We discuss only a narrow range of objects which have recently attracted attention; these are monolayers of some nontransition metals on (111)-type surfaces of diamond-like semiconductors (Si, Ge) with a coverage close to 1/3. Furthermore, we restrict our consideration to reconstructed monolayers of the $\sqrt{3} \times \sqrt{3}$ type in the form of a planar triangular lattice [2]. The question concerning the genesis of such monolayers and the reason for their stability has been repeatedly discussed in the literature (see, e.g., [3]), but a decisive answer to this question has not yet been given. In what follows, a $(\sqrt{3} \times \sqrt{3})$-type monolayer is assumed to exist without specifying the mechanism of the (111)-surface reconstruction which leads to its formation. Among the systems of this type are monolayers of group-III (Al, Ga, In)/Si(111), group-IV (Pb, Sn)/Ge(111), and group-V metals [Sb/Si(111), Bi/Ge(111)], as well as more complex K/Si(111) : B monolayers (see numerous references in [1, 2]).

As for the electronic structure, all the systems indicated above have a fairly narrow surface energy band (of width $W \sim 0.2$–0.5 eV), which is associated with the hybridized orbitals of the metal monolayer and the uppermost atomic layer of the semiconductor.

The surface unit cell consists of a metal atom and three symmetrically arranged atoms of the semiconductor [3]. The filling of the narrow energy band (without regard for charge transfer between the bulk of the semiconductor and its surface) is determined by the redistribution of the electronic density between the sp^3 orbitals of Si or Ge in the uppermost atomic layer and the p (or s) orbitals of the chemisorbed metal. It is easy to verify that, in the pure "chemical" approximation, this redistribution formally results in a half-filled narrow surface band in the case of group-IV metals (Pb, Sn) on the (111) surface of Ge and Si and in the case of a group-I metal (K) on the Si(111) : B surface. In the case of metals of groups III and VI, the narrow surface band is empty and full, respectively. In principle, by varying the composition of the monolayer with the coverage remaining equal to 1/3, the filling of the narrow surface band can be varied over a very wide range without disintegration of the $\sqrt{3} \times \sqrt{3}$ structure and the triangular surface lattice.

The effects of electron correlations in the systems under discussion were accepted to be important after publication [4], in which the photoemission spectra of the K/Si(111) $(\sqrt{3} \times \sqrt{3})$: B structure were studied. Even the simplest estimations show that the effective electron–electron interaction (on-site Coulomb repulsion in the Hubbard model) is of the order of $U \approx 1$–2 eV for the electrons of the surface energy band and, therefore, $U/W \geq 1$. It has been proposed that, everywhere over the temperature range studied, the structure considered in [4] is a Mott insulator and, perhaps, an antiferromagnet, although possible magnetic ordering in it has not yet been investigated. Only quite recently [5] have calculations of the surface electron spectrum been performed for the system treated in [4], and, on the

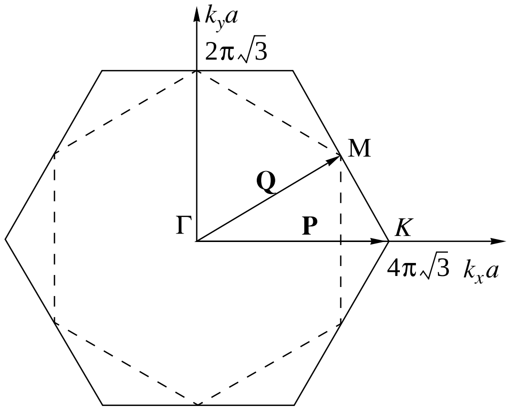

Fig. 1. Brillouin zone of a triangular surface lattice.

whole, the preliminary estimates of the correlation effects have been substantiated.

At the same time, the properties of another group of the structures under discussion, namely, of Pb and Sn monolayers on Ge(111) ($\sqrt{3} \times \sqrt{3}$), are quite different from those exhibited by the K/Si(111) ($\sqrt{3} \times \sqrt{3}$) : B isoelectronic structure mentioned above. It is Pb and Sn monolayers on Ge that undergo a structural transition from the higher-temperature metallic ($\sqrt{3} \times \sqrt{3}$) phase to a lower-temperature reconstructed (3×3) phase with a narrow band gap (Sn/Ge) or a pseudogap (Pb/Ge) (see, e.g., [6, 7] and the references to earlier papers in [2]). The mechanism of this structural transition and the influence of electron correlations on it are debatable at the present time.

The idea that the effect of the electron–electron interaction on the surface energy bands plays an important role in the charge and magnetic ordering of the surface of diamond-like semiconductors has long been considered. It is this interaction that is responsible for the formation of the antiferromagnetic structure in the Pendy quasi-one-dimensional chains on atomically clear (111) (2×1) surfaces of silicon and diamond [6]. Along with chemical dimerization, this interaction also determines the width of the insulating band gap in the spectrum of electronic surface states, as well as the features of chemisorption of some gases and metals in the case of small coverages (see, e.g., [7]) in the systems indicated above.

In this paper, we propose a simple model which qualitatively describes, in a unified way, all available results concerning the charge and spin ordering in monolayers of the $\sqrt{3} \times \sqrt{3}$ type on the (111) surface of silicon and germanium. This model involves the widely known and well-accepted concepts of charge (CDWs) and spin density waves (SDWs), which are successfully used to qualitatively describe electronic phase transitions in a wide range of systems [8]. We analyze different cases in the weak- ($U \ll W$) and strong-interaction ($U \gg W$) limits; only in these limits can the theoretical methods for calculating the electron correlation effects be more or less justified. In the former limit, the model Hamiltonian of interacting fermions in the self-consistent field approximation is used, while in the latter, the effective Hamiltonian of pseudofermions is written in this approximation. On the whole, the results obtained using both approaches correlate well, so that one might expect our conclusions to be also qualitatively valid in the actual case of $U \geq W$.

1. THE ONE-PARTICLE EXCITATION SPECTRUM OF A TRIANGLE LATTICE

Let us consider a system of interacting particles on a triangle lattice with interatomic spacing a. In the simplest tight-binding approximation with only nearest neighbor hopping of electrons, the spectrum of one-particle excitations has the form

$$\varepsilon(\mathbf{k}) = 2t[\cos k_xa + 2\cos(k_xa/2)\cos(\sqrt{3}k_ya/2)], \quad (1)$$

where $t > 0$ is the hopping integral (this sign of the integral corresponds to the case of triangular surface lattices of chemisorbed metals on the (111) surface of semiconductors; see, e.g., recent band spectrum calculations in [5]). The Brillouin zone (Fig. 1) is characterized by two reciprocal lattice vectors:

$$\mathbf{K}_1 = (4\pi/\sqrt{3}a)\mathbf{e}_y, \quad \mathbf{K}_2 = (4\pi/a)(\mathbf{e}_x - \mathbf{e}_y/\sqrt{3}), \quad (2)$$

where $\mathbf{e}_x$ and $\mathbf{e}_y$ are unit vectors. This zone is of the shape of a regular hexagon, and its area is $S_0 = 8\pi^2/(\sqrt{3}\,a^2)$. At $t > 0$, the energy $\varepsilon(\mathbf{k})$ reaches its maximum at point Γ ($\varepsilon_{\max} = 6t$) and its minimum at point K ($\varepsilon_{\min} = -3t$), such that the full width of the allowed energy band is $W = 9t$. The density of states is highly nonuniform in this band and given by

$$N(\varepsilon) = A(\tilde{\varepsilon})/[2\pi^2 t(3 - 2\tilde{\varepsilon})^{1/4}], \quad \tilde{\varepsilon} = \varepsilon/2t, \quad (3)$$

where $A(\tilde{\varepsilon}) = K(k)$ for $k < 1$ and $A(\tilde{\varepsilon}) = k^{-1}K(k^{-1})$ for $k > 1$; $K(k)$ is a complete elliptic integral of the first kind, with its modulus being

$$k = 1/2\sqrt{[2 + (3 - \tilde{\varepsilon}^2)/\sqrt{(3 + 2\tilde{\varepsilon})}]}. \quad (4)$$

We note that $0 \leq k < 1$ if $-1 < \tilde{\varepsilon} \leq 3$ and $k > 1$ if $-3/2 \leq \tilde{\varepsilon} < -1$. It is easy to verify that the density of states in Eq. (3) tends to infinity as $\varepsilon \longrightarrow -2t$ ($\tilde{\varepsilon} \longrightarrow 1$, $k \longrightarrow 1$) and, in the logarithmic approximation, the density of states has a singularity of the van Hove type

$$N(\varepsilon) \approx (3\nu/(4\pi^2 t))\ln(4/|1 + \tilde{\varepsilon}|), \quad (5)$$

where $\nu = 1$ for $\tilde{\varepsilon} > -1$ and $\nu = 2$ for $\tilde{\varepsilon} < -1$. Therefore, the constant-energy "surface" with $\varepsilon_0 = -2t$ is of special interest. Suppose that the Fermi level μ precisely equals ε_0 ($\mu = -2t$). In this case, as can be seen from Eq. (1), the Fermi "surface" is of the shape of a hexagon, with its area being equal to $S = 6\pi^2/(\sqrt{3}\,a^2)$, and the occupation number of electronic states (including the spin factor) is $n_0 = 2[(S_0 - A)/S_0] = 1/2$, i.e., one-half electron per atom. We also note that there are three pairs of segments of the Fermi "surface" (sides of the hexagon) that coincide under translations by vectors $\mathbf{Q}_m$ ($m = 1, 2, 3$), respectively, where

$$\mathbf{Q}_1 = \mathbf{K}_1 + 1/2\mathbf{K}_2, \quad \mathbf{Q}_2 = 1/2\mathbf{K}_2 - 1/2\mathbf{K}_1, \quad \mathbf{Q}_3 = 1/2\mathbf{K}_1 - \mathbf{K}_2. \tag{6}$$

When reduced to the first Brillouin zone, the vectors $\{\mathbf{Q}_m\}$ connect points Γ and M in Fig. 1 (in what follows, we drop the index m and use $\mathbf{Q}$ to denote the ΓM vector in the first Brillouin zone). Note, by the way, that $\varepsilon(\mathbf{Q}) = -2t$ and, therefore, the line along which the singularity occurs in Eq. (5) is the line passing through saddle points of the M type.

Thus, the dominant contribution to the density of states in Eq. (5) comes from the regions around the sides of the hexagon whose vertices are at the M points and even a small shift of the Fermi level μ from the ε_0 level can lead to a noticeable change in the occupation number n relative to its value $n_0 = 1/2$. Assuming $|\delta\mu/W| \ll 1$ (recall that $W = 9t$), where $\delta\mu = \mu - \varepsilon_0$ is the chemical potential shift relative to ε_0, the $n(\delta\mu)$ dependence is found to be

$$n(\delta\nu) = n_0 + (27\nu/2\pi^2)(\delta\mu/W)\ln(8e/9|\delta\mu/W|), \tag{7}$$

where $\nu = 1$ for $\delta\mu > 0$ and $\nu = 2$ for $\delta\mu < 0$.

Even at $\delta\mu/W \approx 0.1$, the change $n(\delta\mu) - n_0$, according to Eq. (7), is equal to $\delta n = n(\delta\mu) - n_0 \approx 0.5$; that is, n is close to half-filling. For this reason, in what follows, we assume that, even at the filling $n \approx 1$, the Fermi level lies near the peak of the density of states in Eq. (5). Band calculations show [2, 5] that this conclusion remains valid for a spectrum of a more complex form than that in Eq. (1), with allowance made for hopping not only between the nearest neighbors, but also between more distant ones. In fact, the latter hopping leads solely to a shift in the energy ε_0 towards higher values, i.e., towards the center of the Brillouin zone, which, in turn, leads to larger values of $n_0 > 1/2$. Therefore, the conclusion that the Fermi level lies near the peak of the density of states $N(\varepsilon)$ and that the states corresponding to the hexagon with its vertices located at the M points have a dominant role in the formation of this peak is fairly general for the systems under discussion and is not closely related to the approximation of $\varepsilon(\mathbf{k})$ by Eq. (1).

Now, let us consider another important characteristic, the one-particle response function $\chi^0(\mathbf{q})$, in terms of which the criterion for instability of the system with respect to the transition to an SDW or CDW state is formulated:

$$\chi^0(\mathbf{q}) = \int[(d\mathbf{k})/(2\pi^2)][(n_{\mathbf{k}} - n_{\mathbf{k}+\mathbf{q}})/(\varepsilon_{\mathbf{k}+\mathbf{q}} - \varepsilon_{\mathbf{k}})], \tag{8}$$

where integration is performed over the first Brillouin zone. For wave vectors close to $\mathbf{q} = \mathbf{Q}$ and $|\delta\mu/W| \ll 1$, an estimation of Eq. (8) with a logarithmic accuracy gives

$$\chi^0(\mathbf{Q}) \sim (1/W)\ln^2|\delta\mu/W|; \tag{9}$$

that is, $\chi^0(\mathbf{q})$ diverges at $\delta\mu = 0$ and $\mathbf{q} \longrightarrow \mathbf{Q}$. It is clear that this divergence is associated with the van Hove singularity of $N(\varepsilon)$ in Eq. (5) and a nesting of sections of the Fermi surface in Fig. 1 at $\delta\mu = 0$. It should be noted that the sharp peak in $\chi^0(\mathbf{q})$ near $\mathbf{q} = \mathbf{Q}$ persists when hopping between more distant neighbors is also taken into account and when the filling n is near unity (see [2]). This is not surprising, since the Fermi level is pinned to the peak of the density of states $N(\varepsilon)$, as indicated above. Therefore, the anomaly of $\chi^0(\mathbf{q})$ for $\mathbf{q} \longrightarrow \mathbf{Q}$ is not heavily dependent on the details of the spectrum $\varepsilon(\mathbf{k})$ and on the approximations made above.

2. THE FORMATION OF CHARGE AND SPIN DENSITY WAVES IN THE WEAK-INTERACTION LIMIT

Let us consider a model Hamiltonian for interacting particles on a triangle lattice:

$$H = \sum_{\mathbf{k},\alpha}\varepsilon(\mathbf{k})a^{+}_{\mathbf{k}\alpha}a_{k\alpha} + U\sum_i n_i\uparrow n_i\downarrow + 1/2V\sum_{i,j}n_i n_j, \tag{10}$$

where $\varepsilon(\mathbf{k})$ is the one-particle excitation spectrum given by Eq. (1), $\mathbf{k}$ is the two-dimensional quasi-momentum, α is the spin index, (i, j) are indices specifying the nearest neighbors on the triangular lattice, U is the on-site (Hubbard) repulsion potential, and V is the Coulomb interaction potential between the nearest neighbors. It is well known that, for a system described by Hamiltonian (10), the generalized criteria for the instability of the ground state with respect to the transitions to a CDW and an SDW state are given by

$$U_c(\mathbf{q})\chi^0(\mathbf{q}) \ge 1, \quad U_c(\mathbf{q}) = -V\sum_{\mathbf{n}}\exp(i\mathbf{qn}) - U, \qquad U_s(\mathbf{q})\chi^0(\mathbf{q}) \ge 1, \quad U_s(\mathbf{q}) = U, \tag{11}$$

respectively. In Eq. (11), summation is performed over the nearest neighbors. It is very important that U_s is independent of the wave vector $\mathbf{q}$, and, therefore, the type of the SDW structure is determined by the peak of $\chi^0(\mathbf{q})$ alone. At the same time, $U_c(\mathbf{q})$ depends heavily on $\mathbf{q}$ (and can even change its sign), and, therefore, the type of the CDW structure is not evident in advance. Indeed, it is easy to verify that $U_c(\mathbf{q})$ reaches its maximum at $\mathbf{q} = \mathbf{P}$ (the vector connecting points Γ and K in Fig. 1), while $\chi^0(\mathbf{q})$ becomes maximal at $\mathbf{q} = \mathbf{Q}$ (the ΓM vector).

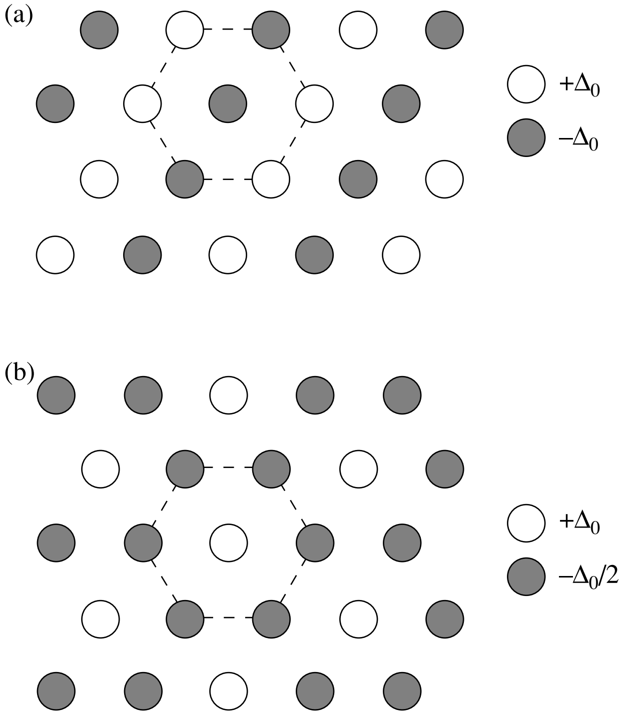

Fig. 2. CDW and SDW structures with wave vectors (a) **Q** and (b) **P**.

Thus, $U_c(\mathbf{P}) = 3V - U$ and $U_c(\mathbf{Q}) = 2V - U$, such that we always have $U_c(\mathbf{Q}) < U_c(\mathbf{P})$. The following cases can occur depending on the relationship between the potentials V and U: (i) at $3V - U < 0$, the transition to the CDW state is impossible; (ii) at $3V - U > 0$, but $2V - U < 0$, only the CDW state with wave vector **P** can arise; and (iii) at $3V - U > 0$ and $2V - U > 0$, the CDW states with wave vectors **P** and **Q** are in competition. In the last case, the result of competition depends on the band filling (i.e., on the value of $\delta\mu$). In the immediate vicinity of the filling value $n = n_0 = 1/2$, the logarithmic singularity of $\chi^0(\mathbf{Q})$ inevitably leads to the formation of the CDW structure with wave vector **Q**, but even for a small departure from n_0 (towards half-filling $n \approx 1$), the CDW structure with wave vector **P** can become more advantageous. In principle, the occurrence of an incommensurate CDW structure is also not ruled out.

In the case of SDWs, we have a much simpler situation. With all other factors being the same, the structure with wave vector **Q** is more advantageous because of the logarithmic singularity of $\chi^0(\mathbf{Q})$ at $n = n_0 = 1/2$. Since $\chi^0(\mathbf{Q})$ remains maximal even at half-filling ($n \approx 1$), as indicated above, it is completely unreasonable to believe that the type of the SDW structure will change.

The possible CDW and SDW structures discussed above are depicted in Fig. 2. We note that the CDW with wave vector **P** most likely corresponds to the experimentally observed 3×3 phase in (Pb, Sn)/Ge(111); the type of the SDW in K/Si(111) : B has not yet been identified.

The self-consistency equation for the order parameter Δ (which is single-component for the CDW and three-component for the SDW) can be relatively easily solved only in the case of ordering with wave vector **Q**. This equation has the form (here and henceforth, we consider only the case of zero temperature, $T = 0$)

$$\Delta = [\Delta U_{c,s}(\mathbf{Q})/\pi^2] \times \int_D \{(dxdy)/[(4t\cos x\cos y)^2 + \Delta^2]^{1/2}\}, \tag{12}$$

where $D(\mu)$ is the region of integration over occupied states in the Brillouin zone. At $\mu = \mu_0$ (the Fermi level is precisely even with the position of the peak of the density of states), a solution to Eq. (12) is given (with a logarithmic accuracy) by the expression

$$\Delta = \Delta_0 = 4t\exp[-4\pi\sqrt{t/U_{c,s}(\mathbf{Q})}]. \tag{13}$$

A detailed calculation of $\Delta(\mu)$ for $\mu \neq \mu_0$ can be performed only numerically; this is a separate problem which is beyond the purpose of this paper. In any case, Eq. (13) can be used as an upper estimate of the order parameter $\Delta(\mu) \leq \Delta_0$ for all types of ordering considered above, when qualitatively analyzing the one-particle spectrum of the rearranged phase.

Now, we discuss the effect of ordering with wave vector **Q** on the density of states $N(\varepsilon)$. This is affected significantly in the vicinity of the energy $\varepsilon = \varepsilon_0 = -2t$. For $|\varepsilon + 2t| > \Delta$, we have

$$N(\varepsilon) \sim (\Delta/t)(\ln t/\Delta)/[(\varepsilon + 2t)^2 - \Delta^2]^{1/2}, \tag{14}$$

while for $\Delta^2/t \ll |\varepsilon + 2t| < \Delta$, we have

$$N(\varepsilon) \sim [\Delta^2 - (\varepsilon + 2t)]^{-1/2}; \tag{15}$$

therefore, there is a square root singularity near the point $\varepsilon = \varepsilon_0$.

In the region $|\varepsilon + 2t| \sim \Delta^2/t \ll \Delta$, there is another, logarithmic, singularity,

$$N(\varepsilon) \sim (1/t)\ln(t/|\varepsilon + 2t|); \tag{16}$$

therefore, the spectrum of one-particle excitations is gapless (more precisely, it has a pseudogap) as before. In the case of ordering of the CDW type with wave vector **P**, the pseudogap 2Δ in the spectrum is even less pronounced than that in Eqs. (14)–(16) and the rearranged system is more likely to be a semimetal in nature. In this case, clearly, the order parameter Δ is described by an expression different from Eq. (13), but, unfortunately, analytical calculation of $\Delta(U_c(\mathbf{P}))$ is impossible.

However, our qualitative conclusion that the energy spectrum of a (3×3)-type CDW phase has a pseudogap (or no gap) does not require such a calculation.

3. THE FORMATION OF A SPIN DENSITY WAVE IN THE STRONG-INTERACTION LIMIT

In the preceding section, we considered the case where the interaction potentials U and V are not very large and the self-consistent field approximation as applied to the original Hamiltonian (10) is justified. It is also appropriate to analyze the other case where the Hubbard on-site repulsion U is large in comparison with the hopping integral t and the intersite repulsion V (i.e., $U \gg t, V$).

In this case, it is convenient to go from the Hamiltonian (10) to the so-called t–J model by introducing the Hubbard $X^i_{\alpha\beta}$ operators in the ordinary way [9]:

$$H_{tJ} = \sum_{\alpha,\, i \neq j} t X^i_{\alpha 0} X^j_{0\alpha} + \sum_{i \neq j} [J\mathbf{S}_i\mathbf{S}_j + (\tilde{V}/2) n_i n_j], \quad (17)$$

where $J = 4t^2/U$, $\tilde{V} = V - 2t^2/U$, $X^i_{\alpha 0}$ is the Hubbard operator for a particle excitation at a site, and $\mathbf{S}_i$ is the spin operator. By going from the Hubbard operators to the auxiliary pseudofermion ($f_{i\alpha}$) and pseudoboson operators (β_i) in the simplest representation ($X^i_{\alpha 0} \longrightarrow f^+_{i\alpha}\beta_i$, $X^i_{\alpha\alpha} \longrightarrow f^+_{i\alpha} f_{i\alpha}$) and treating the pseudoboson operators as c numbers in the saddle-point approximation, we write the effective Hamiltonian in the form

$$H_{\mathrm{eff}} = \sum_{\alpha,\, i \neq j} \tilde{t}_{ij} f^+_{i\alpha} f_{j\alpha} + \sum_{i \neq j} [J\mathbf{S}_i\mathbf{S}_j + (\tilde{V}/2) n_i n_j] - \sum_{i\alpha} \lambda_i f^+_{i\alpha} f_{i\alpha}, \quad (18)$$

where λ_i is the Lagrange multiplier ensuring the conservation of the total number of quasiparticles at a site ($n_i + \beta^+_i\beta_i = 1$), $\mathbf{S}_i = \sum_{\alpha\beta} f^+_{i\alpha}\sigma_{\alpha\beta} f_{i\beta}$, and $n_i = \sum_\alpha f^+_{i\alpha} f_{i\alpha}$. The chemical potential μ is included in the field component λ_0, which is independent of the site index and can be thought of as the chemical potential of pseudofermions ($\lambda_0 = \mu$) in the system without CDWs. The effective hopping integral is $\tilde{t}_{ij} = t\sqrt{(1-n_i)(1-n_j)}$, where n_i and n_j are the average pseudofermion occupation numbers for sites (i, j); in the absence of charge modulation, we have $n_i = n_j = n$ and $\tilde{t}_{ij} = t(1-n)$.

Let us consider the possible formation of a commensurate antiferromagnetic structure in the system with Hamiltonian (18) in the case where there is no charge density redistribution. Earlier, an analogous phenomenon was considered [10] for a one-dimensional chain, which models, in some approximations, the Pendy chain on the (2 × 1) (111)Si surface. In the parameter range where $\tilde{t} = t(1-n) \gg J$ (recall that, for the model with Hamiltonian (18), by definition, we have $J \ll t$, because $t/U \ll 1$), the mean field approximation with respect to the spin density $\mathbf{S}_i$ is justified. By separating the components $\mathbf{S}_\mathbf{q}$ and introducing the order parameter $\Delta_\mathbf{q} = -J_\mathbf{q}\langle\mathbf{S}_\mathbf{q}\rangle$, we arrive at the standard Hamiltonian for a system with an SDW and a fixed chemical potential of pseudofermions μ:

$$H_{\mathrm{eff}} = \sum_{\alpha,\, k} \varepsilon(\mathbf{k}) f^+_{\mathbf{k}\alpha} f_{\mathbf{k}\alpha} - \sum_{\alpha,\,\beta,\, q} [(\Delta_\mathbf{q}\sigma)_{\alpha\beta} f^+_{\mathbf{k}\beta} f_{\mathbf{k}-\mathbf{q}\alpha} + \mathrm{c.c.}] - \sum_\mathbf{q} (|\Delta_\mathbf{q}|^2)/J_\mathbf{q} - \tilde{\mu}\sum_{\alpha,\,\mathbf{k}} \lambda_i f^+_{k\alpha} f_{\mathbf{k}\alpha}, \quad (19)$$

where $\varepsilon(\mathbf{k})$ is the spectrum given by Eq. (1) for a triangle lattice in which the replacement $t \longrightarrow \tilde{t}$ is made.

The effective potential $\tilde{U}_s(\mathbf{q}) = j_\mathbf{q} = -(J/2)\sum_\mathbf{n} \exp(i\mathbf{qn})$ is responsible for the formation of SDWs in the system with Hamiltonian (19); this potential depends on the quasi-momentum $\mathbf{q}$, which essentially distinguishes it from the corresponding potential in the system with Hamiltonian (10) [see Eq. (11)]. The potential $\tilde{U}_s(\mathbf{q})$ reaches its maximum at $\mathbf{q} = \mathbf{P}$, with $\tilde{U}_s(\mathbf{P}) = (3/2)J$, while $\tilde{U}_s(\mathbf{Q}) = J$.

At the same time, according to the Stoner criterion, the paramagnetic state is unstable with respect to the formation of both an SDW with wave vector $\mathbf{Q}$ (when the average filling n is close to 1/2) and an SDW with wave vector $\mathbf{P}$ (when n is not close to 1/2). In both cases ($\mathbf{q} = \mathbf{Q}, \mathbf{P}$), however, we have $U_s(\mathbf{q}) > 0$, and, therefore, the two types of SDWs are in competition, as is the case with the two types of CDWs in the systems with weak interaction (see the preceding section).

We note that, since the average occupation numbers of the fermion (in the original Hamiltonian) and pseudofermion states are equal, the quantity n has the same physical meaning as in the previous sections. However, the physical meaning of $\tilde{\mu}$ becomes quite different; it is the chemical potential of pseudofermions, which is merely a convenient parameter, quite different from the real Fermi level of the primary quasiparticles. Nonetheless, all formulas in Section 1 that relate $\tilde{\mu}$ to n remain valid after the replacement of $t \longrightarrow \tilde{t}$ and $\mu \longrightarrow \tilde{\mu}$ and can be immediately used to analyze the spectrum and density of states of pseudofermions on the triangle lattice. Similarly, after the replacement $U_s(\mathbf{q}) \longrightarrow \tilde{U}_s(\mathbf{q})$, one can use the formulas from Section 2 for the order parameter Δ that characterizes long-range antiferromagnetic ordering in the system with Hamiltonian (18). For example, when ordering with wave vector $\mathbf{q} = \mathbf{Q}$

occurs and the energy band of pseudofermions is a quarter full ($n = n_0 = 1/2$), we have

$$\begin{aligned}\Delta = \Delta_0 &= 4t\exp[-4\pi\sqrt{\tilde{t}/U_s(\mathbf{Q})}] \\ &= 2t\exp[-\pi\sqrt{2U/t}],\end{aligned} \qquad (20)$$

so that $\tilde{\Delta}_0 \ll \tilde{t}$ because of the exponentially small factor in Eq. (20) for $U \gg t$. It should be stressed that the criterion $\tilde{t} \gg J$, which is used when deriving the effective Hamiltonian (19), is not met in the immediate vicinity of half-filling ($n \longrightarrow 1$) and the general Hamiltonian (18) of the t–J model should be used in this case. In the limiting case of $n = 1$, Eq. (18) is equivalent to the Heisenberg Hamiltonian with exchange integral J for a system of local spins $S = 1/2$ on a triangle lattice [11], which cannot be adequately described in terms of the concept of the SDW.

It should be emphasized that the order parameter Δ in the model with Hamiltonian (19) does not have the physical meaning of the maximum amplitude of the spin density at lattice sites; rather, it is the slowly varying envelope of the density of the local spins $\mathbf{S}(\mathbf{r})$ averaged over fast quantum fluctuations. In the limit $U \gg t$, the real spin density is strongly localized on sites ($S = 1/2$), whereas the average static spin density is $\langle\mathbf{S}\rangle = \Delta/\tilde{U}_s \ll 1/2$ for $J \ll \tilde{t}$ and, therefore, the description in terms of SDWs is valid for the system of band pseudofermions. These, of course, have no immediate physical meaning and are nothing more than a graphic description of the mathematical treatment of the system with Hamiltonian (18).

4. CONCLUSION

Thus, we performed qualitative analysis of the electronic spectrum of a planar triangular lattice and of the possible formation of charge and spin density waves in it. By using the tight-binding approximation with only nearest neighbor hopping of electrons, the density of states is shown to have a logarithmically divergent peak (van Hove singularity) at the energy corresponding to the quarter-filled electron energy band ($n = 1/2$). Even when the electron band is half full ($n = 1$), the criterion for instability of the system with respect to the formation of a CDW or an SDW can easily be met, because the Fermi level is pinned. In this case, two possible commensurate structures, with wave vectors $\mathbf{Q} = (\pi/a)[\mathbf{e}_x + (1/\sqrt{3})\mathbf{e}_y]$ and $\mathbf{P} = (4\pi/3)\mathbf{e}_x$ in the first Brillouin zone, can be in competition (incommensurate structures are not considered in this paper). There can occur both a simple stripe-domain structure ($\mathbf{q} = \mathbf{Q}$) near quarter-filling and a more complex triangular (hexagonal) structure ($\mathbf{q} = \mathbf{P}$) near half-filling. In the former case, the nesting of some sections of the Fermi surface at wave vector $\mathbf{Q}$ is of considerable importance, while in the latter case, the increase in the effective interaction potential at wave vector $\mathbf{P}$ plays an important role.

The available experimental data suggest that (Pb, Sn)/Ge(111) monolayers with a coverage of 1/3 are systems in which CDWs arise at wave vector $\mathbf{P}$ and which can adequately be described in the weak interaction approximation [2]. The electronic spectrum of these systems is gapless, or it has a pseudogap. At the same time, K/Si(111) : B monolayers with a coverage of 1/3 most likely belong to systems with SDWs, but questions concerning their SDW structure are still unanswered and a model adequately describing them is lacking. The presence of a gap in the spectrum of electron states favors the strong-interaction model, but the value of the band gap width (about 0.1 eV) is inconsistent with the criterion for strong interaction, which makes one make exotic assumptions about surface relaxation [4], a discussion of which would serve no purpose in this paper.

ACKNOWLEDGMENTS

This work was discussed at the LEPES seminar (CNRS, Grenoble) and at the Solid-State Physics seminar (FIAN, Moscow). One of the authors (V.V.T.) is grateful to Yu.V. Kopaev and A.P. Shotov for useful discussion and encouragement.

REFERENCES

1. V. G. Lifshitz, A. A. Saranin, and A. V. Zotov, *Surface Phases in Silicon* (Wiley, Chichester, 1994).
2. G. Santoro, S. Scandolo, and E. Tosatti, Phys. Rev. B **59** (3), 1891 (1999).
3. B. A. Nesterenko and V. G. Lyapin, *Phase Transitions on Free Faces and Interphase Boundaries in Semiconductors* (Naukova Dumka, Kiev, 1990).
4. H. H. Weitering, X. Shi, and P. D. Johnson, Phys. Rev. Lett. **78** (7), 1331 (1997).
5. C. Hellberg and S. Erwin, Phys. Rev. Lett. **83** (5), 1003 (1999).
6. G. A. Allan and M. Lannoo, Surf. Sci. **63** (1), 11 (1977).
7. V. N. Men'shov and V. V. Tugushev, Zh. Éksp. Teor. Fiz. **104** (5), 3848 (1993) [JETP **77**, 848 (1993)].
8. B. I. Halperin and T. M. Rice, Solid State Phys. **21**, 115 (1968).
9. F. Zhang and T. M. Rice, Phys. Rev. B **37** (7), 3759 (1988).
10. M. Avignon and V. Tugushev, Phys. Lett. A **209**, 198 (1995).
11. P. Fazekas and P. W. Anderson, Philos. Mag. **30**, 423 (1974).

Translated by Yu. Epifanov

Physics of the Solid State, Vol. 43, No. 3, 2001, pp. 569–573. Translated from Fizika Tverdogo Tela, Vol. 43, No. 3, 2001, pp. 549–553.
Original Russian Text Copyright © 2001 by Gomoyunova, Pronin, Valdaĭtsev, Faradzhev.

LOW-DIMENSIONAL SYSTEMS AND SURFACE PHYSICS

Reactive Epitaxy of Cobalt Disilicide on Si(111)

M. V. Gomoyunova, I. I. Pronin, D. A. Valdaĭtsev, and N. S. Faradzhev

Ioffe Physicotechnical Institute, Russian Academy of Sciences, Politekhnicheskaya ul. 26, St. Petersburg, 194021 Russia

Received July 4, 2000

Abstract—A study of the mechanism governing the initial stages in silicide formation under deposition of 1–10 monolayers of cobalt on a heated Si(111) 7 × 7 crystal is reported. The structural data were obtained by an original method of diffraction of inelastically scattered medium-energy electrons, which maps the atomic structure of surface layers in real space. The elemental composition of the near-surface region to be analyzed was investigated by Auger electron spectroscopy. Reactive epitaxy is shown to stimulate epitaxial growth of a *B*-oriented $CoSi_2$(111) film on Si(111). In the initial stages of cobalt deposition (1–3 monolayers), the growth proceeds through island formation. The near-surface layer of a $CoSi_2$(111) film about 30 Å thick does not differ in elemental composition from the bulk cobalt disilicide, and the film terminates in a Si–Co–Si monolayer triad. *© 2001 MAIK "Nauka/Interperiodica".*

Silicon forms the basis of present-day solid-state microelectronics. The latter makes wide use of a variety of microstructures consisting of transition-metal silicides grown on silicon [1]. The Co/Si(111) system has been attracting the interest of many researchers for about two decades [2–12]. It was shown that $CoSi_2$ epitaxial films can be grown on a Si(111) 7 × 7 surface with an atomically sharp interface [13–16]. This feature of the $CoSi_2$/Si(111) heterostructure made it a model system to probe the metal–semiconductor interface and to study the mechanism of Schottky barrier formation [17]. It is also essential that $CoSi_2$ films possess a high conductivity and thermal stability. This combination of properties of the cobalt silicide films on silicon accounts for their widespread use for ohmic and barrier contacts in semiconductor devices.

Three main techniques of growing $CoSi_2$ films in ultrahigh vacuum are known. One of them is solid-state epitaxy, which consists in depositing Co on Si(111) 7 × 7 at room temperature, followed by annealing the sample to 550–600°C. Another method is reactive epitaxy, in which Co is deposited on a heated silicon crystal, and the third is molecular-beam epitaxy. The mechanism itself by which $CoSi_2$ films grow on a heated substrate received only scant attention. The data available to us form only an incomplete picture. For instance, [18] reports the existence of two temperature and coverage regions within which either continuous uniform or island $CoSi_2$ films can grow. The first case is characteristic of lower temperatures and coverages. The above study [18] relates, however, to temperatures and coverages in excess of 550°C and ~15 Å, respectively. As for the earliest stages in the $CoSi_2$ growth for $T < 550°C$, there are indications that the layer-by-layer growth prevails here [8].

This work studies the initial stages in silicide formation under the conditions of reactive epitaxy. The study made use of a new structural method, namely, diffraction of inelastically reflected medium-energy electrons [19–22]. Such diffraction patterns form due to the electron focusing effect consisting essentially in the scattered electrons propagating preferentially along closely packed atomic rows in a crystal, which permits visualization of the atomic structure of a near-surface crystal layer 1–1.5 nm thick in real space. This focusing effect was discovered in studies of the diffraction of photo- and Auger electrons [23–25], which has already found application in the investigation of the structure of silicide films grown by solid-state [5] and molecular-beam epitaxy [26].

1. EXPERIMENTAL

The instrument used in the experiment was described in detail in [27]. We shall discuss here only its principal units. The sample to be studied is irradiated with a 2-keV electron beam. The beam current is 10^{-7} A, and its diameter is 1.0 mm. The electrons hit the surface at grazing incidence, undergo intense scattering in the near-surface layer, and are partially reflected from the sample. The electrons reflected with energy losses not above approximately 10% of the initial energy are detected by a small retarding-field analyzer with two spherical grids. On passing through these grids, the electron flux is amplified by a microchannel plate and initiates luminophor glow, which is observed through the optical window of the vacuum chamber. The LEED optics provide collection of the electrons within a fairly large cone-apex semiangle of 57°. The possibility is provided to observe the important region near the normal to the sample surface, which is inaccessible in standard LEED instruments. The diffractograms are viewed by a videocamera interfaced with a computer. This permits one to record them on a hard disk with a rate of up

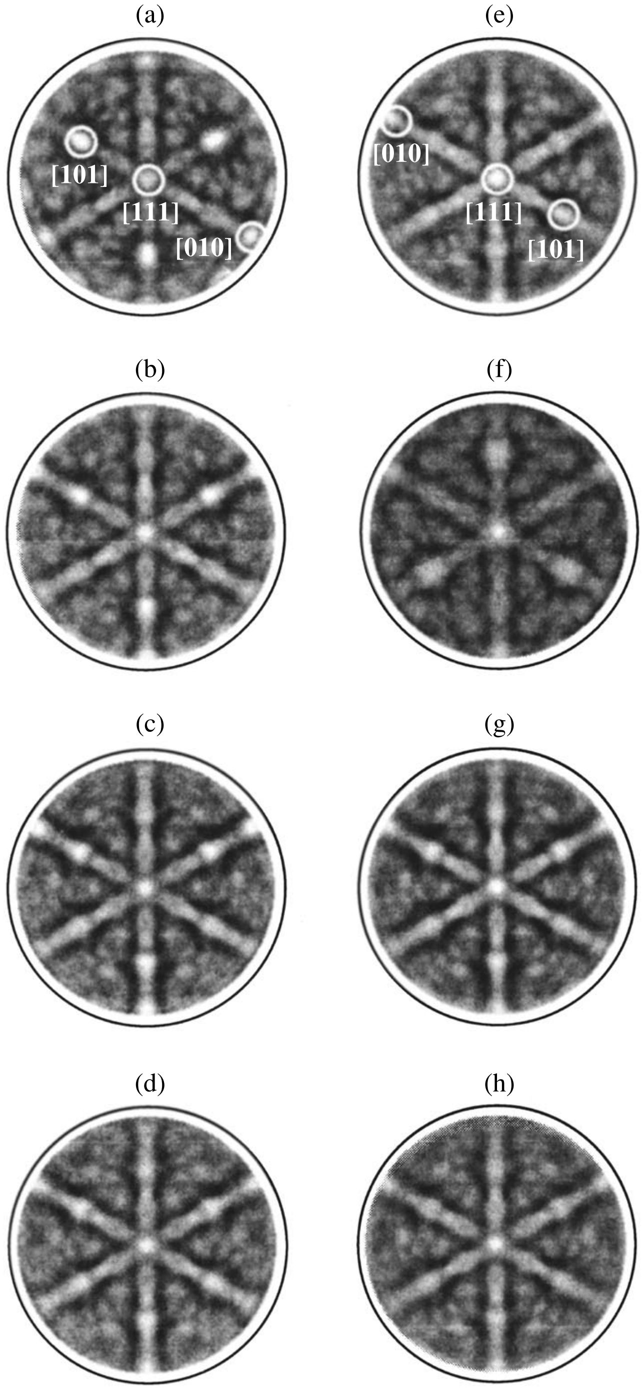

Fig. 1. Diffraction patterns observed in the deposition of cobalt on the surface of a silicon single crystal heated to 450°C. (a) Original pattern from the Si(111) 7 × 7 face; (b)–(d) diffractograms after deposition of one, two, and three Co monolayers, respectively; (e) $CoSi_2(111)$ epitaxial film; (f)–(h) simulations of patterns (e), (c), and (d), respectively.

to 50 frames per second, with their subsequent processing by means of special software. This rate of pattern recording allows studying many atomic processes in real time.

The studies were performed in an ultrahigh vacuum (10^{-8} Pa). The silicon samples on which cobalt was deposited were cut from a KÉF-1 single-crystal plate and measured as 22 × 14 × 0.25 mm. The crystal surface was matched with the (111) face to not worse than 20′. Before mounting them in the chamber, the crystals were thoroughly cleaned by the technique of Shiraki [28]. This was followed by a heat treatment in vacuum, first at $T = 500°C$ for half an hour and then by short stepwise anneals at an ever-increasing temperature (up to 1000°C). Directly before the measurements, the samples were heated for a short time at $T = 1200°C$, which ensured an atomically clean silicon surface with a Si(111) 7 × 7-type reconstruction. During the sample heating, the pressure in the chamber did not rise above 2×10^{-7} Pa. Cobalt was deposited on the crystal maintained at 450°C. The cobalt source was a 1-mm diameter wire of 99.99% purity. The wire was heated by electron bombardment. The cobalt was deposited in approximately one-monolayer steps, at a rate of 0.8 monolayer (ML) per minute. The investigation was carried out over a Co coating range of up to 10 ML. The figure 7.8×10^{14} at/cm^2, which corresponds to the number of Si atoms per 1 cm^2 of the Si(111) face, was accepted for the cobalt monolayer. The cleanness of the original crystal surface and the deposited amount of cobalt were verified by Auger electron spectroscopy. The diffraction patterns were measured at room temperature after the sample had cooled down.

2. RESULTS OF THE MEASUREMENTS AND DISCUSSION

2.1. Dynamics of Diffraction Pattern Variation under Reactive Epitaxy

The results are illustrated by Fig. 1. It displays several diffraction patterns measured on the original Si(111) 7 × 7 crystal (Fig. 1a) and after deposition on it of fixed cobalt amounts (Figs. 1b–1e). The data are presented in the form of stereographically projected, two-dimensional scattered-electron intensity maps in the polar and azimuthal takeoff angles, shown in the nonlinear gray-scale contrast code. The bright regions relate in this case to maxima in the angular distributions, and the black ones, conversely, to their minima. The center of a pattern corresponds to electrons escaping along the surface normal, and the circumference, to their takeoff at a polar angle of 57°. Note that the diffractograms obtained at medium energies and similar to those presented in the figure are frequently called Kikuchi patterns. As can be seen from Fig. 1a, the Kikuchi pattern of the substrate has a threefold symmetry characteristic of the silicon (111) plane. The brightest maxima are observed with electrons escaping along the most closely packed $\langle 110 \rangle$ silicon crystallographic directions lying symmetrically with respect to the pattern center at polar angles $\theta = 35°$. There are also pronounced maxima along the $\langle 111 \rangle$ and $\langle 100 \rangle$ directions.

In Fig. 1a, they are identified by circles. Note also the extended high-intensity bands (Kikuchi bands) along the projections of the closest packed {110} silicon atomic planes. Thus, this pattern does indeed map, in real space, the mutual arrangement of atoms in the near-surface layer of a sample. The thickness of this layer is equal to the average escape depth of the detected electrons, which is about 1.5 nm for an energy of 2.5 keV. A more detailed analysis of the formation of silicon Kikuchi patterns can be found in [29].

Already the deposition of the first cobalt monolayer (Fig. 1b) changes the pattern noticeably. This becomes manifest, first of all, in the weakening of the strongest ⟨110⟩ substrate peaks discussed above, as well as in the change of the fine diffraction structure close to these directions. The maxima in the central part of the image also become slightly stronger. This transformation of the pattern gets still more pronounced on deposition of the second (Fig. 1c) and third (Fig. 1d) cobalt monolayers. Fairly intense maxima at polar angles $\theta = 35°$ appear, which lie azimuthally between the substrate peaks. At higher cobalt coverages, the changes in the pattern become less pronounced, to disappear practically completely after the deposition of five to six cobalt monolayers. The results obtained for this steady-state system are shown in Fig. 1e. Note that it is approximately within this coverage interval that the ratio of the Co(*MMV*) to Si(*LVV*) Auger signals ceases to change, thus implying a constant elemental composition in the probed near-surface layer.

2.2. $CoSi_2(111)$ Epitaxial Film

The pattern displayed in Fig. 1e and showing a distinct diffraction structure provides unambiguous evidence for the silicide layer formed being ordered. As follows from its comparison with Fig. 1a, the pattern itself resembles in many details the one observed for silicon, but turned azimuthally through 180°. It is known that deposition of cobalt on a Si(111) crystal heated to ~450°C results in the growth of a $CoSi_2(111)$ cobalt disilicide film [8]. This similarity between the diffractograms of Si(111) and $CoSi_2(111)$ can be readily understood if one recalls their crystal structures. Both substances crystallize in cubic symmetry, with silicon having a diamond-type structure and $CoSi_2$, a fluorite-type one. The mismatch between the lattice constants is only 1.2% (a_1 = 5.356 Å, a_2 = 5.428 Å). Nevertheless, the differences between these structural types, which are clearly seen in the (110) planes (Fig. 2), complicate the structure of the $CoSi_2$ atomic chains, in particular, along the ⟨110⟩ directions, and change the atom concentrations in them. However, the orientations of the closest-packed directions and planes in both crystals coincide (the ⟨110⟩ directions and {110} planes). Hence, the strongest pattern maxima should be observed at the same takeoff angles of the scattered electrons. This is illustrated by Fig. 3, which schematically shows the mutual orientations of the principal focusing maxima produced by electrons moving along the {110} planes. It is these peaks, as is evident from Figs. 1a and 1e, that are dominant in the diffraction patterns observed. Therefore, these patterns are very similar and their differences are determined by the different relative intensities of the focusing maxima.

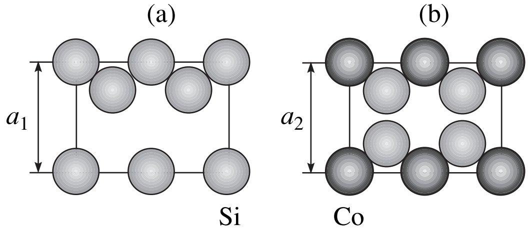

Fig. 2. Schematic presentation of the sections of the (a) Si and (b) $CoSi_2$ unit cells by the (110) plane.

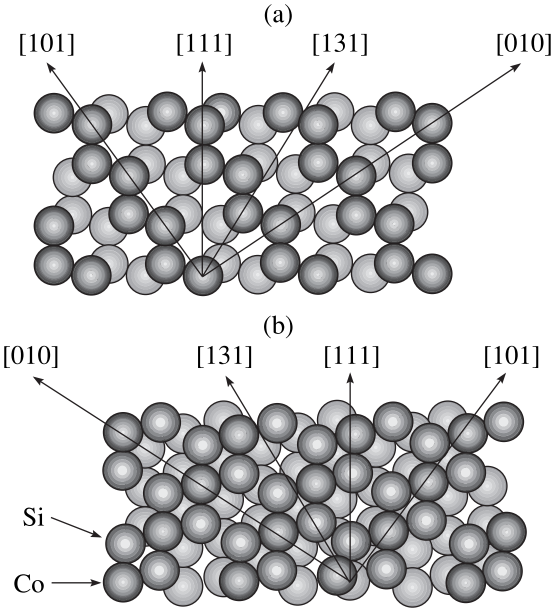

Fig. 3. Schematic illustrating the principal focusing maxima appearing as electrons move along the (110) atomic planes of (a) silicon and (b) cobalt disilicide.

As for the Kikuchi pattern of $CoSi_2(111)$ being turned azimuthally through 180° relative to that of silicon, this is accounted for by the fact that it is this epitaxial orientation of the cobalt disilicide interface that is energetically favorable for the system under study [30]. It is customarily called the *B* orientation, as distinct from the *A* orientation, which coincides with that of the substrate. The orientation of the growing disilicide is determined by its nucleation centers within the unit cell of the reconstructed silicon surface [31]. If these centers are localized on its strained halves, the $CoSi_2(111)$ forms with the *B* orientation, otherwise it will be *A* oriented. It was shown [32] that when Co

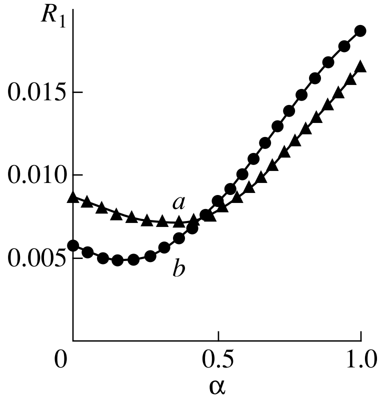

Fig. 4. Dependences of the R_1 factor on parameter α, which characterizes the statistical weight of the substrate in the diffractograms observed after the deposition of (*a*) two and (*b*) three cobalt monolayers.

atoms are deposited on a silicon crystal at room temperature, they are adsorbed and penetrate under the top silicon atom layer within the whole 7 × 7 cell. Indeed, in these conditions, one finds both *A*- and *B*-oriented $CoSi_2(111)$ domains. By contrast, if Co atoms are deposited on a heated crystal in close-to-thermodynamically equilibrium conditions, they migrate over the surface and remain within the strained parts of the cell, and this is what accounts for the growth of the *B*-oriented $CoSi_2(111)$ film in this case.

Thus, when more than ~5 cobalt monolayers are deposited on a Si(111) crystal heated to ~450°C, a continuous epitaxial film of *B*-oriented $CoSi_2(111)$ will grow on it. The ratio of the low-energy $Co(M_{2,3}VV)$ and Si(*LVV*) Auger signals measured for this film is 0.18–0.20, which adjoins the 0.2–0.3 interval quoted in the literature for $CoSi_2$–C [33–35]. It was established that the elemental composition of the surface layers of this phase coincides with that for bulk $CoSi_2(111)$ and terminates with the monolayer triad Si–Co–Si [33, 36]. Note that the surface of Co films annealed to higher temperatures (550–600°C) is enriched in silicon, because it becomes coated by two extra Si monolayers [33–35]. By contrast, the surface of a film with elemental composition coinciding with that of the bulk silicide is called cobalt enriched. The diffraction pattern of $CoSi_2(111)$ with such a surface obtained by computer simulation within the cluster model of single scattering of plane electron waves [19] from a *B*-oriented film is shown in Fig. 1f. It exhibits good agreement with the experiment, thus supporting the validity of the above interpretation of the pattern in Fig. 1e.

2.3. $CoSi_2(111)$ Growth Mode in the Initial Stage of Formation

An analysis of the intermediate diffractograms obtained during the formation of the above Kikuchi pattern with increasing amounts of deposited cobalt (Figs. 1b–1d) yields information on the mechanism of the silicide film growth in the earliest stages of the process. A detailed comparison of these images with the patterns produced by clean silicon (Fig. 1a) and cobalt disilicide (Fig. 1e) shows the intermediate images to contain elements of patterns due to both crystals. This suggests that the intermediate images are actually their superpositions. To check this conjecture, the Kikuchi patterns under study were simulated using images obtained on silicon (Fig. 1a) and cobalt disilicide (Fig. 1e). The intensity $I_t(\theta, \varphi)$ was calculated for each point of the pattern by the expression

$$I_t(\theta, \varphi) = \alpha I_A(\theta, \varphi) + (1-\alpha) I_B(\theta, \varphi), \qquad (1)$$

where $I_A(\theta, \varphi)$ and $I_B(\theta, \varphi)$ are the intensities measured at points in the diffraction patterns (Figs. 1a and 1e) with the angular coordinates (θ, φ) and α is a variable parameter related to the statistical weight of the substrate surface not covered by $CoSi_2(111)$ crystallites.

The optimum value of α can be found by minimizing the difference between the calculated, $I_t(\theta, \varphi)$, and measured, $I_e(\theta, \varphi)$, patterns. These differences are usually estimated by means of reliability factors. One customarily resorts to the R_1 and R_2 factors defined by the relations

$$R_1 = \frac{\sum_{\theta, \varphi} |I_e(\theta, \varphi) - I_t(\theta, \varphi)|}{\sum_{\theta, \varphi} |I_e(\theta, \varphi)|},$$

$$R_2 = \frac{\sum_{\theta, \varphi} [I_e(\theta, \varphi) - I_t(\theta, \varphi)]^2}{\sum_{\theta, \varphi} I_e^2(\theta, \varphi)}. \qquad (2)$$

Here, $I_e(\theta, \varphi)$ and $I_t(\theta, \varphi)$ are the measured and calculated intensities, respectively, for the same point in the diffractogram. The summation is performed over all takeoff angles of the detected scattered electrons. The denominators of the fractions are normalization coefficients.

The calculations using Eqs. (1) and (2) were carried out for α varied in steps of 0.02 within an interval of 0 to 1. The data obtained in this way for the three states of the Co/Si system under study (Figs. 1b–1d) were used to construct $R_1(\alpha)$ and $R_2(\alpha)$ relations. By way of illustration, Fig. 4 shows this relation drawn for R_1 for samples with two and three Co monolayers. These relations are seen to exhibit fairly distinct minima at the values of α of 0.35 and 0.18, respectively. The optimum value of α for one Co monolayer is 0.60. The same results are obtained in estimates made by means of the R_2 factor. The diffractograms calculated for two and three Co monolayers and corresponding to the α values thus found are presented in Figs. 1g and 1h. They are seen to agree very well with the measurements (Figs. 1c, 1d). In contrast to [7], these data indicate that the film forming in the course of deposition of the first few monolayers occupies only a part of the substrate surface, which increases as cobalt is further deposited. For three Co monolayers, it is already 82% and it is probably in this stage that the islands start to coalesce. On deposition of the fourth and fifth monolayers, the $CoSi_2$ film becomes continuous. Estimation of the average thickness of growing islands, made by comparing the amounts of deposited cobalt with the corresponding values of α, shows that, in the earliest stages of the silicide formation, lateral growth of $CoSi_2(111)$ prevails. For instance, an increase in the deposited Co from one to three monolayers results in an increase in the average island thickness by 50%, whereas the area occupied by the islands increases twofold. It is the lateral growth of the islands over the substrate surface that accounts for the formation of fairly perfect epitaxial $CoSi_2$ films in this system.

Thus, the data obtained suggest that the formation of the cobalt disilicide on the Si(111) 7×7 surface at an elevated temperature starts with the nucleation of $CoSi_2(111)$-C islands, followed by their lateral growth. The island coalescence occurs at cobalt amounts of about three monolayers. Deposition of five Co monolayers produces a continuous, *B*-oriented $CoSi_2(111)$ epitaxial film.

ACKNOWLEDGMENTS

This work was supported by the “Surface Atomic Structures” program, project no. 5.10.99.

REFERENCES

1. L. J. Chen and K. N. Tu, Mater. Sci. Rep. **7**, 53 (1991).
2. S. Saitoh, H. Ishiwara, and S. Furukawa, Appl. Phys. Lett. **37** (2), 203 (1980).
3. C. Pirri, J. C. Peruchetti, G. Gewinner, and J. Derrien, Phys. Rev. B **29** (6), 3391 (1984).
4. J. Dirrien, Surf. Sci. **168** (1), 171 (1986).
5. S. A. Chambers, S. B. Anderson, H. W. Chen, and J. H. Weaver, Phys. Rev. B **34** (2), 913 (1986).
6. F. Boschrini, J. J. Joyce, M. W. Ruckman, and J. H. Weaver, Phys. Rev. B **35** (9), 4216 (1987).
7. D. D. Chambliss, T. N. Rhodin, J. E. Rowe, and H. Shigekawa, J. Vac. Sci. Technol. A **7** (3), 2449 (1989).
8. A. Bensaoula, J. Y. Veuillen, T. T. A. Nguyen, *et al.*, Surf. Sci. **241** (3), 425 (1991).
9. H. von Kanel, Mater. Sci. Rep. **8**, 193 (1992).
10. C. W. T. Bulle-Lieuwna, Appl. Surf. Sci. **68** (1), 1 (1993).
11. N. I. Plusnin, A. P. Milenin, and D. P. Prihodko, Phys. Low-Dimens. Semicond. Struct. **9/10**, 107 (1999).
12. Y. Hayashi, M. Yoshinaga, H. Ikeda, *et al.*, Surf. Sci. **438** (1), 116 (1999).
13. C. D. Anterroches, Surf. Sci. **168** (1), 751 (1986).
14. R. T. Tung and J. L. Batstone, Appl. Phys. Lett. **52** (19), 1611 (1988).
15. J. Derrien, M. de Crescenzi, E. Chainet, *et al.*, Phys. Rev. B **36** (12), 6681 (1987).
16. H. von Kanel, C. Schwarz, and S. Goncalves-Conto, Phys. Rev. Lett. **74** (7), 1163 (1995).
17. H. Fujitani and S. Asano, Phys. Rev. B **50** (12), 8681 (1994).
18. F. Arnaud d’Avitayas, S. Delage, *et al.*, J. Vac. Sci. Technol. B **3** (2), 770 (1985).
19. M. V. Gomoyunova, I. I. Pronin, and N. S. Faradzhev, Zh. Éksp. Teor. Fiz. **110** (1), 311 (1996) [JETP **83**, 168 (1996)].
20. N. S. Faradzhev, M. V. Gomoyunova, and I. I. Pronin, Phys. Low-Dimens. Semicond. Struct. **3/4**, 93 (1997).
21. M. Erbudak, M. Hochstrasser, E. Wetli, and M. Zurkirch, Surf. Rev. Lett. **4**, 179 (1997).
22. I. I. Pronin and M. V. Gomoyunova, Prog. Surf. Sci. **59** (1–4), 53 (1998).
23. W. F. Egelhoff, Jr., Crit. Rev. Solid State Mater. Sci. **16**, 213 (1990).
24. S. C. Fadley, in *Synchrotron Radiation Research: Advances in Surface and Interface Science*, Vol. 1: *Techniques*, Ed. by R. Z. Bachrach (Plenum, New York, 1992), Chap. 9, p. 421.
25. S. A. Chambers, Surf. Sci. Rep. **16** (6), 261 (1992).
26. C. Pirri, S. Hong, M. H. Tuilier, *et al.*, Phys. Rev. B **53**, 1368 (1996).
27. I. I. Pronin, D. A. Valdaĭtsev, M. V. Gomoyunova, *et al.*, Zh. Tekh. Fiz. **68** (12), 80 (1998) [Tech. Phys. **43**, 1475 (1998)].
28. A. Ishizaka and Y. Shiraki, J. Electrochem. Soc. **133**, 666 (1986).
29. I. I. Pronin, N. S. Faradzhev, and M. V. Gomoyunova, Fiz. Tverd. Tela (St. Petersburg) **39** (4), 752 (1997) [Phys. Solid State **39**, 666 (1997)].
30. D. R. Haman, Phys. Rev. Lett. **60** (4), 313 (1988).
31. G. Rossi, A. Santaniello, P. de Padova, *et al.*, Europhys. Lett. **11** (3), 235 (1990).
32. P. A. Bennet, D. G. Cahill, and M. Copel, Phys. Rev. Lett. **73** (3), 452 (1994).
33. F. Hellmann and R. T. Tung, Phys. Rev. B **37** (18), 10786 (1988).
34. U. Starke, J. Schardt, W. Weiβ, *et al.*, Surf. Rev. Lett. **5** (1), 139 (1998).
35. A. E. Dolbak, B. Z. Olshanetsky, and S. A. Teys, Phys. Low-Dimens. Semicond. Struct. **3/4**, 113 (1997).
36. D. D. Chambliss, T. N. Rhodin, and J. E. Rowe, Phys. Rev. B **45** (3), 1193 (1992).

Translated by G. Skrebtsov

Physics of the Solid State, Vol. 43, No. 3, 2001, pp. 574–578. Translated from Fizika Tverdogo Tela, Vol. 43, No. 3, 2001, pp. 554–558.
Original Russian Text Copyright © 2001 by Kyasov, Dedkov.

LOW-DIMENSIONAL SYSTEMS AND SURFACE PHYSICS

Fluctuation Electromagnetic Interaction of Moving Particles with a Cylindrical Surface and a Channel

A. A. Kyasov and G. V. Dedkov
Kabardino–Balkar State University, ul. Chernyshevskogo 173, Nalchik, 360000 Russia
e-mail: gv_dedkov@kbsu.ru

Received July 14, 2000

Abstract—The most general (nonrelativistic) analytical formulas are deduced in the framework of the fluctuation electromagnetic theory for the dynamic conservative and dissipative forces experienced by a neutral atom moving parallel to the generatrix of a cylindrical surface. As in the case of a flat surface, a finite friction force proportional to the velocity exists at $T = 0$. *© 2001 MAIK "Nauka/Interperiodica".*

1. INTRODUCTION

Investigation of the dynamic fluctuation electromagnetic interaction (FEI) of atoms and molecules with flat and curved surfaces is of considerable interest for nanotribology [1] and in the context of the possible control of particle beams by means of nanotubes [2, 3]. Furthermore, the information on FEI forces is necessary in studies of the adsorption of particles by surfaces of nanotubes and fullerenes.

This paper is a continuation of our works [4–7] in which the most general nonrelativistic formulas were deduced for the forces of attraction and of viscous friction of atoms and molecules moving parallel to a flat surface. Dissipative FEI forces for a cylindrical surface at temperature $T = 0$ were first considered in [8]. The goal of the present work was to derive the more general formulas for the conservative and dissipative FEI forces acting on a neutral atom moving parallel to the generatrix of a convex (concave) cylindrical surface with a nonrelativistic velocity $V \ll c$ in the case of an arbitrary temperature.

2. ELECTRIC FIELD INDUCED BY A FLUCTUATING ATOMIC DIPOLE ON A SURFACE

As in the case of a flat surface [4–7], let us consider a spherically symmetric atomic particle with the polarizability $\alpha(\omega)$. The medium is specified by the dielectric function $\varepsilon(\omega)$. Figure 1a illustrates the motion above a convex cylindrical surface, and Fig. 1b shows the motion inside a cylindrical channel. For definiteness, in Sections 2–4, we will analyze the former case, and in Section 5, we will consider the latter case.

Our constraints are reduced to the fulfillment of the conditions of validity of the dipole approximation and the neglect of the FEI retardation. In the case demonstrated in Fig. 1a, these requirements constrain the distances between the particle and the surface $h = R - a$ by the range $r_0 \ll h \ll c/\omega_0$, where r_0 is the characteristic size of the atom and ω_0 is the characteristic frequency of excitation of atomic electrons.

Designating the vector of the spontaneous dipole moment of the particle by $\mathbf{d}^{\mathrm{sp}}(t)$, we have the following expression for the vector of electric polarization which is induced in the space by the fluctuations of $\mathbf{d}^{\mathrm{sp}}(t)$ (hereafter, we will use the Gaussian system of units):

$$\begin{aligned}\mathbf{P}^{\mathrm{sp}}(\mathbf{r}, t) &= \delta(x-R)\delta(y)\delta(z-Vt)\mathbf{d}^{\mathrm{sp}}(t)\\ &= \frac{1}{r}\delta(r-R)\delta(\phi)\delta(z)\mathbf{d}^{\mathrm{sp}}(t),\end{aligned} \tag{1}$$

where (r, ϕ, z) are the coordinates of the particle in the cylindrical frame of reference. The Poisson equation for the potential of the electric field induced by the polarization represented by expression (1) ($\Delta\Phi = 4\pi\,\mathrm{div}\mathbf{P}^{\mathrm{sp}}$)

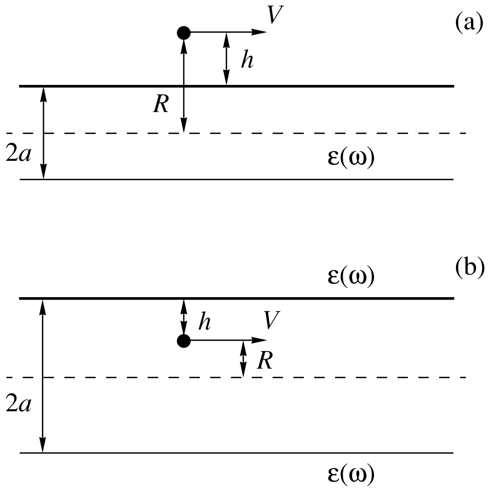

Fig. 1. Diagram of the motion of a neutral particle: (a) parallel to the generatrix of a convex cylindrical surface and (b) inside a cylindrical channel.

has the following form in the cylindrical frame of reference:

$$\begin{aligned}\left(\frac{\partial^2}{\partial r^2}+\frac{1}{r}\frac{\partial}{\partial r}+\frac{1}{r^2}\frac{\partial^2}{\partial \phi^2}+\frac{\partial^2}{\partial z^2}\right)&\Phi(r, \phi, z, t)\\ = 4\pi\Bigg(\frac{1}{r}\frac{\partial}{\partial r}&\delta(r-R)\delta(\phi)\delta(z)d_r^{\mathrm{sp}}(t)\\ +\frac{1}{r}\frac{\partial}{\partial \phi}&\frac{\delta(r-R)}{r}\delta(\phi)\delta(z)d_\phi^{\mathrm{sp}}(t)\\ +\frac{\partial}{\partial z}&\frac{\delta(r-R)}{r}\delta(\phi)\delta(z)d_z^{\mathrm{sp}}(t)\Bigg),\end{aligned} \tag{2}$$

where $d_r^{\mathrm{sp}}(t)$, $d_\phi^{\mathrm{sp}}(t)$, and $d_z^{\mathrm{sp}}(t)$ are the corresponding projections of the vector of dipole moment.

Solving Eq. (2) and taking into account the boundary conditions of the continuity of both the potential and the normal component of electric induction, we obtain the expressions for the vector of the induced electric field of the surface and its components:

$$\begin{aligned}\mathbf{E}^{\mathrm{in}}(r, \phi, z, t) &= \frac{1}{(2\pi)^3}\\ &\times\sum_{n=-\infty}^{\infty}\iint \mathbf{E}_{\omega k}^{\mathrm{in}}(r)e^{in\phi}e^{i(kz-\omega t)}d\omega dk,\end{aligned} \tag{3}$$

$$E_r^{\mathrm{in}}(\omega k;\, r) = -\frac{d}{dr}u_n(\omega k;\, r), \tag{4a}$$

$$E_\phi^{\mathrm{in}}(\omega k;\, r) = -\frac{in}{r}u_n(\omega k;\, r), \tag{4b}$$

$$E_z^{\mathrm{in}}(\omega k;\, r) = -iku_n(\omega k;\, r), \tag{4c}$$

$$\begin{aligned}u_n(\omega k;\, r) = -4\pi\Delta_n(\omega)\Bigg(&K_n(kr)K_n'(kR)kd_r^{\mathrm{sp}}(\omega-kV)\\ &-\frac{in}{R}K_n(kr)K_n(kR)d_\phi^{\mathrm{sp}}(\omega-kV)\\ &-ikK_n(kr)K_n(kR)d_z^{\mathrm{sp}}(\omega-kV)\Bigg),\end{aligned} \tag{5}$$

$$\Delta_n(\omega) = \frac{(\varepsilon(\omega)-1)I_n(ka)I_n'(ka)}{\varepsilon(\omega)I_n'(ka)K_n(ka)-I_n(ka)K_n'(ka)}. \tag{6}$$

For simplicity, argument k (and also a) in formula (6) and, below, in formula (19) is omitted.

The functions $K_n(x)$ and $I_n(x)$ are the cylinder functions of order n, and primes denote their derivatives. The physical meaning of the $\Delta_n(\omega)$ function in Eq. (6) is similar to that of the function $\Delta(\omega) = (\varepsilon(\omega) - 1)/(\varepsilon(\omega) + 1)$ in the case of a flat surface [4–7].

Replacing the Fourier components of the dipole moment in Eqs. (4)–(6) by the corresponding quantum mechanical components of the operator of the dipole moment, expression (3) will be treated as a definition of the operator of the induced electric field of a surface in the Heisenberg representation. All the other vector quantities also have operator meaning.

3. CONSERVATIVE POTENTIAL OF THE INTERACTION OF A PARTICLE WITH A SURFACE

As in the case of a flat surface [4–7], the dynamic potential of the interaction of an atom with a surface in the dipole approximation can be represented in the form of the sum of two independent parts:

$$\begin{aligned}U_{\mathrm{int}} &= -\frac{1}{2}\langle\mathbf{dE}\rangle = -\frac{1}{2}\langle\mathbf{d}^{\mathrm{sp}}\mathbf{E}^{\mathrm{in}}\rangle-\frac{1}{2}\langle\mathbf{d}^{\mathrm{in}}\mathbf{E}^{\mathrm{sp}}\rangle\\ &= U_1+U_2,\end{aligned} \tag{7}$$

where the first and the second terms are associated with the spontaneous fluctuations of the dipole moment of an atom and the electrical field of a surface, respectively.

In order to determine U_1, let us expand the $\mathbf{d}^{\mathrm{sp}}(t)$ operator in the Fourier integral and substitute it into expression (7), together with the operator of the electric field at the point of the particle location $\mathbf{E}^{\mathrm{in}}(R, 0, Vt)$, and then expand the resulting correlators of the dipole moment in a conventional manner with the use of the fluctuation-dissipative theorem (cf. with [6, 7]):

$$\begin{aligned}\langle d_i^{\mathrm{sp}}(\omega)d_k^{\mathrm{sp}}(\omega')\rangle &= 2\pi\delta_{ik}\delta(\omega+\omega')\\ &\times h\alpha''(\omega)\coth(\omega\hbar/2k_{\mathrm{B}}T).\end{aligned} \tag{8}$$

Taking into account the analytical properties of the functions $\alpha(\omega)$ and $\varepsilon(\omega)$, which are associated with the evenness of the real parts and the oddness of the imaginary parts, after a succession of transformations, we bring the expression for U_1 to the form

$$\begin{aligned}U_1(R, V) &= -\frac{\hbar}{2\pi^2R^2}\sum_{n=-\infty}^{\infty}\iint d\omega dk K_n^2(kR)\\ &\times[n^2-(kR)^2+(kR)^2\Phi_n^2(kR)]\coth(\omega\hbar/2k_{\mathrm{B}}T)\\ &\times\alpha''(\omega)[\Delta_n'(\omega-kV)+\Delta_n'(\omega+kV)],\end{aligned} \tag{9}$$

where $\Phi_n(z) \equiv d/dz\ln K_n(z)$ is the logarithmic derivative of the Macdonald function. The functions $\alpha(\omega)$ and $\Delta(\omega)$ with one and two primes in expression (9) and others designate their real and imaginary parts.

In order to find the potential U_2, we expand the $\mathbf{d}^{\mathrm{in}}(t)$ operator in the Fourier frequency integral and $\mathbf{E}^{\mathrm{sp}}$ in the Fourier integral with respect to ω and k and then in a Fourier series in terms of the angular variable ϕ. Then, we substitute the results in expression (7). Proceeding further in a manner identical to the case of the derivation of a similar expression for a flat surface [6, 7], we obtain the following expression for a spectral correlation function of the electric field (at the point of the location of the particle ($r = R$)) which arises in the process of calculation:

$$\begin{aligned}\left\langle \mathbf{E}^{\mathrm{sp}}_{\omega k}(R)\mathbf{E}^{\mathrm{sp}}_{\omega' k'}(R)\right\rangle &= (2\pi)^2\delta(\omega+\omega')\delta(k+k') \\ &\times \frac{2\hbar}{R^2}\coth(\omega\hbar/2k_{\mathrm{B}}T)\sum_{n=-\infty}^{\infty}K_n^2(kR) \\ &\times [n^2+(kR)^2+(kR)^2\Phi_n^2(kR)]\Delta''_n(\omega).\end{aligned} \tag{10}$$

Employing expression (10), integrating the expression for the potential with respect to variables ω' and k', and taking into account the analytical properties of the polarizability and the dielectric function, we have

$$\begin{aligned}U_2(R, V) &= -\frac{\hbar}{2\pi^2R^2}\sum_{n=-\infty}^{\infty}{}'\iint d\omega dk K_n^2(kR) \\ &\times [n^2+(kR)^2+(kR)^2\Phi_n^2(kR)]\coth(\omega\hbar/2k_{\mathrm{B}}T) \\ &\times \Delta''_n(\omega)[\alpha'(\omega-kV)+\alpha'(\omega+kV)].\end{aligned} \tag{11}$$

Finally, summing expressions (9) and (11), we obtain the net result

$$\begin{aligned}U_{\mathrm{int}}(R, V) &= -\frac{\hbar}{\pi^2R^2}\sum_{n=0}^{\infty}{}'\iint d\omega dk K_n^2(kR) \\ &\times [n^2+(kR)^2+(kR)^2\Phi_n^2(kR)]\coth(\omega\hbar/2k_{\mathrm{B}}T) \\ &\times (\Delta''_n(\omega)[\alpha'(\omega-kV)+\alpha'(\omega+kV)] \\ &+ \alpha''(\omega)[\Delta'_n(\omega-kV)+\Delta'_n(\omega+kV)]).\end{aligned} \tag{12}$$

A prime over the summation symbol in formulas (11) and (12) (and also in similar formulas in the following) implies that the term with $n = 0$ is taken with half weight. The integration is carried out with respect to the frequencies and values of the wave vectors which are both positive. The deduced result generalizes the known expression for the static potential of the van der Waals attraction of a neutral spherically symmetric particle to a cylindrical surface at zero temperature [9–11]. In fact, assuming that $V = 0$ and $T = 0$ in formula (12), we obtain

$$\begin{aligned}U_{\mathrm{int}}(R) &= -\frac{2\hbar}{\pi^2R^2}\sum_{n=0}^{\infty}{}'\int_0^{\infty}dk K_n^2(kR) \\ &\times [n^2+(kR)^2+(kR)^2\Phi_n^2(kR)]\,\mathrm{Im}\int_0^{\infty}d\omega\alpha(\omega)\Delta_n(\omega).\end{aligned} \tag{13}$$

After rotating the integration contour through 90°, the frequency integral in formula (13) is put in the form

$$\mathrm{Im}\int_0^{\infty}d\omega\alpha(\omega)\Delta_n(\omega) = \int_0^{\infty}d\omega\alpha(i\omega)\Delta_n(i\omega).$$

Hence, taking into account formula (6), formula (13) is brought to a form which coincides with the results obtained in [9–11]:

$$\begin{aligned}U_{\mathrm{int}}(R) &= -\frac{2\hbar}{\pi^2R^2} \\ &\times \sum_{n=0}^{\infty}{}'\int_0^{\infty}dk K_n^2(kR)[n^2+(kR)^2+(kR)^2\Phi_n^2(kR)] \\ &\times \int_0^{\infty}\frac{\alpha(i\omega)(\varepsilon(i\omega)-1)I'_n(ka)I_n(ka)}{\varepsilon(i\omega)K_n(ka)I'_n(ka)-K'_n(ka)I_n(ka)}d\omega.\end{aligned} \tag{14}$$

4. CALCULATION OF THE FRICTIONAL FORCE

In the case of stationary motion, the lateral force acting on a particle (frictional force) is associated with the Joule dissipation of the fluctuation electromagnetic field energy per unit time:

$$\begin{aligned}-\frac{dW}{dt} &= FV = \int\langle\mathbf{jE}\rangle d\mathbf{r} \\ &= \int\langle\mathbf{j}^{\mathrm{sp}}\mathbf{E}^{\mathrm{in}}\rangle d\mathbf{r}+\int\langle\mathbf{j}^{\mathrm{in}}\mathbf{E}^{\mathrm{sp}}\rangle d\mathbf{r}.\end{aligned} \tag{15}$$

Individual terms in formula (15), as well as in formula (7), are determined by the contributions of the fluctuating dipole moment of an atom and of the fluctuation electromagnetic field of the surface, respectively, where $\mathbf{j}^{\mathrm{sp}} = \partial\mathbf{P}^{\mathrm{sp}}/\partial t$, $\mathbf{P}^{\mathrm{sp}}$ is determined by formula (1), and $\mathbf{j}^{\mathrm{in}}$ is expressed via $\mathbf{E}^{\mathrm{sp}}$ by a linear integral relationship. Carrying out calculations similar to those that were performed for the attractive potential and taking into account the fluctuation-dissipation relationships (8) and (10), we obtain

$$\begin{aligned}F(R, V) &= \frac{2\hbar}{\pi^2R^2V}\sum_{n=0}^{\infty}{}'\iint d\omega dk K_n^2(kR) \\ &\times [n^2+(kR)^2+(kR)^2\Phi_n^2(kR)]\coth(\omega\hbar/2k_{\mathrm{B}}T) \\ &\times \{(\omega+kV)[\Delta''_n(\omega)\alpha''(\omega+kV)-\Delta''_n(\omega+kV)\alpha''(\omega)] \\ &+ (\omega-kV)[\Delta''_n(\omega)\alpha''(\omega-kV)-\Delta''_n(\omega-kV)\alpha''(\omega)]\}.\end{aligned} \tag{16}$$

Formula (16) generalizes the result of the work [8] to the case of finite temperatures and arbitrary nonrelativistic velocities. The structure of the expression in braces in formula (16) [and in formula (12)] is the same as in the calculation of the frictional force (and the attractive potential) in the case of a flat surface [6, 7].

5. AN ATOM MOVING IN A CYLINDRICAL CHANNEL

Let us now consider the motion of a particle in a cylindrical channel (see Fig. 1b). We retain all designations similar to those employed in the case demonstrated in Fig. 1a, but since now $a > R$, the value of h is determined as $h = a - R$.

Without copying the details of the calculations similar to the case of a convex surface, we note that final expressions for the attractive potential and the frictional force are obtained from formulas (12) and (16) by a simple replacement of the Macdonald functions by the modified Bessel functions and vice versa. This results in the expressions

$$\begin{aligned} U_{\text{int}}(R, V) &= -\frac{\hbar}{\pi^2 R^2}\sum_{n=0}^{\infty}{}' \iint d\omega dk I_n^2(kR) \\ &\times [n^2 + (kR)^2 + (kR)^2\Psi_n^2(kR)]\coth(\omega\hbar/2k_{\text{B}}T) \\ &\times (\tilde{\Delta}_n''(\omega)[\alpha'(\omega - kV) + \alpha'(\omega + kV)] \\ &+ \alpha''(\omega)[\tilde{\Delta}_n'(\omega - kV) + \tilde{\Delta}_n'(\omega + kV)]), \end{aligned} \tag{17}$$

$$\begin{aligned} F(R, V) &= \frac{2\hbar}{\pi^2 R^2 V}\sum_{n=0}^{\infty}{}' \iint d\omega dk I_n^2(kR) \\ &\times [n^2 + (kR)^2 + (kR)^2\Psi_n^2(kR)]\coth(\omega\hbar/2k_{\text{B}}T) \\ &\times \{(\omega + kV)[\tilde{\Delta}_n''(\omega)\alpha''(\omega + kV) - \tilde{\Delta}_n''(\omega + kV)\alpha''(\omega)] \\ &+ (\omega - kV)[\tilde{\Delta}_n''(\omega)\alpha''(\omega - kV) - \tilde{\Delta}_n''(\omega - kV)\alpha''(\omega)]\}, \end{aligned} \tag{18}$$

where $\Psi_n(z) \equiv d/dz \ln I_n(z)$ and $\tilde{\Delta}_n''(\omega)$ has the form

$$\tilde{\Delta}_n''(\omega) = \frac{(\varepsilon(\omega) - 1)K_n(ka)K_n'(ka)}{\varepsilon(\omega)K_n(ka)I_n(ka) - K_n(ka)I_n'(ka)}. \tag{19}$$

Formula (17) also generalizes the results of the works [9–11] which were obtained for a static attractive potential in a cylindrical channel at $T = 0$, and it allows one to carry out the calculation of the van der Waals potential for finite velocities and temperatures. Indeed, assuming that $V = 0$ and $T = 0$ in formula (17) and performing transformations similar to those executed during the derivation of formula (14), we obtain a formula identical to those presented in [9–11],

$$\begin{aligned} U_{\text{int}}(R) &= -\frac{2\hbar}{\pi^2 R^2} \\ &\times \sum_{n=0}^{\infty}{}' \int_0^{\infty} dk I_n^2(kR)[n^2 + (kR)^2 + (kR)^2\Psi_n^2(kR)] \\ &\times \int_0^{\infty} \frac{\alpha(i\omega)(\varepsilon(i\omega) - 1)K_n'(ka)K_n(ka)}{\varepsilon(i\omega)I_n(ka)K_n'(ka) - I_n'(ka)K_n(ka)} d\omega. \end{aligned} \tag{20}$$

The passage to the approximation of small velocities in formulas (12) and (16)–(18) is carried out similarly to the case of a flat surface [4–7]. For example, in the linear approximation with respect to the velocity, formula (18) is rearranged to the form

$$\begin{aligned} F(R, V) &= -\frac{2\hbar V}{\pi^2 R^2} \\ &\times \sum_{n=0}^{\infty}{}' \int k^2 C_n(k)[n^2 + (kR)^2 + (kR)^2\Psi_n^2(kR)]dk, \end{aligned} \tag{21}$$

$$\begin{aligned} C_n(k) &= I_n^2(kR) \\ &\times \int_0^{\infty} d\omega \left\{ 2\left[\alpha''(\omega)\frac{d\tilde{\Delta}_n''(\omega)}{d\omega} - \tilde{\Delta}_n''(\omega)\frac{d\alpha''(\omega)}{d\omega}\right] \right. \\ &\left. + \omega\left[\alpha''(\omega)\frac{d^2\tilde{\Delta}_n''(\omega)}{d\omega^2} - \tilde{\Delta}_n''(\omega)\frac{d^2\alpha''(\omega)}{d\omega^2}\right]\right\}\coth\left(\frac{\omega\hbar}{2k_{\text{B}}T}\right). \end{aligned} \tag{22}$$

Let us note that the dependence of the coefficient $C_n(k)$ on the wave vector is determined not only by the factor before the integral, but also by the corresponding dependence of the functions $\tilde{\Delta}_n''(\omega)$ [see formula (19)]. By and large, the expansion of the lateral force in terms of the velocity contains only odd powers and the expansion of the normal force of the attraction to the surface involves only even powers (beginning with the zero power).

In order to carry out practical calculations according to formulas (21) and (22), it is appropriate to remove the factors depending on the wave vector in the numerator and denominator in the $\tilde{\Delta}_n''(\omega)$ function, by combining them with the square of the Bessel function $I_n^2(x)$, after which formula (22) takes the form

$$\begin{aligned} C_n(k) &= A_n(k) \\ &\times \int_0^{\infty} d\omega \left\{ 2\left[\alpha''(\omega)\frac{dD_n(\omega, k)}{d\omega} - D_n(\omega, k)\frac{d\alpha''(\omega)}{d\omega}\right] \right. \\ &\left. + \omega\left[\alpha''(\omega)\frac{d^2 D_n(\omega, k)}{d\omega^2} - D_n(\omega, k)\frac{d^2\alpha''(\omega)}{d\omega^2}\right]\right\} \\ &\times \coth\left(\frac{\omega\hbar}{2k_{\text{B}}T}\right), \end{aligned} \tag{23}$$

$$D_n(\omega, k) = \operatorname{Im}\frac{\varepsilon(\omega) - 1}{\varepsilon(\omega) + B_n(k)}, \tag{24}$$

$$A_n(k) = I_n^2(kR)K_n(ka)/I_n(ka), \tag{25}$$

$$B_n(k) = -\frac{K_n(ka)I_n'(ka)}{K_n'(ka)I_n(ka)}. \tag{26}$$

It is an easy matter to demonstrate with the asymptotics of the cylinder functions that when ka and $kR \gg 1$, we have $\Psi_n^2(kR) \longrightarrow 1$, $B_n(k) \longrightarrow 1$, and $A_n(k) \longrightarrow \exp(-2kh)/2kR$. In this case, the dependence of the integrand obtained in formula (21) on h and on $\varepsilon(\omega)$ is the same as in the case of a flat surface. Nonetheless, the passage to the limit of the flat case, when $R \longrightarrow \infty$, is not a trivial one, since the terms with large indices n contribute significantly to the sum of the cylinder functions in the right-hand side of formula (21). The summation of this series is a separate problem.

If we disregard the possible effect of the temperature on the $\varepsilon(\omega)$ function, the linear temperature dependence of integral (23) manifests itself only in the range of low frequencies when $\coth(\omega\hbar/2k_BT) \longrightarrow 2k_BT/\omega\hbar$. In the case when the absorption spectra of the particle and the surface overlap in the high-frequency range, we have $\coth(\omega\hbar/2k_BT) \longrightarrow 1$. Carrying out integration by parts in formula (23), we obtain

$$C_n(k) = 2A_n(k)\int_0^\infty d\omega\alpha''(\omega)\frac{dD_n(\omega, k)}{d\omega}. \qquad (27)$$

Hence, there always exists a finite frictional force at $T = 0$.

6. CONCLUSION

Thus, employing a minimum of constraints, we derived the most general nonrelativistic formulas for the conservative (attracting) and dissipative (retarding) fluctuation electromagnetic forces exerted on a neutral atom moving parallel to the generatrix of a cylindrical surface. The derived formulas allow one to calculate these forces for arbitrary velocities of the particles, the temperature of the surface, and the dielectric properties of the particle and the surface. When both the velocity and the temperature vanish, the formulas for the conservative potential (van der Waals potential) coincide with the known results of other authors.

The expansion of the fluctuation forces into a power series in terms of the velocity proceeds by even powers for the attracting (conservative) forces and by odd ones for the dissipative forces, which is similar to the case of a flat surface when there exists a nonzero contribution to both forces at $T = 0$.

REFERENCES

1. G. V. Dedkov, Usp. Fiz. Nauk **170** (6), 585 (2000).
2. G. V. Dedkov, Nucl. Instrum. Methods Phys. Res., Sect. B **143** (4), 584 (1998).
3. G. V. Dedkov and B. S. Karamurzov, Surf. Coat. Technol., No. 128/129, 51 (2000).
4. G. V. Dedkov and A. A. Kyasov, Phys. Lett. A **259** (1), 38 (1999).
5. G. V. Dedkov and A. A. Kyasov, Pis'ma Zh. Tekh. Fiz. **25** (12), 10 (1999) [Tech. Phys. Lett. **25**, 466 (1999)].
6. A. A. Kyasov and G. V. Dedkov, Surf. Sci. **453**, 11 (2000).
7. G. V. Dedkov and A. A. Kyasov, Fiz. Tverd. Tela (St. Petersburg) **43** (1), 169 (2001) [Phys. Solid State **43**, 176 (2001)].
8. A. A. Kyasov, Available from VINITI, No. 1407-B91 (1991).
9. M. Schmeits and A. A. Lucas, Surf. Sci. **64** (1), 176 (1977).
10. M. Schmeits and A. A. Lucas, Prog. Surf. Sci. **14** (1), 1 (1983).
11. V. M. Nabutovskiĭ, V. R. Belosludov, and A. M. Korotkikh, Zh. Éksp. Teor. Fiz. **77**, 700 (1979) [Sov. Phys. JETP **50**, 352 (1979)].

Translated by O. Moskalev

Physics of the Solid State, Vol. 43, No. 3, 2001, pp. 579–582. Translated from Fizika Tverdogo Tela, Vol. 43, No. 3, 2001, pp. 559–562.
Original Russian Text Copyright © 2001 by Shul'pina, Ratnikov, Matveev.

LOW-DIMENSIONAL SYSTEMS AND SURFACE PHYSICS

X-ray Diffraction Study of Changes in the CdTe Monocrystal Real Structure Induced by Laser Radiation

I. L. Shul'pina, V. V. Ratnikov, and O. A. Matveev
Ioffe Physicotechnical Institute, Russian Academy of Sciences, Politekhnicheskaya ul. 26, St. Petersburg, 194021 Russia
e-mail: Irene.Shulpina@shuvpop.ioffe.rssi.ru

Received July 27, 2000

Abstract—The changes in the real structure of CdTe monocrystals caused by the thermal action of a high-power laser pulse (1.6–1.97 J/cm^2) were studied by high-resolution x-ray topography and diffractometry methods. It was shown that, under our experimental conditions, in a thin surface layer within the crystal region exposed to the radiation, a dislocation cell structure with an increased dislocation density and with considerable micromisorientations, in comparison with the crystal region unexposed to the radiation, was formed. The characteristics of this modified crystal region were determined, and the thickness of the layer with the changed structure was estimated. *© 2001 MAIK "Nauka/Interperiodica".*

INTRODUCTION

Laser-stimulated impurity intrusion into materials is a modern technological operation, and it is largely used in optoelectronics for the creation of different device structures. However, this procedure is accompanied by heat action which may cause changes in the real structure of the material and in the corresponding electrophysical properties. Therefore, it is of considerable interest to study the structure of crystals exposed to radiation. A specific feature of the laser-stimulated impurity intrusion into CdTe monocrystals is the heating of only a thin surface layer [1]. Thus, the structure is changed only within this surface layer. It was shown in [2, 3] by the x-ray topography method that an increase in the laser beam power from 0.3 to 16 J/cm^2 leads first to a decrease in the number of structural imperfections of the crystal surface layer exposed to radiation, which is due to annealing of the surface defects. Then, there occurs deterioration of the structure, which is accompanied by the formation, development, and degradation of an ordered network of fine twins. Further on, this network is transformed into a dislocation cell structure. This cell structure of an irradiated region cannot be resolved in detail by the single-crystal inverse reflection method for low angles of incidence of the x-ray beam. Only the use of the two-crystal method allowed one to identify the features of this structure. To improve the resolution for observation of the structure details, we used the two-crystal topography method with a low dispersion of the incident beam. This technique was utilized in order to find the optimal conditions for the crystal filming and then to use combined high-resolution x-ray diffractometry methods in order to obtain additional quantitative data about the structure under study for its full description.

At high beam powers, the changes in the CdTe structure induced by the heat action of pulsed laser radiation, in the impurity injection regime, are associated with recrystallization, that is, instant melting and further crystallization of the thin surface layer. In calculations, the thickness of the melted layer is usually determined from the laser power and thermophysical properties of CdTe. A wide range of data on this thickness can be found in the literature [1, 4]. There is even less information on the layer thickness in which the structure changes, despite the fact that this information is of undeniable interest, since it is necessary for the development of different devices. We have not been able to determine this thickness by topography methods; however, there is hope that it can be done by using high-resolution x-ray diffractometry [5].

1. DESCRIPTION OF EXPERIMENTAL SAMPLES

Crystals grown from the melt in the nongradient heat field of a furnace [6] were investigated. The $8 \times 8 \times 1.5$ mm-size samples were cut from monocrystal plates oriented parallel to the (111) plane. The sample surface was prepared by means of mechanical grinding and polishing with further long chemical etching, in order to remove the damaged layer. Samples for investigation were chosen by means of estimation of their real structure using the x-ray back reflection method [2]. The samples chosen did not contain blocks and had the most homogeneous structure. However, they contained subgrains and low-angle grain boundaries. They were characterized by the presence of microstresses and by a mean dislocation density of about $\approx 10^5$ cm^{-2}, which is typical of the best CdTe crystals grown from the melt.

Table 1. Calculated angular dispersion D of a working beam and the half-width ω of the two-crystal reflection curve for determination of the optimal conditions for CdTe crystal filming

Monochromator			CdTe sample, (111)			
Crystal, orientation	*hkl*, geometry	ω_m, arcsec	$-m$, *hkl*	ω_0, arcsec	D, arcsec	ω, arcsec
Ge(111)	111, ac.	3.1	620, ac.	1.8	72	72.1
Ge(111)	333, c.	4.2	620, ac.	1.8	10.8	15.4
Ge(211)	422, c.	10.0	620, ac.	1.8	20.0	22.5
Si(100)	400, c.	3.4	620, ac.	1.8	47.0	47.2
Si(211)	422, c.	2.8	620, ac.	1.8	14.4	15.3
Si(111)	331, ac.	1.25	422, ac.	3.5	5.4	6.7

A pulsed OGM-40 laser with a ruby head (wavelength $\lambda = 0.694$ μm, absorption coefficient $K = 6 \times 10^4$ cm^{-1}) was used to irradiate the samples. The pulse duration was 20 ns. To focus and to homogenize the radiation over the beam cross section, a quartz focon having the form of a truncated cone was used. Its input end had a mat surface, and its output diameter was 0.7 cm. The sample was placed at a distance of 0.05 mm from the focon output end. The 1.61–1.97 J/cm^2 radiation powers were used. The irradiated region had the form of a circle with a diameter of 0.7 cm.

2. METHODS OF INVESTIGATION

High-resolution x-ray topography and diffractometry methods in the Bragg geometry were used in our studies. The two-crystal method with the *n*, –*m* scheme was utilized [5] for topographic studies. The resolution of defect images is improved in this method with lowering of the dispersion of the working beam and with the decreasing width of the two-crystal reflection curve. This allowed us to determine the optimal conditions for crystal filming, first, by means of calculations and, further on, by experimental realization.

The working beam dispersion D and the half-width of the two-crystal reflection curve ω were calculated according to formulas of the dynamic x-ray diffraction theory [7]:

$$D = \Delta\lambda/\lambda(\tan\theta_m - \tan\theta_0), \quad (1)$$

$$\omega = (\omega_m^2 + \omega_0^2 + D^2)^{-1/2}, \quad (2)$$

where

$$\omega_{m,0} = 2C\chi_h\sqrt{\sin(\theta+\alpha)/\sin(\theta-\alpha)}e^{-M}/\sin 2\theta. \quad (3)$$

Here, $\Delta\lambda/\lambda$ is the wavelength dispersion for the Cu$K\alpha_1$ line; θ_m and θ_0 are the Bragg angles for the monochromator and the sample, respectively; ω_m and ω_0 are the half-widths of the reflection curves of the monochromator and the sample, respectively; C is the polarization factor; χ_h is the Fourier component of polarizability; e^{-M} is the heat multiplication factor; and α is the angle between the reflecting plane and the crystal surface. The calculation data are summarized in Table 1.

The optimal conditions for the improvement of the resolution of the structure details corresponded to the last line of Table 1. It was found experimentally that for the asymmetric reflection 331 from a perfect Si crystal (for the (111) surface orientation), it was possible to obtain a working x-ray beam with a low angular divergence and relatively high intensity. When the asymmetric reflection 422 from a CdTe sample was used, it was not necessary to scan the crystal and the photographic plate during the exposure.

The two- and three-crystal methods were utilized for the diffractometric studies. Both the 111 and 333 reflections in the symmetric Bragg geometry and the 620 reflection in the asymmetric geometry for the CuK_{α_1}-radiation were used. For the three-crystal method, the reflection curves were recorded for the θ- and θ–2θ-scanning modes.

3. EXPERIMENTAL RESULTS

(1) Nonirradiated samples. The initial nonirradiated samples were inhomogeneous over their surface and were characterized by a mosaic structure. The fragment sizes ranged from 0.4 to 1 mm. The misorientation of fragments was of the order of 10″–20″. The samples contained low-angle grain boundaries and isolated inclusions (probably, of Te), and there were macrostresses in them. The inclusions were of the dislocation-cell type. The cells had an irregular form. The average linear size of the dislocation cells was 40–50 μm; the mean dislocation density, according to the topographic studies, was approximately ≈10^5 cm^{-2}.

The shape of two-crystal scanning curves of the initial samples was varied when shifting along the crystal. It followed from the analysis of the three-crystal θ and θ–2θ-scanning curves that there were no gradients of the interplanar spacing along the normal to the surface and that the shape of the scanning curves was determined by the misorientation of the crystal fragments due to the residual macrostresses and to the inhomoge-

Table 2. Half-widths ($\omega_{\theta,\,\theta-2\theta}$) of diffraction curves and the density of chaotic (ρ) and small-angle-boundary dislocations (ρ^{c1})

CdTe sample	ω_{θ}^{111}, arcsec	$\omega_{\theta-2\theta}^{111}$, arcsec	ω_{θ}^{333}, arcsec	$\omega_{\theta-2\theta}^{333}$, arcsec	ρ, 10^8 cm^{-2}	ρ^{c1}, 10^6 cm^{-2}
Initial	21	21	38	14		
No. 1	141	31	110	46	0.5	3.5
No. 2	250	38	119	55	1.6	6.3

neously distributed dislocations. At the same time, measurements of the three-crystal curves in the scheme with the fixed position of a sample and with a rotating analyzer, which allowed one to distinguish the dynamic and incoherent components in the diffracted radiation intensity, showed that the scattering is totally incoherent in the 111 reflection (CuK_α radiation, absorption depth 1.7 μm). An analogous result for chemically and mechanically polished samples of CdTe was obtained earlier in [7]. It indicated the presence of a disordered surface layer formed as a result of insufficient chemical polishing.

(2) Irradiated samples. The irradiated region with a diameter of 0.7 cm was characterized by an increased reflected x-ray intensity in comparison with nonirradiated regions of the sample. The structure of the irradiated region was not revealed when studied by the single-crystal back reflection method. When the two-crystal method was used, according to the *n*, –*m* scheme, with the Ge monocrystal as a monochromator in the 111 reflection for CuK_α radiation, the structure of the irradiated region was revealed and it was presumably of the fine dislocation-cell type. The high-resolution topograms, obtained using the Si crystal in the 331 asymmetric reflection, provided support for the cell character of the dislocation structure in the irradiated zone. The dislocation cells had an irregular form, and their mean linear size was 15–20 μm. This is 2.5 times lower than the dislocation cell size in the bulk of crystals and outside the irradiated region. The average density of dislocations inside the irradiated region was estimated to be approximately $\approx 10^6$ cm^{-2}. Due to the higher dislocation density and to the smaller dislocation cell sizes, the structural homogeneity in the irradiated zone was higher than outside it and than in the original crystals. For a low angular dispersion of the working beam, some fragments of the irradiated region ceased to contribute to the reflection.

The data of the diffractometry investigation are shown in Table 2.

The values of the half-width of the reflection curves outside the irradiated zone are represented in the first line of Table 2. The half-widths for the 111 and 333 reflections, calculated by means of the dynamic theory of x-ray scattering, are equal to 20.7′ and 4.7′, respectively. The values of the half-width of the reflection curves for two values of the radiation power of a laser beam are given in the second and third lines of Table 2.

Almost all studied samples possess an imperfect surface layer, which is probably due to insufficient chemical polishing.

The laser radiation leads to considerable broadening of the Bragg curves, which suggests that the dispersion of the reciprocal lattice vector is increased, mainly due to misorientation. The structure homogeneity, in general, is higher inside the irradiated region than outside it. This is because the coherent-scattering regions become finer. The initial crystals, as well as the regions outside the irradiated zone, are characterized by a mosaic structure with fragment misorientation on the order of 10″–20″. The fragment size is about 0.4–1.0 mm. The lattice parameter remains unchanged.

First, we estimated the density of dislocations, according to [8], by assuming their chaotic distribution:

$$\rho = \omega^2/4.35b^2, \tag{4}$$

where $b = 0.458$ nm is the Burgers vector of dislocations.

The corrections, which take into account the intrinsic half-width of the diffraction curves and the sample bend, were added to the experimental values of the half-widths. For the structures of all samples studied, the model of the chaotic distribution of dislocations gives increased dislocation densities up to 0.5×10^8 cm^{-2} for the laser radiation power of 1.61 J/cm^2 and up to 1.6×10^8 cm^{-2} for the 1.97 J/cm^2 power. However, the topographic studies detect such a dislocation density neither in the initial nor in the irradiated crystal samples and indicate the structure for which dislocations are mainly gathered inside the walls of dislocation cells. Then, we used a model in which dislocations produce small-angle boundaries inside the micrograin (or cell) walls. The dislocation density can be calculated in this case by using the formula [9]

$$\rho^{cl} = \omega^2/(2.1b\tau_x), \tag{5}$$

where the value of the spacing between boundaries τ_x was taken from the data on topographic investigations.

Analysis of a considerable broadening of the reflection curves for irradiated crystals in comparison with the initial crystals revealed that the principle reason for this is the misorientation of the diffraction planes or of the coherent scattering regions (cells).

When analyzing the diffraction data, we took into account different x-ray absorption depths, 1.7, 5.0, and 1.5 μm for the 111, 333, and 620 reflections, respectively. Similar values of the absorption depth and of the half-width of the scanning curves for the 111 and 620 reflections, on the one hand, and the abrupt fall of the anisotropy for the reciprocal lattice site for the 333 reflection, on the other, allow us to consider that the diffracted intensity of the 111 and 620 reflections is mainly determined by the surface layer whose structure is different from that of the crystal bulk. The 333 reflection intensity is also determined by the sample region being below this layer. Thus, the thickness of the crystal layer that has a structure modified by laser radiation can be evaluated as the x-ray absorption depth for the 111 and 620 reflections, i.e., a value of about 1.5 μm.

4. DISCUSSION OF RESULTS

We note a good correspondence of the data obtained by the topography and diffractometry methods. A single exception is the evaluation of the density of dislocations by supposing their chaotic distribution. For a correct estimation of this characteristic of the dislocation structure, the correlation of the diffractometric and topographic results of our investigation should be assumed. To our mind, this is due to the fact that in the 5×10^4–1×10^8 cm^{-2} dislocation density interval, a chaotic distribution of dislocations in the bulk crystals is rarely observed. The dislocation cell structure with the dislocation arrangement in more or less dense networks at the boundaries of irregularly shaped cells is more common. Under certain conditions (in the course of epitaxy, impurity diffusion, etc.), regularly shaped cells can arise as elements of a misfit dislocation network. However, the distribution of dislocations is far from being chaotic in this case. This should be taken into consideration when estimating the dislocation density on the basis of a real crystal structure by indirect (rather than direct) methods.

Thus, we observed that, due to the action of the 1.6–2.0 J/cm^2-power pulsed laser radiation, a change in the real structure of an approximately 1.5 μm-thick surface layer took place. The irradiated crystal can be considered as some kind of a sandwich. The greater part of its bulk has a typical large-sized dislocation cell structure, but the thin surface layer has a fine dislocation cell structure with an increased dislocation density and with considerable micromisorientations of the cells. The latter structure occurs quite rarely. That is why it is of interest to study its role in processes of laser-stimulated injection of different impurities and in optical and some other properties of materials [10].

ACKNOWLEDGMENTS

This work was supported by the Russian Foundation for Basic Research, grant no 98-02-18309.

REFERENCES

1. R.O. Bell, M. Toulermonde, and P. Siffert, J. Appl. Phys. **19**, 313 (1979).
2. I. L. Shul'pina, N. K. Zelenina, and O. A. Matveev, Fiz. Tverd. Tela (St. Petersburg) **40** (1), 68 (1998) [Phys. Solid State **40**, 59 (1998)].
3. I. L. Shul'pina, N. K. Zelenina, and O. A. Matveev, Fiz. Tverd. Tela (St. Petersburg) **42** (3), 548 (2000) [Phys. Solid State **42**, 561 (2000)].
4. L. A. Golovan', P. K. Kashkarov, V. M. Lakeenkov, *et al.*, Fiz. Tverd. Tela (St. Petersburg) **40** (2), 209 (1998) [Phys. Solid State **40**, 187 (1998)].
5. D. K. Bowen and B. K. Tanner, *High Resolution X-ray Diffractometry and Topography* (Tailor and Francis, London, 1998), p. 252.
6. Patent No. 143391 (June 20, 1986).
7. V. V. Ratnikov, L. M. Sorokin, V. N. Ivanov-Omskiĭ, *et al.*, Pis'ma Zh. Tekh. Fiz. **14** (15), 1410 (1988) [Sov. Tech. Phys. Lett. **14**, 615 (1988)].
8. P. Gay, P. B. Hirsch, and A. Kelly, Acta Metall. **1** (2), 315 (1953).
9. P. F. Fewster, J. Appl. Crystallogr. **22** (1), 64 (1989).
10. N. K. Zelenina and O. A. Matveev, Pis'ma Zh. Tekh. Fiz. **24** (11), 1 (1998) [Tech. Phys. Lett. **24**, 411 (1998)].

Translated by A. Sonin

Physics of the Solid State, Vol. 43, No. 3, 2001, pp. 583–588. Translated from Fizika Tverdogo Tela, Vol. 43, No. 3, 2001, pp. 563–568.
Original Russian Text Copyright © 2001 by Isakov, Karpel'ev.

LOW-DIMENSIONAL SYSTEMS AND SURFACE PHYSICS

Anomalous Mass Transport in the Vicinity of the Interface of Two Metallic Media

M. G. Isakov and V. A. Karpel'ev

Bardin Central Research Institute for Iron and Steel Industry, Vtoraya Baumanskaya ul. 9/23, Moscow, 107005 Russia
e-mail: ferrumsc@websrv.crifm.gost.ru

Received June 9, 2000; in final form, August 3, 2000

Abstract—Diffusion of nickel in copper was studied experimentally in a temperature range of 250–375°C in the "coating (nickel)–metal (copper)" system using a radioactive isotope ^{63}Ni. Anomalously high values of the diffusion coefficients and an anomalously low value of the activation energy were found. To explain the effect, a new way of describing the diffusion phenomena in the vicinity of the interface of two metallic media is suggested, which takes into account the presence of high gradients of chemical potentials near the boundary. Based on the principles of nonlinear thermodynamics of irreversible processes, a system of differential equations of diffusion in the vicinity of the interface was obtained. Analysis of the kinetics of the diffusion zone formation revealed that chemical-potential gradients significantly accelerate the diffusion process in the vicinity of the interface. A comparison of the calculated kinetics of the formation of a diffusion zone with that obtained upon the experimental investigation of diffusion shows their qualitative agreement. *© 2001 MAIK "Nauka/Interperiodica".*

INTRODUCTION

In practice, there are frequently encountered metallic systems containing various interfaces, e.g., coatings on metallic surfaces, bimetallic compositions, contacts of details made of unlike materials, etc. In many cases, such systems are subjected to additional treatments to improve their physical and mechanical properties, or their service regime corresponds to enhanced temperatures, which causes diffusion redistribution of the components of the contacting metallic materials. On the whole, a well-developed theoretical apparatus exists at present to describe processes of this type, which permits one to make sufficiently reliable predictions [1].

At the same time, when studying diffusion processes in metal–coating systems at low temperatures, experimental data were obtained in some cases that indicated a deviation from the known laws. Thus, based on the investigations of diffusion in various irradiated metal–coating systems, it was, e.g., established [2] that, upon the irradiation of the Mn-coated Ni–10% Mn alloy with gamma photons at room temperature, the diffusion coefficient is close in order of magnitude to the coefficient of thermal diffusion at 850°C. Similar results were observed on other metals with coatings. In terms of radiation-stimulated diffusion, such an increase in diffusion coefficients could not be explained; therefore, an assumption was made that the nature of the observed effect is related to the presence of concentration gradients of the alloy components in the vicinity of the coating–metal interface.

The aim of this work is to experimentally study diffusion in metal–coating systems at low temperatures (below 500°C) and to theoretically describe diffusion processes in regions adjoining the interface with allowance for large gradients of the component concentrations.

1. EXPERIMENTAL INVESTIGATION OF DIFFUSION IN THE METAL–COATING SYSTEMS[1]

The experimental investigation of diffusion in the presence of large concentration gradients was performed with the help of the absorption radiotracer method [3]. The essence of the method is as follows. A sample is covered with a coating containing a radiotracer and is subjected to controlled annealings; then, the kinetics of the activity decay at the surface is studied (the decay is due to the absorption of the radiation of the tracer because of its diffusive penetration into the bulk of the sample during the diffusion annealing). The diffusion coefficient is determined from a comparison of the experimental and theoretical kinetic dependences.

As the samples for the investigation, we used polycrystalline copper; as a coating, nickel was employed, which was labeled with a radioactive isotope ^{63}Ni, having a soft β radiation, and was applied electrolytically onto one of the surfaces of the sample. The coating thickness was 0.02 μm. Annealings were performed in a vacuum chamber. The temperature range of diffusion annealings was between 250 and 375°C. The annealing duration was 4–4.5 h. Despite the relatively low diffusion temperature and relatively short duration of the

---

[1] This work was performed in cooperation with V.A. Lazarev.

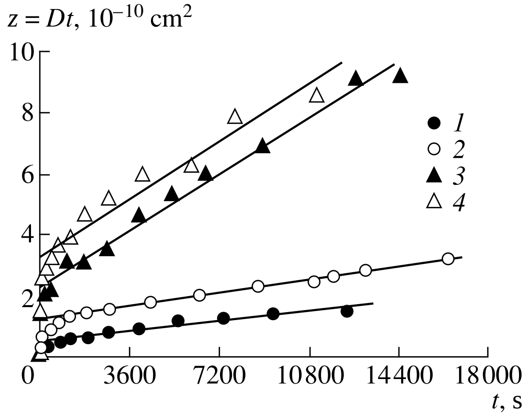

Fig. 1. Experimental and theoretical (Eq. (1)) dependences of the intensity of radiation from a sample for various temperatures of diffusion annealing: (*1*) 250, (*2*) 300, (*3*) 350, and (*4*) 375°C.

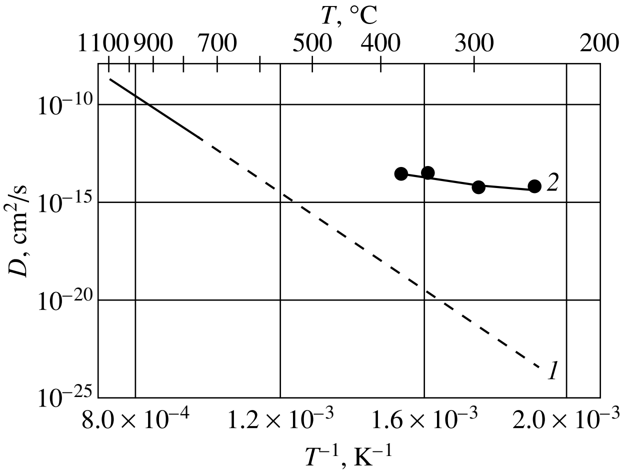

Fig. 2. Temperature dependence of the diffusion coefficients of nickel in copper: (*1*) according to [5] and (*2*) obtained in this work.

diffusion annealing, the large sensitivity of the technique employed [4] permitted us to obtain reliable kinetic dependences of the variation of activity. The experimental kinetic curves were compared with a theoretical dependence of the radiation intensity of the form

$$\frac{I(t)}{I(0)} = \frac{\int\limits_0^{\infty}\left[\operatorname{erf}\left(\frac{l-x}{2\sqrt{Dt}}\right)+\operatorname{erf}\left(\frac{l+x}{2\sqrt{Dt}}\right)\right]\exp(-\mu x)dx}{2l\int\limits_0^{\infty}\exp(-\mu x)dx}, \quad (1)$$

where $I(0)$ is the intensity of radiation from the sample at the initial time moment, $I(t)$ is the current intensity of radiation from the sample, l is the thickness of the coating, x is the coordinate, D is the diffusion coefficient, t is the time, and μ is the absorption coefficient for the β radiation of ^{63}Ni ($\mu = 25000$ cm^{-1}). The results of the comparison are shown in Fig. 1. An analysis of the data shows that the experimental kinetic curves do not correlate with the theoretical linear curves for the entire time of diffusion annealing in the temperature range of 250–375°C. This difference is especially noticeable at the first stages of the diffusion annealing. One of the causes for such a behavior may be the dependence of the diffusion coefficient on time.

However, from the curves of the comparison of experimental and theoretical kinetic dependences (Fig. 1), we can arbitrarily distinguish a certain time moment beginning at which the indicated dependence can satisfactorily be considered to be linear with a constant value of the diffusion coefficient. Such an operation was performed and is shown in Fig. 1. The temperature dependence of the diffusion coefficients calculated without allowance for the initial stages of the diffusion annealing is displayed in Fig. 2 (curve *2*). It is seen that it can satisfactorily be described by the well-known exponential Arrhenius law $D = D_0\exp(-Q/RT)$. For the above temperature range, we have $D_0 = (7.57 \pm 0.16) \times 10^{-11}$ cm^2/s and $Q = 10.5 \pm 2.5$ kcal/mol. For comparison, Fig. 2 displays (curve *1*) data for the diffusion of nickel in copper in the temperature range of 743–1076°C [5] ($D_0 = 2.7$ cm^2/s, $Q = 56.5$ kcal/mol). The extrapolation of the indicated temperature dependence into the region of low temperatures is given in Fig. 2 by the dashed line. The comparison of the activation energy of diffusion for nickel in copper obtained in this work with literature data shows its significant (by more than a factor of five) decrease. This level of the activation energy of diffusion is anomalously low; it is intermediate between the energies of migration of vacancies (≅15 kcal/mol) and interstitials (≅5 kcal/mol) [6]. Depending on the temperature, the diffusion coefficients of nickel obtained by us are lower by 7–13 orders of magnitude than those interpolated from literature data.

The high diffusion mobility of nickel in polycrystalline materials at low temperatures can be explained by the operation of several mechanisms (grain-boundary diffusion, diffusion via defects, etc.). However, the predominance of grain-boundary diffusion at low temperatures leads to a decrease in the activation energy only by a factor of 1.4–2.8 [7]. If we take into account that the transition layer between the coating and the metal is strongly defective, we may assume that this can facilitate diffusion processes. However, the results of [8] indicate that the activation energy of nickel diffusion via defects is ≅26.6 kcal/mol, which is greater by a factor of 2.5 than that obtained in our experiments.

One more mechanism of acceleration of diffusion is the effect of high gradients of chemical potentials in the vicinity of the interface.

2. THEORETICAL DESCRIPTION OF DIFFUSION PROCESSES IN THE COATING–METAL SYSTEM WITH ALLOWANCE FOR HIGH CONCENTRATION GRADIENTS OF COMPONENTS

A detailed analysis of diffusion processes in the presence of large gradients of concentrations and chemical potentials requires a special approach; the usual ways of description of diffusion processes cannot be used in this case. We write, proceeding from the principles of thermodynamics of irreversible processes [9], the expression for the diffusion flux of the component m in the form

$$-J_m = \sum_j L_{mj}\nabla\mu_j + \frac{1}{3!}\sum_{j,k,n} L_{mjkn}\nabla\mu_j\nabla\mu_k\nabla\mu_n, \qquad (2)$$
$$(m, j, k, n = A, B, V),$$

where L_{mj} are the Onsager coefficients, L_{mjkn} are the kinetic coefficients, $\mu(c_j, c_k, c_m)$ are the chemical potentials, and c_m are the concentrations of the component m. The indices A, B, and V correspond to the metal of the coating, the metal of the base, and the vacancies, respectively.

Going from the gradients of chemical potential to gradients of concentration,

$$\nabla\mu_m = \sum_j \frac{\partial\mu_m}{\partial c_j}\nabla c_j, \quad (m, j = A, B, V), \qquad (3)$$

and using the condition of normalization for the concentrations,

$$\sum_m c_m = 1, \quad (m = A, B, V), \qquad (4)$$

we write the expression for the diffusion fluxes in the form

$$-J_m = \sum_j \bar{D}_{mj}\nabla c_j, \quad (m, j = A, B, V). \qquad (5)$$

In this expression, we have

$$\bar{D}_{mn} = (-1)^k c_V R_{mn}\begin{cases} k = 0, \text{ at } m = n \\ k = 1, \text{ at } m \neq n \end{cases}$$
$$(m, n = A, B),$$
$$\bar{D}_{AV} = -c_A R_{AV}, \qquad (6)$$
$$\bar{D}_{BV} = -c_B R_{BV},$$
$$R_{mn} = r_{mn} + \alpha_{mn}(\nabla c_A)^2 + \beta_{mn}(\nabla c_V)^2,$$
$$(m, n = A, B, V),$$

where r_{mn}, α_{mn}, and β_{mn} are the combinations of Onsager coefficients and derivatives of chemical potentials with respect to the concentrations of the components. In addition, the diffusion coefficients $\bar{D}_{mj}$ are related as follows [10]:

$$\sum_m \bar{D}_{mA} = 0, \quad \sum_m \bar{D}_{mB} = 0, \quad \sum_m \bar{D}_{mV} = 0, \qquad (7)$$
$$(m = A, B, V).$$

Using Eqs. (4)–(6) and taking into account the conditions of the limiting transition to a quasibinary system, we can show that the set of equations of diffusion of the components in the vicinity of the coating–metal interface is written as

$$\frac{\partial c_A}{\partial t} = \frac{\partial}{\partial x}\left(D_{AA}\frac{\partial c_A}{\partial x}\right) - \frac{\partial}{\partial x}\left(D_{AV}\frac{\partial c_V}{\partial x}\right),$$
$$\frac{\partial c_V}{\partial t} = -\frac{\partial}{\partial x}\left(D_{VA}\frac{\partial c_A}{\partial x}\right) + \frac{\partial}{\partial x}\left(D_{VV}\frac{\partial c_V}{\partial x}\right), \qquad (8)$$
$$c_A + c_B + c_V = 1.$$

Here,

$$D_{AA} = \bar{D}_{AA} - \bar{D}_{AB} = c_V\left[D_A + |\alpha_{AA} - \alpha_{BB}|\left(\frac{\partial c_A}{\partial x}\right)^2\right],$$
$$D_{AV} = \bar{D}_{AV} - \bar{D}_{AB} = c_A D_A,$$
$$D_{VA} = \bar{D}_{VA} - \bar{D}_{VB} = c_V(D_A - D_B),$$
$$D_{VV} = \bar{D}_{VV} - \bar{D}_{VB} = c_A D_A + (1 - c_A - c_V)D_B.$$

D_m ($m = a, B$) are the coefficients of the mobility of the component m and α_{AA} and α_{BB} are the kinetic coefficients.

The set of equations (8) is nonlinear; therefore, we used numerical calculations to analyze the kinetics of the formation of a diffusion zone in the vicinity of the coating–metal interface. The calculations were performed using the finite-difference scheme for the approximate solution of systems of nonlinear differential equations of the parabolic type [11].

The set of equations (8) was solved for two variants of the model of the interface: (i) the interface between two homogeneous semibounded media; and (ii) the interface between a thin coating and a semibounded medium.

2.1. Diffusion in the Vicinity of the Interface between Two Homogeneous Semibounded Media

Diffusion calculations for the model of the interface between two semibounded media were performed for the set of equations (8) with the initial conditions

$$c_A(x, 0) = c_A^1, \quad c_V(x, 0) = c_V^1, \quad (-\infty < x \le 0),$$
$$c_A(x, 0) = c_A^2, \quad c_V(x, 0) = c_V^2, \quad (0 \le x < +\infty) \qquad (9)$$

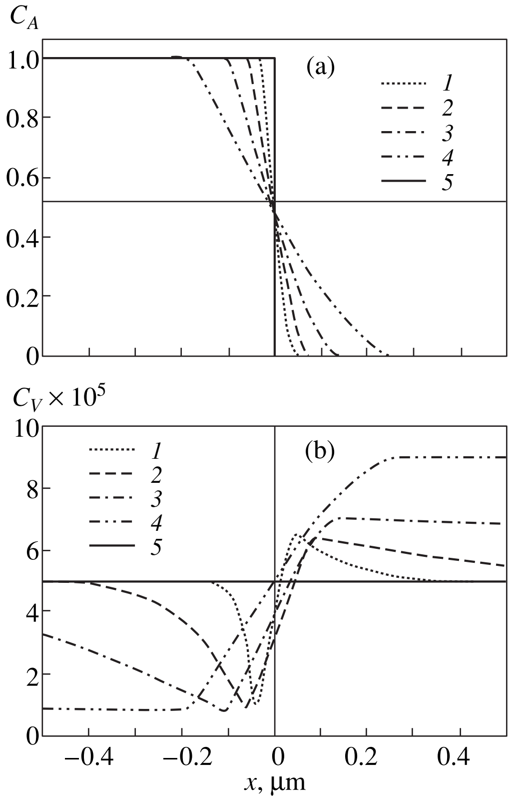

Fig. 3. Distribution of (a) the component A and (b) vacancies in the diffusion zone in the vicinity of the interface between two semibounded media as a function of time: t = (*1*) 1.25, (*2*) 12.5, (*3*) 125, (*4*) 1250 s, and (*5*) initial distribution. $D_A = 1 \times 10^{-11}$ cm²/s, $D_B = 1 \times 10^{-10}$ cm²/s, $c_V^1 = c_V^2 = 5 \times 10^{-5}$, and $\alpha = 10^{-17}$.

and boundary conditions

$$\begin{aligned} c_A(-\infty, t) &= c_A^1, \quad c_V(-\infty, t) = c_V^1, \\ c_A(+\infty, t) &= c_A^2, \quad c_V(+\infty, t) = c_V^2, \end{aligned} \tag{10}$$

where c_A^1 is the initial concentration of the component A in medium 1, c_A^2 is the initial concentration of the component A in medium 2, c_V^1 is the initial concentration of vacancies in medium 1, and c_V^2 is the initial concentration of vacancies in medium 2.

The solution of the set of equations (8) with the initial and boundary conditions (9), (10) was solved for various relations between the coefficients of mobility of the components. The cases $D_A = D_B$, $D_A < D_B$, and $D_A > D_B$ were considered. The initial concentration of vacancies in both media was the same; i.e., $c_V^1 = c_V^2$.

The effect of the magnitude of the gradient of concentration of the component A on its diffusion redistribution in the vicinity of the interface was studied by specifying various values of the kinetic coefficient $\alpha = |\alpha_{AA} - \alpha_{BB}|$. The results of the calculations indicate a substantial effect of the kinetic parameter α and of the gradient of concentration of the component A on the diffusion processes in the vicinity of the interface. As the parameter α increases, the zone of the redistribution of the components increases for any relationship between the mobility coefficients. Note also that the allowance for the gradient of concentration of the component A in the set of equations (8) noticeably changes the form of the kinetic dependences of diffusion in the vicinity of the interface. For $\alpha = 0$, the coordinates of points with a given concentration are proportional to $\sqrt{t}$. If $\alpha \neq 0$, the kinetic dependences deviate significantly from this law. The most intense development of diffusion processes near the interface is observed at the initial time moment, when the effect of the gradient of concentration of the component is particularly noticeable. As the diffusion time increases, the effect of the gradient decreases. This is connected with the magnitude of the gradient, which is maximum at $t \longrightarrow 0$. A mathematical treatment of the kinetic curves showed that for the initial time moments, the coordinate x is proportional to $\sqrt[4]{t}$.

The calculations showed that, for the cases $D_A < D_B$ and $D_A > D_B$, there is observed a redistribution of vacancy concentrations in the vicinities of the interface of the two semibounded regions considered (Fig. 3b), which is related to the difference in the mobilities of atoms in these regions. This difference leads to the appearance of a flux of vacancies from the region with a lower mobility to the region with a greater mobility. The observed distribution of vacancies corresponds to the idea of Bardeen and Herring that was employed by them for the explanation of the Kirkendall effect, according to which a redistribution of vacancies occurs with time under the effect of diffusion so that the extremal points are displaced further from the interface and the concentration of vacancies tends to fit to the magnitude of the coefficients of mobility of the components. The zone of the redistribution of vacancies exceeds the zone of the redistribution of component A (Fig. 3a).

2.2. Diffusion in the Vicinities of the Interface between a Thin Coating and a Semibounded Medium

Simulation of diffusion processes in the vicinity of the interface between a coating and a metal was performed with the use of the set of equations (8) with the initial conditions

$$\begin{aligned} c_A(x, 0) &= c_A^1, \quad c_V(x, 0) = c_V^1, \quad (-l < x \le 0), \\ c_A(x, 0) &= c_A^2, \quad c_V(x, 0) = c_V^2, \quad (0 \le x < +\infty) \end{aligned} \tag{11}$$

and boundary conditions

$$\begin{aligned} &J_A(-l, t) = 0, \quad J_V(-l, t) = 0, \\ &c_A(+\infty, t) = c_A^2, \quad c_V(+\infty, t) = c_V^2, \end{aligned} \tag{12}$$

where l is the thickness of the coating, J_A is the flux of component A, J_V is the flux of vacancies, c_A^1 is the initial concentration of component A in the coating, c_A^2 is the initial concentration of component A in the metal, c_V^1 is the initial concentration of vacancies in the coating, and c_V^2 is the initial concentration of vacancies in the metal.

The solution to the set of equations (8) with the initial and boundary conditions (11)–(12) was performed for various values of the coating thicknesses and various relationships between the coefficients of mobility of the components. Like in the case of two semibounded homogeneous media, we considered the variants $D_A = D_B$, $D_A < D_B$, and $D_A > D_B$. The initial concentration of vacancies in the coating and in the metal was assumed to be the same; i.e., $c_V^1 = c_V^2$.

Figure 4a displays the redistribution of component A in the diffusion zone for a 0.05-μm coating at a fixed time moment without allowance for the gradient of the concentration (curve *2*) and with allowance for this gradient (curve *3*). The mobility of component A is higher by an order of magnitude than that of component B; i.e., the condition $D_A > D_B$ is fulfilled. The allowance for the concentration gradient leads to a more significant redistribution of the components in the diffusion zone, which is analogous to an increase in the diffusion coefficient. The distribution of vacancies in this zone (Fig. 4b) correlates with the distribution of component A.

The allowance for the concentration gradient for the case where the mobility of the component of the coating is less than that of the base, i.e., $D_A < D_B$, just as in the case of $D_A > D_B$, leads to a faster diffusion redistribution of the components in the vicinity of the interface. The distribution of vacancies in the diffusion zone in this case correlates with the distribution of component B.

At equal mobilities of the components ($D_A = D_B$), there also occurs an acceleration of the diffusion redistribution in the vicinities of the interface with allowance for the gradient of concentrations of the components.

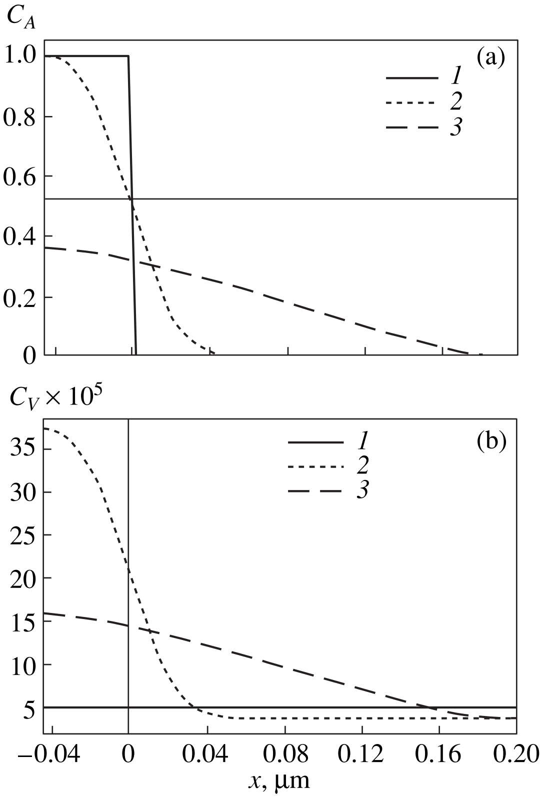

Fig. 4. Distribution of (a) the component A and (b) of vacancies in the diffusion zone in the vicinity of the interface between the coating and the metal ($D_A = 1 \times 10^{-10}$ cm^2/s, $D_B = 1 \times 10^{-11}$ cm^2/s, $c_V^1 = c_V^2 = 5 \times 10^{-5}$, $t = 5 \times 10^2$ s): (*1*) initial, (*2*) for $\alpha = 0$, and (*3*) for $\alpha = 10^{-17}$.

Based on the investigated regularities of the formation of the diffusion zone in the vicinity of the interface between the coating and the base metal, we simulated the kinetics changes in the intensity of radiation from the surface of the sample in the diffusion experiment. We assumed that a coating 0.02 μm thick of component A (containing the nickel isotope ^{63}Ni) was applied to the metallic base representing component B. The initial intensity of radiation $I(t)$ was determined in accordance with the expression $I(t) = \int_0^\infty c_A(x, t)\exp(-\mu x)dx$, where t is the time, x is the coordinate, μ is the absorption coefficient of the β radiation of ^{63}Ni, and $c_A(x, t)$ is the current concentration of nickel in the diffusion zone, which was determined from the solution of the set of equations (8) with the initial and boundary conditions (11), (12). The calculated values of $I(t)$ were normalized to the intensity of radiation at the initial time moment $I(0)$. The calculated kinetic curve of the intensity of radiation was compared, as in the case of the experiment, with the theoretical curve described by Eq. (1). The results of the comparison are given in Fig. 5. Note that in the case where the gradient of concentrations of the components has not been taken into account, a linear dependence is observed (curve *1*) between the calculated kinetic curve and the theoretical one. When the gradient of concentration was allowed for, a significant deviation of the comparison curve (curve *2*) from the linear dependence was observed. Such a course of curve *2* (Fig. 5) correlates sufficiently well with experimental data presented in

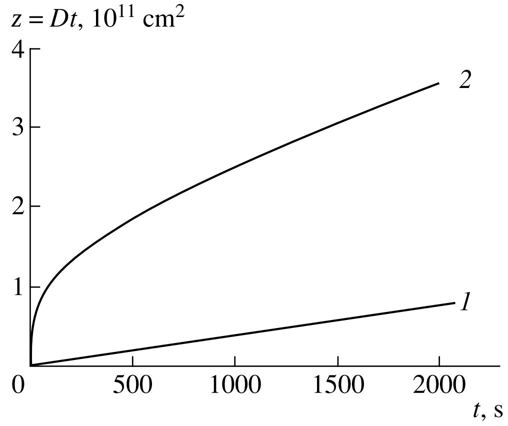

Fig. 5. Comparison of the calculated dependences of the change in the intensity of radiation at the surface of the sample with the theoretical curve (Eq. (1)): (*1*) without allowance for the gradient of concentration of the components ($\alpha = 0$) and (*2*) with allowance for the gradient of concentration ($\alpha = 10^{-20}$). The coating thickness is 0.02 μm, $D_A = D_B = 1 \times 10^{-10}$ cm^2/s.

Fig. 1 and, to a certain extent, corroborates the assumption on the effect of gradients of concentrations of the components on the kinetics of diffusion processes in the vicinities of the interface between two media. This effect should be especially pronounced at the initial time moments, when the gradients are large.

REFERENCES

1. N. D. Potekhina, Fiz. Tverd. Tela (St. Petersburg) **41** (9), 1712 (1999) [Phys. Solid State **41**, 1569 (1999)].
2. A. M. Shalaev, *Radiation-Enhanced Processes in Metals* (Énergoatomizdat, Moscow, 1988).
3. V. M. Golikov and V. T. Borisov, *Problems of Metallography and Physics of Metals* (Metallurgizdat, Moscow, 1955), Vol. 4, p. 528.
4. P. L. Gruzin, V. A. Lazarev, and S. G. Urytu, Zavod. Lab. **48** (5), 32 (1982).
5. C. A. Macliet, Phys. Rev. **109** (6), 1964 (1958).
6. A. C. Damask and G. J. Dienes, *Point Defects in Metals* (Gordon and Breach, New York, 1963; Mir, Moscow, 1966).
7. B. S. Bokshteĭn, *Diffusion in Metals* (Metallurgiya, Moscow, 1978).
8. S. D. Gertsriken and T. K. Yanenko, *Problems of Physics of Metals and Metallography* (Kiev, 1961), p. 135.
9. I. Gyarmati, *Non-Equilibrium Thermodynamics* (Springer-Verlag, Berlin, 1970; Mir, Moscow, 1974).
10. A. V. Nazarov and K. P. Gurov, Fiz. Met. Metalloved. **45** (4), 885 (1978).
11. A. A. Samarskiĭ, *The Theory of Difference Schemes* (Nauka, Moscow, 1977).

Translated by S. Gorin

Physics of the Solid State, Vol. 43, No. 3, 2001, pp. 589–595. Translated from Fizika Tverdogo Tela, Vol. 43, No. 3, 2001, pp. 569–575.
Original Russian Text Copyright © 2001 by Skryshevskiĭ, Vakhnin.

POLYMERS AND LIQUID CRYSTALS

Phototransformations in Polysilane Films

Yu. A. Skryshevskiĭ and A. Yu. Vakhnin

Institute of Physics, National Academy of Sciences of Ukraine, pr. Nauki 46, Kiev, 03039 Ukraine
e-mail: kadash@iop.kiev.ua

Received May 10, 2000

Abstract—The absorption (T = 295 K) and luminescence (T = 5 and 295 K) spectra of films of alkyl and aryl substituted polysilanes, namely, poly(dihexylsilane) (PDHS) and poly(methylphenylsilane) (PMPS), are investigated as functions of the time and the wavelength of light irradiation at T_{irr} = 5 and 295 K. It is shown that the photodegradation in polysilane films depends on the temperature, irradiation wavelength, and the structure of side substituents. The absorption of light by short chain segments in polysilanes at room temperature leads to competitive processes such as the transfer of excitation energy to longer segments, the scission of σ bonds between Si atoms, and the radiationless dissipation of excitation. It is revealed that, at T_{irr} = 295 K, the photodegradation of PDHS films is accompanied by the transformation of certain chain segments from a low-temperature *trans* conformation with an ordered arrangement of side hexyl groups to a high-temperature helical conformation with a disordered arrangement of side groups. *© 2001 MAIK “Nauka/Interperiodica”.*

1. INTRODUCTION

Polysilanes of the general formula $[–\text{Si}(\text{R}_1\text{R}_2)–]$ are the organosilicon polymers in which the main chains consist of Si atoms linked by σ bonds and R_1 and R_2 are the side organic groups. These compounds are characterized by a strong absorption in the near UV range, large quantum yields of luminescence and charge carrier photogeneration, high drift mobilities of holes [1–3], and nonlinear properties [2–4]; moreover, they also are known as highly sensitive self-developing photoresists [2, 5].

According to modern concepts [1–3], a polymer chain in polysilanes, like in π-conjugated polymers, contains different-sized segments which are separated by conformational defects. As follows from the estimates, a segment involves, on average, 20–25 monomer units. The lowest-lying excited state in the chain corresponds to the $^1(\sigma\sigma^*)$ transition of an electron delocalized along the segment axis. The absorption spectrum of polysilanes in the range of the $^1(\sigma\sigma^*)$ transition exhibits a structureless inhomogeneously broadened band whose shape is determined by the size distribution of chain segments. The spectrum of excited states in polysilanes was described within the models of Frenkel, Wannier–Mott, and mixed-type one-dimensional excitons [1, 3, 4, 6–10]. It seems likely that the properties of the lowest-lying excited state in polysilanes are most adequately described by the model of Frenkel one-dimensional excitons with a weak exciton–phonon bond [1, 3, 7, 8, 10].

Investigations into the dynamics of excited states in polysilanes revealed that the short-wavelength excitation leads to a fast (for τ = 0.7 ps) energy relaxation from high-lying excited states to the lowest-lying excited state [7, 10]. It was assumed that this process is attended with the scattering of electrons by phonons. Then, the energy is slowly (τ > 1 ps) transferred from short segments to the longer segments which are characterized by a lower excitation energy. This process occurs through the tunneling (jumps) of excitons over a system of disordered energy levels. The luminescence spectrum of polysilanes is associated with radiative transitions in long chain segments; in this case, the Stokes shift between absorption and emission in long chain segments is insignificant [1, 7].

It is known that exposure of polysilanes to light results in their degradation, which is accompanied by a decrease in the molecular weight of polymers and a decline in the absorption in the range of the $^1(\sigma\sigma^*)$ transition [2, 5, 11]. According to [2, 11], the photodegradation of a polymer starts with the scission of one or two σ bonds between Si atoms in a segment and with the formation of silyl and silylene radicals, respectively. Then, these radicals in polymers are involved in different chemical reactions, in particular, the attachment of oxygen and the formation of cyclic structures. Moreover, the cross-linking of polymer chains occurs in polysilanes which contain aryl side groups directly attached to Si atoms of the main chain. The induced absorption spectra of the alkyl and aryl substituted polysilane solutions and films irradiated with light pulses of lengths from 0.7 ps to 10 μs were studied by the flash photolysis technique in [7, 12–15]. It was found that the spectra depend on the structure of side groups in polymer chains, the pulse length, the wavelength of the incident light (λ_{irr} = 266–355 nm), and the delay time between light pulses and the onset of recording. Introduction of special quenchers into the solutions made it possible to reveal and identify absorption bands

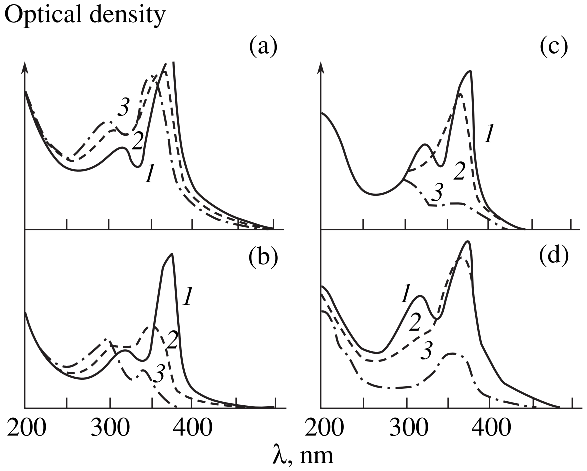

Fig. 1. Absorption spectra of PDHS films (T = 295 K) irradiated at T_{irr} = 295 K with light at wavelengths λ_{irr} = (a) 405, (b) 365, (c) 313, and (d) 265 nm. Irradiation time t_{irr}: (a) (*1*) 0, (*2*) 3, and (*3*) 15 min; (b) (*1*) 0, (*2*) 5, and (*3*) 70 s; (c) (*1*) 0, (*2*) 1, and (*3*) 3 min; and (d) (*1*) 0, (*2*) 3, and (*3*) 6 min.

which are associated with the formation of silyl and silylene radicals.

The absorption spectra of frozen solutions and films of poly(dihexylsilane) (PDHS) were examined by the spectral hole burning method [8, 16, 17]. It was shown that, after the selective excitation of short segments, the energy is transferred to longer chain segments followed by their photodegradation. In our earlier work [18], we revealed that the degradation processes in poly(methylphenylsilane) (PMPS) films considerably differ upon light irradiation in the ranges which correspond to the absorption of the main chain segments and side phenyl groups. In the present work, we investigated how the transfer of excitation energy between segments and also from the side substituents to the polymer chain segments affects the photodegradation processes in alkyl and aryl substituted polysilane films. For this purpose, the absorption (at T = 295 K) and luminescence (at T = 5 and 295 K) spectra of PDHS and PMPS films were studied as functions of the time t_{irr} of light irradiation at wavelengths λ_{irr} = 405, 365, 313, and 265 nm at T_{irr} = 295 K. The choice of the aforementioned polymers was motivated by the fact that their electronic properties were investigated in greater detail [1–3].

2. EXPERIMENTAL TECHNIQUE

The PDHS and PMPS films with thickness d = 0.5–10 μm were prepared by pouring toluene solutions of polymers onto fused silica substrates. The absorption spectra (T = 295 K) were recorded on a KSVU-23 spectrometric computer complex, and the luminescence spectra (T = 5–295 K) were measured on an SDL-1 spectrometer. The low-temperature investigations were performed using an optical temperature-controlled helium cryostate with quarts windows and an automatic system of control and stabilization of the temperature which was measured with a copper–constantan differential thermocouple. For excitation of luminescence or photodegradation, the polysilane films in air or a helium atmosphere in the cryostate were irradiated with a DRSh-250-2 ultrahigh-pressure mercury lamp through the absorption light filters. The relative photon distribution with account for the filtration at λ = 405, 365, 313, and 265 nm was equal to 4 : 8 : 1.5 : 1. The power densities Φ of lamp radiation at λ = 365 nm upon irradiation of films in air and in the cryostate were equal to 60 and 20 mW cm^{-2}, respectively.

3. EXPERIMENTAL RESULTS

At T = 295 K, the absorption spectrum of the PDHS film in the range λ = 200–500 nm consists of two broad bands with $\lambda_{\max}$ = 317 and 375 nm (Figs. 1a–1d). These bands are associated with the $^1(\sigma\sigma^*)$ electronic transitions in the polymer chain segments which adopt helical and *trans* conformations, respectively [1, 19]. Exposure of films to light ($\lambda_{\mathrm{irr}} \le 405$ nm) at T_{irr} = 295 K leads to irreversible changes in the absorption spectra of these films; the character of the observed changes depends on λ_{irr} and t_{irr}. The irradiation with light at λ_{irr} = 405 and 365 nm results in a hypsochromic shift of two absorption bands. In this case, the absorption decreases for the long-wavelength band and increases for the short-wavelength band. These spectral changes become more pronounced with an increase in t_{irr}. Specifically, after the irradiation at λ_{irr} = 405 nm for t_{irr} = 15 min or at λ_{irr} = 365 nm for t_{irr} = 70 s, the shift is equal to 25–30 nm (Figs. 1a, 1b). The irradiation of films with light at λ_{irr} = 313 nm for t_{irr} = 1 min or at λ_{irr} = 265 nm for t_{irr} = 3 min brings about a noticeable decrease in both absorption bands, which is attended by an insignificant hypsochromic shift of the long-wavelength band (curves *1*, *2* in Figs. 1c, 1d). An increase in the time of film exposure to the light at λ_{irr} = 313 nm up to $t_{\mathrm{irr}} \ge 3$ min leads to a drastic decrease in the long-wavelength absorption band, a weaker decrease in the short-wavelength band, and a hypsochromic shift of its maximum (Fig. 1c, curve *3*). At the same time, an increase in the time of film exposure to the light at λ_{irr} = 265 nm up to t_{irr} = 6 min brings about virtually the complete disappearance of the short-wavelength band and only the long-wavelength band at $\lambda_{\max}$ = 360 nm remains in the absorption spectrum (Fig. 1d, curve *3*).

At T = 5 K and λ_{exc} = 313 nm, the luminescence spectrum of the PDHS film exhibits a narrow exciton luminescence band (half-width Δ = 300–400 cm^{-1}) at $\lambda_{\max}$ = 371 nm and a very weak structureless background in the range λ = 400–600 nm whose intensity is 50–100 times less than the intensity of the exciton band at a maximum (Figs. 2a–2d, curves *1*). This background is attributed to the impurity luminescence [1]. An increase in the temperature results in a decrease in the intensity of the exciton luminescence band, an increase in its half-width, and a bathochromic shift of its maximum. At $T = 295$ K, the maximum of the exciton band is located at $\lambda_{max} = 381$ nm and its half-width Δ is equal to 1000 cm^{-1}.

It is found that, after the irradiation of the PDHS films with light at $\lambda_{irr} \le 405$ nm at $T_{irr} = 295$ K in air or a helium atmosphere, the luminescence spectra measured at $T = 5$ and 295 K are characterized by the same irreversible changes irrespective of the presence of oxygen. Particularly, exposure of the films to light at $\lambda_{irr} = 405$ or 365 nm ($t_{irr} = 30$ min) brings about a decrease in the intensity of the exciton band, an increase in its half-width by a factor of 1.5–3, and a hypsochromic shift of its maximum by 5–10 nm (Figs. 2a, 2b). Similar changes are observed in the luminescence spectra of films irradiated with light at $\lambda_{irr} = 313$ nm and $T_{irr} = 295$ K. However, the hypsochromic shift in the maximum of the exciton luminescence band in this case is small and equal only to 0.5–1.0 nm (Fig. 2c). Unlike the illumination of PDHS films at $\lambda_{irr} = 405$, 365, and 313 nm, the irradiation with light at $\lambda_{irr} = 265$ nm leads only to a decrease in the intensity of the exciton luminescence band without change in the location of its maximum (Fig. 2d).

At $T_{irr} = 5$ K, the irradiation of the PDHS films with light at $\lambda_{irr} = 313$ nm and $\Phi = 2$ mW cm^{-2} for $t_{irr} = 2$ h does not lead to substantial changes in the luminescence spectra at $T = 5$ K. However, the irradiation with light at $\lambda_{irr} = 365$ nm and $\Phi = 20$ mW cm^{-2} for $t_{irr} \ge 3$ min at $T_{irr} = 5$ K results in the appearance of a new very weak band at $\lambda_{max} = 377$ nm in the luminescence spectrum. The intensity of this band is approximately 50 times less than that of the exciton band at a maximum. After the irradiation with light at $\lambda_{irr} = 265$–365 nm, $\Phi = 100$ mW cm^{-2}, $t_{irr} \ge 15$ min, and $T_{irr} = 5$ K, the intensity of the band at $\lambda_{max} = 377$ nm increases by a factor of approximately 10. Simultaneously, the hypsochromic shift by approximately 1 nm is observed for the exciton band, and its intensity decreases by 5–10%. These changes in the exciton band after the irradiation of the PDHS film by light at $T_{irr} = 5$ K are irreversible. However, the band at $\lambda_{max} = 377$ nm disappears after the photodegradation of the film exposed to light at $\lambda_{irr} = 313$ nm for $t_{irr} \ge 60$ min and $T_{irr} = 295$ K and does not appear after repeated irradiation with light at $T_{irr} = 5$ K. It seems likely that this band corresponds to the luminescence of polymer chain defects, which are formed upon irradiation of the polymer within its absorption band at $T_{irr} = 5$ K and annihilate after the irradiation at $T_{irr} = 295$ K.

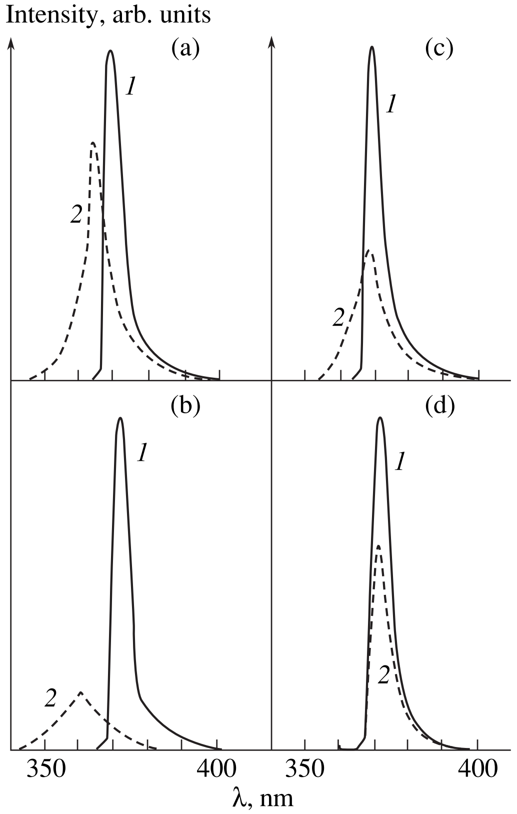

Fig. 2. Luminescence spectra of PDHS films ($T = 5$ K, $\lambda_{exc} = 313$ nm) irradiated at $T_{irr} = 295$ K with light at wavelengths $\lambda_{irr} =$ (a) 405, (b) 365, (c) 313, and (d) 265 nm for time $t_{irr} =$ (*1*) 0 and (*2*) 60 min.

At $T = 295$ K, the absorption spectrum of the PMPS films involves two bands at $\lambda_{max} = 337$ and 275 nm, which are attributed to the $^1(\sigma\sigma^*)$ and $^1(\pi\pi^*)$ transitions in the main chain segments and side phenyl groups, respectively [20] (Figs. 3a–3c, curves *1*). Exposure of the films to light at $\lambda_{irr} \le 365$ nm and $T_{irr} = 295$ K leads to irreversible changes in the absorption spectra. These changes, as for the PDHS films, depend on λ_{irr} and become more pronounced with an increase in t_{irr}. The irradiation with light at $\lambda_{irr} = 365$ nm brings about a decrease in the absorption in the long-wavelength band, which is attended by its hypsochromic shift. In particular, the shift at $t_{irr} = 50$ min is equal to approximately 25 nm (Fig. 3a). The irradiation of films at $\lambda_{irr} = 313$ and 265 nm, unlike the irradiation at $\lambda_{irr} = 365$ nm, results in a considerable decrease in the absorption in the $^1(\sigma\sigma^*)$ band; however, the location of its maximum changes insignificantly (Figs. 3b, 3c).

At $T = 5$ K and $\lambda_{exc} = 313$ nm, the luminescence spectrum of the PMPS films of thickness $d \le 5$ μm contains two bands (Figs. 4a–4c, curves *1*). The narrow band ($\Delta = 700$–800 cm^{-1}) is associated with the exciton luminescence of long chain segments. It is found that the location of its maximum depends on the film thickness and varies in the range $\lambda_{max} = 350$–354 nm with an increase in the thickness d from 0.5 to 5.0 μm. The

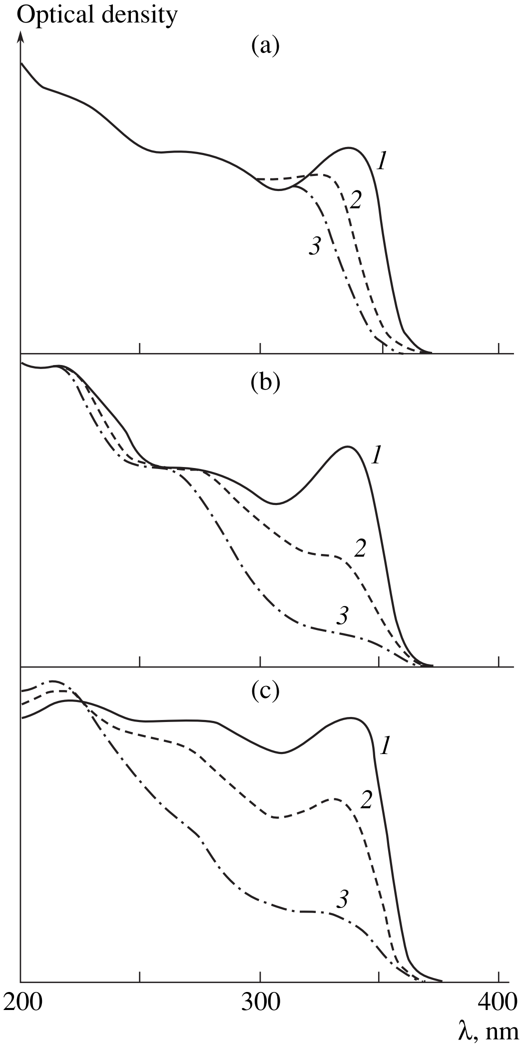

Fig. 3. Absorption spectra of PMPS films (T = 295 K) irradiated at T_{irr} = 295 K with light at wavelengths λ_{irr} = (a) 365, (b) 313, and (c) 265 nm. Irradiation time t_{irr}, min: (a) (*1*) 0, (*2*) 3, and (*3*) 50; (b) (*1*) 0, (*2*) 1, and (*3*) 4; and (c) (*1*) 0, (*2*) 10, and (*3*) 30.

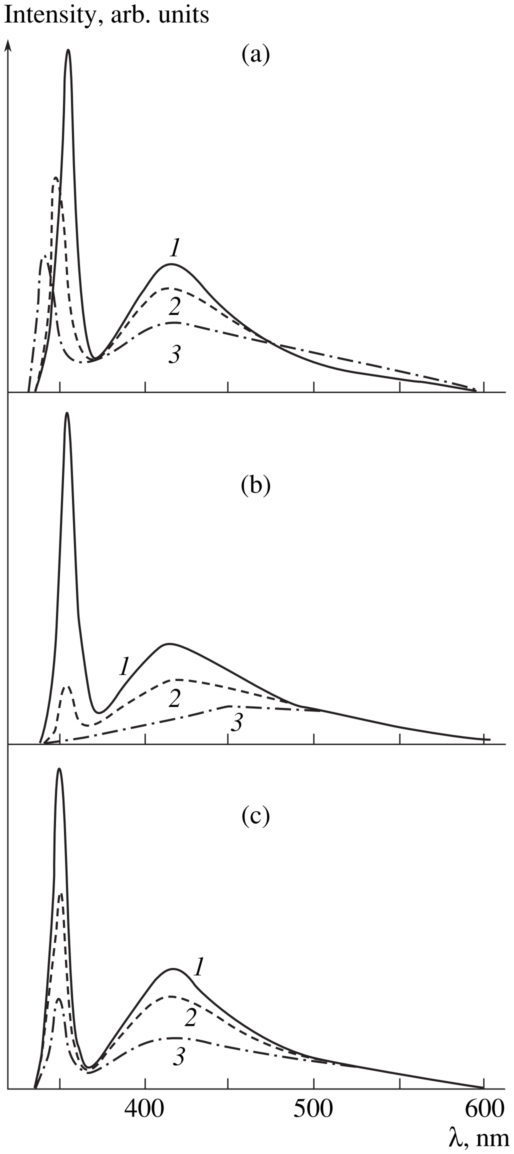

Fig. 4. Luminescence spectra of PMPS films (T = 5 K, λ_{exc} = 313 nm) irradiated at T_{irr} = 295 K with light at wavelengths λ_{irr} = (a) 365, (b) 313, and (c) 265 nm for the time t_{irr} = (*1*) 0, (*2*) 5, and (*3*) 60 min.

broad band is observed in the range λ = 380–600 nm, and its maximum is located at λ_{max} = 415 nm. This band is assigned to the radiative transition from the $^1(\pi^*\sigma)$ state, which is formed as a result of the transition of the σ electron (delocalized over a segment of the main polymer chain) to the π^* orbital of the phenyl ring [20, 21]. As the temperature T increases, the intensity of this band rapidly decreases and the spectrum at $T \geq 77$ K involves a weak band at λ_{max} = 500 nm whose intensity varies only slightly upon heating to T = 295 K. According to [1, 20, 22], this band is attributed to the luminescence of defects in the PMPS polymer chain.

As follows from our results, the luminescence spectra of the PMPS films preliminarily irradiated with light at $\lambda_{irr} \leq 365$ nm in air or a helium atmosphere at T_{irr} = 295 K coincide at T = 5 K. Since the films rapidly degrade during the recording of the luminescence spectra at T = 295 K, the spectra prior to and after the irradiation of samples were measured only at T = 5 K. The irradiation of the PMPS films with light at $\lambda_{irr} \leq 365$ nm and T_{irr} = 295 K leads to a decrease in the intensity of the exciton band. Moreover, upon irradiation at λ_{irr} = 365 nm, an increase in the luminescence in the range $\lambda > 500$ nm is observed in the spectra of thin films ($d < 5$ μm). In the spectra of thick films, the luminescence in this range increases upon irradiation at λ_{irr} = 313 and 265 nm. In [18, 23], it was demonstrated that an increase in the luminescence in the range $\lambda > 500$ nm is explained by the cross-linking between polymer chains. According to our data, the irradiation of films with light at λ_{irr} = 365 nm for t_{irr} = 60 min leads to the hypsochromic shift in the maximum of the exciton band by approximately 10 nm (Fig. 4a). Exposure to light at λ_{irr} = 313 nm for t_{irr} = 5 min brings about a decrease in the intensity of the exciton band by a factor of approximately 5 and the hypsochromic shift in its maximum by approximately 1.5 nm. A further increase in t_{irr} results in complete disappearance of the exciton band (Fig. 4b). Unlike the irradiation at λ_{irr} = 365 and 313 nm, the irradiation of the films at λ_{irr} = 265 nm does not lead to a shift in the maximum of the exciton luminescence band (Fig. 4c).

The PMPS films, as the PDHS films, also degrade upon light irradiation at T_{irr} = 5 K. For example, the irradiation of the PMPS films with light at λ_{irr} = 265–365 nm, Φ = 100 mW cm^{-2}, t_{irr} = 15 min, and T_{irr} = 5 K results in an irreversible decrease in the intensity of the exciton band and an increase in the intensity of luminescence in the range $\lambda > 500$ nm by 5–10%. As t_{irr} increases, these changes in the luminescence spectrum become more pronounced.

4. DISCUSSION

The results obtained demonstrate that changes in the absorption and luminescence spectra of polysilane films irradiated by light with different wavelengths differ substantially. Note that changes in the shape and location of the maxima associated with the exciton transitions in the absorption and luminescence spectra of a photodegraded film clearly correlated with the position of λ_{irr} with respect to its absorption spectrum.

As is known, the shape of the lowest-lying absorption band $^1(\sigma\sigma^*)$ for polysilanes is governed by the size distribution of segments and the location of the exciton luminescence band at a maximum is determined by the radiative transitions in long chain segments and depends on their length [1, 2]. Therefore, it can be assumed that the change in shape of the lowest-lying absorption band after the photodegradation of a polymer is caused by the change in the size distribution of segments, and the hypsochromic shift of the luminescence maximum is associated with the prevailing scission of σ bonds between Si atoms in the longest segments. The latter segments depending on λ_{irr} can be excited either under direct light absorption or through energy transfer after the light absorption by short segments.

Let us consider how the irradiation of films with light at wavelengths λ_{irr} = 405 and 365 nm affects the shape and location of the long-wavelength absorption bands which are attributed to the $^1(\sigma\sigma^*)$ transitions either in PDHS chain segments characterized by the *trans* conformation or in segments of the main PMPS chain (Figs. 1a, 1b, 3a). It is seen from these figures that an increase in the time t_{irr} of irradiation with light at a wavelength which corresponds to the long-wavelength edge or a maximum of the band associated with the $^1(\sigma\sigma^*)$ transition leads to a decrease in the absorption predominantly in the long-wavelength edge of this band and its hypsochromic shift. A similar hypsochromic shift is observed for the exciton luminescence band (Figs. 2a, 2b, 4a). Therefore, the changes observed in the spectra can be uniquely attributed to the photodegradation of the longest chain segments. Note that the concentration of short segments, which are formed after the scission of σ bonds in long segments and absorb in the spectral range under consideration, can increase at certain t_{irr}. This results in an increase in the absorption in the short-wavelength edge of the band assigned to the $^1(\sigma\sigma^*)$ transition (Fig. 1a, curves *1–3*; Fig. 1b, curves *1*, *2*).

It should be noted that changes determined by specific properties of polymers are also observed in the absorption spectra of the PDHS and PMPS films after their photodegradation. These changes can be assigned to the occurrence of two conformations of a polymer chain at T = 295 K in the case of PDHS and to the cross-linking between polymer chains in PMPS. It is known that PDHS polymer chains at T = 295 K can exhibit two conformations: a low-temperature *trans* conformation with an ordered arrangement of side hexyl groups and a high-temperature helical conformation, which are responsible for the absorption bands at λ_{max} = 375 and 317 nm, respectively [1, 19, 24]. The transition from the *trans* conformation to the helical conformation takes place at T = 315 K and is attended by heat absorption due to the disordering (“fusion”) of side hexyl groups. As is seen from Figs. 1a and 1b, the irradiation of films with light at λ_{irr} = 405 and 365 nm leads to a decrease in the absorption in the long-wavelength band and also to an increase in the absorption in the short-wavelength band and its hypsochromic shift. Consequently, the short segments which are formed upon scission of σ bonds in long segments with the ordered *trans* conformation partly transform into segments with a disordered helical conformation. Most likely, the excitation of long segments characterized by the *trans* conformation results in the scission of σ bonds and also in the local heating of segments, which stimulates the conformation transition observed.

As follows from Fig. 3a, the radiation at λ_{irr} = 365 nm corresponds to the range of a very weak absorption of the PMPS film for which the concentration of absorbing long segments is small. At the same time, prolonged irradiation of the polymer brings about a large hypsochromic shift in the maximum of the absorption band (approximately by 25 nm at the band half-width Δ = 30 nm for t_{irr} = 50 min). So large a shift can be explained by photochemical reactions that proceed upon photodegradation of a polymer chain. It can be seen from Fig. 4a that the luminescence intensity in the range $\lambda > 500$ nm increases in the luminescence spectrum after the irradiation of the film with light at λ_{irr} =

365 nm. This luminescence is caused by structural defects formed as a result of the cross-linking between polymer chains [18, 23]. Therefore, it can be assumed that the cross-linking changes the morphology of a polymer chain and leads to the formation of additional conformational defects. As a consequence, the segment length decreases, which is responsible for the change observed in the shape and the location of maxima of the absorption band.

Now, we dwell on the changes in the spectra of films after the irradiation with light at λ_{irr} = 313 nm [near the maximum of the short-wavelength absorption band of PDHS and at the short-wavelength edge of the band associated with the $^1(\sigma\sigma^*)$ transition in PMPS]. An increase in the time t_{irr} for the PDHS films results in a decrease in the intensity of both absorption bands in the spectrum and is accompanied by the hypsochromic shift of the short-wavelength band (Fig. 1c). For the PMPS films, an increase in t_{irr} brings about a decrease in the intensity of the absorption band attributed to the $^1(\sigma\sigma^*)$ transition (Fig. 3b). The exciton luminescence intensity decreases in the luminescence spectra of the PDHS and PMPS films. Note that the hypsochromic shift in the maximum of the exciton band is very insignificant (Figs. 2c, 4b). The changes in the absorption spectra of the PMPS films irradiated with light at the wavelength λ_{irr} = 265 nm [the range of the $^1(\pi\pi^*)$ transition in side phenyl groups] are similar to those observed upon irradiation at λ_{irr} = 313 nm (Fig. 3c). For the PDHS films, at λ_{irr} = 265 nm (at the short-wavelength edge of the absorption band corresponding to segments in the helical conformation), an increase in t_{irr} is attended by a fast decrease in the intensity of this band and a slower drop in the intensity of the absorption band assigned to segments in the *trans* conformation (Fig. 1c). At the same time, only a decrease in the intensity of the exciton luminescence without change in the location of its maximum is observed in the luminescence spectra of the PDHS (T = 5 and 295 K) and PMPS (T = 5 K) films (Figs. 2d, 4c). Consequently, the irradiation of films with light at λ_{irr} = 313 and 265 nm results in the scission of σ bonds and the degradation of both long and short chain segments.

It is evident that the photodegradation of polymers considerably depends not only on λ_{irr} but also on the temperature T_{irr}, which determines the conformation of chain segments and the mobility of segments themselves and their particular fragments. Therefore, the photodegradation of the polysilanes studied in this work is retarded with a decrease in the temperature T_{irr}. However, the above results demonstrate that an insignificant degradation of the PDHS and PMPS films also occurs at T_{irr} = 5 K. This finding is in agreement with observations of hole burning in the spectra of frozen solutions and films of polysilanes [8, 16, 17].

The results obtained in the present work allow us to draw the inferences about the dynamics of excited states in polysilanes. Holzer *et al.* [25] observed the dependences of the absorption spectra for π-conjugated polymers on λ_{irr}, which are similar to those shown in Figs. 1 and 3. However, these authors interpreted their results under the assumption that the photodegradation of π-conjugated polymers proceeds after the energy transfer from short segments to long segments whose excitation is responsible for the luminescence spectrum. Our results suggest that the radiationless dissipation of the excitation energy of short segments due to the scission of σ bonds or thermal relaxation in polysilanes competes with the energy transfer to long segments whose excitation determines the location of the exciton luminescence maximum.

The above assumption is confirmed by the data available in the literature. In [3, 10], the dependences of the quantum yield of luminescence for the *PHDS* and PMPS films on λ_{exc} were measured within the band attributed to the $^1(\sigma\sigma^*)$ transition. It was revealed that the quantum yield of luminescence upon excitation within the range of the short-wavelength edge of the aforementioned band (which correspond to the absorption of short segments) is less than that upon direct excitation of long chain segments. Consequently, after the excitation of short segments, the transfer of energy to long segments is accompanied by processes of its radiative dissipation. In [7, 12], the flash photolysis technique was applied to measure the rise times for the induced absorption bands of the products formed upon irradiation of PDHS and PMPS solutions with light pulses at wavelengths λ_{exc} = 312 and 355 nm, respectively. It was found that the rise time for the band at λ_{max} = 375 nm in the spectra of PDHS solutions is equal to 100 ps and coincides with the rise time for the exciton luminescence which decays with a time constant of 150 ps. According to [7], this band is attributed to the transitions from the lowest-lying excited state to the biexciton state. At the same time, this band was assigned to the absorption of silyl radicals in [13] and to the absorption of silyl radical cations in [14]. In [12], it was proved that the rise time for the band at λ_{max} = 450 nm (associated with the absorption of silylene radicals) in the spectra of PMPS solutions is equal to 40 ps and coincides with the rise time for the exciton luminescence for which the decay time is 70 ps. Therefore, the scission of σ bonds between Si atoms and the formation of radicals occur simultaneously with the formation of excited states in long chain segments.

5. CONCLUSION

Thus, in the present work, we demonstrated that the photodegradation processes in polysilane films depend on the temperature, irradiation wavelength, and the structure of side substituents. It was established that the absorption of light by short chain segments in polysilanes leads to the transfer of excitation energy and its radiationless dissipation due to the scission of σ bonds between Si atoms or thermal relaxation. These processes compete with each other and determine the dynamics of excited states in polysilanes. It was found that the photodegradation of the *PHDS* films at $T_{\rm irr}$ = 295 K is attended by the transformation of certain chain segments from the low-temperature *trans* conformation with an ordered arrangement of side hexyl groups to the high-temperature helical conformation with a disordered arrangement of side groups.

ACKNOWLEDGMENTS

We are grateful to Dr. S. Suto (Tohoku University, Sendai, Japan) for supplying the polysilane samples and A.K. Kadashchuk (Senior Researcher of the Institute of Physics, National Academy of Sciences of Ukraine) for his participation in discussions of the results.

REFERENCES

1. M. Pope and C. E. Swenberg, *Electronic Processes in Organic Crystals and Polymers* (Oxford Univ. Press, New York, 1999), p. 877.
2. R. D. Miller and J. Michl, Chem. Rev. **89**, 1359 (1989).
3. R. G. Kepler and Z. G. Soos, in *Primary Photoexcitations in Conjugated Polymers: Molecular Exciton versus Semiconductor Band Model*, Ed. by N. S. Sariciftci (World Scientific, Singapore, 1997), p. 363.
4. T. Hasegawa, Y. Iwasa, H. Sunamura, *et al.*, Phys. Rev. Lett. **69**, 668 (1992).
5. M. Sawodny, J. Stumpe, and W. Knoll, J. Appl. Phys. **69**, 1927 (1991).
6. J. R. G. Thorne, Y. Ohsako, J. M. Zeigler, and R. M. Hochstrasser, Chem. Phys. Lett. **162**, 455 (1989).
7. J. R. G. Thorne, S. T. Repinec, S. A. Abrash, *et al.*, Chem. Phys. **146**, 315 (1990).
8. A. Tilgner, H. P. Trommsdorff, J. M. Zeigler, and R. M. Hochstrasser, J. Chem. Phys. **96**, 781 (1992).
9. H. Tachibana, M. Matsumoto, Y. Tokura, *et al.*, Phys. Rev. B **47**, 4363 (1993).
10. M. Shimizu, S. Suto, T. Goto, *et al.*, Phys. Rev. B **58**, 5032 (1998).
11. P. Trefonas, R. West, and R. D. Miller, J. Am. Chem. Soc. **107**, 2737 (1985).
12. Y. Ohsako, J. R. G. Thorne, C. M. Phillips, *et al.*, J. Phys. Chem. **93**, 4408 (1989).
13. A. Watanabe and M. Matsuda, Macromolecules **25**, 484 (1992).
14. A. Eckhardt and W. Schnabel, J. Inorg. Organomet. Polym. **6**, 95 (1996).
15. S. Nespurek, V. Herden, W. Schnabel, and A. Eckhardt, Czech. J. Phys. **48**, 477 (1998).
16. A. Tilgner, J. R. G. Thorne, J. P. Pique, *et al.*, J. Lumin. **48–49**, 193 (1991).
17. H. P. Trommsdorff, J. M. Zeigler, and R. M. Hochstrasser, Chem. Phys. Lett. **154**, 463 (1989).
18. V. M. Zaika, A. K. Kadashchuk, N. I. Ostapenko, *et al.*, Ukr. Fiz. Zh. **45**, 1246 (2000).
19. J. F. Rabolt, D. Hefer, R. D. Miller, and G. N. Fickes, Macromolecules **19**, 611 (1986).
20. O. Ito, M. Terazima, T. Azumi, *et al.*, Macromolecules **22**, 1718 (1989).
21. M. Terazima, O. Ito, and T. Azumi, Chem. Phys. Lett. **160**, 319 (1989).
22. Y. Kanemitsu, K. Suzuki, S. Kyushin, and H. Matsumoto, Phys. Rev. B **51**, 13103 (1995).
23. L. A. Harrah and J. M. Zeigler, J. Polym. Sci., Part C: Polym. Lett. **25**, 205 (1987).
24. A. J. Lovinger, F. C. Schilling, F. A. Bovey, and J. M. Zeigler, Macromolecules **19**, 2657 (1986).
25. W. Holzer, A. Penzkofer, M. Pichlmaier, *et al.*, Chem. Phys. **248**, 273 (1999).

Translated by O. Borovik-Romanova

Physics of the Solid State, Vol. 43, No. 3, 2001, p. 596. Translated from Fizika Tverdogo Tela, Vol. 43, No. 3, 2001, p. 576.
Original Russian Text Copyright © 2001 by the Editorial Board.

PERSONALIA

Academician of the RAS, Yuriĭ Andreevich Osip’yan Turned 70

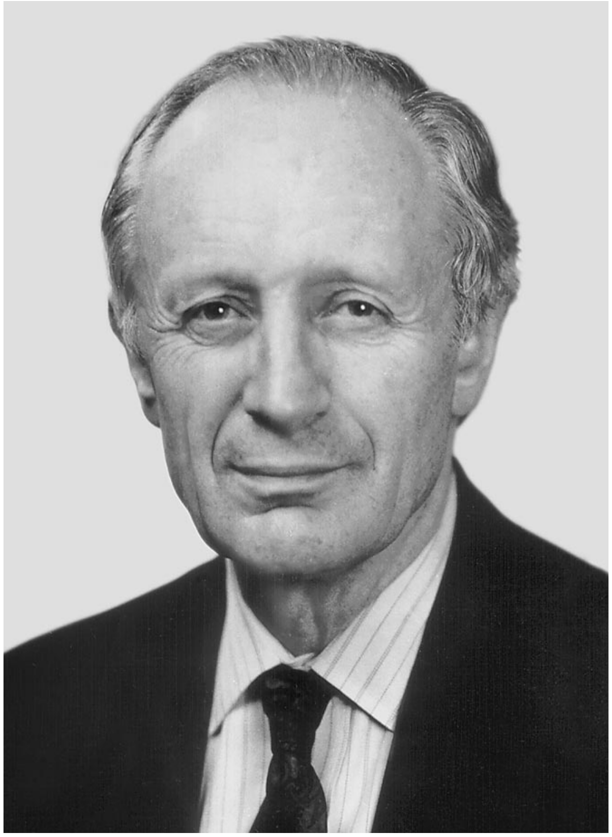

Dear Yuriĭ Andreevich!

The Editorial Board of *Physics of the Solid State* heartily congratulates you on your birthday and hopes that you live to be a hundred and continue to show the same creative enthusiasm that you have always used to tackle the most interesting problems in our shared science, modern solid state physics.

We cannot but mention your scientific style and favorite trends in physics: the quantum-mechanical approach to problems in the physics of strength, studies on photoplasticity and spin-dependent carrier recombination on dislocations, investigations of metallic glasses and the problems of formation of ice and its strength, and finally, comprehensive research in high-temperature superconductors and fullerenes.

You are also a great scientific manager, knowing many ways to approach scientists, who can sometimes be as obstinate and capricious as prima donnas. It is your innate talent, along with your enormous vital energy, that allowed you to organize a pearl of Russian physics, the RAS Institute of Solid State Physics in Chernogolovka, where you harmoniously developed different trends of our science with tact and the sense of proportion so characteristic of you. What excellent scientists you have trained!

You are not only a gifted scientist and organizer and even a talented statesman, but also an excellent orator. Who else can relate sophisticated scientific studies in such an absorbing and spirited manner? Nobody can. You are a maestro in delivering a scientific lecture!

You know very well that not only do we consider you our brother scientist, we also regard you as our “Phystech” brother, for we remember that you are a scientific grandson of “father” Ioffe, and one may always depend on you.

We wish you health, good spirits, every success in science, and an even larger number of prizes and titles than you have now!

Editorial Board

1063-7834/01/4303-0596$21.00 © 2001 MAIK “Nauka/Interperiodica”